Ossa-Morena Zone Variscan 'calc-alkaline' hybrid rocks: interaction of mantle- and crustal-derived magmas as a result of intra-orogenic extension-related intraplating.

Aitor Cambeses Torres

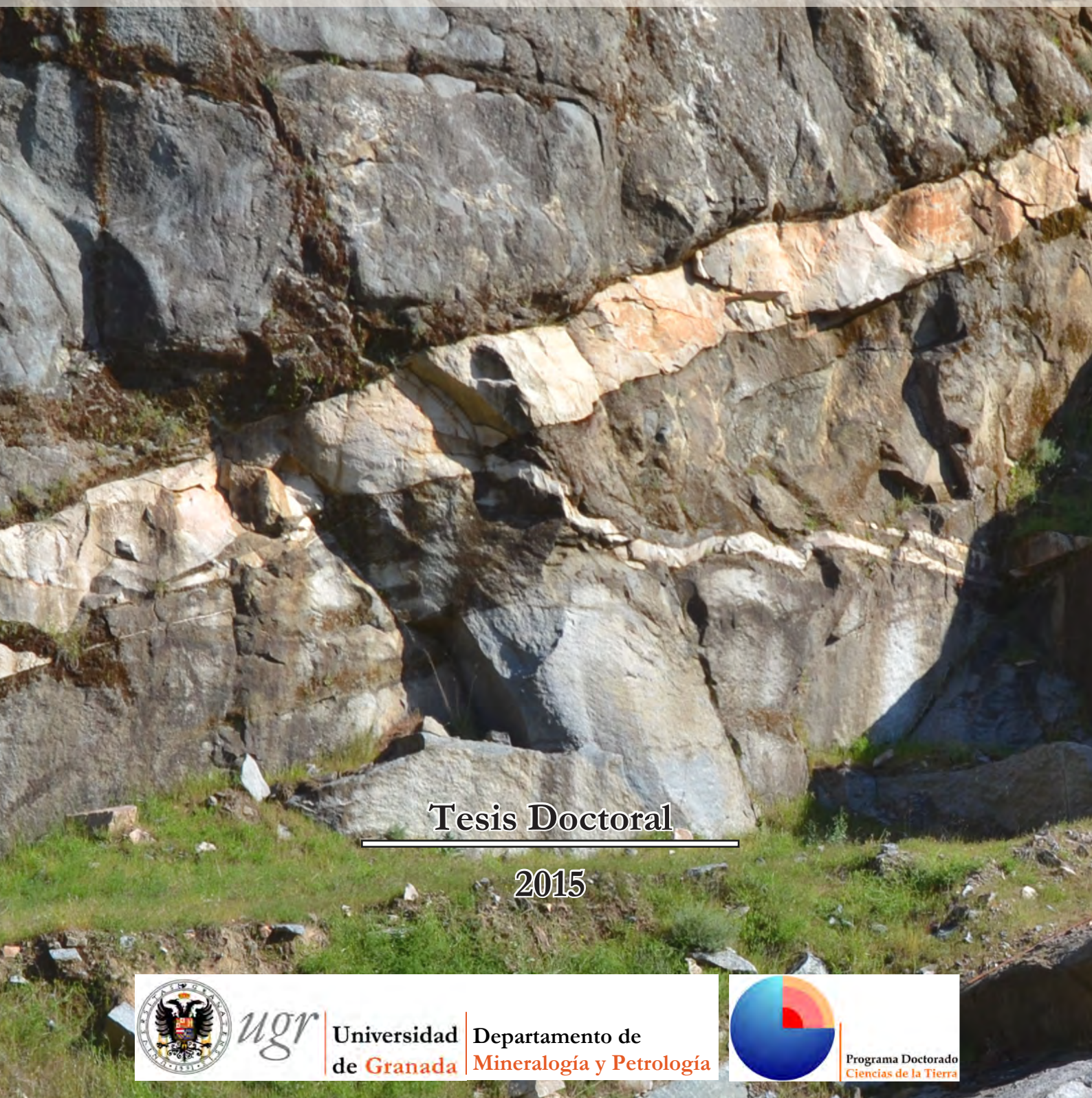

Tesis Doctoral

2015

ugr Universidad de Granada | Departamento de Mineralogía y Petrología

Programa Doctorado Ciencias de la Tierra

Editorial: Universidad de Granada. Tesis Doctorales
Autor: Aitor Cambeses Torres
ISBN: 978-84-9125-270-2
URI: http://hdl.handle.net/10481/40693

University of Granada

Department of Mineralogy and Petrology

Ossa-Morena Zone Variscan 'calc-alkaline' hybrid rocks: interaction of mantle- and crustal-derived magmas as a result of intra-orogenic extension-related intraplating

Aitor Cambeses Torres

Doctoral Thesis

University of Granada

2015

Departamento de Mineralogía y Petrología

Universidad de Granada

Ossa-Morena Zone Variscan 'calc-alkaline' hybrid rocks: interaction of mantle- and crustal-derived magmas as a result of intra-orogenic extension-related intraplating

Memoria de Tesis Doctoral presentada por el Licenciado en Geología
D. Aitor Cambeses Torres para optar al Grado de Doctor por
la Universidad de Granada.

Granada, 21 de julio de 2015

Fdo. D. Aitor Cambeses Torres

VºBº del Director

VºBº de la Directora

Fdo. Dr. D. Fernando Bea Barredo

Fdo. Dra. Dña. Jane Hannah Scarrow

Esta Tesis Doctoral ha sido financiada por los proyectos CGL2008-02864 y CGL-2013-40785-P (Ministerio de Economía y Competitividad), los proyectos RNM1595 y P12-RNM2163 (Junta de Andalucía), el Grupo de Investigación RNM 302 de la Junta de Andalucía, así como por la beca disfrutada por el doctorando del programa de Formación del Profesorado Universitario (FPU) por el Ministerio de Educación, Cultura y Deporte. El trabajo de investigación se ha llevado a cabo en el Departamento de Mineralogía y Petrología de la Universidad de Granada (UGR) y en el Centro de Instrumentación Científica (CIC) ambos sitos en Granada

El doctorando Aitor Cambeses Torres y los directores de la tesis Fernando Bea Barredo y Jane Hannah Scarrow. Garantizamos, al firmar esta tesis doctoral, que el trabajo ha sido realizado por el doctorando bajo la dirección de los directores de la tesis y hasta donde nuestro conocimiento alcanza, en la realización del trabajo, se han respetado los derechos de otros autores a ser citados, cuando se han utilizado sus resultados o publicaciones.

Granada 21 de julio de 2015

El Doctorando

Fdo. D. Aitor Cambeses Torres

El Director

Fdo. Dr. D. Fernando Bea Barredo

La Directora

Fdo. Dra. Dña. Jane Hannah Scarrow

A mis padres

A Leticia

Agradecimientos

Me gustaría expresar mi más sincera y profunda gratitud a todos aquellos que han contribuido en el desarrollo de este trabajo, y sin los cuales no hubiera sido posible.

En primer lugar, a mis directores Fernando Bea y Jane H. Scarrow. Muchas gracias por haberme dado la oportunidad de formar parte de este grupo de investigación y por guiarme durante este periodo. Muchas gracias Jane, por toda la dedicación que has invertido en esta tesis, por buscar un hueco siempre que ha sido necesario, aunque no lo hubiera, para que esta tesis haya podido terminarse. Gracias por todo lo que he aprendido en todos estos años y sobre todo por la amistad y confianza que has demostrado en todo momento. Trabajando contigo he aprendido a ser paciente, constante y un poquito más ordenado, si al final lo has conseguido, me llevo multitud de recuerdos, enseñanzas y experiencias de lo cual te estaré siempre agradecido. Muchas gracias Fernando, por confiar en mí, por apoyarme, por poner a mi disposición todos los medios necesarios para el desarrollo de esta tesis y por todo lo que me ha enseñado y aportado tanto a nivel científico como personal.

También quiero agradecer de manera muy especial a Pilar Montero toda la ayuda y el apoyo mostrado durante todos estos años. Gracias por tener siempre palabras de ánimo y por atender cualquier consulta relacionada con la geocronología y la geología isotópica de esta tesis, que han sido muchas.

A Jose Francisco Molina Palma agradecerle todo el apoyo recibido durante todo este tiempo, por todos los 'Pepe tienes un momento', y que siempre fueron respondidos de manera afirmativa. Gracias por los largos ratos de discusión sobre la geoquímica, temobarometría y el 'anfíbol'.

A Antonio García Casco, gracias por toda la confianza y el ánimo transmitido durante estos años y por los largos ratos de discusión sobre temas científicos y de la vida en general. Gracias por pasar todas las noches por el despacho antes de terminar la larga jornada laboral y por todos los buenos momentos que hemos compartido fuera y dentro de la facultad.

Otro especial agradecimiento va dirigido al apoyo institucional del Departamento de Mineralogía y Petrología de la Universidad de Granada, especialmente para Miguel Ortega Huertas y Nicolás Velilla Sánchez, directores del Departamento durante el desarrollo de esta Tesis Doctoral. No me quiero olvidar de los buenos amigos que he conocido en el departamento, especialmente a los técnicos y personal de administración empezando por Sandra, Inés, Noelia,

Emi y Jesús, que de tantos apuros me ha sacado, que en otros ya nos hemos metido nosotros solos, y con el que siempre se puede contar, para un roto o al ataque¡¡¡¡¡. Gracias también a todo el personal del IACT que conocí cuando empecé mi andadura por el departamento, cómo no, a Sonia a quien le tocó en su día enseñarme como moler una piedra¡¡¡, y al personal del Centro de Instrumentación Científica. Vaya también dirigido un agradecimiento de manera especial a Isabel Nieto, que a lo largo de estos años me ha echado más de un cable y no solo para enseñarme a separar circones, muchas gracias.

Agradecer también a los integrantes de los Departamentos de Estratigrafía y Paleontología y Geodinámica, especialmente a Fernando Simancas y David Poyatos por toda la ayuda que me han prestado para entender un poco de la complejidad geológica que esconde la Zona de Ossa-Morena.

También me gustaría mostrar mi gratitud a mis compañeros de 'fatigas' diarias, Claudio, Anika, Encarni, Vicente y con mucho cariño a mí 'vecina' Concha, gracias por acogerme tan bien en los desayunos, y por favor que no se pierda ese grupo de wassap que me da la vida¡¡¡¡

No me quisiera olvidar de Patricia Ruano, que tanto me ha cuidado y se ha preocupado por mi todos estos años, gracias, espero poder devolverte esa cariño en forma de paellas¡¡¡

Un gran agradecimiento va dedicado, sin duda a mis compañeros de doctorado y cómo no a los que formaban parte del mítico despacho 29, a Pili, Veronica, Marta, Silvia, David, Anna Pedro, Rute, Iñaki, Idael, Carlos, Erwin y como no a mi Carmela¡¡¡¡ cómo me acuerdo de los buenos ratos que pasábamos en la Happy hour, gracias a todos por acogerme tan bien cuando era un novatillo, la consecución de esta tesis es también gracias a vosotros¡¡¡ Me gustaría agradecer de una manera especial a Juan mi amigo chileno, que aunque hace tiempo que no nos vemos, se merece este reconocimiento por todo el cariño que nos tenemos. Por supuesto a Vane, si tu no sabías que me ibas a decir a mi cuando defendiste tu tesis, ¿Qué te puedo decir yo? Empezaré por darte las gracias por todos estos años, gracias por estar hay siempre para un 'tele poleo' y por saber que en algún sitio siempre habrá una persona en la que confiar y con la que se puede contar, ya sabes que aquí estamos 'pa lo que haga falta'. Gracias por recibirme tan bien en Frankfurt, y por extensión gracias a mi equipo Alemán: Vane, Maria, Nando, Angela y Paula, que bien me lo pase con vosotros por tierras germanas¡¡¡¡¡

No me quiero olvidar de mis compañeros de estos últimos años, muchas gracias Vinicius, el master-class de la orogenia intracontinental, Juan Antonio, Eduardo, Juanillo, Jose Antonio, Irene y, al reciente fichaje, Lidia, gracias por estar tan pendiente estos últimos meses de fin de tesis¡¡¡ Muchas gracias Thais, amiga.

También me gustaría mostrar mi más sincero agradecimiento a Louis Dinn Scarrow. Gracias por llevar con nosotros las responbsabiladad de esta tesis, por las jornadas de campo y por los muchos fines de semana, especialmente en estos últimos meses, que te he 'quitado'. Gracias por tu altruismo y por ponerle ese toque soñador a nuestras conversaciones, eres buena gente y te deseo lo mejor.

También quiero acordarme de mi amiga 'Cartagenera', Belén. Muchas gracias por el ánimo, el apoyo y por e cariño que me has mostrado desde que nos conocimos. Me has enseñado a ver las cosas con puntos de vista diferentes, con y sin submarino, me siento muy afortunado de formar parte de tu vida. Cómo no, hago extensivo este agradecimiento a Luis y a Nacho.

Gracias también a Faouziya Haissen, por todo el apoyo desde la distancia y por tenerme siempre presente. Gracias por tu cercanía, confianza y amistad.

También me gustaría agradecer a mucha gente ajena al ámbito profesional pero que sin duda me han guiado en esta travesía. Me gustaría acordarme en primer lugar de mis profesores de Instituto, 'mis maestros', Juan Manuel Sánchez, Ángel González-Palencia Lagunilla (que ganas tenis a de escribir tu nombre completo), María Flores y María José Guillén entre otros. Gracias por depositar un voto de confianza en mí por todas las enseñanzas que me habéis brindado todos estos años. Espero que la consecución de esta tesis os reporte un poco de todo lo que vosotros me habéis dado. Muchas gracias mis amigos, Celso, Jose Benito, Benito, Pedro, Carlos, Claudio, Rubén, y espeCILmente a Moi y a Rubén Lora. Sois un apoyo único, y para mi es una auténtica satisfacción poder considerados mis amigos. Sin duda el conoceros ayudó y mucho, si no quizá todavía estaría en la calle de atrás, a que este viaje termine en buen puerto, muchas gracias a todos. Gracias también a todas las personas que no puedo nombrar por limitaciones de espacio pero que han estado a mi lado durante todos estos años, Fernando, Alejandro, Jesús a toda la gente de la Cabaña, Irene, Paco, Antonia, Carmina,…, en definitiva muchas gracias a todos.

Y por último, y no menos importante me gustaría agradecer a mi familia, comenzando por el clan Barcos, gracias a todos por hacerme sentir como uno más de la familia y, aunque el número de sobrinos crezca de manera 'exponencial', aquí tenéis cuñado para rato. A mis hermanos y cuñados, el clan Cambeses, Cesar, Sara, Claudio, María del Carmen, María Dolores y Maite, por cuidarme y estar siempre ahí por todo el cariño, paciencia y comprensión que he recibido de vuestra parte. También el más sentido agradecimiento a mis padres, Cesar y Dolores, todo este trabajo va dedicado, sin duda, a vosotros que sois los referentes que me han ayudado a llevarlo a cabo. Gracias.

Finalmente a Leticia. Gracias. Gracias por estar a mi lado en esta larga travesía. Gracias por la paciencia y compresión que siempre has mostrado y por ponerle siempre una sonrisa a las situaciones más adversas. Tu apoyo ha sido fundamental en todo este proceso, por ello quiero hacerte partícipe de este trabajo tanto como yo.

Table of Contents

Abstract

Resumen

Abstract

This thesis considers the petrogenesis of three Ossa-Morena Zone Variscan plutonic bodies: the Burguillos del Cerro plutonic complex; the Valencia del Ventoso plutonic complex; and the Brovales pluton. Consideration of these compositionally diverse ultramafic-felsic bodies provides insights into crustal growth and reworking. Orogenic magmatism may be the product of addition of new material to the crust or recycling of pre-existing crust or a combination of these. Determining the relative importance of these processes to identify and assess crustal growth cycles depends upon the recognition of juvenile and ancient magmatic components.

Mafic stocks are commonly produced associated with felsic plutons during orogenesis. The Ossa-Morena Variscan magmatism is unusual, and particularly useful, in this respect in that it is characterised by intrusions with a relatively large abundance of mafic rocks. Study of these heterogeneous intrusions is the key to unravelling the role and relative importance of mantle- and crustal-derived material. Here we show that the petrogenesis of these 'calc-alkaline' hybrid rocks involved complex interaction of asthenosphere-, lithosphere- and metasedimentary basement-derived magmas as a result of intra-orogenic extension-related intraplating.

SHRIMP U-Pb zircon dating has constrained the age of three Ossa-Morena Zone Variscan plutonic bodies to Carboniferous, Visean-Bashkirian, 340-320 Ma: i. the Burguillos del Cerro plutonic complex age is 336 ± 1 Ma; ii. the Valencia del Ventoso plutonic complex has an age range of 334 to 320 Ma; iii. the Brovales pluton age is 340 ± 2 Ma. These new ages dissociate the magmatism from collision-related subduction. It is fixed instead to a period of high temperature low pressure metamorphism and sedimentary basin formation in an extensional/transtensional context between the two main Variscan collisional episodes in the region.

The complexes comprise ultramafic to felsic, alkaline to subalkaline, metaluminous to peraluminous compositions. Despite this diversity, similarities in the petrography, mineral chemistry and whole-rock major and trace element and Sr and Nd isotopic compositions allows correlation of the different units in the three plutonic bodies into five broad groups: *Ultramafic-Mafic; Alkaline; Subalkaline Mafic-Intermediate* and *Intermediate-Felsic;* and, *Peraluminous*.

Initial field-based interpretations regarding the importance of hybridisation, accumulation and fractionation processes were confirmed by petrographic textures. These revealed evidence of minerals in equilibrium and disequilibrium and cumulus and in situ crystallisation. Discrimination of mineral chemistry compositional variations, particularly in the hydrous ferromagnesian minerals biotite and amphibole, and also plagioclase, was central to untangling these petrogenetic

processes. This, combined with whole-rock compositional data, led to identification of three different magmatic end-member components: alkaline, tholeiitic and peraluminous. All these were affected by a complex interplay of magmatic differentiation.

Explanation of the observed compositional diversity requires involvement of two different mantle sources: the lithosphere producing basic alkaline melts and the asthenosphere producing basic tholeiitic melts. A further, third, crustal source was tapped, Ossa-Morena Zone basement metasediments, giving rise to acid peraluminous melts.

How these sources came to interact in an extensional context may be explained by a simple model of lithospheric stretching resulting in asthenospheric upwelling and melting causing localised fusion of the overlying lithospheric mantle and crust.

In the absence of a thermal anomaly, low volume asthenospheric melt resulted from limited extension of the lithosphere. Ascent of asthenospheric, subalkaline tholeiitic, magma combined with the effect of extension-related adiabatic uplift caused fusion of the most fertile metasomatised parts, veins, of a heterogeneous lithospheric mantle producing alkaline melts. Ascending subalkaline and alkaline magmas coalesced forming intraplated intrusions in the middle crust. Conductive heat transfer from the crystallizing magma to the surrounding crust resulted in localised partial melting of the crust above and below the mafic body. Crustal-derived acid magmas are less dense than mafic magma thus only the basal melts would rise inducing hybridisation.

Mixing and crystallisation led to the formation of variably hybrid, cumulate and fractionated rocks. The Burguillos del Cerro *Ultramafic-Mafic* and *Alkaline* groups represent the mantle-derived mafic melts forming the pluton itself; the *Peraluminous Group* the 'pure' basement crustal-derived melt overlying the pluton; and the *Subalkaline* groups that, significantly, intrude the *Ultramafic-Mafic* and *Alkaline* groups, the ascending basal pluton-country rock contact mixed magma that are also preserved in the Valencia and Brovales plutonic bodies. This petrogenetic model relating the groups is consistent with intrusive and mixing relationships observed in the field.

To place the Variscan magmatism in a broader temporal and spatial context the pre-Variscan paleogeographic position of the Ossa-Morena Zone was investigated. During the Cambro-Ordovician the Ossa-Morena Zone was one of a series of north Gondwana terranes that juxtaposed during the Variscan Orogeny. An association with the Tuareg Shield north Gondwana, African, terrane is indicated by all geochronological data: Nd model ages; detrital zircon ages; and, pre-magmatic and magmatic ages. This positions the Ossa-Morena Zone to the

east of the Anti-Atlas West African Craton where it had been located to date. Consistent with this is the sedimentological and magmatic evidence of diachronous west to east (Paleozoic position) opening of the Rheic Ocean, or a branch of this, between the Cadomian and Variscan orogenies. Rift-related magmatism is more extensive in the Ossa-Morena Zone than in the more easterly (Paleozoic position) Central Iberian Zone and Galicia Tras-os-Montes Zone. Stratigraphical and paleontological sequences record that the Ossa-Morena Zone sediments were deeper water than those of the Galicia Tras-os-Montes Zone and Central Iberian Zone. Subsequent Variscan amalgamation of Iberia, joined the Ossa-Morena Zone and the Central Iberian Zone by sinistral transpression along the Badajoz-Cordoba shear zone.

Abstract

Resumen

Esta Tesis Doctoral trata sobre la petrogénesis de tres complejos plutónicos de la Zona de Ossa-Morena emplazados durante la orogenia Varisca. Estos complejos son; Burguillos del Cerro, Valencia del Ventoso y Brovales. El amplio espectro composicional observado en estos complejos, desde rocas ultramáficas hasta diferenciados félsicos, proporciona una información detallada de los procesos de formación y crecimiento cortical. El magmatismo orogénico puede ser el producto tanto de la adición de nuevo material a la corteza como de un proceso de reciclaje de una corteza pre-existente o una combinación de ambos. Establecer el aporte de cada uno de estos procesos para evaluar y determinar las causas del crecimiento cortical necesita el reconocimiento y caracterización de componentes magmáticos juveniles y antiguos.

Los procesos de intrusión de rocas máficas en la corteza están, generalmente, asociados a la formación de magmatismo de características félsicas durante el proceso orogénico. El magmatismo de la Zona de Ossa-Morena es presenta una marcada diferencia con el magmatismo del resto de Zonas del Macizo Ibérico, principalmente por la abundancia del magmatismo máfico frente al félsico. La caracterización de estas intrusiones, heterogéneas, es la clave para determinar cuál es el papel y la importancia de los derivados mantélicos y corticales. En este trabajo se estudia la petrogénesis de rocas 'calco-alcalinas' de características híbridas donde están implicadas en su formación magmas de distintas fuentes; astenosféricas, litosféricas y del basamento sedimentario.

Las dataciones mediante U-Pb en circón con SHRIMP establecieron la edad de tres complejos plutónicos Variscos de la Zona de Ossa-Morena en un rango de 340-320 Ma (Viseense-Bashkiriense): i. el complejo plutónico de Burguillos del Cerro con una edad de 336 ± 1 Ma; ii. el complejo plutónico de Valencia del Ventoso con un rango de edades de 334-320 Ma; y iii. el plutón de Brovales con una edad de 340 ± 2 Ma. Esta caracterización temporal relaciona el magmatismo con un evento metamórfico de alta temperatura y baja presión así como como con el desarrollo de cuencas sedimentarias. Estos eventos se enmarcan en un contexto tectonomagmático de intrusión intra-placa relacionado con la extensión/transtensión de un proceso de orogenia-intracontinental descrito en la región.

Los complejos estudiados abarcan composiciones ultramáficas a félsicas, tanto alcalinas como sub-alcalinas metaluminosas o peraluminosas. La gran variación de las relaciones petrográficas, el quimismo de las fases minerales y la composición de elementos mayores, traza y de isotópos (Sr y Nd) de roca total permitieron agrupar a este conjunto de rocas en cinco grandes grupos composicionales: *Ultramáfico-Máfico; Alcalino; Subalcalino Máfico-Intermedio, Subalcalino*

Intermedio-Félsico y *Peraluminoso*.

Las relaciones de campo muestran la importancia de los procesos de hibridación, acumulación y fraccionación, confirmados por las relaciones texturales y petrográficas. Las relaciones texturales, además, indican procesos de equilibrio-desequilibrio, acumulación y cristalización in-situ. La variación composicional del quimismo mineral en piroxeno, anfíbol, biotita y plagioclasa permite esclarecer en gran medida el proceso petrogenético asociado a las rocas estudiadas en esta tesis. Combinando estos datos juntos con los de composición de roca total permitió establecer la presencia de tres componentes magmáticos implicados en el proceso petrogenético: alcalino, toleiitico y peraluminoso. En estos se produjeron complejos procesos de interacción y diferenciación magmática.

Para poder explicar la amplia variabilidad composicional es necesario la presencia de dos fuentes mantélicas; la primera litosférica a la que estrían asociados los derivados máficos alcalinos; y la segunda astenosférica la cual generaría los magmas de composición toleiitica. La tercera fuente implicada en este proceso se relaciona con la fusión parcial de la corteza, los sedimentos que dan forma al basamento de la Zona de Ossa-Morena, produciendo los fundidos félsicos peraluminosos.

Como estas fuentes pudieron interactuar en un contexto extensional se explica por un modelo simple del estiramiento de la litosfera dando como el resultado el ascenso de la astenosfera la fusión parcial de esta última, del manto litosférico adyacente y de la corteza.

En ausencia de una anomalía térmica, se pueden producir pequeñas cantidades de fundido derivado de la astenosfera con limitado estiramiento de la litosfera. El ascenso de los magmas derivados de la astenosfera y la descompresión adiabática del manto provocarían la fusión del manto litosférico metasomatizado, produciendo los líquidos alcalinos. El ascenso y la coalescencia de estos magmas máficos, sub-alcalinos y alcalinos, provocaría la intrusión de pequeños sills a niveles de la corteza media. La transferencia de calor del magma máfico al encajante favoreciendo la fusión parcial de la corteza en el contorno de la intrusión máfica. Al ser estos derivados corticales menos densos, ascenderían desde la base y través de los magmas máficos provocando los procesos de hibridación entre ambos magmas.

Los procesos de mezcla y cristalización dieron lugar al amplio cortejo de rocas, híbridas, cumulíticas y fraccionadas que se observan en los tres complejos plutónicos estudiados. En el complejo plutónico de Burguillos del Cerro los grupos *Ultramáfico-Máfico* y *Alcalino* representan los componentes derivados del manto. El *Grupo Peraluminoso* representa el magma, 'puro', derivado de la corteza. Por otro lado los grupos *Subalcalinos*, que además intruyen a los grupos

Ultramáfico-Máfico y *Alcalino*, representarían las rocas híbridas, rocas que se preservan en mayor medida en el complejo de Valencia del Ventoso y en plutón de Brovales. Este modelo petrogenético es consistente con las relaciones de intrusión y mezcla observadas en el campo.

Para contextualizar el magmatismo Varisco de la Zona de Ossa-Morena en un rango de tiempo y espacio más amplio se investigó en esta tesis la posición paleogeográfica de la Zona de Ossa-Morena durante en el transito Cámbrico-Ordovícico. En ese periodo de tiempo la Zona de Ossa-Morena formaba parte de las áreas periféricas del norte de Gondwana, las cuales se amalgamaron durante la orogenia Varisca. En términos de paleoposición, se puede correlacionar el Escudo del Tuareg, norte de África, con la Zona de Ossa-Morena, como así lo indican los datos geocronológicos de distribución de edades modelo de Nd, de circones detríticos y circones pre- y magmáticos. Esta nueva posición paleogeográfica difiere de la previamente definida en las inmediaciones del Escudo Oeste Africano, en el Anti-Atlas. En este periodo de tiempo se enmarca, además, la apertura del Océano Rhéico a lo largo del margen norte de Gondwana. En consecuencia la expresión magmática de este evento se registra de manera más leve en los terrenos, de acuerdo con su posición paleogeográfica en el Paleozoico, situados en la parte más oriental, como es el caso de la Zona Centro-Ibérica o los terrenos parautóctonos de la Zona de Galicia Tras-os-Montes. Mientras que el evento magmático Cámbrico-Ordovícico es más evidente en las zonas localizadas en una posición paleogeográfica más occidental, como la que se propone en este trabajo para la Zona de Ossa-Morena. El modelo que explicaría esta evolución magmática estaría asociado con la propagación de una 'rama' o 'brazo' del Océano Rhéico que se preservaría actualmente en la zona de cizalla transpresiva izquierda de Badajoz-Córdoba, como consecuencia de la amalgamación de la Zona Centro-Ibérica y la Zona de Ossa-Morena durante la orogenia Varisca.

Chapter 1: Introduction

1.1 Problem Definition

1.2 Objectives

1. Introduction

1.1 Problem Definition

Syn-orogenic igneous rocks record tectonomagmatic processes, providing information about mantle and crustal sources tapped during terrane accretion. Unpicking the components of hybrid magmas is the key to assessing the importance of mantle and crustal contributions. Whether magmatism is the result of addition of new material to the continental crust, crustal growth, or recycling of pre-existing crust is a subject of considerable debate (e.g., Rapp and Watson, 1995; Kemp et al., 2005; Roberts et al., 2015). As noted by Condie (2014) a first step in assessing the relative rates of growth and recycling is to understand more about how and when new, juvenile, crust is preserved in orogens. This raises the question, then, of the significance of minor, but widespread, mafic-intermediate intrusions associated with granitoid batholiths. Coeval mafic magmatism may play a role in crustal melting through heat transfer by mantle wedge convection, asthenospheric upwelling or under- and intraplating of mafic magmas into the crust (e.g., England and Thompson, 1986, Fyfe, 1973; Huppert and Sparks, 1988; Clemens, 1998; 2006; Brown, 2007; 2010). So, is maybe not necessarily be a matter of 'either-or' but rather 'what, how much and how'.

Throughout the European Variscan orogenic province mafic-intermediate 'calc-alkaline' stocks are common within granitoid plutons (Pitcher, 1993 and references therein). However, the extent to which such magmas may be used as markers of tectonomagmatic context is a matter of some discussion (e.g., Arculus, 2003; Scarrow et al., 2009; Eyal et al., 2010; Seghedi et al., 2011; Erkül, 2011; Zhang et al., 2011; Kurt et al., 2013). The Iberian Massif is the most extensive expression of the Variscan province magmatism. In the south of the massif, the Ossa-Morena Zone (OMZ) continental block, formed of Neoproterozoic to Carboniferous rocks, juxtaposed with the Central Iberian Zone (CIZ) and the South Portuguese Zone (SPZ) during the latest Devonian-earliest Carboniferous (Fig. 1.1) (Matte, 2001 and references therein).

The early Carboniferous igneous rocks of the Ossa-Morena Zone have historically been the focus of considerable interest for two main reasons:

i. First, the Variscan plutons in the Ossa-Morena Zone have a wider compositional spectrum than the CIZ. They are typically compositionally diverse comprising gabbros and diorites through quartz diorites to granodiorites and granites (Fig. 1.1) (e.g., Pons, 1982; Casquet and Galindo, 2004; Ordoñez-Casado et al., 2008) suggesting complex interplay of magmas derived from mantle and crustal sources.

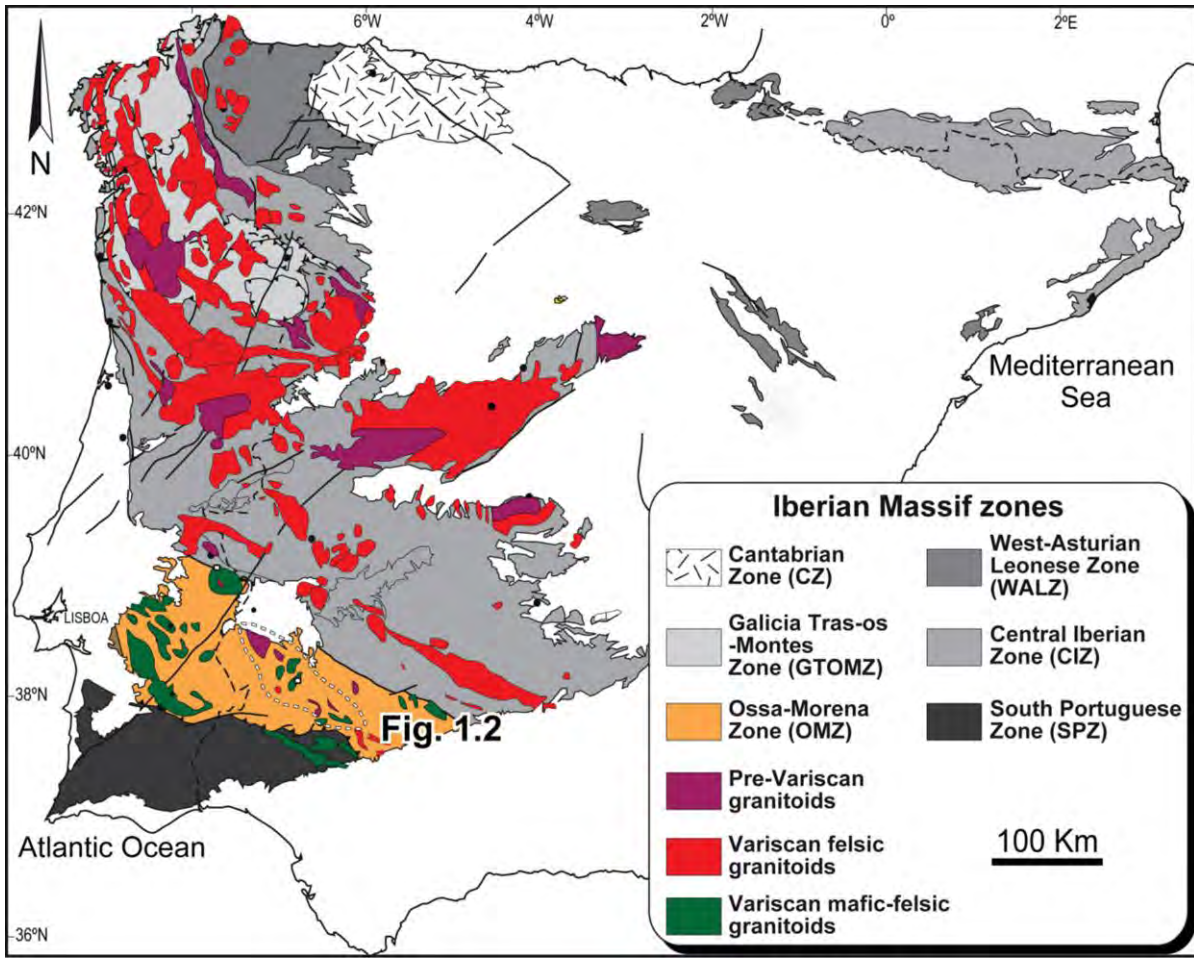

Figure 1.1. Zones of the Iberian Massif indicating the distribution of mafic and felsic granitoids throughout the Massif. Modified from Bea et al., (2006) and Martinez-Catalán, (2011).

ii. Second, the calc-alkaline character of the OMZ Variscan magmatism (Fig. 1.2) has led to it being linked with subduction (e.g., Pons, 1982; Giese et al. 1994; Quesada et al., 1994; Castro et al., 1996; Sarrionandia, 2005). But, it is not clear whether all calc-alkaline rocks should be directly linked with active or ancient subduction zones (e.g., Arculus, 2003; Pearce, 2008; Scarrow et al., 2009). Furthermore, in Iberia, contemporaneous with the early Carboniferous magmatism, a short-lived intra-orogenic extensional event occurred during the main Variscan collision 350-330 Ma (Apraiz and Eguiluz, 2002; Simancas et al., 2003; Pereira et al., 2007; Rosas et al., 2008),. At the same time there was: sedimentary basin development (Quesada et al., 1990; Giese et al., 1994; Simancas et al. 2003); mid-crustal intraplating of the 'IBERSEIS Reflective Body', interpreted to be ultramafic-mafic sills (Simancas et al., 2003; Palomeras et al., 2010; Brown et al., 2012); extensive mineralisation (Tornos et al., 2006; Romero et al., 2006); MT/HT-LP metamorphism (Bard, 1969; Ordoñez-Casado, 1998; Pereira et al., 2003; 2009; Díaz-Azpiroz et al., 2004; 2006); and the main OMZ Olivenza-Monesterio antiform magmatism (Fig. 1.2)

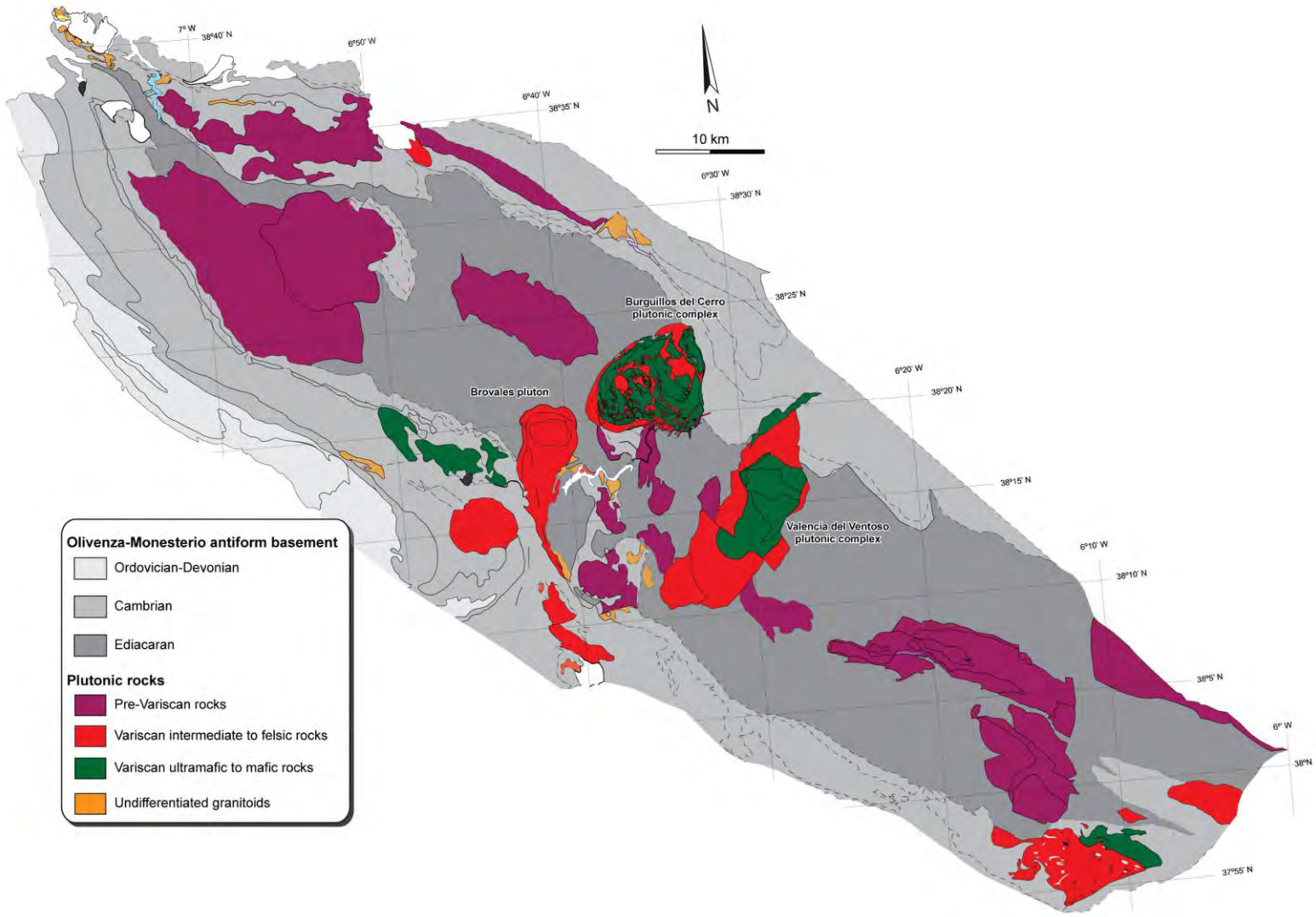

Figure 1.2. The Olivenza-Monesterio antiform showing the pre-Variscan and Variscan plutonic complexes and highlighting the Variscan mafic to felsic magmatism. Modified from Expósito, (2000).

(Dallmeyer et al. 1995; Montero et al., 2000; Ordóñez-Casado, 2008).

The difficulty in constraining the origin of the magmatism in this area arises from the complex multi-component nature of the hybrid rocks and thus the problem of identifying the end-members in the mixing process. To date, the study of the Ossa Morena early Carboniferous magmatism has lacked access to: new micro-analytical techniques such as analysis of O isotopes and U-Pb zircon dating by SHRIMP; compilations of 'big data' now available in the literature; current regional structural reinterpretations of geodynamic events; and, recently developed numerical models of crustal melting and magma mixing processes.

1.2 Objectives

The main goal of this work is to provide new constraints on, and insights into, the petrogenesis of the early Carboniferous Ossa-Morena Variscan plutons. This should shed light on mantle-crustal sources and growth-recycling processes involved in intra-orogenic magmatism. To do this, we carried out a systematic study of the geochronology and composition of three representative plutonic bodies: Burguillos del Cerro, Valencia del Ventoso and Brovales. In particular we aim to determine:

i. The age of the magmatism using SHRIMP U-Pb zircon dating and the presence and significance of pre-magmatic zircons.
ii. The petrographic, mineral chemistry, whole-rock major and trace element geochemistry, Sr and Nd and zircon SHRIMP O isotope composition of the plutonic bodies and their related basement.
iii. The character of the Ossa-Morena Zone basement of the plutonic bodies in relation to northern Gondwana terranes and its context prior to Variscan amalgamation of Iberia.
iv. The timing of the magmatism in relation to the main Variscan regional geodynamic events and its possible link with an intra-orogenic extensional context.
v. The processes involved in the generation of diverse alkaline–subalkaline–peraluminous compositions by numerical modelling of magma mixing involving mafic mantle-derived and felsic crustal-derived components.

The results of this work have yielded the following paper:

i. SHRIMP U-Pb zircon dating of the Valencia del Ventoso plutonic complex, Ossa-Morena Zone, SW Iberia: Early Carboniferous intra-orogenic extension-related 'calc-alkaline' magmatism. Cambeses, Scarrow, Montero, Molina and Moreno. Gondwana Research (in press).

Other manuscripts in preparation include:

i. The paleogeographic position of the Ossa-Morena Zone during Cambro-Ordovician times: evidence from Proterozoic-Paleozoic zircons. (to be submitted to International Geology Review).

ii. Deciphering the geodynamic significance of mantle and crustal sources tapped during orogenesis. SHRIMP U-Pb ages and oxygen isotope composition of zircon from the Brovales mixed syn-orogenic Variscan pluton, Ossa-Morena Zone, SW Iberia. (to be submitted to Tectonophysics).

iii. Producing new crust whilst reworking old: identification of multiple mantle and crustal mixed magma end-members in Variscan Central Iberian plutons. (to be submitted to Journal of Petrology).

Chapter 2: Geological Setting

2.1 The Variscan Belt

2.2 The Iberian Massif

2.3 The Ossa-Morena Zone

2. Geological Setting

2.1 The Variscan Belt

The Variscan belt preserves the most extensive assemblage of pre-Mesozoic rocks in central and western Europe and parts of north Africa (e.g., Matte, 2001; Michard et al., 2010) (Fig. 2.1A). The Variscan continental crust has been variably overprinted and incorporated into younger orogens such as the Alps (von Raumer and Neubauer, 1993), the Betic Cordillera (Foucault and Paquet, 1971; Martín-Algarra, 1983; Martín-Algarra et al., 2000; Navas-Parejo, 2012), the Carpathians and Balkanides (Haydoutov, 1989), and the Hellenides (Stampfli et al., 2002). Parts of Anatolia (Okay et al., 2010) and the Caucasus (Mayringer et al., 2011) also contain rocks recording Variscan influence (Fig. 2.1).

The Variscan belt formed as a consequence of collision of Laurussia and Gondwana and the resulting closure of the Rheic Ocean during the late Carboniferous to early Permian (Matte and Ribero, 1975; Matte, 1986; Stampfli and Borel, 2002; Nance et al., 2010; Kroner and Romer, 2013) (Fig. 2.1B). This event led to a complex tectonic evolution that generated strongly deformed and metamorphosed belts and abundant magmatism. The European Variscan massifs (as described in, amongst others, Kossmat, 1927; Julivert et al., 1972; Tait et al. 1996; Matte, 2001; Martínez-Catalán, 2011; 2012) (Fig. 2.2) include the Iberian Massif, the Amorican Massif, the Massif Central of France, the Bohemian Massif, the Rhenish Massif and the Urals (Burg and Matte., 1978; Bard et al., 1980; Matte, 1986) (Fig. 2.2).

In Iberia, the main deformed metamorphic and magmatic rocks crop out in a wide band in the central part of the orogen, flanked by less deformed regions (Fig. 2.2). The massifs were classified in seven main zones on the basis of their magmatic, metamorphic and structural features (e.g., Lotze, 1945; Carey, 1955; Lotze, 1956b; Julivert et al., 1972): i. External thrust belt and foreland basins preserved in the Avalonia terrane; ii. Gondwana affinity areas with a strong Cadomian orogeny imprint; iii. Gondwana affinity areas that preserve Early Ordovician magmatism; iv. Allocthonous terranes, including ophiolites and high-pressure rocks; v. Variscan orocline and metamorphic belts and vi-vii. Variscan foreland fold and thrust belts (e.g., Martínez-Catalán, 2011; 2012) (Fig. 2.2). Subsequent strike-slip shearing and oroclinal bending also affected the Iberian region (Bard et al., 1971; Ribeiro et al., 1995; Matte, 2001; Gutiérrez-Alonso et al., 2004; Martínez-Catalán, 2011; Simancas et al., 2013) (Fig. 2.2).

2.2 The Iberian Massif

The Iberian Massif is the westernmost and most extensive expression of the European

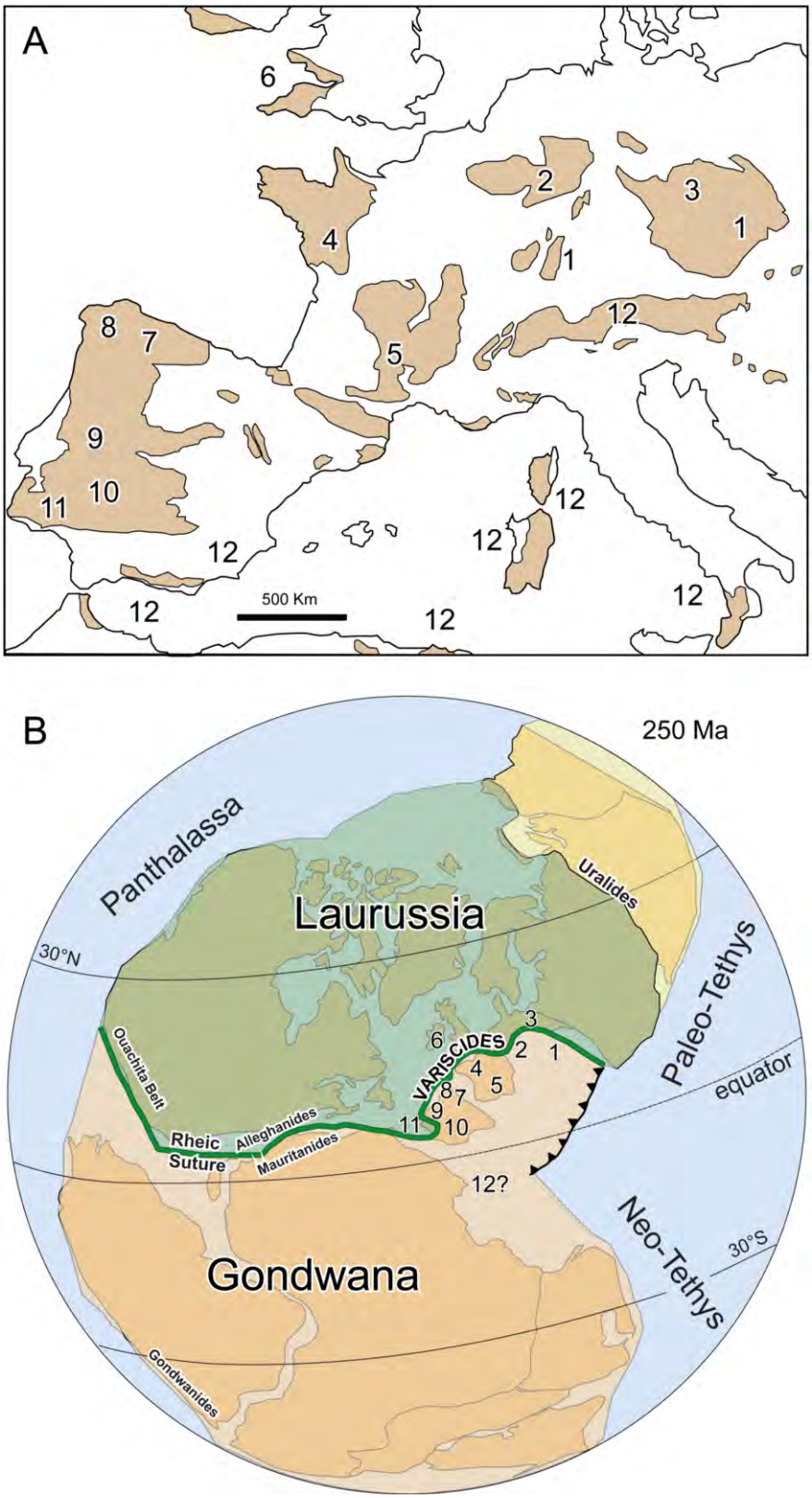

Figure 2.1. A) Paleozoic terranes in central and western Europe and north Africa (modified from Navas-Parejo, 2012). B) The Variscan orogen in the context of Pangea, at 250 Ma (modified from Kroner and Romer, 2013). Numbering refers to the European Variscide terranes; 1: Bohemian Masif, 2: Rhenish Massif, 3: Saxo-Turingia, 4: Armorican Massif, 5: Massif Central, 6: Lizard Front, 7: Cantabrian and West-Asturian Leonese zones, 8: Galicia Tras-os-Montez Zone, 9: Central Iberian Zone, 10: Ossa-Morena Zone, 11: South Portuguese Zone and 12: Intra-Alpine terranes.

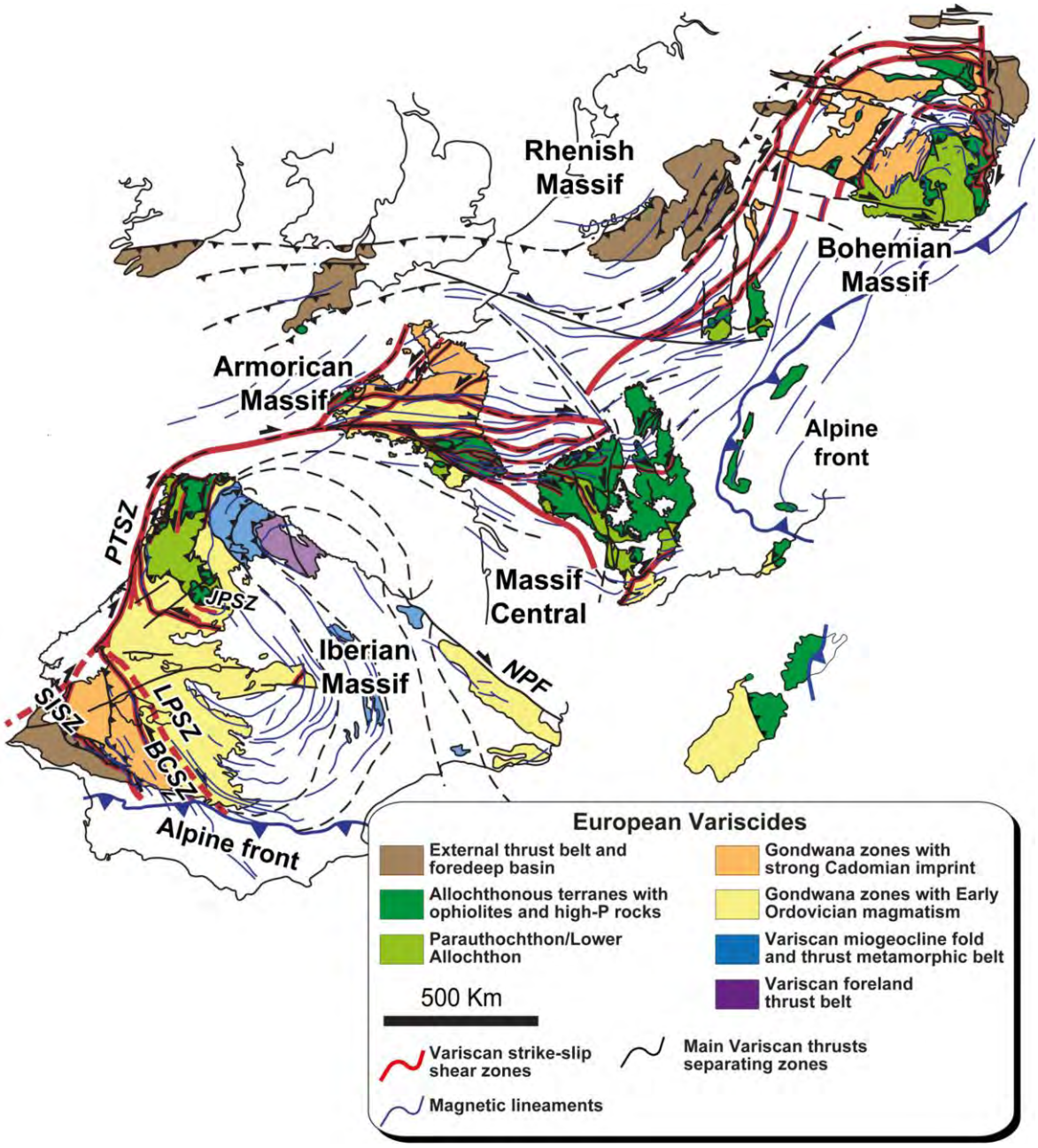

Figure 2.2. Geological map of the European Variscides, after Martínez-Catalán (2011). JPSZ: Juzbado-Penalva shear zone; LPSZ: Los Pedroches shear zone; BCSZ: Badajoz-Cordoba shear zone; PTSZ: Porto-Tomar shear zone; SISZ: Sudiberica shear zone.

Variscides (Bard et al., 1973; 1980; Burg and Matte., 1978; Matte, 1986; Pérez-Estaún and Bea, 2004). The massif has been divided into six main zones, broadly from north to south: Cantabrian (CZ); West Asturian-Leonese (WALZ); Galicia Tras-os-Montes (GTZ); Central Iberian (CIZ); Ossa-Morena (OMZ) and South Portuguese (SPZ), (Fig. 2.3; Lotze, 1945; Julivert et al., 1972; Ribeiro et al., 1990; Martínez-Catalan et al., 1999).

The Cantabrian Zone is located in the north-east of the Iberian Massif, it is composed of Neoproterozoic to Palaeozoic sequences (Pérez-Estaún, 2004). The CZ was affected by fold-and-

thrust deformation thin-skinned tectonics (cf., Pérez-Estaún et al., 1988). Magmatic rocks are scarce in the CZ only being represented by pre-Variscan volcanic rocks and late Variscan plutonic rocks (Gallastegui et al., 1992; 2004).

The West Asturian-Leonese Zone comprises thick Cambro-Ordovician stratigraphic series, with the youngest materials being Devonian (Marcos et al., 2004). These rocks were affected by two stages of Variscan folding. The first formed recumbent folds with that verge to the east and were affected by thrusts; the second formed vertical folds (Marcos, 1973; Marcos et al., 1980; 2004; Gutiérrez-Alonso, 2004). The WALZ magmatic rocks include volcanic and plutonic pre-Variscan and Variscan series (Bellido et al., 1987; Corretgé et al. 1990).

The Galicia Tras-os-Montes Zone is a composite of parautochtonous sequences and allochthonous complexes thrust over the CIZ and CZ (Arenas, 1984; Martínez-Catalán et al., 2007; 2009) (Fig. 2.3). The parautochthonous sequences (Farias et al., 1987; Riberio et al., 1990) comprise latest Ediacaran and latest Cambrian rocks (Díez-Fernandez et al., 2010) whereas the allochthonous complexes *s. s.* include the remnants of the Variscan suture (Arenas et al., 2007; Sánchez-Martínez et al., 2012). The allochthonous complexes have an intricate internal structure, comprising three terranes with contrasting origin, structure and tectonothermal evolution (Arenas, 1985). Nappe piles, late Variscan synforms, may be divided from base to top in: basal, ophiolitic and upper units. Magmatic rocks are abundant and include a Cambro-Ordovician magmatic event, ophiolitic suites and Variscan-related magmatism (Arenas, 1985; Montero et al., 1998; 2009b; Sánchez-Martínez et al., 2011; Arenas et al., 2004; 2013, 2014).

The Central Iberian Zone forms the middle of the Iberian Massif (Fig. 2.3). It has been divided into two domains: the Ollo de Sapo formation to the north and the Schist-Greywacke Complex domain to the south (Pérez-Estaún et al., 2004). Both domains comprise late Ediacaran to early Carboniferous rocks (Parga-Pondal et al., 1964; Martínez-García, 1973; Martínez-Catalán, 1985; Díez-Balda, 1986). Both pre-Variscan and Variscan deformation is recorded in the region. The pre-Variscan deformation is marked by several discordances formed during the Cadomian, or Pan-African, orogeny (Ortega-Girones and Gonzaléz-Lodeiro, 1986; Capdevila et al., 1971; Díez-Balda et al., 1990). The Variscan deformation took place during the Late Devonian to late Carboniferous in three main phases: i. formation of recumbent folds that verge to the east (Matte, 1986; Azor et al., 1994a); ii. generation of thrusts, that cut previous folds and formation of folds with a vertical axial plane; and iii. late-orogenic extension (Escuder-Viruete et al., 1994; 2000; Díez-Balda et al., 1995). Both pre-Variscan and Variscan magmatic rocks are abundant in the CIZ (Bea et al., 1987). The pre-Variscan rocks are essentially Cambro-Ordovician, mostly derived from Pan-African materials (Bea et al., 2006, 2007; Montero et al., 2007, 2009a). They

crop

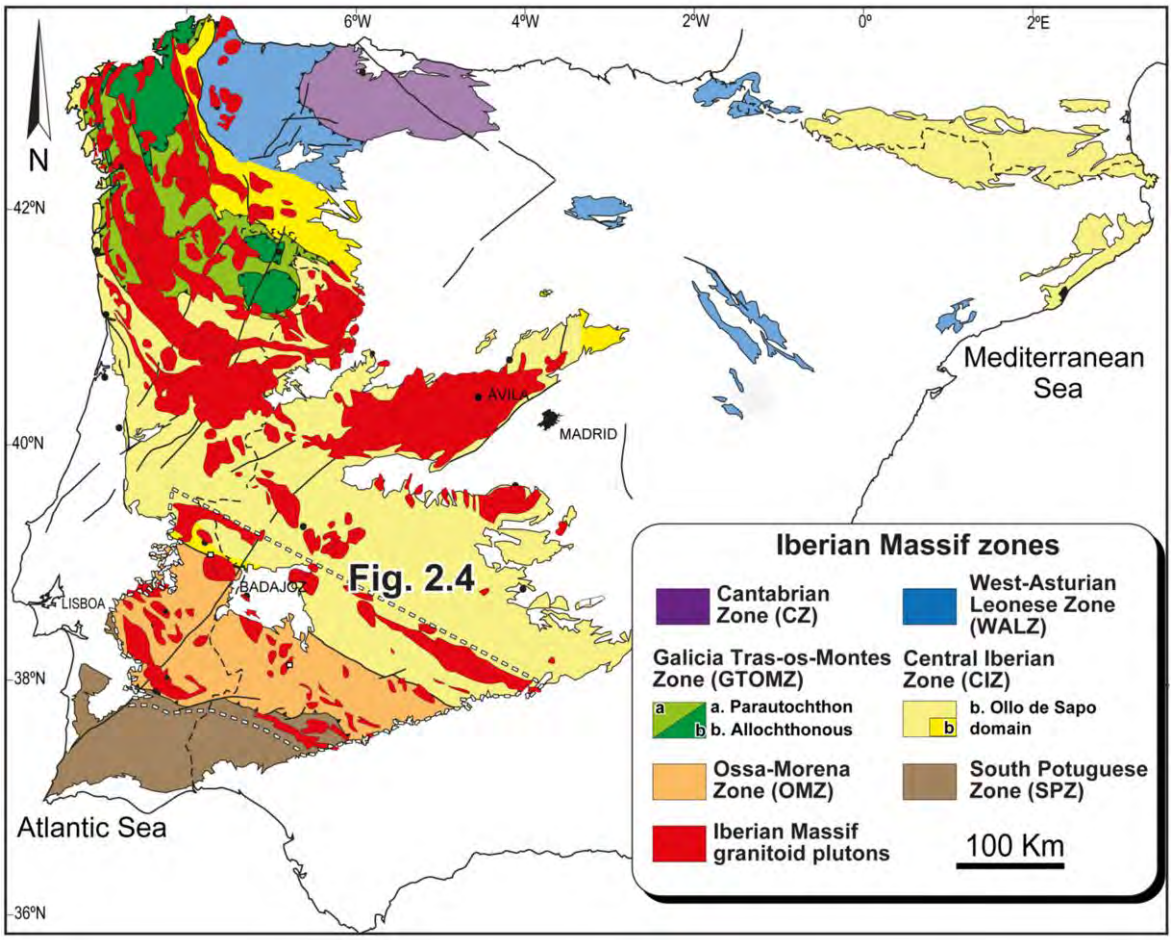

Figure 2.3. Zones of the Iberian Massif indicating the distribution of granitoids, modified from Bea et al., (2006) and Martinez-Catalán, (2011).

out in i. the Ollo de Sapo and ii. the Guadarrama orthogneiss complex. The CIZ Variscan magmatism, 350-295 Ma, records voluminous plutonism (Bea, 1991; 2004; Montero et al., 2004).

The Ossa-Morena Zone is situated between the CIZ and SPZ. The Variscan magmatic rocks of this region are the focus of the current work so the zone will be discussed in detail in the following sections.

The South Portuguese Zone constitutes an external orogenic domain unrelated to the other zones of the Iberian Variscan Massif (Simancas, 2004 and references therein). Its northern contact with the Ossa-Morena Zone includes units that have an oceanic affinity: possible ophiolitic rocks, Beja-Acebuches amphibolites, and accretionary prism sediments, the Pulo do Lobo Unit (Silva et al., 1990; Crespo-Blanc, 1991; Eden and Andrews, 1990; Quesada et al., 1994; Castro et al., 1996; Braid et al., 2010). Late Devonian to late Carboniferous metasedimentary and metavolcanic rocks in the region (Simancas, 1983; Fonseca and Ribeiro, 1993) were affected by

southwest vergent folds and thrusts and low-grade metamorphism (Simancas, 2004; Abad et al., 2004). The SPZ Variscan magmatism includes both volcanic and plutonic rocks. The former were related to the formation of the Pyrite Belt massive sulphide deposit formations (Schermerhön, 1971; Sáez et al., 1997; Barriga et al., 1997; Sánchez-España et al., 2003). The latter are restricted to the north-east SPZ and comprise bimodal magmatism, gabbros to granites (De la Rosa, 1992; De la Rosa et al., 2002; Gladney et al., 2014).

2.3 The Ossa-Morena Zone

The Ossa-Morena Zone is a continental block that represents part of the most northern margin of Gondwana (Robardet, 2003). The OMZ preserves evidence of a complex evolution during the late Neoproterozoic Cadomian orogeny, 650-550 Ma, and subsequent Cambro-Ordovician, 510-480 Ma, extension (Eguiluz et al., 2000; Expósito, 2000; Expósito et al., 2003; Sánchez-García et al., 2003; 2010). Furthermore, during the Carboniferous Variscan orogeny the region was deformed, as reflected in two complex contacts that register convergence at its northern and southern margins (Bard, 1977; Bard and Moine 1979; Ábalos et al., 1991; Quesada, 1991; Castro et al., 1996; Matte, 2001; Simancas et al., 2005) (Fig. 2.4).

The contact with the Central Iberian Zone, to the north, is marked by the Badajoz-Cordoba fault, interpreted by some authors as a major Variscan intra-continental shear zone (Burg et al., 1981; Azor et al., 1994b; Gómez-Pugnaire et al., 2003; Simancas et al., 2005, Pereira et al., 2007; 2009; 2010a; 2010b; 2012a) (Fig. 2.4). However, other authors consider that the OMZ-CIZ boundary is a fault that was originally active during the Cadomian orogeny that was subsequently reactivated during the Variscan (Ábalos et al., 1991; Quesada, 1991; Ábalos and Díaz-Cusi, 1995; Eguiluz et al., 1995; 2000).

The contact with the South Portuguese Zone, to the south, is marked by the aforementioned Beja-Acebuches amphibolites (BAA) and the Pulo do Lobo shear zone (Fonseca and Ribeiro, 1993; Quesada et al., 1994; Araujo et al., 2005; Azor et al., 2008; Braid et al., 2010) (Fig. 2.4). The amphibolites have been interpreted as remnants of the Rheic Ocean (e.g., Quesada et al., 1994; Castro et al., 1996). However, more recently, this idea has been refuted on the basis of new, younger than previously thought, post-collisional radiometric ages, 340-330 Ma, for the BAA (Azor et al., 2008).

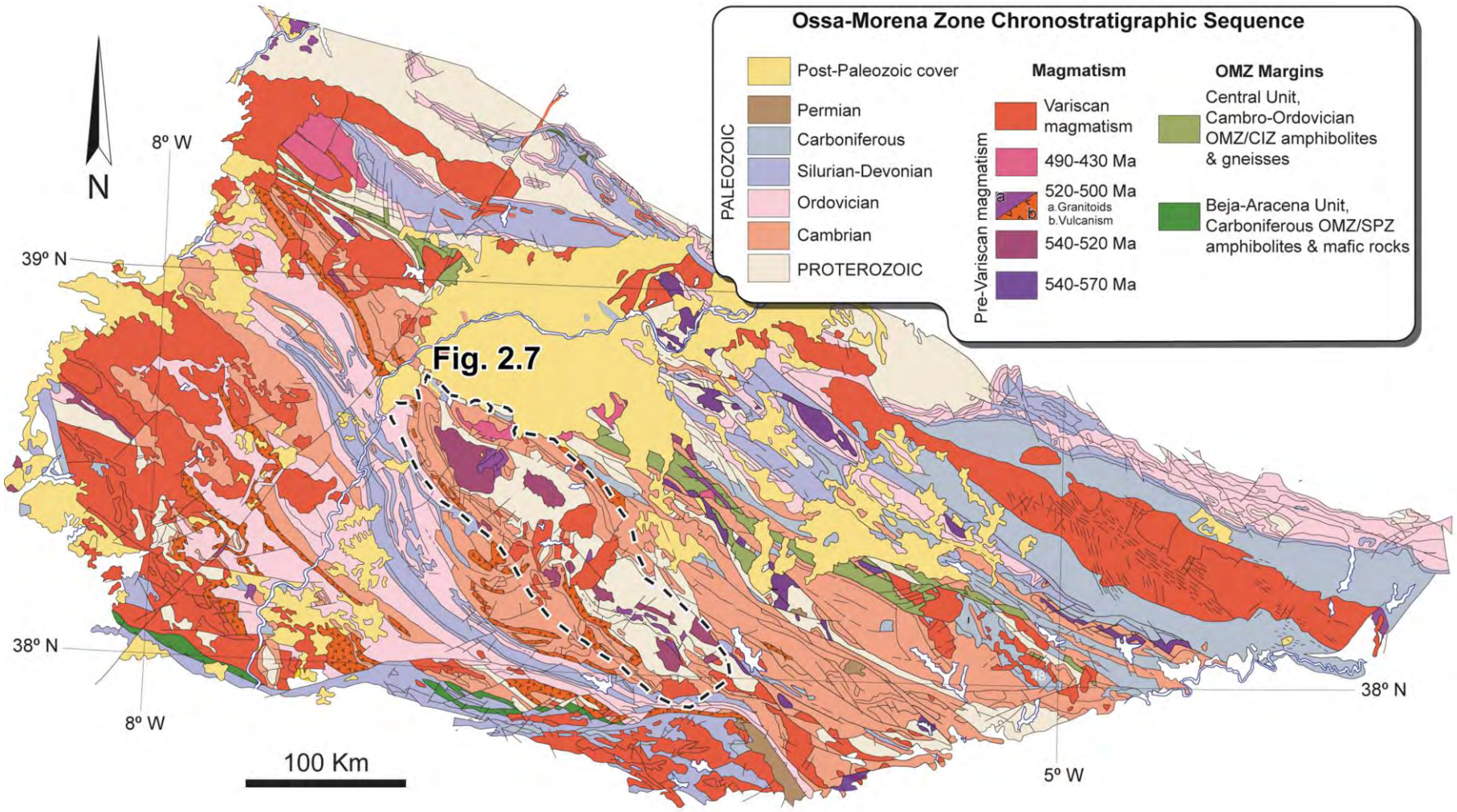

Figure 2.4. Chronostratigraphic sequence of the Ossa-Morena Zone showing the different stages and the Ossa-Morena Zone boundaries with the Central Iberian Zone and the South Portuguese Zone, modified from Gabaldón et al., (2001).

2.3.1 OMZ Stratigraphy

The OMZ stratigraphic succession includes rocks of Ediacaran to early Carboniferous age. The sedimentary sequence is particularly well-exposed in the eastern part of the OMZ close to the Olivenza Monesterio Antiform (Fig. 2.4 and 2.5).

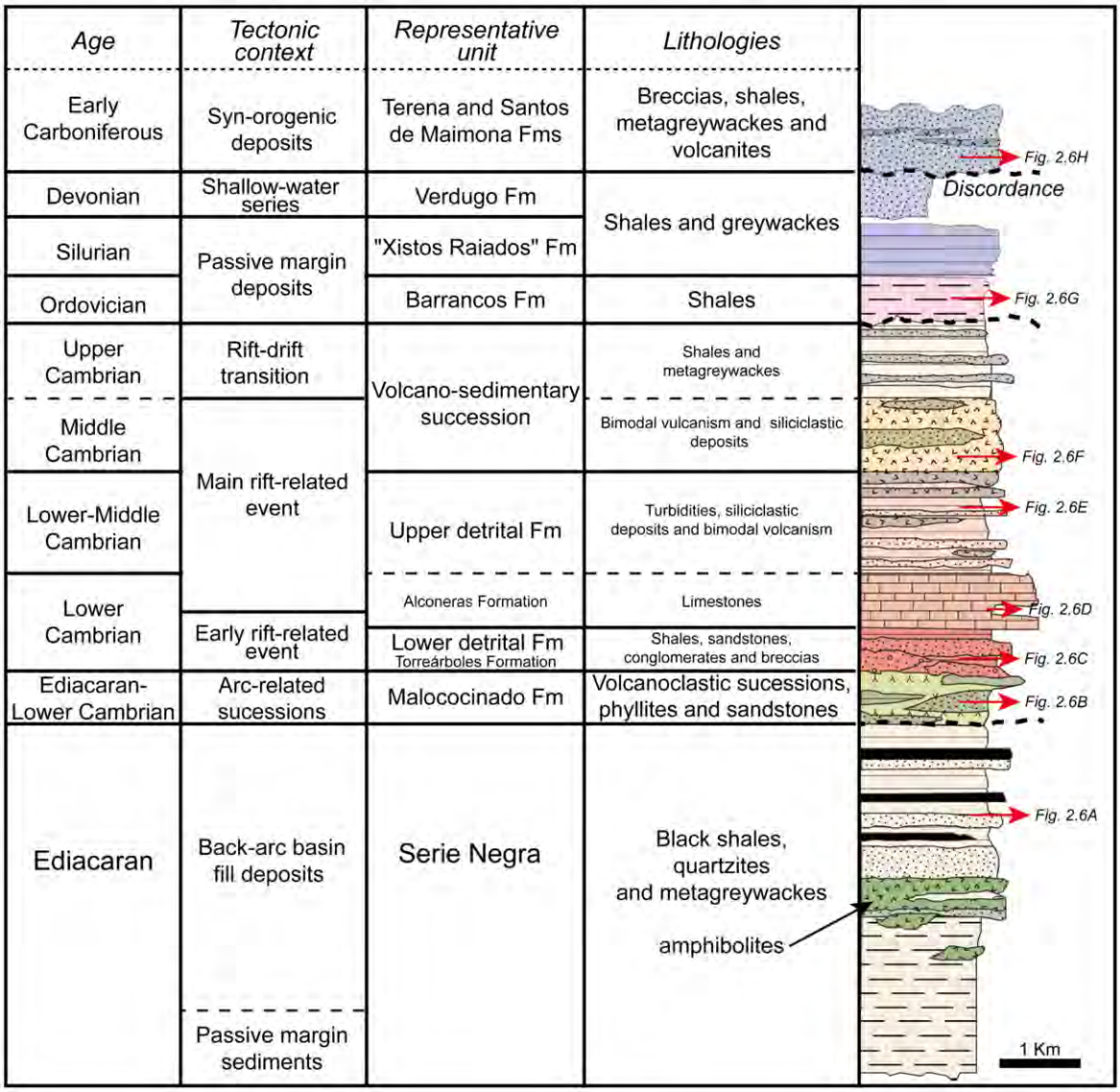

Figure 2.5. Summary of the Ossa-Morena Zone stratigraphic sequence (modified from Expósito, 2000) with the age, tectonic context, representative units and the lithologies in the area.

2.3.1.1 Precambrian to Cambrian

The OMZ basement is formed of Neoproterozoic Ediacaran Serie Negra black shales, quartzites and metagreywackes (Fig. 2.4, 2.5 and 2.6A) (Alía 1963; Carvalhosa 1965; Chacón, et al., 1984; Schäfer et a., 1993; López-Guijarro, 2006) that can be divided in two main formations:

the Montemolín Formation passive margin sediments, and the Tentudía Formation back-arc basin fill deposits (Eguiluz, 1988; Quesada, 1990). Comparable sequences, the Mosteiros Formation and the Besteiros Amphibolites unit, crop out further to the west in Portugal (Gonçalves, 1971; Oliveira et al., 1991; Pereira and Silva, 2001; Pereira et al., 2006). Radiometric U-Pb ages on detrital zircons indicate a maximum Neoproterozoic deposition age for the Serie Negra of 590-540 Ma (Pereira et al., 2008; 2012b; Linnemann et al., 2008). The Montemolín Formation has a maximum sedimentation age of *c.* 590 Ma (Ordoñez-Casado, 1998). The Tentudía Formation has a somewhat younger maximum depositional age of *c.* 565 Ma in the Olivenza-Monesterio Antiform, younging northward to *c.* 545 Ma close to the OMZ-CIZ boundary (Schäfer et al., 1993; Linnemann et al., 2008).

The Precambrian-Cambrian Malcocinado Formation (Fricke, 1941), overlies the OMZ Serie Negra and crops out beneath Cambrian units (Fig. 2.4, 2.5 and 2.6). This formation is composed of Cadomian arc volcanoclastic successions, metagreywackes, phyllites, sandstones and conglomerates (Fig. 2.6B) (Sánchez-Carretero et al., 1989; 1990; Quesada et al., 1990b; Eguiluz et al., 2000; Pin et al., 2002). The youngest detrital zircons obtained from it give a sedimentation age of *c.* 522 Ma (Ordoñez-Casado, 1998).

2.3.1.2 Cambrian and Ordovician

The transition from the OMZ Precambrian formations to the Cambrian sediments is, often, marked by an unconformable contact associated with a stage of rifting (Fig. 2.4) (Liñán and Quesada, 1990; Expósito et al., 2003; Sánchez-García et al., 2003; 2010; Chichorro et al., 2008). The Cambrian rift succession (Liñán and Quesada, 1990) can be divided into four main components, from base to top. The oldest, the lower detrital formation, is, from fossil evidence, early Cambrian (Liñán and Quesada, 1990; Liñán et al. 2002) It is formed of fluvial to shallow marine shelf deposits related to an early transgression, e.g., the OMZ Torrearboles Formation (Fig. 2.4, 2.5 and 2.6C) (cf., Liñán, 1984). In agreement with this, Ediacaran-early Cambrian sediments from the lower detrital formation, close to the boundary between the OMZ and the CIZ, have a maximum sedimentation age of 536-532 Ma (Pereira et al., 2011) although Linnemann et al., (2008) recorded ages of *c.* 567 Ma. The second component of the Cambrian rift succession is an early Cambrian shallow marine carbonate unit, the Olivenza-Monesterio Antiform Alconera Formation (Fig. 2.4, 2.5 and 2.6D) (Liñán, 1978; Liñán and Perejón, 1981). The third component, is the early to middle Cambrian upper detrital formation, which is characterised by turbiditic and shelf siliciclastic sediments deposited during a collapse-related extensional process (Fig. 2.5 and 2.6E) (Liñán and Quesada, 1990; Liñán and Gámez-Vintaned, 1993; Sánhez-García et al., 2003). The final component, a volcano-sedimentary succession, has

Figure 2.6. Examples of representative units of the Ossa-Morena Zone stratigraphic sequence: A) Serie Negra shales and metagreywackes. B) Rhyolites from the Malcocinado Formation. C) Torrearboles Formation metagreywackes (Lower detrital Formation). D) Limestone from the Alconera Formation (Upper detrital Formation). E) Upper detrital Formation turbidites. F) Mafic rocks from the volcano-sedimentary succession. G) Ordovician shales. H) Early Carboniferous syn-orogenic shales and metagreywackes.

been dated as middle to late Cambrian (Fig. 2.4, 2.5 and 2.6F) (Liñán and Quesada, 1990; Pereira et al., 2006; Sánchez-García et al., 2008; López-Guijarro et al., 2008). A gap in sedimentation in the late Cambrian transition is associated with an exhumation processes linked to the emplacement of extension-related magmatic bodies that resulted in uplift and erosion (Fig. 2.5) (Quesada, 1991, Sánchez-García et al., 2003; 2010; Quesada et al., 2006).

Early Ordovician deposits are dominated by detrital to open marine sediments (Oliveira et al., 1992; Giese et al., 1994), whereas the Late Ordovician succession is composed of passive margin deposits (Robardet, 1981; Gutiérrez-Marco et al., 1984; 1990a; 2002) (Fig. 2.4, 2.5 and 2.6G). In the north of the OMZ, at the contact with the CIZ, a Lower Ordovician, *c.* 522 Ma, maximum sedimentation age was defined for the Oguela Formation quartzite (Linnemann et al., 2008).

2.3.1.3 Silurian to Carboniferous

Overlying the Ordovician sediments is a monotonous series of Silurian black shales (Fig. 2.4 and 2.5) (Llandovery, Robardet and Gutierrez-Marco, 1990a; Gutiérrez-Marco et al., 1998). By the Early Devonian the upper part of the succession comprised more shallow-water terrigenous series intercalated with the black shales (Fig. 2.4 and 2.5) (Ludfordian to Lochkovian, Oliveira et al., 1991). The transition from Early to Middle-Late Devonian is marked by an unconformity related to the beginning of the Variscan collision (Fig. 2.5) (Oliveira et al., 1986, Expósito, 2000). Principally, greywackes, shales and volcano-sedimentary sequences compose the synorogenic successions (Fig. 2.6H) (cf., Apalategui et al., 1985; Quesada et al., 1990b; Pereira et al., 2006; 2007). The age of these sequences straddles the Late Devonian (Quesada et al., 1990b; Giese et al., 1994) and early Carboniferous, Tournasian-Visean (Wagner, 1978; Wagner at al., 1983; Giese et al., 1994). The succession has been interpreted as flyschs and molasses from foreland basins in the lower part of the series and continental basin deposits in the upper part of the series (e.g., Quesada et al., 1990b, Giese et al., 1994; Expósito, 2000, Simancas et al., 2003).

Early Carboniferous turbidites (Tournaisian-Visean) in the OMZ, Cabrela Formation, have a detrital zircon maximum sedimentation age of *c.* 352 Ma (Pereira et al., 2012c).

2.3.2 OMZ Structure

Pre-Variscan structures are preserved in the LP-HT metamorphic regions of the Olivenza-Monesterio antiform: Valuengo and Monesterio (Fig. 2.7) (Expósito et al., 2003; Sánchez-García et al., 2003; 2010). These areas record intense metamorphism (see next section) and syn-metamorphic extensional shearing (Expósito, 2000; Expósito et al., 2003). This deformation generated a milonitic foliation with a northeast-oriented stretching lineation (Apraiz and Eguiluz,

1996; Expósito et al., 2003). Such pre-Variscan structures were overprinted by the Variscan deformation so producing the complex structural relationships characteristic of this area.

The Variscan structures preserve evidence of an initial collisional event between 390-345 Ma (Simancas et al., 2001; 2003; Expósito et al., 2002; Braid et al., 2011; Pereira et al., 2012b) followed, 345-330 Ma, by extension/transtension (Apraiz and Eguiluz, 2002; Simancas et al., 2003; Pereira et al., 2007; 2009; Rosas et al., 2008) and a subsequent, 330-305 Ma, second collisional event (Simancas et al., 2003; 2006; Azor et al., 2008).

In the OMZ Olivenza-Monesterio antiform the initial collisional event resulted in large recumbent southwest vergent folds (Fig. 2.7). This folding was related to low-grade metamorphic conditions and development of a plano-linear fabric parallel to the axial foliation plane (Expósito et al., 2002). This first collisional event also generated thrusts that cut the recumbent folds (Fig. 2.7). The most significant is the Monesterio thrust (Fig. 2.7) (Eguiluz, 1987; Expósito, 2000; Eguiluz et al., 2000; Expósito et al., 2002) which cuts the axial trace of the Olivenza-Monesterio antiform, displacing the roof block to the south-west (Fig. 2.7). It has caused a brittle-ductile fabric, that is preserved in some Variscan plutons (Fig. 2.7). Simancas et al., (2003) concluded that it had a mid-crustal detachment level, comparable to other, associated, more minor structures.

Following the initial compression, the deformation style changed from transpressive to transtensive. The second stage resulted in recumbent fold and thrust collapse, and in the formation of Carboniferous basins that filled with olistrostomic deposits (Munhá, 1983; Oliveira, 1990; Simancas et al., 2003). Simultaneously normal faults developed in other regions also forming Caboniferous basins (Azor, 1994).

The final stage of deformation, the second collisional event, generated upright folds, which deformed previous structures. These folds verge to the southwest and northeast (Fig. 2.7). The normal faults and Carboniferous basins were affected by this deformational event (Martínez-Poyatos, 1997). The upright folds were subsequently cut by post-Variscan high-angle reverse faults.

Deformation in the OMZ-CIZ Badajoz-Cordoba boundary shear zone was predominantly ductile as reflected in the development of a plano-linear fabric (Azor, 1994; Azor et al., 2004). This stretching lineation records sinistral lateral displacement (Azor, 1994). The OMZ-SPZ boundary shear zone was folded recumbently (Crespo-Blanc, 1989; 1992; Crespo-Blanc and Orozco, 1991).

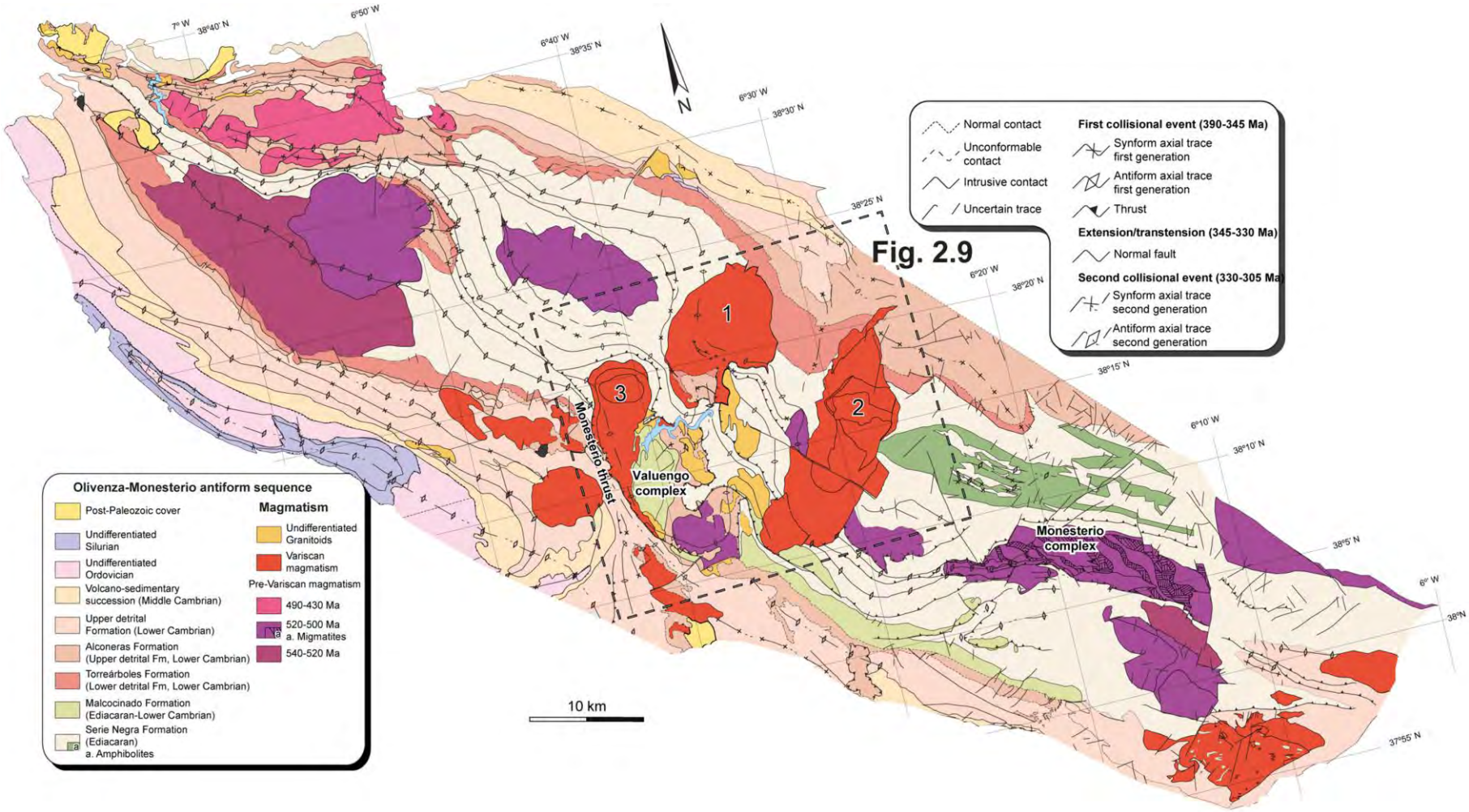

Figure 2.7. Olivenza-Monesterio antiform chronostratigraphic sequence showing the different stages and highlighting the structure pattern and magmatism, from Expósito, (2000). 1: Burguillos del Cerro plutonic complex, 2: Valencia del Ventoso plutonic complex and 3: Brovales pluton.

Kinematic indicators reveal composite movement including reverse, normal and sinistral components. This deformation was associated with development of northwest-southeast mylonitic foliation that dips steeply to the northeast (Crespo-Blanc, 1989; 1992), and which was folded during the second collisional event (Crespo-Blanc, 1989; Díaz-Azpiroz, 2001).

2.3.3 OMZ Metamorphism

The metamorphism that has affected the OMZ was low-grade except in the Valuengo and Monesterio complexes, the Badajoz-Cordoba shear zone, and the Évora-Aracena-Lora del Rio metamorphic belt, where the metamorphism reached high-grade (Expósito et al., 2003; Simancas et al., 2004; Pereira et al., 2009).

In the first region, the Valuengo and Monesterio complexes, the high-grade metamorphic event was pre-Variscan (Fig. 2.7). The Valuengo Complex consists of high-grade gneissic-migmatitites with an association of sillimanite+alkali feldspar+reddish brown biotite±garnet in the core and low-grade metapelites with green biotite as the only index mineral in the border. The HT-LP conditions occurred at *c.* 532 Ma (orthogneiss, Montero et al., 2000) and *c.* 480 Ma (undeformed microgranite, Montero et al., 2000). In the Monesterio complex the highest grade metamorphic rocks contain andalusite+cordierite+sillimanite+alkali feldspar (Eguiluz, 1988). This metamorphic event occurred, as in the Valuengo complex, between 530-500 Ma (Schäfer, 1990; Oschner, 1993; Ordoñez Casado, 1998; Montero et al., 1999). The high-grade metamorphism in both complexes has been related to a Cambro-Ordovician rifting context associated with Rheic Ocean opening (e.g., Sánchez-García et al., 2003; 2010; Nance et al., 2010; 2012) (see section 11.1).

The second and third regions record the OMZ Variscan metamorphism: the Badajoz-Cordoba shear zone and the Évora-Aracena-Lora del Rio metamorphic belt. In these areas the metamorphism occurred in two steps: LT/HT-HP and HT-LP.

The first stage was LT/HT-HP evidenced in the Badajoz-Cordoba shear zone, by garnet-bearing amphibolites that record eclogite conditions (550 ºC and 19 kbar, López Sánchez-Vizcaíno et al., 2003) but were strongly retrogressed to amphibolite facies during shearing (Fig. 2.8) (Azor et al., 1994b). This high pressure metamorphic event was also recorded in other regions of the OMZ, in the Coimbra sector of this shear zone, for example the Campo Maoir

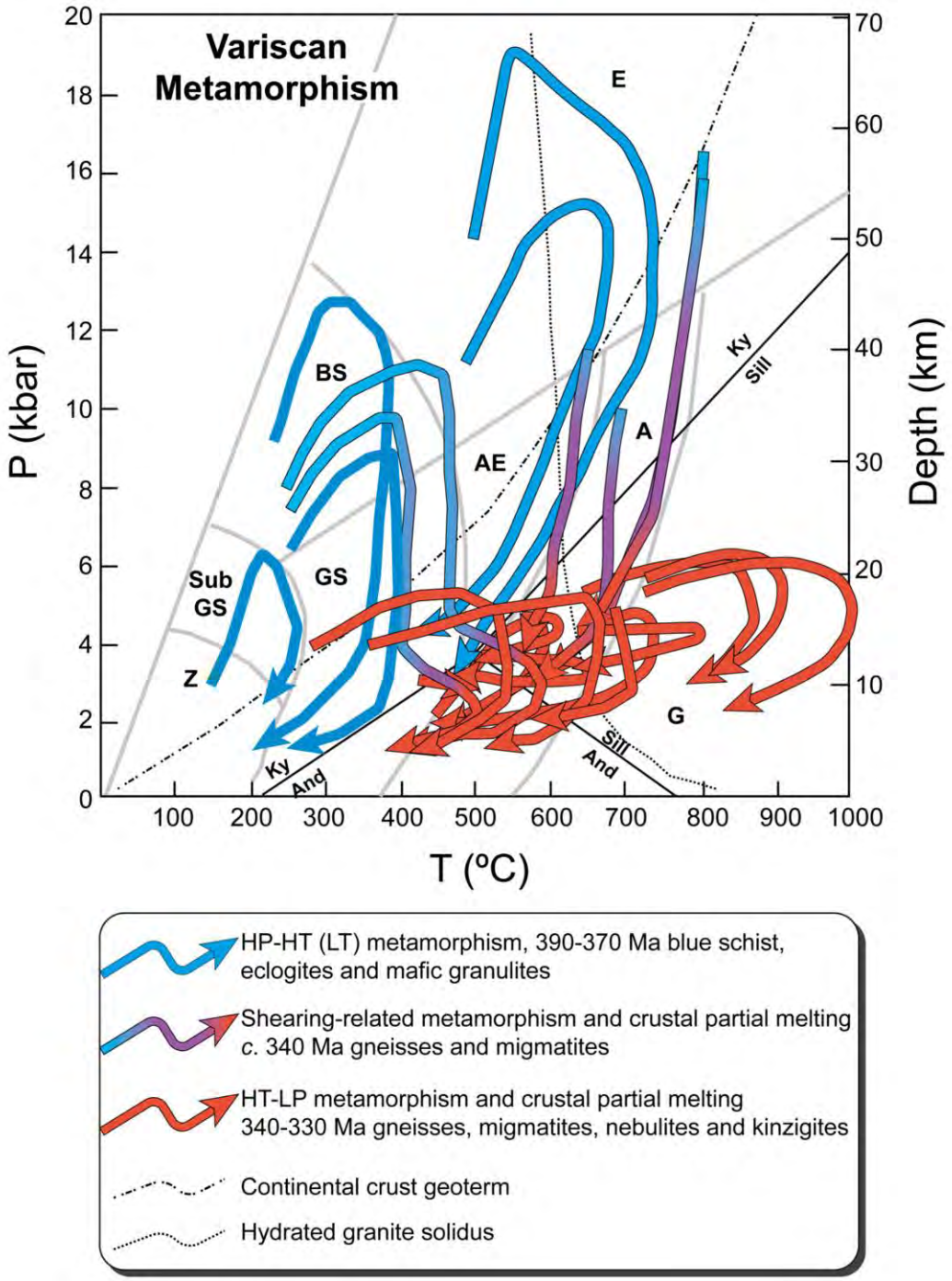

Figure 2.8. Summary of the P–T–t path for the Variscan metamorphism in the OMZ. The HP-HT metamorphism is compiled from Lopéz Sánchez-Vizcaíno et al., (2003) Araujo et al., (2005), Booth-Rea et al., (2006) and Rubio-Pascual et al., (2013). Shear-related metamorphism is taken from Pereira et al., (2010b). The HT-LP metamorphism is compiled from Évora (Pereira et al., 2007), Aracena (Díaz-Azpiroz et al., 2006; Rubio-Pascual et al., 2013) and the Lora del Rio metamorphic belt (Apraiz and Eguiliz 2002). Z: Zeolite facies; Sub GS: Sub-greenschist facies; AE: Amphibolite with epidote facies; A: Amphibolite facies; G: Granulite facies; BS: Blueschist facies; E: Eclogite facies; And: Andalucite; Sil; Sillimanite; Ky: Kyanite.

unit HT-HP mafic granulites (880-725 ºC and 17-13 kbar, Pereira et al., 2010a; 2010b) (Fig. 2.8). It is also preserved in the adjacent MP/HP rocks, the Safira-Viana do Alentejo eclogites and the Moura LT-HP blueschists (310-450 ºC and 12-7 kbar) (Araújo et al. 2005; Booth-Rea et al., 2006; Ribeiro et al. 2007; Rubio-Pascual et al., 2013) (Fig. 2.8).

The age of the metamorphism was dated prior to early Carboniferous (*c.* 340 Ma; Ordoñez-Casado, 1998; Pereira et al., 2010a; 2010b). The Moura blueschists are Middle-Late Devonian (390-370 Ma, Araújo et al. 2005; Moita et al., 2005c). The Campo Maoir unit decompression and shearing began later at *c.* 340 Ma (Pereira et al., 2010a; 2010b). The retrograde metamorphism at low- to medium-grade conditions occurred at *c.* 330 Ma (Dallmeyer, 1993; Azor, 1994b; Pereira et al., 2010a; 2010b) related to exhumation (cf., Azor et al., 2004).

The second Variscan metamorphic event was characterised by HT-LP conditions. It is best exposed in the Évora-Aracena-Lora del Rio metamorphic belt (Pereira et al., 2009). The P-T evolution of this high-grade metamorphism was isobaric, but with a significant temperature variation (Díaz-Azpiroz et al., 2004; 2006; Pereira et al., 2009). For example, in the Évora Massif high-grade terranes both garnet cordierite-rich paragneisses and diatexites with plagioclase, alkali feldspar, sillimanite and cordierite are common (Pereira et al., 2007; 2009). Similar P-T conditions are recorded in the Aracena metamorphic belt and the Lora del Rio massif: paragneisses (600-700 ºC and 3-4 kbar); migmatites (850-900ºC and 4-4.5 kbar); and, kinzigitic gneisses (955 ºC and 5 kbar) (Fig. 2.8) (Patiño-Douce et al., 1997; Ábalos et al., 1991; Apraiz, 1998; El-Biad, 2000; Díaz-Azpiroz, 2001; Díaz-Azpiroz et al., 2004; 2006). This metamorphism has a Visean-Serpukhovian age in all regions: the Évora Massif (340±6 Ma and 337±4 Ma, U-Pb SHRIMP, Pereira et al., 2009); the Aracena metamorphic belt (351±58 Ma, 331±27 Ma and 323±4 Ma, Rb-Sr Castro et al., 1999); and, the Lora del Rio massif (c. 340 Ma, U-Pb SHRIMP Ordoñez-Casado, 1998). It was coeval with the OMZ transtensive event and early Carboniferous magmatism (see section 11.2)

2.3.4 OMZ Magmatism

The OMZ magmatism can be divided into three main stages: Neoproterozoic-Cambrian Cadomian collision-related; Cambro-Ordovician, extension-related; and Carboniferous Variscan to Permian collision- and extension-related (Galindo and Casquet, 2004 and references therein). The stages are described briefly here and considered in more detail below in Chapter 3 and Chapter 11.

The Neoproterozoic magmatism occurred between 585-544 Ma. It comprises metamorphosed basic igneous rocks, amphibolites, and diorites–granites which have been

interpreted as subduction-related (Bellon et al., 1979; Quesada, 1990b; Schäfer, 1990; Oschner, 1993; Bandrés et al., 2004; Sánchez-Lorda et al., 2013).

The early Cambrian magmatism, occurred between 537-503 Ma. It is composed of peraluminous to metaluminous granites produced during initiation of extension (Galindo, 1989; Schäfer, 1990; Oschner, 1993; Galindo and Casquet, 2004; Chichorro et al., 2008; Sánchez-García et al., 2010; 2013; Pereira et al., 2011). Late Cambrian alkaline granitoids emplaced between 505-498 Ma, formed associated with an extensional event (Galindo and Casquet, 1985; Galindo et al, 1990; Montero et al., 1999; Salman, 2002). Cambro-Ordovician plutonic rocks intruded between 510-480 Ma have an anorogenic character related to progression of the extension that started in the Cambrian (Ábalos, 1992; Oschner, 1993; Sánchez-García et al., 2003; 2010).

The Carboniferous magmatism, 350-330 Ma, was a product of the Variscan Orogeny (e.g., Dallmeyer et al., 1995; Montero et al., 2000; Casquet and Galindo, 2004; Ordoñez-Casado et al., 2008; Pin et al., 2008). It comprises ultrabasic to acid, metaluminous alkaline to calc-alkaline, plutons and peraluminous dykes (Casquet and Galindo, 2004). Numerous plutons were emplaced in the Olivenza-Monesterio antiform related to this event, these massifs include: Bazana, Valuengo, Brovales, Valencia del Ventoso and Burgillos del Cerro in the central region and Santa Olalla to the southeast (Fig. 2.7). The last magmatic event in the region was Permian, extension-related, intrusion of dolerite dykes (Galindo et al., 1991).

2.3.5 OMZ Geophysical Overview

During the last 20-30 years numerous heat-flow, gravimetric, magnetometric and seismic studies have been carried out in the OMZ (e.g., Mueller et al., 1973; Prodehl et al., 1975; González et al., 1996; Simancas et al., 2003; Sánchez-Jiménez, 2004; García-Lobón, 2004; Carbonell et al., 2004; Palomeras et al., 2009; Brown et al., 2012).

Marzán et al., (1996) determined a value of 50 ± 14 mW/m^{-2} for the OMZ heat flux, which is comparable to that of the whole Iberian Massif (65 mW/m^{-2}, Fernández et al., 1998).

Gravimetric and magnetometric data indicate that the OMZ upper crust is 13-17 km thick and has a density of 2.73 g/cm^3 (Sánchez-Jiménez, 2004); the middle and lower crust are 15-17 km thick with densities of 2.82 g/cm^3 and 2.93 g/cm^3 respectively (Sánchez-Jiménez, 2004). Furthermore, at the Moho density increases to 3.3 g/cm^3.

The OMZ has a strong magnetic variability (Sánchez-Jiménez, 2004; García-Lobón, 2004; García-Lobón et al., 2006) especially in the Olivenza-Monesterio antiform

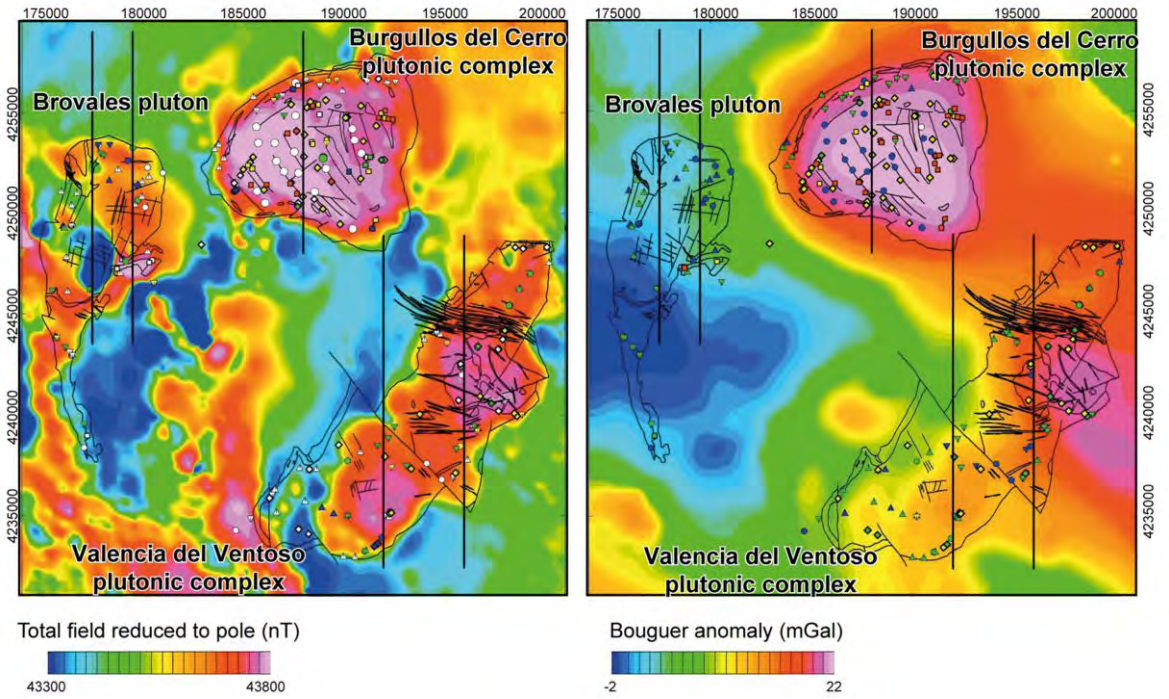

Figure 2.9. Total field reduced to pole magnetic and Bouguer gravity-density anomaly maps centred on the plutonic complexes of Burguillos del Cerro, Valencia del Ventoso and Brovales (modified from García-Lobón, 2004). Symbols are selected samples of García-Lobón, (2004) for petrophysical study that are not considered in this work.

which consists of a magnetic basement at a depth of 13.28 ± 0.23 km and some localised more magnetic minor bodies (García-Lobón, 2004; Sánchez-Jiménez, 2004)

The punctual magnetic and gravimetric variations are spatially associated with plutonic bodies that are well-exposed in the Olivenza-Monesterio antiform (García-Lobón, 2004; García-Lobón et al., 2006), namely the Burguillos del Cerro plutonic complex, the Valencia del Ventoso plutonic complex and the Brovales pluton the density and magnetic properties of which show notable differences (García-Lobón, 2004; García-Lobón et al., 2006) (Fig. 2.9). Such variations are the result of the lithological variations in each centre. In Burguillos del Cerro gabbros and diorites cause positive density and magnetic anomalies (Fig. 2.9) (García-Lobón, 2004; García-Lobón et al., 2006). In the Valencia del Ventoso plutonic complex the anomalies are related to the presence of hornblende in the monzodioritic and tonalitic rocks (Fig. 2.9) (García-Lobón, 2004; García-Lobón et al., 2006). By contrast, the Brovales pluton has less marked magnetic and gravimetric anomalies as a result of its more felsic tonalitic to granitic composition (Fig. 2.9) (García-Lobón, 2004; García-Lobón et al., 2006). Considered together the three complexes comprise a compositional range from ultrabasic to acid rocks and are, therefore, representative of the heterogeneous OMZ early Carboniferous magmatism.

Numerous deep seismic profiles have been done across the Iberian Massif (see review in Simancas et al., 2013). One of the most revealing of these was the IBERSEIS seismic profile (Fig. 2.10A) (Simancas et al., 2003) that runs for some 300 km, roughly northeast-southwest, crossing the SPZ, OMZ and CIZ and their tectonic boundaries (Fig. 2.10A) (Simancas et al., 2003). The profile shows a complete section of the Variscan belt crust in southwest Iberia, which is characterised by numerous well-defined reflectors (Fig. 2.10B) (Simancas et al., 2003). The profile shows that the Moho, detected as a strong drop in reflectivity at 10.5 s, is at a depth of 33 km (Figs. 2.10B and 2.10C) (Simancas et al., 2003). Moreover, the reflexion pattern is more marked and tilted in the upper crust than in the middle and lower crust (Figs. 2.10B and 2.10C) (Simancas et al., 2003). The profile also shows a band of high reflectivity located in the middle crust in the OMZ, terminates in the southern CIZ and is present at a shallower depth with a more diffuse character in the SPZ upper crust. (Fig. 2.10B and 2.10C) (Simancas et al., 2003). The feature was named the IBERSEIS Reflective Body (IRB) by Simancas et al., (2003), it is described in the next section (Figs. 2.10B and 2.10C) (Simancas et al., 2003).

2.3.5.1. The IBERSEIS Reflective Body

The IBERSEIS Reflective Body (IRB) band of mid-crustal high reflectivity marks a basal detachment plane for thrust and normal faults, including the Monesterio thrust. It can be traced to the surface and correlated with surface geology and, in particular, the OMZ structural features (Fig. 2.10C). The age of formation and nature of this prominent feature are questions that need to be addressed when interpreting the formation of the OMZ lithosphere.

2.3.5.1.1 The IBERSEIS Reflective Body Age

There are three main lines of evidence for constraining the age of the IRB, the relationship of the body with: i. the previously described regional Variscan structures, ii. the aforementioned widespread early Carboniferous high-medium-grade metamorphic event, and iii. the OMZ early Carboniferous ultramafic to mafic magmatism, specifically in the Santa Olalla plutonic complex.

The maximum age of the IRB is given by its relationship with structures related to the first collisional event recorded in the OMZ. Given that the IRB reflectors cut the traces of latest Devonian–earliest Carboniferous compressional structures, for example the Monesterio thrust, it can be fixed at 390-345 Ma (Simancas et al., 2003; Azor et al., 2008) (Fig. 2.10D). The first compression was followed by an intra-orogenic extensional/transtensional event (Apraiz and Eguiluz, 2002; Pereira et al., 2007).

The minimum age of the IRB is given by its relationship with structures related to the second collisional event because the IRB reflectors are cut by the traces of late Carboniferous

compressional structures (Fig. 2.10D) (Simancas et al., 2003), it can be fixed at 330-305 Ma (cf., Azor et al., 2008).

Significantly, the IRB age range suggested by the regional structures coincides with the high-medium-grade metamorphism that is well-exposed in Évora-Aracena-Lora del Río metamorphic belt (cf., Bard, 1969; Ordoñez-Casado, 1998; Apraiz and Eguiluz, 2002; Pereira et al., 2003; 2007; 2009; Díaz-Azpiroz et al., 2004; 2006). Pereira et al., (2009) related this localised HT-LP metamorphism and coeval magmatism, 350-335 Ma, to an intra-orogenic extensional event. Prior to geophysical evidence having revealed the IRB, Castro et al., (1999) had concluded that the metamorphism, recorded in the Beja-Acebuches amphibolites, and related magmatism such as the Aracena norites and gabbros, was the resulted of subduction of an ocean ridge beneath the OMZ. By contrast, Simancas et al. (2003) invoked emplacement of the IRB as the heat source for both the metamorphism and the melting so, linking its formation to the Variscan orogeny and ruling out the idea that it formed during the OMZ Cambro-Ordovician extensional event as suggested by Sarrionandia et al., (2012).

2.3.5.1.2 The IBERSEIS Reflective Body Nature

The geophysical properties of the mid-crustal IRB are the main source of information constraining its composition. Aeromagnetic data reveal that the OMZ has a widespread positive magnetic anomaly. Simancas et al. (2003) interpreted this as the result of an extensive sill-like mafic body at depth with numerous local magnetic anomalies that coincide with mafic rock outcrops (Ardizone et al., 1989).

The normal incidence reflection pattern and P- and S-wave velocity characteristics of the IRB resulted in it being interpreted as a sub-horizontal sill-like complex of mantle-derived ultramafic–mafic rocks and interlayered metasediments (Simancas et al., 2003; Carbonell et al., 2004). Further analysis using wide-angle data confirmed that the IRB is a high velocity zone, with a high Poission's ratio, supporting the interpretation that it comprises ultramafic–mafic bodies (Palomeras et al., 2011). Density models developed by these authors based on the velocity data are also consistent with the presence of mid-crustal high density bodies. A recent petrophysical study by Brown et al. (2012) focused on the geophysical properties of igneous and metamorphic rocks that crop out along the contact between the OMZ and SPZ. They concluded that the P- and S-wave seismic velocities and the density of the studied rocks are consistent with the interpretation of the IRB as an intraplated mafic sill. Notably, mafic igneous bodies have also been proposed as the source of conspicuous reflectivity in the upper crust of the adjacent SPZ (Schmelzbach et al., 2008).

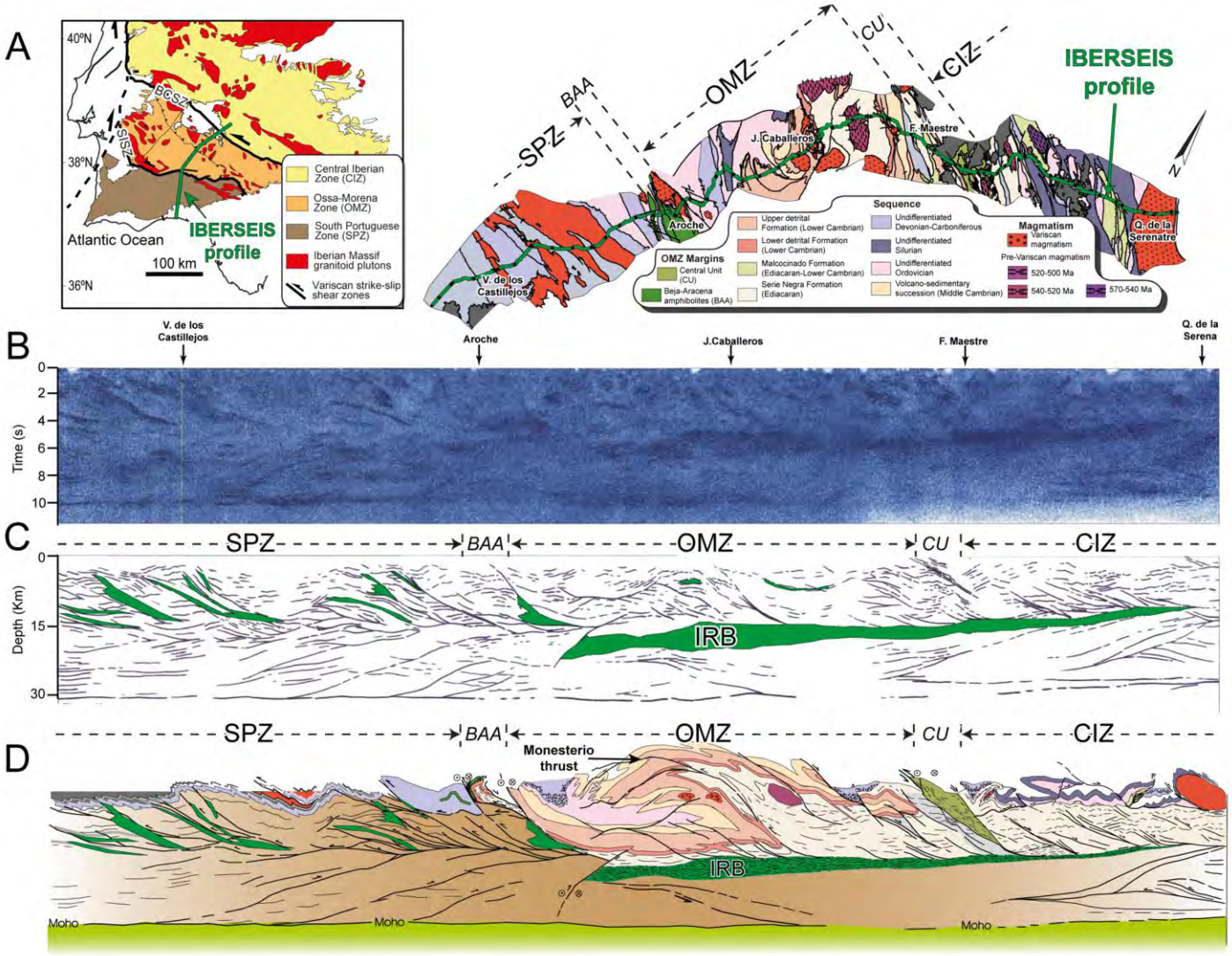

Figure 2.10. A) Trace of the IBERSEIS seismic profile in the SPZ, OMZ and CIZ. B) Time-migrated stack image and C) line drawing of the IBERSEIS deep seismic reflection profile. D) Geological interpretation of the crustal seismic structure of the IBERSEIS profile. All images and geological models are taken and modified from Simancas et al., (2003).

2.3.5.1.3 The Relationship between the IBERSEIS Reflective Body and the OMZ Carboniferous Magmatism

The suggestion of a link between underplated or intraplated mafic magmas and granitic magma production is not new (cf., Clemens, 1998; 2006; Brown, 2007; 2010).

Simancas et al., (2003), in their interpretation of the IBERSEIS deep seismic reflection profile, tentatively suggested a link between the IRB and the Carboniferous magmatism. They proposed that the sill-like body played an important role in the development of magmatism and related mineralization in the OMZ. Tornos et al., (2005; 2006) and Ordoñez-Casado et al., (2008) proposed that the IRB was key in the development of the mineralization of the alkaline-calc-alkaline Santa Olalla plutonic complex, that includes the Aguablanca mafic-ultramafic stock (cf., Romero et al., 2006; Ordoñez-Casado et al., 2008).

The Aguablanca stock Ni-Cu-PGE deposits led Lunar et al., (1997) and, later, Ortega et al., (2001; 2004), to propose an extensional context for their formation. In the absence of geochronological constraints these authors suggested a petrogenetic link with the well-established regional Cambro-Ordovician extensional event. However, subsequent dating has revealed that the Santa Olalla plutonic complex has an early Carboniferous age, 347-340 Ma (Romero et al., 2006; Ordoñez-Casado, 2008) thus constraining the tectonomagmatic context at that time as extensional.

In this thesis we shall investigate the possible link between the IRB and the OMZ plutonic rocks based on three main criteria: i. the coincident location; ii. the coeval age; and iii. the comparable composition.

Chapter 3: Previous Work

3.1 Pre-Variscan Magmatism

3.2 Variscan Magmatism

3.3 Post-Variscan Magmatism

3. Previous Work

Numerous studies have focused on the magmatic evolution of the Ossa-Morena Zone (OMZ) (e.g., Pascual, 1981, Pons, 1982; Castro, 1984; Eguiluz, 1988; Galindo, 1989; Abalos, 1990; García-Casquero, 1991; Quesada, 1991, Oschner, 1993; Azor, 1994; Ordoñez-Casado, 1998; Salman, 2002; Sarrionandia, 2005; Piña, 2006; Moita, 2007). These studies highlight the main differences between the magmatism of the OMZ and other Iberian Massif zones.

Compared with the other zones the OMZ magmatism is characterised by smaller sized intrusions, greater abundance of mafic magmatism and a longer age range Neoproterozoic to Permian (Fig. 3.1) (cf., Galindo and Casquet, 2004). The OMZ igneous rocks can be divided into three main stages: i. Pre-Variscan Neoproterozoic-Cambrian and Cambro-Ordovician rocks; ii. Variscan volcanic and plutonic Carboniferous rocks and iii. Post-Variscan Permian intrusions (Casquet and Galindo, 2004 and references therein). What follows summarises the previous work done in the area.

3.1 Pre-Variscan Magmatism

The brief description of the pre-Variscan magmatism given here is discussed in more detail in section 11.1.

3.1.1 Neoproterozoic-Cambrian

The OMZ Neoproterozoic magmatism (Fig. 3.1), 611-544 Ma, is related to the Cadomian Orogeny. Basic igneous rocks, now metamorphosed to amphibolites, 590-550 Ma, (Ordoñez-Casado, 1998) with a volcanic arc signature are interbedded in the Serie Negra (e.g., Eguiluz, 1988; Sánchez-Carretero. 1989; Sánchez-Lorda et al., 2013). Furthermore, subduction-related calc-alkaline intermediate to felsic plutonic and volcanic rocks crop out in the Malcocinado Formation (Bellon et al., 1979; Quesada, 1990a; Pin et al., 2002; Bandrés et al., 2004; Kröner and Romer, 2013 and references therein).

The early Cambrian magmatism (Fig. 3.1), 540-520 Ma, is composed of metaluminous to peraluminous rocks produced during initiation of extension, the 'early rift-related event' (Galindo, 1989; Oschner, 1993; Sánchez-García et al., 2010; 2013). Middle Cambrian, 520-500 Ma, magmatism comprises mafic, OIB- and MORB-like, and felsic, alkaline and peraluminous, compositions associated with progression of the early Cambrian extension that led to the 'main rift-related event' (Galindo and Casquet, 1985; Galindo et al, 1990; Montero et al., 1999; Salman, 2002; Sánchez-García et al., 2003).

3.1.2 Cambro-Ordovician

The OMZ Cambro-Ordovician magmatism (Fig. 3.1), 490-470 Ma, has an anorogenic character (Ábalos, 1992; Oschner, 1993; Sánchez-García et al., 2003; 2010). This stage is characterised by bimodal compositions: mafic, N-MORB-like (Ordoñez-Casado, 1998); and felsic, peralkaline and peraluminous, rocks (Sánchez-Carretero et al., 1999; Montero et al., 1999; Chichorro et al., 2008; Díez-Fernández et al., 2014).

3.1.3 Pre-Variscan Plutons

The Olivenza-Monesterio pre-Variscan plutonic rock are represented by: Barcarrota (505±5 Ma Rb-Sr WR, Galindo et al., 1990; 501+5-2 Ma U-Pb TIMS, Oschner, 1993); Táliga (525± 1 Ma, U-Pb monazite TIMS, Oschner, 1993); Salvatierra (516+9-3 Ma, U-Pb TIMS, Oschern, 1993); Almendral (470±10 Ma, WR K-Ar, Galindo unpublished data in Casquet and Galindo, 2004); Castillo (502±8 Ma KOBER method, Salman, 2002); Culebrin (532±4 Ma KOBER method, Salman, 2002) and Monesterio (510±4 Ma in granodiorite, KOBER method, Salman and Montero, 1999 and 511±40 Ma for migmatite, Rb-Sr WR, Salman, 2002) (Fig. 3.2). These plutonic intrusions are related to the Cambro-Ordovician rifting event recorded in the OMZ (see Chapter 11) (Oschner, 1993; Sánhez-García et al., 2003, Linnemann et al., 2008).

3.2 Variscan Magmatism

The OMZ Variscan magmatism is abundant (Fig. 3.1), it includes minor volcanism, interbedded in Carboniferous sediments, and extensive plutonism. The plutonic bodies are spread throughout the OMZ in five main regions: i. the La Coronada-Villaviciosa complex (Apalategui et al., 1985, Delgado-Quesada et al., 1985), ii. the Nisa-Santa Eulalia plutons (González-Menéndez and Bea, 2004; Solá, 2007; Solá et al., 2009), iii. the Évora Massif (Pereira et al., 2003; 2009; 2015; Moita et al., 2009; Lima et al., 2012), iv. the Beja-Aracena intrusive complex (Fonseca and Ribeiro, 1993; Quesada et al., 1994; Castro et al., 1996; Pin et al., 2008) and v. the Olivenza-Monesterio complex, see below (Fig. 3.1A).

3.2.1 Early Carboniferous Volcanic Rocks

Variscan volcanism is well-represented in the La Coronada-Villaviciosa complex and the Olivenza-Monesterio complex (Delgado-Quesada, 1971; Chaumerail, 1975; Eguiluz et al., 1985; Giese et al., 1994). The volcanic rocks are basaltic andesites and dacites in the lower part of the sequence, all of which are cut by hypabyssal rocks (cf., Eguiluz et al., 1985). By contrast, the upper part of the sequence comprises more evolved rocks, rhyolitic volcaniclastic deposits (Odriozola et al., 1983; Giese et al., 1994, Sanchez-Carretero et al., 1990). Fossils found in the

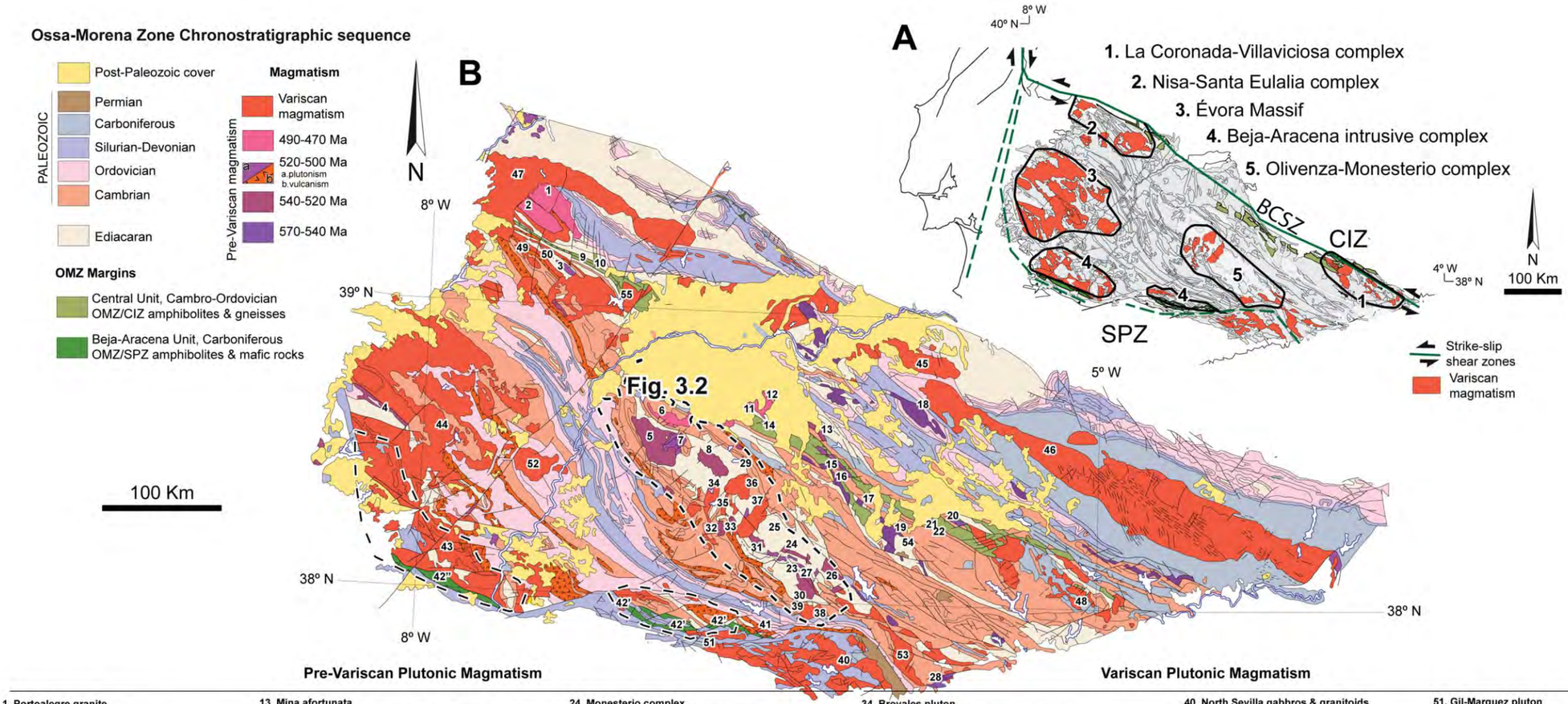

1. Portoalegre granite
493±4 Ma U-Pb SHRIMP (Sola, 2007)

2. Carrascal granodiorite
486±7 Ma U-Pb LA-ICP-MS (Sola, 2007)

3. Barquete granite
526±4 Ma U-Pb SHRIMP (Pereira et al., 2011)

4. Évora Massif gneiss
527-505 Ma U-Pb SHRIMP (Chichorro et al., 2008)

5. Taliga granite
525±2,5 Ma Rb-Sr, (Galindo et al., 1990)
525±1 Ma TIMS monacite, (Ochsner, 1993)

6. Almedral granite
450±12 Ma K-Ar, (Galindo & Portugal-Ferreira, 1988)
481±10 Ma K-Ar, (Galindo & Portugal-Ferreira, 1988)

7. Barcarrota granite
505±5 Ma Rb-Sr, (Galindo et al., 1990)
501+4-3 Ma TIMS zircon (Ochsner, 1993)
503+5-2 Ma TIMS zircon (Ochsner, 1993)

8. Salvatierra granite
516+9-3 Ma TIMS Zircon (Ochsner, 1993)

9. Campo Maior gneiss
488±2 Ma U-Pb SHRIMP (Pereira et al., 2010b)

10. Aroches migmatite
465±4 Ma U-Pb SHRIMP (Ordoñez-Casado, 1998)

11. Aceuchal gneiss
477±5 Ma TIMS zircon (Ochsner, 1993)

12. Almendradejo gneiss
475+10-6 Ma TIMS zircon (Ochsner, 1993)

49. Barreiros granite
525±1 Ma TIMS zircon (Sánchez-Garcia et al., 2013)

13. Mina afortunata
507+9-6 Ma TIMS Monacite, granodiorite (Ochsner, 1993)
523±7 Ma U-Pb SHRIMP, leucosome (Ordoñez-Casado, 1998)
554±16 Ma U-Pb SHRIMP, amphibolite (Ordoñez-Casado, 1998)
532±4 Ma TIMS Zircon, leucosome (Sánchez-García et al., 2008)

14. El pocico amphibolite
483±13 Ma U-Pb SHRIMP, (Ordoñez-Casado, 1998)

15. Ribera del fresno gneiss
475±7 Ma U-Pb SHRIMP, (Ordoñez-Casado, 1998)

16. Mosquil tonalite
544+6-5 Ma TIMS zircon, (Ochsner, 1993)

17. Higuera gneiss
460±4 Ma U-Pb SHRIMP, (Ordoñez-Casado, 1998)

18. Serena granitoid
573±14 Ma U-Pb SHRIMP, (Ordoñez-Casado, 1998)

19. Ahillones
585±5 Ma TIMS zircon, granodiorite (Schäfer, 1990)
550±10 Ma U-Pb SHRIMP, granite (Ordoñez-Casado, 1998)

20. Las Minillas gneiss
556+159-67 Ma TIMS zircon, (Ochsner, 1993)

21. Arroyo Argallón
525±13 Ma U-Pb SHRIMP, amphibolite (Ordoñez-Casado, 1998)
509±8 Ma U-Pb SHRIMP, gneiss (Ordoñez-Casado, 1998)
514±8 Ma U-Pb SHRIMP, leucosome (Ordoñez-Casado, 1998)

22. Las mesas retrogressed eclogite
596±14 Ma U-Pb SHRIMP, (Ordoñez-Casado, 1998)

23. Calera de Leon granite
524±4 Ma KOBER (Salman & Montero, 1999)

50. Peralkaline orthogneis
490-470 Ma LA-ICP-MS zircon (Díez-Fernández et al., 2014)

24. Monesterio complex
527+10-7 Ma TIMS xenotime, granodiorite (Ochsner, 1993)
510±4 Ma KOBER, granodiorite (Montero et al., 1999)
533±8 Ma U-Pb SHRIMP, leucosome (Ordoñez-Casado, 1998)
495±8 Ma TIMS Zircon, granodiorite (Schäfer, 1990)
507±21 Ma TIMS Apatite, granodiorite (Schäfer, 1990)

25. Monteagudo gabro
536±11 Ma U-Pb SHRIMP, (Ordoñez-Casado, 1998)

26. Pallares granodiorite
518±15 Ma U-Pb SHRIMP, (Ordoñez-Casado, 1998)

27. Culebrin Tonalite
532±4 Ma KOBER (Salman, 2002)

28. Lora del Rio granodiorite
600±13 Ma U-Pb SHRIMP (Ordoñez-Casado, 1998)

29. Sierra Vieja granite
518±5 Ma TIMS zircon, (Sánchez-García et al., 2008)

30. Castillo granite
498+10-7 Ma TIMS zircon, (Ochsner, 1993)
502±8 Ma KOBER, (Salman, 2002)

31. Tablada granite
511±8 Ma TIMS monazite, (Ochsner, 1993)
512±8 Ma TIMS xenotime, (Ochsner, 1993)

32. Remedios granite
517±2 Ma TIMS zircon, (Sánchez-García et al., 2008)

33. Leucogranite
510±3 Ma U-Pb SHRIMP, (Present work)

34. Brovales pluton
340±4 Ma Pb-Pb Kober Method, (Montero et al., 2000)
339±4 Ma U-Pb SHRIMP, q-monzodiorite (Present work)
341±4 Ma U-Pb SHRIMP, gabbronorite (Present work)
339±4 Ma U-Pb SHRIMP, syenogranite (Present work)
340±2 Ma U-Pb SHRIMP, aplite (Present work)

35. Valuengo gabbro
342±4 Ma Pb-Pb Kober Method, (Montero et al., 2000)

36. Burguillos del Cerro plutonic complex
342-335 Ma Ar-Ar, (Dallmeyer et al., 1995)
330±9 Ma Rb-Sr, leucogranite (Bachiller et al., 1997)
336±2 Ma U-Pb SHRIMP, gabbronorite (Present work)
338±4 Ma U-Pb SHRIMP, diorite (Present work)
335±2 Ma U-Pb SHRIMP, alkaline feldspar granite (Present work)
335±2 Ma U-Pb SHRIMP, q-diorite (Present work)
335-330 Ma, two-mica granite (Present work)

37. Valencia Ventoso plutonic complex
338±3 Ma U-Pb SHRIMP, diorite (Present work)
330±4 Ma U-Pb SHRIMP, q-Monzodiorite (Present work)
333±2 Ma U-Pb SHRIMP, granodiorite (Present work)
336±2 Ma U-Pb SHRIMP, monzogranite (Present work)
329±6 Ma U-Pb SHRIMP, leucogranite (Present work)

38. Santa Olalla-Agua Blanca complex
344±2 Ma U-Pb SHRIMP, gabbro (Ordoñez-Casado et al., 2008)
338±3 Ma Ar-Ar phologopite, grabbronorite (Tornos et al., 2004)
339±1 Ma TIMS Zircon, diorite (Romero et al., 2006b)
341±2 Ma TIMS Zircon, mingled body (Romero et al., 2006b)
342±3 Ma TIMS Zircon, tonalite (Romero et al., 2006b)
341±2 Ma TIMS Zircon, Hb tonalite (Romero et al., 2006b)
347±3 Ma U-Pb SHRIMP, granodiorite (Ordoñez-Casado et al., 2008)
339±3 Ma Ma TIMS Zircon, granite (Romero et al., 2006b)

39. Teuler granite
348±4 Ma Pb-Pb Kober Method (Montero et al., 2000)
338±2 Ma TIMS zircon (Romero et al., 2006b)

40. North Sevilla gabbros & granitoids
c. 336 Ma Rb-Sr (De la Rosa et al., 1993)

41. Aracena belt norites, nebulites and migmatites
328±4 Ma Rb-Sr (Castro et al., 1999)
340±23 Ma Sm-Nd (Castro et al., 1999)
323±4 Ma Rb-Sr (Castro et al., 1999)
331±7 Ma Rb-Sr (Castro et al., 1999)

42. Beja-Acebuche amphibolite & metagabbros 42'.
335±3 Ma Ar-Ar, (Castro et al., 1999)
334±3 Ma U-Pb SHRIMP, (Azor et al., 2008)
42".
342±2 Ma Ar-Ar, (Castro et al., 1999)
339±4 Ma U-Pb SHRIMP, (Azor et al., 2008)

43. Beja Igneous complex
352±2 Ma TIMS zircon, (Pin et al., 2008)
342±9 Ma U-Pb SHRIMP, (Jesus et al., 2006)

44. Évora Massif
323±5 Ma Ar-Ar, (Moita et al., 2005c)
340±6 Ma U-Pb SHRIMP, (Pereira et al., 2009)
337±4 Ma U-Pb SHRIMP, (Pereira et al., 2009)
339-341 Ma U-Pb SHRIMP, (Pereira et al., 2012)
328-317 Ma U-Pb SHRIMP, (Lima et al., 2012)

45. Pedroches granodiorite
314±2 Ma TIMS zircon, (Carracedo et al., 2009)

46. Pedroches granite
308±1 Ma TIMS zircon, (Carracedo et al., 2009)

47. Nisa granite
307±4 Ma U-Pb SHRIMP, (Sola et al., 2009)

48. Villaviciosa granite
316±16 Ma K-Ar, (Bellon et al., 1979)
332±17 Ma K-Ar, (Bellon et al., 1979)

51. Gil-Marquez pluton
354-335 Ma LA-ICP-MS zircon (Gladney et al., 2014)

52. Regueros de Mosaraz pluton
337±16 Ma TIMS zircon (Antunes et al., 2011)

54. Azuaga orthogneis
347-341 Ma U-Pb SHRIMP, (Ordoñez-Casado, 1998)

53. Lora del Rio granodiorite
c. 340 Ma U-Pb SHRIMP, (Ordoñez-Casado, 1998)

55. Campo Maior gneisses
340-334 Ma LA-ICP-MS zircon (Pereira et al., 2010a; 2010b)

Figure 3.1. The Ossa-Morena Zone with respect to the South Portuguese Zone (SPZ) and the Central Iberian Zone (CIZ) highlighting the main Variscan intrusive complexes. B) Chronostratigraphic sequence of the Ossa-Morena Zone indicating the different types of pre-Variscan and Variscan magmatism in the area, modified from Gabaldón et al., (2001).

sediments interbedded with the volcanic rocks indicate a Tournaisian-Visean early Carboniferous age for the deposits (Expósito, 2000). The igneous rocks have a K-rich calc-alkaline signature (Chaumerail, 1975, Giese et al., 1994). The volcanism was associated with early Carboniferous extension that also resulted in intrusion of plutons, particularly in the La Coronada-Villaviciosa complex (Delgado-Quesada et al., 1985).

3.2.2 Early Carboniferous Plutonic Rocks

Numerous pre-Variscan and Variscan magmatic intrusions are emplaced throughout Olivenza-Monesterio complex in the central part of the OMZ (Fig. 3.1 and 3.2).

The Variscan magmatism in the Olivenza-Monesterio complex comprises several epizonal plutons (Fig. 3.2). These complexes are composed of mafic to felsic rocks with, in general, a calc-alkaline composition (Casquet and Galindo, 2004). A common characteristic is zonation with mafic rocks in the core of the plutons and more felsic rocks at the rim (Casquet and Galindo, 2004) (Fig. 3.2). In detail, the complexes are composed of gabbros, in some cases ultramafic rocks, and tonalites-granodiorites to granites (Fig. 3.2). The main plutonic bodies are:

i. The Burguillos del Cerro plutonic complex with ultramafic to felsic rocks (Fig. 3.2, 337±3 Ma amphibole Ar-Ar Dallmeyer et al., 1995; García-Casquero, 1991; Bachiller et al., 1997).

ii. The Valencia del Ventoso plutonic complex composed of gabbros to granites (349±28 Ma WR Rb-Sr Sarrionandia et al., 2007).

iii. The Brovales pluton composed of quartz diorites to granites (342±4 Ma, KOBER method, granodiorite, Montero et al., 2000; Galindo and Casquet, 2004).

iv. The La Bazana late-Variscan granitic pluton (Galadí-Enriquez et al., 2000; 2003).

v. The Santa Olalla-Aguablanca plutonic complex comprises ultramafic to intermediate rocks (Fig. 3.2) (344±3 Ma U-Pb SHRIMP Ordoñez-Casado et al., 2008; Tornos et al., 2006; Romero et al., 2006a; 2006b).

The first three plutons are the focus of this study and will be considered in detail below. Here a brief summary of them is given into permit comparison with the other complexes described in the next sections.

3.2.2.1 Burguillos del Cerro Plutonic Complex

The Burguillos del Cerro plutonic complex is composed of ultramafic-mafic, intermediate and subordinate felsic rocks (Pons, 1975, 1982; García-Casquero, 1991; 1995; Dallmeyer et al., 1995; Bachiller et al., 1997; Casquet and Galindo, 2004). It may be divided into four main units: a gabbroic layered association; a gabbroic non-layered association; a dioritic association; and, a

granitic association (Fig. 3.2) (Pons, 1982; García-Casquero et al., 1991). The age of the complex is given by: two amphibole-bearing gabbros from the gabbroic layered association, 342±1 Ma and 336±2 Ma (Ar-Ar amphibole, Dallmeyer et al., 1995); two quartz monzodiorites from the gabbroic non-layered association, 336±2 and 329±1 Ma (Ar-Ar amphibole, Dallmeyer et al., 1995); one diorite from the dioritic association, 338±1 Ma (Ar-Ar amphibole, Dallmeyer et al., 1995); and, leucogranites from the granitic association, 330±9 Ma (Rb-Sr WR, Bachiller et al., 1997).

Two main petrogenetic models have been proposed for the Burguillos del Cerro plutonic complex. The first suggested production of calc-alkaline composition rocks by differentiation from a tholeiitic parental magma (Pons, 1982) The second proposed a multi-stage evolution. Cambro-Ordovician emplacement of the gabbroic layered association, gabbroic non-layered association and alkaline granites related to rifting. Then, during the Variscan Orogeny, emplacement of the dioritic association, which intruded the other units and reset their Ar-Ar ages (García-Casquero, 1991).

3.2.2.2 Valencia del Ventoso Plutonic Complex

The Valencia del Ventoso plutonic complex is principally composed of intermediate and, minor, mafic rocks (Pons, 1982; Sarrionandia, 2005; García-Lobón et al., 2006; Sarrionandia et al., 2007; 2011). The complex has been divided into four main bodies: the Valencia del Ventoso main pluton; the Medina de las Torres stock; the Cortijo del Pozuelo stock; and, the Intrusive dyke complex (Fig. 3.2, Pons, 1982; Sarrionandia, 2005). The granodiorites and granites yielded a Rb-Sr WR age of 349±28 Ma (Sarrionandia et al., 2007). The complex was interpreted to be the result of partial melting of a supra-subduction enriched spinel, amphibole and phlogopite lherzolite in a transtensional context related to OMZ and SPZ collision during the Tournasian (*c.* 349 Ma) (Pons, 1982; Sarrionandia, 2005). The compositional range was attributed to fractional crystallization (Pons, 1982; Sarrionandia, 2005).

3.2.2.3 Brovales Pluton

The Brovales pluton is concentrically zoned with quartz diorites and tonalites at its core, surrounded by granodiorites and fine grain granites at the outer rim (Fig. 3.2) (Brun and Pons, 1981; Pons, 1982). The pluton is asymmetric, recording the main stages of Variscan deformation (Pons, 1982; Expósito, 2000; Eguiluz et al., 2004). Granodiorites were dated at 340±7 Ma (KOBER method, Montero et al., 2000). Pons, (1982), concluded that the compositional variations in the pluton resulted from fractional crystallization of a subduction-related calc-alkaline parental magma.

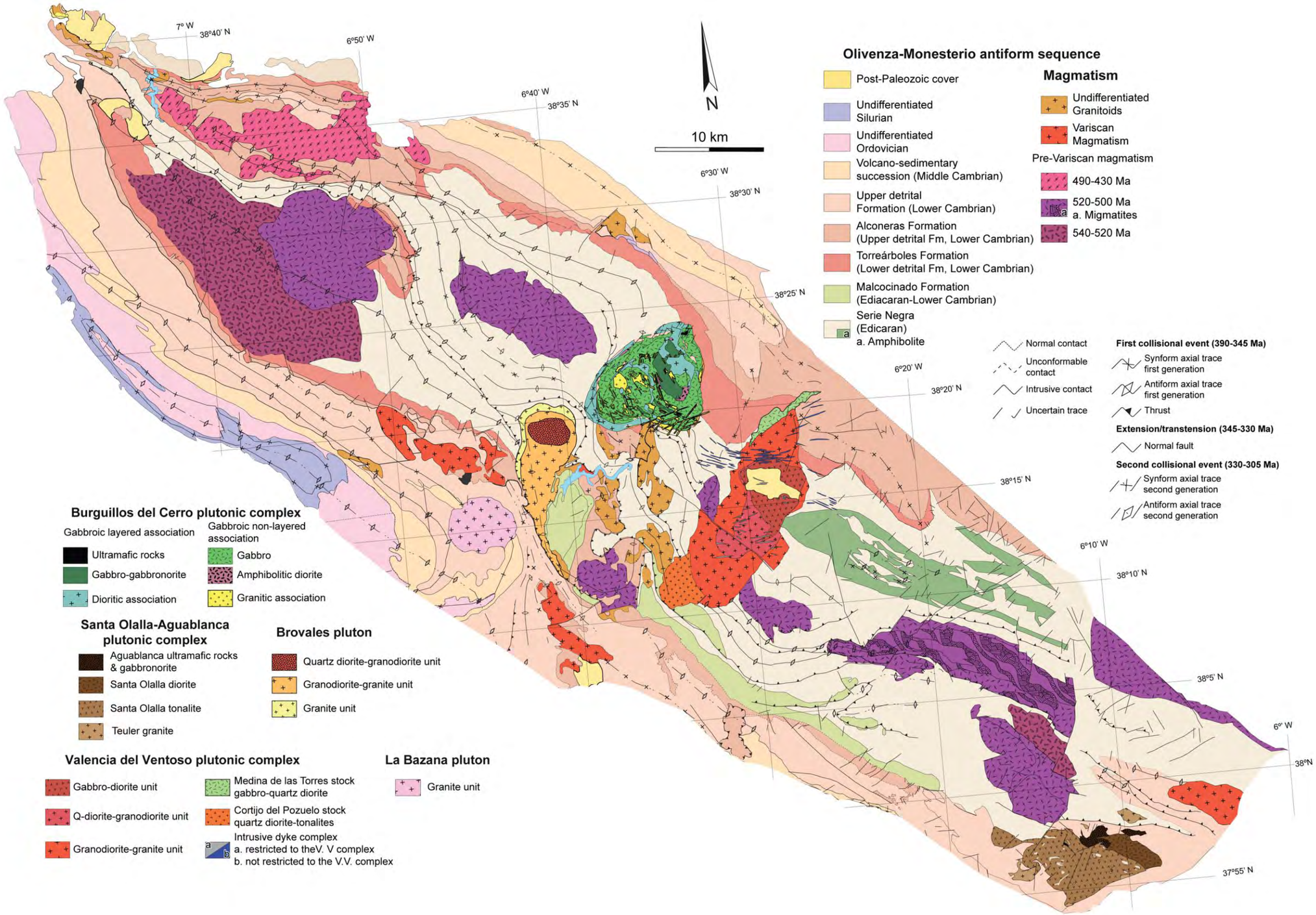

Figure 3.2. Geological map of the Olivenza-Monesterio Complex. Note the different fold generations and principal intrusive bodies of the pre-Variscan magmatism and migmatites and the main Variscan intrusions highlighting the Burguillos del Cerro plutonic complex, Santa Olalla-Aguablanca plutonic complex, Brovales pluton, Valencia del Ventoso plutonic complex and La Bazana pluton, modified from Pons, (1982), García-Casquero, (1991), Expósito (2000), Gabaldón et al., (2001), Tornos et al., (2004), Piña, (2006) and Ordoñez-Casado et al., (2008).

3.2.2.4 La Bazana Pluton

The La Bazana pluton crops out in the south of the Olivenza-Monesterio antiform cutting Cambrian sediments and the Variscan structures (Fig. 3.2). It is a small diameter *c.* 6 km circular pluton composed of medium-grained peraluminous monzogranites with plagioclase, alkali feldspar, quartz, biotite and primary muscovite (Fernández-Carrasco et al., 1981; Galadí-Enríquez et al., 2000; 2003). Expósito (2000) interpreted it as late-orogenic, the last expression of Variscan magmatism in the OMZ, 330-305 Ma.

3.2.2.5 Santa Olalla-Aguablanca Plutonic Complex

The Santa Olalla-Aguablanca plutonic complex is located close to the OMZ southeast boundary with the SPZ (Fig. 3.1 and 3.2). It cuts Serie Negra and Cambrian sediments (Fig. 3.2) and comprises three main intrusions: i. the Santa Olalla pluton, main intrusion; ii. the Aguablanca stock; and, iii. the Teuler granite (Fig. 3.2) (Casquet, 1980; Eguiluz, 1988; Eguiluz et al., 1989; Casquet et al., 1998; Salman, 2002; Tornos et al., 2006; Piña, 2006; Ordoñez-Casado et al., 2008).

The Santa Olalla pluton is composed of diorites-tonalites, granodiorites and granitic dykes (Velasco and Amigó, 1981; Casquet et al., 2001; Salman, 2002). These rocks were dated at: tonalites 341±3 Ma (U-Pb zircon TIMS, Romero et al., 2006b); granodiorites 347±3 Ma (U-Pb SHRIMP Ordoñez-Casado et al., 2008) and granites 339±3 Ma (U-Pb zircon TIMS, Romero et al., 2006b).

The diorites are coarse- to medium-grained and composed of amphibole, biotite, plagioclase, alkali feldspar and quartz. Tonalites, volumetrically the most important composition, contain amphibole, biotite, plagioclase and quartz. All the intermediate rocks are subalkaline (SiO_2 54-63 wt %, Na_2O+K_2O 4-7 wt %) metaluminous to slightly peraluminous (ASI 0.1-1.1) with an intermediate content of K_2O (1.5-3.5 wt %) and variably ferroan character (molar $FeO_T/(FeO_T+MgO)$ ≈ 0.3-0.7). Chondrite-normalised rare earth element diagrams show an enrichment in LREE relative to HREE with some rocks having negative Eu anomalies. The isotopic compositions have a marked crustal signature $\varepsilon Nd_{332\ Ma}$ of -6 to -8 and $^{87}Sr/^{86}Sr_{332\ Ma}$, 0.709235-0.710557.

The granitic rocks are composed of aggregates of pyroxene-amphibole-biotite and individual crystals of biotite, plagioclase, alkali feldspar and quartz. These rocks have both alkaline to subalkaline (SiO_2 67-74 wt%, Na_2O+K_2O 7-9 wt %) peraluminous (ASI 0.01-1) and peralkaline-metaluminous compositions (AGPI 0.73-6.42). Moreover, they have a variable ferroan character (molar $FeO_T/(FeO_T+MgO)$ 0.31-0.70) and K_2O (0.84-5.1 wt %), Na_2O (3-7 wt %), Zr (105-1010 ppm) and Nb (20-133 ppm).

The Aguablanca stock is emplaced to the north of the Santa Olalla pluton (Fig. 3.2). It is mainly formed of gabbros and gabbronorites with subordinate diorites. Notably, mingling relationships were described between the gabbroic rocks and diorites (Casquet, 1980, Tornos et al., 2001; 2006; Romero et al., 2006a; 2006b; Piña et al., 2006). The age of the Aguablanca stock was determined for: a gabbronorite, 338±3 Ma (Ar-Ar phlogopite, Tornos et al., 2004); a gabbro, 344±2 Ma (U-Pb SHRIMP, Ordoñez-Casado et al., 2008); a diorite dyke, 339±1 Ma (U-Pb zircon TIMS, Romero et al., 2006b); and a mingled body, 341±2 (Ma TIMS zircon, Romero et al., 2006b).

The Aguablanca stock, gabbronorites and gabbros are composed of orthopyroxene, clinopyroxene and plagioclase. The diorites also contain orthopyroxene, clinopyroxene, amphibole, phlogopite, plagioclase and quartz. The rocks have alkaline to subalkaline, (SiO_2 49-61 wt%, Na_2O+K_2O 2-7 wt %) compositions with variable TiO_2 (1-1.5 wt %) and Mg# (0.6-0.8). Silicate Earth-normalised trace elements diagrams show enrichment in incompatible elements and cumulitic features with strong positive anomalies in U, Pb, Sr and Eu.

Notably, mineralised host rocks have a similar mineralogical association to the non-mineralised rocks. Ore deposits, Ni–Cu-PGM, were identified in the stock (Ortega et al., 2004; Piña et al., 2008). In general, the mineralization is massive and is found in the ultramafic-mafic rocks: wehrlites, harzburgites, dunites, gabbros and anorthosites (Tornos et al., 2005; 2006; Romeo et al., 2006a; 2006b; 2007; Piña, 2006; Piña et al., 2010). Mineralised host rocks were classified as cumulates with $MgO/SiO_2 \approx 0.05\text{-}1.05$, $Al_2O_3 \approx 0.75\text{-}33$ wt % and Mg# ≈ 0.36-0.84. Chondrite-normalised rare earth element diagrams for dunites and pyroxenites have low contents of LREE and HREE and no Eu anomaly. On the other hand, gabbros and gabbronorites are more enriched in LREE relative to HREE with slight Eu negative anomalies. The isotopic compositions may be divided into two main groups: i. the first is composed of unmineralised rocks with $\varepsilon Nd_{338\ Ma}$ of -5 to -7 and $^{87}Sr/^{86}Sr_{338\ Ma}$ 0.70800-0.710765 similar to the Santa Olalla main pluton; and, ii. the second, of mineralised rocks, has $\varepsilon Nd_{338\ Ma}$ of -4 to -6 and $^{87}Sr/^{86}Sr_{338\ Ma}$, 0.706863-0.710557. In the latter group some samples have a more primitive character, $\varepsilon Nd_{338\ Ma}$ up to 9 and $^{87}Sr/^{86}Sr_{338\ Ma}$ 0.701707 (Casquet et al., 2001; Tornos et al., 2006).

The Teuler granite crops out to the south of the Santa Olalla pluton (Fig. 3.2). Mainly composed of granitic rocks with minor intermediate enclaves, it was dated at 348±4 Ma (KOBER method, Montero et al., 2000) and 338±2 Ma (U-Pb TIMS zircon, Romero et al., 2006b). Another intrusion in the region that is compositionally comparable to the Teuler granite is the Helenchoso granite to the north of Santa Olalla (Casquet, 1980; Eguiluz, 1987; Eguiluz et al., 1989; Salman, 2002).

The granite is fine- to medium-grained, with holocrystalline hypidiomophic textures and biotite, plagioclase, alkali feldspar and quartz. The more intermediate enclaves are fine-grained quartz monzonites and monzogranites composed of allotrimorphic biotite and plagioclase, alkali feldspar and quartz. The granite is subalkaline (SiO_2 68-72 wt%, Na_2O+K_2O 7-8 wt %) and peraluminous (ASI 1-1.15) with elevated K_2O (4-5 wt%). Silicate Earth-normalised trace elements diagrams show enrichment in incompatible elements with positive anomalies in U, Pb, and Zr and negative anomalies in Nb, P, Ti, Sr and Eu. The isotopic composition of this granite indicates a crustal component with $\varepsilon Nd_{348\ Ma}$ of -7 and $^{87}Sr/^{86}Sr_{348\ Ma}$, 0.709381 (Salman, 2002).

Geological, geochemical and geochronological studies indicate that the different rock types from the Santa Olalla-Aguablanca plutonic complex are petrogenetically linked (Casquet et al., 2001; Salman, 2002; Tornos et al., 2006; Romero et al., 2006b). The formation of this complex has been associated with the early Carboniferous extension-related event (Tornos et al, 2006; Romero et al., 2006a; 2006b; Ordoñez-Casado, 2008).

3.3 Post-Variscan Magmatism

Post-Varsican dolerite dykes cut the OMZ Variscan plutons and sedimentary sequences (Fig. 3.2, Casquet, 1980, Pons, 1982, Galindo and Casquet, 1985; Galindo, 1989). These dykes are oriented northwest-southeast (Fig. 3.2). Compositional data reveal that they are olivine tholeiites (Casquet and Galindo, 2004). This extension-related magmatism has a Permian age of 250±5 in the Olivenza-Monesterio antiform, (K-Ar WR, Galindo et al., 1991) and of *c.* 257 Ma in Arouca, Portugal (Portugal-Ferreira et al., 1982).

Chapter 4: Field Relations

4.1 Burguillos del Cerro Plutonic Complex

4.2 Valencia del Ventoso Plutonic Complex

4.3 Brovales Pluton

4.4 Cambrian leucogranite

and Serie Negra metasediment

4. Field Relations

4.1 Burguillos del Cerro Plutonic Complex

The Burguillos de Cerro plutonic complex crops out over an area of about 100 km^2 in the central part of the Olivenza-Monesterio antiform (Fig. 4.1 and Fig. 3.2). It has a rounded morphology and comprises, predominantly, ultramafic to mafic layered and gabbroic rocks (Fig. 4.1). The plutonic complex cuts structures, both thrusts and folds, related to the first compressional phase of deformation 390-345 Ma (Fig. 4.1) (Expósito, 2000). It principally intruded the OMZ basement Ediacaran Serie Negra, (Fig. 4.1). In the northeast and southwest, however, the complex intruded the OMZ basement Neoproterozoic to lower Cambrian Malcocinado and lower Cambrian Torreárboles and Alconeras formations (Fig. 4.1).

Pons (1982) and García-Casquero, (1991) studied the Burguillos del Cerro plutonic complex in detail. These authors observed that the complex comprises ultramafic to granitic rocks but is predominantly gabbroic (Fig. 4.1). Both works concluded that the complex is formed by a central core of layered gabbros intruded by diorites and granodiorites (Fig. 4.1). Nevertheless, important differences exist between the two studies in terms of the cartography and classification of the main rock types.

Pons (1982) defined four main rock groups based on petrographic and structural criteria: i. ultramafic 'early cumulates' that include olivine gabbros and also gabbros and gabbronorites with distinctive poikilitic amphibole, known locally as the 'ojo de culebra', snake eye, facies ii. 'blue' facies gabbros and diorites with amphibole and biotite. These two groups form the main mass of the complex, they are bordered by; iii. peripheral facies amphibole- and biotite-bearing diorites and granodiorites; and cut by iv. granites veins that are mainly found in the central part of the complex.

García-Casquero (1991) also defined four groups on the basis of petrographic and structural criteria i. a gabbroic association which he divided into a layered series (Pons' group 1) and an unlayered series (including rocks from Pons' groups 1 and 2); ii. a dioritic association (all the intermediate rocks from Pons' groups 2 and 3); iii. a feldspathic association of alkaline granites (not described by Pons); and iv. a late peraluminous granite and aplite association (Pons' group 4).

The fieldwork undertaken in the current work was based on the aforementioned maps with an aim to clarify the main differences between them. From an iterative process of combining field relations information with mineralogical, petrographic, and compositional characteristics

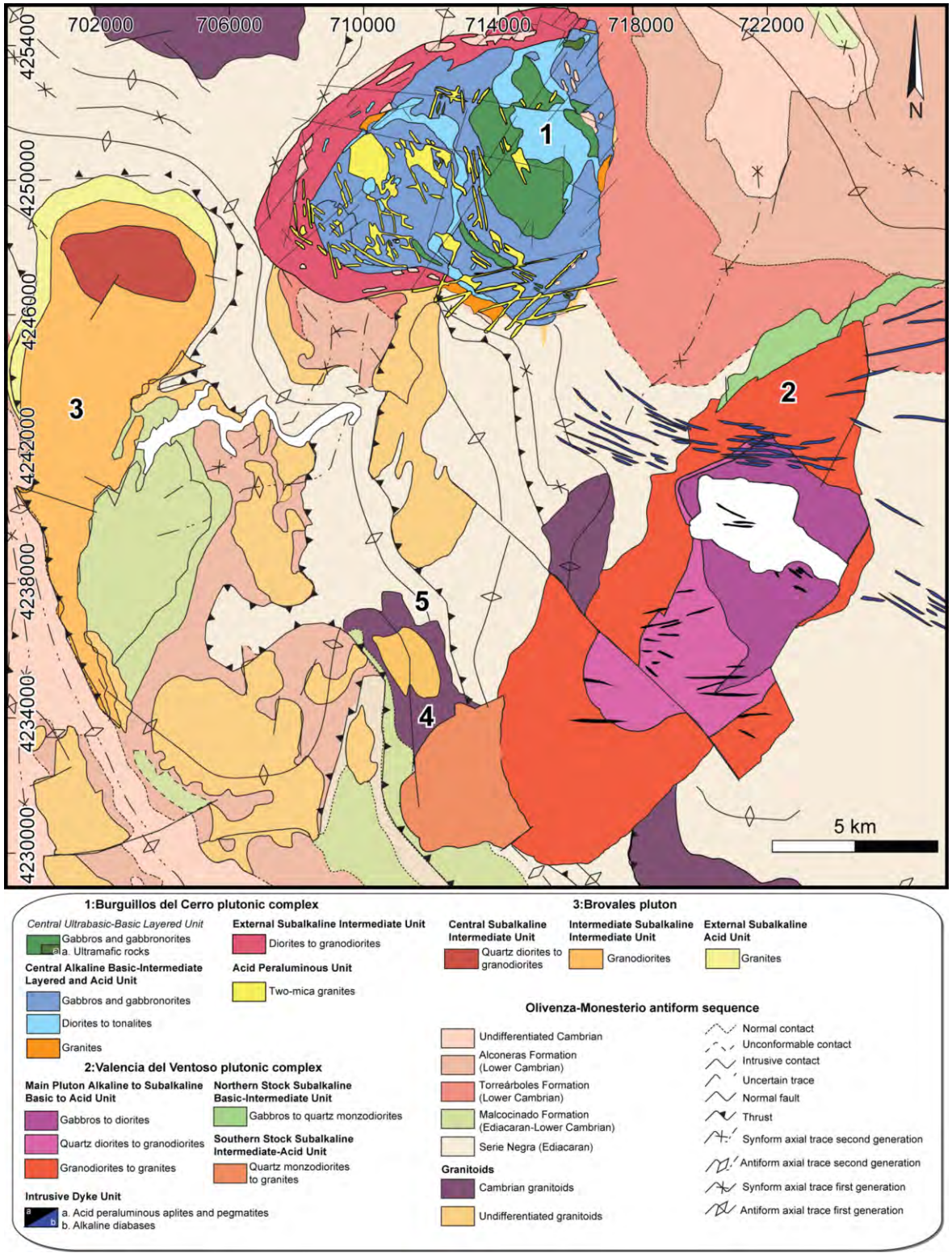

Figure 4.1. Schematic geological map of the Olivenza-Monesterio antiform, modified from Expósito (2000). 1: Burguillos del Cerro plutonic complex (modified from Pons, 1982 and García-Casquero, 1991), 2: Valencia del Ventoso plutonic complex and 3: Brovales pluton both modified form Pons, (1982), 4: Cambrian leucogranite and 5: Metasediment from Serie Negra.

here we define four main Burguillos del Cerro plutonic complex rock groups (Fig. 4.1):

i. The *Central Ultrabasic-Basic Layered Unit.*

ii. The *Central Alkaline Basic-Intermediate Layered and Acid Unit.*

iii. The *External Subalkaline Intermediate Unit.*

iv. The *Acid Peraluminous Unit.*

4.1.1 Central Ultrabasic-Basic Layered Unit

This unit only crops out in the central part of the complex (Fig. 4.1). It corresponds to Pons' group 1 and part of García-Casquero's group 1 layered series. The unit has a marked compositional layering that is well-defined by alternating dark, ferromagnesian, and light, feldspathic, bands.

The ultramafic rocks are websterites and lherzolites that grade to olivine gabbros where plagioclase is more abundant. They crop out as small black bodies in the main gabbroic mass (Fig. 4.1), mappable because of the high modal proportion of ferromagnesian minerals (Fig. 4.2A and 4.2B). The main minerals are olivine and pyroxenes with, less abundant phlogopite and amphibole. The modal proportion of plagioclase varies gradationally from less than 5% in the ultramafic rocks (Fig. 4.2C) to more than 10% marking the transition to gabbros (Fig. 4.2D).

The mafic rocks are olivine gabbros and, most typically, gabbros s. s. and gabronorites with distinctive poikilitic amphibole (Fig. 4.2E). This group crops out in the northeast of complex (Fig. 4.1). It is also found as small bodies within the *Central Alkaline Basic-Intermediate Layered and Acid Unit* gabbros from which it may be distinguished in the field by its coarser grain size (Fig. 4.2F), that in places is pegmatitic (Fig. 4.2G), dark green colour, and mottled appearance resulting from the centimetric-scale, poikilitic amphiboles (Fig. 4.2H).

4.1.2 Central Alkaline Basic-Intermediate Layered and Acid Unit

This unit comprises the main core of layered gabbros, intermediate rocks from the central part of the complex, and syenites and alkali feldspar granites (Fig. 4.1). The mafic rocks correspond to Pons' group 2 blue gabbros and García-Casquero's group 1 layered and unlayered series. The intermediate rocks also correspond to Pons' group 2. García-Casquero, (1995) conversely grouped all intermediate rocks into a dioritic association, his group 3. However, as we shall see below, there are significant differences between the diorites of this unit and those of our group 3, *External Subalkaline Intermediate Unit.* To misquote H. H. Read, in Burguillos 'there are diorites and diorites'. Fittingly, given that D'Aubisson in 1891 came up with the term diorite from

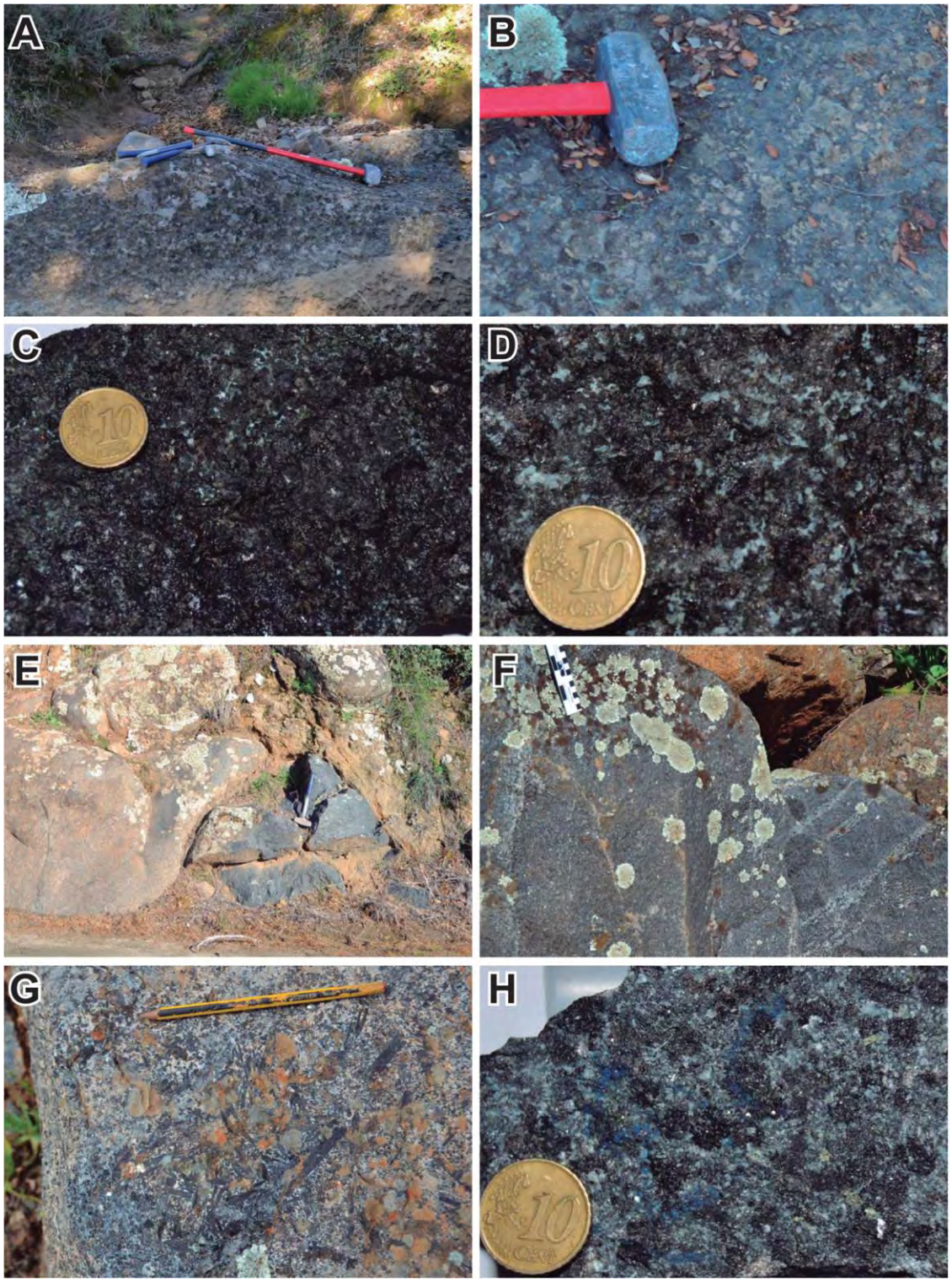

Figure 4.2. Burguillos del Cerro plutonic complex Central Ultrabasic-Basic Layered Unit field relations: A) Ultramafic block in gabbro. B) Detail of the ultramafic block in gabbro, note the dark colour. C) Hand specimen of ultramafic rock, lherzolite (BUAW-9). D) Hand specimen of mafic rock, olivine gabbro (BUAW-8). E) Outcrop of gabbro and gabbronorite with poikilitic amphibole known locally as 'ojo de culebra', snake eye. F) Detail of the dark, ferromagnesian, light, feldspathic layering. G) Detail of a pegmatitic patch in the poikilitic amphibole gabbro. H) Hand specimen of mafic rock, poikilitic amphibole gabbro, note the centimetric size of the minerals (BUAW-4).

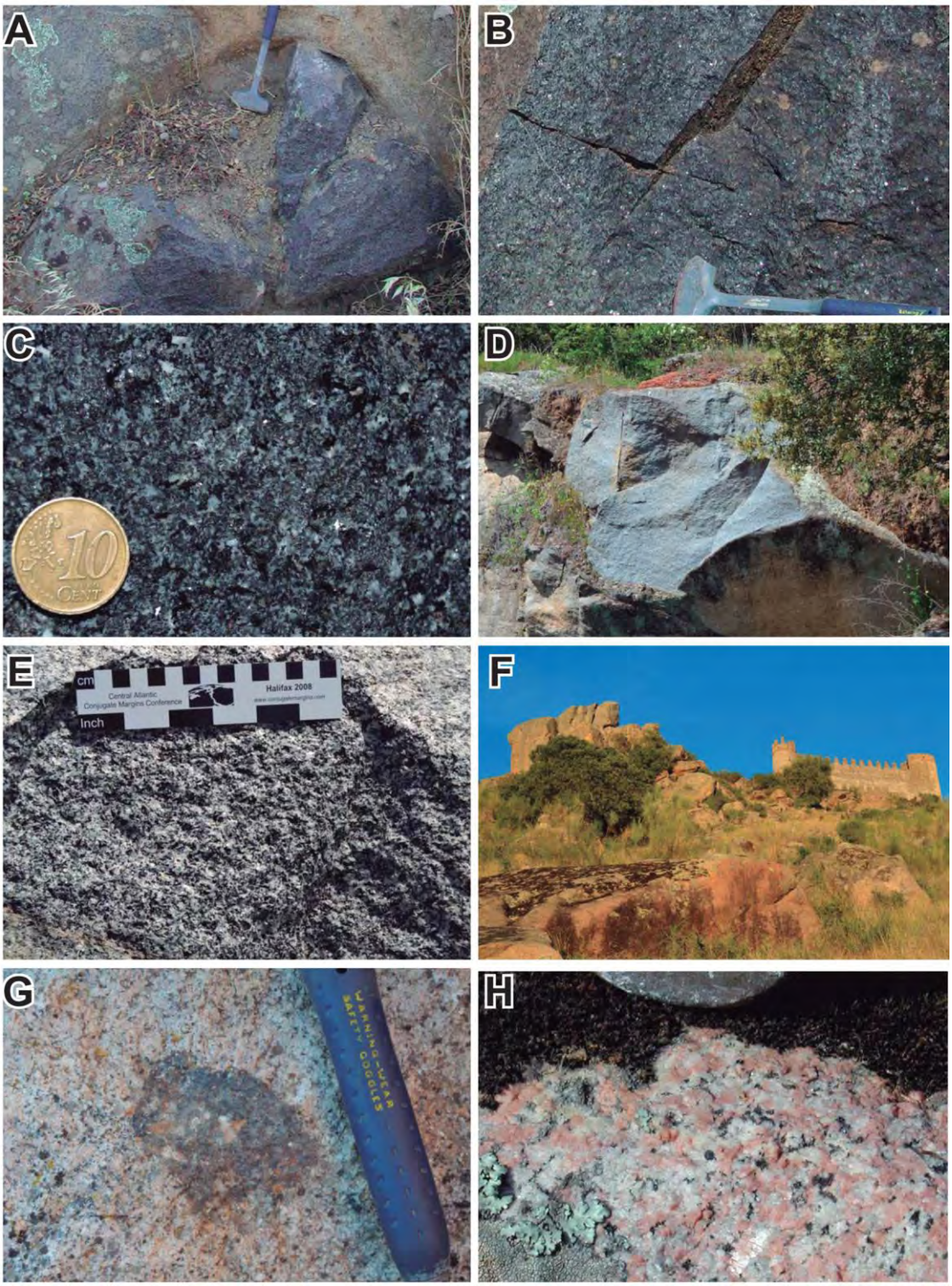

Figure 4.3. Burguillos del Cerro plutonic complex Central Alkaline Basic-Intermediate Layered and Acid Unit field relations: A) Outcrop of blue-grey gabbro. B) Detail of the gabbro, note the coarse grain size and the blueish color. C) Hand specimen of the gabbro, note the abundant pyroxene, plagioclase and biotite. D) Outcrop of diorite, note the lighter grey color compared with the gabbros. E) Hand specimen of diorite, note the lower color index and the abundance of plagioclase and biotite. F) Outcrop of alkali feldpsar granite below the medieval town castle. G) Hand specimen of alkali feldspar granite, note the pink color and the mafic enclave. H) Pegmatite facies in the alkali feldspar granite.

the Greek word for 'distinguish', these rocks will prove to be the key to understanding the complex Burguillos petrogenesis (Chapter 11.3). The felsic rocks of this unit correspond to García-Casquero's group 3, Pons however did not describe these alkaline granites.

The mafic rocks are gabbros and gabbronorites which have a blueish colour and an inequigranular coarse-grained texture (Fig. 4.3A). The main minerals are pyroxenes, plagioclase and biotite (Fig. 4.3C). Notably both olivine and amphibole are absent. Biotite, on the other hand, is ubiquitous and abundant. A light to dark, in places patchy, compositional layering, reflects lesser or greater proportions of ferromagnesian minerals. The layering is weaker than in the previous *Central Ultrabasic-Basic Layered Unit* which gives most of this *Central Alkaline Basic-Intermediate Layered Unit* a more massive appearance (Fig. 4.3B**)**.

The intermediate rocks are diorites and, less commonly, tonalites which crop out in the central part of the complex intermingled with more mafic components of this unit surrounding the *Central Ultrabasic-Basic Layered Unit* (Fig. 4.1). The rocks have an inequigranular, coarse-grained texture and a grey colour with centimetric scale ferromagnesian minerals (Fig. 4.3D). The main minerals are rare pyroxenes, amphibole, biotite and plagioclase with quartz in the most evolved facies (Fig. 4.3E).

The acid syenites and alkali feldspar granites crop out in the southern sector and in the central region below the medieval town castle (Fig. 4.3F). The rocks have coarse-grained, in some place pegmatitic, texture and pinkish white colour caused by alkali feldspar alteration (Fig. 4.3G and H). The other main minerals are quartz and, less abundant, amphibole and biotite (Fig. 4.3G and H). The rocks contain enclaves that have a similar mineralogy to the blue gabbros (Fig. 4.3G).

4.1.3 External Subalkaline Intermediate Unit

This unit forms an external ring that surrounds and intrudes the main central gabbro of the *Central Alkaline Basic-Intermediate Layered Unit* (Fig. 4.1). It corresponds to Pons' group 3. As mentioned above, García-Casquero (1991) grouped all the intermediate rocks into a single dioritic association, his group 3. Nevertheless, we have detected significant compositional differences between the central and external diorites: namely a lower modal proportion of pyroxene and biotite and a higher modal proportion of amphibole in the latter.

The *External Subalkaline Intermediate Unit* is composed of intermediate diorites to granodiorites and acid granites (Fig. 4.1). Outcrops are discontinuous, typically forming blocky mounds (Fig. 4.4A). The rocks have a coarse-grained massive texture and are light grey with

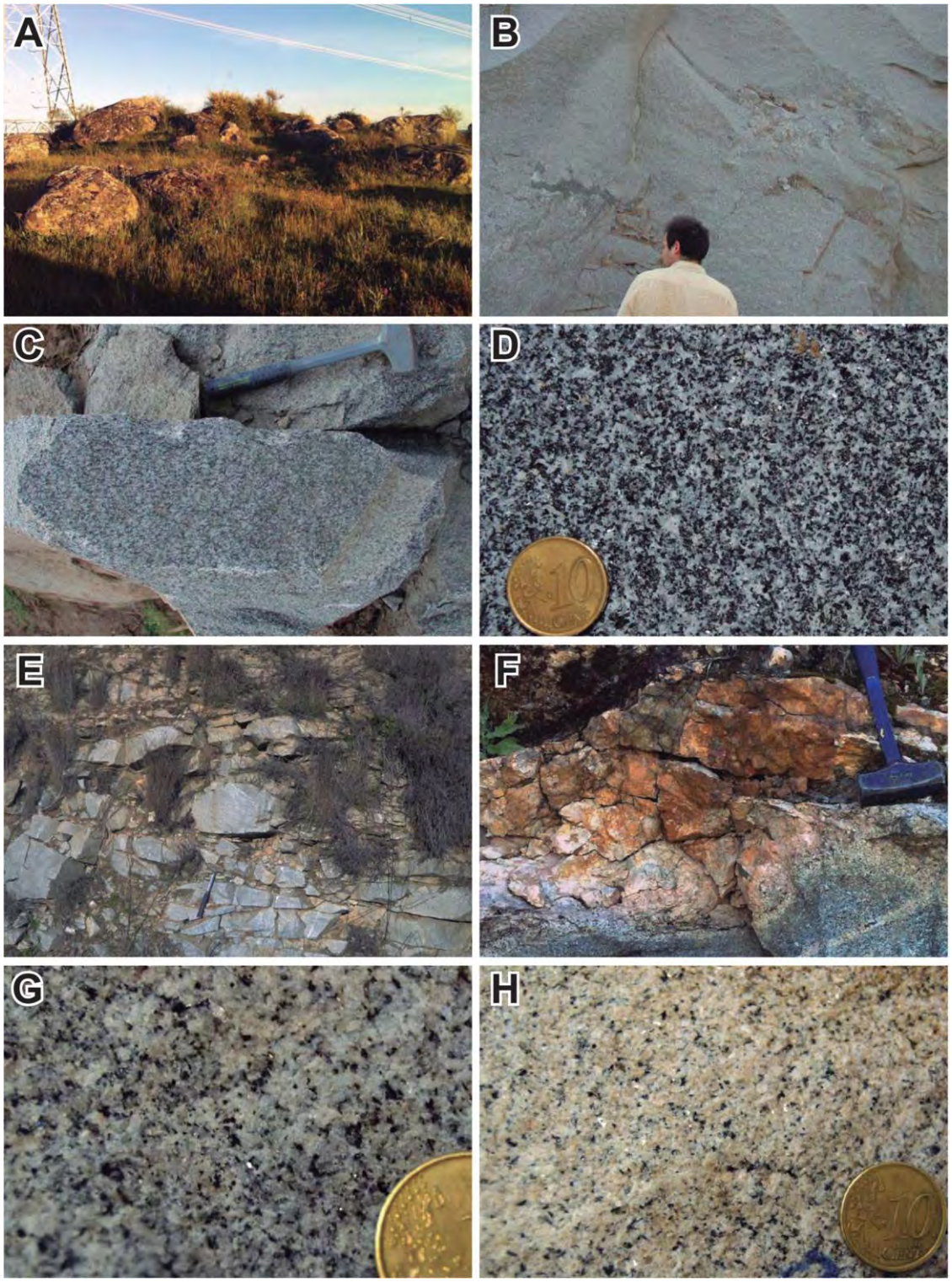

Figure 4.4. Burguillos del Cerro plutonic complex External Subalkaline Intermediate Unit field relations: A) Panoramic view of the external part of the Burguillos del Cerro plutonic complex, looking to the southwest in the southern part of the main pluton, note the typical blocky discontinuous outcrops. B) Outcrop of quartz diorite, note the light grey color, massive texture and irregular coarse-fine melanocratic-leucocratic patches. C) Hand specimen of quartz diorite. D) Hand specimen of tonalite, note the abundance of amphibole relative to biotite. Burguillos del Cerro plutonic Acid Peraluminous Unit field relations: E) General view of a two-mica granite. F) Detail of the pegmatitic facies. G) Hand specimen of two-mica granite. H) Hand specimen of two-mica granite, note that this sampe has less biotite.

darker ferromagnesian minerals (Fig. 4.4B). The main minerals are amphibole, biotite, plagioclase, alkali feldspar and quartz (Fig 4.4C and 4.4D).

4.1.4 Acid Peraluminous Unit

This unit comprises granite, aplite and pegmatite dykes and stocks (Fig. 4.1, Fig. 4.4E and F). It corresponds to both Pons' and García-Casquero's group 4. The mineralogy is quite homogenous: biotite, primary-looking muscovite, alkali feldspar and quartz (Fig. 4.4G). The most evolved rocks have less biotite and more alkali feldspar (Fig. 4.4H). The granitic dykes strike 90º to 110º and 170º to 180º (Fig. 4.1). They abound in the *Central Ultrabasic-Basic Layered Unit* and the *Central Alkaline Basic-Intermediate Layered and Acid Unit*, but are much less common in the *External Subalkaline Intermediate Unit* (Fig. 4.1). Complex intrusive and mingling relationships between these granitic rocks and the other Burguillos del Cerro plutonic complex units are discussed in the next section.

4.1.5 Intrusive and Mingling Relationships

Diverse and complex intrusive and interaction relationships are observed between the Burguillos del Cerro plutonic complex units (Fig. 4.5 and 4.6).

In the central part of the complex the intermediate rocks of the *Central Alkaline Basic-Intermediate Layered and Acid Unit* appear mingled with the basic rocks (Fig. 4.5B). The contacts are interdigitated and rounded (Fig. 4.5B) with locally abundant mafic enclaves in the intermediate rocks (Fig. 4.5C).

The *Acid Peraluminous Unit* bodies have a preferential alignment in the central part of the complex (Fig 4.1). Their contacts with the other rock types, however, are not generally sharp but rather branched (Fig. 4.5D) or curved (Fig. 4.5E). Accordingly, the contacts with the more mafic host rock are gradational rather than abrupt (Fig. 4.5F). The transitional nature of the contact is also evident petrographically in an incremental change in the proportion of the ferromagnesian minerals from the more mafic host to the granitic intrusion (Fig. 4.5F) which, in places, results in irregular mixed intermediate composition patches (Fig. 4.5G).

The *Acid Peraluminous Unit* intrusions are rare in the external ring that surrounds the main central gabbro (Fig. 4.1). By contrast evidence of interaction between the *External Subalkaline Intermediate Unit* and the mafic rocks of the *Central Alkaline Basic-Intermediate Layered and Acid Unit* is common (Fig. 4.6). Field relations indicate that the *External Subalkaline Intermediate Unit* intrudes the basic rocks of the *Central Alkaline Basic-Intermediate Layered and Acid Unit* (Fig. 4.6A). The contact, however, is not sharp but irregular and gradational, mixed, further from the contact the

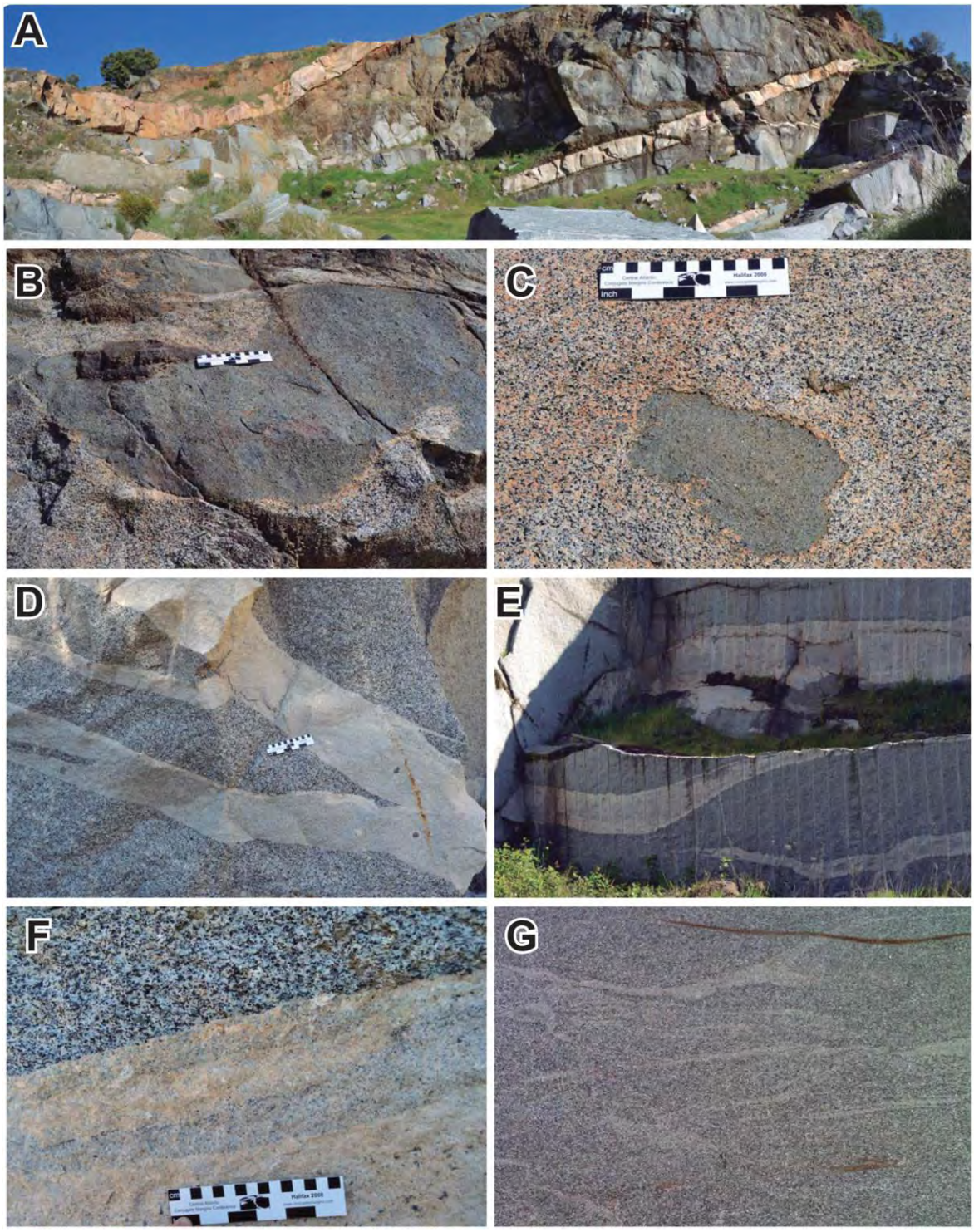

Figure 4.5. A) Panoramic view of the interacion between Acid Peraluminous Unit granite dykes and the Central Alkaline Basic-Intermediate Layered and Acid Unit gabbros and diorites. B) Intrusive and mingling relations between the Central Alkaline Basic-Intermediate Layered and Acid Unit coarser grained diorite that is intruding the finer grained gabbro. C) Detail of more advanced mingling, note the rounded dismembered block of gabbro in the diorite. D) Intrusive and mingling relations between the Acid Peraluminous Unit, granites and diorites from the Central Alkaline Basic-Intermediate Layered and Acid Unit, note the branched structure. E) Outcrop of granite dykes cutting diorites, note the curved, irregular, nature of the contact. F) Hand specimen of the granite and diorite gradational contact. G) Detail of an advanced state of interaction between the granite and diorite.

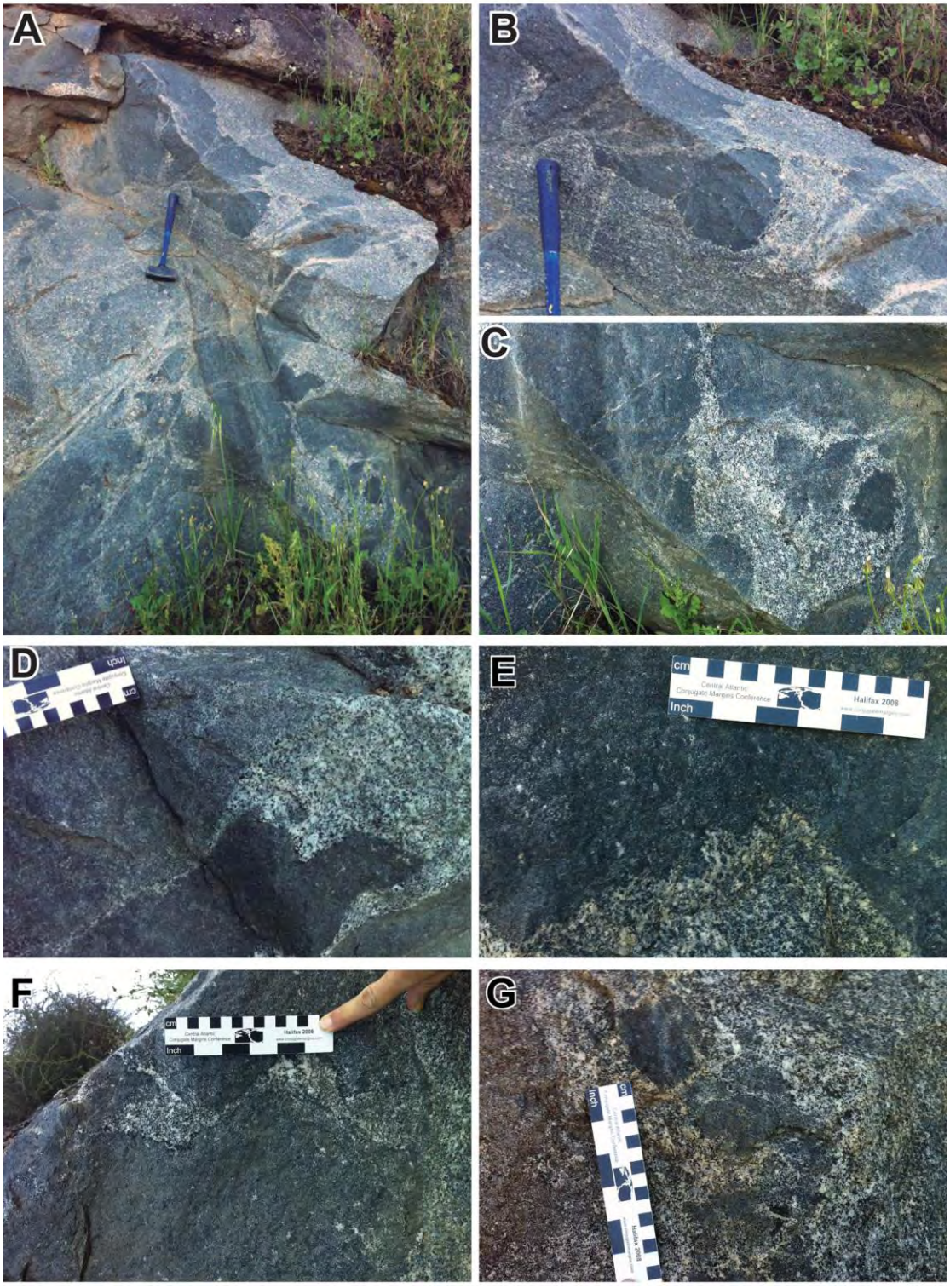

Figure 4.6. A) Intrusive and mingling relations between the External Subalkaline Intermediate Unit, quartz diorites and tonalites and Central Alkaline Basic-Intermediate Layered and Acid Unit gabbros. B) Detail of the rounded irregular contact between the intermediate and basic rocks. C) Detail of blocks of gabbro in an intermediate host, e4vidence of progression of mingling: D) Intrusion of intermediate rocks in the gabbros, note the irregular contacts. E) Detail of a lobulate contact between the intermediate and basic rocks, indicating the initiation of mingling. F) Boudins of intermediate material in the mafic rocks. G) Chaotic mingling between the two rock types, an advanced state of interaction indicated by the dismembering of the mafic material in an irregular mass.

proportion of mafic facies diminishes and the external intermediate compositions dominate, this results in blocks of mafic material in a mass of intermediate composition (Fig. 4.6B to G). In detail, the interaction between the two rock types progresses from dendritic and intrusive (Fig. 4.6D and E) to zones of mingling between the mafic and intermediate compositions that surround remnant mafic blocks (Fig. 4.6F and G).

4.2 Valencia del Ventoso Plutonic Complex

The Valencia del Ventoso plutonic complex was emplaced in the central part of the Olivenza-Monesterio antiform where it crops out over an area of about 150 km^2 (Fig. 4.1). This plutonic complex has an oval morphology that is elongated northeast-southwest (Fig. 4.1). As was the case in Burguillos, the main pluton cuts structures related to thrusts related to the first compressional phase of deformation 390-345 Ma (Fig. 4.1) (Expósito, 2000) but it is cut by a second, oblique, compressional phase fault (Fig. 4.1).

The plutonic complex intruded the Ediacaran Serie Negra except in the southwest where it also intruded the Neoproterozoic to lower Cambrian Malcocinado Formation and cuts a Cambrian leucogranite and in the northwest where it intruded the lower Cambrian Torreárboles Formation (Fig. 4.1).

Pons (1982) defined four main rock groups based on petrographic and structural criteria: i. the Valencia del Ventoso main pluton, which is concentrically zoned from a mafic centre to a felsic rim; ii. the Medina de las Torres stock in the north; iii. the Cortijo del Pozuelo stock in the south; iv. the Intrusive dyke complex (Fig. 4.1).

Sarrionandia (2005) followed the general division of Pons (1982) but subdivided the four main groups according to their petrography. In the main pluton he identified a central stock of layered mafic rocks and divided the rest of the pluton into a basic unit and an acid unit. A quartz monzodiorite facies was mapped in the gabbros of the Medina de las Torres stock. The Cortijo del Pozuelo stock was also divided in two, a central facies and a peripheral facies. Sarrionandia (2005) also split the Intrusive dyke complex into two groups: the aplite and pegmatite veins that just crop out in the plutonic complex; and, dolerite dykes that cut both the plutonic complex and the surrounding country rocks.

Here we combine the work of Pons (1982) and Sarrionandia (2005) with our own field, mineralogical, petrographic, and compositional data to define four main rock groups (Fig. 4.1):

i. The *Main Pluton Alkaline to Subalkaline Basic-Acid Unit,* which encompasses the Valencia del Ventoso main pluton.

ii. The *Northern Stock Subalkaline Basic-Intermediate Unit,* which corresponds to the Medina de las Torres stock.

iii. The *Southern Stock Subalkaline Intermediate-Acid Unit,* equivalent to the Cortijo del Pozuelo stock.

iv. The *Intrusive Dyke Unit,* like the Intrusive dyke complex.

4.2.1 Main Pluton Alkaline to Subalkaline Basic-Acid Unit

The *Main Pluton Alkaline to Subalkaline Basic-Acid Unit* is concentrically zoned (Fig. 4.1). In the central part of the intrusion mafic and intermediate rocks comprise gabbros and diorites. The gabbros are equigranular, fine-grained and black. The main minerals are pyroxene, biotite and plagioclase. Increasing proportions of amphibole and, to a lesser extent, quartz mark the transition to the diorites. The diorites are massive, equigranular, fine-grained and grey (Fig. 4.7C and D). The main minerals are pyroxene, amphibole, biotite, plagioclase and minor quartz (Fig. 4.7E). Coarser-grained granitic enclaves are present in this facies (Fig. 4.7D).

The central part of the plutonic complex is surrounded by intermediate quartz diorites and granodiorites (Fig. 4.1). These rocks are inequigranular, coarse-grained and blue-grey (Fig. 4.7F and Fig. 4.7G). The main minerals are pyroxene, amphibole, biotite, plagioclase, and more minor alkali feldspar and quartz (Fig. 4.7H). Oriented amphibole and biotite mark a planolinear foliation, that strikes between 75º and 175º and dips from 20º to 60º to the northeast (Pons, 1982; Sarrionandia, 2005) (Fig. 4.7H).

The outer, volumetrically largest, part of the plutonic complex comprises the most evolved granodiorites and granites (Fig. 4.1). As for other units, the outcrops of these rocks are discontinuous, typically forming blocky mounds (Fig. 4.8A and B). The rocks are inequigranular, coarse- to very coarse-grained and light grey to pinkish where the alkali feldspar is somewhat altered (Fig 4.8C and D). The main minerals are biotite, plagioclase, alkali feldspar and quartz with minor pyroxene and amphibole, (Fig. 4.8C). This outer unit also has a planolinear foliation, although this is less well-developed than in the more intermediate facies (Fig. 4.8C). Significantly, throughout the pluton, field relations reveal patchy interaction between more mafic and more felsic components (see below).

4.2.2 Northern Stock Subalkaline Basic-Intermediate Unit

The *Northern Stock Subalkaline Basic-Intermediate Unit* is composed of gabbros to quartz monzodiorites. It has a tectonic, apparently emplacement-related, foliation perpendicular to the main regional compressional structures (Pons, 1982; Expósito, 2000). The southern contact, with

Figure 4.7. Valencia del Ventoso plutonic complex Main Pluton Alkaline to Subalkaline Basic-Acid Unit field relations: A) Gabbro outcrop, central part of the complex. B) Detail of the gabbro, note the fine grain size and dark colour. C) Diorite outcrop. D) Detail of the diorite outcrop, central part of the complex, note the granitic enclave. E) Hand specimen of diorite. F) Outcrop of quartz diorite, note the aplite dyke cutting the intermediate plutonic rock. G) Detail of the quartz diorite, note the coarser grain size and blue-grey color. H) Hand specimen of the quartz diorite, note the foliation marked by the preferential orientation of the amphibole and biotite.

Figure 4.8. Valencia del Ventoso plutonic complex Main Pluton Alkaline to Subalkaline Basic-Acid Unit field relations: A) Panoramic view of the external part of the Valencia del Ventoso plutonic complex, looking to the north from the south of the main pluton, note the typical blocky discontinuous outcrops. B) Outcrop of granodiorite. C) Detail of the granodiorite, note the coarse grain size and pink colour. D) Hand specimen of the granodiorite, note the foliation marked by the preferential orientation of the abundant biotite. E) Valencia del Ventoso main pluton granodiorite-granite. Intrusive Dyke Unit field relations: E) Aplite dyke cutting granodiorite. F) Detail of the aplite, note the fine grain size, leucocratic colour index and the clots of tourmaline G) Dolerite dyke cutting in a central diorite.

the Valencia del Ventoso main pluton, is faulted (Fig. 4.9A and B). The rocks are greenish black to grey with fine to medium grained, equigranular textures (Fig. 4.9C). The main minerals are olivine, in the mafic facies, pyroxenes, amphibole, biotite, and plagioclase, plus alkali feldspar and quartz in the most evolved facies (Fig. 4.9D).

4.2.3 Southern Stock Subalkaline Intermediate-Acid Unit

The *Southern Stock Subalkaline Intermediate-Acid Unit* comprises quartz monzodiorites and quartz diorites to tonalites. Outcrops are discontinuous, typically forming blocky mounds (Fig. 4.9E). The rocks have fine to coarse-grained inequigranular porphyritic textures (Fig. 4.9F) and contain two types of enclaves: i. fine grained, with the same mineralogy as the host intrusion, pyroxene, amphibole, biotite, plagioclase and quartz (Fig. 4.9F and 4.9G); and, ii. metapelitic similar to the Serie Negra rocks (Fig. 4.9H).

4.2.4 Intrusive Dyke Unit

The *Intrusive Dyke Unit* is composed of two quite different groups of rocks. The first are acid peraluminous aplite and syenite veins that are spatially restricted to the Valencia del Ventoso plutonic complex (Fig. 4.1). These veins cut the *Main Pluton Alkaline to Subalkaline Basic-Acid Unit* (Fig. 4.7F and 4.8E). The pink rocks are generally equigranular and fine-grained with some pegmatitic patches (Fig. 4.8F). The main minerals are alkali feldspar and quartz with rare biotite with primary-looking muscovite and sparse aggregates of tourmaline (Fig. 4.8F). The second group of rocks is formed of a swarm of dykes, composed of fine-grained microgabbros (Fig. 4.8G), andesites and rhyolites, that cut across both the main pluton and the country rocks (Fig. 4.1, Pons, 1982, Sarrionandia, 2005). Field relations suggest that the first group were syn-magmatic whereas the second group are younger, maybe related to a Permian dyke swarm that cuts other plutons in the region (e.g., Galindo et al., 1991; Sarrionandia, 2005).

4.2.5 Interaction and Mingling Relationships

Interaction between rocks with mafic and felsic compositions are observed in the *Main Pluton Alkaline to Subalkaline Basic-Acid Unit*. Such features are particularly well-exposed in the southwest part of the main plutonic complex where acid rocks dominate over mafic. Pons (1982) and Sarrionandia (2005) regarded it as evidence of magma mixing. Variably-shaped more mafic enclaves, with rounded irregular borders, are set in a granitic host (Fig. 4.10A). The contacts between the different rock types are lobulate rather than sharp (Fig 4.10B and C), they vary from: i. somewhat distinct and curved (Fig. 4.10D); to ii. complex with interdigitation of the two rock types (Fig. 4.10E); and iii. diffuse with the mafic phase disaggregated in the granite (Fig. 4.10F).

Figure 4.9. Valencia del Ventoso plutonic complex Northern Stock Subalkaline Basic-Intermediate Unit field relations: A) Outcrop of quartz monzodiorite affectected by dextral faults. B) Detail of faulted quartz monzodiorites. C) Detail of the quartz monzodiorites, note the massive unbanded texture. D) Hand specimen of the quartz monzodiorites. Valencia del Ventoso plutonic complex Southern Stock Subalkaline Intermediate-Acid Unit field relations: E) Outcrop of granodiorite, note the blocky nature. F) Detail of quartz monzodiorites, note the massive, coarse-grained texture. G) Hand specimen of the quartz monzodiorites, note the fine-grained enclaves. H) Detail of a partially assimilated basement metapelitic enclave.

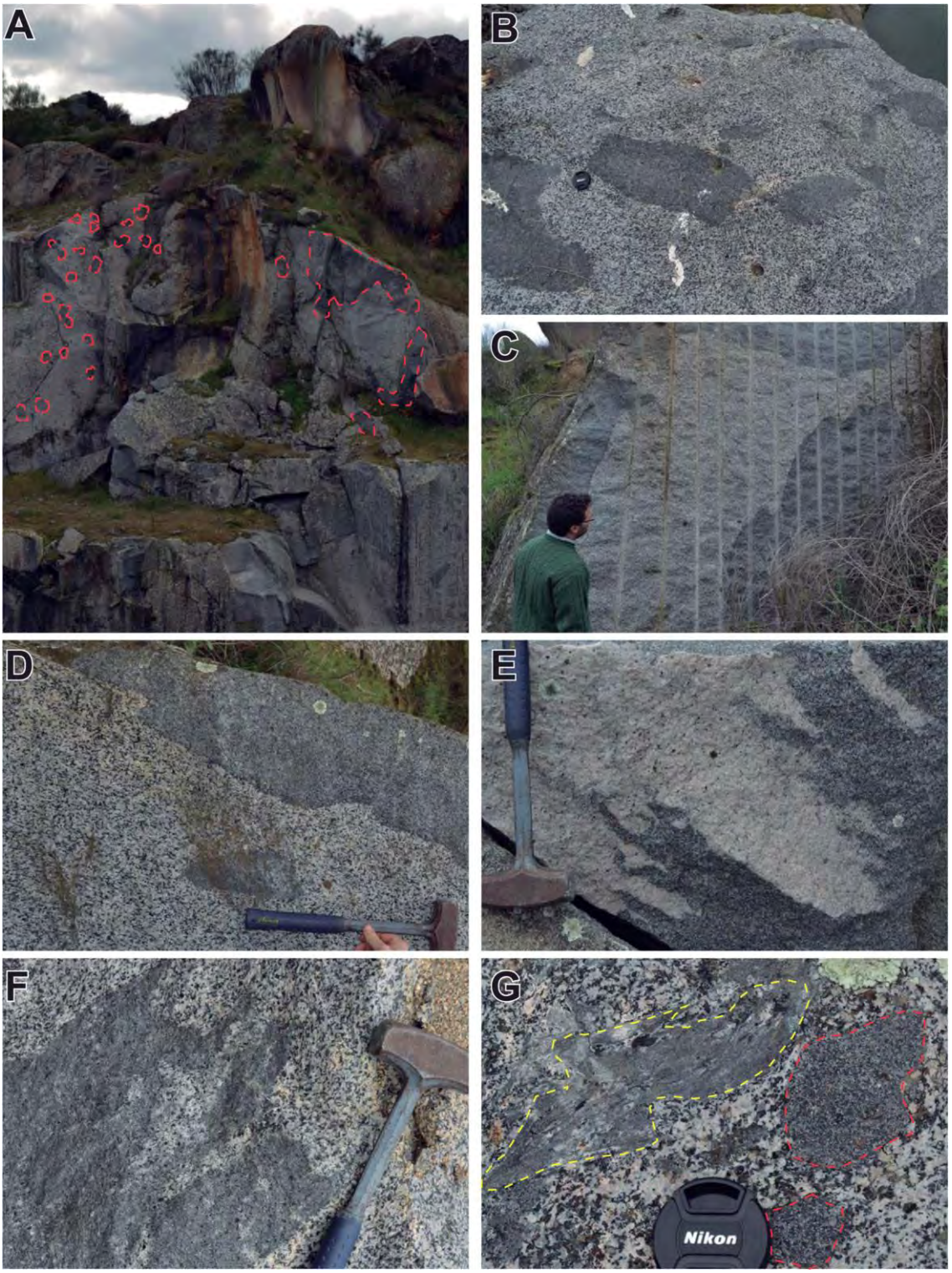

Figure 4.10. Valencia del Ventoso plutonic complex Main Pluton Alkaline to Subalkaline Basic-Acid Unit mingling relations: A) Quarry face showing extensive mingling between gabbros-diorites (marked by a discontinuous line) and granodiorites-granites. B) Enclaves of diorite in granodiorite, note their rounded shape. C) Irregular contacts between the diorite and granodiorite, evidence of progression of mingling: D) Detail of the irregular lobulate contact between the diorite and granodiorite, indicating the initiation of mingling. E) Complex interdigitation of the diorite and granodiorite. F) Disaggregation of the diorite in the granodiorite. G) Detail of a partially assimilated basement metapelitic enclave.

Such interactions are also evident, albeit less so, in the mafic rocks of the *Main Pluton Alkaline to Subalkaline Basic-Acid Unit* in the central part of the complex (Fig. 4.7D). The granites also contain partially assimilated metapelitic enclaves (Fig. 4.10G).

4.3 Brovales Pluton

The Brovales pluton was emplaced in the central part of the Olivenza-Monesterio antiform where it crops out over an area of about 75 km^2 (Fig. 4.1). This pluton has a plan view north-south 'inverted-drop' morphology (Fig. 4.1). Its style of emplacement was related to the regional structures, principally affected by the Monesterio thrust (Fig. 4.1). This thrust is related to the first compressional phase of deformation 390-345 Ma (cf., Simancas et al., 2003). It is dextral and marks the western boundary of the pluton, indicating its syn-tectonic character (Eguiluz, 1988; Expósito et al., 2002; Eguiluz et al., 2004).

In the north the pluton intruded the Ediacaran Serie Negra, (Fig. 4.1). In the east the pluton also intruded the Neoproterozoic to lower Cambrian Malcocinado Formation (Fig. 4.1). In the west it intruded the lower Cambrian Formation volcano-sedimentary series, and lower Cambrian Alconeras Formation limestones (Fig. 4.1).

The Brovales pluton has been studied in detail, from the point of view of its geochemical and geochronological features (Brun and Pons, 1981; Pons, 1982; Montero et al., 2000) and its structural relationship with the Monesterio thrust (Eguiluz et al., 2004; Expósito, 2000). Pons (1982) deduced that the pluton was concentrically zoned and divided it in three: Central Unit diorites and granodiorites at the core; surrounded by Intermediate Unit granodiorites and granites; with External Unit and Aplitic dykes and granites at the outer rim (Fig. 4.1).

Here we combine the mapping of Pons (1982) with our own field, mineralogical, petrographic, and compositional data to define four main rock groups (Fig. 4.1):

i. The *Central Subalkaline Intermediate Unit.*
ii. The *Intermediate Subalkaline Intermediate Unit.*
iii. The *External Subalkaline Acid Unit*
iv. *Intrusive, Acid Peraluminous, Dykes*

4.3.1 Central Subalkaline Intermediate Unit

The Central Unit comprises quartz diorites to quartz monzodiorites, tonalites and granodiorites (Fig. 4.1). These rocks have medium to coarse-grained inequigranular textures (Fig. 4.11A and B). They have a foliation marked by the orientation of, in places deformed, mafic

Figure 4.11. Brovales pluton Central Subalkaline Intermediate Unit field relations: A) General view of the quartz diorite, note the foliation. B) Detail of the quartz monzodiorite with a fine-grained dioritic enclave, both of them with foliation. C) Hand specimen of a quartz monzodiorite, note the dioritic enclave. D) Hand specimen of a granodiorite. Brovales pluton Intermediate Subalkaline Intermediate Unit field relations: E) Granodiorites showing the fine and coarse grain facies, note the interaction of these two facies. F) Detail of unfoliated granodiorites, note the intrusive relationship of coarse grain in fine grain facies. G) Hand specimen of the fine-grained granodiorite. H) Hand specimen of the coarse-grained granodiorite.

minerals, that strikes from 70º to 90º east with a dip of 0º to 30º to the northeast-northwest, (Figs 4.11B and C). The main minerals are amphibole, biotite, plagioclase, alkali feldspar and quartz (Fig. 4.11C and D). The rocks contain fine-grained foliated dioritic enclaves that are compositionally quite similar to the host intrusion but with more amphibole and biotite and less quartz (Figs 4.11B and C).

4.3.2 Intermediate Subalkaline Intermediate Unit

The Intermediate Unit is composed of tonalites, granodiorites and granites (Fig. 4.1). The unit includes undeformed granodioritic facies as well as facies deformed by the Monesterio thrust (Figs 4.11E-H and 4.12A-D). The undeformed granodiorites may be divided into two sub-types: the first, which is fine-grained, is more abundant, the second is coarse-grained (Fig. 4.11E and F). Complex interaction relationships exist between the two sub-types with intrusive contacts and enclaves in both facies (Fig. 4.11E and F). The fine-grained facies is equigranular and light grey (Fig. 4.11G). By contrast the coarse-grained facies is inequigranular with poikilitic amphibole and biotite (Fig. 4.11H). The main minerals in both facies are amphibole, biotite, plagioclase, alkali feldspar and quartz (Fig. 4.11G and H).

In the western part of the pluton the deformed intermediate unit (Fig. 4.12A) has well-developed S-C structures (Fig. 4.12B and D). A marked foliation strikes 170º to 10º east and dips 70º to 90º east, coincident with the orientation of the Monesterio thrust in the region (Fig. 4.1). Mineralogically comparable deformed and undeformed fine-grained rocks are found in the same outcrop (Fig. 4.12C).

4.3.3 External Subalkaline Acid Unit and Intrusive, Acid Peraluminous, Dykes

The *External Subalkaline Acid Unit* is composed of monzogranites and syenogranites at the contact between the Brovales pluton and the Serie Negra (Fig. 4.12E). The granites have a foliation that strikes 80º to 110º east and dips 20º to 50º to the northeast-northwest. These rocks have medium- to fine-grained equigranular textures. The main minerals are biotite, alkali feldspar and quartz (Fig. 4.12F).

The volumetrically minor *Intrusive, Acid Peraluminous, Dykes* crop out through the pluton cutting all the aforementioned units. In the west of the pluton aplite dykes cut the *Intermediate Subalkaline Intermediate Unit* and are affected by the same Monesterio thrust-related deformation as the granodiorite (Fig. 4.12G). The aplites are equigranular, fine-grained and pink (Fig. 13G and H). The main minerals are scare biotite, alkali feldspar and quartz (Fig. 4.12H).

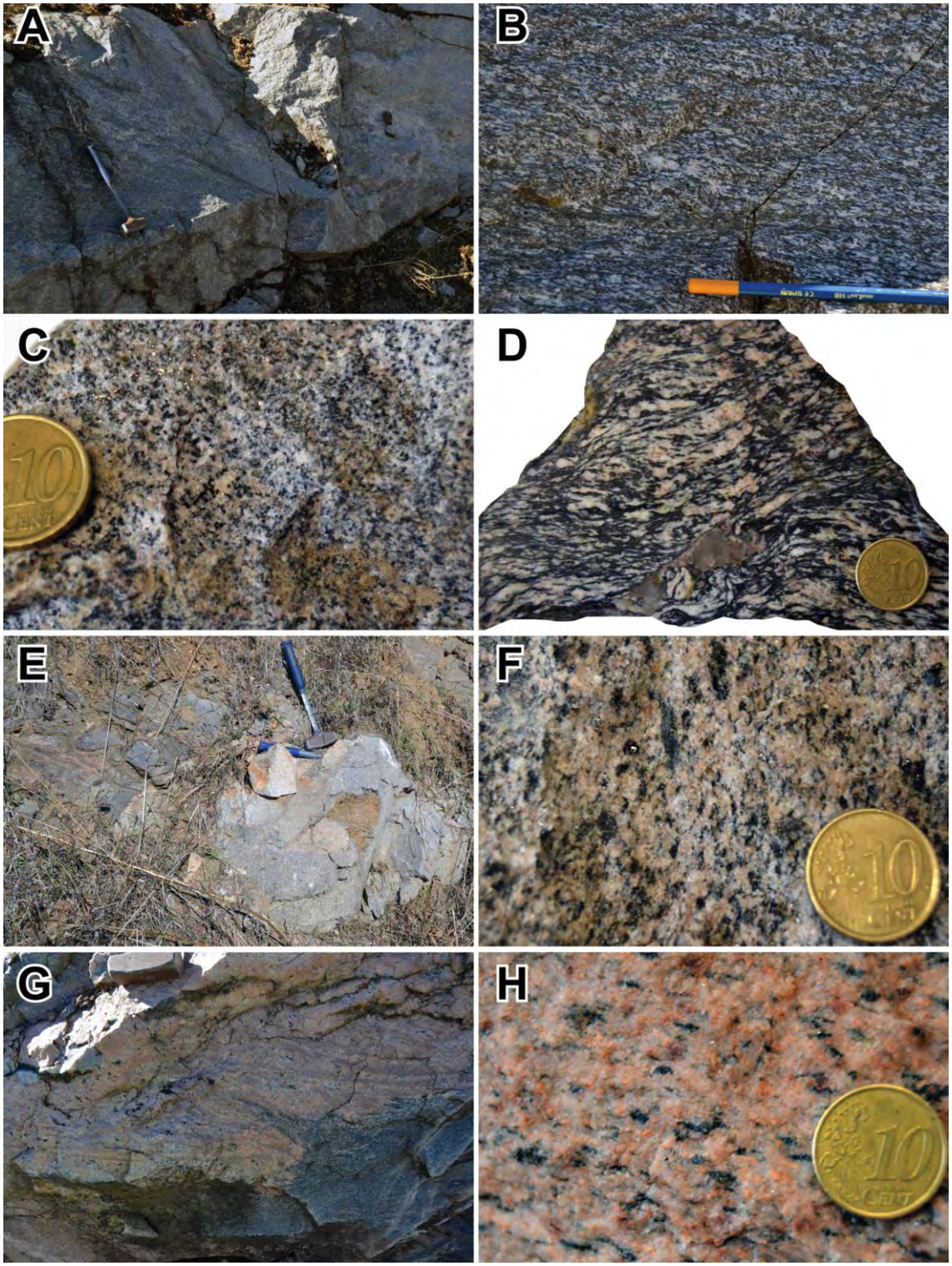

Figure 4.12. Brovales pluton Intermediate Subalkaline Intermediate Unit field relations: A) Outcrop scale view of deformed granodiorites, related to the Monesterio thrust, and undeformed granodiorites. B) Detail of strong deformation pattern in the granodiorites provoked by the Monesterio thrust. C) Hand specimen of the undeformed granodiorite. D) Hand specimen of the deformed granodiorite. Brovales pluton External Subalkaline Acid Unit and Intrusive, Acid Peraluminous, Dykes field relations: E) Contact of the syenogranite with the Serie Negra country rocks. F) Hand specimen of syenogranite. G) Aplite cutting the foliated granodiorite within the Monesterio thrust trace, note that the aplite has the same strong deformation pattern as the granodiorite. H) Hand specimen of aplite, note the light pink colour and the foliation marked by the orientation of the biotites.

4.4 Cambrian Leucogranite and Serie Negra Metasediment

The Cambrian leucogranite studied in the present work intruded the central part of the Olivenza-Monesterio antiform (Fig. 4.1) where it crops out over an area of about 20 km^2. The pluton has an oval shaped outcrop that is elongated northwest-southeast (Fig 4.1). It cuts the Tentudía Formation metasediment (Fig. 4.13B to D), the contact with the Serie Negra in the north is sharp contact; whereas the contact with the Malcocinado Formation to the south is more irregular and gradational. The eastern contact of the leucogranite pluton is itself cut by the early Carboniferous Valencia del Ventoso plutonic complex (Fig. 4.1). Outcrops are discontinuous, typically forming blocky mounds. The granite has an equigranular texture and white colour as a result of the paucity of ferromagnesian minerals (Fig. 4.13A). The main minerals are alkali feldspar and quartz.

The Serie Negra Tentudía formation fine-grained black metasediment sampled in this study shows evidence of partially assimilation by the Cambrian leucogranite (Fig. 4.13B-D). The contact with the leucogranite is complex and interdigitated (Fig 4.13D), in places, the metasediment crops out as irregular decimetric-scale stoped blocks (Fig. 4.13B). Near the granite contact the metasediment is massive, lacking the well-defined regional foliation that is generally observed in the Serie Negra (Fig. 4.13 D).

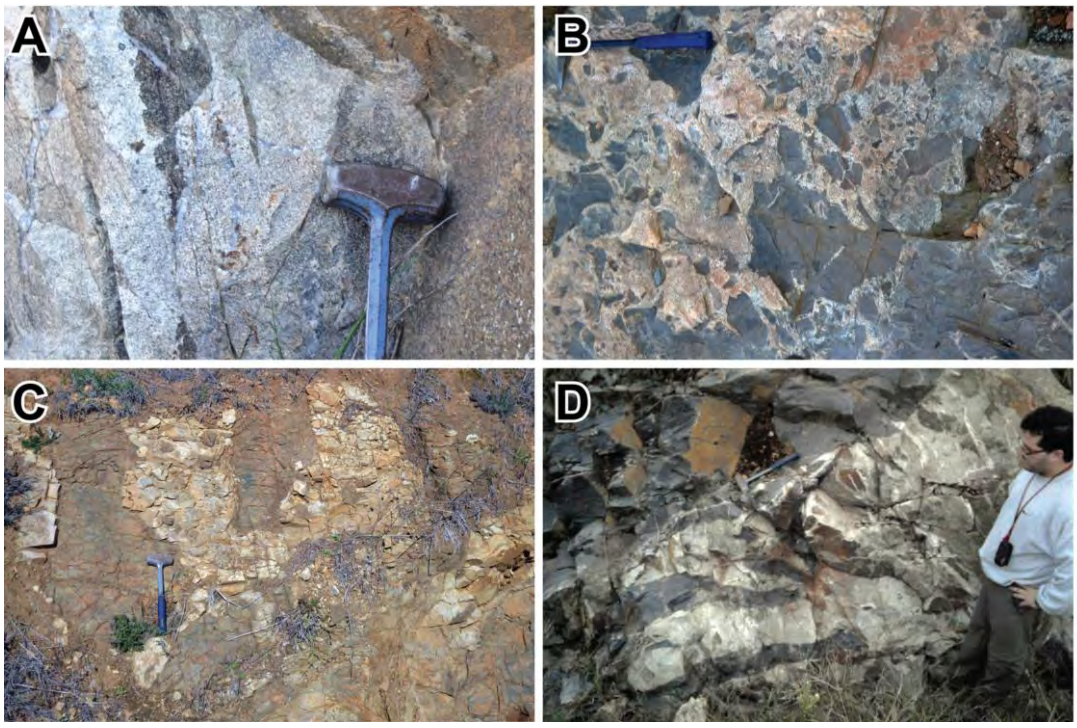

Figure 4.13. Field relations: A) Cambrian leucogranite. B) Cambrian leucogranite and Serie Negra metasediment showing complex interactions, including contact interdigitation, C) intrusion and D) irregular decimetric scale blocks of metasediment within the leucogranite.

Chapter 5: Samples and Methods

5. Samples and Methods

This study has focused on three representative Ossa-Morena Zone (OMZ) Variscan plutonic bodies: i. the Burguillos del Cerro plutonic complex; ii. the Valencia del Ventoso plutonic complex; and, iii. the Brovales pluton (Fig. 5.1). Chapter 3, summarized the results of the various studies of OMZ magmatism. The available data are combined here with new analyses of characteristic samples from each of the three aforementioned bodies. Table 5.1 summarizes information regarding representative samples from the current work including unit, rock type, location and distinctive petrographic characteristics.

5.1 Database

One of the first tasks that we undertook was to compile geochemical and geochronological data for pre-Variscan and Variscan rocks from the OMZ and related Iberian and north African terranes (Appendix I).

The resultant database comprises major, trace and Sr and Nd isotope data for:

i. OMZ pre-Variscan Cambro-Ordovician igneous rocks.

(Galindo, 1989; Oschern, 1993; Ordóñez-Casado, 1998; Salman, 2002; Gómez-Pugnaire et al., 2003; Pereira et al., 2006; Solá, 2007; Chichorro et al., 2008; López-Guijarro et al., 2008; Solá et al., 2008; Sarrionandia et al., 2012; Sánchez-García et al., 2010; 2013).

ii. OMZ Ediacaran to Ordovician sedimentary rocks.

(Schäfer, 1990; Casquet et al., 2001; Pereira et al., 2006; López-Guijarro et al., 2006; 2008; Chichorro et al., 2008).

iii. OMZ Variscan Carboniferous igneous rocks.

Of particular note, in terms of previous work, are the PhD theses of Pons (1982) who studied Burguillos del Cerro, Valencia del Ventoso and Brovales (as well as Salvatierra de los Barros), García-Casquero (1991) regarding Burguillos del Cerro, and Sarrionandia (2005) concerning Valencia del Ventoso.

(Pons, 1982; García-Casquero, 1991; Bateman et al., 1991; Castro et al., 1996; Bachiller, 1996; El Hmidi, 2000; Casquet et al., 2001; Sarrionandia, 2005; Piña, 2006; Tornos et al., 2006; Azor et al., 2008; Pin et al., 2008; Pereira et al., 2008; Moita et al., 2009; Antunez et al., 2010) (Appendix I).

To complement the OMZ pre-Variscan data we also included Nd isotope data for:

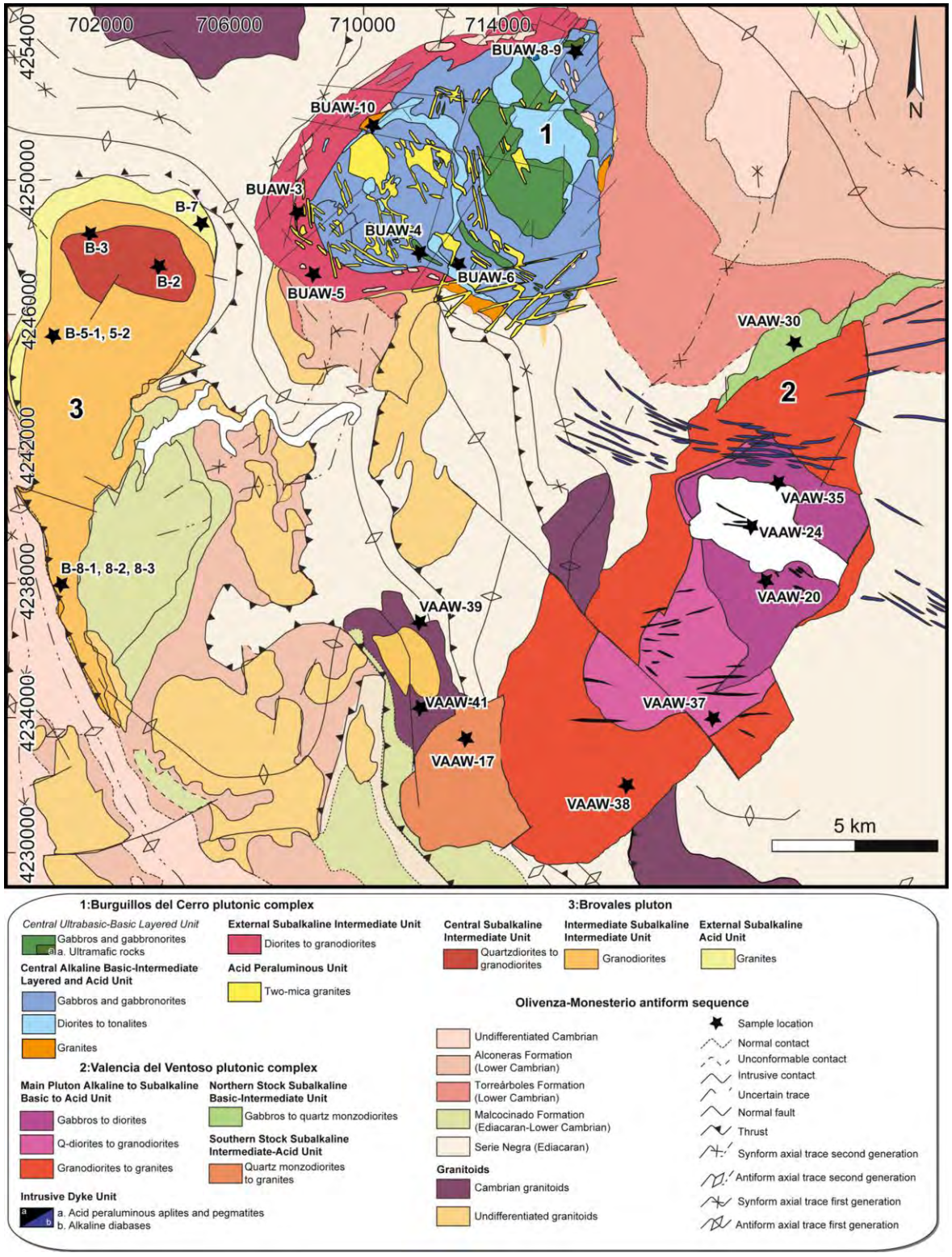

Figure 5.1. Schematic geological map of the Olivenza-Monesterio antiform, modified from Expósito (2000). 1: Burguillos del Cerro plutonic complex (modified from Pons, 1982 and García-Casquero, 1991), 2: Valencia del Ventoso plutonic complex and 3: Brovales pluton both modified form Pons, (1982), 4: Cambrian leucogranite and 5: Serie Negra metasediment.

i. Pre-Variscan sedimentary rocks from the Central Iberian Zone (CIZ).

(Schäfer, 1990; Casquet et al., 2001; Chichorro et al., 2008; López-Guijarro et al., 2008).

ii. Pan-African granitoids, potential OMZ sediment sources, from the three main North African terranes were also incorporated: the Anti-Atlas, West African Craton.

(Blanc et al., 1992; Barbey et al., 2001; Thomas et al., 2002; Samson et al., 2004; Gasquet et al., 2005; Errami et al., 2009; Tahiri et al., 2010; Tounmmite et al., 2013), the Tuareg Shield (Liégeois et al., 1994; Ferré et al., 1996; Acef et al., 2003; Azzouni-Sekkal et al., 2003; Abdallah et al., 2007); and, the Sahara Metacraton (Harms et al., 1990; Bea et al., 2011).

Geochronological data were also collated. These include Neoproterozoic, Cambrian and Ordovician U-Pb single and population zircon data and Rb-Sr whole-rock ages for:

i. OMZ pre-Variscan igneous rocks.

(Galindo and Portugal-Ferreira, 1988; Galindo et al., 1990; Oschner, 1993; Ordónez-Casado, 1998; Montero et al., 1999; Salman, 2002; Romero et al., 2006; Solá, 2007; Chichorro et al., 2008; Sánchez-García et al., 2008; Pereira et al., 2010b; 2011; 2012b) sedimentary rocks (Schäfer et al., 1993; Ordóñez-Casado, 1998; Fernández-Suárez et al., 2002b; Linnemann et al., 2008; Pereira et al., 2010a; 2010b; 2011; 2012b).

ii. OMZ Variscan igneous rocks.

(Bellon et al., 1979; De la Rosa et al., 1993; Dallmeyer et al., 1993; 1995; Bachiller et al., 1997; Ordoñez-Casado, 1998; Montero et al., 2000; Tornos et al., 2005; Romero et al., 2006b; Jesus et al., 2007; Azor et al., 2008; Pin et al., 2008; Pereira et al., 2009; 2015; Ordoñez-Casado et al., 2008; Antunez et al., 2011; Lima et al., 2012; Gladney et al., 2014).

iii. OMZ Variscan metamorphic rocks.

(Dallmeyer et al., 1993; Castro et al., 1999; Pereira et al., 2009).

iv. Late Devonian to early Carboniferous sedimentary rocks.

(Braid et al., 2011; Pereira et al., 2012c).

For comparison with the OMZ ages we added U-Pb single and population zircon data and whole-rock ages of contemporaneous magmatic and sedimentary rocks from the other autochthonous Iberian Massif Zones:

i. The Central Iberian Zone.

(Gutiérrez-Alonso et al., 2003; Bea et al., 2006; 2007; Pereira et al., 2012a; Talavera et al., 2012; 2013; Fernández-Suárez et al., 2014; Shaw et al., 2014).

ii. the Cantabrian Zone.

(Fernández-Suárez et al., 2014; Shaw et al., 2014).

iii. the Galicia Tras-os-Montes Zone parautochthonous units.

(Montero et al., 2009b; Díez-Fernández et al., 2010; 2012; Talavera et al., 2013).

In addition, the database was completed with north African single and population zircon and whole-rock ages for Neoproterozoic and Cambrian magmatic and sedimentary rocks from:

i. the Anti-Atlas, West African Craton.

(Ducrot and Lancelot, 1977; Comptson et al., 1992; Aït Malek et al., 1998; Chalot-Prat et al., 2001; Gasquet et al., 2001; 2004; 2005; Thomas et al., 2002; Walsh et al., 2002; Barbey et al., 2004; Samson et al., 2004; Inglis et al., 2004; 2005; Peucat et al., 2005; D'Lemos et al., 2006; Eddif et al., 2007; Abati et al., 2010a; Tahiri et al., 2010; Avigad et al., 2012; Tounmmite et al., 2013)

ii. the Tuareg Shield.

(Snelling, 1964; Tougarinov et al., 1968; van Bremen et al., 1977; Caby et al., 1982;1985; 1989; Okeke and Fitton, 1982; Lancelot et al., 1983; Caen-Vachette and Umeji, 1983; Tubosun et al., 1984; Bertrand et al., 1986a; 1986b; Liégeois et al., 1987; 1994; 2003; Caby and Andreopoulos-Renard, 1989; Barbey et al., 1989; Dada and Respaut, 1989; Dada et al., 1989; 1993; Küster, 1995; Ferré et al., 1996; 2002; Paquette et al., 1998; Hadj-Kaddour et al., 1998; Kröner et al., 2001; Ferkous and Monié, 2002; Azzouni-Sekkal et al., 2003; Peucat et al., 2003; Abdallah et al., 2007;Bendaoud et al., 2008; Henry et al., 2009; Linnemann et al., 2011)

iii. the Sahara Metacraton.

(Bea et al., 2010; Meinhold et al., 2011; Morton et al., compiled in Meinhold et al., 2013).

5.2 Samples

All three of the studied plutonic bodies have varied compositions that overlap to a greater or lesser extent. The Burguillos del Cerro and the Valencia del Ventoso plutonic complexes show the greatest diversity from ultramafic-mafic to felsic whereas the Brovales pluton comprises intermediate to felsic rock types (Fig. 5.1). Some 141 Burguillos samples were selected for detailed study: 31 rocks from the *Central Ultrabasic-Basic Layered Unit*; 49 from the *Central Alkaline Basic-Intermediate Layered Unit* mafic-intermediate rocks and 10 felsic rocks; 45 from the

Complex	Unit	Rock type	Coordinates		Description
Burguillos del Cerro plutonic complex	*Central Ultrabasic-Basic Layered Unit*	Ultramafic rocks (BUAW-9)	716566	4253804	Fresh ultramafic rock with abundant phlogopite and amphibole
		Olivine gabbros (BUAW-8)	716614	4253692	Ultramafic rock with cumulitic textures and abundant plagioclase and phlogopite
		Poikilitic amphibole gabros and gabbronorites (BUAW-4)	711921	4247490	Gabbroic rock with large plagioclase and poikilitic amphibole with minor amount of biotite ('ojo de culebra' facies)
	Central Alkaline Basic-Intermediate Layered and Acid Unit	Gabbros and diorites (BUAW-6)	712737	4247219	Medium to coarse-grained inequigranular rock plagioclase and pyroxene, with slight orientation of biotite.
		Alkali feldspar granites (BUAW-10)	710379	4251411	Coarse-grained granite less content in biotite and amphibole. In some places it has minor mafic enclaves.
	External Subalkaline Intermediate Unit	Quartz diorites to tonalites (BUAW-5)	708753	4247357	Medium-grained equigranular rock with amphibole, biotite, plagioclase and rare quartz.
	Acid Peraluminous Unit	Two mica granites (BUAW-3)	708255	4249014	Medium- to fine-grained equigranular granitic dyke, which cuts gabbroic rocks, with abundant biotite and primary muscovite
Valencia del Ventoso plutonic complex	*Main Pluton Alkaline to Subalkaline Basic-Acid Unit*	Gabbros (VAAW-20)	721339	4237741	Fine-grained gabbro with minor amounts of amphibole and mica
		Diorites (VAAW-35)	722633	4241171	Medium-grained rock with more amphibole than pyroxene. In some areas shows intermediate rocks enclaves
		Quartz diorites (VAAW-37)	720521	4233932	Coarse-grain intermediate rock with slightly oriented amphibole and biotite, also cut by aplitic dykes
		Granodiorites to granites (VAAW-38)	718456	4232771	Coarse-grained granodiorite with mingling relationship with mafic rocks

Table 5.1. Representative samples from the Burguillos del Cerro and Valencia del Ventoso plutonic complexes and the Brovales pluton. Text in brackets is the sample number. The coordinates are UTM WGS1984.

Complex	Unit	Rock type	Coordinates		Description
Valencia del Ventoso plutonic complex	*Northern Stock Subalkaline Basic-Intermediate Unit*	Quartz monzodiorites (VAAW-30)	723608	4245488	Medium-grained intermediate rock with orthopyroxene
	Southern Stock Subalkaline Intermediate-Acid Unit	Quartz monzodiorites (VAAW-17)	713722	4233769	Medium-grained intermediate rock with amphibole and biotite
	Intrusive Dyke Unit	Aplites (VAAW-24)	721566	4239988	Intrusive dyke restricted to the plutonic complex. In some places it has pegmatitic textures with tourmaline and muscovite
Brovales pluton	*Central Subalkaline Intermediate Unit*	Quartz diorites (B-2)	704242	4247457	Intermediate rock with strong foliation and mafic enclaves
		Granodiorites (B-3)	702487	4248440	Rock with strong foliation marked by the orientation of mafic minerals that, in some cases, are deformed
	Intermediate Subalkaline Intermediate Unit	Granodiorites (B-5-1)	700592	4245121	Undeformed facies with fine-grain size and patchy interaction with coarse-grain size rocks
		Granodiorites (B-5-2)	700592	4245121	Undeformed facies with coarse-grain size and patchy interaction with fine-grain size rocks
		Granodiorites (B-8-1, B-8-3)	700961	4239038	Variable deformed granodiorite with large feldspar and development of S-C structures
	External Subalkaline Acid Unit	Granites (B-7)	705211	4248041	Medium- to fine-grained granite, with slightly orientation of micas
	Intrusive, Acid Peraluminous, Dykes	Aplites (B-8-2)	700961	4239038	Strongly deformed aplite emplaced in the deformed Intermediate Unit granodiorites
Olivenza-Monesterio basement	Cambrian leucogranite (VAAW-41)		711586	4234982	Granite with Serie Negra blocks
	Serie Negra metasediment (VAAW-39)		712335	4236249	Fine-grained metagreywacke with recrystallized textures

Table 5.1. Continued

External Subalkaline Intermediate Unit; and six from the *Acid Peraluminous Unit*. Of these, samples from each group, six in total, were chosen for U-Pb SHRIMP dating, however it was only possible to separate zircons from four of these because the ultramafic sample did not contain any (see Table 5.1). Fig. 5.1 shows the location of all the samples dated in this work.

For Valencía de Ventso we complemented the data of Sarrionandia (2005) with analyses of representative samples some of which were picked out for geochronological study (see Table 5.1): one sample from the *Northern* (Medina de las Torres) *Stock,* another from the *Southern* (Cortijo del Pozuelo) *Stock*, three from the *Main Pluton* and an *Acid Peraluminous Dyke* (Fig. 5.1). A similar approach was taken for the Brovales pluton. The data of Pons (1981) were supplemented by selected analyses of samples that we dated (see Table 5.1): one from the *Central Subalkaline Intermediate Unit*, another from the *Intermediate Subalkaline Intermediate Unit*, one *External Subalkaline Acid Unit* sample and an *Acid Peraluminous Dyke* (Fig. 5.1). A pre-Variscan Cambrian alkaline leucogranite cut by the Valencia del Ventoso plutonic complex and an Olivenza-Monesterio Antiform Serie Negra metasediment were also analysed and dated (Table 5.1, Fig. 5.1).

Whole-rock major and trace element compositions were determined for all the selected samples (Appendix II). The Sr and Nd isotopes compositions were also obtained in 32 Burguillos del Cerro plutonic complex samples, six Valencia del Ventoso plutonic complex samples and four Brovales pluton samples (Appendix II). Moreover, the Cambrian leucogranite and metasediment were also analysed for Sr and Nd isotopes (Appendix II). We analysed the mineral compositions in 12 samples from the Burguillos 6 from the Valencia plutonic complexes and 4 from the Brovales pluton, as well as in the Cambrian leucogranite and metasediment (Appendix III). The zircons separated from eight of the 17 dated samples were also analysed 8 for O isotopes using the IBERSIMS SHRIMP (Appendix IV).

5.3 Methods

All the analyses were performed at the Scientific Analytical Centre (CIC, Centro de Instrumentación Científica), University of Granada.

5.3.1 Mineral Chemistry

5.3.1.1. Scanning Electron Microscopy (SEM)

Electron images were obtained by scanning electron microscopy (SEM) and energy-dispersive spectrometry (EDX) with a Zeiss DSM-950 scanning microscope equipped with a Link Isis series 300 Analytical Pentafet system, operated at 20 kV and 1-2 nA bean current. Natural and synthetic standards were employed in the analyses of mineral major elements.

Precision was better than ± 1.5 proportion for analyte concentrations of 1 wt % proportion.

5.3.1.1. Electron Microbeam Probe Analysis (EMPA)

Major element analyses of minerals were obtained at the University of Granada by wavelength dispersive analyses with a Camebax SX-100 electron microprobe, using synthetic standards. Accelerating voltage was 20 kV, and beam current was 15 nA. Coefficients of variation were, respectively, close to 1 %, 2.5 %, and 5 % for 10 wt %, 1 wt %, and 0.25 wt % for the synthetic standards run as unknowns and analyte concentration.

5.3.2 Whole-Rock

5.3.2.1. X-Ray Fluorescence (XRF)

Major element determinations were performed by X-ray fluorescence, after fusion with lithium tetraborate. Typical precision was better than ±1.5% for an analyte concentration of 10 wt %. Zirconium was determined by X-ray fluorescence on the same disks, with a precision better than ± 4% for 100 ppm Zr.

5.3.2.2. Inductively Coupled Plasma Mass Spectrometry (ICP-MS)

Trace element determinations were done by ICP-mass spectrometry (ICP-MS) after HNO_3+HF digestion of 0.1000 g of sample powder in a Teflon-lined vessel at ~180 °C and 200 psi for 30 min, evaporation to dryness, and subsequent dissolution in 100 ml of 4 vol.% HNO_3. Instrument measurements were carried out in triplicate with a PE SCIEX ELAN-8000 spectrometer using rhodium as an internal standard. Precision, as determined from standards WSE, BR and AGV run as unknowns, was better than ±2% and ±5% for analyte concentrations of 50 and 5 ppm, respectively.

5.3.2.3. Thermal Ionization Mass Spectrometry (TIMS)

Samples for Sr and Nd isotope analysis (0.1000 g) were digested with HNO_3 + HF in a Teflon-lined vessel at 200 p.s.i. The elements were separated with ion-exchange resins, and the Sr and Nd isotope ratios were determined by thermal ionization mass spectrometry (TIMS) with a Finnigan Mat 262. All reagents were ultra clean. Normalization values were $^{86}Sr/^{88}Sr = 0.1194$ and $^{146}Nd/^{144}Nd = 0.7219$. Blanks were 0.6 and 0.09 ng for Sr and Nd. The external precision (2σ), estimated by analyzing 10 replicates of the standard WS-E (Govindaraju et al., 1994), was better than ± 0.003% for $^{87}Sr/^{86}Sr$ and ±0.0015% for $^{143}Nd/^{144}Nd$. $^{87}Rb/^{86}Sr$ and $^{147}Sm/^{144}Nd$ were directly determined by ICP-MS following the method developed by Montero and Bea (1998), with a precision better than ±1.2% and ±0.9% (2σ) respectively.

5.3.3 U-Pb and O Isotopes SHRIMP Dating

Zircon was separated using panning, first in water and then in ethanol. This was followed by magnetic extraction of Fe-rich minerals with a Nd magnet. Finally, zircons were handpicked using a binocular microscope. The zircons were cast on "megamounts", i.e., 35 mm epoxy discs fixed on the front of a mount holder so that no metallic parts or surface discontinuities faced the secondary ions extraction plate. The minerals were carefully studied with optical (reflected and transmitted light) and scanning electronic microscopy (backscattering and cathodoluminescence) prior to SHRIMP analyses with the IBERSIMS SHRIMP IIe/mc ion microprobe at the University of Granada.

Zircons were analysed for U-Th-Pb following the method described by Williams and Claesson (1987). The mount was coated with a ≈ 12 nm thick gold layer. Each spot was rastered with the primary beam for 120 s prior to analysis and then analysed for 6 scans following the isotope peak sequence $^{196}Zr_2O$, ^{204}Pb, $^{204.1}$background, ^{206}Pb, ^{207}Pb, ^{208}Pb, ^{238}U, ^{248}ThO, ^{254}UO. Every peak of every scan was measured sequentially 10 times with the following total counting times per scan: 2 s for mass 196; 5 s for masses 238, 248, and 254; 15 s for masses 204, 206, and 208; and 20 s for mass 207. The primary beam, composed of $^{16}O^{-16}O^{+}$, was set to an intensity of about 5 nA, with a 120 microns Kohler aperture, which generated 17 x 20 micron elliptical spots on the target. The secondary beam exit slit was fixed at 80 microns, achieving a resolution of about 5000 at 1% peak height. All calibration procedures were performed on the standards included on the same mount. Mass calibration was done on the REG zircon (ca. 2.5 Ga, very high U, Th and common lead content). The analytical session started by measuring the SL13 zircon (Claoue-Long et al., 1995), which was used as a concentration standard (238 ppm U). The TEMORA zircon (416.8 ± 1.1 Ma; Black et al., 2003), used as an isotope ratios standard, was then measured every 4 unknowns. Data reduction was done with the SHRIMPTOOLS software (available from www.ugr.es/~fbea), which is a new implementation of the PRAWN software originally developed for the SHRIMP. Errors are reported at the 95% confidence interval (≈2 sigma). Standard errors (95% C.I) on the 37 replicates of the TEMORA standard measured during the analytical session were ± 0.35% for $^{206}Pb/^{238}U$ and ± 0.83 % for $^{207}Pb/^{206}Pb$

Zircon oxygen isotopes were analysed following, "grosso modo", the method described by Ickert et al. (2008) on the megamounts previously used for U-Th-Pb determinations. After slight repolishing, the mount was recoated with a 12 nm thick gold layer. The primary beam consisted of a 15 kV and 3 to 3.5 nA Cs ion beam focused to produce a 17 x 20 μm elliptical spot on the sample. The electrical charge of the non-conductive zircons caused by the primary beam was neutralised with an electron beam that impacted the sample in a ≈ 200 μm diameter spot concentric with the Cs beam. The source slit was fixed at 150 μm and the secondary ^{18}O and ^{16}O

were measured simultaneously in static mode on two Faraday cups with entry slits of 300 μm. The sample was pre-sputtered for 180 s prior to analysis. During the last 90 s of the pre-sputtering time the secondary beam and the electron beam were focused to obtain the maximum signal on the Faraday cups. The measurement consisted of two sets of six scans, each scan lasted 10 s. The mass fractionation caused by the Earth's magnetic field was compensated with Hemholtz coils operated at -309 mA. This compensation also eliminated the mass fractionation related to the horizontal steering of the secondary beam. Electron-induced secondary-ion emission (EISI) was measured for 10 s both at the beginning of each scan and at the end of the measurement, it was then and subtracted accordingly. Data reduction was performed using the POXI software developed by Peter Lanc and Peter Holden at the ANU. The zircon standard TEMORA-2 ($\delta^{18}O$ = 8.2 ± 0.3 ‰, Black et al., 2004) was measured several times at the beginning of the session and every four unknowns it was cross-checked against the 91500 zircon standard ($\delta^{18}O$ = 9.86 ± 0.11 ‰, Wiedenbeck et al., 2004), ten to fifteen replicates of which were measured as unknowns interspersed throughout the analytical session.

Chapter 6: Petrography

6.1 Burguillos del Cerro Plutonic Complex

6.2 Valencia del Ventoso Plutonic Complex

6.3 Brovales Pluton

6.4 Cambrian Leucogranite and the Serie Negra Metasediment

6.5 Petrographic Comparison of the Main Units of the Three Plutonic Bodies

6. Petrography

6.1 Burguillos del Cerro Plutonic Complex

The Burguilos del Cerro plutonic complex comprises ultramafic to felsic rocks (Pons, 1982; García-Casquero, 1991). In Chapter 4, using field relations, petrography and whole-rock compositions, we defined four main Burguillos del Cerro plutonic complex rock groups (Fig. 4.1): i. the *Central Ultrabasic-Basic Layered Unit*; ii. the *Central Alkaline Basic-Intermediate Layered and Acid Unit*; iii. the *External Subalkaline Intermediate Unit* and iv. the *Acid Peraluminous Unit*. Here we summarize the main petrographic features of each of our newly defined groups, this information is summarised in Table 6.1 which also includes representative samples for each unit.

6.1.1 Central Ultrabasic-Basic Layered Unit

6.1.1.1 Ultramafic and Mafic Rocks

The ultramafic rocks of this unit are lherzolites, harzburgites and olivine websterites. They contain variable proportions of olivine, orthopyroxene (enstatite), clinopyroxene (dipsode-augite), phlogopite, amphibole (hastingsites-pargasites) and plagioclase (bytownite-labradorite) (Fig 6.1A). Accessory phases include chromite, magnetite, ilmenite and apatite.

These rocks have inequigranular textures with orthopyroxene and amphibole showing particularly variable grain size. Cumulate textures are common, although often more obvious at outcrop rather than thin-section scale: euhedral to subhedral olivine, clinopyroxene and reddish brown amphibole are cumulate phases (Fig 6.1B and C) whereas the intercumulus phases are colourless amphibole and orthopyroxene (Fig 6.1D and E). The role of phlogopite is ambiguous, it is not poikilitic but does contain inclusions of olivine and, in turn, is included in the clearly intercumulus phases (Fig. 6.1F). The relative modal proportion of cumulus and intercumulus phases is *c.* 50:50, indicating that the rock is an orthocumulate.

The olivine, *c.* 30 vol. %, contains inclusions chromite (Fig. 6.1G) and commonly has a marked veinlike network of serpentine (Fig. 6.1A). In places, olivine crystals are texturally related to phlogopite and amphibole either as rounded inclusions within them or partially resorbed by them (Fig. 6.1E and F). Orthopyroxene, 25-30 vol. %, is present as large poikilitic crystals with inclusions of olivine, clinopyroxene, phlogopite and reddish brown primary amphibole (Fig. 6.1H). Notably the inclusions show no evidence of a change in grain size or mineral phases from core to rim, this is consistent with late-stage growth of the orthopyroxene. The phlogopite represents about 10 vol. %. Its interference colours change from core to rim indicating that it is concentrically zoned (Fig. 6.1B and C). Abundant individual crystals of primary amphibole,.

Main complex	*Rock group unit*	*Facies*	*Ol*	*Opx*	*Cpx*	*Amp*	*Amp (sec)*	*Bt*	*Plg*	*Kfs*	*Qtz*	*Mus*	*Mt*	*Ilm*	*Ap*	*Zrn*	*Ttn*	*Ep*	*Chl*
Burguillos del Cerro plutonic complex	*Central Ultrabasic-Basic Layered Unit*	Ultramafic rocks,(BUAW-9), lherzolites, hazburgites and olivinic websterites	xxx	xxx	x	x	x	x (Phl)					x	x	x				
		Olivine gabbros, BUAW-8	x	xx	xxx	xx	x	x (Phl)	xx				x	x	x				
		Poikilitic amphibole and biotite gabbronorites to gabbros (BUB-3)		xx	xx	xxx		xx	xxx				x	x	x	x			
		Poikilitic amphibole gabbronorites to gabbros (BUAW-4)		x	xx	xxx			xxx				x	x	x	x			
	Central Alkaline Basic-Intermediate Layered and Acid Unit	Gabbros, gabbronorites and diorites (BUB-1)		xx	xx		x	xxx	xxx				xx	xx	xxx	xx			
		Gabbros with amphibole (BUB-15 and BUB-16)		xx	xx	x	xx	xx	xxx				xx	xx	xxx	xx			
		Diorites to quartz diorites (BUAW-6 and BUB-11)			x	xx	x	xx	xxx	x	x		x	x	xxx	xx			
		Syenites and alkali feldspar granites (BUAW-10 and BUB-17)			x	x		x	xx	xxx	xxx		x	x	x	x			
	External Subalkaline Intermediate Unit	Diorites to granodiorites, (BUAW-5, BUB-12 BUB-13 and BUB-14)			x	xxx	xx	xx	xx	x	x		xx	x	x	xx	xx		
	Acid Peraluminous Unit	Two-mica granites, aplites and pegmatites (BUAW-3)						x	xx	xxx	xxx	x	x		x	xx			

Table 6.1. Summary of the main petrographic characteristics. The abundance of each mineral is indicated by the number of crosses from one to three. Ol: Olivine; Opx: Othopyroxene; Cpx: Clinopyroxene; Amp: Amphibole; Amp (sec): Secondary amphibole; Bt: Biotite; Phl: phlogopite; Plg: Plagioclase; Kfd: Alkali feldspar; Qtz; Quartz; Mus: Muscovite; Mt: Magnetite; Ilm: Ilmenite; Ap: Apatite; Zrn: Zircon; Ttn: Titanite; Ep: Epidote; Chl: Chlorite.

Main complex	*Rock group unit*	*Facies*	*Ol*	*Opx*	*Cpx*	*Amp*	*Amp (sec)*	*Bt*	*Plg*	*Kfs*	*Qtz*	*Mus*	*Mt*	*Ilm*	*Ap*	*Zrc*	*Ttn*	*Ep*	*Chl*
Valencia del Ventoso plutonic complex	*Main Pluton Alkaline to Subalkaline Basic-Acid Unit*	Gabbros and diorites (VAAW-20)			xx			xxx	xxx				x	x	xx	x			
		Diorites to quartz diorites (VAAW-35)			x	xx	x	xx	xx	x	x		x	x	x	x	x		
		Quartz monzodiorites to granites (VAAW-37-38)			x	xx	x	xx	xx	xx	xx		x	x	x	x	xx	x	
	Northern Stock Subalkaline Basic-Intermediate Unit	Gabbros to quartz monzodiorites (VAAW-30)	x	xx	x		xxx	xx	xxx	x	x		x	x	x	x	x		
	Southern Stock Subalkaline Intermediate-Acid Unit	Quartz monzodiorites, quartz diorites and tonalites (VAAW-17)			x		xxx	xx	xx	x	x		x	x	x	x			
	Intrusive Dyke Unit	Syenites and aplites (VAAW-24)						x	xx	xxx	xxx	x	x		x	xx			
Brovales pluton	*Central Subalkaline Intermediate Unit*	Quartz monzodiorites to granodiorites (B-2 and B-3)				xx		xx	xx	xx	x		x	x	x	x	x		
	Intermediate Subalkaline Intermediate Unit	Granodiorites (B-5-1, B-5-2 and B-8-1)				xx		xx	xx	xx	xx		x	x	x	x	x	x	
	External Subalkaline Acid Unit	Monzogranites and syenogranites (B-7)						x	x	xxx	xx		x	x	x	x		x	
	Intrusive, Acid Peraluminous, Dykes	Aplites (B-8-2)						x	x	xxx	xxx		x		x	x			
Olivenza-Monesterio basement	*Cambrian leucogranite*	Leucogranite (VAAW-41)							xx	xxx	xxx				x	x			
	Serie Negra metasediment	Metagreywacke (VAAW-39)						xx				x		x	x	x			x

Table 6.1. Continued.

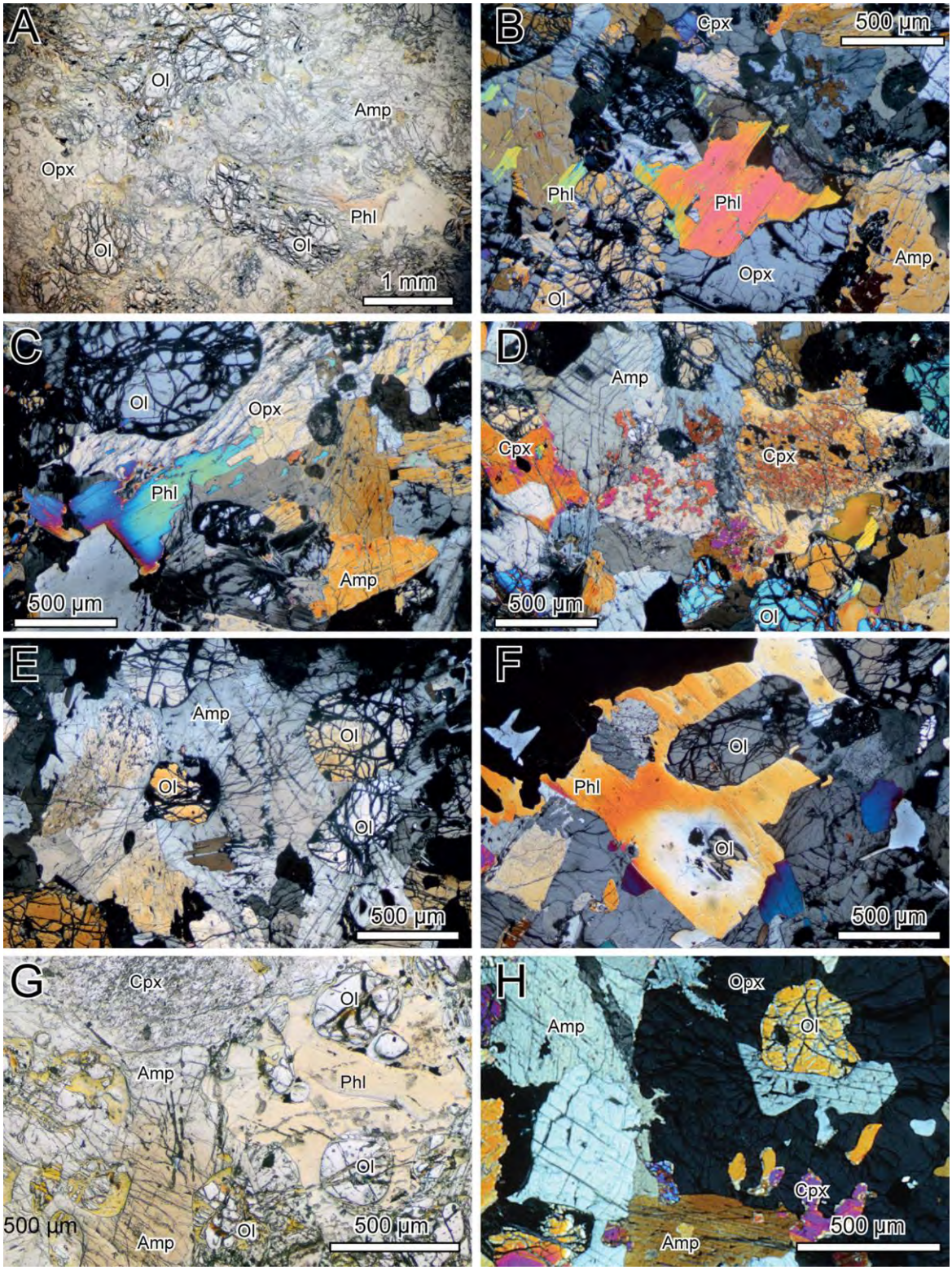

Figure 6.1: Burguillos del Cerro plutonic complex Central Ultrabasic-Basic Layered Unit ultramafic rocks. A) Coarse-grained ultramafic rock from Burguillos Central ultrabasic-basic layered unit, xp. B) and C) Cumulus olivine and pyroxene, intercumulus phlogopite and amphibole, xp. D) Clinopyroxene transformation to secondary amphibole, xp. E) Rounded olivine partially reabsorbed by amphibole, xp. F) Rounded olivine partial reabsorbed by phlogopite, xp. G) Chromite in olivine, ppl. H) Poikilitic orthopyroxene with the inclusions include olivine, clinopyroxene, phlogopite and reddish brown primary amphibole, xp. Ol: Olivine; Cpx: Clinopyroxene; Opx: Orthopyroxene; Amp: Amphibole; Phl: Phlogopite. (xp and ppl crossed polars and plane-polarized light respectively)

some 10 vol. %, are zoned with reddish brown cores and colourless rims or are completely colourless (Fig 6.1E, G and H). Clinopyroxene is a minor phase. It commonly transforms to secondary pale green amphibole, actinolite (Fig. 6.1D).

The apparent order of order of crystallisation of the main mineral phases is: olivine, clinopyroxene, phlogopite, reddish brown amphibole, orthopyroxene and colourless amphibole.

These cumulate rocks may be considered the only real products of gravitational segregation. The other layered rocks represent cumulates formed by crystal growth at the juncture between the cumulate pile and the melt - provoking in situ crystallisation (cf., Langmuir, 1989).

This unit also includes rocks that have somewhat more than 10 modal% plagioclase and so may be considered as gabbros (Fig. 6.2A to D). Their textures and mineralogy are comparable to the ultramafic samples, with the addition of intercumulus plagioclase (Fig. 6.2E). Thus they representing the transition between the ultramafic rocks (described above) and the 'true' gabbros and gabbronorites from this unit (described below). Clinopyroxene, 30-40 vol. %, is much more abundant than in the ultramafic rocks. It also shows the same transformation to secondary amphibole (Fig. 6.2F). Orthopyroxene, 25-30 vol %, is present as large poikilitic crystals with numerous inclusions of olivine, clinopyroxene and plagioclase (Fig. 6.2B and D). Plagioclase, *c.*10 vol. %, is euhedral with a tabular habit and polysynthetic twins, it shows no textural evidence of disequilibrium (Fig. 6.2C). Reddish brown to pale yellow poikilitic amphibole, *c.* 10 vol. %, is also common (Fig. 6.2H), it includes plagioclase, which is smaller than in the surrounding matrix (Fig. 6.2H). The texture of the amphibole is similar to that of the 'gabbros and gabbronorites with poikilitic amphibole' (see below) in which this phase is much more abundant. Phlogopite, by contrast, is less abundant, <5 vol. %, than in the ultramafic rocks and has a poikilitic texture with inclusions of olivine (Fig. 6.2G).

The apparent order of crystallisation of the main mineral phases is: olivine, clinopyroxene, phlogopite, plagioclase, orthopyroxene and amphibole.

6.1.1.2 Gabbros and Gabbronorites

The gabbroic rocks from this unit are poikilitic amphibole gabbros and gabbronorites and minor olivine gabbronorites and troctolites. All the rocks contain variable proportions of plagioclase (bytownite-labradorite), amphibole (pargasites-magnesiohastingsites), biotite, olivine, clinopyroxene (diopside-augite), orthopyroxene (enstatite), (Fig. 6.3). Accessory phases include apatite, abundant magnetite, ilmenite and zircon. All the amphibole gabbros and gabbronorites in this group have large poikilitic crystals of amphibole (Fig. 6.3). The rocks are inequigranular,

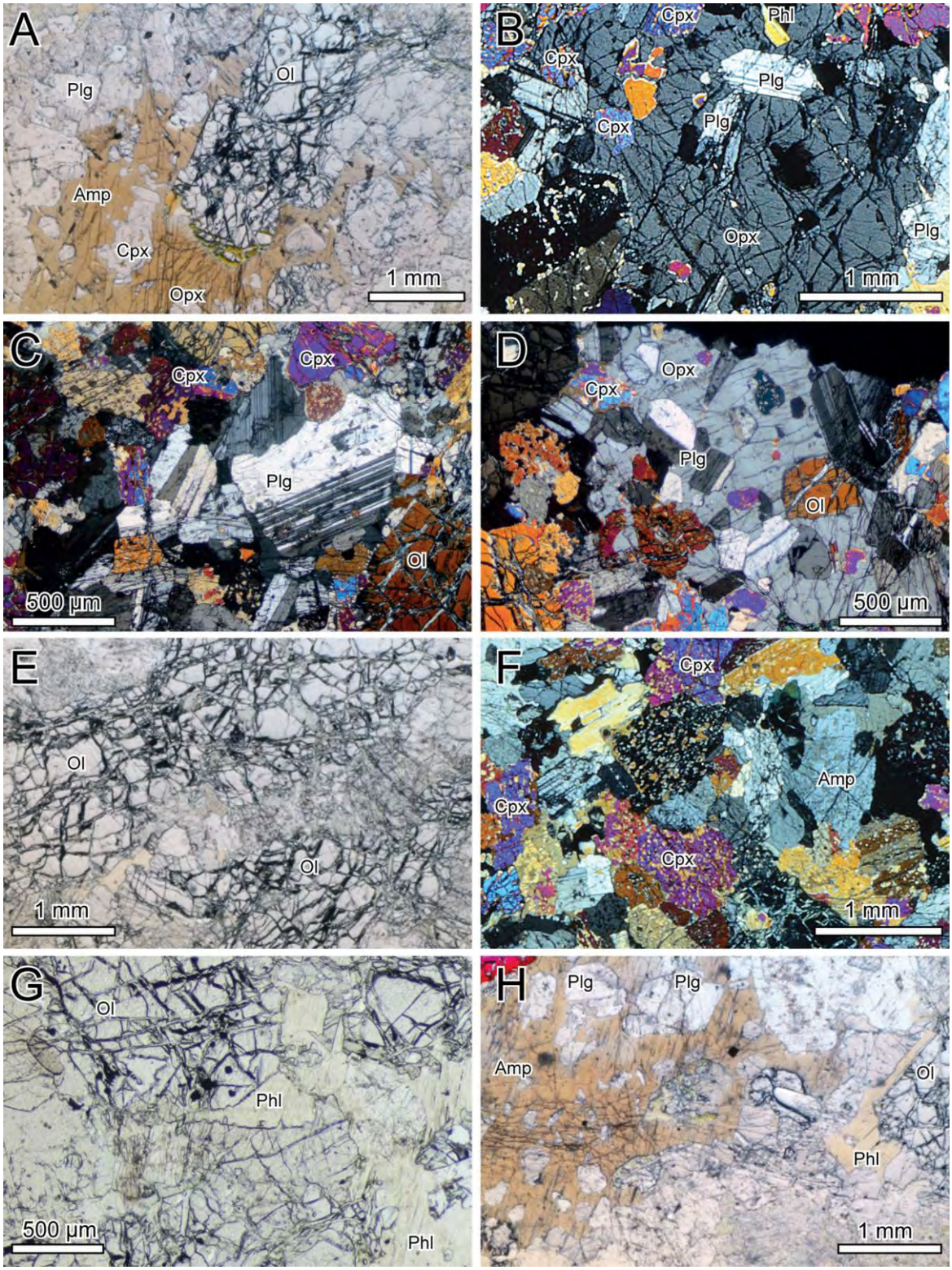

Figure 6.2: Burguillos del Cerro plutonic complex Central Ultrabasic-Basic Layered Unit olivine gabbros. A) Olivine gabbro, ppl. B) Poikilitic orthopyroxene with numerous inclusions of olivine, clinopyroxene and plagioclase, xp. C) Euhedral plagioclase with a uniform internal structure, a tabular habit and polysynthetic twins, xp. D) Poikilitic orthopyroxene with numerous inclusions of olivine, clinopyroxene and plagioclase, xp. E) Olivine gabbro, ppl. F) Clinopyroxene transformation to secondary amphibole, xp. G) Poikilitic phlogopite with numerous inclusions of olivine, xp. H) Reddish brown to pale yellow pleochroic poikilitic amphibole, ppl. Ol: Olivine; Cpx: Clinopyroxene; Opx: Orthopyroxene; Amp: Amphibole; Phl: Phlogopite; Plg: Plagioclase. (xp and ppl crossed polars and plane-polarized light respectively)

particularly regarding the size of the plagioclase and amphibole. The amphibole, *c.* 40 vol. %, and to a lesser extent the biotite, 0-5 vol. %, are poikilitic with pyroxene, plagioclase, and apatite inclusions (Fig. 6.3A to D). The texture is adcumulate, with the cumulus phases including olivine, pyroxene, plagioclase, biotite and amphibole. The only intercumulus phase appears to be Fe-Ti oxide. This facies may be the product of in situ crystallisation (cf., Langmuir, 1989).

Plagioclase is the most abundant phase, c. 50 % vol., the grains have a seriate texture, tabular subhedral form and polysynthetic twins (Fig. 6.3E). Some grains of this mineral show at least three different textures indicative of disequilibrium: i. crystal aggregates formed during distinct crystallisation stages overgrown by common rims (Fig. 6.3F), ii. crystals with patchy zoned cores and overgrowth rims (Fig 6.3G); iii. resorbed, rounded, plagioclase cores overgrown by a later phase of plagioclase (Fig. 6.3H). Amphibole, 20-45 % vol., is always poikilitic, it shows a clear dark brown to pale yellow pleochroism (Fig. 6.3A). Biotite, *c.* 1-10 % vol, has two habits: in some samples it is poikilitic and strongly pleochroic, varying from dark red to pale yellow (Fig. 6.3B) in other samples it is only present as euhedral crystals included in the poikilitic amphibole (Fig. 6.3C).

The textural relationships between the biotite and amphibole permitted us to identify two petrographic facies. The first facies has poikilitic amphibole and, less abundant, poikilitic biotite (Fig. 6.3B). The second facies only contains poikilitic amphibole with inclusions of subhedral biotite plus olivine, clinopyroxene and plagioclase (Fig. 6.3C).

In contrast to the poikilitic intercumulus orthopyroxene and colourless amphibole in the ultramafic rocks, changes in both grain-size and mineral phases of inclusions are observed from the cores to the rims of poikilitic amphibole and biotite in this unit. Olivine and clinopyroxene are more common in the centres of the oikocrysts than in the rims (Fig. 6.3A and D). Plagioclase, by contrast, is spread throughout the oikocrysts. All inclusions vary in size from smaller in the centres to larger at the rims, and larger still in the matrix (Fig. 6.3A).

The variations in the distribution of the inclusions in the poikilitic amphibole and biotite and may be explained by the amphibole beginning to crystallise early with a low nucleation but high growth rate, resulting in large, up to centimetric-scale, crystals. This 'pegmatitic-like' growth probably resulted from an elevated H_2O content in the magma. Other mineral phases, by contrast, had a higher nucleation rates but slower growth rates - perhaps a result of their dry nature. So, as the amphibole grew it surrounded and shielded olivine, clinopyroxene and, especially, plagioclase preventing them from further growth Unshielded crystals in the magma continued to grow until

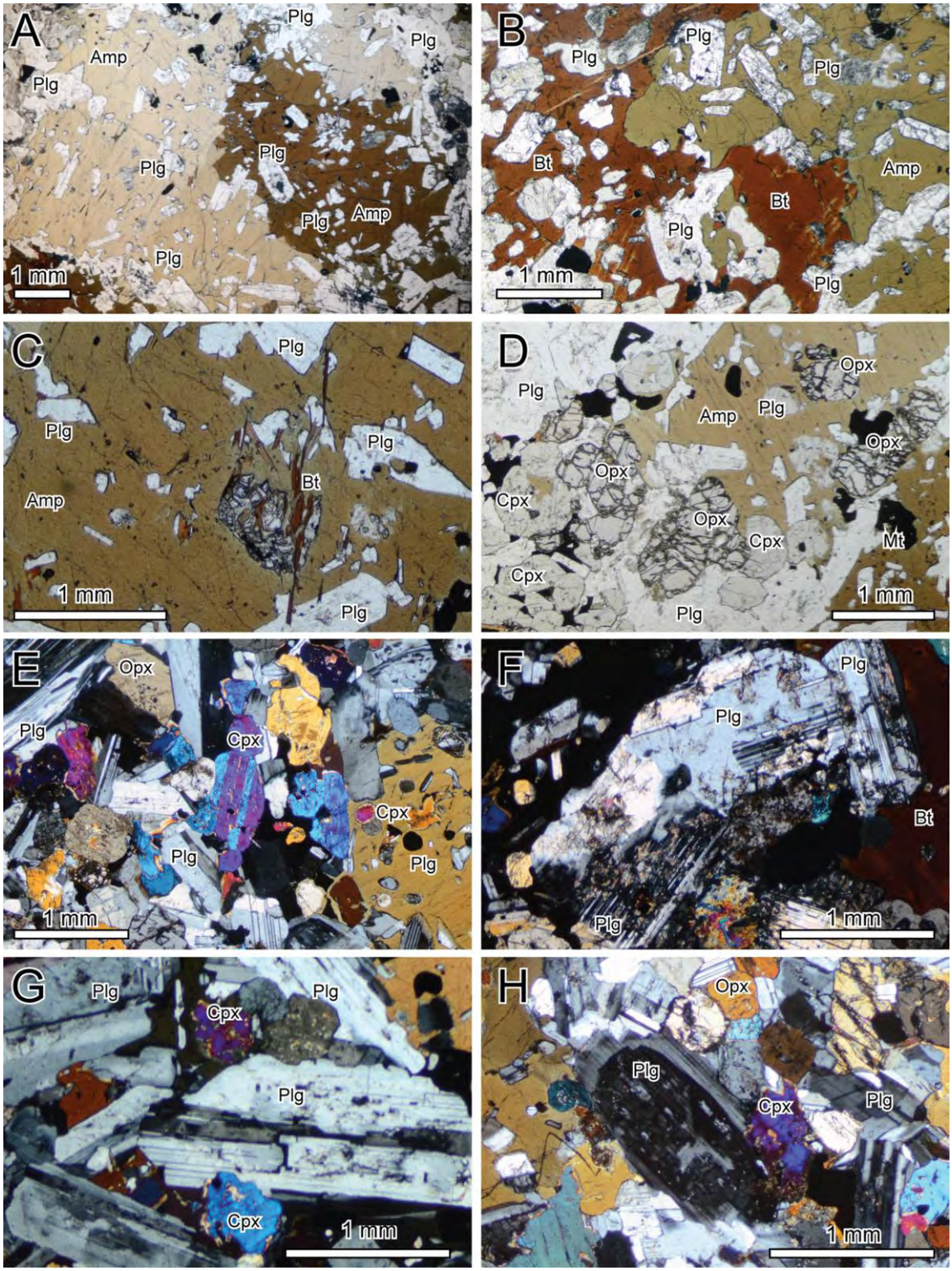

Figure 6.3: Burguillos del Cerro plutonic complex Central Ultrabasic-Basic Layered Unit gabbros and gabbronorites: A) Amphibole gabbro, note the large size poikilitic amphibole, ppl. B) Poikilitic amphibole and biotite with inclusions of pyroxene, plagioclase, and apatite, ppl. C) Poikilitic amphibole with inclusions of plagioclase, biotite and pyroxene, ppl. D) Poikilitic amphibole and biotite with inclusions of pyroxene, plagioclase, and Fe-Ti oxides, ppl. E) Plagioclase with seriate grain size and a uniform internal structure with polysynthetic twin, note the grain-size of the inclusions in the poikilitic amphibole, xp. F) Complex growth zoned plagioclase, xp. G) Zoned plagioclase with, at least, two crystallisation steps, xp. H) Plagioclases with cumulitic and recrystallized textures, xp. Cpx: Clinopyroxene; Opx: Orthopyroxene; Amp: Amphibole; Bt: Biotite; Plg: Plagioclase (xp and ppl crossed polars and plane-polarized light respectively).

they too were surrounded. Thus, progressive crystallisation resulted in large crystals of amphibole englobing ever bigger crystals of the other minerals. Many crystals, however, were not 'caught' because of the low amphibole nucleation rate, these grew to a medium grain size (Fig. 6.3E).

The order or crystallisation in the unit is amphibole with olivine, pyroxenes, plagioclase, biotite and Fe-Ti oxides.

6.1.2 Central Alkaline Basic-Intermediate Layered and Acid Unit

The mafic and intermediate rocks of this group are the most abundant in the Burguillos del Cerro plutonic complex. They comprise gabbronorites to gabbros, diorites to quartz diorites, minor granodiorites, syenites and alkali feldspar granites.

6.1.2.1 Gabbros and Gabbronorites

The gabbronorites and gabbros are composed of plagioclase (labradorite), biotite, orthopyroxene (enstatite), clinopyroxene (diopside-augite), and rare amphibole (pargasites-magnesiohastingsites) (Fig. 6.4A and B). Accessory phases are magnetite, ilmenite and abundant large apatite and zircon. The lack of olivine, the near absence of amphibole and the abundance of large euhedral apatite in biotites and plagioclases marks an important difference with the gabbros of the *Central Ultrabasic-Basic Layered Unit* described above.

The rocks of this unit have an inequigranular orthocumulate texture, which is most clearly marked by oriented plagioclase, 50-60 vol. %, (Fig. 6.4C). The biotite, 15-30 vol. %, is poikilitic with large inclusions of apatite, and smaller inclusions of pyroxenes and rare plagioclase (Fig. 6.4A, B and D). Large, 0.5-1 mm, pyroxenes, *c.* 10 vol. %, are the other main cumulus phases (Fig. 6.4A and Fig. 6.4B).

Plagioclase is the most abundant mineral, > 50% vol. In contrast to the *Central Ultrabasic-Basic Layered Unit* gabbros, in this unit plagioclase is euhedral, twinned with little evidence of disequilibrium textures (Fig. 6.4G and 6.4H). The biotite is dark red to pale brown pleochroic (Fig. 6.4A y 6.4B), it is intergrown with the Fe-Ti oxides (Fig. 6.4D). The relative proportions of the pyroxenes vary from norites to gabbros *s.s.* (Fig. 6.4B y 6.4E). Albeit a minor phase, two generations of amphibole may be identified: i) primary, *c.* 5 vol. %, subhedral dark green poikilitic crystals that are present in the 'gabbros with amphibole' of this unit (see below) and ii) secondary anhedral green patchy crystals pseudomorphing pyroxenes (Fig. 6.4D and 6.4F).

The apparent order of crystallisation for these mafic rocks is: apatite, pyroxenes, plagioclase, biotite and amphibole.

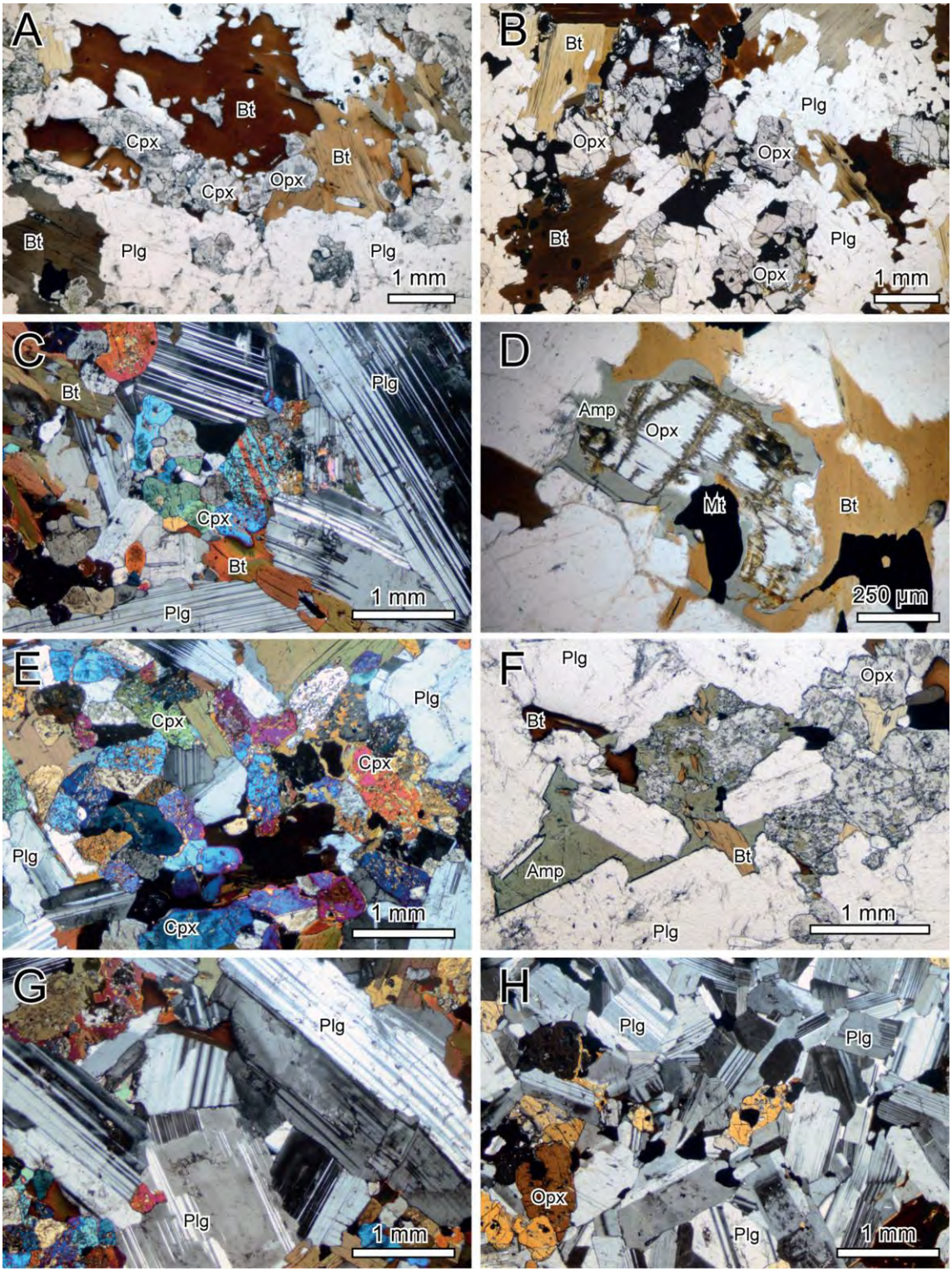

Figure 6.4: Burguillos del Cerro plutonic complex Central Alkaline Basic-Intermediate Layered and Acid Unit gabbros: A) Gabbro with large size poikilitic biotite and pyroxenes, primary amphibole is absent, ppl. B) Detail of orthopyroxene and biotite intergrown with ores. Note that biotite has both euhedral and poikilitic xenomorphic textures, ppl. C) Clinopyroxene with exolution lamellae, ppl. D) Orthopyroxene transformed to green amphibole surrounded by biotite, ppl. E) Clinopyroxene transformed to secondary actinolite, xp. F) Interstitial green amphibole with replacement textures after orthopyroxene. Note that this green amphibole also includes some crystals of biotite, xp. G) Cumulitic plagioclase, xp. H) Cumulitic plagioclase, xp. Cpx: Clinopyroxene; Opx: Orthopyroxene; Amp: Amphibole; Bt: Biotite; Plg: Plagioclase; Mt: Magnetite (xp and ppl crossed polars and plane-polarized light respectively).

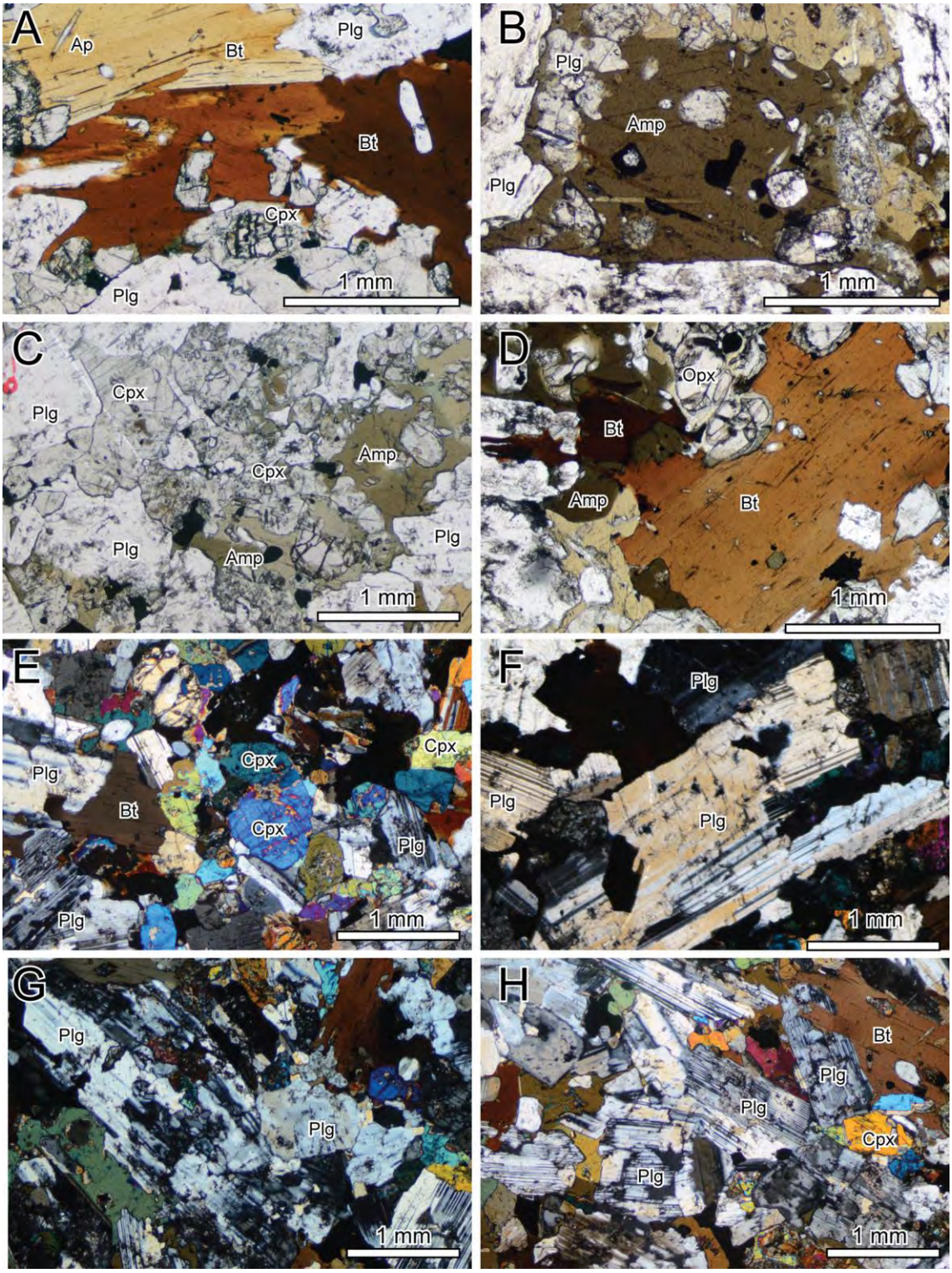

Figure 6.5: Burguillos del Cerro plutonic complex Central Alkaline Basic-Intermediate Layered and Acid Unit amphibole gabbros: A) Amphibole gabbro with abundant poikilitic biotite with abundant inclusions of apatite and intergrowths of Fe-Ti oxides, ppl. B) Dark green subhedral, poikilitic amphibole that has inclusions of all the other minerals, ppl. C) Clinopyroxene partially transformed to secondary actinolite, ppl. D) Poikilitic biotite with abundant inclusions of apatite and intergrowths of Fe-Ti oxides and euhedral biotite included in amphibole, ppl. E) Amphibole gabbro with biotite, clinopyroxene and plagioclase, xp. F) Aggregates of inequigranular, bimodal plagioclase, xp. G) Plagioclase with patchy zoned cores, xp. H) Plagioclase with overgrowth rims, xp. Cpx: Clinopyroxene; Opx: Orthopyroxene; Amp: Amphibole; Bt: Biotite; Plg: Plagioclase; Mt: Magnetite (xp and ppl crossed polars and plane-polarized light respectively).

A few rocks of this unit have more abundant modal amphibole leading us to name them 'amphibole gabbros'. These rocks have a similar mineralogy to the other gabbros of this unit (Fig. 6.5A) but are compositionally transitional towards the *Central Ultrabasic-Basic Layered Unit* gabbros.

They comprise dark green subhedral, poikilitic amphibole that includes all the other minerals: pyroxenes, plagioclase, and poikilitic biotite (Fig. 6.5A to 6.5D). As in the *Central Ultrabasic-Basic Layered Unit* gabbros which, it is worth bearing in mind, also had poikilitic amphibole, the plagioclases here also have textures indicative of disequilibrium for example i. aggregates of crystals formed during distinct crystallisation stages (Fig. 6.5F); ii. crystals with patchy zoned cores and overgrowth rims (Fig 6.5G) and; iii. resorbed, rounded, plagioclase cores overgrown by a later phase of plagioclase (Fig. 6.5H). The poikilitic biotite has abundant inclusions of apatite and intergrowths of Fe-Ti oxides (Fig. 6.5A and 6.5D). It is, however, included in the amphibole indicating early crystallisation, like in the other *Central Alkaline Basic-Intermediate Layered and Acid Unit* rocks (Fig. 6.5D). Plagioclases are inequigranular bimodal (Fig. 6.5E and 6.5F).

6.1.2.2 Diorites to Tonalites

The major minerals of the intermediate rocks of this unit are plagioclase (labradorite), biotite, amphibole (magnesiohastingsites-magnesiohornblendes), clinopyroxene (dipside-augite) and quartz (Fig. 6.6). Accessory phases are magnetite, ilmenite, apatite and zircon. The rocks are inequigranular with large crystals of plagioclase oriented in an adcumulate texture (Fig. 6.6A to D). Both biotite and amphibole are poikilitic with the former included in the latter (Fig. 6.6D).

Plagioclase accounts for up to 40 % vol. (Fig. 6.6E). It forms two generations of euhedral crystals: i. with polysynthetic twins (Fig. 6.6G) and ii) with complex internal structures and discontinuous zoning that indicate distinct crystallisation events (Fig. 6.6H). Biotite is present, up to 15 vol. %, but decreases in the more evolved samples. It has a dark red light brown pleochroism (Fig. 6.6D), and as in the gabbros of this unit, it is poikilitic with abundant apatite inclusions (Fig. 6.6F). Notwithstanding, in the most evolved samples biotite is no longer poikilitic but instead partially surrounded by the amphibole (Fig. 6.6A and D**)**. The primary amphibole 10-15 vol. %, is euhedral with dark green brown cores and lighter rims (Fig. 6.6C). Its modal proportion increases in the more evolved samples as the biotite decreases (more biotite: Fig. 6.6A and 6.6B; more amphibole: Fig. 6.6C and 6.6D).

The apparent order of crystallisation in these rocks is apatite, zircon, clinopyroxene, plagioclase, Fe-Ti oxides, biotite, amphibole, quartz.

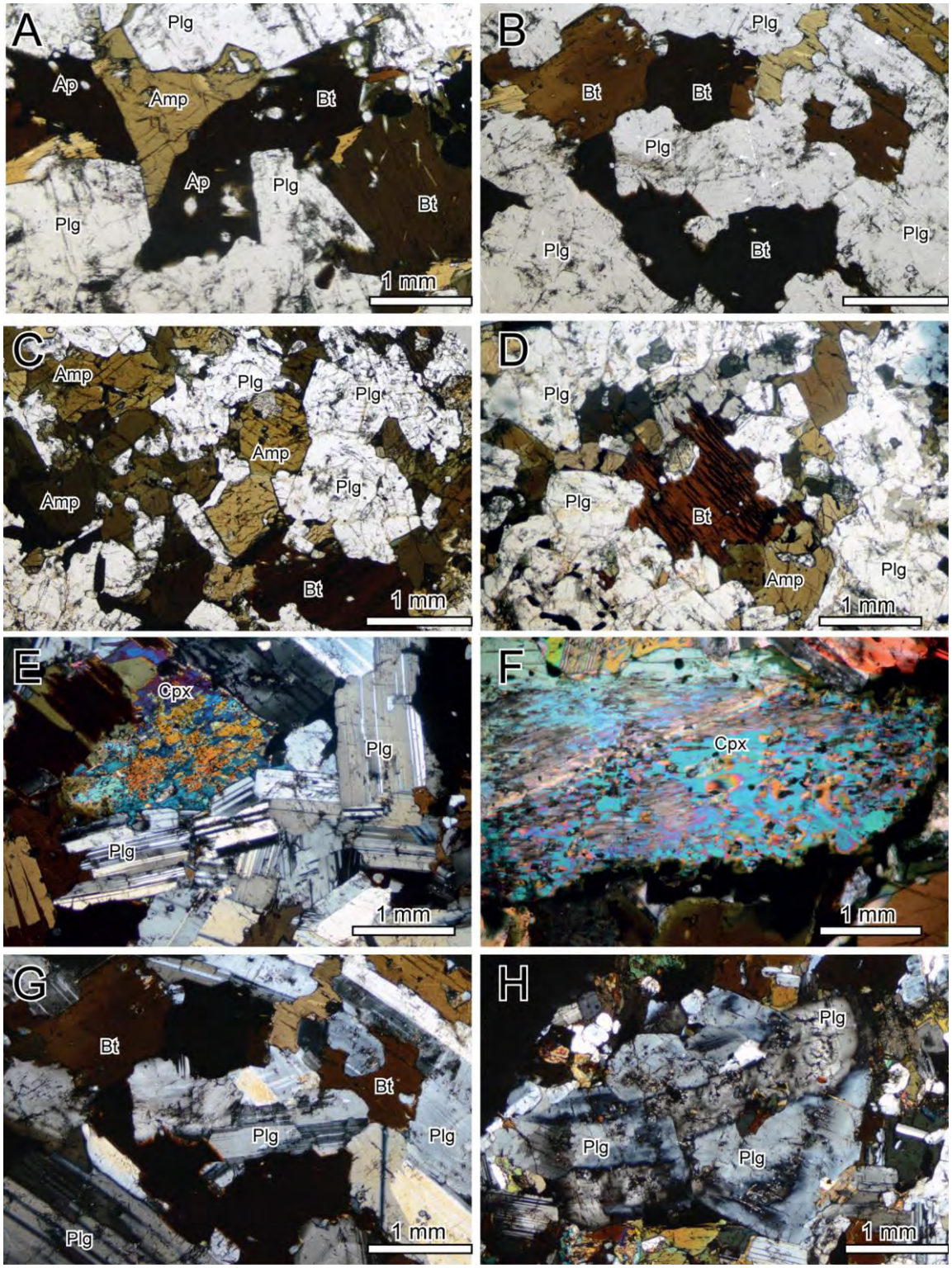

Figure 6.6: Burguillos del Cerro plutonic complexCentral Alkaline Basic-Intermediate Layered and Acid Unit diorites and quartz diorites: A) Coarse-grained diorite, note the amphibole in addition to the poikilitic biotite, ppl. B) Reddish brown biotite surrounding plagioclase, ppl. C) and D) Relationship between reddish biotite and amphibole. The latter is medium-grained it includes the biotite. Notably, amphibole shows a zonation from brown cores to green rims, ppl. E) Coarse-grained tonalite, note the abundance in biotite rather than amphibole and the oriented plagioclase, xp. E) Clinopyroxene partially transformed to secondary amphibole, xp. G) Plagioclase with uniform internal structures and polysynthetic twins, xp. H) Plagioclase with complex internal structures and discontinuous zoning, xp. Mineral abbreviations as Fig. 6.4 (xp and ppl crossed polars and plane-polarized light respectively).

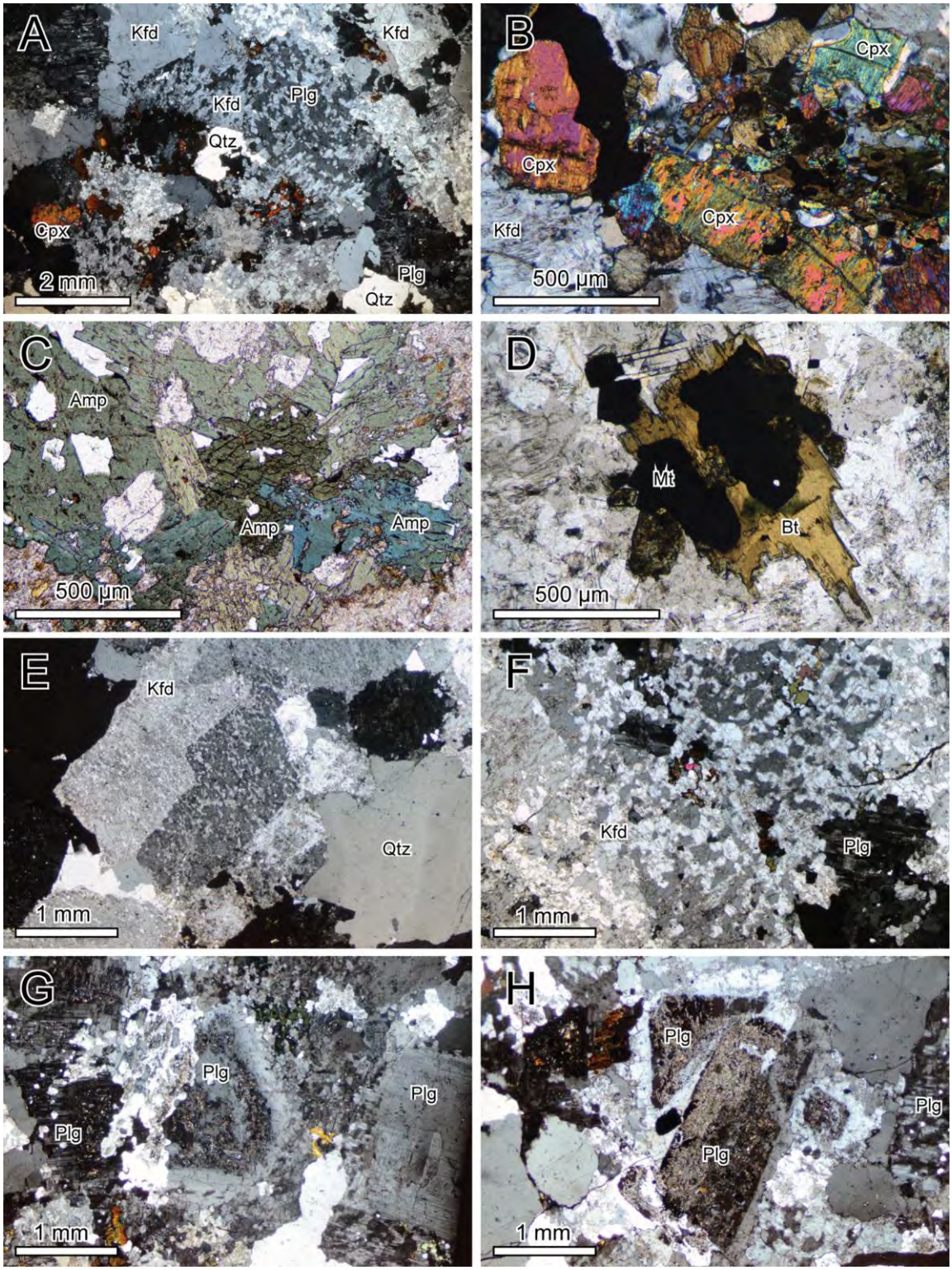

Figure 6.7: Burguillos del Cerro plutonic complex Central Alkaline Basic-Intermediate Layered and Acid Unit granites: A) Medium-grained syenite, xp. B) Clinopyroxene partially transformed to secondary amphibole, xp. C) Poikilitic, subhedral inequigranular green amphibole, ppl. D) Subhedral biotite intergrown with Fe-Ti oxides, ppl. E) Perthitic alkali feldspar and quartz, ppl. F) Detail of the alkali feldspar with inclusions of biotite and plagioclase, xp. G) Plagioclase with complex internal structures and discontinuous zoning, xp. H) Transformed plagioclase with a fresh albitic rim, ppl. Cpx: Clinopyroxene; Amp: Amphibole; Bt: Biotite; Plg: Plagioclase; Kfd: Alkali feldspar; Qtz: Quartz; Mt: Magnetite (xp and ppl crossed polars and plane-polarized light respectively).

6.1.2.3 Syenites and Alkali Feldspar Granites

Felsic rocks from this group are syenites and alkali feldspar granites. These rocks are composed of alkali feldspar-albite, as granular perthite, and quartz with minor amounts of clinopyroxene (hedenbergite-augite), amphibole (ferroedenite-ferrohornblende) and biotite (Fig. 6.7A and 6.7B). Accessory phases are ilmenite, magnetite, apatite and zircon.

Alkali feldspar with patchy perthite exsolutions is the most abundant phase in these rocks with the Na-rich plagioclase it makes up 70 vol. % (Fig. 6.7A, 6.7E and 6.7F). The alkali feldspar contains numerous inclusions of ferromagnesian minerals, plagioclase and quartz. In addition to the perthite exsolutions (Fig. 6.7E) a second type of plagioclase forms large grains with disequilibrium textures with albitic rims (Fig. 6.7G and 6.7H). Amphibole, *c.* 5 vol. %, is present as euhedral inequigranular crystals with marked dark teal green to light green pleochroism (Fig. 6.7C). It is the most abundant ferromagnesian phase and is typically poikilitic. Biotite, <5 vol. %, is much less abundant. It is present as isolated euhedral crystals associated with the Fe-Ti oxides (Fig. 6.7D).

The apparent order of crystallisation was apatite and zircon, clinopyroxene, amphibole, Fe-Ti oxides, biotite, alkali feldspars and quartz.

6.1.3 External Subalkaline Intermediate Unit

This group mainly comprises diorites, quartz diorites, tonalites, and granodiorites that are composed of amphibole (magnesiohornblendes-edenites-magnesiohastingsites), plagioclase (labradorite-andesine), biotite, clinopyroxene (diopside) and varying proportions of alkali feldspar and quartz (Fig. 6.8A). Accessory phases are magnetite, ilmenite, titanite, apatite and zircon. The rocks are mostly equigranular, only plagioclase is somewhat coarser (Fig. 6.8B). This unit may be petrographically distinguished from the *Central Ultrabasic-Basic Layered Unit* by its lack of poikilitic amphibole and from the *Central Alkaline Basic-Intermediate Layered and Acid Unit* by its low modal proportion of biotite (Fig. 6.8A, 6.8C and 6.8D). In addition, the rocks do not have layered cumulate textures.

Amphibole, *c.* 25 vol. %, is the most abundant ferromagnesian phase (Fig. 6.8A). It is equigranular and euhedral with dark to light brown pleochroic cores and paler rims (Fig. 6.8E and 6.8F). Most of the plagioclase, *c.* 30 vol. %, is euhedral, tabular, with well-developed polysynthetic twins (Fig. 6.8G). Nevertheless, some plagioclase grains show evidence of disequilibrium including: recrystallisation; patchy zoning; and, abundant inclusions of amphibole, biotite and

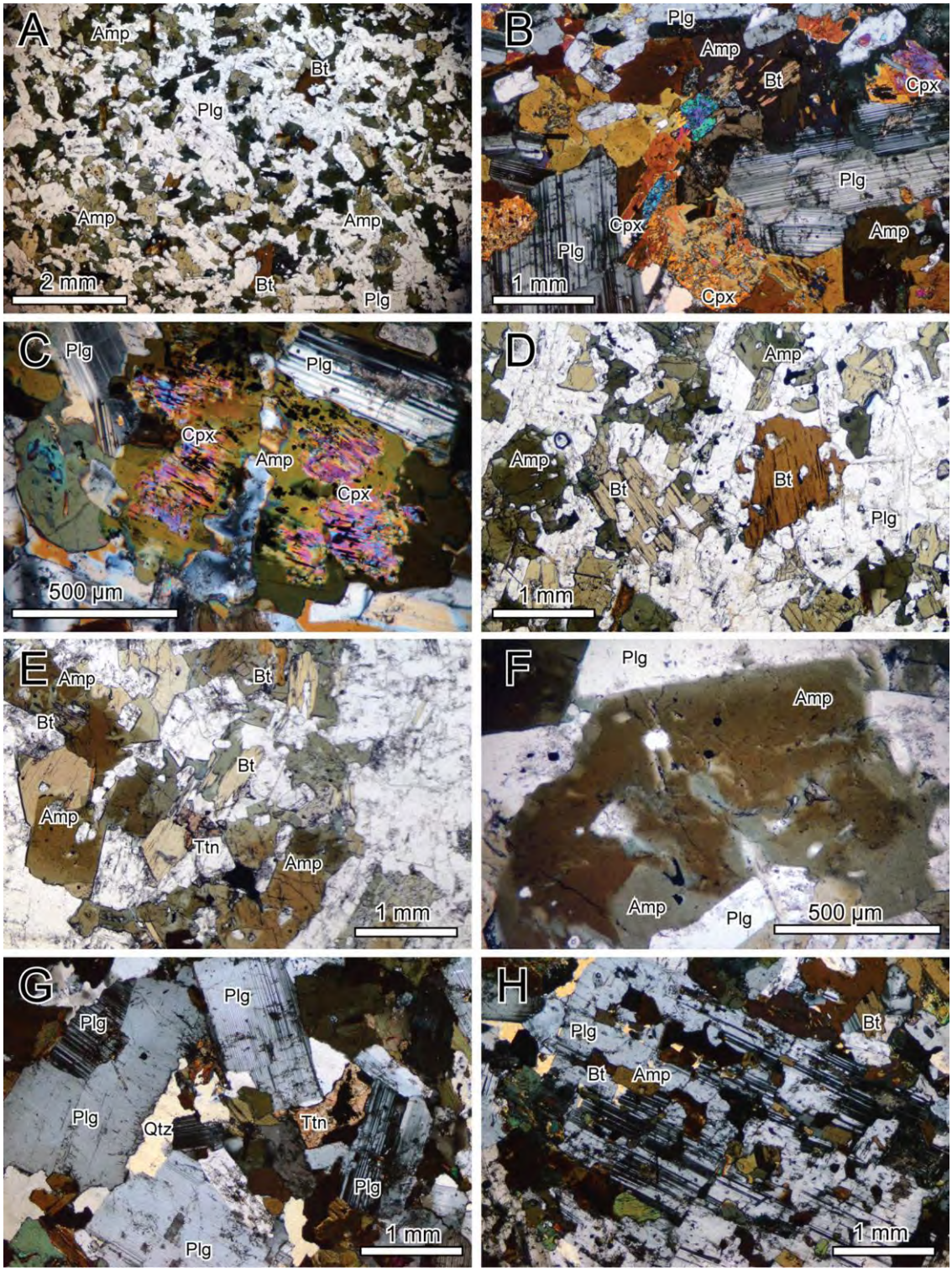

Figure 6.8: Burguillos del Cerro plutonic complex External Subalkaline Intermediate unit quartz diorites to tonalites. A) Fine-grained diorite, note the abundance of amphibole over biotite, ppl. B) Detail of a medium-grained diorite, note that the biotite is included in the amphibole, xp. C) Clinopyroxene partially replaced by secondary actinolite, xp. D) Amphibole with dark to light brown pleochroism in the crystal cores but paler rims. E) Zoned amphibole with brown cores to green rims, note that small-grained biotites are include in amphibole, ppl. F) Detail of zoned amphibole with a brown core and green rim, ppl. G) Plagioclase with uniform internal structure and well developed polysynthetic twins, ppl. H) Plagioclase with numerous inclusions of amphibole, biotite and Fe-Ti oxides, xp. Cpx: Clinopyroxene; Amp: Amphibole; Bt: Biotite; Plg: Plagioclase; Qtz: Quartz; Ttn: Titanite (xp and ppl crossed polars and plane-polarized light respectively).

Fe-Ti oxides oriented in fractures (Fig. 6.8H). Biotite, *c.* 10 vol. %, with dark red to light brown pleochroism is a minor phase compare with the amphibole (Fig. 6.8A). It is euhedral with inclusions of plagioclase, apatite and zircon, but is itself included in the amphibole (Fig. 6.8D). Euhedral titanite is present in all the rocks of this unit. Its modal proportion increases with SiO_2 (Fig. 6.8E and 6.8H).

The apparent order of crystallisation was apatite, titanite, pyroxene, plagioclase, Fe-Ti oxides, biotite, amphibole, alkali feldspar and quartz.

6.1.4 Acid Peraluminous Unit

This group comprises two-mica granites, aplites and pegmatites. The two-mica granites have medium- to fine-grained predominantly equigranular textures. They contain quartz, perthitic alkali feldspar, plagioclase (albite), biotite, primary-looking muscovite, and cordierite (Fig. 6.9). Typical accessory phases are apatite, zircon and rare andalucite. The aplites have a comparable mineralogy, albeit it richer in quartz, perthitic alkali feldspar and plagioclase. The pegmatitic bodies also contain aggregates of quartz and tourmaline.

The apparent order of crystallisation was biotite, plagioclase, alkali feldspar, quartz and muscovite.

6.2 Valencia del Ventoso Plutonic Complex

The Valencia del Ventoso plutonic complex is a mafic to felsic pluton with mafic stocks (Pons, 1982; Sarrionandia, 2005). As indicate in the Chapter 4 the complex is divided in four main units: i. the *Main Pluton Alkaline to Subalkaline Basic-Acid Unit*; ii. the *Northern Stock Subalkaline Basic-Intermediate Unit;* iii. the *Southern Stock Subalkaline Intermediate-Acid Unit* and iv. *Intrusive Dyke Unit*. The petrographic features of each unit are summarised below.

6.2.1 Main Pluton Alkaline to Subalkaline Basic-Acid Unit

The *Main Pluton Alkaline to Subalkaline Basic-Acid Unit* is concentrically zoned with gabbros and diorites at its core, surrounded by quartz diorites to granodiorites and granites at the outer rim. The main mineralogical assemblage consists of plagioclase, amphibole, biotite, alkali feldspar, quartz and clinopyroxene, (Pons, 1982; Sarrionandia, 2005). The accessory assemblage is apatite, zircon, magnetite, ilmenite, titanite and epidote (Pons, 1982; Sarrionandia, 2005).

6.2.1.1 Gabbros and Diorites

In general gabbros from the inner part of the pluton are composed of plagioclase (labradorite-andesine), biotite, clinopyroxene (diopside-augite) (Fig. 6.10A and 6.10B). They have

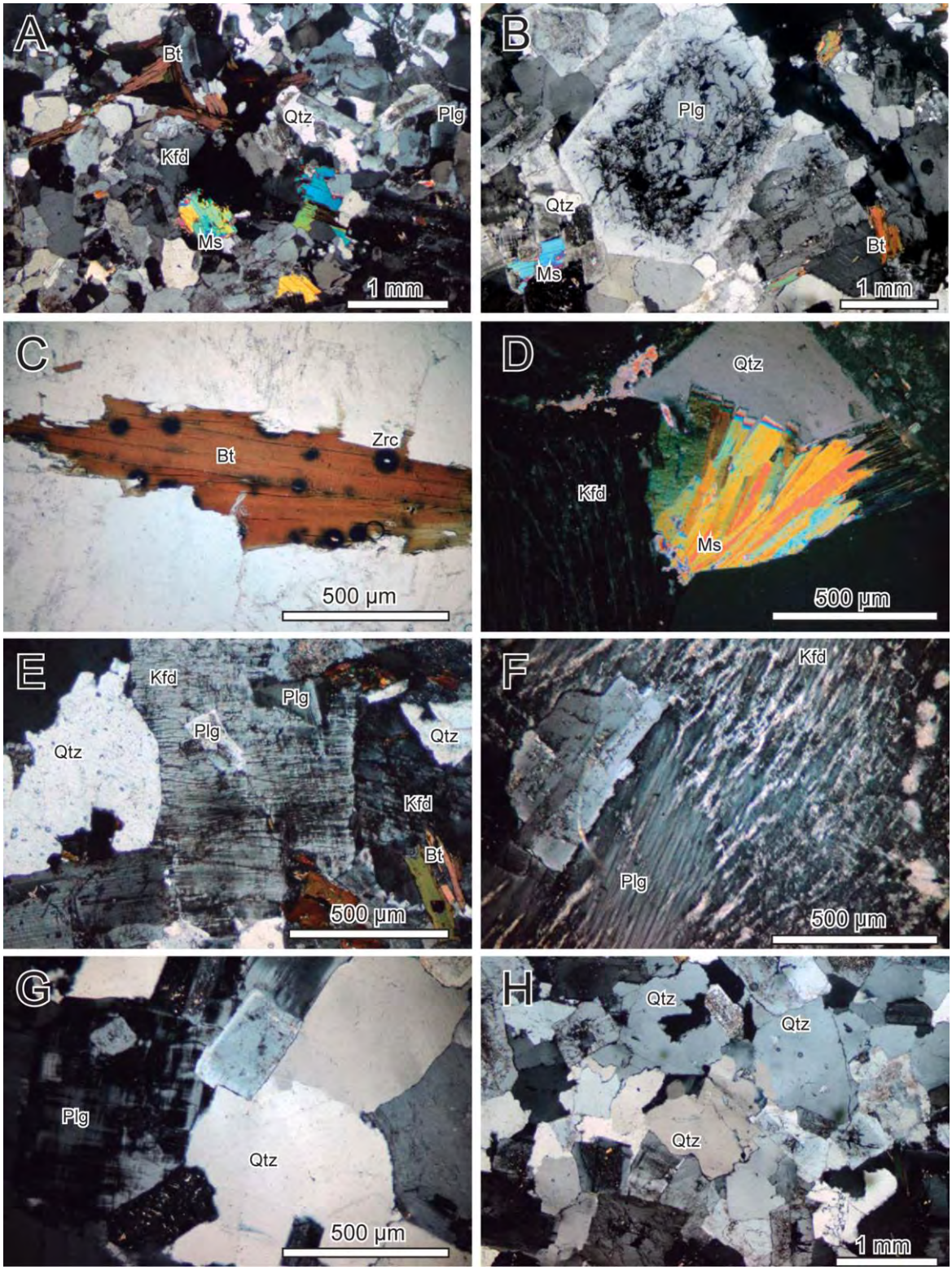

Figure 6.9: Burguillos del Cerro plutonic complex Acid Peraluminous Unit granite: A) Two mica granite with biotite, primary muscovite, plagioclase, perthite alkali feldspar and quartz, xp. B) Coarser.granied irregualr zoned plagioclase, xp. C) Reddish brown biotite with abundant zircon, ppl. D) Radial primary muscovite aggregate, xp. E) Perthitic alkali feldspar with inclusions of plagioclase and biotite, xp. F) Perthitic alkali feldspar and plagioclase, xp. G) Quartz partially surrounding plagiocase, xp. H) Mosaic of quartz and alkali feldspar, xp. Bt: Biotite; Plg: Plagioclase; Kfd: Alkali feldspar; Qtz: Quartz; Ms: Muscovite; Zrc; Zircon (xp and ppl crossed polars and plane-polarized light respectively).

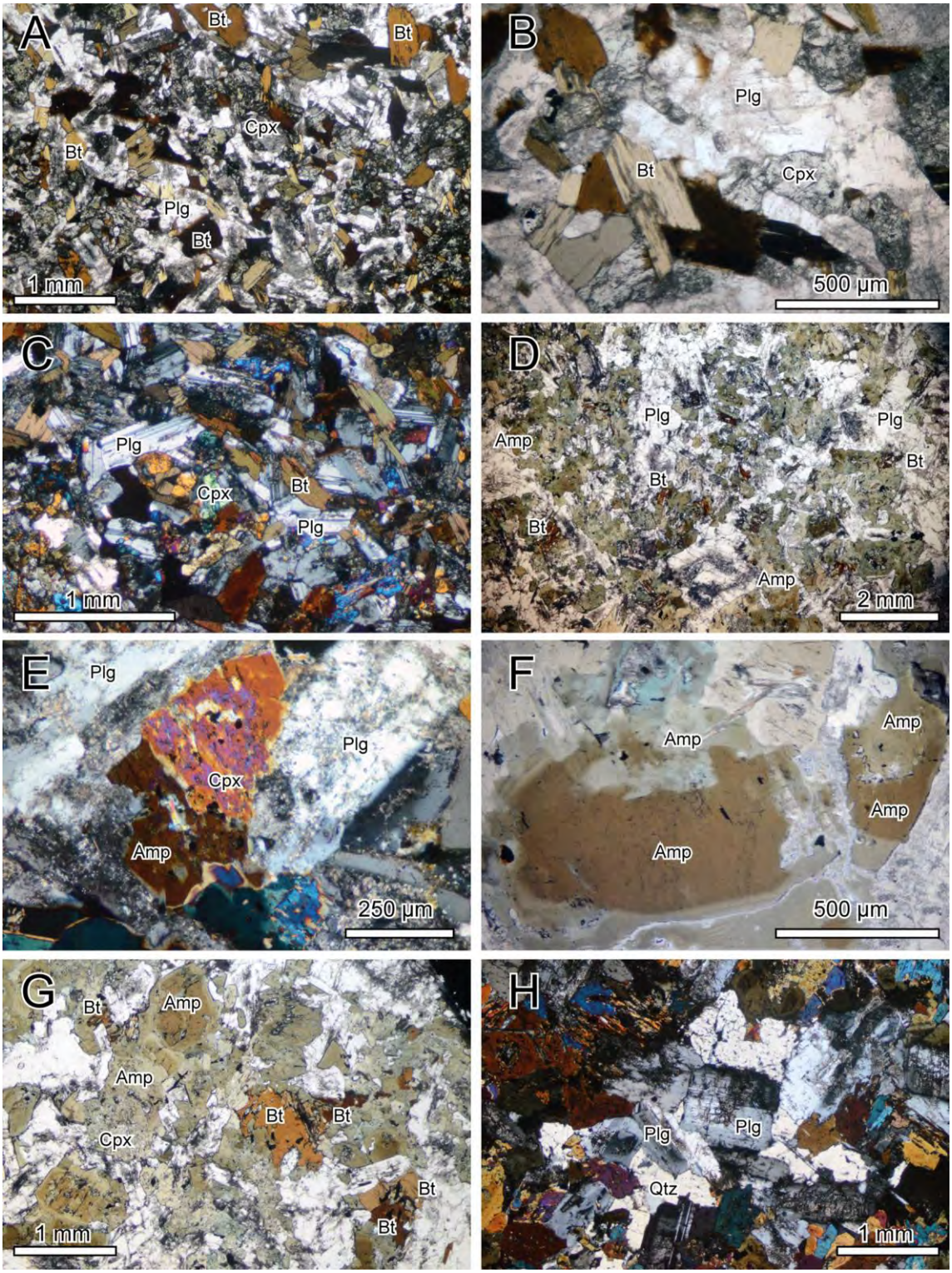

Figure 6.10. Valencia del Ventoso plutonic complex Main Pluton Alkaline to Subalkaline Basic-Acid Unit gabbro and diorite. A) Fine-grained gabbro, ppl. B) Detail of the gabbro, showing biotite, clinopyroxene and plagioclase, ppl. C) Plagioclase with a uniform internal structure and polysynthetic twins and mesocumulitic texture, xp. D) Medium-grained diorite, note the main abundance in amphibole, ppl. E) Clinopyroxene partially transformed to pale green secondary actinolite, xp. F) Zoned amphibole with brown cores to green rims, compare with Fig. 6.8F, ppl. G) Detail of biotite included in zoned amphibole, ppl. H) Subhedral zoned plagioclase crystals with complex zonation and others with uniform internal structure, xp. Cpx: Clinopyroxene; Amp: Amphibole; Bt: Biotite; Plg: Plagioclase; Qtz: Quartz (xp and ppl crossed polars and plane-polarized light respectively).

fine-grained, inequigranular mesocumulate textures (Fig. 6.10C). Plagioclase, *c.* 60 vol. %, is euhedral and tabular with polysynthetic twins (Fig. 6.10C). Biotite, 15-30 vol. %, is pleochroic, euhedral with inclusions of Fe-Ti oxides and apatite (Fig. 6.10B).

The apparent order of crystallisation was apatite, clinopyoxene, Fe-Ti oxides, plagioclase and biotite.

The diorites are composed of plagioclase (labradorite-oligoclase), amphibole (magnesiohastingsites-magnesiohornblendes), biotite, clinopyroxene (diopside) and quartz (Fig. 6.10D and 6.10E). Accessory phases are apatite, zircon, ilmenite, magnetite and titanite. They are medium-grained and inequigranular.

Plagioclase is abundant, up to 60 % vol., it shows some evidence of disequilibrium, but it also concentrically zoned with polysynthetic twins (Fig. 6.10E and 6.10H). The rocks contain two generations of amphibole: i. primary (magnesiohastingsites-magnesiohornblendes), *c.* 20 vol. %, with darker brown to lighter brown pleochroism in the core and more greenish rims; ii. secondary pale green, actinonlite, associated with the transformed clinopyroxene (Fig. 6.10E and Fig. 6.10F). Biotite, <10 %, is less abundant than amphibole. It is present as individual crystals or as inclusions in amphibole (Fig. 6.10G). The individual crystals are euhedral, show intergrowths with Fe-Ti oxides and are rich in inclusions (Fig. 6.10G). The diorites of this unit have euhedral titanite, but here it is fine-grained and rare.

The apparent order of crystallisation was apatite, pyroxenes, plagioclase, titanite, Fe-Ti oxides, biotite, amphibole and quartz.

6.2.1.2 Quartz Diorites to Granites

The coarse-grained quartz diorites are composed of plagioclase (andesine), amphibole (magnesiohastingsites-magnesiopargasite), biotite and minor alkali feldspar and quartz (Fig. 6.11A). Accessory phases are zircon, apatite magnetite, ilmenite and titanite.

Plagioclase is abundant, *c.* 60 vol. %. It is generally euhedral and tabular with well-developed polysynthetic twins (Fig. 6.11C). Just a few crystals have patchy zoning with marked discontinuities in the concentric zones, indicative of recrystallisation and more than one phase of growth respectively (Fig. 6.11C). Amphibole, *c.* 30 vol. %, is subhedral with darker brown to lighter brown pleochroism in the core and, as in the diorites, more greenish rims (Fig. 6.11B). Biotite, *c.* 10 % vol., is present either as i. fine-grained inclusions in amphibole and plagioclase (Fig. 6.11A to B); or as, ii. coarse-grained, large anhedral crystals with a poikilitic texture showing numerous inclusions of apatite (Fig. 6.11A).

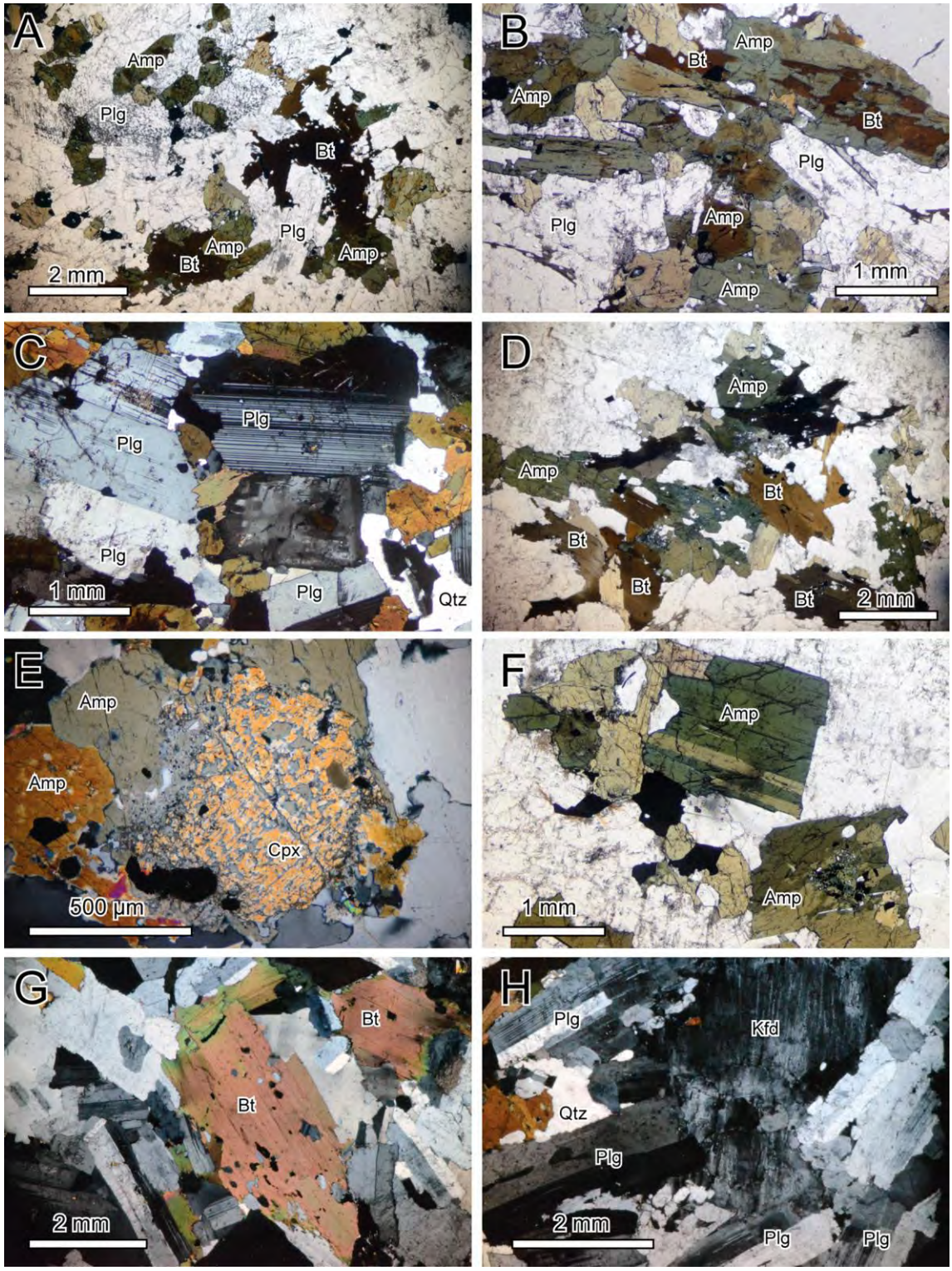

Figure 6.11 Valencia del Ventosos plutonic comlex Main Pluton Alkaline to Subalkaline Basic-Acid Unit quartz diorite and granodiorite: A) Medium-grained quartz diorite, ppl. B) Detail of the relationship between amphibole and biotite, the latter is included in amphibole, ppl. C) Euhedral and tabular plagioclase with well-developed polysynthetic twins, xp. D) Medium-grained granodiorite, ppl. E) Clinopyroxene transformed to pale secondary amphibole, xp. F) Detail of amphibole with marked green pleochroism, ppl. G) Zoned biotite with numerous inclusions of Fe-Ti oxides and plagioclase but fewer apatites than the quartz diorite biotites (see Fig. 6.11G), xpl H) Plagioclase with uniform internal structure and medium-grained and anhedral alkali feldspar and interstitial quartz, xp. Cpx: Clinopyroxene; Amp: Amphibole; Bt: Biotite; Plg: Plagioclase; Kfd: Alkali feldspar; Qtz: Quartz (xp and ppl crossed polars and plane-polarized light respectively).

The apparent order of crystallisation was apatite, titanite, Fe-Ti oxides, biotite, plagioclase and amphibole.

The granodiorites to granites, contain plagioclase (andesine-oligoclase), amphibole (magnesiohornblendes-edenites), alkali feldspar, quartz, biotite and relict clinopyroxene (diopside) (Fig. 6.11D). Accessory phases are large zircon, apatite, magnetite, ilmenite and abundant titanite. Plagioclase is abundant, *c.* 30 % vol., and has euhedral tabular forms with polysynthetic twins (Fig. 6.11H). The rocks contain two generations of amphibole: i. primary, magnesiohornblende *c.* 30 vol. %, euhedral to subhedral with green to lighter green pleochroism (Fig. 6.11F); ii. secondary, actinolite, anhedral pale green, associated with the transformed clinopyroxene (Fig. 6.11E). Biotite, *c.* 10 vol. %, is less abundant than the amphibole (Fig. 6.11D). It is presents as subhedral, coarse-grained crystals. These are zoned with numerous inclusions of Fe-Ti oxides and plagioclase but fewer apatites than the biotites of the quartz diorite (Fig. 6.11G).

The apparent order of crystallisation was apatite and zircon, titanite, Fe-Ti oxides, biotite, plagioclase, amphibole, alkali feldspar, and quartz.

6.2.2 Northern Stock Subalkaline Basic-Intermediate Unit

This unit is composed of a gabbro to quartz monzodiorite association. The main mineralogical assemblage consists of rare olivine restricted to the more mafic rocks, plagioclase (labradorite-oligoclase), biotite, amphibole (magnesiohornblende), orthopyroxene (enstatite) and clinopyroxene (diopside-augite), alkali feldspar and, in the more evolved rocks, quartz (Fig. 6.12). The accessory minerals are apatite, zircon, rutile, ilmenite, magnetite and titanite.

Plagioclase, *c.* 50 % vol., has the highest modal proportion, it is euhedral and tabular with coarse- to medium-grained textures (Fig. 6.12F and 6.12G). It shows two different zonation patterns: i. the first consists of discontinuous surfaces that reveal various growths steps (Fig. 6.12F); ii. the second is regular with well-developed polysynthetic twins (Fig. 6.12G and 6.12H). Biotite, *c.* 10 % vol., forms euhedral to anhedral, medium- to coarse-grained crystals (Fig. 6.12A) with brown-reddish to pale-yellow pleochroism (Fig. 6.12A and 6.12E). They show intergrowths with Fe-Ti oxides and include abundant apatite, and zircon (Fig. 6.12A and 6.12E). Orthopyroxene, <5 vol. %, is euhedral, medium- to fine-grained, it is typically present included in other ferromagnesian phases (Fig. 6.12B and 6.12C). Alkali feldspar and quartz are anhedral, interstitial, and, in places, show graphic intergrowths (Fig. 6.12G and 6.12H).

The apparent order of crystallisation was apatite, pyroxenes, Fe-Ti oxides, biotite, amphibole, plagioclase, alkali feldspar and quartz.

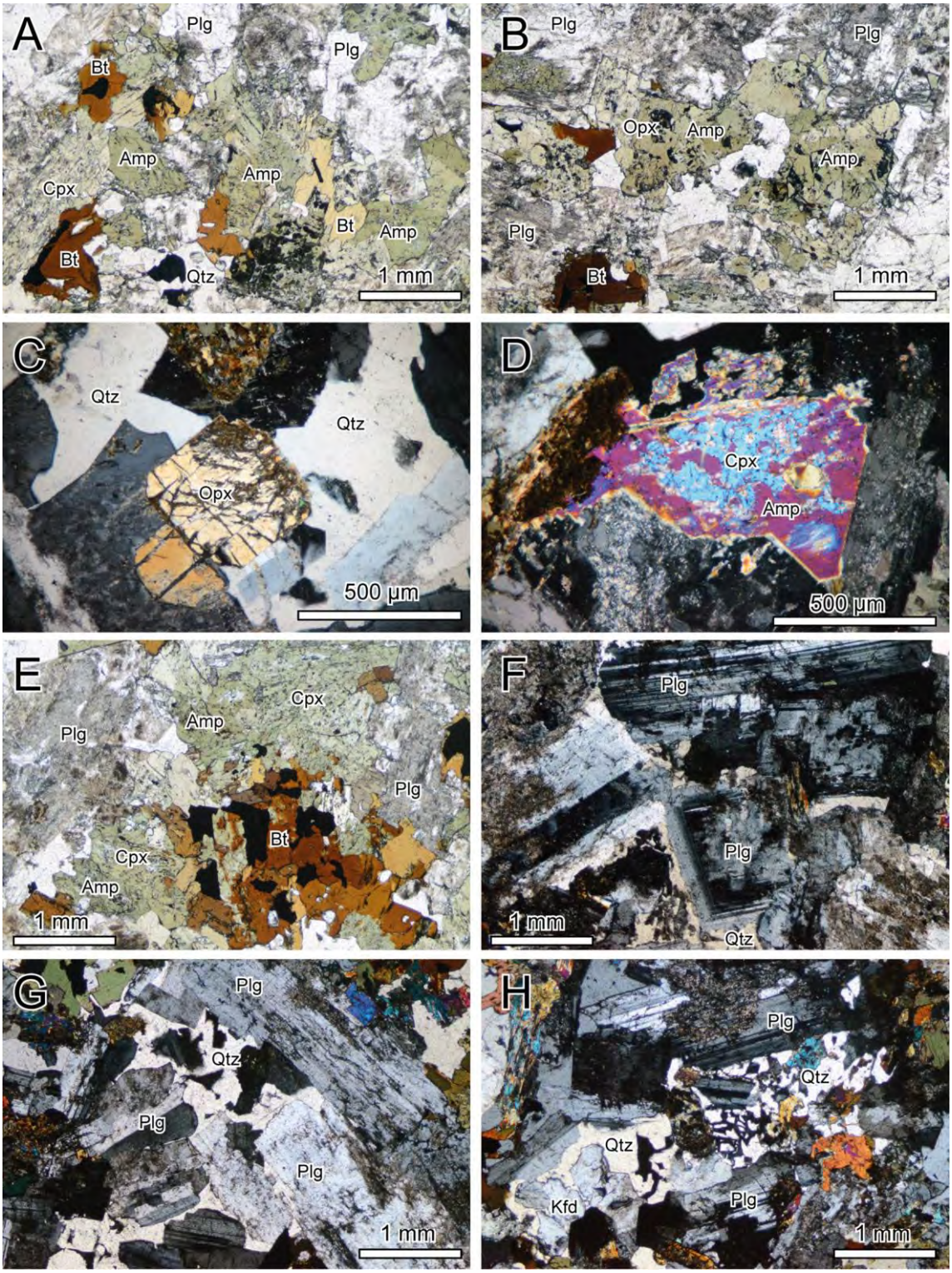

Figure 6.12: Valencia del Ventoso Northern Stock Subalkaline Basic-Intermediate unit quartz monzodiorite. A) and B) Medium-grained quartz monzodiorite, note the reddish biotite intergrown with Fe-Ti oxides and green amphibole and pyroxene, ppl. C) Small-grained euhedral of orthopyroxene, xp. D) Clinopyroxene partially transformed to secondary actinolite, xp. E) Aggregate of reddish biotite intergrown with Fe-Ti oxides and and greenish amphibole and pyroxene, ppl. F) Plagioclase with discontinuous zoning, xp. G) Plagiocase with uniform with well-developed polysynthetic twins, xp. H) Anhedral, interstitial quartz and alkali feldspar graphic intergrowths, xp. Cpx: Clinopyroxene; Opx: Orthopyroxene;Amp: Amphibole; Bt: Biotite; Plg: Plagioclase; Kfd Alkali feldspar; Qtz: Quartz (xp and ppl crossed polars and plane-polarized light respectively).

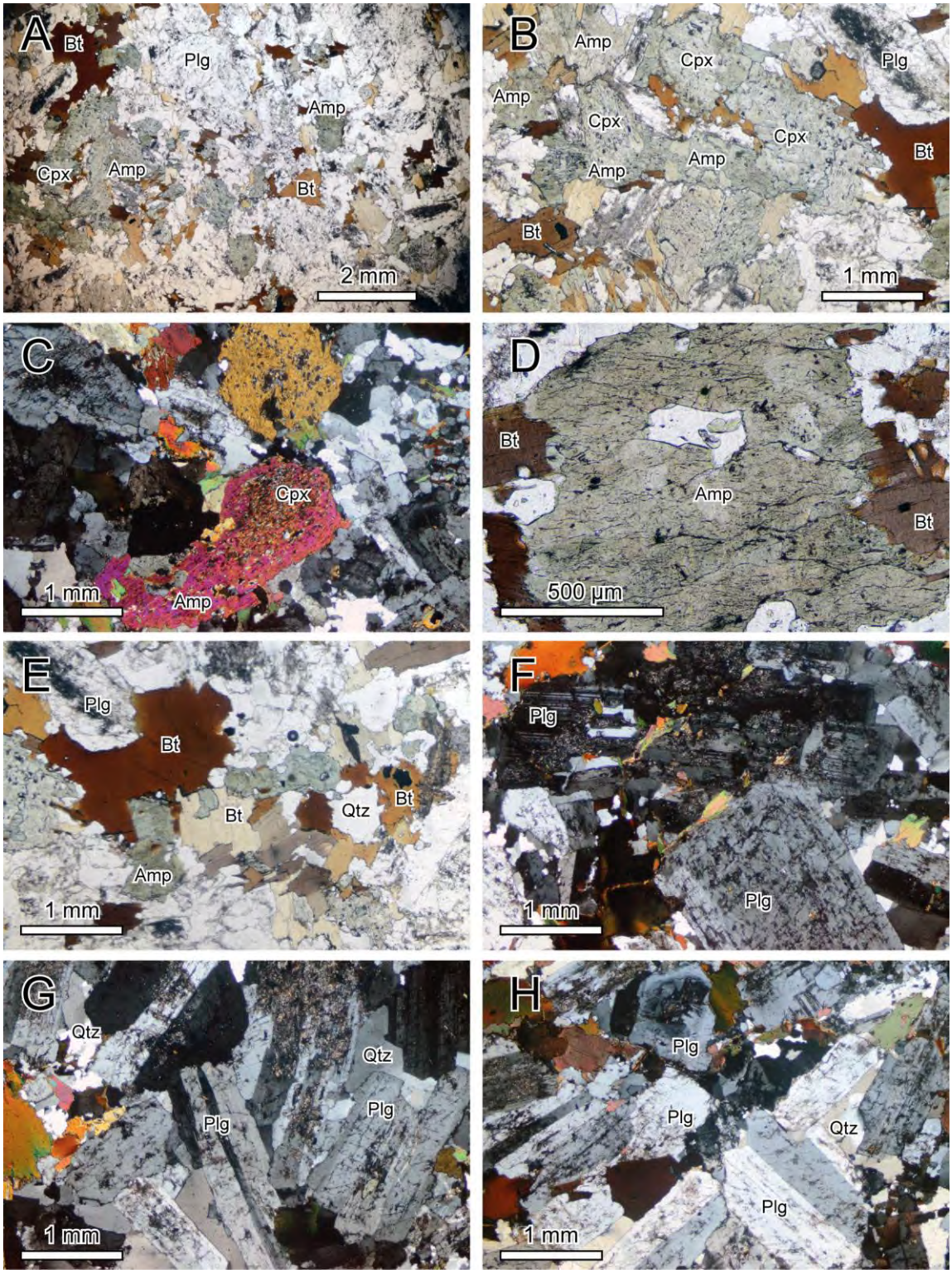

Figure 6.13: Valencia del Ventoso plutonic complex Southern Stock Subalkaline Intermediate-Acid Unit: A) Coarse-grained quartz monzodiorite, note the presence of reddish and abundant green amphibole, ppl. B) Clinopyroxene partially transformed to secondary actinolite, xp. C) Detail of the quartz monzodiorite, xp. D) Detail of secondary green amphibole, note that biotite is not include in amphibole, ppl. E) Subhedral biotite in places intergrown with Fe-Ti oxides, ppl. F) Subhedral and zoned plagioclases with complex zonation, discontinuous surfaces and numerous inclusions of biotite and secondary amphibole, xp. G) Subhedral zoned plagioclases with well-developed polysynthetic twins xp. H) Subhedral zoned plagioclase crystals with complex zonation and others with polysynthetic twins, xp. Cpx: Clinopyroxene; Amp: Amphibole; Bt: Biotite; Plg: Plagioclase; Qtz: Quartz (xp and ppl crossed polars and plane-polarized light respectively).

6.2.3 Southern Stock Subalkaline Intermediate-Acid Unit

This unit comprises quartz monzodiorites and quartz diorites to tonalites. The main minerals are plagioclase (labradorite-oligoclase), biotite, clinopyroxene (diopside-augite), amphibole (magnesiohornblende), alkali feldspar and quartz (Fig. 6.13A and 6.13B). The accessory assemblage consists of apatite, zircon, magnetite, ilmenite, titanite and epidote.

Plagioclase, up to 50 % vol., is the most abundant mineral, it is typically euhedral, inequigranular and tabular with developed polysynthetic twins and concentric zonation and little evidence of disequilibrium textures (Fig. 6.13F to 6.13H). Some grains, do show evidence of disequilibrium with complex zonation, discontinuous surfaces and numerous inclusions of biotite and secondary actinolite (Fig. 6.13F). Biotite, *c.* 10 % vol., is the main ferromagnesian phase. It is euhedral with reddish brown to pale yellow pleochroism and commonly includes several of the accessory phases (Fig. 6.13E). Only a few crystals have a clear relationship with Fe-Ti oxide intergrowths (Fig. 6.13E). The only amphibole observed in these rocks is pale green, secondary actinolite replacing clinopyroxene (Fig. 6.13B to 6.13D).

The apparent order of crystallisation was apatite, pyroxenes, Fe-Ti oxides, biotite, plagioclase, alkali feldspar and quartz.

6.2.4 Intrusive, Acid Peraluminous, Dyke Unit

The *Intrusive, Acid Peraluminous, Dyke Unit* is composed of aplite and syenite veins. The main minerals in these aplites are alkali feldspar, quartz, biotite, and primary muscovite (Fig. 6.14). Accessory minerals include apatite, zircon, tourmaline and magnetite.

The rocks are fine- to medium-grained and inequigranular (Fig. 6.14). Quartz and alkali feldspars show graphic intergrowths (Fig. 6.14G and 6.14H).

The apparent order of crystallisation was biotite, alkali feldspar, muscovite and quartz.

6.3 Brovales Pluton

The Brovales pluton comprises intermediate to felsic rocks (Pons, 1982). It is divided into three main units: i. the *Central Subalkaline Intermediate Unit*; ii. the *Intermediate Subalkaline Intermediate Unit* and; iii. the *External Subalkaline Acid Unit and Intrusive, Acid Peraluminous, Dykes*. The following paragraphs describe the main petrographic characteristics of each unit.

6.3.1 Central Subalkaline Intermediate Unit

This unit comprises quartz monzodiorites to granodiorites. The main minerals in this unit are plagioclase (andesine-oligoclase), amphibole (ferroedenites-edenites), biotite, alkali feldspar

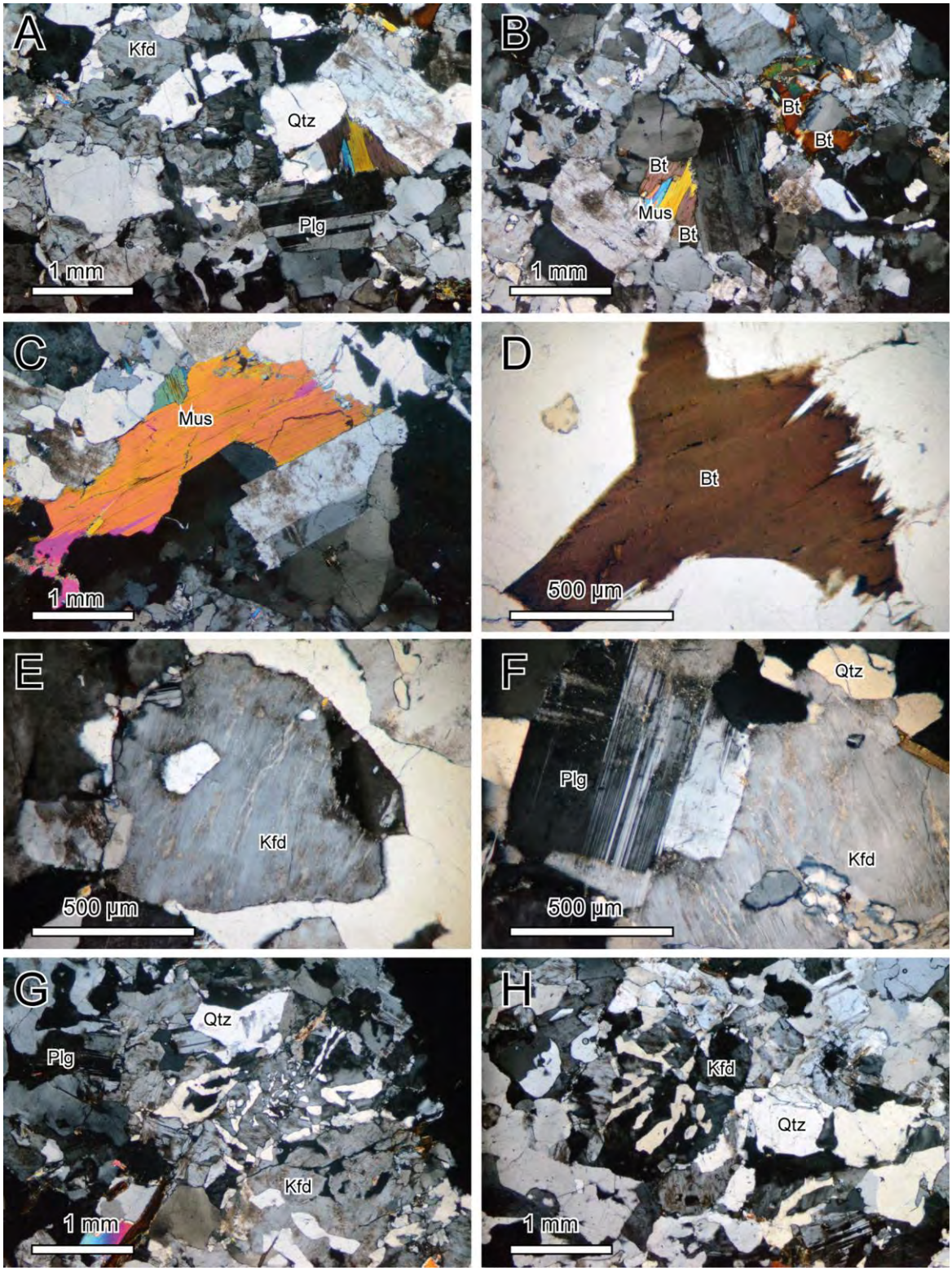

Figure 6.14: Valencia del Ventoso plutonic complex Intrusive, Acid Peraluminous, Dyke Unit aplite: A) and B) Medium-grained aplite, note the primary biotite and muscovite, xp. C) Detail of a large single primary muscovite crystal, xp. D) Detail of a single crystal of biotite that has a pale-brown to yellowish pleochroism, ppl. E) and F) Cross-polarised light microphotographs of abundant alkali feldspar with a well-defined perthite textures, xp. G) and H) Fine-grained plagioclase crystals and graphic intergrowth of quartz and alkali feldspar, xp. Bt: Biotite; Plg: Plagioclase; Hfd: Alkali feldspar; Qtz: Quartz; Mus: Muscovite (xp and ppl crossed polars and plane-polarized light respectively).

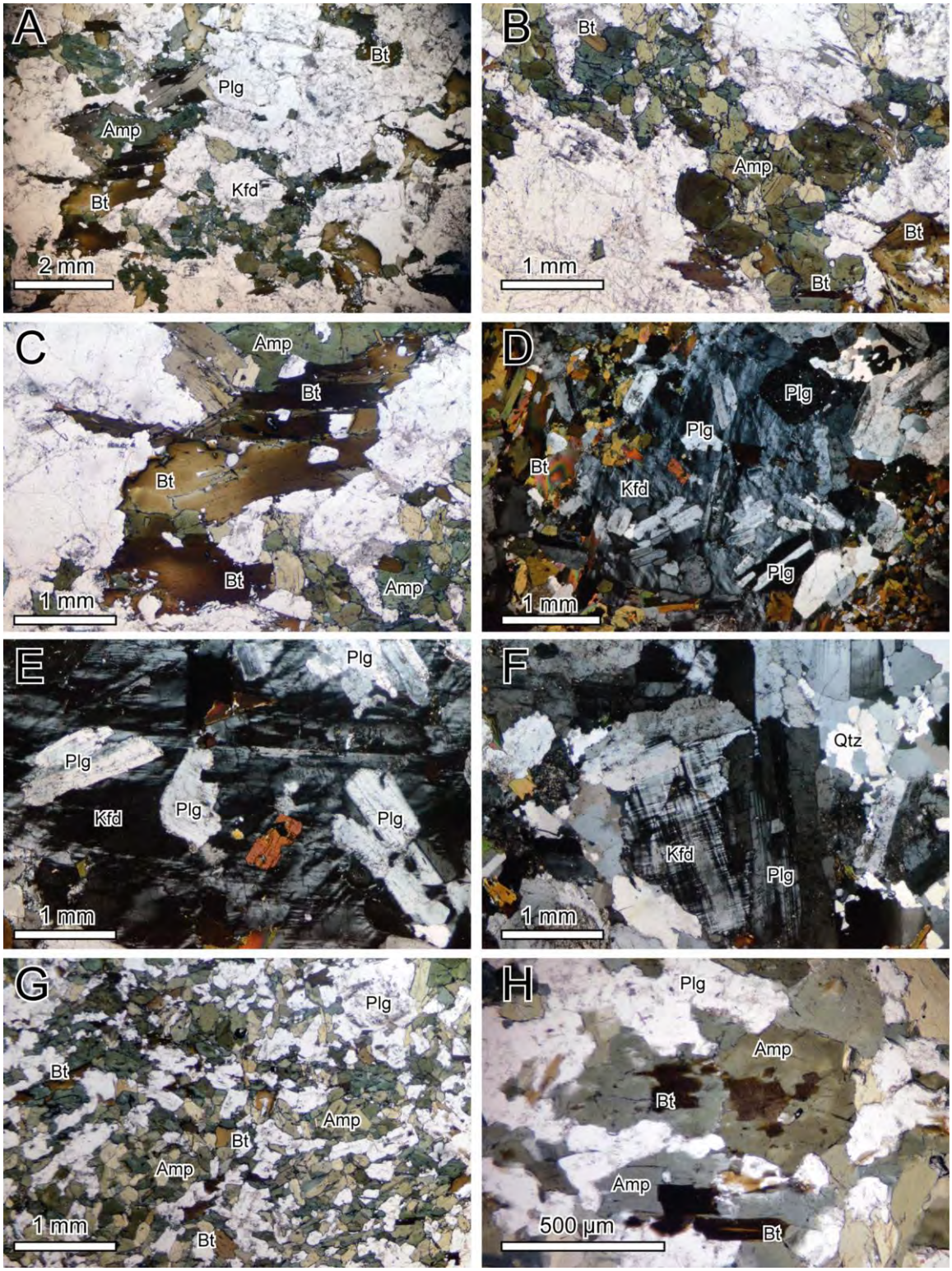

Figure 6.15: Brovales pluton Central Subalkaline Intermediate Unit: A) Medium-grained quartz diorite, note the indication of deformation shown by slightly oriented amphibole and, principally, biotite, ppl. B) Aggregate of amphibole which is zoned with dark green cores and light green rims with some small biotite inclusions, ppl. C) Detail of biotite which is deformed with a marked dark brown to yellowish pleochorism, ppl. D), E) and F) Plagioclase included in anhedral microcline alkali feldspar, quartz is anhedral and interstitial and interstitial position. G) Fine-grained dioritic enclave, note the greater amphibole content, ppl. H) Detail of the dioritic enclave, the amphibole has a slight zonation from brownish cores to green rims and inclusions of biotite, ppl. Amp: Amphibole; Bt: Biotite; Plg: Plagioclase; Kfd: Alkali feldspar; Qtz: Quartz (xp and ppl crossed polars and plane-polarized light respectively).

and quartz (Figs 6.15A) with apatite, zircon, magnetite, allanite and epidote as accessories.

The rocks are generally coarse-grained and inequigranular with a foliation marked by the orientation of ferromagnesian minerals that, in places, are deformed (Fig. 6.15A, 6.15B and 6.15C). Plagioclase accounts for, *c.* 60 % vol. It is present as subhedral tabular crystals and as irregular-shaped crystals included in alkali feldspar (Fig. 6.15D and 6.15E). Amphibole, *c.* 30 vol. %, is inequigranular and oriented. It is zoned with dark green cores and light green rims (Fig. 6.15B). Biotite, *c.* 10 vol. %, is commonly included in amphibole (Fig. 6.15A, Fig. 6.15B and Fig. 6.15C). It is coarse-grained and deformed with a marked dark brown to yellowish pleochorism (Fig. 6.15C). Microcline, *c.* 5 vol. %, is anhedral with numerous inclusions of others minerals, such as biotite, amphibole and plagioclase (Fig. 6.15E and 6.15F). The most important accessory phases in these rocks are allanite, which is commonly altered, and primary epidote.

The apparent order of crystallisation was apatite, zircon, allanite, plagioclase, biotite, amphibole, alkali feldspar and quartz.

Fine-grained foliated dioritic enclaves are common in this unit (Fig 6.15G). Their main minerals are amphibole, plagioclase, biotite (Fig. 6.15G) with apatite, zircon and magnetite as the most abundant accesories. The enclaves are fine-grained and equigranular. Amphibole, *c.* 50 vol. %, is subhedral and dark green to light green pleochroic (Fig 6.15G). Plagioclase, *c.* 40 vol. %, is euhedral with a uniform, polysynthetic twinned, internal structure. Biotite, <10 vol. %, is less abundant than the amphibole, in which it is commonly included, it has a reddish brown to pale brown pleochroism (Fig 6.15G and 6.15H).

The apparent order of crystallisation was apatite, zircon, plagioclase, biotite and amphibole.

6.3.2 Intermediate Subalkaline Intermediate Unit

The *Intermediate Subalkaline Intermediate Unit* is mainly composed of granodiorites that may be divided into three different facies; fine-grained, coarse-grained, and deformed. All three facies have comparable mineralogy: plagioclase (andesine-oligoclase), poikilitic green amphibole (hastingsite-ferropargasite), biotite, alkali feldspar and quartz; with accessory zircon, apatite, magnetite, ilmenite and titanite (Fig. 6.16).

Plagioclase, *c.* 50 vol. %, is subhedral and tabular with concentric zonation. More than one stage of growth and disequilibrium are indicated by: discontinuities in core to rim zonations and patchy, recrystallised internal structures (Fig. 6.16A and 6.16B). In the fine-grained facies the green amphibole, *c.* 20 vol. %, is anhedral and poikilitic (Fig. 6.16A). Biotite, *c.* 20 vol. %, is more

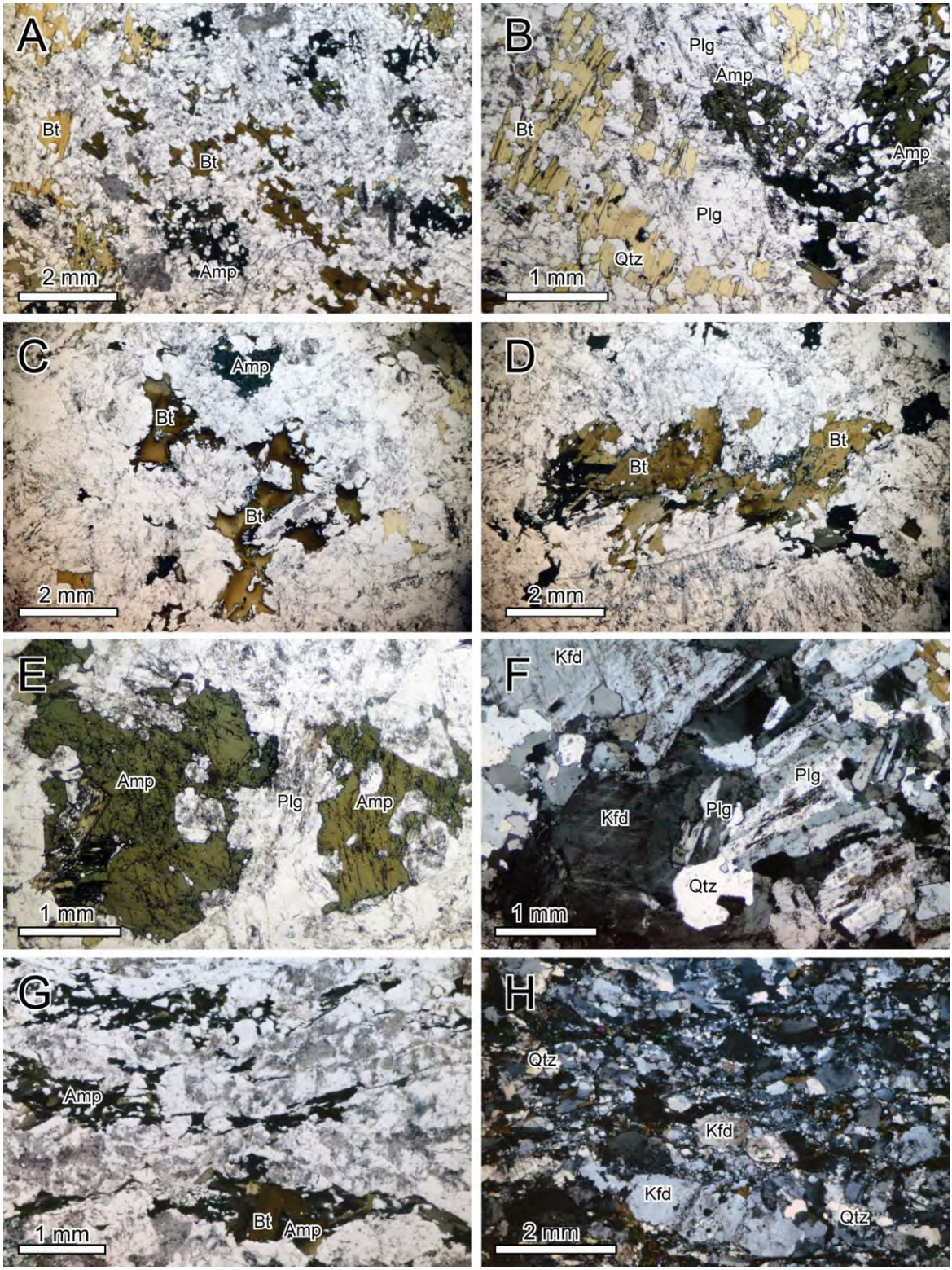

Figure 6.16: Brovales pluton Intermediate Subalkaline Intermediate Unit: A) Fine-grained granodiorite, ppl. B) Detail of poikilitic textures of amphiboles and biotite, ppl. C) Coarse-grained granodiorite, ppl. D) Detail of an aggregate of biotite in the coarse-grained granodiorite, ppl. E) Detail of subhedral amphibole with a green pleochroism, note the slight zonation with green brownish cores, ppl. F) Microcline, plagioclase and quartz, xp. G) Strongly deformed granodiorite, note the orientation of the biotites, ppl. H) Deformed granodiorite, note the oriented porphyroclasts of alkali feldspar and the general mylonitic texture, xp.. Amp: Amphibole; Bt: Biotite; Plg: Plagioclase; Kfd: Alkali feldspar; Qtz: Quartz (xp and ppl crossed polars and plane-polarized light respectively).

abundant than amphibole but has a similar anhedral poikilitic texture (Fig. 6.16A). Notably, in this facies amphibole does not contain inclusions of biotite. Microcline alkali feldspar is interstitial (Fig. 6.16B).

In the coarse-grained facies plagioclase, *c.* 50 vol. %, is subhedral and tabular with the same multiple growth stages and disequilibrium textures identified in the fine-grained facies (Fig. 6.16F). The amphibole and biotite, *c.* 20 vol. % each, have similar features to those of the fine-grained facies (Fig. 6.16C, 6.16D and 6.16E). In the coarser rocks the biotite forms oriented clots (Fig. 16C). Microcline, *c.* 10 vol. %, is coarse-grained (Fig. 6.16F).

The apparent order of crystallisation for both facies was apatite and zircon, amphibole, plagioclase, biotite, alkali feldspar and quartz.

In the foliated facies deformation resulted in grain-size reduction that locally formed granitic ultramylonites. The texture is dominated by a fine-grained matrix with a few large relict alkali feldspar porphyroclasts that show deformation-preferred growth (Fig. 6.16G and 6.16H). Biotite and amphibole are strongly oriented, in some cases they show concentric zoning. Quartz is recrystallised to a micromosaic texture (Fig. 6.16G and 6.16H).

6.3.3 External Subalkaline Acid Unit and Intrusive, Acid Peraluminous, Dykes

This unit comprises monzo- and syenogranites. The main minerals are plagioclase (oligoclase), alkali feldspar, biotite, and quartz (Figs 6.17A) with zircon, apatite and minor magnetite as the main accessory phases.

These rocks are medium-grained, inequigranular with a foliation marked by the biotite. Plagioclase, *c.* 30 vol. %, is euhedral and zoned; multiple growth stages are indicated by inclusion-rich cores overgrown by a second-stage inclusion-free rim (Fig. 6.17A and 6.17C). Alkali feldspar, *c.* 30 vol. %, is present as both large euhedral crystal with some inclusions, such as biotite, and also as anhedral interstitial grains (Fig. 6.17C and 6.17D). Biotite accounts for 15-20 vol. %, and is present as both inequigranular, subhedral, medium and fine-grained glomeroporphyritic anhedral interstitial crystals (Fig. 6.17B).

The apparent order of crystallisation was plagioclase, biotite, alkali feldspar and quartz.

The aplites, e.g., B-8-2, have equigranular fine-grained textures (Fig. 6.17E). They are composed of biotite, alkali feldspar and quartz (Figs 6.17E, to 6.17H). The accessory phases are zircon and apatite. Some are deformed as revealed by distorted micas and oriented polycrystalline quartz and feldspar aggregates (Fig. 6.17F).

The apparent order of crystallization was apatite, zircon, biotite, alkali feldspar and quartz.

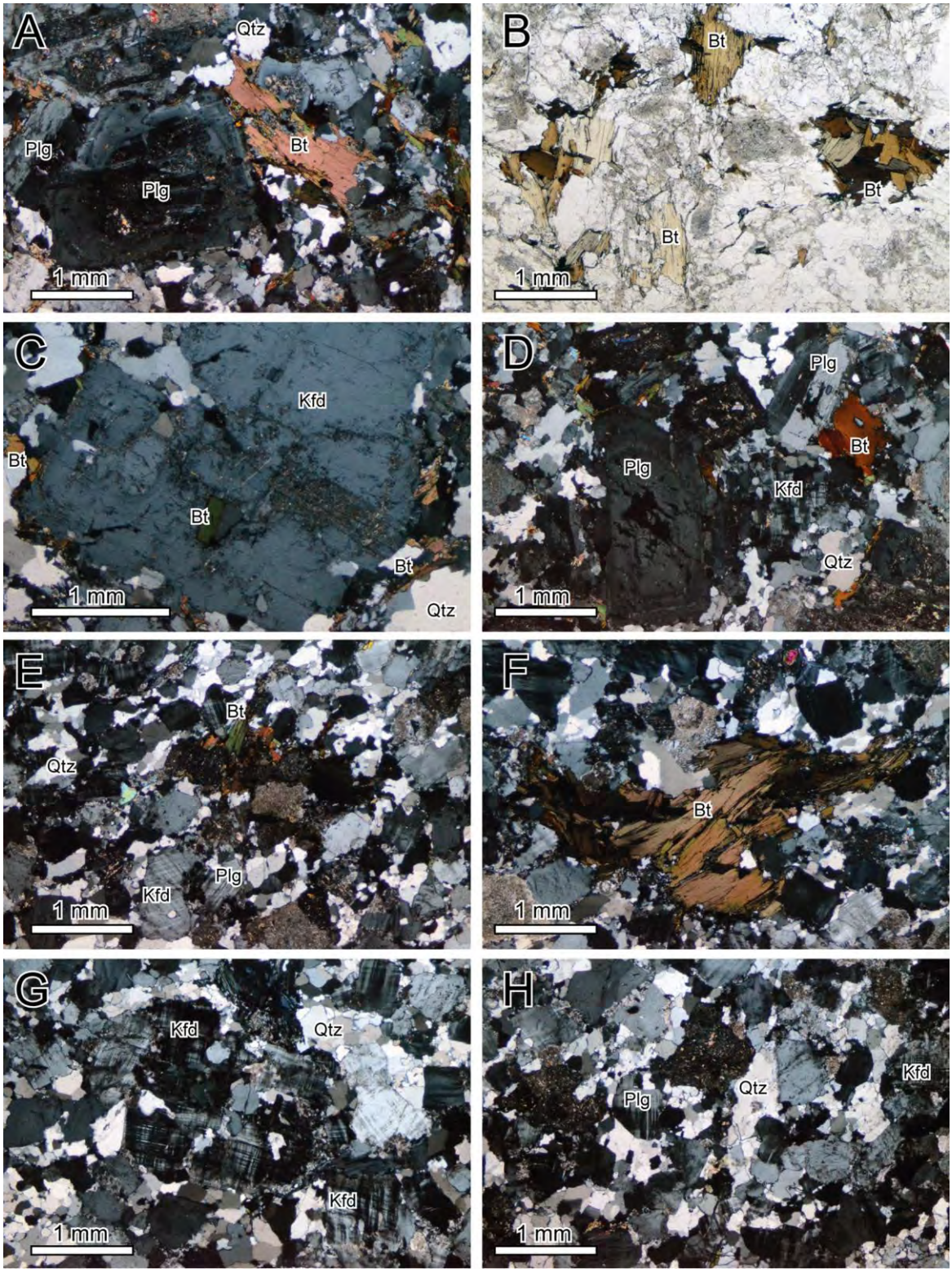

Figure 6.17: Brovales pluton External Subalkaline Acid Unit and Intrusive, Acid Peraluminous, Dykes aplite: A) Medium-grained syenogranite, note the coarse-grained irregularly zoned plagioclase, xp. B) Detail of the inequigranular somewhat oriented aggregates of biotite, ppl. C) Medium-grained syenogranite, note the coarse-grained irregularly zoned plagioclase with an overgrowth rim, xp. D) Detail of a large subhedral crystal of alkali feldspar, note the biotite growth at the rim, xp. E) Aplite comprising biotite, alkali feldspar and quartz, xp. F) Detail of deformed biotite in the aplite, xp. G) and H) Aplite showing biotite, microcline alkali feldspar, plagioclase and quartz, xp. Bt: Biotite; Plg: Plagioclase; Kfd: Alkali feldspar; Qtz: Quartz (xp and ppl crossed polars and plane-polarized light respectively).

6.4 Cambrian Leucogranite and the Serie Negra Metasediment

Two samples of pre-Variscan rocks were also studied, a leucogranite and a basement metasediment collected from the Ossa-Morena Zone Olivenza-Monesterio Antiform.

6.4.1 Cambrian Leucogranite

The coarse-grained leucogranite has biotite, alkali feldspar and quartz as major minerals and zircon, apatite and rutile as accessories. It is inequigranular and has graphic textures (Fig. 6.18A and 6.18B). Perthite alkali feldspar is coarser grained than the other minerals (Fig. 6.18A). Quartz is abundant, it is present as anhedral individual crystals and as graphic intergrowths with alkali feldspar (Fig. 6.18B).

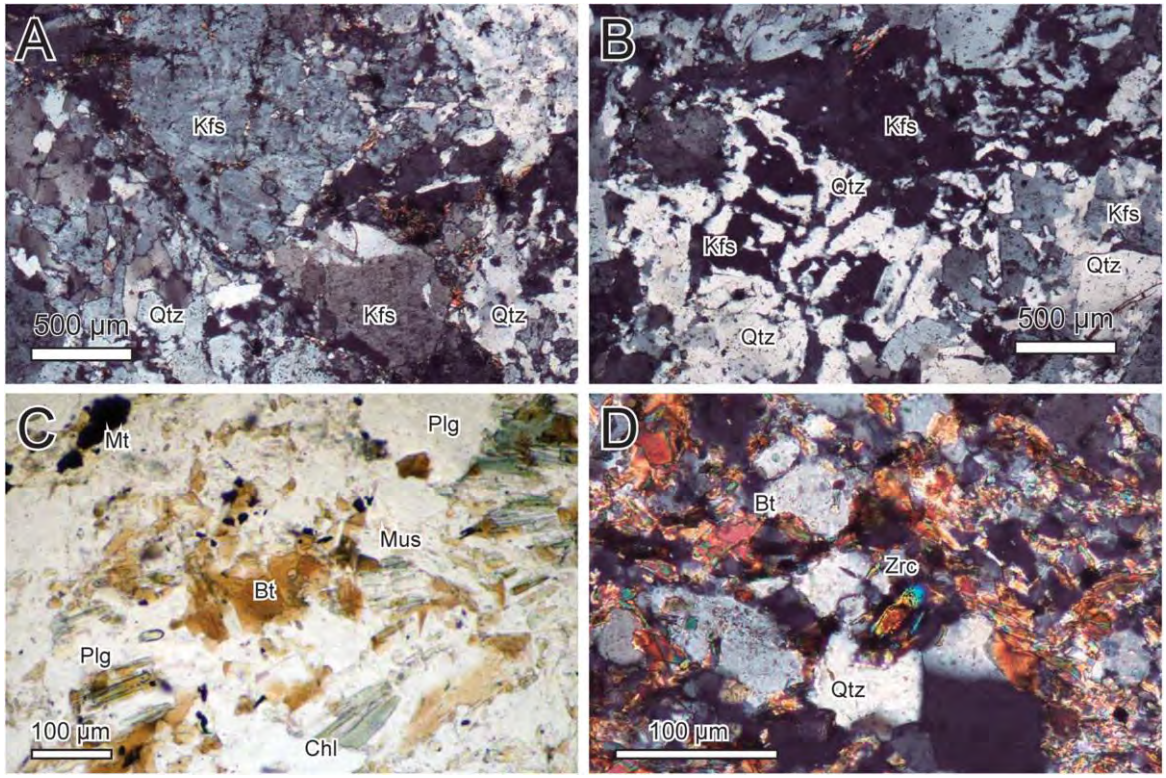

Figure 6.18: Cambrian leucogranite and Serie Negra metasediment: A) Coarse-grained leucogranite with biotite, alkali feldspar and quartz, and inequigranular and graphic textures, xp. B) Graphic intergrowth between quartz and alkali feldspar, xp. C) Metasediment with plagioclase, biotite, chlorite and muscovite, ppl. D) Metasediment with plagioclase, biotite, chlorite, muscovite and accessory zircon, note the triple points between the quartz crystals, xp. Bt: Biotite; Plg: Plagioclase; Kfs: Alkali feldspar; Qtz: Quartz; Mus: Muscovite; Chl: Chlorite; Zrc: Zircon (xp and ppl crossed polars and plane-polarized light respectively).

6.4.2 Serie Negra Metasediment

The Serie Negra metasediment studied here comprises plagioclase, biotite, chlorite, muscovite, albite with accessory ilmenite, apatite and zircon (Fig. 6.18C and 6.18D). It has a fine-grained recrystallised texture with triple-point boundaries (Fig. 6.18D). The coexistence of

biotite+chlorite+muscovite+albite+oligoclase, as a peristerite gap association (cf., Maruyama et al., 1982), suggests low- to medium-grade conditions of metamorphism. The absence of preferred phyllosilicate orientation combined with the triple-point recrystallisation textures is consistent with contact metamorphism (Fig. 6.18D).

6.5 Petrographic Comparison of the Main Units of the Three Plutonic Bodies

The different rock units reveal significant textural and mineralogical differences (Table 6.1).

6.5.1 Textural Characteristics

The first textural division that may be made is between cumulitic and massive plutonic bodies. The best examples of cumulitic textures are observed in the Burguillos del Cerro plutonic complex (Pons, 1982; García-Casquero, 1991): in the *Central Ultrabasic-Basic Layered Unit,* defined by ferromagnesian minerals such as olivine, pyroxene and amphibole (Fig. 6.1B and 6.3A); in the *Central Alkaline Basic-Intermediate Layered Acid Unit* plagioclase marks the cumulitic texture and the ferromagnesian minerals are less abundant (Fig. 6.4H). In the Valencia del Ventoso plutonic complex cumulates, defined by variable proportions of olivine, pyroxene and plagioclase, are restricted to the *Northern Stock Subalkaline Basic-Intermediate Unit* gabbros and the most mafic, central, part of the *Main Pluton Alkaline to Subalkaline Basic-Acid Unit*. Cumulitic textures are not observed in the intermediate-felsic Brovales pluton.

Rocks with massive textures crop out in the three plutonic complexes. In Burguillos, they are only present in the *External Subalkaline Intermediate Unit* (Fig. 6.8A). In Valencia del Ventoso, by contrast, rocks with massive textures are much more common, comprising the *Main Pluton Alkaline to Subalkaline Basic-Acid Unit* (Fig. 6.11A) and the *Southern Stock Subalkaline Intermediate-Acid Unit* (Fig. 6.13A). The three Brovales pluton units have massive textures (Fig. 6.15).

6.5.2 Mineralogical Characteristics

Noteworthy mineralogical features in the three complexes include:

Olivine, always a cumulus phase, is only present in the ultramafic rocks and olivine gabbros and gabbronorites of the Burguillos *Central Ultrabasic-Basic Layered Unit* (Fig. 6.1A and 6.2A) and the mafic rocks of the Valencia *Northern Stock Subalkaline Basic-Intermediate Unit*.

*Orthopyroxen***e** is abundant in the Burguillos and Valencia ultramafic and mafic facies, albeit texturally distinct in each. In the ultramafic rocks of the Burguillos *Central Ultrabasic-Basic Layered Unit* it crystallised late forming large poikilitic crystals with inclusions of all the

main mineral phases with no core to rim compositional or grain-size variations (Fig. 6.2D). By contrast, it is subhedral in the mafic rocks of that same unit, those of the Burguillos *Central Alkaline Basic-Intermediate Layered and Acid Unit* (Fig. 6.4B) and the *Valencia Northern Stock Subalkaline Basic-Intermediate Unit* (Fig. 6.12C).

Clinopyroxene is common in the Burguillos and Valencia complexes, mainly in the mafic rocks but also in the intermediate rocks. In the Brovales pluton it is absent. In the Burguillos *Central Alkaline Basic-Intermediate Layered and Acid Unit* its modal proportion is inversely related to the amount of orthopyroxene (Fig. 6.4A and 6.4B).

Amphibole is one of the most ubiquitous phases in the studied plutonic complexes. Its widespread distribution combined with its textural and compositional variety (see Chapter 7) makes it extremely useful as a marker to distinguish between the main units defined in this thesis.

In the mafic rocks of the Burguillos *Central Ultrabasic-Basic Layered Unit* amphibole (hastingsites-pargasites) is pleochroic with a poikilitic texture that characterises the facies (Fig. 6.3A). The modal proportion changes from minor in the ultramafic rocks, to abundant and coarse-grained in the gabbros (Fig. 6.2H and 6.3A). The gabbros of the *Burguillos Central Alkaline Basic-Intermediate Layered and Acid Unit,* on the other hand, hardly contain primary amphibole (pargasites-magnesiohastingsites), although it is more typical in the intermediate rocks and more rarely in the alkali feldspar granites (Fig. 6.6C; Fig. 6.7C). In all cases, textural relationships indicate that amphibole crystallised after biotite. In the Burguillos *External Subalkaline Intermediate Unit* intermediate rocks 'un-poikilitic' brown-green amphibole (magnesiohornblendes-edenites-magnesiohastingsites) is characteristic surrounding the biotite (Fig. 6.8F).

In the Valencia *Main Pluton Alkaline to Subalkaline Basic-Acid Unit* comparable features to the Burguillos *Central Alkaline Basic-Intermediate Layered and Acid Unit* are observed: amphibole is absent in the gabbros but present surrounding biotite in the diorites (magnesiohastingsites-magnesiohornblendes) (Fig. 6.10F and Fig. 6.10G and Fig. 6.6A for the two units respectively). In the most evolved rocks of the Valencia *Main Pluton Alkaline to Subalkaline Basic-Acid Unit* the amphibole (magnesiohastingsites-magnesiopargasite) is dark green and biotite inclusion-free (Fig. 6.11F).

In the Brovales pluton amphibole is a common phase (Fig. 6.15C). In the dioritic enclaves (ferroedenite-edenite) it has inclusions of biotite like in the more alkaline diorites from the other complexes (Fig. 6.15H). In the granodiorite is poikilitic (hastingsite-ferropargasite),

(Fig. 6.16A) similar to granodiorites of the Valencia *Main Pluton Alkaline to Subalkaline Basic-Acid Unit* (Fig. 6.16E).

Biotite, and in the ultramafic rocks *phlogopite*, is another abundant mineral, present in all the units of the three complexes. Once more it is a useful mineral to discriminate between the different units because of its prevalence, varied composition and distinctive textures in particular in relation to the amphibole.

In the ultramafic rocks of the Burguillos *Central Ultrabasic-Basic Layered Unit* the brown mica is phlogopite (Fig. 6.1F), it includes olivine and is included in orthopyroxene and amphibole (Fig. 6.1C). As noted above in the gabbros of this unit the character of the biotite permits identification of two facies i. the first has poikilitic biotite and, more abundant, poikilitic amphibole, (Fig. 6.3B) i. the second only contains biotite as inclusions the poikilitic amphibole (Fig. 6.3C). In the Burguillos *Central Alkaline Basic-Intermediate Layered and Acid Unit* gabbros biotite is the main hydrous ferromagnesian mineral (Fig. 6.4A and 6.5A). It usually grows around Fe-Ti oxides (Fig. 6.4B). It is also common in the intermediate rock of this unit, although its proportion decreases as amphibole increases in the more evolved samples (Fig. 6.6C). In the felsic rocks of this unit biotite is a minor phase (Fig. 6.7D).

Similar to the Burguillos *Central Alkaline Basic-Intermediate Layered and Acid Unit*, in the Valencia *Main Pluton Alkaline to Subalkaline Basic-Acid Unit* and the biotite dominates over amphibole in the gabbros (Fig. 6.10A) but its proportion decreases as amphibole increases in the more evolved samples (Fig. 6.11B). In the *Northern Stock Subalkaline Basic-Intermediate Unit* the biotite, which is reddish, is usually found associated with Fe-Ti oxides (Fig. 6.12E). In the *Southern Stock Subalkaline Intermediate-Acid Unit,* some biotites have Fe-Ti oxide inclusions but most are inclusion-free similar to those seen in the more evolved facies of the *Main Pluton Alkaline to Subalkaline Basic-Acid Unit* (Fig. 6.13E).

Significantly, in both the Burguillos *External Subalkaline Intermediate Unit* and the Valencia *Main Pluton Alkaline to Subalkaline Basic-Acid Unit* granodiorites the biotites are concentrically zoned (Fig. 6.11G). The Brovales pluton biotites are comparable to those in the intermediate rocks of the other complexes, but they are less zoned (Fig. 6.15C).

Biotite is typically included in amphibole, indicating that it crystallised first, in the intermediate rocks of: the Burguillos Central *Alkaline Basic-Intermediate Layered and Acid Unit* (Fig. 6.6C), the Valencia *Main Pluton Alkaline to Subalkaline Basic-Acid Unit* (Fig. 6.11B) and the Brovales dioritic enclaves of the *External Subalkaline Acid Unit* (Fig. 6.15H).

Plagioclase is the commonest mineral in the three complexes, particularly in the mafic rocks. Textural variations make it useful for distinguishing the different units.

In the Burguillos *Central Ultrabasic-Basic Layered Unit* ultramafic rocks plagioclase (bytownite-labradorite) modal proportion varies and, as it increases, marks the transition to the mafic rocks. In the gabbros of this unit it has a bimodal grain-size: the smaller crystals are included in the poikilitic amphibole whereas the larger crystals with complex patchy, recrystallised, internal structures form cumulate layers (Fig. 6.3A, Fig. 6.3F and Fig. 6.3G respectively). By contrast, the plagioclases (labradorites) in the Burguillos *Central Alkaline Basic-Intermediate Layered and Acid Unit* gabbros are quite different, euhedral with regular polysynthetic twins; the intermediate and felsic rocks once more show evidence of recrystallisation and complex zoning (Fig. 6.4H).

In the Valencia *Main Pluton Alkaline to Subalkaline Basic-Acid Unit* the plagioclases have either a euhedral habit with regular polysynthetic twins or recrystallised textures (Fig. 6.10H). This duality is more common in the mafic and intermediate rocks than in the felsic rocks in which the plagioclases are more uniform (Fig. 6.11G). In both the *Northern Stock Subalkaline Basic-Intermediate Unit* and the *Southern Stock Subalkaline Intermediate-Acid Unit* the plagioclases shows evidence of disequilibrium (Fig. 6.12F and Fig. 6.13F respectively).

In the Brovales pluton the *Central Subalkaline Intermediate Unit* has euhedral uniform crystals (Fig. 6.15F) whereas the *Intermediate Subalkaline Intermediate Unit* plagioclases show evidence of recrystallisation (Fig. 6.16F).

Alkali feldspar and *quartz* are present in the most evolved units of the three complexes. In the Burguillos *Central Alkaline Basic-Intermediate Layered and Acid Unit* granites and *Acid Peraluminous Unit* and the Valencia *Intrusive Dyke Unit* the feldspars are perthitic (Fig. 6.7E, 6.9F and 6.14E respectively).

Primary muscovite is only present in the Burguillos *Acid Peraluminous Unit* and the Valencia *Intrusive Dyke Unit* where it is subhedral and medium- to coarse-grained, the latter in the pegmatite facies (Fig. 6.9D and 6.14C respectively).

Apatite is the most noteworthy accessory mineral aside from *zircon* which is discussed in detail in Chapter 9. Apatite is present in all the units of the three complexes, in some of which it is quite distinctive. In the mafic and intermediate rocks of the Burguillos *Central Alkaline Basic-Intermediate Layered and Acid Unit* it is much more abundant than in the gabbros of the Burguillos *Central Ultrabasic-Basic Layered Unit* (Fig. 6.4A and 6.3A respectively) or for that matter, any other unit of the three complexes other than the quartz

diorite of the Valencia *Main Pluton Alkaline to Subalkaline Basic-Acid Unit* (Fig. 6.10A). Zircon is also present in all the units of the three complexes and, in some units, has a characteristic form and size (see Chapter 9). Other accessory minerals include primary *titanite* and *epidote*. In Burguillos, however, titanite is restricted to the *External Subalkaline Acid Unit,* increasing in abundance in the more evolved rocks (Fig. 6.8H). It is also present in the intermediate and felsic rocks of the Valencia *Main Pluton Alkaline to Subalkaline Basic-Acid Unit* (Fig. 6.11F). In Brovales sparse titanite is observed, by contrast, primary epidote is common.

Chapter 7: Mineral Chemistry

7.1 Olivine

7.2 Pyroxene

7.3 Amphibole

7.4 Biotite

7.5 Plagioclase

7.6 Alkali Feldspar

7.7 Fe-Ti Oxides

7.8 Mineral Chemistry Indications of the Magma Compositons of the Main Units of the Three Plutonic Bodies

7. Mineral Chemistry

This chapter describes the chemical composition of the major minerals: olivine, pyroxenes, amphiboles, biotite, feldspar and Fe-Ti oxides (mineral analyses are given in Appendix III).

7.1 Olivine

Olivine is only found in the ultramafic and mafic rocks of the Burguillos del Cerro plutonic complex *Central Ultrabasic-Basic Layered Unit* and the Valencia del Ventoso plutonic complex *Northern Stock Subalkaline Basic-Intermediate Unit* (Table 7.1).

Complex	Burguillos del Cerro plutonic complex					
Rock group unitit	*Central Ultrabasic-Basic Layered Unit*					
Facies	Ultramafic rocks			Olivine gabbros		
Sample	BUAW-9			BUAW-8		
Major elements (wt %)						
SiO_2	38.83	39.52	39.32	38.94	39.13	38.86
TiO_2	0.01	0.01		0.02	0.01	
Al_2O_3				0.00		
Cr_2O_3	0.01	0.02				0.01
NiO	0.19	0.20	0.22	0.10	0.13	0.10
FeO_T	17.45	17.73	17.67	18.78	18.64	19.22
MnO	0.25	0.30	0.27	0.25	0.25	0.26
MgO	43.11	43.09	43.13	42.77	42.55	42.26
CaO	0.06	0.04	0.02	0.05	0.01	0.03
Na_2O	0.09	0.02	0.04	0.01	0.03	0.01
K_2O	0.02	0.01	0.02	0.01	0.01	0.01
Sum	100.19	101.07	100.80	101.07	100.92	100.90
Formula based on 4 oxygens						
Si	0.985	0.995	0.992	0.983	0.990	0.986
Ti	0.000	0.000		0.000	0.000	
Al				0.000		
Cr	0.000	0.000				0.000
Ni	0.004	0.004	0.005	0.002	0.003	0.002
Fe^{3+}	0.035	0.010	0.019	0.034	0.021	0.030
Fe^{2+}	0.335	0.364	0.354	0.363	0.373	0.378
Mn	0.005	0.006	0.006	0.005	0.005	0.005
Mg	1.629	1.618	1.622	1.610	1.605	1.597
Ca	0.002	0.001	0.001	0.001	0.000	0.001
Na	0.004	0.001	0.002	0.000	0.001	0.001
K	0.001	0.000	0.001	0.000	0.000	0.000
Fo %	81.28	80.99	81.08	80.02	80.06	79.45

Table 7.1. Representative analyses of olivine from ultramafic rocks and olivine gabbros from the Burguillos Central Ultrabasic-Basic Layered Unit.

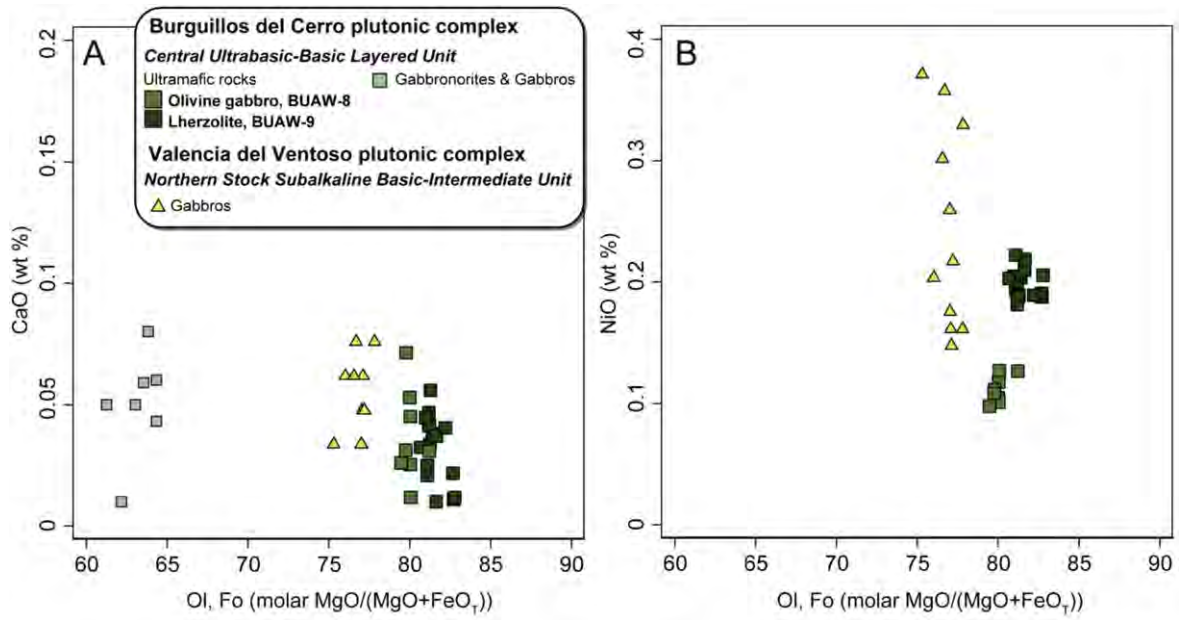

Figure 7.1. Compositional variation of olivine from the ultramafic rocks and olivine gabbros and gabbronorites of the Burguillos Central Ultrabasic-Basic Layered Unit (smaller lighter symbols - data from García-Casquero, 1991); and olivine from the gabbros of the Valencia Northern Stock Subalkaline Basic-Intermediate Unit (data from Sarrionandia, 2005).

Olivine is always a cumulus phase in the rocks of this study. In the Burguillos *Central Ultrabasic- Basic Layered Unit* ultramafic rocks its composition varies from Fo_{80-84} then to Fo_{79-81} in the plagioclase-bearing rocks (Fig. 7.1). In the olivine gabbros and poikilitic amphibole gabbros of the same unit the olivine has a composition of Fo_{61-65} (Fig. 7.1A). The Valencia *Northern Stock Subalkaline Basic-Intermediate Unit* olivines are in the range Fo_{75-78}, (Fig. 7.1). Notably, none of the olivines are sufficiently rich in Mg to be in equilibrium with mantle compositions, Fo > 88. Brey and Köhler, (1990) suggested that the Ca content of olivine may be used as a geobarometer. It is therefore interesting to note that all units have a comparable range of CaO (Fig. 7.1), which might indicate comparable pressures of crystallisation.

The NiO content of the olivines varies significantly between the groups (Fig. 7.1B). In the Burguillos *Central Ultrabasic-Basic Layered Unit* the olivines from the ultramafic rocks have NiO ≈ 0.18-0.22 wt % whereas those from the more plagioclase-rich facies have lower NiO ≈ 0.10-0.12 wt % (Fig. M1A). The Valencia *Northern Stock Subalkaline Basic-Intermediate Unit* olivines, have the greatest range and highest NiO values ≈ 0.18-0.36 wt %.

7.2 Pyroxene

Both orthopyroxene and clinopyroxene are common in the ultramafic and mafic rocks of the Burguillos del Cerro and Valencia del Ventoso plutonic complexes. Only clinopyroxene is present in the intermediate rocks, it commonly alters to secondary amphibole. However,

pyroxene is absent in the Brovales pluton.

In Figure 7.2, the pyroxenes are all calcic-ferro-magnesian not calcic-sodic or sodic (cf., Morimoto et al., 1988). The clinopyroxenes are mostly diopside and augite with some hedenbergites in the alkali feldspar granites; the orthopyroxenes are predominantly enstatite with a few pigeonites (Fig. 7.3, Table 7.2 and 7.3).

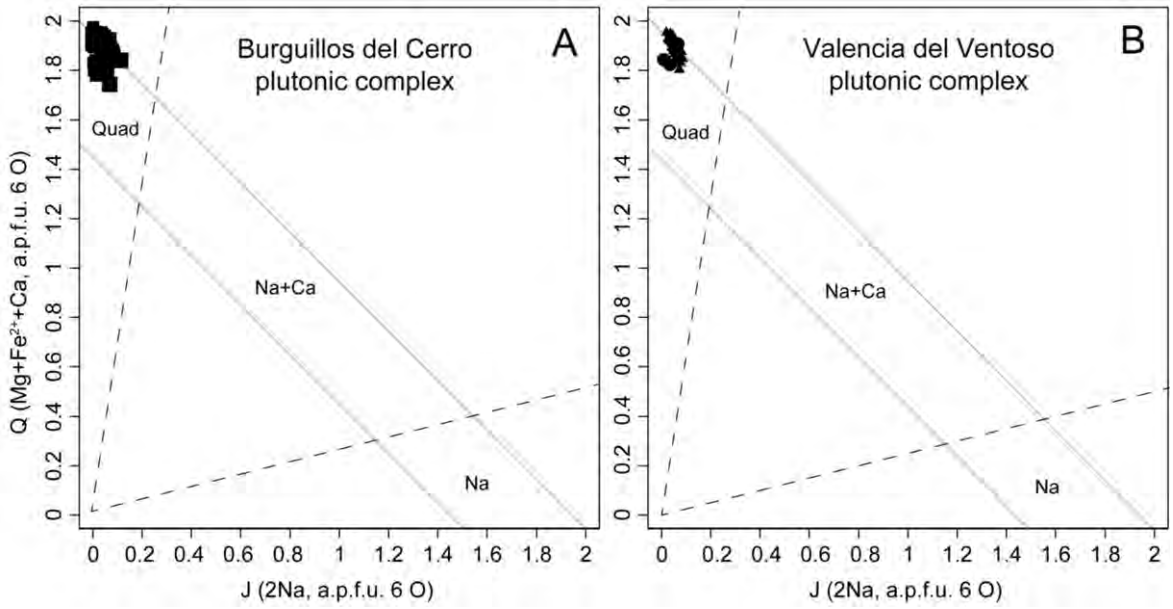

Figure 7.2. Classification of pyroxenes from: A) Burguillos del Cerro; and B) Valencia del Ventoso plutonic complexes. Fields from Morimoto et al., (1988). Note that all the pyroxenes fall in the 'Quad' Ca-Fe- Mg pyroxene field (smaller symbols data from García-Casquero, 1991 and Sarrionandia, 2005).

7.2.1 Orthopyroxene

Orthopyroxene, like olivine, is typical in the Burguillos *Central Ultrabasic-Basic Layered Unit,* it is also found in the Burguillos *Central Alkaline Basic-Intermediate Layered and Acid Unit* (Fig. 7.3). In the Valencia del Ventoso plutonic complex, however, it is restricted to the *Northern Stock Subalkaline Basic-Intermediate Unit* (Fig. 7.3B). Almost all these orthopyroxenes are enstatites with a solid solution compositional variation of Wo_{1-8}-En_{49-85}-Fe_{15-41} (Fig. 7.3).

In Burguillos the orthopyroxene has different compositions in the two main units. In the *Central Ultrabasic-Basic Layered Unit* ultramafic rocks and olivine gabbros the poikilitic intercumulus orthopyroxene is Wo_{1-2}-En_{80-85}-Fe_{14-18} (Table 7.2, Fig. 7.3A). By contrast, in the gabbros and gabbronorites of this unit with characterisitic poikilitic amphibole the orthopyroxenes, which are less abundant, are less magnesian with a composition of $Wo_{1-8}En_{60-70}$-Fe_{29-37} (Fig. 73A, Table 7.2). Orthopyroxene in the gabbros and diorites of the *Central Alkaline Basic-Intermediate Layered and Acid Unit* have a similar composition with MgO≈ 20-23 wt % and an end-member compositional

Complex	Burguillos del Cerro plutonic complex											
Rock group unit	*Central Ultrabasic-Basic Layered Unit*											
Facies	Ultramafic rocks			Olivine gabbros			Poikilitic amphibole and biotite gabbronorites and gabbros			Poikilitic amphibole gabbronorites and gabbros		
Sample	BUAW-9			BUAW-8			BUB-3			BUAW-4		
Major elements (wt %)												
SiO_2	56.61	56.08	56.02	55.25	55.37	55.52	52.13	51.01	52.71	52.59	52.63	52.50
TiO_2	0.00	0.09	0.10	0.22	0.25	0.18	0.21	0.53	0.18	0.27	0.26	0.24
Al_2O_3	0.46	0.97	1.01	1.19	1.24	1.13	1.07	1.06	1.12	1.04	0.96	0.78
Cr_2O_3	0.01	0.13	0.16	0.14	0.15	0.10		0.10			0.02	
NiO	0.04	0.03	0.03	0.02	0.03	0.03						
FeO_T	10.40	10.16	9.90	11.26	11.71	11.56	19.86	23.75	20.61	23.02	21.38	21.31
MnO	0.25	0.28	0.25	0.26	0.26	0.29	0.54	0.47	0.54	0.66	0.62	0.61
MgO	31.76	31.65	31.58	30.73	30.18	30.62	21.85	21.88	21.64	22.12	23.76	23.48
CaO	0.80	0.93	0.92	1.05	1.14	1.04	3.91	1.14	2.94	1.17	0.75	1.14
Na_2O	0.04	0.05	0.04	0.05	0.03	0.02	0.30		0.17	0.02	0.01	0.03
K_2O	0.01	0.02	0.02	0.02	0.01	0.01	0.02		0.02	0.01	0.01	0.02
Sum	100.39	100.39	100.04	100.19	100.38	100.51	99.90	99.93	99.92	100.90	100.41	100.10
Formula based on 6 oxygens												
Si	1.979	1.960	1.964	1.945	1.952	1.951	1.930	1.909	1.959	1.946	1.938	1.940
Ti	0.000	0.002	0.003	0.006	0.007	0.005	0.006	0.015	0.005	0.007	0.007	0.007
Al	0.019	0.040	0.042	0.050	0.051	0.047	0.047	0.047	0.049	0.045	0.042	0.034
Cr	0.000	0.003	0.004	0.004	0.004	0.003		0.003			0.001	
Ni	0.001	0.001	0.001	0.001	0.001	0.001						
Fe^{3+}	0.025	0.036	0.025	0.050	0.030	0.041	0.102	0.100	0.035	0.050	0.069	0.075
Fe^{2+}	0.279	0.261	0.266	0.281	0.315	0.299	0.512	0.643	0.605	0.662	0.590	0.583
Mn	0.007	0.008	0.007	0.008	0.008	0.009	0.017	0.015	0.017	0.021	0.019	0.019
Mg	1.655	1.649	1.651	1.613	1.586	1.604	1.206	1.221	1.199	1.220	1.304	1.294
Ca	0.030	0.035	0.035	0.040	0.043	0.039	0.155	0.046	0.117	0.046	0.030	0.045
Na	0.003	0.003	0.003	0.003	0.002	0.002	0.022		0.012	0.002	0.001	0.002
K	0.001	0.001	0.001	0.001	0.000	0.000	0.001		0.001	0.000	0.000	0.001
Wo %	1.50	1.76	1.75	1.98	2.18	1.97	7.79	2.26	5.92	2.31	1.47	2.23
En %	82.90	82.90	83.24	80.98	80.01	80.55	60.51	60.29	60.76	61.03	64.84	64.16
Fer %	15.59	15.34	15.01	17.03	17.81	17.48	31.70	37.44	33.32	36.65	33.69	33.61

Table 7.2. Representative analyses of orthopyroxene from the Burguillos del Cerro and Valencia del Ventoso plutonic complexes.

Complex	Burguillos del Cerro plutonic complex					Valencia del Ventoso plutonic complex			
Rock group unit	*Central Alkaline Basic-Intermediate Layered and Acid Unit*					*Northern Stock Subalkaline Basic-Intermediate Unit*			
Facies	Gabbros with amphibole			Gabbros	Diorites	Quartz monzodiorites			
Sample	BUB-15			BUB-16	BUB-1	VAAW-30			
Major elements (wt %)									
SiO_2	52.35	53.56	53.52	56.79	53.26	52.02	52.36	51.52	52.11
TiO_2	0.14	0.21	0.21	0.18	0.36	0.29	0.33	0.25	0.24
Al_2O_3	0.67	0.99	1.01	0.92	1.22	0.69	0.60	0.49	0.50
Cr_2O_3		0.02			0.10	0.03	0.03	0.00	0.02
NiO						0.04	0.03		0.02
FeO_T	24.79	23.30	23.49	18.93	19.57	24.68	24.15	26.87	24.30
MnO	1.03	0.64	0.63	0.64	0.45	0.48	0.53	0.63	0.49
MgO	19.83	23.29	22.83	19.79	22.54	20.32	20.67	19.23	20.49
CaO	0.99	0.87	0.99	2.33	2.20	1.33	1.65	1.20	1.49
Na_2O	0.20	0.02	0.02	0.38	0.21	0.05	0.06	0.05	0.06
K_2O		0.01	0.02		0.08	0.02	0.01	0.02	0.03
Sum	100.00	102.91	102.72	99.97	99.98	99.94	100.40	100.26	99.76
Formula based on 6 oxygens									
Si	1.978	1.937	1.943	2.121	1.968	1.963	1.963	1.956	1.967
Ti	0.004	0.006	0.006	0.005	0.010	0.008	0.009	0.007	0.007
Al	0.030	0.042	0.043	0.041	0.053	0.031	0.027	0.022	0.022
Cr		0.001			0.003	0.001	0.001	0.000	0.001
Ni						0.001	0.001		0.001
Fe^{3+}	0.021	0.075	0.063		0.007	0.030	0.033	0.057	0.034
Fe^{2+}	0.762	0.630	0.650	0.591	0.598	0.749	0.724	0.796	0.733
Mn	0.033	0.020	0.019	0.020	0.014	0.015	0.017	0.020	0.016
Mg	1.117	1.255	1.235	1.102	1.241	1.143	1.155	1.088	1.153
Ca	0.040	0.034	0.038	0.093	0.087	0.054	0.066	0.049	0.060
Na	0.015	0.001	0.001	0.027	0.015	0.004	0.004	0.004	0.004
K		0.000	0.001		0.004	0.001	0.000	0.001	0.001
Wo %	2.03	1.67	1.92	5.16	4.47	2.70	3.31	2.42	3.01
En %	56.61	62.36	61.58	61.00	63.76	57.41	57.91	54.14	57.77
Fer %	41.37	35.97	36.50	33.84	31.78	39.89	38.78	43.44	39.22

Table 7.2. Continued.

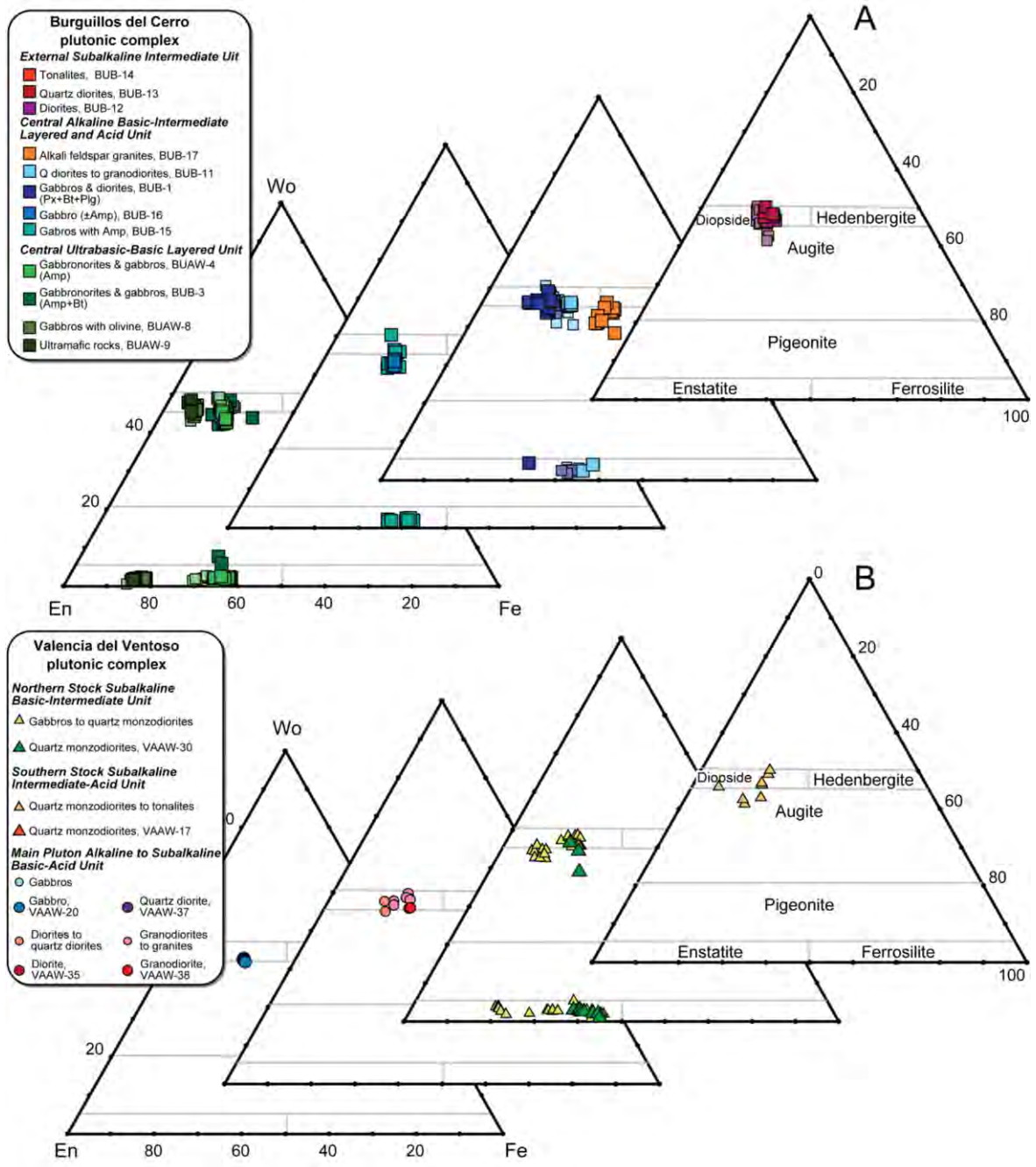

Figure 7.3. Classification of pyroxenes from: A) Burguillos del Cerro; and B) Valencia del Ventoso in the diagram En-Wo-Fe of Morimoto et al., (1988). (smaller lighter symbols data from García-Casquero, 1991 and Sarrionandia, 2005). En: Enstatite; Wo: Wollastonite; Fe: Ferrosilite.

range of Wo_{2-5}-En_{55-64}-Fe_{32-43} (Fig. 7.3A).

The orthopyroxene compositions in the gabbros to quartz monzodiorites of the Valencia *Northern Stock Subalkaline Basic-Intermediate Unit* cover almost the whole compositional range found in the Burguillos complex, MgO ≈ 19-29 wt % and $Wo_{1-5}En_{53-77}$-Fe_{20-45} (Table 7.2, Fig. 7.3B). The quartz monzodiorite orthopyroxenes have MgO ≈ 20-21 wt % and Wo_{2-3}-En_{54-59}-Fe_{37-43} (Fig. 7.3B, Table 7.2).

Complex	Burguillos del Cerro plutonic complex									
Rock group unit	*Central Ultrabasic-Basic Layered Unit*								*Central Alkaline Basic-Intermediate Layered and Acid Unit*	
Facies	Ultramafic rocks		Olivine gabbros		Poikilitic amphibole and biotite gabbronorites and gabbros		Poikilitic amphibole gabbronorites and gabbros		Gabbros with amphibole	
Sample	BUAW-9		BUAW-8		BUB-3		BUAW-4		BUB-15	
Major elements (wt %)										
SiO_2	54.45	54.37	52.46	53.88	52.57	52.32	51.70	51.85	53.09	53.17
TiO_2	0.04	0.04	0.35	0.04	0.32	0.41	0.62	0.41	0.37	0.43
Al_2O_3	0.20	0.24	1.91	0.66	2.09	2.06	2.15	1.70	1.72	1.63
Cr_2O_3	0.24	0.18	0.23	0.08	0.02			0.01		0.02
NiO	0.01	0.01	0.02	0.01	0.01	0.06		0.01		
FeO_T	2.92	3.12	4.82	4.16	8.38	8.21	9.24	9.60	9.73	9.46
MnO	0.12	0.12	0.14	0.12	0.31	0.30	0.31	0.33	0.27	0.25
MgO	17.24	16.87	17.07	16.93	14.70	14.32	14.08	14.39	15.23	14.96
CaO	24.27	24.54	22.04	23.83	21.71	22.42	21.82	21.10	20.76	21.50
Na_2O	0.19	0.18	0.24	0.12	0.38	0.36	0.38	0.32	0.28	0.28
K_2O	0.02	0.01	0.01	0.01	0.02	0.01	0.01	0.01	0.02	0.01
Sum	99.71	99.69	99.30	99.83	100.51	100.47	100.32	99.73	101.47	101.71
Formula based on 6 oxygens										
Si	1.988	1.989	1.928	1.971	1.938	1.932	1.918	1.935	1.943	1.943
Ti	0.001	0.001	0.010	0.001	0.009	0.011	0.017	0.011	0.010	0.012
Al	0.009	0.010	0.083	0.028	0.091	0.090	0.094	0.075	0.074	0.070
Cr	0.007	0.005	0.007	0.002	0.001			0.000		0.001
Ni	0.000	0.000	0.001	0.000	0.000	0.002		0.000		
Fe^{3+}	0.020	0.018	0.053	0.034	0.043	0.049	0.063	0.056	0.039	0.039
Fe^{2+}	0.069	0.078	0.095	0.093	0.215	0.205	0.224	0.244	0.258	0.250
Mn	0.004	0.004	0.004	0.004	0.010	0.009	0.010	0.010	0.008	0.008
Mg	0.939	0.920	0.935	0.923	0.808	0.788	0.779	0.801	0.831	0.815
Ca	0.949	0.962	0.868	0.934	0.857	0.887	0.867	0.844	0.814	0.842
Na	0.013	0.013	0.017	0.008	0.027	0.026	0.027	0.023	0.020	0.020
K	0.001	0.001	0.000	0.001	0.001	0.000	0.001	0.001	0.001	0.000
Wo %	47.93	48.54	44.38	46.97	44.35	45.76	44.65	43.16	41.72	43.09
En %	47.38	46.45	47.82	46.45	41.79	40.67	40.10	40.98	42.59	41.72
Fer %	4.69	5.01	7.80	6.59	13.86	13.56	15.25	15.86	15.69	15.19

Table 7.3. Representative analyses of clinopyroxene from the Burguillos del Cerro and Valencia del Ventoso plutonic complexes.

	Burguillos del Cerro plutonic complex									
Rock group unit	*Central Alkaline Basic-Intermediate Layered and Acid Unit*						*External Subalkaline Intermediate Unit*			
Facies	Diorites		Quartz diorites		Alkali feldspar granites		Diorites		Quartz diorites and tonalites	
Sample	BUB-1		BUB-11		BUB-17		BUB-12		BUB-13	
Major elements (wt %)										
SiO_2	52.56	52.52	52.18	52.12	52.09	51.75	52.61	53.45	53.23	53.14
TiO_2	0.38	0.41	0.14	0.11	0.22	0.23		0.07	0.04	
Al_2O_3	1.59	1.57	0.69	0.72	0.78	1.03	0.36	0.27	0.79	0.29
Cr_2O_3	0.09	0.08	0.07		0.01	0.04			0.03	0.07
NiO		0.05			0.02	0.03				
FeO_T	10.17	9.78	11.80	12.41	17.01	16.53	10.14	9.78	9.16	8.72
MnO	0.31	0.38	0.53	0.53	0.75	0.65	0.88	0.63	0.54	0.47
MgO	14.07	14.13	11.80	11.63	10.30	9.80	12.05	12.74	12.77	12.37
CaO	21.64	21.52	22.38	22.20	19.56	20.40	23.43	22.61	23.02	24.70
Na_2O	0.35	0.33	0.26	0.26	0.45	0.39	0.51	0.44	0.32	0.19
K_2O	0.02	0.03	0.04		0.04	0.15			0.04	0.04
Sum	101.18	100.80	99.90	99.97	101.23	101.00	99.98	100.00	99.93	100.00
Formula based on 6 oxygens										
Si	1.939	1.944	1.976	1.976	1.979	1.972	1.980	2.005	1.995	1.995
Ti	0.011	0.011	0.004	0.003	0.006	0.007		0.002	0.001	
Al	0.069	0.068	0.031	0.032	0.035	0.046	0.016	0.012	0.035	0.013
Cr	0.003	0.002	0.002		0.000	0.001			0.001	0.002
Ni		0.001			0.001	0.001				
Fe^{3+}	0.055	0.044	0.027	0.028	0.030	0.032	0.062	0.005		0.012
Fe^{2+}	0.259	0.259	0.347	0.365	0.511	0.495	0.257	0.302	0.287	0.262
Mn	0.010	0.012	0.017	0.017	0.024	0.021	0.028	0.020	0.017	0.015
Mg	0.774	0.780	0.666	0.657	0.583	0.557	0.676	0.713	0.713	0.692
Ca	0.855	0.853	0.908	0.902	0.796	0.833	0.944	0.909	0.924	0.993
Na	0.025	0.024	0.019	0.019	0.033	0.029	0.037	0.032	0.023	0.014
K	0.001	0.001	0.002		0.002	0.007			0.002	0.002
Wo %	43.80	43.81	46.21	45.79	40.95	42.99	48.00	46.64	47.60	50.30
En %	39.63	40.03	33.91	33.37	30.01	28.74	34.36	36.58	36.73	35.07
Fer %	16.56	16.15	19.88	20.84	29.04	28.27	17.64	16.78	15.66	14.63

Table 7.3. Continued.

	Valencia del Ventoso plutonic complex					
Rock group unit	*Main Pluton Alkaline to Subalkaline Basic-Acid Unit*				*Northern Stock Subalkaline Basic-Intermediate Unit*	
Facies	Gabbros and diorites		Granodiorites and granites		Quartz monzodiorites	
Sample	VAAW-20		VAAW-38		VAAW-30	
Major elements (wt %)						
SiO_2	52.17	51.81	52.61	52.27	52.57	51.85
TiO_2	0.16	0.19	0.18	0.14	0.06	0.44
Al_2O_3	0.96	1.06	0.77	0.75	0.46	1.10
Cr_2O_3	0.02	0.01		0.01	0.07	0.03
NiO		0.00	0.03	0.02	0.01	0.00
FeO_T	10.52	10.65	11.56	11.65	10.74	12.39
MnO	0.54	0.59	0.46	0.52	0.33	0.35
MgO	13.02	12.74	11.95	11.81	13.02	13.85
CaO	22.22	21.80	22.00	22.07	21.70	18.94
Na_2O	0.30	0.51	0.45	0.43	0.30	0.47
K_2O	0.02	0.03	0.02	0.02	0.03	0.02
Sum	99.93	99.40	100.02	99.68	99.29	99.43
Formula based on 6 oxygens						
Si	1.959	1.955	1.985	1.981	1.988	1.956
Ti	0.005	0.005	0.005	0.004	0.002	0.013
Al	0.042	0.047	0.034	0.034	0.021	0.049
Cr	0.000	0.000		0.000	0.002	0.001
Ni		0.000	0.001	0.000	0.000	0.000
Fe^{3+}	0.053	0.070	0.020	0.029	0.021	0.048
Fe^{2+}	0.278	0.266	0.345	0.340	0.319	0.343
Mn	0.017	0.019	0.015	0.017	0.010	0.011
Mg	0.729	0.717	0.672	0.667	0.734	0.779
Ca	0.894	0.882	0.889	0.896	0.879	0.766
Na	0.022	0.037	0.033	0.031	0.022	0.034
K	0.001	0.001	0.001	0.001	0.001	0.001
Wo %	45.37	45.13	45.82	45.98	44.78	39.33
En %	36.99	36.70	34.64	34.22	37.39	40.02
Fer %	17.64	18.17	19.54	19.80	17.83	20.64

Table 7.3. Continued.

7.2.2 Clinopyroxene

Clinopyroxene is present in the ultramafic to intermediate Burguillos del Cerro and Valencia del Ventoso units. It is mostly diopside and augite with some hedenbergitic augites in the alkali feldspar granites (Table 7.3, Fig., 7.3 and Fig., 7.4).

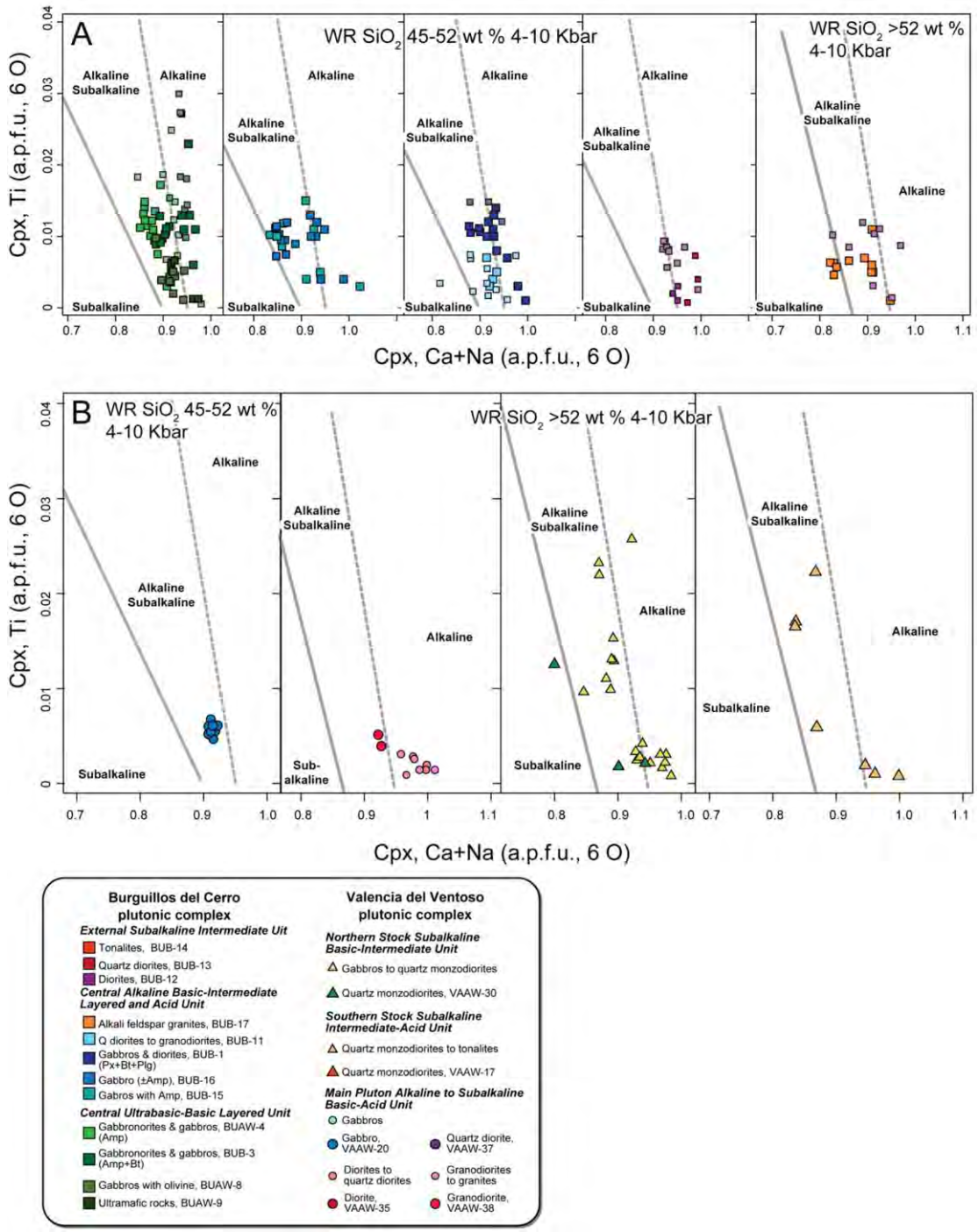

Figure 7.4. Composition of the clinopyroxene from A) Burguillos del Cerro and Valencia del Ventoso plutonic complexes. Ti versus Ca+Na considering a pressure of 4 kbar and basic to acid compositions, fields from Molina et al., (2009). (smaller lighter symbols data from García-Casquero,1991 and Sarrionandia, 2005).

The clinopyroxenes in the Burguillos *Central Ultrabasic-Basic Layered Unit* ultramafic rocks and olivine gabbros are $Wo_{43-49}En_{46-49}$-Fe_{5-8} (Table 7.2, Fig., 7.3A). The gabbros and gabbronorites from that unit and the Burguillos *Central Alkaline Basic-Intermediate Layered and Acid Unit* gabbros and diorites have comparable clinopyroxene compositions: Wo_{42-50}-En_{37-43}-Fe_{10-20} (Fig. 7.3A and 7.4A). A similar range is observed in gabbros and quartz monzodiorites from the Valencia *Northern Stock Subalkaline Basic-Intermediate Unit* clinopyroxenes which have $Wo_{39-49}En_{36-48}$-Fe_{8-21} (Fig. 7.3B, Table 7.3); and also the mafic rocks from the Valencia *Main Pluton Alkaline to Subalkaline Basic-Acid Unit* with $Wo_{45-46}En_{36-37}$-Fe_{17-18} (Fig. 7.3A).

The clinopyroxenes in the more intermediate rocks is commonly partially transformed to secondary amphibole. In the other Burguillos rocks as well as in all the Valencia units clinopyroxene is less abundant and extensively transformed to actinolite. The clinopyroxenes in the intermediate rocks have similar compositions to those in the mafic rocks (Table 7.2 and Fig. 7.4B), having end-member compositions of $Wo_{42-50}En_{34-40}$-Fe_{12-24} (Fig. 7.3A).

The clinopyroxene of the alkali-feldspar granites from the Burguillos *Central Alkaline Basic-Intermediate Layered and Acid Unit* is hedenbergitic augite $Wo_{38-46}En_{24-30}$-Fe_{28-34} (Fig. 7.3A, Table 7.3).

7.3 Amphibole

Amphibole is one of the most abundant minerals in the three plutonic bodies. All the amphiboles are calcic albeit with a broad compositional range that comprises pargasites, hastingsites, edenites, magnesiohornblendes and actinolites (Fig. 7.5, 7.6 and 7.7). Textural evidence indicates that the rocks contain both primary magmatic and secondary amphibole, these have to be separated. We used petrographic and textural data to preliminarily identify secondary amphiboles as the pale green mineral that formed from the subsolidus transformation of clinopyroxene (see Chapter 6).

Mineral chemistry data may be used to support this interpretation. The complexity of amphibole compositions permit its use to deduce information about the magma composition from which it crystallised and, as we shall see below in Chapter 9 its P-T conditions of formation. Molina et al., (2009) established that low $(Na+K)_A$, Al_{IV} and TiO_2 in amphiboles is indicative of low temperature subsolidus reequilibration (e.g., Gilbert et al., 1982; Deer et al., 1997). The corollary of this, as applied by Molina et al. (2009), is that primary amphiboles eddinite-pargasite-hastingsite may be identified as those with $(Na+K)_A$ greater than 0.5, relatively high Al_{IV} and, usually, high TiO_2 (Fig. 7.8). Primary magnesiohornblende, on the other hand, has $(Na+K)_A$ less than 0.5 but may be distinguished from the secondary actinolite by their higher TiO_2 > 1.1-2 wt. % and Al_{IV} > 1 (Fig. 7.8). Applying these criteria to the amphiboles of the

Burguillos del Cerro, Valencia and Brovales complexes permitted us to confirm the aforementioned petrographic identification of secondary actinolite and identify the primary amphiboles for further consideration (Fig. 7.8).

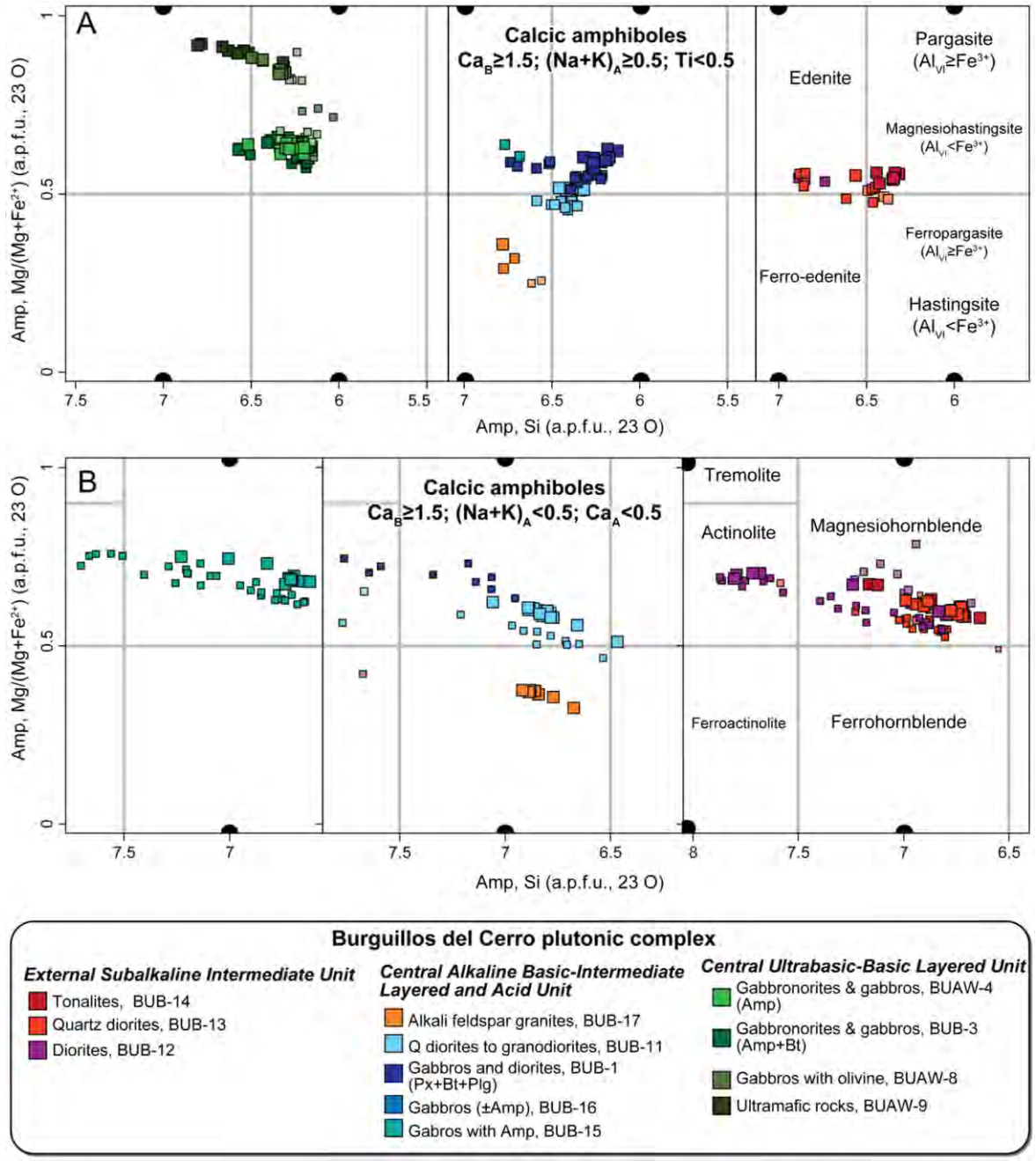

Figure 7.5. Classification of amphiboles from the Burguillos del Cerro plutonic complex, fields for all diagrams given in right side figure from Leake et al., (1997). Note that the amphiboles are calcic and that each of the units is compositionally varied (smaller lighter symbols - data from Pons, 1982 and García-Casquero, 1991).

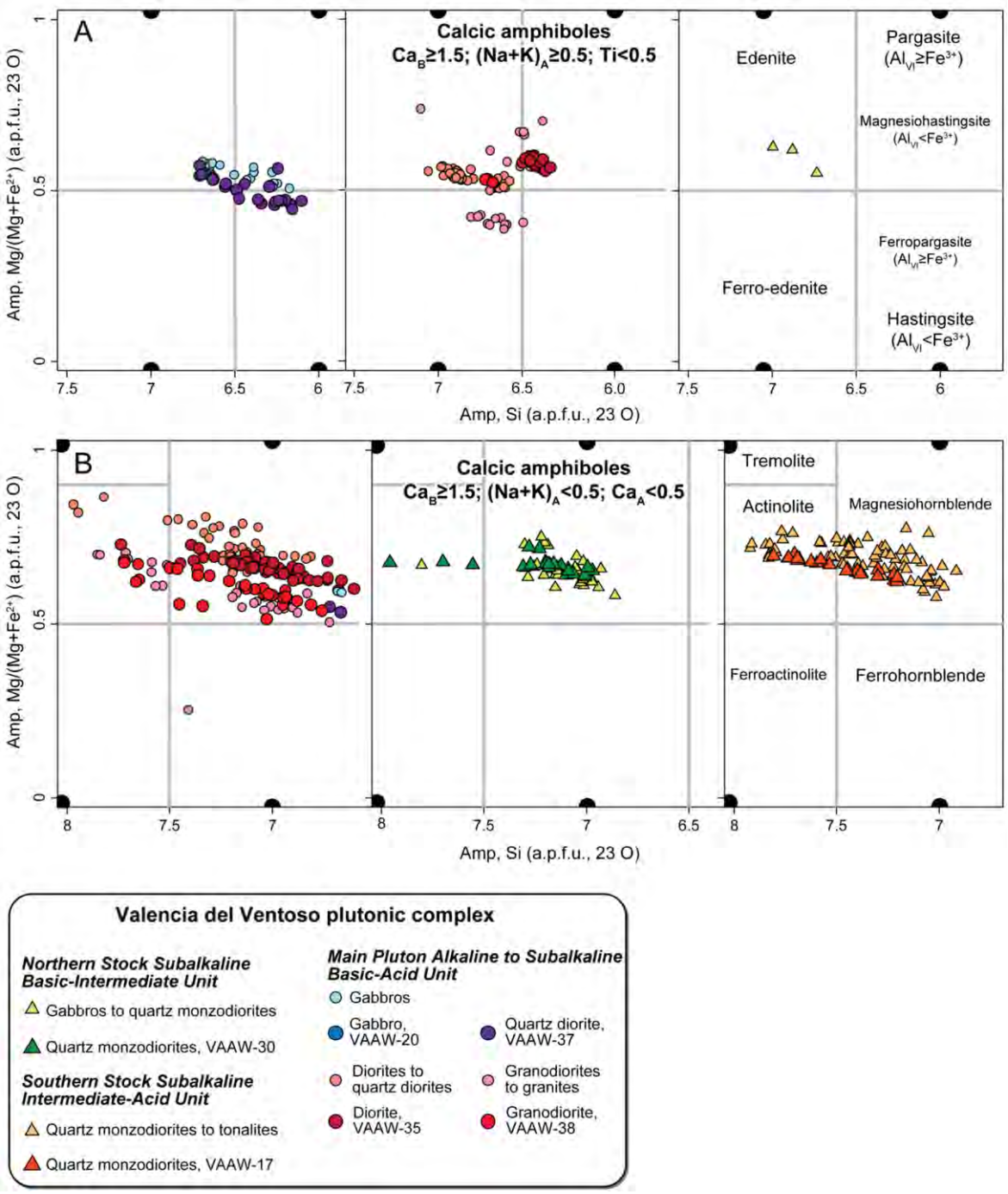

Figure 7.6. Classification of amphiboles from the Valencia del Ventoso plutonic complex, fields from Leake et al., (1997). Note that the amphiboles are calcic and that each of the units is compositionally varied (smaller lighter symbols - Sarrionandia, 2005).

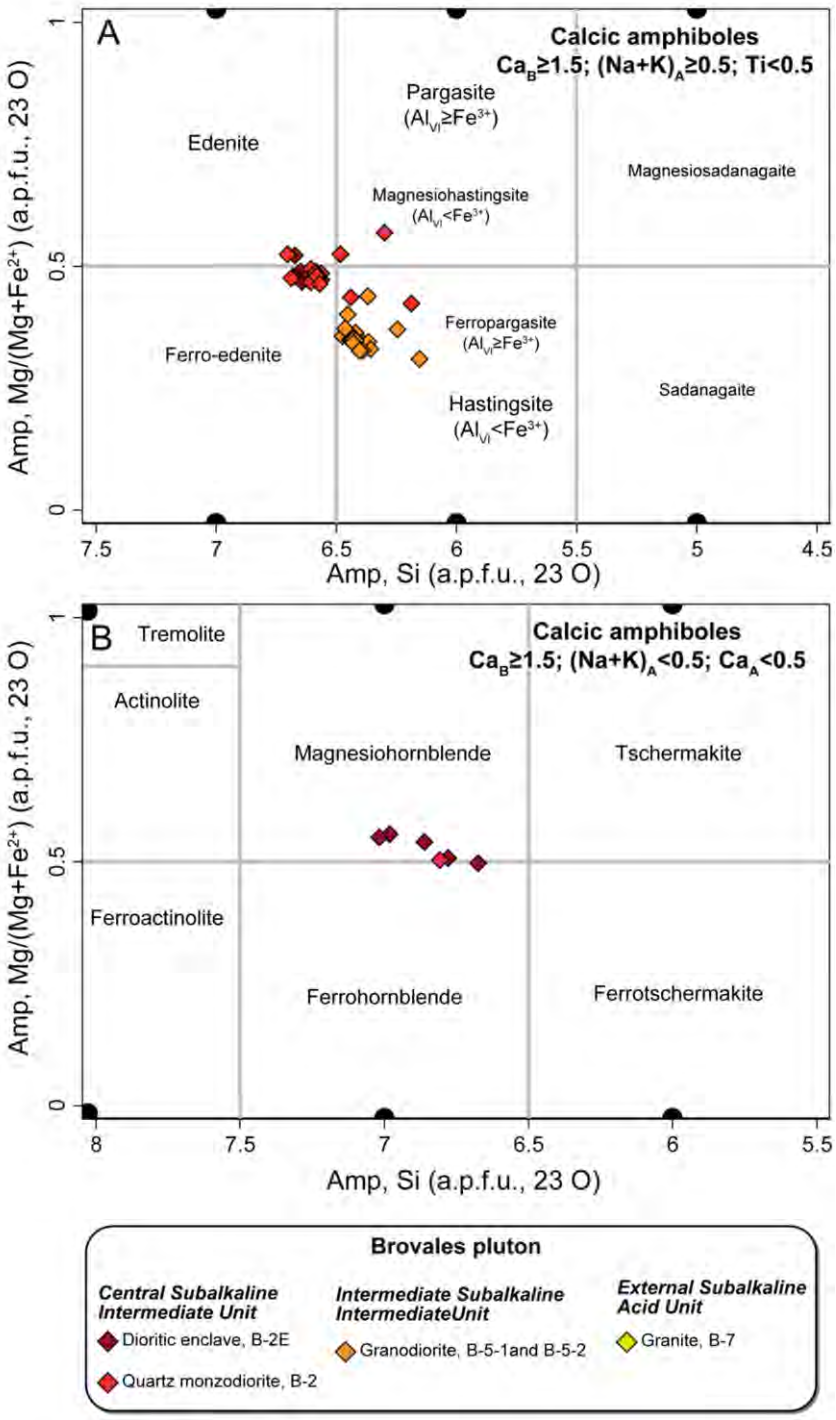

Figure 7.7. Classification of amphiboles from the Brovales pluton, fields from Leake et al., (1997). Note that all the amphiboles are calcic and that the majority have high Na+K in the A-site.

Complex	Burguillos del Cerro plutonic complex										
Rock group unit	*Central Ultrabasic-Basic Layered Unit*									*Central Alkaline Basic-Intermediate Layered and Acid Unit*	
Facies	Ultramafic rocks		Olivine gabbros		Poikilitic amphibole and biotite gabbronorites and gabbros		Poikilitic amphibole gabbronorites and gabbros			Gabbros with amphibole	
Sample	BUAW-9		BUAW-8		BUB-3		BUAW-4			BUB-15	
Textual position	core	rim	core	rim	rim	core	core	rim	rim	core	core
Major elements (wt %)											
SiO_2	43.70	45.64	43.44	45.14	43.06	42.63	41.63	43.67	45.72	46.06	45.75
TiO_2	2.01	0.36	2.80	1.04	2.66	2.42	3.81	2.48	1.93	2.10	1.95
Al_2O_3	11.22	10.56	11.10	10.88	10.28	11.34	11.05	9.41	8.00	8.45	8.68
Cr_2O_3	1.37	0.43	0.59	0.57	0.01		0.02	0.02			
NiO	0.04	0.05	0.02	0.06	0.01	0.01	0.00	0.00		0.03	
FeO_T	6.01	6.62	7.37	7.24	14.21	14.25	13.94	14.64	14.34	15.51	15.81
MnO	0.09	0.08	0.09	0.08	0.17	0.17	0.20	0.17	0.20	0.28	0.25
MgO	17.17	18.17	16.54	17.17	12.68	12.58	12.24	12.39	13.20	13.41	13.23
CaO	11.67	11.48	11.71	11.76	11.58	11.56	11.45	11.69	11.48	11.37	11.45
Na_2O	2.84	2.73	2.23	1.96	1.84	1.86	1.74	1.32	1.25	1.28	1.20
K_2O	0.91	0.68	0.99	0.79	1.16	1.27	1.25	1.16	0.94	0.95	1.02
F	0.16	0.15	0.18	0.11	0.24	0.23	0.28	0.38	0.36	0.37	0.38
Cl	0.30	0.35	0.13	0.21	0.50	0.53	0.64	0.67	0.64	0.50	0.49
Sum	97.51	97.29	97.21	97.01	98.40	98.85	98.26	98.02	98.04	100.31	100.21
Formula based on 23 oxygens											
Si_T	6.318	6.543	6.305	6.495	6.388	6.291	6.209	6.518	6.765	6.650	6.618
Al_T	1.682	1.457	1.695	1.505	1.612	1.709	1.791	1.482	1.235	1.350	1.382
Al_C	0.231	0.328	0.203	0.340	0.185	0.263	0.152	0.173	0.160	0.088	0.098
Ti_C	0.219	0.039	0.306	0.113	0.297	0.269	0.427	0.279	0.214	0.228	0.212
Fe^{3+}_C	0.171	0.377	0.224	0.378	0.256	0.321	0.235	0.274	0.299	0.529	0.576
Cr_C		0.034			0.004					0.001	
Mg_C	3.700	3.883	3.579	3.683	2.804	2.768	2.722	2.757	2.911	2.887	2.853
Fe^{2+}_C	0.555	0.339	0.670	0.486	1.454	1.380	1.464	1.517	1.416	1.268	1.262
Mn_C	0.012	0.000	0.011	0.000	0.000	0.000	0.000	0.000	0.000	0.000	0.000
Fe^{2+}_B	0.000	0.078	0.000	0.006	0.053	0.058	0.040	0.036	0.059	0.076	0.075
Mn_B	0.000	0.010	0.000	0.009	0.021	0.021	0.025	0.022	0.025	0.034	0.031
Ca_B	1.807	1.763	1.821	1.813	1.840	1.828	1.830	1.869	1.819	1.759	1.774
Na_B	0.193	0.149	0.179	0.171	0.085	0.093	0.106	0.073	0.096	0.131	0.120
Na_A	0.604	0.609	0.449	0.376	0.444	0.439	0.396	0.309	0.261	0.228	0.217
K_A	0.168	0.124	0.184	0.146	0.220	0.239	0.238	0.221	0.177	0.175	0.188
A-vacancy	0.228	0.267	0.367	0.478	0.337	0.322	0.365	0.470	0.562	0.597	0.595
Classification	Pg	Ed	Mg-Hst	Mg-Hst	Mg-Hst	Mg-Hst	Mg-Hst	Ed	Mg-Hbn	Mg-Hbn	Mg-Hbn

Table 7.4. Representative analyses of calcic amphibole from the Burguillos del Cerro and Valencia del Ventoso plutonic complexes and the Brovales pluton. Fe-Kt: Ferrokaersutite, Pg: Pargasite, Fe-Pg: Ferropargasite; Mg-Hst: Magnesiohastingsite, Hst: Hastingsite, Ed: Edenite, Fe-Ed: Ferroedenite, Mg-Hbn: Magnesiohornblende and Fe-Hbn, Ferrohornblende.

Complex	Burguillos del Cerro plutonic complex								
Rock group unit	*Central Alkaline Basic-Intermediate Layered and Acid Unit*						*External Subalkaline Intermediate Unit*		
Facies	Diorites		Quartz diorites		Alkali feldspar granites		Diorites	Quartz diorites and tonalites	
Sample	BUB-1		BUB-11		BUB-17		BUB-12	BUB-13	BUB-14
Textual position	core	rim	core	rim	single	single	single	core	rim
Major elements (wt %)									
SiO_2	41.82	42.20	42.40	46.28	44.71	44.80	46.12	42.62	47.28
TiO_2	4.14	3.29	3.45	1.61	1.76	1.71	1.66	3.57	1.27
Al_2O_3	11.51	10.89	10.25	7.84	7.20	7.16	8.06	10.48	7.20
Cr_2O_3	0.03		0.02			0.02	0.05	0.06	0.02
NiO	0.01		0.04		0.03		0.02	0.01	
FeO_T	15.05	17.07	18.95	18.06	25.66	25.59	17.03	17.31	17.27
MnO	0.21	0.26	0.30	0.36	0.48	0.52	0.35	0.29	0.34
MgO	11.78	10.88	9.69	11.32	7.03	7.14	11.62	10.63	12.34
CaO	11.17	11.37	10.87	10.99	10.69	10.62	11.43	11.27	11.56
Na_2O	2.11	1.77	1.84	1.13	1.47	1.56	1.28	1.84	1.10
K_2O	1.14	1.18	1.05	0.74	0.85	0.84	0.90	1.05	0.75
F	0.30	0.29	0.25	0.29	0.32	0.27	0.24	0.21	0.28
Cl	0.34	0.40	0.71	0.65	0.45	0.42	0.49	0.52	0.22
Sum	99.61	99.60	99.82	99.27	100.65	100.65	99.25	99.86	99.63
Formula based on 23 oxygens									
Si_T	6.156	6.261	6.335	6.823	6.772	6.781	6.799	6.314	6.888
Al_T	1.844	1.739	1.665	1.177	1.228	1.219	1.201	1.686	1.112
Al_C	0.152	0.165	0.139	0.186	0.057	0.058	0.199	0.144	0.124
Ti_C	0.458	0.367	0.388	0.179	0.200	0.195	0.184	0.398	0.139
Fe^{3+}_C	0.275	0.313	0.340	0.452	0.385	0.363	0.307	0.276	0.465
Cr_C	0.005	0.003	0.002		0.002			0.001	
Mg_C	2.585	2.407	2.158	2.488	1.587	1.611	2.554	2.348	2.680
Fe^{2+}_C	1.524	1.745	1.972	1.695	2.768	2.773	1.756	1.833	1.591
Mn_C	0.000	0.000	0.000	0.000	0.000	0.000	0.000	0.000	0.000
Fe^{2+}_B	0.053	0.060	0.055	0.079	0.097	0.102	0.036	0.036	0.047
Mn_B	0.026	0.033	0.038	0.045	0.062	0.067	0.044	0.036	0.042
Ca_B	1.761	1.807	1.740	1.736	1.735	1.722	1.805	1.789	1.804
Na_B	0.160	0.100	0.167	0.140	0.107	0.109	0.115	0.139	0.106
Na_A	0.442	0.410	0.366	0.183	0.325	0.349	0.251	0.389	0.204
K_A	0.214	0.223	0.200	0.139	0.164	0.162	0.169	0.198	0.139
A-vacancy	0.344	0.367	0.434	0.678	0.511	0.489	0.580	0.412	0.656
Classification	Mg-Hst	Mg-Hst	Mg-Hst	Mg-Hbn	Fe-Hbn	Fe-Ed	Mg-Hbn	Mg-Hst	Mg-Hbn

Table 7.4. Continued.

Complex	Valencia del Ventoso plutonic complex									
Rock group unit	*Main Pluton Alkaline to Subalkaline Basic-Acid Unit*				*Main Pluton Alkaline to Subalkaline Basic-Acid Unit*				*Northern Stock Subalkaline Basic-Intermediate Unit*	
Facies	Diorites		Quartz diorites		Granodiorites to granites				Quartz monzodiorites	
Sample	VAAW-35		VAAW-37		VAAW-38				VAAW-30	
Textual position	core	rim	core	rim	core	rim	core	rim	single	core
Major elements (wt %)										
SiO_2	41.81	44.84	39.39	43.82	44.41	46.06	43.89	45.04	46.51	46.09
TiO_2	3.33	2.32	5.26	2.33	1.77	1.14	1.77	1.27	1.31	1.35
Al_2O_3	9.91	7.92	10.26	8.33	7.85	6.83	8.12	7.51	6.16	5.99
Cr_2O_3	0.01	0.02		0.02		0.01		0.03	0.32	0.04
NiO	0.00		0.02					0.00	0.04	
FeO_T	15.21	15.19	18.12	18.06	18.81	17.76	18.97	18.17	15.01	14.77
MnO	0.18	0.21	0.30	0.29	0.33	0.30	0.36	0.40	0.20	0.14
MgO	11.05	12.35	8.49	10.48	10.48	11.12	10.12	10.70	13.22	13.31
CaO	11.17	10.94	11.87	11.32	11.26	11.64	11.14	11.59	10.80	10.50
Na_2O	1.93	1.61	2.06	1.58	1.60	0.94	1.53	1.13	1.61	1.55
K_2O	0.95	0.81	1.01	1.03	1.04	0.81	1.10	0.96	0.76	0.74
F	0.23	0.20	0.31	0.36	0.41	0.33	0.41	0.40	0.50	0.46
Cl	0.54	0.51	0.60	0.58	0.54	0.29	0.57	0.38	0.49	0.55
Sum	96.31	96.91	97.70	98.20	98.49	97.25	97.98	97.59	96.92	95.48
Formula based on 23 oxygens										
Si_T	6.389	6.728	6.119	6.630	6.708	6.939	6.675	6.810	6.971	6.993
Al_T	1.611	1.272	1.881	1.370	1.292	1.061	1.325	1.190	1.029	1.007
Al_C	0.175	0.129		0.115	0.105	0.151	0.130	0.148	0.059	0.065
Ti_C	0.383	0.261	0.615	0.266	0.201	0.129	0.203	0.144	0.147	0.154
Fe^{3+}_C	0.154	0.301		0.244	0.305	0.347	0.315	0.363	0.333	0.366
Cr_C	0.004	0.016	0.001			0.004	0.005		0.022	0.006
Mg_C	2.518	2.762	1.966	2.364	2.359	2.498	2.295	2.413	2.954	3.011
Fe^{2+}_C	1.766	1.531	2.355	2.011	2.030	1.870	2.052	1.933	1.484	1.398
Mn_C	0.000	0.000	0.040	0.000	0.000	0.000	0.000	0.000	0.000	0.000
Fe^{2+}_B	0.023	0.073	0.000	0.030	0.041	0.020	0.045	0.002	0.064	0.110
Mn_B	0.024	0.026	0.000	0.038	0.042	0.039	0.046	0.051	0.025	0.018
Ca_B	1.828	1.758	1.976	1.835	1.822	1.879	1.814	1.877	1.734	1.707
Na_B	0.125	0.142	0.024	0.098	0.095	0.062	0.094	0.069	0.177	0.165
Na_A	0.445	0.327	0.596	0.366	0.373	0.213	0.358	0.263	0.292	0.290
K_A	0.185	0.155	0.200	0.199	0.201	0.156	0.214	0.186	0.145	0.143
A-vacancy	0.370	0.518	0.204	0.434	0.426	0.631	0.429	0.552	0.563	0.567
Classification	Pg	Mg-Hbn	Fe-Kt	Ed	Ed	Mg-Hbn	Ed	Mg-Hbn	Mg-Hbn	Mg-Hbn

Table 7.4. Continued.

Complex	Brovales pluton										
Rock group unit	*Central Subalkaline Intermediate Unit*							*Intermediate Subalkaline Intermediate Unit*			
Facies	Dioritic enclaves				Quartz monzodiorites to granodiorites			Granodiorites			
Sample	B-2E				B-2			B-5-1		B-5-2	
Textual position	single	core	rim	single	core	rim	single	single	single	core	rim
Major elements (wt %)											
SiO_2	45.95	44.02	44.15	43.47	40.36	43.38	43.27	41.56	41.25	41.23	40.68
TiO_2	1.09	1.43	1.26	1.44	2.78	1.58	1.58	2.21	1.96	2.24	1.61
Al_2O_3	7.34	8.60	8.90	9.12	11.32	8.83	8.87	9.13	9.40	9.17	9.74
Cr_2O_3	0.03	0.06	0.07	0.10	0.05	0.03	0.04		0.00	0.00	
NiO		0.00	0.02	0.00		0.00					
FeO_T	19.08	20.31	18.66	20.24	20.96	20.66	20.63	23.61	24.32	23.97	25.05
MnO	0.42	0.43	0.41	0.44	0.45	0.45	0.47	0.63	0.68	0.52	0.70
MgO	10.52	9.31	9.95	9.17	7.70	8.85	9.02	6.57	6.39	6.49	5.97
CaO	11.75	11.48	11.53	11.39	11.33	11.27	11.28	10.49	10.59	10.70	10.71
Na_2O	1.06	1.36	1.34	1.39	1.91	1.56	1.59	1.78	1.87	1.81	1.87
K_2O	0.86	1.09	1.10	1.18	1.10	1.05	0.99	1.53	1.47	1.49	1.51
F	0.36	0.43	0.37	0.42	0.42	0.39	0.40	0.40	0.44	0.34	0.42
Cl	0.43	0.67	0.68	0.60	0.56	0.84	0.76	1.84	1.55	1.84	1.51
Sum	98.89	99.20	98.44	98.95	98.94	98.92	98.90	99.75	99.90	99.80	99.76
Formula based on 23 oxygens											
Si_T	6.862	6.648	6.672	6.581	6.188	6.606	6.576	6.474	6.419	6.435	6.358
Al_T	1.138	1.352	1.328	1.419	1.812	1.394	1.424	1.526	1.581	1.565	1.642
Al_C	0.153	0.179	0.257	0.208	0.233	0.191	0.165	0.149	0.142	0.121	0.151
Ti_C	0.122	0.163	0.143	0.164	0.320	0.182	0.180	0.259	0.230	0.263	0.189
Fe^{3+}_C	0.394	0.381	0.312	0.397	0.290	0.343	0.402	0.322	0.375	0.315	0.459
Cr_C	0.008				0.006	0.004	0.004	0.000			
Mg_C	2.342	2.095	2.242	2.069	1.760	2.009	2.044	1.525	1.482	1.511	1.391
Fe^{2+}_C	1.981	2.182	2.046	2.162	2.392	2.271	2.203	2.743	2.771	2.791	2.810
Mn_C	0.000	0.000	0.001	0.000	0.000	0.000	0.000	0.000	0.000	0.000	0.000
Fe^{2+}_B	0.007	0.003	0.000	0.004	0.005	0.017	0.016	0.010	0.018	0.021	0.004
Mn_B	0.053	0.055	0.051	0.056	0.059	0.058	0.060	0.082	0.090	0.069	0.093
Ca_B	1.879	1.858	1.867	1.847	1.861	1.838	1.836	1.750	1.766	1.788	1.794
Na_B	0.061	0.084	0.082	0.094	0.075	0.087	0.088	0.157	0.127	0.122	0.110
Na_A	0.247	0.314	0.309	0.315	0.493	0.373	0.380	0.380	0.436	0.425	0.458
K_A	0.163	0.210	0.212	0.228	0.214	0.204	0.193	0.305	0.291	0.297	0.301
A-vacancy	0.590	0.476	0.479	0.456	0.293	0.423	0.427	0.315	0.273	0.278	0.241
Classification	Mg-Hbn	Fe-Ed	Ed	Fe-Ed	Hst	Fe-Ed	Fe-Ed	Hst	Hst	Hst	Hst

Table 7.4. Continued.

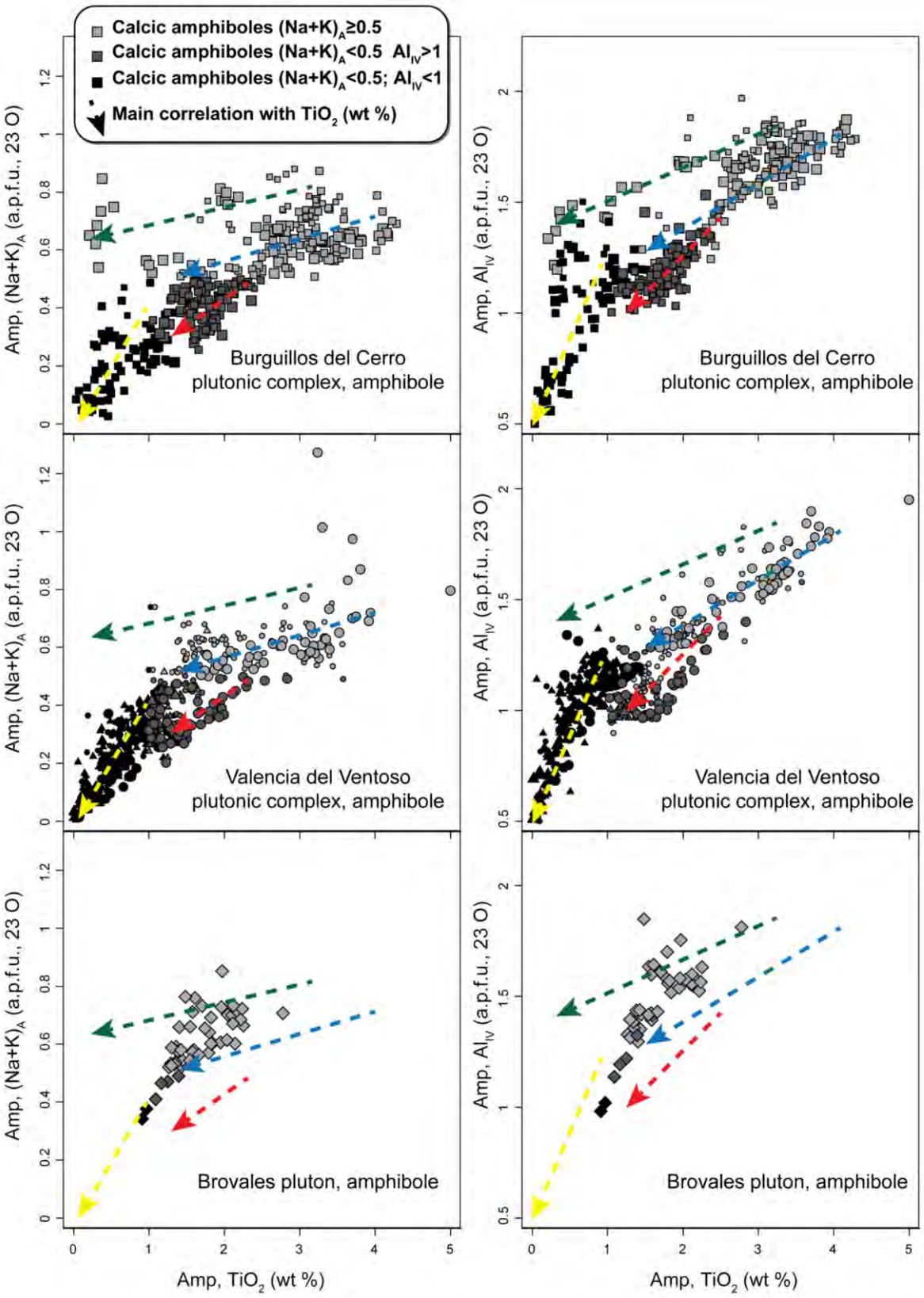

Figure 7.8. Composition of amphibole from the three complexes: left column) occupancy of Na+K in A-site versus TiO_2 (wt %); right column) occupancy of Al in tetrahedral site versus TiO_2 (wt %). Note the main correlations between these components, a function of temperature dependence, which allowed us to define the primary and secondary amphiboles. Lines represent the main correlation

7.3.1 Compositional Variations in the Primary Amphiboles

Having identified the primary amphiboles, we describe their compositional variations.

The amphiboles in the Burguillos *Central Ultrabasic-Basic Layered Unit* ultramafic rocks and olivine gabbros are compositionally diverse, with a bimodal distribution of TiO_2 (Table 7.4, Fig. 7.8A to C). The highest TiO_2 concentrations are found in brown cores and amphibole inclusions in orthopyroxene. The lowest TiO_2 concentrations are in colourless rims or individual crystals. The brown amphiboles are pargasites and magnesiohastingsites with $TiO_2 \approx$ 1-3 wt %, $K_2O \approx$ 0.5-1.1 wt % and $Al_2O_3 \approx$ 10-11 wt % and moderate MgO ≈ 16-18 wt % (Fig. 7.9A to C). The colourless amphibole is edenite with very low $TiO_2 \approx$ 0.2-0.53 wt %, moderate $K_2O \approx$ 0.3-7 wt % and $Al_2O_3 \approx$ 8-11 wt %, and higher MgO ≈ 18-19 wt % concentrations (Fig. 7.9A to C).

The large poikilitic amphiboles, pargasites and magnesiohastingsites, in the gabbronorites and gabbros of this same *Central Ultrabasic-Basic Layered Unit* are different from the amphiboles of the ultramafic and olivine gabbro in that they have lower MgO ≈ 11-13 wt % (Fig. 7.9A); restricted, generally high, $TiO_2 \approx$ 2-4 wt % only a few crystals have as little as *c.* 1 wt %; variable $K_2O \approx$ 1-2 wt %; and variable $Al_2O_3 \approx$ 8-12 wt % (Fig. 7.9B and C).

The amphiboles in the ultramafic rocks and olivine gabbros have low F ≈ 0.15-0.2 wt %; the gabbronorites and poikilitic amphibole gabbros have higher contents, with a clear division between the facies with poikilitic biotite and amphibole ≈ 0.2-0.3 wt % and that with just poikilitic amphibole ≈ F 0.3-0.4 wt % (Table 7.4). These differences correlate positively with TiO_2. The same relationships can be seen in the amphiboles Cl contents of these amphiboles as a function of TiO_2 and the type of facies (Table 7.4).

Amphiboles are generally present in the intermediate and felsic rocks of the Burguillos *Central Alkaline Basic-Intermediate Layered and Acid Unit* (Table 7.4). Pyroxene and biotite are the principal ferromagnesian phases in the gabbros and diorites of this unit with amphibole only commonly found in the volumetrically minor amphibole gabbros (Table 7.4, Fig. 7.9D to I). In contrast to the amphiboles of the previous unit they are magnesiohornblendes with intermediate concentrations of $TiO_2 \approx$ 1-2 wt %, MgO ≈ 12-14 wt %, $K_2O \approx$ 0.6-1 wt % and $Al_2O_3 \approx$ 7-9 wt % (Fig. 7.9D to F). The scarse amphiboles in the gabbros and diorites of this unit are pargasite, magnesiohastingsite and edenite. So they are quite different from the amphibole gabbros magnesiohornblendes in having more $TiO_2 \approx$ 2-4 wt %, $K_2O \approx$ 0.7-1.2 wt % and $Al_2O_3 \approx$ 7-12 wt %, but less MgO ≈ 10-13 wt % (Fig. 7.9G and H). They are zoned with brown high-TiO_2 cores and lower-TiO_2 pale green rims. The same tendency is observed in the quartzdiorite ferro-pargasites, magnesiohastingsite and magnesihornblendes from this unit (Fig. 7.9G to H).

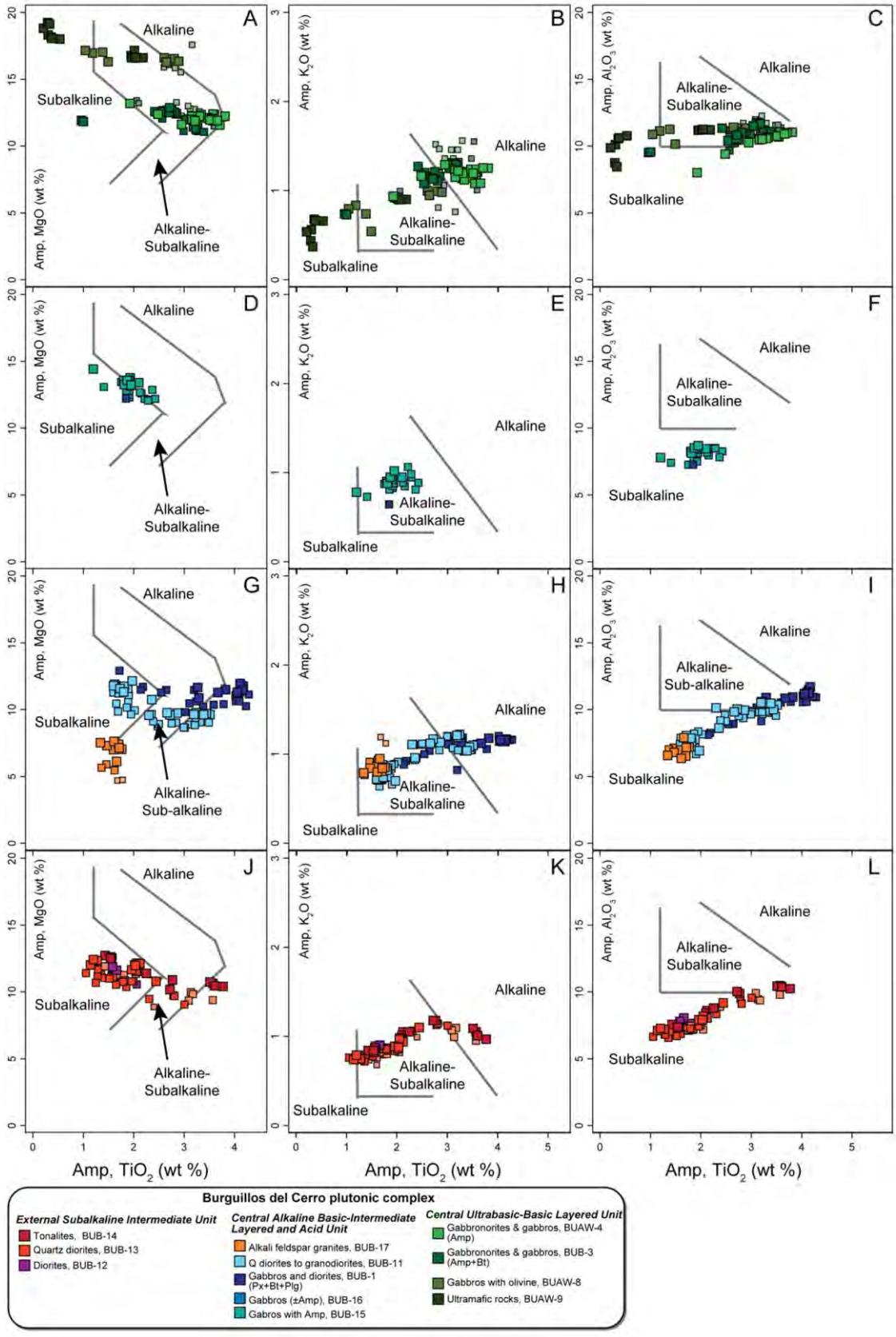

Figure 7.9. Composition of primary igneous amphiboles MgO vs. TiO_2, K_2O vs TiO_2 and Al_2O_3 vs TiO_2 from the Burguillos del Cerro plutonic complex A-C) Central Ultrabasic-Basic Layered Unit D-I) Central Alkaline Basic-Intermediate Layered and Acid Unit and J-L) External Subalkaline Intermediate Unit. Alkaline to subalkaline fields are from Molina et al., (2009). (smaller lighter symbols – García-Casquero, 1991).

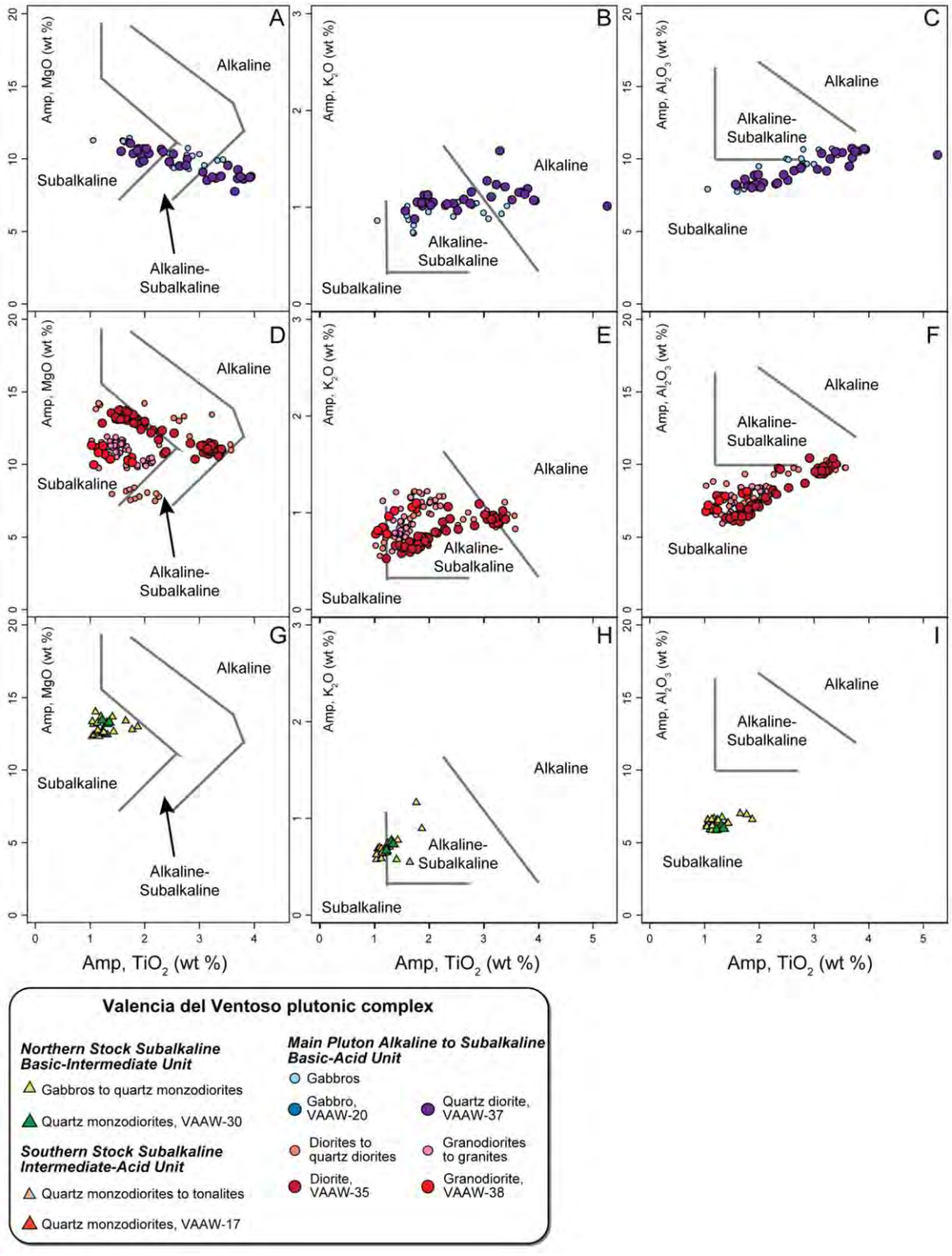

Figure 7.10. Composition of primary igneous amphiboles MgO vs. TiO_2, K_2O vs. TiO_2 and Al_2O_3 vs. TiO_2 from the Valencia del Ventoso plutonic complex A-F) Main Pluton Alkaline to Subalkaline Basic-Acid Unit J-L) Northern Stock Subalkaline Basic-Intermediate Unit. Alkaline to subalkaline fields are from Molina et al., (2009). (smaller lighter symbols - Sarrionandia, 2005).

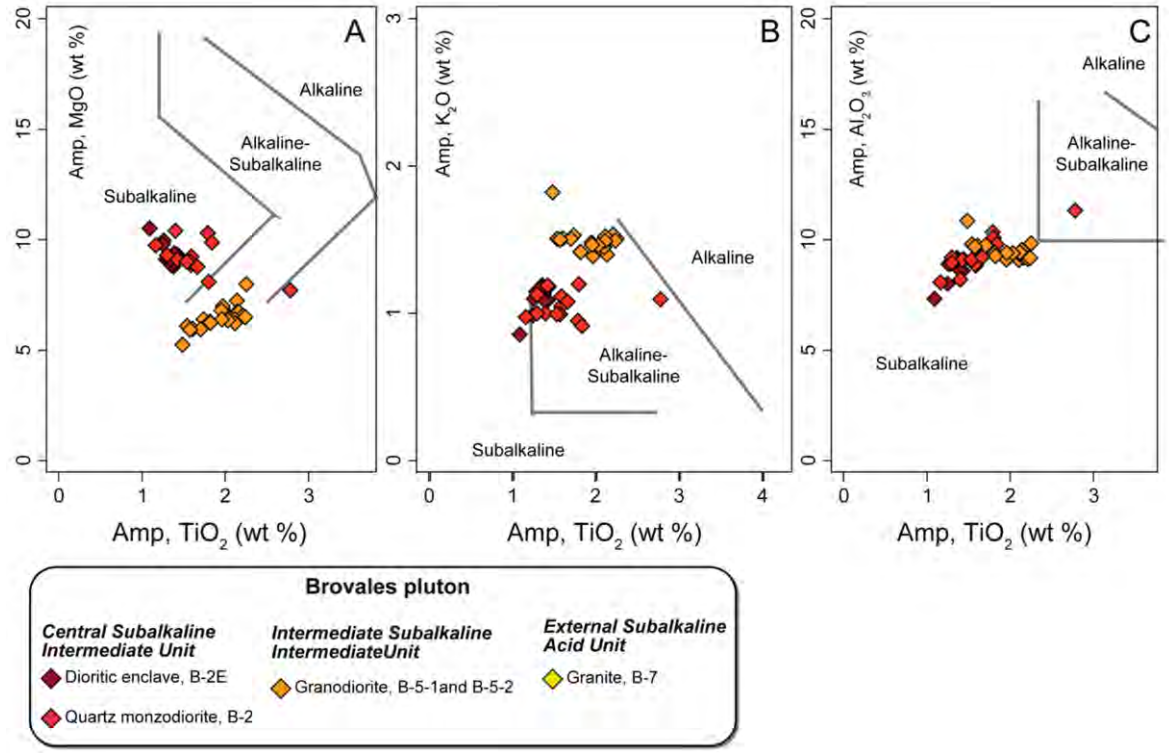

Figure 7.11. Composition of primary igneous amphiboles MgO vs. TiO_2, K_2O vs. TiO_2 and Al_2O_3 vs. TiO_2 from the Brovales pluton A-C) Central and Intermediate Subalkaline Intermediate Unit. Alkaline to subalkaline fields are from Molina et al., (2009).

The amphiboles in the more evolved alkali feldspar granites of the *Central Alkaline Basic-Intermediate Layered and Acid Unit* are ferro-edenites and ferrohornblendes (Fig. 7.5). They have relatively low TiO_2 ≈ 1.3-1.7 wt %, MgO ≈ 5-8 wt %, K_2O ≈ 0.8-1.2 wt % and Al_2O_3 ≈ 6-8 wt % (Fig. 7.9G and H). No core to rim zonation is observed.

The amphibole in this unit has a constant value of F ≈ 0.25-0.4 wt % (Table 7.4). Its Cl content is moderate ≈ 0.5-1 wt % and systematically higher in the intermediate rocks than in the mafic rocks (Table 7.4).

The amphiboles from the Burguillos *External Subalkaline Intermediate Unit* are pargasite, hastingsite, edenite and magnesiohornblende (Fig. 7.5) with TiO_2 ≈ 1-3.7 wt %, MgO ≈ 9-12 wt %, K_2O ≈ 0.6-1.2 wt % and Al_2O_3 ≈7-10 wt % (Table 7.4, Fig. 7.9J to L). They are zoned with brown TiO_2-rich, ≈ 2-3 wt %, core and lighter brown to dark greenish rims with lower TiO_2 ≈ 1-2 wt % which is also the composition of individual crystals (Fig. 7.9J to L).

The amphiboles in this unit have F contents of *c.* 0.25 wt % at the limit of the flourine species field (Table 7.4). The Cl shows more variation 0.25-0.5 wt % and a weak positive correlation with TiO_2 (Table 7.4).

The amphiboles in the quartz diorites of the Valencia *Main Pluton Alkaline to Subalkaline*

Basic-Acid Unit are kaersutite, pargasite, hastingsite and edenite with high TiO_2 ≈ 1.6-5 wt %, and K_2O ≈ 0.8-1.5 wt % and Al_2O_3 ≈ 8-11 wt % (Fig. 7.7 and Fig. 7.10A to C).

The amphiboles in the diorites and granodiorites of the *Main Pluton Alkaline to Subalkaline Basic-Acid Unit,* are pargasite, magnesoihastingsite, and magnesiohornblende (Fig. 7.6). Those in the diorites are zoned with high TiO_2 ≈ 2.5-3.2 wt % core and lower TiO_2 ≈ 1-2.5 wt % rims. Other elements such as K_2O ≈ 0.5-1 wt % and Al_2O_3 ≈ 6-9 wt % are also higher in the cores than the rims (Fig. 7.10D to F). The amphiboles in granodiorites have lower TiO_2 ≈ 1-2 wt %, K_2O ≈ 0.6-1.2 wt % and Al_2O_3 ≈ 6-8 wt % (Fig. 7.10D to F).

The amphiboles from this unit have variable contents in F (Table 7.4). The diorites have lowish F ≈ 0.15-0.2 wt %; the quartz diorites, that has high TiO_2 also has high F ≈ 0.25-0.35 wt % and intermediate values of Cl ≈ 0.5-1.2 wt % that shows a positive correlation with TiO_2 (Table 7.4). The amphiboles in the granodiorites are the most F-rich ≈ 0.3-0.4 wt % (Table 7.4) but their Cl are the lowest ≈ 0.25-0.5 wt % albeit positively correlated with TiO_2.

Almost all the amphiboles in the Valencia *Northern Stock Subalkaline Basic-Intermediate Unit* and *Southern Stock Subalkaline Intermediate-Acid Unit* are secondary, actinolites and magnesiohornblendes (Fig. 7.6). However, a few magnesiohornblendes from the *Northern Stock Subalkaline Basic-Intermediate Unit*, may be considered primary with low TiO_2 ≈ 1-2 wt %, K_2O ≈ 0.5-1 wt % and Al_2O_3 ≈ 6-7 wt % (Fig. 7.10G to I).

The amphiboles of the intermediate rocks from the Brovales pluton are somewhat more compositionally restricted than in the other two complexes. Two main compositional groups, may be defined (Table 7.4). Ferroedenite and magnesiohornblende are found in the quartz monzodiorite and the diorite enclave of the Brovales pluton *Central Subalkaline Intermediate Unit* they have moderate TiO_2≈ 1-2.7 wt %, MgO ≈ 8-11 wt %, K_2O ≈ 0.8-1.2 wt % and Al_2O_3 ≈ 7-11 wt % (Fig. 7.11A to C). Hastingsites are found in the granodiorites of the *Intermediate Subalkaline Intermediate Unit* (Fig. 7.7) and have TiO_2 ≈ 1.5-2.3 wt %, K_2O ≈ 1.4-1.8 wt % and Al_2O_3 ≈ 9-11 wt % and MgO ≈ 5-8 wt % (Fig. 7.11A to C). The *External Subalkaline Intermediate Unit* does not contain amphiboles.

The amphiboles from Brovales have the highest concentration of volatiles of the three complexes F ≈ 0.3-0.5 wt %, and variable contents of Cl that are high 0.5-0.9 wt % in the *Central Subalkaline Intermediate Unit* but even higher ≈ 1-2 wt % in the *Intermediate Subalkaline Intermediate Unit* (Table 7.4).

7.4 Biotite

Biotite is ubiquitous in the three complexes. In the classification scheme of Tischendorf et

al., (2007) most of the micas are biotites, phlogopites are only found in the Burguillos *Central Ultrabasic-Basic Layered Unit* and the Valencia *Northern Stock Subalkaline Basic-Intermediate Unit* (Fig. 7.12).

Phlogopites in the Burguillos *Central Ultrabasic-Basic Layered Unit* ultramafic rocks and olivine gabbro have homogeneous $FeO_T \approx$ 5-7 wt % and $Al_2O_3 \approx$ 15-17 wt % but variable $TiO_2 \approx$ 0.2-2.4 wt % (Figs.7.12A, 7.13A and 7.14A). They are zoned, as was observed in the amphiboles. Larger crystals have TiO_2-rich cores whereas rims of these crystals and smaller individual grains have lower TiO_2 (Table 7.5). The biotites in the gabbronorites and gabbros of this unit they are different from the phlogopites (Figs 7.13A, 7.14A and 7.15A). Most of the micas are biotite reflected in a higher FeO_T content ≈ 15-18 wt % (Fig. 7.14A) although a few plot in the phlogopite field (Fig.14A). There seems to be little compositional difference between the two textural types of biotite that were identified in this facies: i. poikilitic biotite $Al_2O_3 \approx$ 13-15 wt % and $TiO_2 \approx$ 5-7 wt % and ii. euhedral biotite inclusions in pokilitic amphibole $Al_2O_3 \approx$ 13-14 wt % and $TiO_2 \approx$ 5-6 wt % (Fig. 7.14A and Table 7.5).

Biotite is common in the Burguillos *Central Alkaline Basic-Intermediate Layered and Acid Unit* (Fig. 7.12B and 7.12C). It has a similar compositions in both the amphibole gabbros ($FeO_T \approx$ 16-20 wt %, $Al_2O_3 \approx$ 13-15 wt % and $TiO_2 \approx$ 5-8 wt %) and those in which biotite is the only hydrated ferromagnesian mineral ($FeO_T \approx$ 17-19 wt %, $Al_2O_3 \approx$ 14-15 wt % and $TiO_2 \approx$ 6-7 wt %) (Fig. 7.13B-C, 7.14B-C and 7.15B-C). The biotites in the intermediate rocks of this unit, on the other hand, have similar $Al_2O_3 \approx$ 13-14 wt % to the gabbros but less $TiO_2 \approx$ 4-5 wt % and more $FeO_T \approx$ 20-21 wt % (Fig. 7.13B-C and 7.14B-C and 7.15B-C). These differences are more obvious still in the felsic rocks from this unit (Fig. 7.12C), compared to the intermediate rocks the biotites are scarce, and have higher $FeO_T \approx$ 29-30 wt % (Fig, 7.13C), somewhat lower $Al_2O_3 \approx$ 12-14 wt % but comparable $TiO_2 \approx$ 3-5 wt % (Fig, 7.14C and 7.15C). Thus the Burguillos *Central Alkaline Basic-Intermediate Layered and Acid Unit* biotites define a compositional trend with a negative correlation between Al_2O_3 and FeO_T a positive one between Al_2O_3 and TiO_2 (Fig. 7.13C, 7.14C and 7.15C).

The biotites in the Burguillos *External Subalkaline Intermediate Unit* rocks, (Fig. 7.12D), have uniform $FeO_T \approx$ 18-20 wt % (Fig. 7.13D) but more varied $Al_2O_3 \approx$ 18-20 wt % and, particularly, $TiO_2 \approx$ 2-7 wt % (Fig. 7.14D and 7.15D). As was the case for the amphiboles, the biotites are zoned. Their cores have more TiO_2 and less Al_2O_3 than their rims (Table 7.5).

The F and Cl composition of the biotites varies significantly in the different units of the three complexes (Table 7.5). Those in the ultramafic rocks and olivine gabbros of the Burguillos

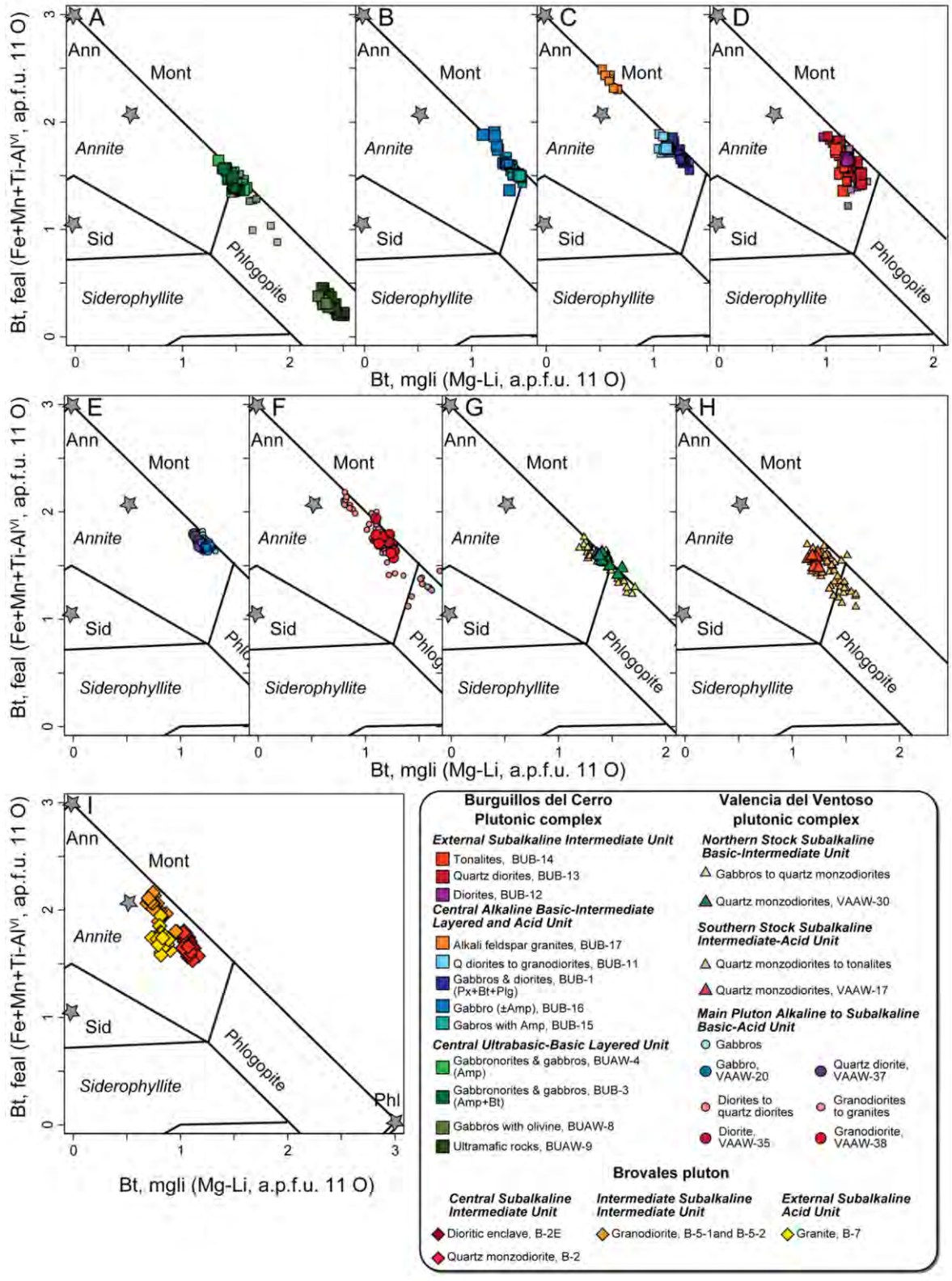

Figure 7.12. Classification of biotites in the diagram of Tischendorf et al., (2007): Burguillos del Cerro plutonic complex A) Central Ultrabasic-Basic Layered Unit, B-C) Central Alkaline Basic-Intermediate Layered and Acid Unit and D) External Subalkaline Intermediate Unit; Valencia del Ventoso plutonic complex E-F) Main Pluton Alkaline to Subalkaline Basic-Acid Unit, G) Northern Stock Subalkaline Basic-Intermediate Unit and H) Southern Stock Subalkaline Intermediate-Acid Unit; I) Brovales pluton. (smaller lighter symbols – García-Casquero, 1991 and Sarrionandia, 2005).

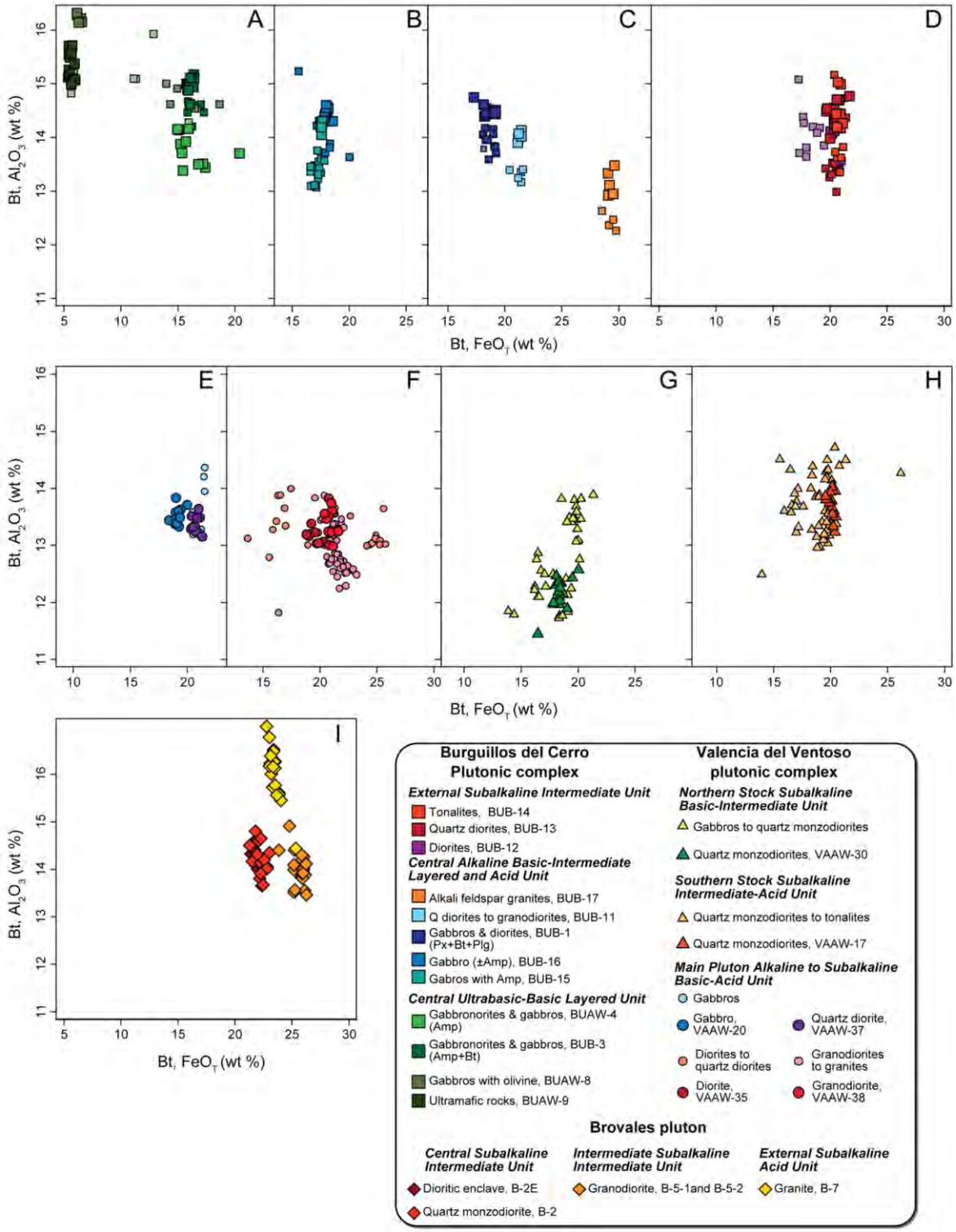

Figure 7.13. Compositional variation of biotites, Al_2O_3 vs. FeO_T from: Burguillos del Cerro plutonic complex A) Central Ultrabasic-Basic Layered Unit, B-C) Central Alkaline Basic-Intermediate Layered and Acid Unit and D) External Subalkaline Intermediate Unit; Valencia del Ventoso plutonic complex E-F) Main Pluton Alkaline to Subalkaline Basic-Acid Unit, G) Northern Stock Subalkaline Basic-Intermediate Unit and H) Southern Stock Subalkaline Intermediate-Acid Unit; I) Brovales pluton. (smaller lighter symbols – García-Casquero, 1991 and Sarrionandia, 2005).

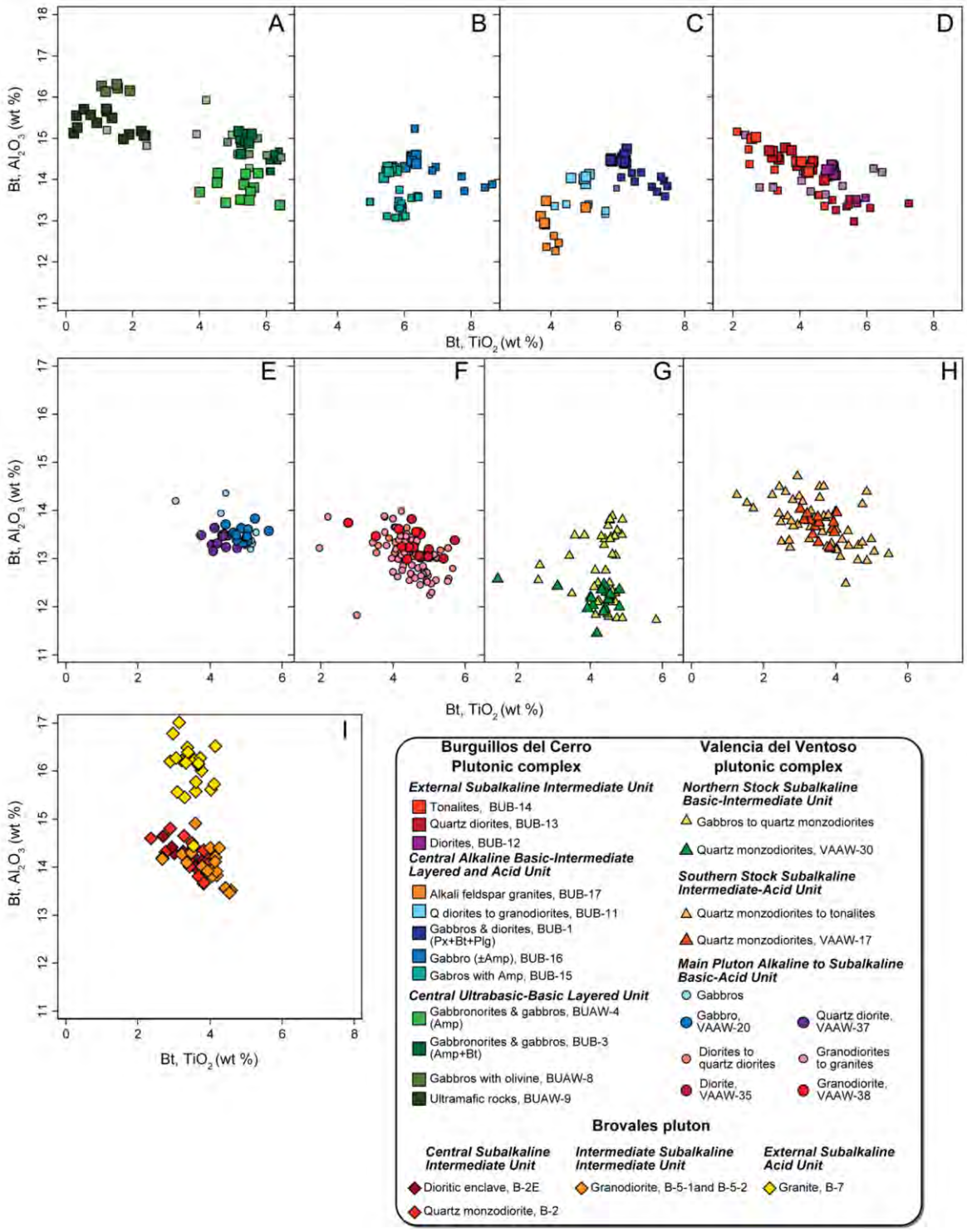

Figure 7.14. Compositional variation of biotites, Al_2O_3 vs. TiO_2 from: Burguillos del Cerro plutonic complex A) Central Ultrabasic-Basic Layered Unit, B-C) Central Alkaline Basic-Intermediate Layered and Acid Unit and D) External Subalkaline Intermediate Unit; Valencia del Ventoso plutonic complex E-F) Main Pluton Alkaline to Subalkaline Basic-Acid Unit, G) Northern Stock Subalkaline Basic-Intermediate Unit and H) Southern Stock Subalkaline Intermediate-Acid Unit; I) Brovales pluton. (smaller lighter symbols – García-Casquero, 1991 and Sarrionandia, 2005).

Central Ultrabasic-Basic Layered Unit have low F and Cl relative to the gabbros and gabbronorites of the same unit (Table 7.5). The biotite in all the facies of the Burguillos *Central Alkaline Basic-Intermediate Layered and Acid Unit* have high F and Cl (Table 7.5). The Burguillos *External Subalkaline Intermediate Unit* biotites have intermediate concentrations of F and Cl (Table 7.5).

The biotites in the Valencia *Main Pluton Alkaline to Subalkaline Basic-Acid Unit* gabbro and quartz diorites have $FeO_T \approx$ 18-21 wt %, $Al_2O_3 \approx$ 13-14 wt % although with slightly less $TiO_2 \approx$ 3-5 wt % (Fig. 7.13E, 7.14E and 7.15E). The biotites, and rare phlogopites (Fig. 7.12F), in the diorites have quite variable $FeO_T \approx$ 14-26 wt % but similar Al_2O_3 12-14 ≈ wt % and $TiO_2 \approx$ 3-5 wt % (Fig. 7.13F, 7.14F and 7.15F). The biotites in the granodiorites and granites of this unit (Fig. 7.12F), have $FeO_T \approx$ 20-23 wt %, $Al_2O_3 \approx$ 12-14 wt % and $TiO_2 \approx$ 2-5 wt % (Fig. 7.13F, 7.14F and 7.15F). The cores have higher TiO_2 and lower Al_2O_3 than the rims (Table 7.5).

The Valencia *Main Pluton Alkaline to Subalkaline Basic-Acid Unit* (Table 7.5) gabbros have high F and Cl. The quartz diorites and granites biotites in this unit have intermediate concentrations of F and Cl (Table 7.5), the diorites have lower F (Table 7.5).

Pholgopites and biotites in the Valencia *Northern Stock Subalkaline Basic-Intermediate Unit* (Fig. 7.12G), have $Al_2O_3 \approx$ 11-14 wt %, some of the lowest values in the three complexes (Fig. 7.13G, 7.14G and 7.15G). Other elements are quite variable in these micas $FeO_T \approx$14-21 wt % and $TiO_2 \approx$ 1-6 wt % (Fig. 7.13G and 7.14G), The biotites and less abundant phlogopites in the Valencia *Southern Stock Subalkaline Intermediate-Acid Unit,* (Fig. 7.12H), have more $FeO_T \approx$ 14-26 wt % (Fig. 7.13H), with $Al_2O_3 \approx$ 13-15 wt % but comparable $TiO_2 \approx$ 1-6 wt %.

The biotites from the Brovales pluton are broadly comparable to those from the other plutonic bodies (Fig. 7.12I). Compositional differences exist between the different units in the pluton. Biotites in the *Central Subalkaline Intermediate Unit* quartz diorite and diorite enclave have the same highish $FeO_T \approx$ 21-23 wt % with $Al_2O_3 \approx$ 14-15 wt % and $TiO_2 \approx$ 2-4 wt %. The *Intermediate Subalkaline Intermediate Unit* biotites have more $FeO_T \approx$ 24-26 wt % (Fig. 7.13I) but comparable $Al_2O_3 \approx$ 13-15 wt % and $TiO_2 \approx$ 3-5 wt % (Fig. 7.14I). The *External Subalkaline Acid Unit* biotites are higher in $Al_2O_3 \approx$ 14-17 wt % but have the same concentrations of $FeO_T \approx$ 23-25 wt % and $TiO_2 \approx$ 3-4 wt % (Fig. 7.13I, 7.14I and 7.15I).

All the biotites in the three units of the Brovales pluton have high F contents (Table 7.5). The higher Cl of the biotites from the Brovales *External Subalkaline Acid Unit* is a distinguishing feature in the volatile contents of the micas (Table 7.5).

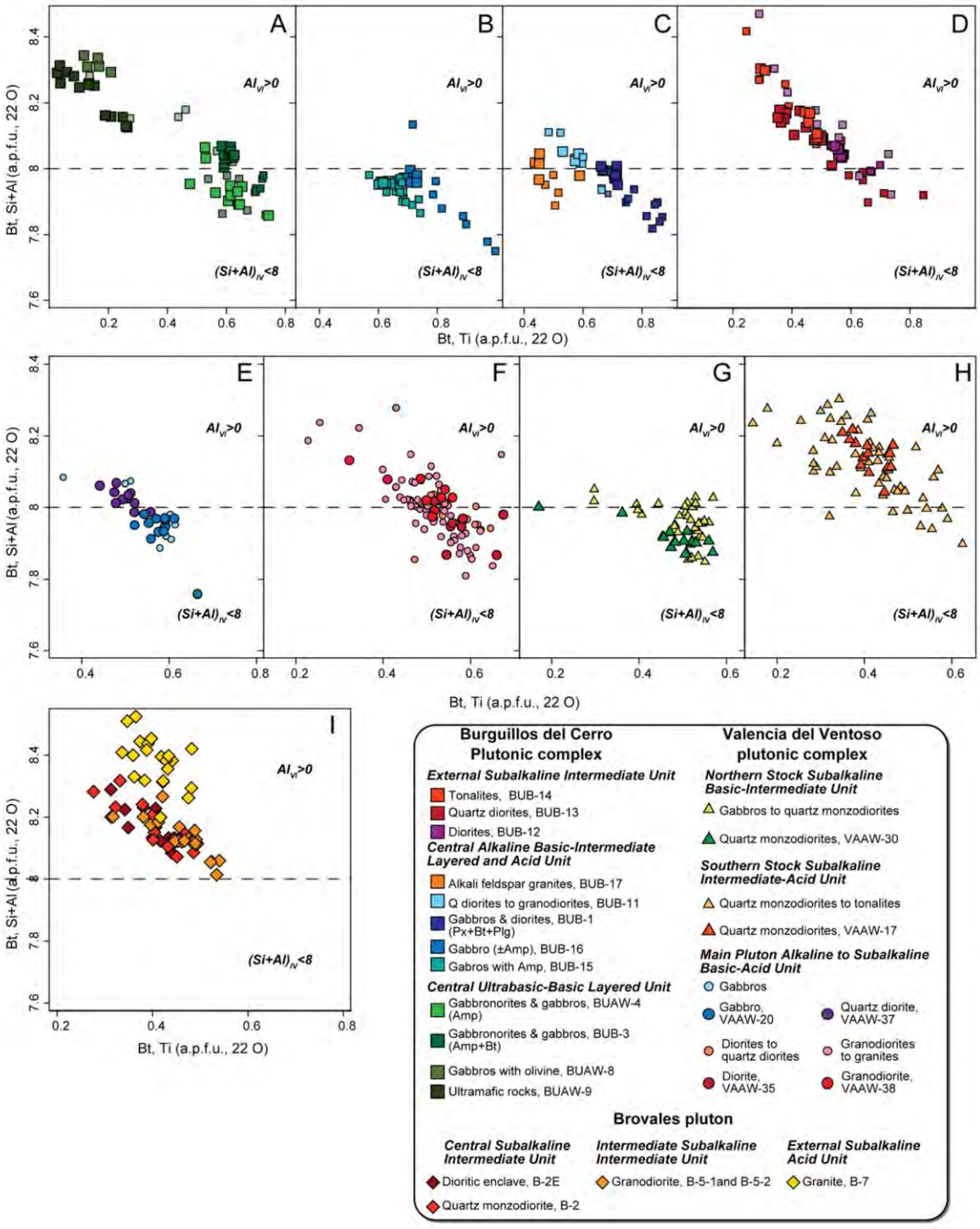

Figure 7.15. Relationship between Si+Al and Ti (apfu, 22 O) in the biotites from: Burguillos del Cerro plutonic complex A) Central Ultrabasic-Basic Layered Unit, B-C) Central Alkaline Basic-Intermediate Layered and Acid Unit and D) External Subalkaline Intermediate Unit; Valencia del Ventoso plutonic complex E-F) Main Pluton Alkaline to Subalkaline Basic-Acid Unit, G) Northern Stock Subalkaline Basic-Intermediate Unit and H) Southern Stock Subalkaline Intermediate-Acid Unit; I) Brovales pluton. Note that the values of Si+Al<8 indicates a cation deficieny in the tetrahedral layer in of the biotites. (smaller lighter symbols – García-Casquero, 1991 and Sarrionandia, 2005).

Complex	Burguillos del Cerro plutonic complex									
Rock group unit	*Central Ultrabasic-Basic Layered Unit*								*Central Alkaline Basic-Intermediate Layered and Acid Unit*	
Facies	Ultramafic rocks		Olivine gabbros		Poikilitic amphibole and biotite gabbronorites and gabbros		Poikilitic amphibole gabbronorites and gabbros		Gabbros with amphibole	
Sample	BUAW-9		BUAW-8		BUB-3		BUAW-4		BUB-15	
Textural position	core	rim	core	rim	core	rim	single	single	rim	core
Majors elements (wt %)										
SiO_2	38.61	39.27	38.41	38.61	35.92	35.65	35.25	35.54	37.01	36.30
TiO_2	1.23	0.32	1.91	1.55	5.33	5.25	6.41	5.53	5.76	6.03
Al_2O_3	15.65	15.55	16.15	16.22	14.99	14.90	13.38	13.71	14.21	13.11
Cr_2O_3	0.51	0.31	0.32	0.30	0.02	0.01	0.01		0.02	0.09
NiO	0.12	0.13	0.08	0.07			0.00	0.00		
FeO_T	5.68	5.44	6.57	6.48	15.89	15.84	15.45	15.36	17.50	16.95
MnO	0.02	0.03	0.04	0.04	0.09	0.12	0.07	0.09	0.11	0.15
MgO	22.10	22.83	21.16	21.57	14.10	14.06	13.10	13.55	13.42	12.66
CaO	0.01	0.00		0.02	0.01	0.02	0.01	0.05		
Na_2O	1.51	1.44	1.01	0.94	0.42	0.39	0.29	0.19	0.21	0.24
K_2O	7.99	8.29	8.59	8.61	8.83	8.65	8.91	9.16	9.29	9.06
F	0.13	0.17	0.19	0.10	0.19	0.24	0.29	0.31	0.53	
Cl	0.38	0.41	0.27	0.28	0.42	0.48	0.59	0.62	0.65	0.41
Sum	94.60	94.54	95.11	95.14	96.21	95.61	95.14	95.61	98.71	95.00
Formula based on 22 oxygens										
Si_{IV}	5.589	5.669	5.545	5.559	5.383	5.380	5.429	5.452	5.476	5.540
Al_{IV}	2.411	2.331	2.455	2.441	2.617	2.620	2.429	2.478	2.478	2.358
Ti_{VI}	0.134	0.035	0.208	0.168	0.601	0.596	0.742	0.638	0.641	0.692
Al_{VI}	0.259	0.313	0.293	0.311	0.030	0.030	0.000	0.000	0.000	0.000
Cr_{VI}	0.058	0.035	0.036	0.035	0.002	0.001	0.001		0.002	0.011
Ni_{VI}	0.013	0.015	0.009	0.009			0.000	0.000		
$Fe^{2+}{}_{VI}$	0.687	0.656	0.794	0.780	1.991	1.999	1.990	1.970	2.165	2.163
Mn_{VI}	0.003	0.003	0.004	0.005	0.011	0.015	0.010	0.012	0.014	0.019
Mg_{VI}	4.770	4.913	4.555	4.629	3.150	3.163	3.009	3.098	2.960	2.881
VI-vacancy	0.075	0.029	0.100	0.064	0.215	0.195	0.249	0.282	0.218	0.234
Ca_{XII}	0.001	0.000		0.003	0.002	0.003	0.001	0.008		
Na_{XII}	0.424	0.403	0.282	0.262	0.122	0.114	0.088	0.058	0.060	0.071
K_{XII}	1.476	1.526	1.582	1.582	1.688	1.665	1.751	1.792	1.753	1.764
XII-vacancy	0.099	0.071	0.137	0.154	0.189	0.217	0.160	0.142	0.186	0.164
F	0.060	0.079	0.087	0.045	0.090	0.115	0.142	0.151	0.248	
Cl	0.093	0.101	0.066	0.067	0.107	0.123	0.153	0.162	0.163	0.105

Table 7.5. Representative analyses of biotite from the Burguillos del Cerro and Valencia del Ventoso plutonic complexes and the Brovales pluton.

Complex	Burguillos del Cerro plutonic complex											
Rock group unit	*Central Alkaline Basic-Intermediate Layered and Acid Unit*						*External Subalkaline Intermediate Unit*					
Facies	Diorites		Quartz diorites		Alkali feldspar granites		Diorites		Quartz diorites and tonalites			
Sample	BUB-1		BUB-11		BUB-17		BUB-12		BUB-13		BUB-14	
Textural position	core	rim	core	rim	single	single	core	rim	single	rim	rim	single
Major elements (wt %)												
SiO_2	34.97	35.31	36.01	35.71	35.29	35.70	35.50	36.56	35.42	36.86	36.86	36.67
TiO_2	7.38	6.19	4.60	5.05	3.80	5.04	5.40	4.79	5.62	3.75	3.89	2.68
Al_2O_3	13.97	14.49	14.04	14.07	12.95	13.33	13.35	14.24	12.99	14.71	14.44	15.03
Cr_2O_3					0.04	0.01			0.12	0.07	0.06	0.05
NiO		0.01			0.02					0.04		
FeO_T	18.52	18.38	21.44	21.23	29.49	29.05	20.72	20.42	20.56	20.59	20.64	20.70
MnO	0.23	0.09	0.10	0.12	0.18	0.18	0.23	0.15	0.11	0.22	0.19	0.18
MgO	11.01	11.83	10.69	10.40	6.75	5.98	9.95	11.17	10.40	11.29	11.00	11.05
CaO		0.01	0.03	0.01	0.03	0.02		0.02	0.02	0.07	0.01	0.10
Na_2O		0.19	0.17	0.16	0.04	0.03	0.26	0.13	0.05	0.07	0.11	0.06
K_2O	8.53	8.77	8.92	8.73	8.46	9.06	9.25	9.33	9.50	9.37	9.32	9.51
F		0.37	0.40	0.39	0.31	0.32		0.32		0.35	0.36	0.34
Cl	0.37	0.56	1.22	1.19	0.46	0.42	0.34	0.58	0.21	0.42	0.35	0.44
Sum	95.00	96.20	97.62	97.06	97.82	99.14	95.00	97.71	95.00	97.81	97.23	96.81
Formula based on 22 oxygens												
Si_{IV}	5.370	5.379	5.517	5.495	5.562	5.541	5.530	5.530	5.514	5.561	5.591	5.596
Al_{IV}	2.528	2.601	2.483	2.505	2.405	2.438	2.451	2.470	2.383	2.439	2.409	2.404
Ti_{VI}	0.853	0.709	0.530	0.584	0.450	0.588	0.632	0.545	0.658	0.425	0.444	0.308
Al_{VI}	0.000	0.000	0.052	0.046	0.000	0.000	0.000	0.068	0.000	0.176	0.172	0.299
Cr_{VI}					0.005	0.001			0.015	0.008	0.007	0.006
Ni_{VI}		0.001			0.003					0.005		
$Fe^{2+}{}_{VI}$	2.378	2.341	2.747	2.731	3.886	3.770	2.699	2.583	2.676	2.597	2.618	2.641
Mn_{VI}	0.030	0.012	0.013	0.016	0.024	0.024	0.030	0.019	0.015	0.028	0.024	0.023
Mg_{VI}	2.520	2.687	2.442	2.386	1.586	1.384	2.311	2.519	2.413	2.539	2.487	2.514
VI-vacancy	0.219	0.250	0.216	0.237	0.046	0.233	0.327	0.266	0.223	0.221	0.248	0.209
Ca_{XII}		0.002	0.005	0.002	0.005	0.003		0.003	0.004	0.011	0.002	0.016
Na_{XII}		0.056	0.050	0.048	0.012	0.009	0.079	0.038	0.015	0.020	0.032	0.018
K_{XII}	1.671	1.704	1.743	1.713	1.701	1.794	1.837	1.800	1.887	1.803	1.803	1.851
XII-vacancy	0.329	0.238	0.201	0.237	0.282	0.194	0.084	0.159	0.094	0.165	0.163	0.115
F		0.178	0.194	0.190	0.155	0.157		0.153		0.167	0.173	0.164
Cl	0.097	0.145	0.317	0.310	0.123	0.110	0.090	0.149	0.056	0.107	0.090	0.114

Table 7.5. Continued.

Complex	Valencia del Ventoso plutonic complex											
Rock group unit	*Main Pluton Alkalineto Subalkaline Basic-Acid Unit*								*Northern Stock Subalkaline Basic-Intermediate Unit*		*Southern Stock Subalkaline Intermediate-Acid Unit*	
Facies	Gabbros and diorites		Diorites		Quartz diorites		Granodiorites to granites		Quartz monzodiorites		Quartz monzodiorites	
Sample	VAAW-20		VAAW-35		VAAW-37		VAAW-38		VAAW-30		VAAW-17	
Textural position	single	single	core	core	core	rim	core	rim	core	core	core	single
Major elements (wt %)												
SiO_2	33.34	35.07	35.03	35.88	35.06	35.62	36.15	35.99	37.26	36.91	36.53	36.79
TiO_2	5.63	4.87	5.72	4.42	5.02	3.75	4.57	4.45	4.41	4.08	3.84	3.02
Al_2O_3	13.57	13.63	13.38	13.22	13.32	13.48	13.24	13.23	11.97	12.04	13.24	14.04
Cr_2O_3	0.04	0.02	0.07	0.05	0.04		0.04	0.01	0.02	0.13	0.04	0.09
NiO			0.02	0.04		0.00			0.07	0.05	0.06	0.02
FeO_T	19.00	19.43	19.26	19.62	20.71	20.82	20.75	21.04	18.35	18.42	20.38	20.14
MnO	0.19	0.20	0.13	0.18	0.16	0.12	0.20	0.16	0.07	0.08	0.18	0.17
MgO	12.64	11.13	10.21	11.24	10.24	10.84	10.30	10.56	13.20	13.11	11.31	11.27
CaO	1.24	0.00	0.02	0.01	0.01	0.03		0.01	0.00	0.03	0.00	0.00
Na_2O	0.12	0.11	0.12	0.13	0.16	0.33	0.16	0.27	0.30	0.24	0.07	0.09
K_2O	6.39	9.31	8.68	9.04	8.62	8.99	9.19	9.35	8.98	9.03	9.48	9.33
F	0.57	0.56	0.19	0.24	0.48	0.49	0.57	0.58	0.69	0.66	0.43	0.45
Cl	0.61	0.89	0.59	0.54	0.52	0.88	0.51	0.51	0.82	0.97	0.84	0.89
Sum	94.13	96.57	94.76	94.92	95.59	95.68	96.48	96.74	96.25	95.80	96.59	96.40
Formula based on 22 oxygens												
Si_{IV}	5.242	5.465	5.503	5.589	5.504	5.574	5.607	5.576	5.710	5.699	5.637	5.664
Al_{IV}	2.515	2.503	2.477	2.411	2.464	2.426	2.393	2.415	2.162	2.191	2.363	2.336
Ti_{VI}	0.666	0.571	0.675	0.518	0.592	0.442	0.533	0.518	0.508	0.473	0.445	0.349
Al_{VI}	0.000	0.000	0.000	0.017	0.000	0.060	0.028	0.000	0.000	0.000	0.044	0.210
Cr_{VI}	0.005	0.003	0.009	0.006	0.005		0.005	0.001	0.002	0.015	0.005	0.010
Ni_{VI}			0.002	0.005		0.000			0.009	0.006	0.007	0.002
Fe^{2+}_{VI}	2.498	2.532	2.530	2.555	2.718	2.724	2.691	2.725	2.352	2.378	2.629	2.592
Mn_{VI}	0.025	0.026	0.017	0.024	0.021	0.016	0.026	0.021	0.009	0.010	0.024	0.022
Mg_{VI}	2.964	2.587	2.391	2.612	2.398	2.528	2.382	2.440	3.017	3.018	2.603	2.586
VI-vacancy	0.000	0.281	0.376	0.263	0.266	0.230	0.334	0.295	0.103	0.099	0.243	0.228
Ca_{XII}	0.209	0.000	0.003	0.002	0.002	0.006		0.002	0.001	0.004	0.000	0.001
Na_{XII}	0.036	0.033	0.036	0.040	0.050	0.099	0.047	0.081	0.089	0.073	0.021	0.025
K_{XII}	1.282	1.851	1.740	1.797	1.726	1.793	1.819	1.848	1.756	1.779	1.866	1.832
XII-vacancy	0.473	0.117	0.222	0.161	0.145	0.082	0.134	0.069	0.155	0.144	0.113	0.142
F	0.282	0.277	0.092	0.119	0.237	0.245	0.282	0.284	0.332	0.321	0.210	0.220
Cl	0.163	0.235	0.156	0.144	0.137	0.234	0.134	0.135	0.213	0.254	0.220	0.232

Table 7.5. Continued.

Complex	Brovales pluton									
Rock group unit	*Central Subalkaline Intermediate Unitt*				*Intermediate Subalkaline Intermediate Unit*				*External Subalkaline Acid Unit*	
Facies	Dioritic enclaves		Quartz monzodiorites to granodiorites		Granodiorites				Granites	
Sample	B-2E		B-2		B-5-1		B-5-2		B-7	
Textural position	single	single	rim	core	single	single	single	rim	core	single
Majors elements (wt %)										
SiO_2	36.68	35.94	35.95	36.41	35.48	35.41	35.26	35.44	34.28	35.47
TiO_2	3.82	3.25	2.36	3.28	4.58	4.43	3.22	2.68	4.03	3.21
Al_2O_3	13.65	14.32	14.60	14.65	13.51	13.56	14.27	14.17	15.61	16.22
Cr_2O_3	0.05	0.04	0.00	0.04	0.01			0.02	0.02	0.01
NiO	0.02	0.03		0.01				0.00		
FeO_T	22.36	21.42	22.08	22.29	25.18	25.27	26.03	26.02	23.85	23.21
MnO	0.27	0.28	0.28	0.27	0.24	0.27	0.39	0.39	0.20	0.19
MgO	10.05	9.61	10.00	9.59	7.32	7.49	7.46	7.64	7.67	7.94
CaO	0.00	0.01	0.02			0.00	0.05			0.00
Na_2O	0.10	0.12	0.10	0.08	0.07	0.09	0.09	0.16	0.10	0.08
K_2O	9.63	9.91	9.61	9.84	9.71	9.69	8.83	9.65	9.62	9.74
F	0.68	0.67	0.55	0.58	0.61	0.64	0.63	0.70	0.51	0.56
Cl	0.77	0.71	0.69	0.71	1.26	1.29	1.23	1.33	0.88	0.89
Sum	98.39	96.52	96.44	97.91	98.30	98.49	97.80	98.41	97.39	97.64
Formula based on 22 oxygens										
Si_{IV}	5.620	5.601	5.602	5.590	5.563	5.550	5.553	5.575	5.376	5.488
Al_{IV}	2.380	2.399	2.398	2.410	2.437	2.450	2.447	2.425	2.624	2.512
Ti_{VI}	0.441	0.381	0.277	0.379	0.540	0.522	0.381	0.317	0.476	0.374
Al_{VI}	0.085	0.232	0.282	0.241	0.060	0.054	0.201	0.202	0.263	0.445
Cr_{VI}	0.007	0.005	0.000	0.005	0.001			0.002	0.002	0.001
Ni_{VI}	0.002	0.003		0.001				0.000		
$Fe^{2+}{}_{VI}$	2.864	2.791	2.877	2.862	3.302	3.311	3.427	3.422	3.128	3.003
Mn_{VI}	0.035	0.037	0.037	0.035	0.032	0.035	0.052	0.052	0.027	0.024
Mg_{VI}	2.295	2.233	2.323	2.195	1.711	1.750	1.750	1.792	1.793	1.831
VI-vacancy	0.271	0.318	0.204	0.282	0.354	0.328	0.189	0.213	0.312	0.321
Ca_{XII}	0.000	0.002	0.003			0.000	0.008			0.001
Na_{XII}	0.031	0.037	0.030	0.024	0.021	0.028	0.028	0.048	0.030	0.024
K_{XII}	1.882	1.969	1.909	1.927	1.943	1.938	1.774	1.936	1.926	1.922
XII-vacancy	0.087	-0.008	0.058	0.049	0.036	0.034	0.189	0.015	0.045	0.054
F	0.327	0.329	0.269	0.284	0.302	0.317	0.312	0.346	0.253	0.275
Cl	0.201	0.188	0.182	0.185	0.334	0.343	0.329	0.355	0.235	0.234

Table 7.5. Continued

7.5 Plagioclase

Plagioclase is the most abundant mineral in the different units of the three complexes, it ranges in composition from bytownite An_{90} to oligoclase An_{10} (Fig. 7.16). The textures and zoning of the crystals varies in the different units (Table 7.6).

The plagioclase in the Burguillos *Central Ultrabasic-Basic Layered Unit* varies from bytownite to labradorite, An_{90-55} (Fig. 7.16A).

In Chapter 6, we described complex zonation and recrystallisation disequilibrium textures. The Burguillos *Central Ultrabasic-Basic Layered Unit* olivine gabbros contain scarce labradorite An_{55}, as inclusions in larger crystals of bytownite An_{70-90}, (Fig. 7.16A and Table 7.6). The bytownite is, in turn, included in late-stage poikilitic orthopyroxene, demonstrating that it crystallised before the ferromagnesian mineral. In the gabbros and gabbronorites of this unit the same compositional relationship is evident: labradorite, An_{53-70}, cores are generally in disequilibrium with bytownite, An_{70-90}, rims (Fig, 7.16A and Table 7.6).

The plagioclases of the Burguillos *Central Alkaline Basic-Intermediate Layered and Acid Unit* also show compositional variations but in this case correlated with the facies. In the amphibole gabbros the plagioclase has the same compositional and disequilibrium textural characteristics as those of in the *Central Ultrabasic-Basic Layered Unit* poikilitic amphibole gabbro and gabbronorite: Carlsbad twinned crystals with a transition from common labradorite, An_{50-70}, cores to less abundant bytownite, An_{74-82}, rims and individual crystals (Fig, 7.16A and Table 7.6). This compositional transition is more obvious in the facies in which amphibole is more abundant, the facies that has less amphibole only has labradorite, An_{50-58}, (Fig. 7.16A and Table 7.6). In the *Central Alkaline Basic-Intermediate Layered and Acid Unit* gabbros and diorites without amphibole, the plagioclases have a uniform composition: labradorite, An_{48-63} (Fig. 7.16A and Table 7.6). These minerals are mostly unzoned, but some have a slight variation in composition from core to rim (Fig. 7.16A and Table 7.6). The plagioclase composition in the intermediate rocks of this same unit is andesine An_{32-50}, with zonation from the cores to somewhat less Ca-rich rims (Fig. 7.16A and Table 7.6). In the felsic rocks from this unit the plagioclase is oligoclase, An_{14} (Fig. 7.16A and Table 7.6).

The plagioclase in the Burguillos *External Subalkaline Intermediate Unit* is mostly andesine An_{31-50} (Fig. 7.16A and Table 7.6). Evidence of textural disequilibrium includes labradorite, An_{59-63}, cores overgrown by andesine (Fig. 7.16A and Table 7.6).

The plagioclases in the amphibole-free gabbros and diorites of the Valencia *Main Pluton*

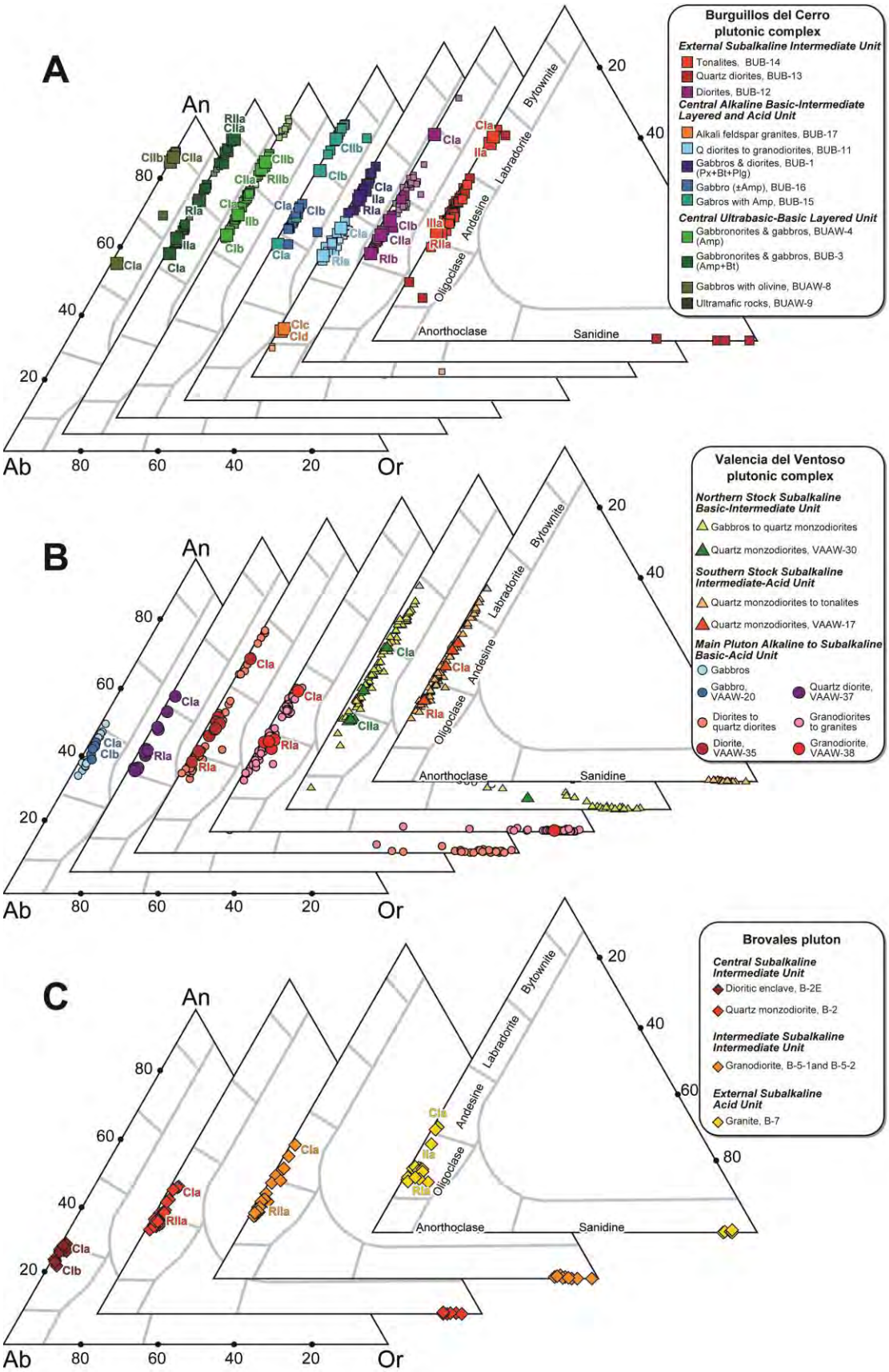

Figure 7.16. Classification of feldspars based on their content in An-Ab-Or. A) Burguillos del Cerro plutonic complex B) Valencia del Ventoso plutonic complex and C) Brovales pluton. The textural relationship of representative analyses refers to information given in Table M6. (smaller lighter symbols – García-Casquero, 1991 and Sarrionandia, 2005).

Complex	Burguillos del Cerro plutonic complex																		
Rock roup unit	*Central Ultrabasic-Basic Layered Unit*													*Central Alkaline Basic-Intermediate Layered and Acid Unit*					
Facies	Olivine gabbros			Poikilitic amphibole and biotite gabbronorites and gabbros					Poikilitic amphibole gabbronorites and gabbros						Gabbros with amphibole			Gabbros		Diorites	
Sample	BUAW-8			BUB-3					BUAW-4						BUB-15			BUB-16		BUB-1	
Texture	CIIb	CIa	CIIa	RIa	IIa	CIa	RIIa	CIIa	CIIa	CIa	RIIb	CIIb	CIb	IIb	CIa	CIb	CIIb	CIa	CIb	CIa	RIa
Major elements (wt %)																					
SiO_2	45.56	53.12	44.88	50.74	53.40	55.29	46.15	46.85	47.90	51.89	48.75	48.05	53.77	52.18	57.09	51.17	48.85	54.80	55.62	54.51	55.31
TiO_2	0.01	0.02	0.01	0.08	0.11	0.08			0.02	0.01	0.02	0.01	0.01		0.08			0.05	0.02	0.04	0.03
Al_2O_3	34.10	28.87	34.26	30.98	29.17	27.90	33.88	33.90	31.79	29.95	32.18	32.34	28.52	29.66	27.08	30.46	32.19	28.97	28.36	29.25	28.55
FeO_T	0.15	0.28	0.25	0.37	0.31	0.34	0.40	0.54	0.49	0.29	0.39	0.35	0.32	0.30	0.31	0.41	0.51	0.29	0.24	0.33	0.29
MnO	0.00		0.00	0.03				0.10	0.00				0.00	0.01	0.03	0.03	0.03		0.01		
MgO	0.02	0.02	0.02	0.06	0.13			1.94	0.18	0.02	0.03	0.02	0.02	0.02			0.02	0.02	0.01	0.03	
CaO	17.61	11.62	17.97	14.21	12.03	11.04	18.14	15.46	15.39	12.71	15.25	15.55	11.31	12.57	9.40	14.23	15.88	11.05	10.44	11.50	10.84
Na_2O	1.52	4.85	1.34	3.31	4.66	5.13	1.34	1.08	2.69	4.34	2.86	2.59	5.04	4.35	5.82	3.50	2.41	5.00	5.35	4.85	5.20
K_2O	0.03	0.28	0.06	0.11	0.11	0.16	0.02	0.11	0.12	0.21	0.11	0.10	0.26	0.24	0.18	0.18	0.09	0.27	0.26	0.29	0.26
Sum	99.00	99.06	98.81	99.89	99.93	99.95	99.93	99.98	98.58	99.43	99.59	99.01	99.26	99.35	100.00	99.98	99.98	100.45	100.31	100.80	100.48
Formula based on 8 oxygens																					
Si	2.114	2.422	2.088	2.315	2.418	2.501	2.126	2.148	2.219	2.363	2.234	2.218	2.446	2.379	2.573	2.332	2.239	2.465	2.502	2.445	2.486
Ti	0.000	0.001	0.000	0.003	0.004	0.003			0.001	0.000	0.001	0.000	0.000		0.003			0.002	0.001	0.001	0.001
Al	1.865	1.552	1.879	1.666	1.556	1.488	1.840	1.832	1.736	1.607	1.738	1.759	1.529	1.594	1.438	1.636	1.739	1.536	1.503	1.546	1.512
Fe_T	0.006	0.011	0.010	0.014	0.012	0.013	0.016	0.021	0.019	0.011	0.015	0.014	0.012	0.012	0.012	0.016	0.019	0.011	0.009	0.012	0.011
Mn	0.000		0.000	0.001				0.004	0.000				0.000	0.000	0.001	0.001	0.001		0.000		
Mg	0.001	0.002	0.001	0.004	0.009			0.133	0.013	0.002	0.002	0.001	0.001	0.002			0.001	0.001	0.001	0.002	
Ca	0.875	0.568	0.896	0.694	0.583	0.535	0.895	0.759	0.764	0.620	0.749	0.769	0.551	0.614	0.454	0.695	0.780	0.533	0.503	0.553	0.522
Na	0.137	0.429	0.121	0.293	0.409	0.450	0.119	0.096	0.241	0.383	0.254	0.232	0.445	0.385	0.509	0.309	0.214	0.436	0.466	0.422	0.453
K	0.002	0.016	0.004	0.007	0.006	0.009	0.001	0.007	0.007	0.012	0.007	0.006	0.015	0.014	0.010	0.010	0.005	0.015	0.015	0.017	0.015
An %	86.31	56.05	87.79	69.90	58.39	53.80	88.12	88.08	75.47	61.08	74.15	76.37	54.51	60.62	46.65	68.50	78.02	54.11	51.10	55.77	52.72
Ab %	13.49	42.35	11.85	29.45	40.96	45.29	11.75	11.16	23.83	37.73	25.19	23.04	43.99	37.99	52.28	30.47	21.46	44.31	47.39	42.56	45.77
Or %	0.20	1.60	0.36	0.65	0.65	0.92	0.13	0.75	0.70	1.19	0.66	0.59	1.50	1.40	1.07	1.02	0.52	1.57	1.52	1.67	1.51

Table 7.6. Representative analyses of plagioclase from the Burguillos del Cerro and Valencia del Ventoso plutonic complexes and the Brovales pluton. Textural codes; C: core, I: intermediate core rim position; R: rim. I, II and III numbers of different plagioclases in the same grain a, b or c. See Fig. 7.16.

Complex	Burguillos del Cerro plutonic complex												Valencia del Ventoso plutonic complex							
Rock group unit	*Central Alkaline Basic-Intermediate Layered and Acid Unit*				*External Subalkaline Intermediate Unit*								*Main Pluton Alkaline to Subalkaline Basic-Acid Unit*							
Facies	Quartz diorites		Alkali feldspar granites		Diorites				Quartz diorites and tonalites				Gabbros and diorites		Diorites		Quartz diorites		Granodiorites to granites	
Sample	BUB-11		BUB-17		BUB-12				BUB-14				VAAW-20		VAAW-35		VAAW-37		VAAW-38	
Texture	CIa	RIa	CIc	CId	CIa	RIa	CIb	Rib	RIIa	CIa	IIa	IIIa	CIb	CIa	RIa	CIa	CIa	RIa	CIa	RIa
Major elements (wt %)																				
SiO_2	59.88	57.57	66.19	65.90	51.23	59.71	58.13	60.88	60.57	53.67	53.31	60.92	56.24	55.92	61.13	53.04	54.43	58.89	56.85	61.49
TiO_2		0.02			0.04		0.02	0.02		0.04	0.03		0.01	0.01		0.06	0.05	0.01	0.02	
Al_2O_3	26.52	27.53	22.45	22.58	30.99	25.59	27.28	25.48	25.31	30.00	30.31	25.43	27.05	27.03	23.34	28.75	28.06	25.33	26.34	23.73
FeO_T	0.42	0.16	0.40	0.48	0.24	0.17	0.24	0.09	0.15	0.28	0.19	0.18	0.30	0.30	0.15	0.21	0.26	0.19	0.15	0.21
MnO						0.07		0.03	0.02		0.01	0.02	0.01	0.00			0.01		0.01	0.03
MgO	0.01	0.01				0.10	0.01		0.01				0.01	0.01	0.01	0.01	0.01	0.01	0.01	0.01
CaO	7.50	9.10	2.93	3.06	13.86	7.47	8.82	6.78	6.73	12.17	12.52	6.70	9.38	9.43	5.55	11.71	10.76	7.51	8.59	5.63
Na_2O	7.29	6.19	10.13	9.96	3.56	6.60	6.45	7.72	7.69	4.56	4.34	7.80	6.19	6.14	8.07	4.55	5.24	7.07	6.33	7.90
K_2O	0.10	0.21	0.19	0.25	0.07	0.30	0.31	0.30	0.33	0.20	0.18	0.15	0.28	0.29	0.25	0.22	0.24	0.39	0.35	0.58
Sum	101.72	100.79	102.29	102.23	99.98	100.00	101.26	101.30	100.81	100.92	100.89	101.20	99.47	99.13	98.49	98.55	99.07	99.41	98.65	99.56
Formula based on 8 oxygens																				
Si	2.631	2.565	2.852	2.844	2.332	2.680	2.575	2.679	2.678	2.408	2.395	2.683	2.537	2.532	2.761	2.437	2.477	2.647	2.584	2.750
Ti		0.001			0.001		0.001	0.001		0.001	0.001		0.000	0.000		0.002	0.002	0.000	0.001	
Al	1.373	1.446	1.140	1.148	1.663	1.354	1.424	1.321	1.319	1.587	1.605	1.320	1.438	1.442	1.243	1.557	1.505	1.342	1.411	1.251
Fe_T	0.015	0.006	0.014	0.017	0.009	0.007	0.009	0.003	0.006	0.011	0.007	0.007	0.011	0.011	0.006	0.008	0.010	0.007	0.006	0.008
Mn						0.003		0.001	0.001		0.000	0.001	0.000	0.000			0.000		0.000	0.001
Mg	0.001	0.001				0.007	0.001		0.001				0.001	0.001	0.000	0.001	0.001	0.000	0.001	0.000
Ca	0.353	0.434	0.135	0.141	0.676	0.359	0.419	0.320	0.319	0.585	0.603	0.316	0.453	0.457	0.269	0.576	0.525	0.362	0.418	0.270
Na	0.621	0.535	0.846	0.833	0.315	0.574	0.554	0.659	0.659	0.397	0.378	0.666	0.542	0.539	0.707	0.406	0.462	0.616	0.558	0.685
K	0.006	0.012	0.010	0.014	0.004	0.017	0.018	0.017	0.019	0.011	0.010	0.008	0.016	0.017	0.014	0.013	0.014	0.023	0.020	0.033
An %	36.04	44.28	13.64	14.31	67.97	37.77	42.28	32.12	31.99	58.91	60.81	31.91	44.84	45.16	27.14	57.95	52.43	36.16	41.99	27.31
Ab %	63.39	54.50	85.31	84.30	31.63	60.44	55.95	66.19	66.14	39.94	38.15	67.23	53.59	53.21	71.42	40.77	46.18	61.59	55.97	69.33
Or %	0.57	1.22	1.05	1.39	0.39	1.79	1.77	1.69	1.87	1.15	1.04	0.85	1.57	1.63	1.44	1.29	1.39	2.25	2.05	3.36

Table 7.6. Continued.

Complex	Valencia del Ventoso plutonic complex				Brovales pluton								
Rock group unit	*Northern Stock Subalkaline Basic-Intermediate Unit*		*Southern Stock Subalkaline Intermediate-Acid Unit*		*Central Subalkaline Intermediate Unit*				*Intermediate Subalkaline Intermediate Unit*		*External Subalkaline Acid Unit*		
Facies	Quartz monzodiorites		Quartz monzodiorites		Dioritic enclaves		Quartz monzodiorites to granodiorites		Granodiorites		Granites		
Sample	VAAW-30		VAAW-17		B-2E		B-2		B-5-1		B-7		
Texture	CIa	CIIa	CIa	RIa	CIa	CIb	CIa	RIIa	RIIa	CIa	RIa	IIa	CIa
Majors elements (wt %)													
SiO_2	55.57	61.04	59.06	62.29	60.31	62.26	58.31	60.78	62.48	57.83	63.70	61.42	59.98
TiO_2	0.04	0.06	0.04	0.01	0.00		0.01	0.01	0.01	0.02	0.01	0.00	
Al_2O_3	27.02	23.29	25.08	23.41	24.61	23.77	26.05	24.73	23.35	26.58	22.17	24.41	25.37
FeO_T	0.30	0.28	0.09	0.02	0.14	0.13	0.16	0.11	0.09	0.10	0.02	0.04	0.02
MnO					0.01		0.00	0.01					
MgO	0.02	0.01	0.01	0.00	0.00	0.00	0.01			0.00	0.04	0.00	0.00
CaO	9.87	5.47	7.12	5.09	6.27	4.99	7.95	6.18	4.74	8.37	3.34	5.58	6.68
Na_2O	5.58	8.04	7.30	8.50	7.91	8.68	6.98	7.98	8.94	6.81	9.28	8.33	7.87
K_2O	0.35	0.50	0.32	0.26	0.22	0.37	0.34	0.31	0.20	0.21	0.19	0.38	0.21
Sum	98.74	98.70	99.00	99.57	99.48	100.21	99.80	100.11	99.80	99.94	98.75	100.18	100.12
Formula based on 8 oxygens													
Si	2.535	2.752	2.662	2.776	2.697	2.754	2.611	2.700	2.771	2.588	2.851	2.721	2.664
Ti	0.001	0.002	0.001	0.000	0.000		0.000	0.000	0.000	0.001	0.000	0.000	
Al	1.453	1.238	1.332	1.229	1.297	1.239	1.375	1.295	1.220	1.402	1.169	1.275	1.328
Fe_T	0.011	0.011	0.003	0.001	0.005	0.005	0.006	0.004	0.003	0.004	0.001	0.001	0.001
Mn					0.000		0.000	0.000					
Mg	0.001	0.001	0.000	0.000	0.000	0.000	0.000			0.000	0.003	0.000	0.000
Ca	0.482	0.264	0.344	0.243	0.301	0.236	0.382	0.294	0.225	0.401	0.160	0.265	0.318
Na	0.493	0.703	0.638	0.734	0.686	0.744	0.606	0.688	0.768	0.591	0.805	0.716	0.677
K	0.020	0.029	0.018	0.015	0.013	0.021	0.019	0.017	0.011	0.012	0.011	0.022	0.012
An %	48.42	26.53	34.39	24.49	30.08	23.59	37.89	29.44	22.40	39.98	16.41	26.44	31.55
Ab %	49.54	70.58	63.80	74.02	68.65	74.30	60.18	68.81	76.48	58.84	82.48	71.41	67.26
Or %	2.03	2.89	1.82	1.49	1.27	2.11	1.93	1.75	1.12	1.18	1.11	2.15	1.18

Table 7.6. Continued.

Alkaline to Subalkaline Basic-Acid Unit (Fig. 7.16B and Table 7.6) range in composition from oligoclase to labradorite An_{25-52}. The plagioclases of these rocks show evidence of disequilibrium. The diorites and quartz diorites contain labradorite, An_{53-66} rimmed by andesine to oligoclase, An_{22-45} (Fig. 7.16B and Table 7.6). The granodiorites and granites from this unit also contain andesine to oligoclase, An_{15-42}, (Fig. 7.16B and Table 7.6).

The plagioclases in the Valencia *Northern Stock Subalkaline Basic-Intermediate Unit* and *Southern Stock Subalkaline Intermediate-Acid Unit* are quite varied from labradorite cores to oligoclase rims, An_{18-70} the largest range observed in any of the units (Fig. 7.16B and Table 7.6). Both the units contain plagioclases with disequilibrium textures such as complex internal zoning. Individual crystals of oligoclase, however, are uniform and unzoned.

The plagioclase in the Brovales pluton is transitional between andesine and oligoclase, An_{15-40} (Fig. 7.16C and Table 7.6). The finer-grained diorite enclave from the *Central Subalkaline Intermediate Unit* has a very limited compositional range of plagioclase: oligoclase, An_{24-30} (Fig. 7.16C and Table 7.6). However, the plagioclases in the host quartz diorites is of two different populations: andesine, An_{35-40} (Fig. 7.16C and Table 7.6) and oligoclase, An_{25-30} (Fig. 7.16C and Table 7.6). The plagioclases in the *Intermediate Subalkaline Intermediate Unit* show evidence of disequilibrium: cores of andesine An_{30-40}, with overgrowth rims of oligoclase, An_{19-29} (Fig. 7.16C and Table 7.6). The *External Subalkaline Acid Unit* plagioclase is strongly zoned from andesine cores to, predominantly, oligoclase rims An_{15-32}, (Fig. 7.16C and Table 7.6).

7.6 Alkali Feldspar

Alkali feldspar is not common in the studied complexes. In is only present in some of the intermediate and felsic rocks.

In the Burguillos del Cerro plutonic complex alkali feldspar was only analysed from the *External Subalkaline Intermediate Unit* where it has Or_{74-98}. This broad range of compositions, here and in the other complexes, may be attributable to the presence of cryptoperthites (Fig. 7.16A).

In the Valencia *Main Pluton Alkaline to Subalkaline Basic-Acid Unit* alkali feldspars are relatively common in the intermediate rocks, Or_{50-98} (Fig. 7.16B; Sarrionandia, 2005). In the *Northern Stock Subalkaline Basic-Intermediate Unit* the quartz monzodiorites have alkali feldspar, Or_{79-91}, (Fig. 7.16B; Sarrionandia, 2005). In the *Southern Stock Subalkaline Intermediate-Acid Unit* the alkali feldspar has a more restricted composition, Or_{87-97}, (Fig7.16B; Sarrionandia, 2005;).

Alkali feldspar is present in the three main units of the Brovales Pluton (Fig. 7.16C). It has a moderate range of compositions, Or_{79-99} (Fig. 7.16C).

7.7 Fe-Ti Oxides

The Fe-Ti oxides, magnetite and ilmenite, are found in all the units of the three complexes.

Magnetite is quite homogeneous. In Burguillos del Cerro it has Fe_2O_3 64-72 wt % and FeO 31-38 wt % and low TiO_2 0-3 wt % (Fig. 7.17A) (calculated from the electron microprobe data). In the Valencia del Ventoso plutonic complex the magnetites are compositionally similar

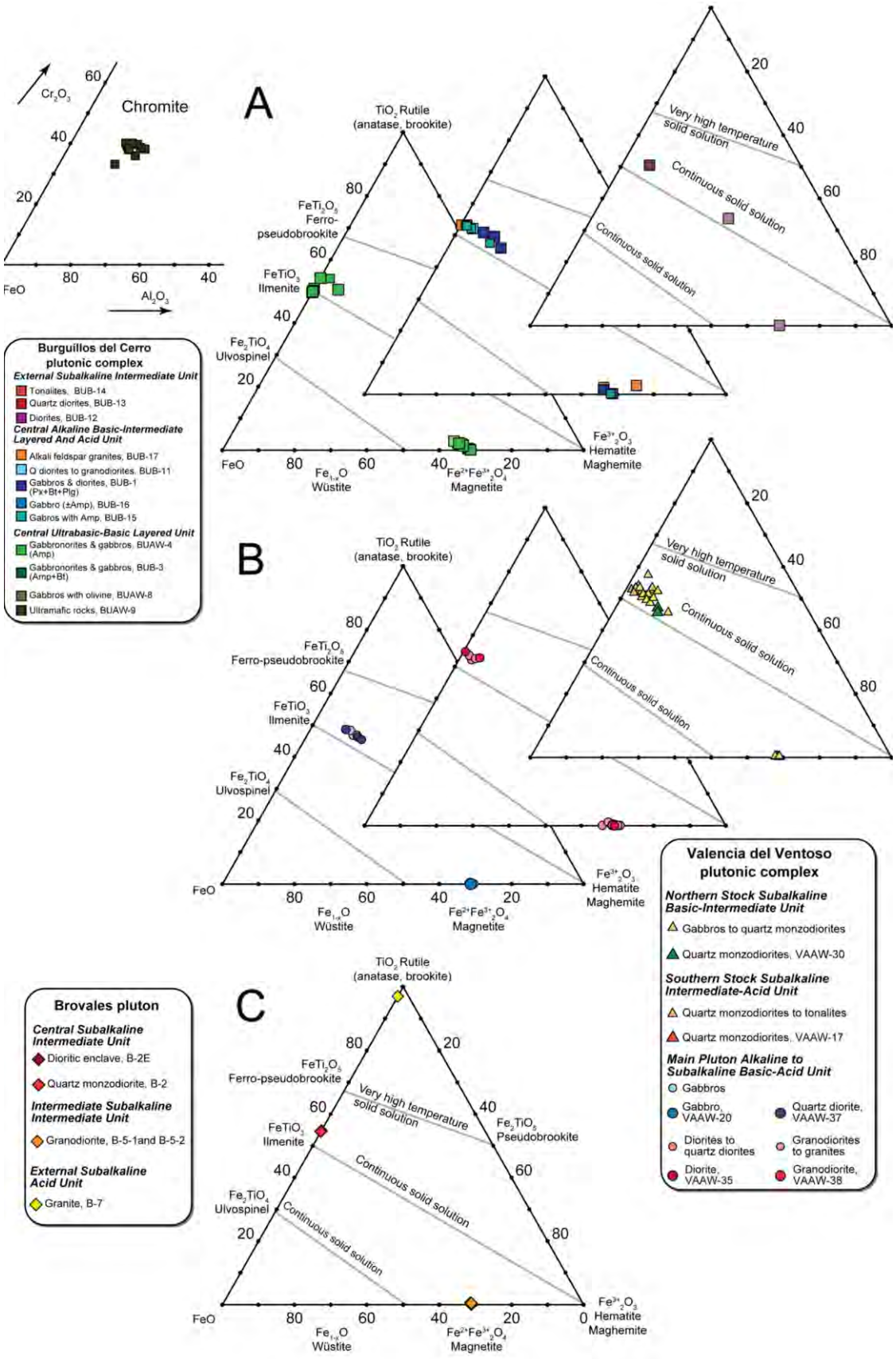

Figure 7.17. Classification of Fe-Ti oxides based on their Fe_2O_3-FeO- TiO_2 calculated from electron microprobe results A) Burguillos del Cerro plutonic complex, chromites from this complex are also shown B) Valencia del Ventoso plutonic complex and C) Brovales pluton. (smaller lighter symbols are from García-Casquero, 1991 and Sarrionandia, 2005).

Fe_2O_3 ≈ 58-73 wt % and FeO ≈ 30-32 wt % and low TiO_2 ≈ 0-1 wt % (Fig. 7.17B); as are the few data available for the Brovales pluton, Fe_2O_3 ≈ 70 wt % and FeO ≈31-32 wt % and low TiO_2 ≈ 0-1 wt % (Fig. 7.17C).

In the Burguillos del Cerro plutonic complex ilmenite has Fe_2O_3 ≈ 0-15 wt % and FeO ≈ 37-49 wt % and low TiO_2 ≈ 45-52 wt % (Fig. 7.17A) (calculated from the electron microprobe data). In the Valencia del Ventoso plutonic complex the ilmenites have Fe_2O_3 ≈ 0-15 wt %, FeO ≈ 38-45 wt % and TiO_2 ≈ 41-58 wt % (Fig. 7.17B; Sarrionandia, 2005). Once more, few data are available for the Brovales pluton, Fe_2O_3 ≈ 0 wt % and FeO ≈ 40-41 wt % and low TiO_2 ≈ 47-50 wt % (Fig. 7.17C).

Chromite is only present as inclusions in olivine in the Burguillos del Cerro plutonic complex *Central Ultrabasic-Basic Layered Unit* ultramafic rocks, it has a composition of Cr_2O_3 ≈ 28-37 wt %, Al_2O_3 ≈ 14-20 wt % and FeO_T ≈ 35-43 wt % (Fig. 7.17A).

Rutile is only found in the Brovales *External Subalkaline Acid Unit* granite (Fig. 7.17C).

7.8 Mineral Chemistry Indications of the Magma Compositions of the Main Units of the Three Plutonic Bodies

7.8.1 Clinopyroxene

The composition of clinopyroxene, in particular Ti and Ca+Na, may be used to establish the affinity of the magma from which the crystals formed (Leterrier et al., 1982; Molina et al., 2009).

Clinopyroxenes consistent with crystallisation from an alkaline magma are those from: the Burguillos *Central Alkaline Basic-Intermediate Layered and Acid Unit* gabbros (Fig. 7.4B) and the *External Subalkaline Intermediate Unit*, this latter belies their whole-rock compositions but is consistent with the textural evidence that this mineral was an early formed phase in these rocks (see Chapter 6, Fig. 7.4A and 7.4B),as was the case for the Valencia intermediate rocks of the *Main Pluton Alkaline to Subalkaline Basic-Acid Unit.*

Clinopyroxenes consistent with crystallisation from a transitional alkaline-subalkaline magma are those from: the Burguillos *Central Ultrabasic-Basic Layered Unit* gabbro and gabbronorite (Fig. 7.4A) and the *Central Alkaline Basic-Intermediate Layered and Acid Unit* amphibole gabbros and intermediate rocks (Fig. 7.4A); the Valencia *Northern Stock Subalkaline Basic-Intermediate Unit* and the *Southern Stock Subalkaline Intermediate-Acid Unit* basic to intermediate rocks (Fig. 7.4B).

Clinopyroxenes consistent with crystallisation from a subalkaline magma are those from:

the Burguillos *Central Ultrabasic-Basic Layered Unit* ultramafic rocks and olivine gabbros (Fig. 7.4A).

7.8.2 Amphibole

Whether amphiboles crystallised from a magma with an alkaline, transitional or subalkaline composition may be determined, to a great extent, by their TiO_2, MgO, K_2O and Al_2O_3 contents (Molina et al., 2009) (Fig. 7.9, 7.10 and 7.11).

Amphiboles consistent with crystallisation from an alkaline magma are: cores from the gabbros and diorites of the Burguillos *Central Alkaline Basic-Intermediate Layered and Acid Unit*; in Valencia such compositions are found in cores from gabbros and quartz diorites of the *Main Pluton Alkaline to Subalkaline Basic-Acid Unit.*

Amphiboles consistent with crystallisation from a transitional alkaline-subalkaline magma are those from: the Burguillos *Central Ultrabasic-Basic Layered Unit*, rims of crystals from the *Central Alkaline Basic-Intermediate Layered and Acid Unit* gabbros and diorites, and cores from the *External Subalkaline Intermediate Unit* diorites to granodiorites; the Valencia *Main Pluton Alkaline to Subalkaline Basic-Acid Unit* diorites; and the Brovales *Central Subalkaline Intermediate Unit* quartz diorites and *Intermediate Subalkaline Intermediate Unit* granodiorites.

Amphiboles consistent with crystallisation from a subalkaline magma include: rims from the Burguillos *Central Ultrabasic-Basic Layered Unit* ultramafic rocks and olivine gabbros, individual crystals from the *Central Alkaline Basic-Intermediate Layered and Acid Unit* amphibole gabbros, and both rims and individual crystals from the *External Subalkaline Intermediate Unit* diorites and granodiorites. The Valencia examples include rims from the *Main Pluton Alkaline to Subalkaline Basic-Acid Unit* diorites and individual crystals in granodiorites from the same unit and also the *Northern Stock Subalkaline Basic-Intermediate Unit.*

7.8.3 Biotite

Whether micas crystallised from an alkaline or subalkaline magma is reflect by the presence or absence of a cation deficiency in the tetrahedral layer; i.e. if there was insufficient or sufficient, respectively, Si+Al (>8 apfu for 22 O) to complete the layer (Fig. 7.15). Biotites that have a cation deficiency also have elevated Ti contents, indicative of an alkaline magma. Those with no deficiency have less Ti, consistent with a subalkaline composition magma (Fig. 7.15). As shown above, the compositional variation between the biotites from the three complexes is reflected in their Al_2O_3 and TiO_2 variations.

Biotites consistent with crystallisation from an alkaline magma are those from: all the Burguillos *Central Alkaline Basic-Intermediate Layered and Acid Unit* rocks (Fig. 7.15B), even the

amphibole gabbros (Fig. 7.15C) and the *External Subalkaline Intermediate Unit* dark brown Ti rich cores (Fig. 7.15D) and in the Valencia *Main Pluton Alkaline to Subalkaline Basic-Acid Unit* gabbros and some of the intermediate rocks (Fig. 7.15E and 7.15F).

Biotites consistent with crystallisation from a transitional alkaline-subalkaline magma are those from: the Burguillos *Central Ultrabasic-Basic Layered Unit* gabbro and gabbronorite (Fig. 7.15A) some of the Valencia *Main Pluton Alkaline to Subalkaline Basic-Acid Unit* intermediate rocks (Fig. 7.15F).

Biotites consistent with crystallisation from a subalkaline magma are those from: the Burguillos *Central Ultrabasic-Basic Layered Unit* ultramafic rocks and olivine gabbro phlogopites, even albeit to a lesser extent, the brown, more Ti-rich, cores (Fig. 7.15A) and the *External Subalkaline Intermediate Unit* colourless Ti-poor rims and individual crystals (Fig7.15D); some of the Valencia *Main Pluton Alkaline to Subalkaline Basic-Acid Unit* intermediate rocks (Fig. 7.15F) and the *Southern Stock Subalkaline Intermediate-Acid Unit* intermediate rocks (Fig. 7.15H); and, all the Brovales units (Fig. 17.5I).

7.8.4 Plagioclase

The relationship between mineral chemistry and magma composition is not so direct for plagioclase as it is for the other minerals. Smith and Brown (1988) concluded that a labradorite, An_{50-60} composition is typical for liquidus plagioclase in alkali basalts, whereas plagioclases crystallised from tholeiitic magmas tend to be more Ca-rich bytownite. This compositional variation reveals that the less calcic plagioclase, labradorite-andesine, crystallised from more alkaline magmas, for example those that crystallised to the gabbros to quartz diorites of the Burguillos *Central Alkaline Basic-Intermediate Layered and Acid Unit* and the Valencia gabbros and quartz diorites of the *Main Pluton Alkaline to Subalkaline Basic-Acid Unit*. Labradorite is found in disequilibrium in the Burguillos *Central Ultrabasic-Basic Layered Unit* rocks, in cores of crystals with bytownite, the latter also being the composition of individual crystals formed.

In the subalkaline diorites to tonalites of the Burguillos *External Subalkaline Intermediate Unit* and the diorites of the Valencia *Main Pluton Alkaline to Subalkaline Basic-Acid Unit* labradorite cores show evidence of desequilibrium with andesine rims and individual crystals. In the Valencia *Main Pluton Alkaline to Subalkaline Basic-Acid Unit* and Brovales granodiorites and granites andesine and oligoclase crystallised apparently in equilibrium

Chapter 8: Whole-rock Geochemical Composition

8. Whole-rock Geochemical Composition

Here we describe the whole-rock major and trace element and Rb-Sr isotope compositions of the Burguillos del Cerro plutonic complex, the Valencia del Ventoso plutonic complex and the Brovales pluton including both data from this study and the literature (Pons, 1982; Sarrionandia, 2005). At the end of the chapter the different units from the three complexes are considered together highlighting similitudes.

Representative major and trace element data and Rb-Sr and Sm-Nd isotopes are given in Tables 8.1 to 8.3 and shown in Figs 8.1 to 8.17; the full dataset is given in Appendix II.

8.1 Burguillos del Cerro Plutonic Complex

8.1.1 Central Ultrabasic-Basic Layered Unit

8.1.1.1 Ultramafic and Mafic Rocks

The lherzolites to websterites and olivine gabbros major element concentrations are SiO_2 ≈ 43-50 wt %, Na_2O+K_2O ≈ 0.7-2.6 wt % with FeO_T/MgO ≈ 0.3-0.6, being rich in MgO ≈10-30 wt % and having FeO_T ≈6-10 wt %, TiO_2 ≈0.2-0.5 wt %, Al_2O_3 ≈ 4.5-19 wt %, CaO ≈ 6-16 wt %, K_2O ≈ 0.2-1 wt % and P_2O_5 ≈ 0-0.2 wt % (Fig. 8.2).

They are, therefore, low-medium-K, subalkaline, calc-alkaline, metaluminous, with an aluminium saturation index, ASI, (molar $((Al_2O_3)/(Na_2O+K_2O))$ ≈ 0.25-0.62), and an index of Borodin (1987) that indicates they are tholeiitic (Acidity, AC, is calculated as 4Si/(1.5Ti+6Al+5(Fe+Mn)+5.5(Mg+Ca)+17Na+19K)) where the elements are expressed as molecular numbers of the oxides) (Fig. 8.1).

In silicate Earth-normalised diagrams these rocks have negative anomalies in Nb, Ta, P, Zr and Ti and positive anomalies in U, K, Pb and Sr (Fig. 8.3A). Furthermore, they have chondrite-normalised enrichment in LREE relative to HREE, La_N/Lu_N ≈ 3.9-13.3, and variable small, negative and positive, Eu anomalies, Eu/Eu^* ≈ 0.70-1.80 (Fig. 8.3B).

The ultramafic and mafic rocks present a range of $\varepsilon Nd_{335\ Ma}$ ≈ -3.8 to -2.5 and $^{87}Sr/\ ^{86}Sr_{335\ Ma}$ values 0.706285-0.706541 (Fig. 8.4). They have high $^{147}Sm/^{144}Nd$ ≈ 0.152-0.176 and old Nd model ages 1.5 to 2.4 Ga calculated according to DePaolo (1981) (Fig. 8.4).

8.1.1.2 Gabbros and Gabbronorites

This group comprises two facies the first is alkaline (poikilitic biotite and amphibole) and the second is subalkaline (poikilitic amphibole).

The major element compositions of the gabbro and gabbronorite alkaline rocks are SiO_2 ≈

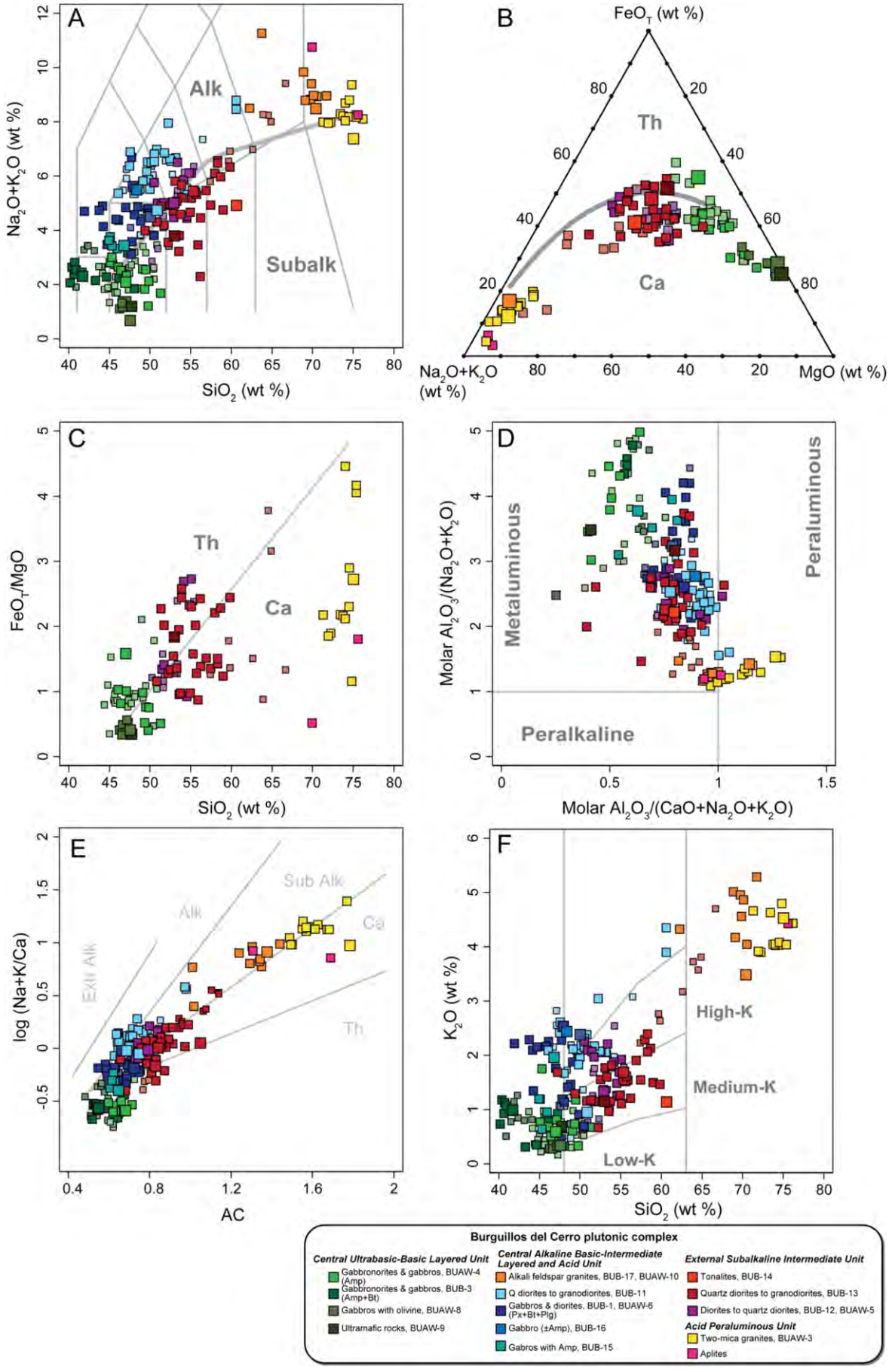
A
Alk
Subalk
Na_2O+K_2O (wt %)
SiO_2 (wt %)
B
FeO_T (wt %)
Th
Ca
Na_2O+K_2O (wt %)
MgO (wt %)
C
Th
Ca
FeO_T/MgO
SiO_2 (wt %)
D
Metaluminous
Peraluminous
Peralkaline
Molar $Al_2O_3/(Na_2O+K_2O)$
Molar $Al_2O_3/(CaO+Na_2O+K_2O)$
E
Sub Alk
Alk
Ca
Th
log (Na+K/Ca)
AC
F
High-K
Medium-K
Low-K
K_2O (wt %)
SiO_2 (wt %)
Burguillos del Cerro plutonic complex
Central Ultrabasic-Basic Layered Unit
Gabbronorites & gabbros, BUAW-4 (Amp)
Gabbronorites & gabbros, BUB-3 (Amp+Bt)
Gabbros with olivine, BUAW-8
Ultramafic rocks, BUAW-9
Central Alkaline Basic-Intermediate Layered and Acid Unit
Alkali feldspar granites, BUB-17, BUAW-10
Q diorites to granodiorites, BUB-11
Gabbros & diorites, BUB-1, BUAW-6 (Px+Bt+Plg)
Gabbro (±Amp), BUB-16
Gabros with Amp, BUB-15
External Subalkaline Intermediate Unit
Tonalites, BUB-14
Quartz diorites to granodiorites, BUB-13
Diorites to quartz diorites, BUB-12, BUAW-5
Acid Peraluminous Unit
Two-mica granites, BUAW-3
Aplites

39-48 wt %, Na_2O+K_2O ≈ 1.8-3.4 wt % with FeO_T/MgO ≈ 0.9-3.1 (Fig. 8.1). Their MgO contents vary from ≈ 3.7-9.2 wt % with FeO_T ≈ 4-17 wt %, TiO_2 ≈ 0.6-2.8 wt %, Al_2O_3 ≈ 15.4-26 wt %, CaO ≈ 11.5-16 wt %, K_2O ≈ 0.3-1.2 wt % and P_2O_5 ≈ 0-0.5 wt % (Fig. 8.2). SiO_2 is negatively correlated with TiO_2, MgO and FeO_T (Fig. 8.2).

The major element compositions of the subalkaline rocks are SiO_2 ≈ 42-51 wt %, Na_2O+K_2O ≈ 1.1-3.5 wt % with FeO_T/MgO ≈ 0.4-3 (Fig. 8.1). Their MgO contents vary from 3.4-13.4 wt % with FeO_T ≈ 4.2-10.6 wt %, TiO_2 ≈ 0.3-2 wt %, Al_2O_3 ≈ 10.2-24.8 wt %, CaO ≈ 10.2-17.1 wt %, K_2O ≈ 0.2-1.7 wt % and P_2O_5 ≈ 0-0.7 wt % (Fig. 8.2). The subalkaline poikilitic amphibole gabbros show the same negative correlations between SiO_2 and TiO_2, MgO, FeO as the alkaline gabbros but have higher values of MgO and lower FeO_T (Fig. 8.2).

These rocks are low-K, alkaline to subalkaline-transitional, tholeiitic to calc-alkaline, metaluminous (ASI ≈ 0.40-0.90), with a tholeiitic to, rarely, calc-alkaline Borodin index (Fig. 8.1).

In silicate Earth-normalised diagrams the alkaline mafic rocks have negative anomalies in Nb, Ta, P and Ti and positive anomalies in Ba, U, K, Pb, Sr and variable Zr (Fig. 8.3C). This group is enriched in LREE relative to HREE, La_N/Lu_N ≈ 2.9-5.6, with positive Eu anomalies, Eu/Eu^* ≈ 0.9-1.5 (Fig. 8.3D).

In silicate Earth-normalised diagrams the subalkaline mafic compostions have weak negative anomalies in Nb, Ta, P, Zr and Ti and positive anomalies in Ba, K and, to a lesser extent, Sr (Fig. 8.3E). This group, uniquely in the whole plutonic complex, has a slight overall chondrite-normalised enrichment in LREE relative to HREE, La_N/Lu_N ≈ 2.7-4.8, but with a somewhat flattened LREE profile giving the pattern an upwards convex saddle-like appearance (Fig. 8.3F). The Eu anomalies change systematically throughout the group from weakly to negative, Eu/Eu^* ≈ 0.8-1.1 (Fig. 8.3F).

The mafic rocks present a range of $\varepsilon Nd_{335\ Ma}$ ≈ -4.3 to -2.3 and $^{87}Sr/\ ^{86}Sr_{335\ Ma}$ values of 0.706328-0.707433 (Fig. 8.4). Like the previous facies, the mafic rocks $^{147}Sm/^{144}Nd$ is high 0.150-0.179 which gives them old Nd model ages, 1.5 to 2.4 Ga (Fig. 8.4).

Figure 8.1: Burguillos del Cerro plutonic complex whole-rock compositions. A) Total alkalis vs SiO_2 (TAS) (fields from Le Maitre et al., 1989). B) (Na_2O+K_2O) - FeO_T - MgO (AFM) (fields from Kuno, 1968). C) FeO_T /MgO vs SiO_2 (fields from Frost et al., 2001). D) Molar $Al_2O_3/(Na_2O+K_2O)$ vs Molar $Al_2O_3/(CaO+ Na_2O+K_2O)$ (fields from Shand, 1947). E) Borodin index. F) K_2O vs SiO_2. (smaller lighter symbols data from Pons, 1982). Th: Tholeiitic; Ca: Calc-alkaline; SubAkl: Subalkaline; Alk: Alkaline.

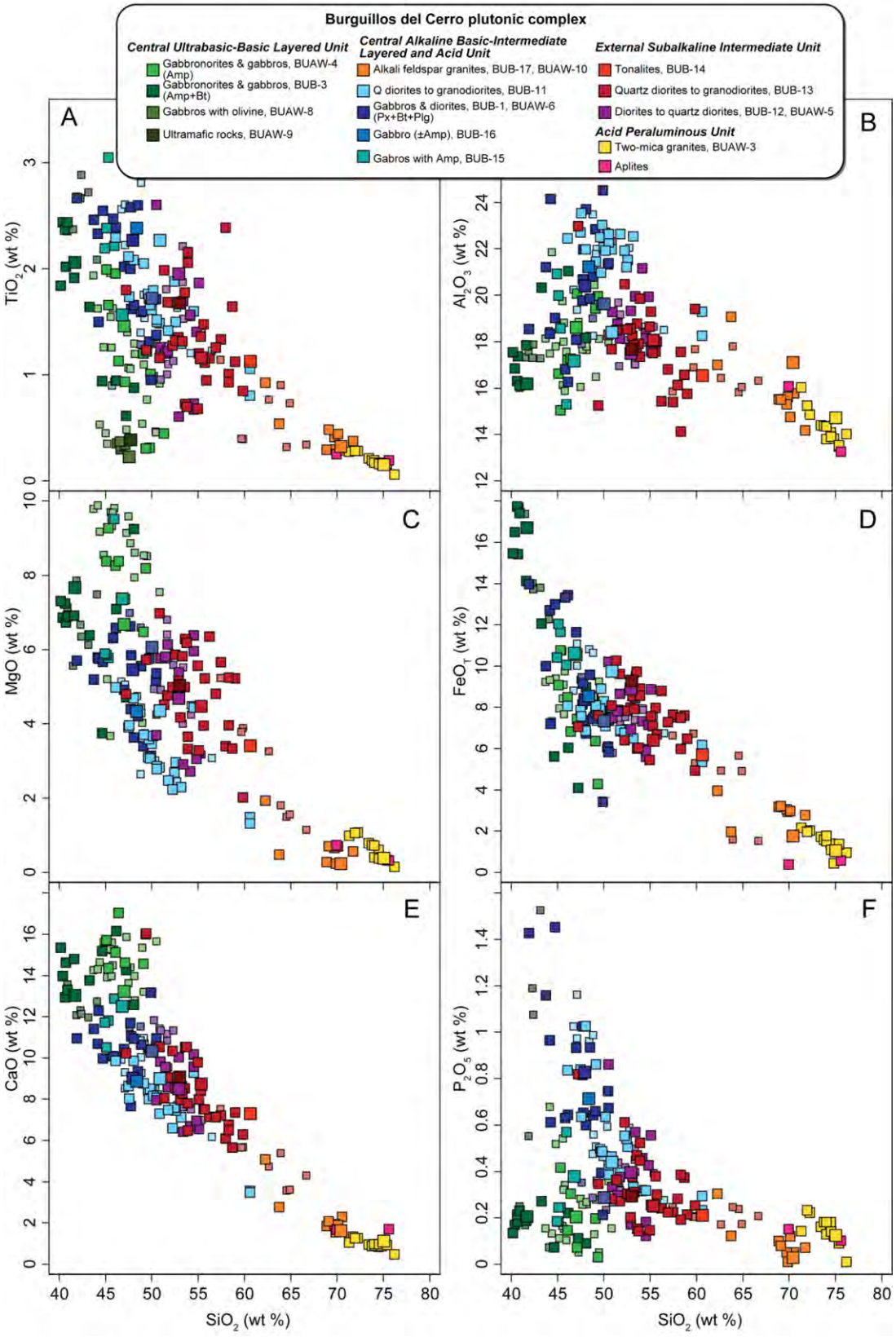

Figure 8.2: Burguillos del Cerro plutonic complex Harker diagrams: A) TiO_2 vs SiO_2. B) Al_2O_3 vs SiO_2 C) MgO vs SiO_2. D) FeO_T vs SiO_2. E) CaO vs SiO_2. F) P_2O_5 vs SiO_2 (smaller lighter symbols data from Pons, 1982).

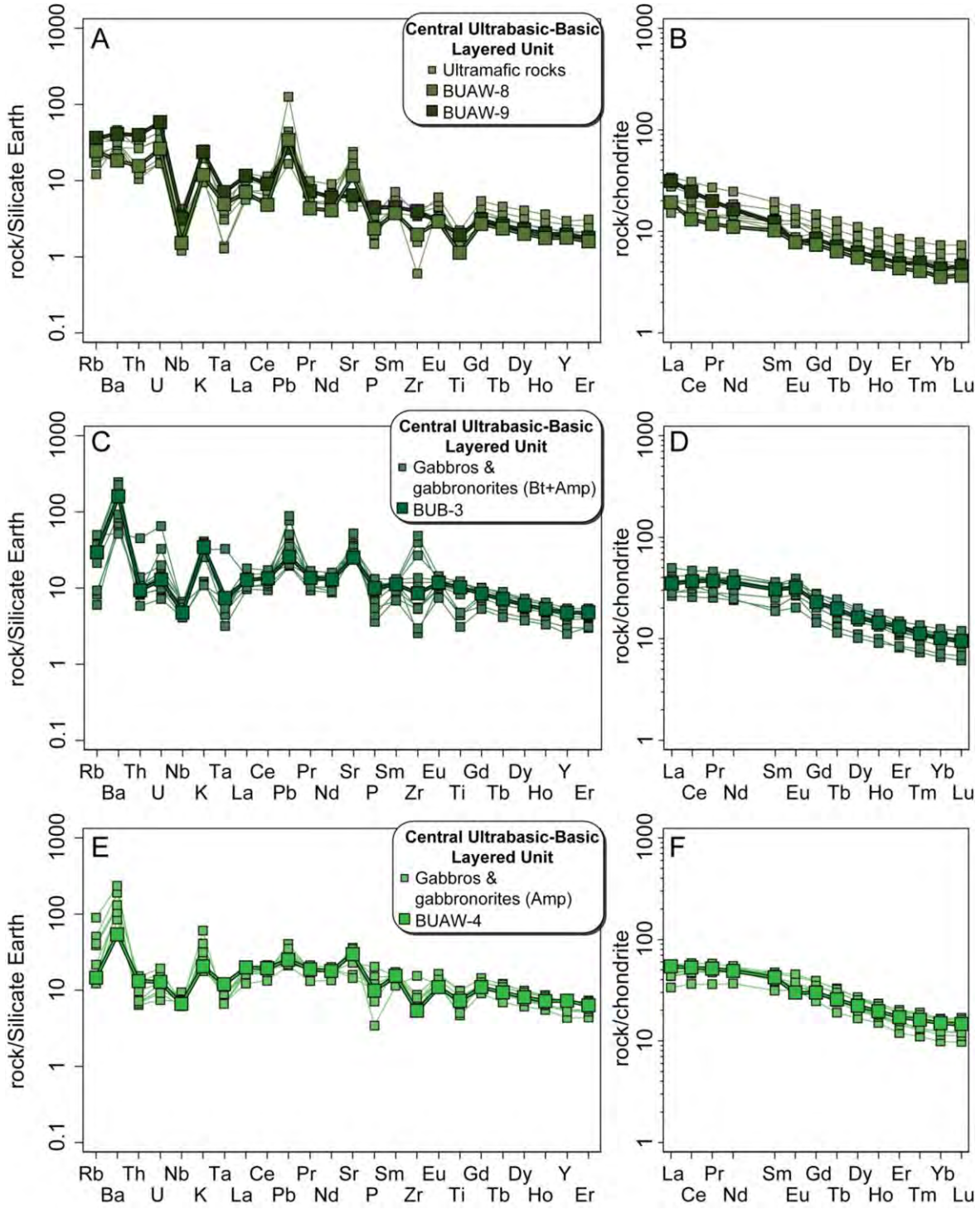

Figure 8.3: Burguillos del Cerro plutonic complex silicate Earth- and chondrite-normalised diagrams (normalization values from McDonough and Sun (1995). A) and B) Central Ultrabasic-Basic Layered Unit ultramafic rocks. C) and D) Central Ultrabasic-Basic Layered Unit gabbros and gabbronorites with amphibole and biotite. E) and F) Central Ultrabasic-Basic Layered Unit gabbros and gabbronorites with amphibole.

8.1.2 Central Alkaline Basic-Intermediate Layered and Acid Unit

8.1.2.1 Gabbros and Gabbronorites

This group includes two facies the first is subalkaline (amphibole gabbros) and the second is alkaline (gabbros and gabbronorites with biotite).

The major element composition of the amphibole gabbros is SiO_2 ≈ 44-47 wt %, Na_2O+K_2O ≈ 3.3-5.5 wt %, with a high FeO_T/MgO ratio ≈ 1.1-2.1 (Fig. 8.1). They have variable contents of MgO ≈ 4.2-9.3 wt %, FeO_T ≈ 8.3-11.9 wt %, TiO_2 ≈ 1.5-3 wt %, Al_2O_3 ≈ 15-21 wt %, CaO ≈ 8.6-12.7 wt %, K_2O ≈ 0.6-2.4 wt %, and P_2O_5 ≈ 0.2-0.7 wt % (Fig. 8.2)

These rocks are subalkaline, metaluminous (ASI ≈ 0.54-0.89) and are richer in Na_2O+K_2O than the poikilitic amphibole gabbros of the previous unit, with a tholeiitic to calc-alkaline Borodin index (Fig. 8.1).

The major element compositions of the gabbros with biotite are SiO_2 ≈ 41-50 wt %, Na_2O+K_2O ≈ 3.1-6.7 wt % with a high FeO_T /MgO ratio ≈ 1.1-2.5 (Fig. 8.1). They have variable contents of MgO ≈ 3.1-6.8 wt %, FeO_T ≈ 3.4-13.8 wt %, TiO_2 ≈ 0.9-2.6 wt %, Al_2O_3 ≈ 15.6-24 wt %, CaO ≈ 7.6-13 wt %, K_2O ≈ 0.5-2.5 wt % and P_2O_5 ≈ 0.2-1.4 wt % (Fig. 8.2). The SiO_2 is strongly positively correlated with Al_2O_3; negative correlations exist between SiO_2 and TiO_2, MgO, FeO, CaO and P_2O_5 (Fig. 8.2).

Theses rocks are high-K, to ultra high-K, alkaline and metaluminous (ASI ≈ 0.66-0.94) with a subalkaline to calc-alkaline Borodin index (Fig. 8.1).

In silicate Earth–normalised diagrams the amphibole gabbros have weak negative anomalies in Nb, Ta and Ti and positive anomalies in Ba, K, and Sr and variable Zr and P (Fig. 8.5A). The rocks show variable enrichment in LREE relative to HREE, La_N/Lu_N ≈ 3.3-11.2, those with more LREE enrichment have strong positive Eu anomalies, Eu/Eu^* ≈ 0.94-2.0, but those with flatter patterns do not (Fig. 8.5B). The variability of the patterns is transitional between the gabbros with biotite from this unit and the *Central Ultrabasic-Basic Layered Unit* amphibole gabbros.

The gabbros with biotite have weak negative anomalies in Nb and Ta and positive anomalies in Ba, U, K, Pb, and Sr, and variable P and Zr (Fig. 8.5C). They show enrichment in LREE relative to HREE, La_N/Lu_N ≈ 4.9-13.6, and strong positive Eu anomalies, Eu/Eu^* ≈ 1.20-3.07 (Fig. 8.5D).

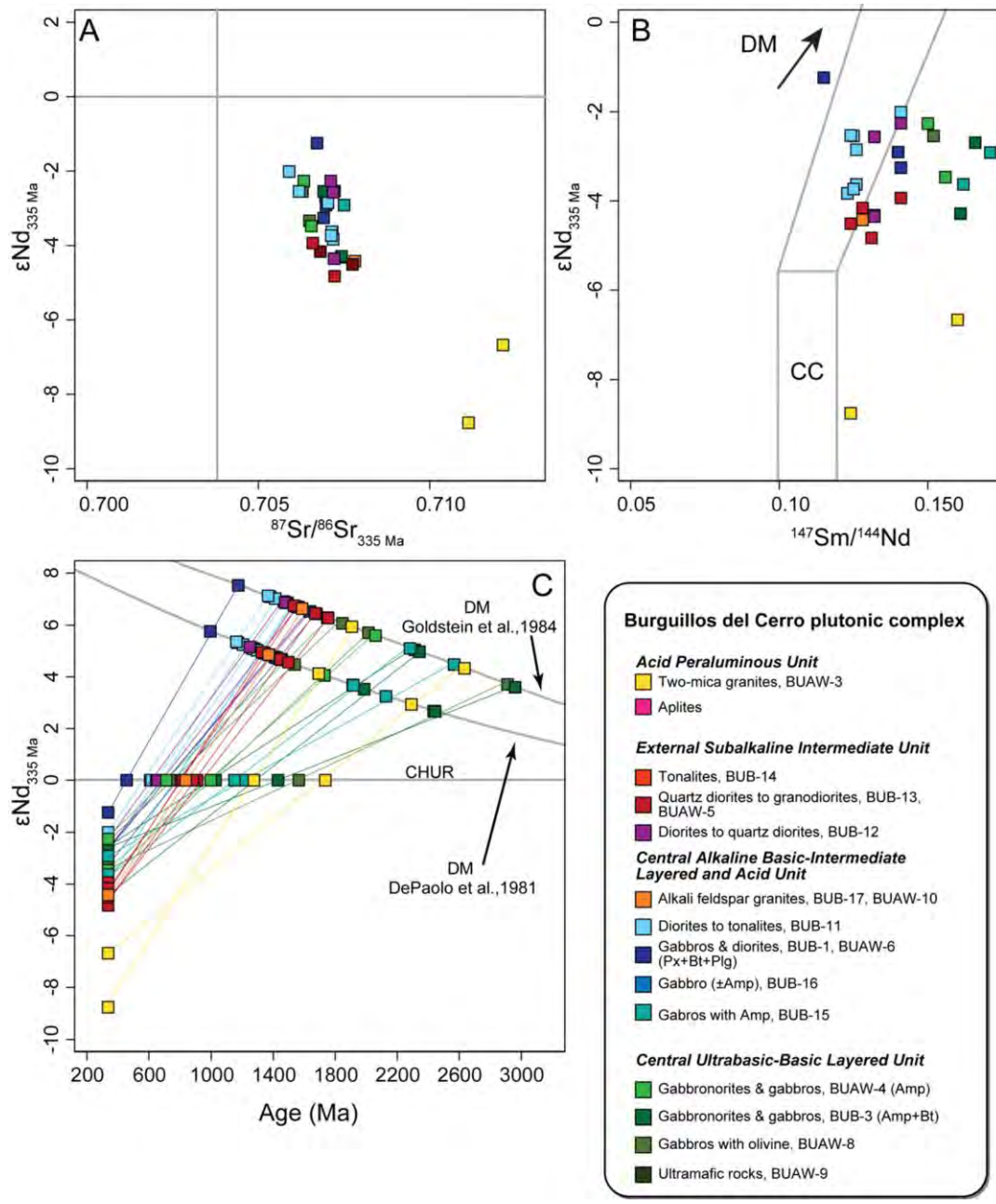

Figure 8.4: Burguillos del Cerro plutonic complex A) $\varepsilon Nd_{335\ Ma}$ vs $^{87}Sr/^{86}Sr_{335\ Ma}$. B) $\varepsilon Nd_{335\ Ma}$ vs $^{147}Sm/^{144}Nd$. C) $\varepsilon Nd_{335\ Ma}$ vs age. DM, depleted mantle (i.e., MORB-like source); OIB, ocean island basalt source; FM, fertile mantle (derived by 1–7% of partial melting of an OIB source, Swinden et al. 1990); and C) Nd model ages calculated for all rocks using the method of DePaolo, (1981) (TDM) and Goldstein et al., (1984) (TCR). CHUR normalisation taken from DePaolo (1988) and Wasserburg et al. (1981).

The isotopic composition of the amphibole gabbros is $\varepsilon Nd_{335\ Ma} \approx$ -3.6 to -1.3 and $^{87}Sr/^{86}Sr_{335\ Ma}$ values 0.707157-0.707496 (Fig. 8.4) with $^{147}Sm/^{144}Nd \approx$ 0.162-0.171 and Nd model ages from 1.9 to 2.1 Ga (Fig. 8.4). The isotopic composition of gabbros and gabbronorites with biotite is $\varepsilon Nd_{335\ Ma} \approx$ -3.3 to -1.2 and $^{87}Sr/^{86}Sr_{335\ Ma}$ values 0.706703-0.706971 (Fig. 8.4) with $^{147}Sm/^{144}Nd \approx$ 0.115-0.141 and Nd model ages from 0.9 to 1.4 Ga (Fig. 8.4).

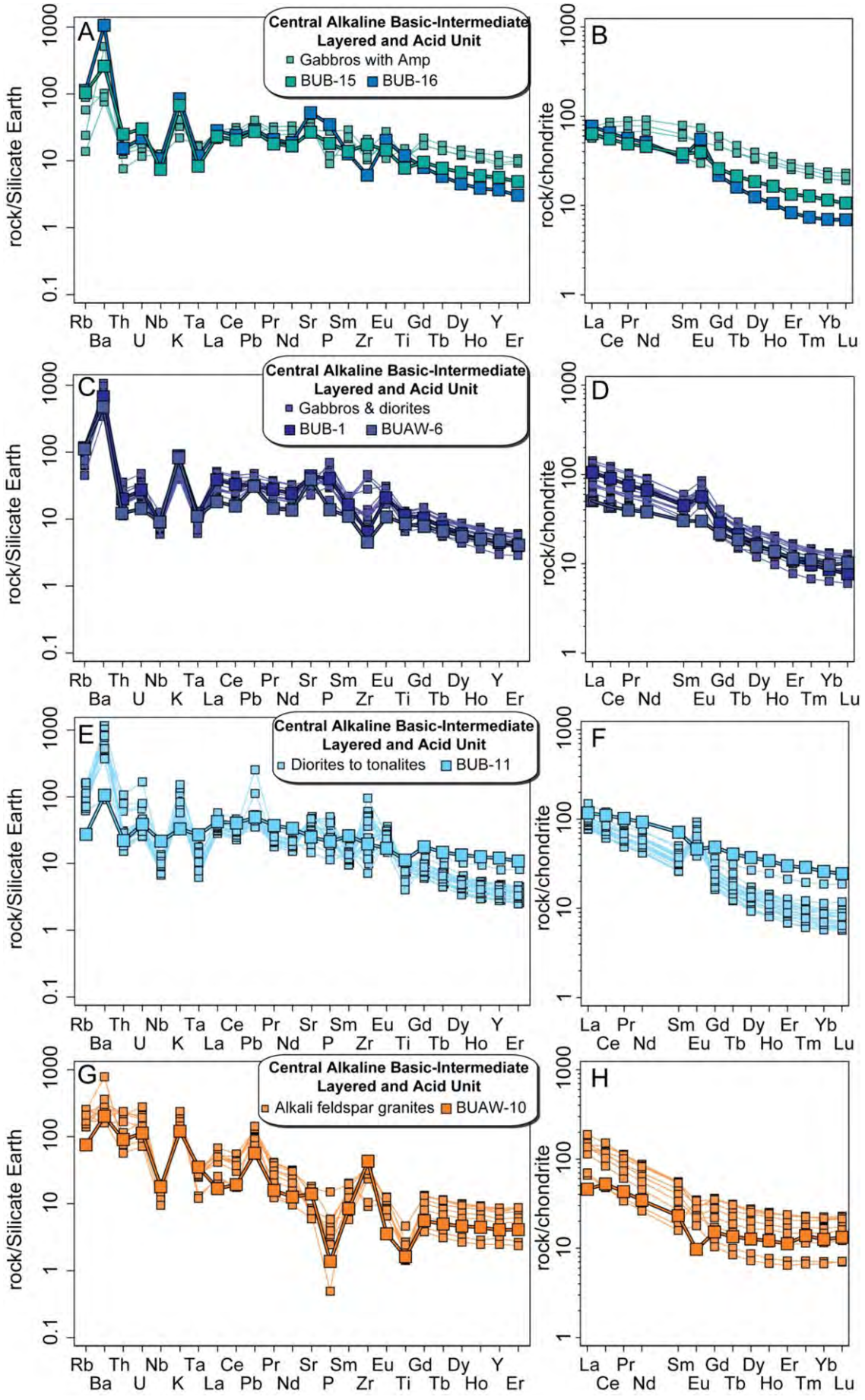
A
Central Alkaline Basic-Intermediate Layered and Acid Unit
Gabbros with Amp
BUB-15
BUB-16
B
C
Central Alkaline Basic-Intermediate Layered and Acid Unit
Gabbros & diorites
BUB-1
BUAW-6
D
E
Central Alkaline Basic-Intermediate Layered and Acid Unit
Diorites to tonalites
BUB-11
F
G
Central Alkaline Basic-Intermediate Layered and Acid Unit
Alkali feldspar granites
BUAW-10
H
rock/Silicate Earth
rock/chondrite
0.1
1
10
100
1000
Rb Th Nb Ta Ce Pr Sr Sm Eu Gd Dy Y
Ba U K La Pb Nd P Zr Ti Tb Ho Er
La Pr Sm Gd Dy Er Yb
Ce Nd Eu Tb Ho Tm Lu

8.1.2.2 Diorites to Tonalites

The major element compositions of the diorites, quartz diorites and tonalites in this unit are SiO_2 ranges from 45-60 wt %, $Na_2O+K_2O \approx$ 3.8-8.8 wt % with a high FeO_T/MgO ratio ≈ 1.3-4.1 (Fig. 8.1), variable contents of MgO ≈ 1.3-4.9 wt %, $FeO_T \approx$ 5.2-10.6 wt %, $TiO_2 \approx$ 0.8-2.7 wt %, $Al_2O_3 \approx$ 17.4-23.3 wt %, CaO ≈ 3.4-10.6 wt %, $K_2O \approx$ 0.5-4.3 wt % and $P_2O_5 \approx$ 0.2-1.1 wt % (Fig. 8.2).

These intermediate rocks are high-K to ultra-high K, alkaline and generally metaluminous but trend more towards the peraluminous field than either of the gabbros facies (ASI ≈ 0.72-1.05). Their Borodin index is alkaline to subalkaline (Fig. 8.1).

The major elements of this facies shows the same variations with SiO_2 as the gabbros with biotite from this unit. That is to say: strong positive correlation with Al_2O_3 and negative correlations between SiO_2 and TiO_2, MgO, FeO, CaO and P_2O_5 (Fig. 8.2).

In silicate Earth–normalised diagrams these intermediate compositions have negative anomalies in Nb, Ta and Ti and positive anomalies in Ba, K, Pb and Eu and variable Th, U, Sr, P and Zr (Fig. 8.5E). The rocks show variable enrichment in LREE relative to HREE, $La_N/Lu_N \approx$ 4.7-16.8, those with more LREE enrichment have strong positive Eu anomalies, the flatter patterns have slight negative anomalies, $Eu/Eu^* \approx$ 0.78-4.23 (Fig. 8.5F).

The isotopic composition of these rocks is $\varepsilon Nd_{335\ Ma} \approx$ -3.8 to -2.0 and $^{87}Sr/\ ^{86}Sr_{335\ Ma}$ values 0.705895-0.707223 (Fig. 8.4) with $^{147}Sm/^{144}Nd \approx$ 0.123-0.141 and Nd model ages from 1.1 to 1.3 Ga (Fig. 8.4).

8.1.2.3 Syenites and Alkali Feldspar Granites

The acid rocks from this unit are syenites and alkali feldspar granites, typical major element concentrations are $SiO_2 \approx$ 61-71 wt %, $Na_2O+K_2O \approx$ 8.4-11.3 wt % with high FeO_T/MgO ratio ≈ 2-12.6 (Fig. 8.1). They have a low content of MgO ≈ 0.2-1.9 wt % and $FeO_T \approx$ 1.7-3.9 wt %, moderate $TiO_2 \approx$ 0.3-0.9 wt % and CaO ≈ 1.3-5.0 wt %, high $Al_2O_3 \approx$ 14-18.1 wt % and $K_2O \approx$ 3.5-6.8 wt %, and $P_2O_5 \approx$ 0-0.3 wt % (Fig. 8.2). SiO_2 is negatively correlated with all the major elements except K_2O with which it has a weak positive correlation (Fig. 8.2).

Figure 8.5: Burguillos del Cerro plutonic complex silicate Earth- and chondrite-normalised diagrams (normalisation values from McDonough and Sun (1995). A) and B) Central Alkaline Basic-Intermediate Layered And Acid Unit gabbros with amphibole. C) and D) Central Alkaline Basic-Intermediate Layered And Acid Unit gabbros and diorites. E) and F) Central Alkaline Basic-Intermediate Layered And Acid Unit diorites and tonalities. G) and H) Central Alkaline Basic-Intermediate Layered And Acid Unit alkali feldspar granite.

These rocks are evolved metaluminous to peraluminous, (ASI ≈ 0.82-1.14) (Fig. 8.1).

In silicate Earth–normalised diagrams these acid rocks have negative anomalies in Th, Nb, P, and Ti and positive anomalies in Ba, K, Pb and Zr, and variable Ta (Fig. 8.5G). Furthermore, they all have chondrite-normalised enrichment in LREE relative to HREE, La_N/Lu_N ≈ 3.5-9.8, less evolved samples show positive Eu anomalies, whereas in more evolved samples the anomalies are negative, Eu/Eu^* ≈ 0.51-2.34 (Fig. 8.5H).

The acid alkaline rocks present $\varepsilon Nd_{335\ Ma}$ ≈ -4.4 and $^{87}Sr/^{86}Sr_{335\ Ma}$ values 0.707203-0.707813 and $^{147}Sm/^{144}Nd$ ≈ 0.128 and Nd model ages of 1.4 Ga like the alkaline gabbros to diorites (Fig. 8.4).

8.1.3 External Subalkaline Intermediate Unit

This unit includes abundant diorites, quartz diorites, tonalites, granodiorites and rare granites that may be divided into two groups: the first is transitional with the *Central Alkaline Basic-Intermediate Layered and Acid Unit* rocks and the second is subalkaline.

The major element concentrations of the first, transitional, group are SiO_2 ≈ 50-55 wt %, Na_2O+K_2O ≈ 4.5-6.5 wt % with FeO_T /MgO ≈ 0.9-2.9 (Fig. 8.1). This first group has a variable content of MgO ≈ 2.7-6.3 wt %, FeO_T ≈ 5.6-10.1 wt %, TiO_2 ≈ 0.6-2.6 wt %, Al_2O_3 ≈ 16-21 wt %, CaO ≈ 6.3-10.8 wt %, K_2O ≈ 1.2-2.5 wt % and P_2O_5 ≈ 0.1-0.9 wt % (Fig. 8.2).

The rocks of this group are medium-K to high-K, transitional, metaluminous to weakly peraluminous (ASI ≈ 0.67-1.01), and subalkaline to calc-alkaline according to their Borodin index (Fig. 8.1).

The second, main, group is quite different from the Burguillos *Central Alkaline Basic-Intermediate Layered and Acid Unit*. The major element concentrations of the second subalkaline, subgroup are SiO_2≈ 47-65 wt %, Na_2O+K_2O ≈ 2.8-9.4 wt % with FeO_T /MgO ≈ 0.9-3.8 (Fig. 8.1) with variable contents of MgO ≈ 1.1-9.9 wt %, FeO_T ≈ 1.5-10.1 wt %, TiO_2 ≈ 0.3-2.4 wt %, Al_2O_3 ≈ 9.4-22.6 wt %, CaO ≈ 3.3-15.8 wt %, K_2O ≈ 0.6-4.5 wt % and P_2O_5 ≈ 0.1-0.8 wt % (Fig. 8.2).

They are medium-K, subalkaline tholeiitic to calc-alkaline, metaluminous trending towards the peraluminous field (ASI ≈ 0.39-1.02), and with a subalkaline to tholeiitic Borodin index (Fig. 8.1).

Neither the transitional nor the subalkaline intermediate rocks of this unit show any obvious major element correlations with SiO_2, the distribution appears more dispersed (Fig. 8.2).

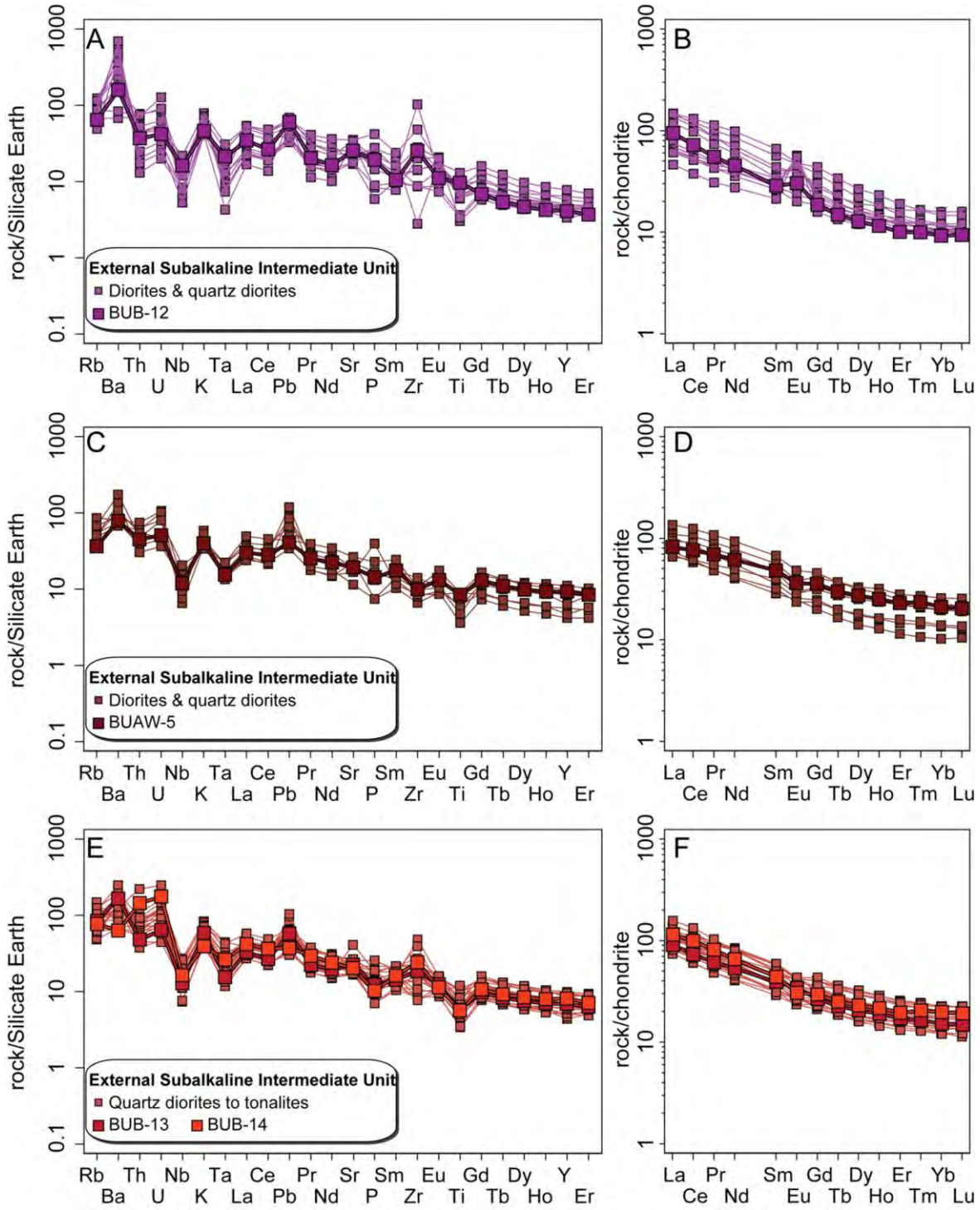

Figure 8.6: Burguillos del Cerro plutonic complex silicate Earth- and chondrite-normalised diagrams (normalisation values from McDonough and Sun (1995). A) and B) External Subalkaline Intermediate Unit diorites and quartz diorites. C) and D) External Subalkaline Intermediate Unit Diorites & quartz diorites. E) and F) External Subalkaline Intermediate Unit Quartz diorites to tonalites

In silicate Earth–normalised diagrams the transitional rocks have negative anomalies in Th, Nb, Ta and Ti and positive anomalies in Ba, K, Pb and to a lesser extent in Sr, and variable Zr and P (Fig. 8.6A). They show variable enrichment in LREE relative to HREE, $La_N/Lu_N \approx 4.3$-

15.1, that correlates with a variation from strongly positive to slightly negative Eu anomalies, $Eu/Eu^{*} \approx 0.89\text{-}3.09$ (Fig. 8.6B).

On the other hand, in silicate Earth–normalised diagrams the main group of subalkaline rocks have negative anomalies in Nb, Ta and Ti and positive anomalies in Ba, K and Pb, and variable Th, Sr, Zr and P (Fig. 8.6C - diorites and quartz diorites; Fig. 8.6E - quartz diorites to tonalites). These rocks show enrichment in LREE relative to HREE, $La_N/Lu_N \approx 3.4\text{-}12.7$, and slightly negative to positive Eu anomalies, $Eu/Eu^{*} \approx 0.73\text{-}1.90$ (Fig. 8.6D - diorites and quartz diorites; Fig. 8.6F - quartz diorites to tonalites).

The isotopic composition of these rocks is $\varepsilon Nd_{335\ Ma} \approx -4.8$ to -2.3 and $^{87}Sr/\ ^{86}Sr_{335\ Ma}$ values 0.706591-0.707745 (Fig. 8.4) and $^{147}Sm/^{144}Nd \approx 0.124\text{-}0.141$ and Nd model ages from 1.3 to 1.5 Ga which are intermediate, relative to the other units of the complex (Fig. 8.4). The transitional samples tend to have the more primitive values (see Chapter 11).

8.1.4 Acid Peraluminous Unit

This unit is formed of granites, as dykes and small plutons and aplites.

Their major element concentrations are $SiO_2 \approx 69\text{-}76$ wt %, $Na_2O+K_2O \approx 7.4$ to 10.8 wt % with low FeO_T/MgO ratio ≈ 0.5-6.3 (Fig. 8.1). They have low contents of MgO ≈ 0.2-1.1 wt %, $FeO_T \approx 0.4\text{-}2.1$ wt %, $TiO_2 \approx 0.1\text{-}0.3$ wt %, CaO ≈ 0.5-1.7 wt %, high $Al_2O_3 \approx 13\text{-}16$ wt %, $K_2O \approx 3.9\text{-}8.6$ wt %, and low $P_2O_5 \approx 0.02$ wt% (Fig. 8.2). Despite the restricted compositional range of this unit, SiO_2 is negatively correlated with all the major elements except K_2O with

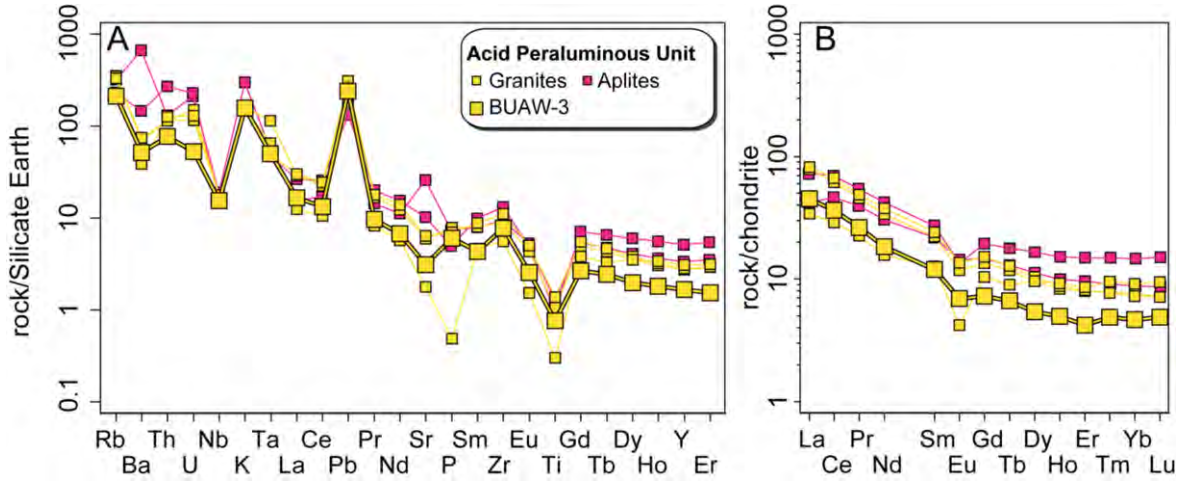

Figure 8.7: Burguillos del Cerro plutonic complex silicate Earth- and chondrite-normalised diagrams (normalisation values from McDonough and Sun (1995) A) and B) Acid Peraluminous Unit granites and aplites

	Burguillos del Cerro plutonic complex						
	Central Ultrabasic-Basic Layered Unit						
	Lherzolite	Lherzolite	Olivine gabbro	Poikilitic amphibole and biotite gabbro	Poikilitic amphibole and biotite gabbronorite	Poikilitic amphibole gabbronorite	Poikilitic amphibole gabbronorite
	BUAW-9	BUB-126	BUAW-8	BUB-45	BUB-3	BUAW-4	BUB-48
Major elements (wt %)							
SiO_2	45.67	45.27	46.28	39.92	40.71	46.00	45.74
TiO_2	0.37	0.29	0.22	1.98	2.01	1.43	1.11
Al_2O_3	5.30	9.36	11.54	17.02	15.79	18.21	17.01
FeO	9.43	8.95	7.65	15.12	16.31	10.33	6.73
MnO	0.18	0.15	0.14	0.14	0.15	0.14	0.12
MgO	27.25	21.51	18.83	6.60	7.49	6.53	8.26
CaO	6.24	10.39	11.96	14.33	12.72	12.95	16.78
Na_2O	0.49	0.77	0.33	1.66	1.28	1.46	1.99
K_2O	0.66	0.35	0.33	1.10	0.97	0.58	0.50
P_2O_5	0.09	0.07	0.05	0.18	0.20	0.20	0.30
LOI	2.46	1.05	1.12	0.57	1.08	0.35	1.20
Total	98.14	98.17	98.44	98.61	98.71	98.18	99.74
Trace elements (ppm)							
Li	16.0	6.7	8.8	6.6	4.1	4.3	6.0
Rb	22	14	15	21	18	9	7
Cs	1.3	0.5	1.7	1.3	0.4	0.3	0.2
Be	0.7	0.6	0.6	0.8	0.7	0.7	0.9
Sr	126	221	230	499	498	590	543
Ba	271	177	121	1229	1060	355	556
Sc	23.1	33.1	34.5	39.1	42.1	40.9	46.5
V	91.8	108.1	100.6	770.5	807.8	420.4	241.6
Cr	1882.3	1294.8	889.5	123.8	33.8	34.3	439.1
Co	96.2	86.2	76.8	83.1	106.6	45.4	37.4
Ni	753.8	491.9	429.1	86.3	23.4	14.7	106.6
Cu	31.1	31.0	108.8	144.0	148.0	47.0	49.6
Zn	71.4	67.2	51.2	77.4	79.1	87.0	46.1
Ga	5.9	7.5	9.6	19.1	20.0	19.1	15.2
Y	8.4	7.2	7.6	19.8	20.3	31.0	23.8
Nb	2.1	1.4	1.0	3.6	3.1	4.3	6.1
Ta	0.3	0.2	0.2	0.2	0.3	0.4	0.4
Zr	42	36	21	415	89	56	73
Hf	1.0	1.1	0.5	14.4	3.7	1.9	2.9
Sn	0.8	0.3	0.6	1.5	1.3	1.7	1.4
Tl	0.2	0.2	0.2	0.2	0.2	0.1	0.1
Pb	4	4	5	5	4	4	4
U	1.18	0.71	0.53	0.29	0.26	0.26	0.20
Th	3.2	2.1	1.2	0.8	0.7	1.0	0.6
La	7.4	4.8	4.6	8.4	8.3	12.8	13.3
Ce	15.1	10.8	8.0	22.2	22.6	32.3	35.6
Pr	1.8	1.4	1.1	3.5	3.4	4.8	5.4
Nd	7.5	5.9	5.1	17.2	16.2	22.3	25.0
Sm	1.81	1.54	1.51	4.67	4.52	6.22	6.18
Eu	0.44	0.46	0.44	1.74	1.80	1.68	1.93
Gd	1.67	1.44	1.47	4.70	4.56	5.95	6.07
Tb	0.25	0.22	0.23	0.72	0.71	0.93	0.90
Dy	1.52	1.31	1.35	4.15	3.99	5.46	5.03
Ho	0.30	0.26	0.26	0.79	0.79	1.07	0.95
Er	0.78	0.68	0.69	1.99	2.10	2.75	2.40
Tm	0.12	0.10	0.10	0.27	0.28	0.40	0.33
Yb	0.69	0.62	0.57	1.63	1.62	2.40	1.98
Lu	0.11	0.09	0.09	0.25	0.23	0.36	0.31
Isotopes							
$^{87}Rb/^{86}Sr$		0.182		0.122			0.039
$^{87}Sr/^{86}Sr$		0.707155		0.707535			0.706512
$^{87}Sr/^{86}Sr_{335\ Ma}$		0.706285		0.706955			0.706328
$^{147}Sm/^{144}Nd$		0.152		0.166			0.150
$^{143}Nd/^{144}Nd$		0.512410		0.512434			0.512419
$^{143}Nd/^{144}Nd_{335\ Ma}$		0.512076		0.512069			0.512090
$\varepsilon Nd_{335\ Ma}$		-2.6		-2.7			-2.3
$T_{DM\ (Ga)}$		1.5		1.9			1.5

Table 8.1: Representative major and trace element and Rb-Sr and Sm-Nd isotope data for the Burguillos del Cerro plutonic complex. Nd model ages calculated for all rocks using the method of DePaolo, (1981) (TDM)

	Burguillos del Cerro plutonic complex									
	Central Alkaline Basic-Intermediate Layered And Acid Unit									
	Gabbro with amphibole	Gabbro with amphibole	Diorite	Gabbro	Gabbro	Diorite	Quartz diorite	Diorite	Quartz syenite	Alkali feldspar granite
	BUB-15	BUB-119	BUB-16	BUB-1	BUB-63	BUAW-6	BUB-11	BUB-1	BUB-112	BUAW-10
Major elements (wt %)										
SiO_2	45.75	43.82	47.13	47.49	42.98	49.10	49.81	49.25	61.33	69.75
TiO_2	1.53	2.14	2.32	2.24	2.27	1.69	2.22	1.59	0.91	0.32
Al_2O_3	16.79	20.41	20.69	20.20	17.85	19.26	18.02	21.74	16.74	16.94
FeO	10.40	10.17	8.33	8.30	12.38	7.20	9.55	8.18	3.89	1.74
MnO	0.14	0.11	0.08	0.08	0.15	0.11	0.17	0.09	0.07	0.04
MgO	7.21	5.75	4.22	5.41	5.63	5.95	4.26	3.41	1.90	0.23
CaO	12.23	11.43	8.64	8.93	10.40	10.14	8.82	8.37	5.00	1.61
Na_2O	1.44	2.37	2.97	3.06	2.72	2.08	3.71	3.50	4.12	4.96
K_2O	1.92	1.17	2.38	2.51	2.04	2.34	0.93	1.94	4.26	3.45
P_2O_5	0.37	0.18	0.70	0.82	0.94	0.28	0.43	0.46	0.30	0.03
LOI	0.56	0.98	1.05	0.36	1.75	0.36	0.47	0.42	0.58	0.34
Total	98.33	98.53	98.50	99.41	99.11	98.51	98.39	98.95	99.10	99.40
Trace elements (ppm)										
Li	6.8	19.6	24.9	8.1	5.1	4.6	9.2	5.5	12.4	6.1
Rb	62	54	68	70	49	68	16	45	94	45
Cs	1.5	1.6	1.7	0.7	0.6	1.0	0.6	0.3	1.0	0.7
Be	1.0	1.3	1.1	1.2	0.9	1.0	1.4	0.9	3.2	3.3
Sr	532	641	1036	884	527	792	493	901	334	277
Ba	1708	598	6972	4454	4531	3141	696	5101	2387	1330
Sc	48.9	42.6	18.1	19.5	38.5	23.9	34.5	14.3	14.1	4.6
V	374.3	528.1	222.7	239.3	456.3	192.4	283.9	176.7	125.5	5.4
Cr	47.2	47.4	17.2	52.3	32.2	157.9	24.7	55.7	127.2	14.2
Co	50.5	52.0	29.6	58.5	41.0	26.8	36.1	20.2	7.9	12.6
Ni	26.9	40.7	16.9	20.2	14.6	27.2	13.9	18.9	22.2	2.0
Cu	31.2	137.9	30.7	25.6	81.3	16.7	22.2	18.6	4.9	6.2
Zn	68.7	62.2	70.8	66.7	77.4	56.0	87.6	52.5	42.3	24.8
Ga	18.3	22.3	20.4	21.7	20.4	18.8	20.5	20.9	19.1	21.0
Y	24.3	40.4	15.8	19.2	26.3	20.6	51.6	13.6	31.9	17.5
Nb	4.9	8.3	7.1	5.9	5.2	6.0	14.2	4.8	10.7	11.8
Ta	0.3	0.6	0.4	0.4	0.3	0.4	1.0	0.3	1.1	1.3
Zr	183	118	64	67	101	48	206	543	110	447
Hf	1.1	4.4	0.6	1.9	3.8	1.3	2.6	19.3	3.7	6.2
Sn	1.6	3.9	0.9	0.9	1.5	0.7	1.3	0.7	2.5	1.8
Tl	0.4	0.3	0.3	0.4	0.3	0.3	0.1	0.3	0.4	0.3
Pb	4	6	4	5	6	5	7	6	14	8
U	0.61	0.36	0.44	0.56	0.51	0.29	0.78	0.64	3.38	2.30
Th	2.0	1.1	1.2	1.6	1.6	1.0	1.7	1.7	9.2	7.2
La	15.0	16.7	18.3	25.0	24.2	11.9	27.6	18.2	31.0	10.8
Ce	34.1	47.3	39.9	55.3	54.7	26.4	67.4	38.1	73.0	32.2
Pr	4.5	7.2	5.2	7.0	7.2	3.7	9.4	4.9	9.4	4.0
Nd	20.9	35.5	23.2	30.3	32.7	17.1	42.3	20.7	37.4	15.7
Sm	5.61	9.30	5.12	6.60	7.57	4.46	10.55	4.31	7.94	3.41
Eu	2.23	2.87	3.09	3.18	3.57	1.66	2.59	3.93	1.89	0.54
Gd	5.17	9.27	4.34	5.64	7.09	4.28	9.65	3.90	6.92	3.02
Tb	0.77	1.40	0.58	0.76	0.96	0.66	1.46	0.51	1.10	0.49
Dy	4.53	8.35	3.05	4.08	5.60	3.77	9.10	2.75	6.23	3.10
Ho	0.90	1.68	0.57	0.74	1.09	0.74	1.86	0.52	1.33	0.66
Er	2.14	4.33	1.32	1.75	2.58	1.82	4.78	1.23	3.79	1.80
Tm	0.32	0.61	0.18	0.24	0.35	0.27	0.71	0.16	0.55	0.34
Yb	1.85	3.50	1.12	1.38	2.07	1.53	4.18	0.95	3.49	2.02
Lu	0.26	0.52	0.17	0.19	0.29	0.25	0.60	0.15	0.52	0.33
Isotopes										
$^{87}Rb/^{86}Sr$		0.243			0.268			0.145	0.813	
$^{87}Sr/^{86}Sr$		0.708316			0.708250			0.707823	0.711688	
$^{87}Sr/^{86}Sr_{335\ Ma}$		0.707157			0.706971			0.707132	0.707813	
$^{147}Sm/^{144}Nd$		0.162			0.140			0.126	0.128	
$^{143}Nd/^{144}Nd$		0.512376			0.512365			0.512298	0.512261	
$^{143}Nd/^{144}Nd_{335\ Ma}$		0.512021			0.512057			0.512021	0.511980	
$\varepsilon Nd_{335\ Ma}$		-3.6			-2.9			-3.6	-4.4	
$T_{DM\ (Ga)}$		1.9			1.4			1.3	1.4	

Table 8.1: Continued.

	Burguillos del Cerro plutonic complex									
	External Subalkaline Intermediate Unit							*Acid Peraluminous Unit*		
	Diorite	Quartz diorite	Quartz diorite	Quartz diorite	Quartz monzo diorite	Tonalite	Tonalite	Two mica granite	Two mica granite	Aplite
	BUB-24	BUB-12	BUAW-5	BUB-23	BUB-13	BUB-14	BUB-83	BUAW-3	BUB-103	BUB-113
Major elements (wt %)										
SiO_2	49.88	51.84	51.87	48.48	54.46	59.74	54.42	74.18	72.59	69.23
TiO_2	2.57	1.91	1.64	1.21	1.14	1.11	1.34	0.15	0.21	0.25
Al_2O_3	18.05	17.13	17.30	14.96	17.77	16.29	17.23	14.54	14.23	15.92
FeO	10.08	8.70	9.06	7.47	6.31	5.62	6.97	1.03	1.70	0.37
MnO	0.12	0.18	0.16	0.42	0.12	0.11	0.13	0.04	0.06	0.02
MgO	3.65	4.59	4.93	5.62	4.40	3.36	4.42	0.38	0.78	0.72
CaO	7.86	8.33	8.89	15.75	8.60	7.20	8.28	1.11	0.94	1.67
Na_2O	3.46	3.60	2.58	2.65	3.70	3.73	3.86	2.81	3.62	2.08
K_2O	2.23	1.30	1.13	1.27	1.66	1.12	1.51	4.48	4.58	8.56
P_2O_5	0.85	0.39	0.29	0.34	0.25	0.21	0.24	0.12	0.16	0.15
LOI	0.67	0.47	0.42	0.85	0.42	0.62	0.35	0.34	0.60	0.68
Total	99.42	98.44	98.27	99.02	98.83	99.10	98.75	99.18	99.47	99.65
Trace elements (ppm)										
Li	13.8	9.6	8.0	12.7	10.3	11.9	13.4	41.1	72.6	8.4
Rb	69	39	22	51	50	46	44	127	212	190
Cs	0.7	1.0	1.1	1.7	1.3	2.1	0.9	5.3	10.1	3.0
Be	1.4	1.3	1.2	1.9	1.5	2.1	1.7	2.5	7.5	4.2
Sr	695	500	382	438	449	403	438	62	118	510
Ba	1852	1050	518	530	1092	416	1116	341	453	4413
Sc	29.1	19.7	27.7	22.9	27.6	20.0	25.8	2.2	4.4	5.2
V	174.4	225.3	223.5	198.6	140.2	139.3	191.8	9.6	25.8	27.3
Cr	80.0	92.7	24.8	238.1	115.9	90.8	176.7	28.6	228.5	195.7
Co	19.3	38.3	36.1	31.4	33.4	33.9	25.0	16.2	4.2	1.1
Ni	35.1	39.2	11.4	83.7	36.6	28.6	39.4	3.6	24.8	12.8
Cu	21.7	33.1	23.0	32.5	32.2	18.6	27.1	3.2	3.5	5.1
Zn	87.4	89.8	101.1	92.9	58.9	55.4	64.9	38.2	22.5	12.1
Ga	21.4	17.7	18.4	18.2	17.7	17.5	17.8	13.7	17.0	11.5
Y	33.2	17.6	39.8	24.2	29.4	34.8	29.2	7.1	11.7	14.4
Nb	14.4	10.6	7.8	8.3	8.5	10.8	11.3	10.1	11.5	12.4
Ta	1.1	0.8	0.6	0.8	0.6	1.0	0.9	1.8	4.2	2.0
Zr	504	263	105	84	194	252	196	81	95	99
Hf	18.4	1.2	2.3	3.0	2.0	2.1	7.5	1.6	3.5	3.5
Sn	1.5	1.2	1.8	1.4	1.3	3.2	1.9	2.2	2.3	1.4
Tl	0.4	0.3	0.2	0.3	0.3	0.3	0.3	0.9	1.3	0.8
Pb	10	9	6	18	9	6	11	36	46	27
U	0.96	0.85	1.04	2.13	1.30	3.55	1.38	1.07	2.33	4.31
Th	3.4	2.9	3.6	5.9	3.8	11.4	4.9	6.1	9.3	10.3
La	34.5	22.3	19.4	23.8	21.3	27.2	24.4	10.7	18.6	9.9
Ce	80.1	44.1	46.6	52.1	44.6	60.8	53.4	22.3	37.7	28.6
Pr	10.4	5.1	6.4	6.3	5.7	7.5	6.9	2.5	4.2	3.7
Nd	44.8	20.6	28.0	25.4	24.4	29.8	28.7	8.4	15.4	14.0
Sm	9.72	4.23	7.11	5.30	5.78	6.51	6.82	1.76	3.26	3.23
Eu	2.68	1.70	2.03	1.45	1.92	1.73	2.14	0.39	0.66	0.81
Gd	8.66	3.69	7.06	4.89	5.30	5.83	6.68	1.44	2.67	2.92
Tb	1.22	0.53	1.08	0.72	0.81	0.91	1.02	0.24	0.43	0.47
Dy	6.53	3.14	6.67	4.25	5.06	5.64	6.17	1.33	2.36	2.76
Ho	1.26	0.63	1.37	0.87	1.03	1.18	1.20	0.27	0.45	0.54
Er	3.03	1.60	3.66	2.32	2.74	3.09	3.15	0.67	1.27	1.53
Tm	0.41	0.25	0.58	0.35	0.41	0.51	0.47	0.12	0.19	0.22
Yb	2.35	1.49	3.40	2.17	2.44	3.17	2.84	0.75	1.23	1.41
Lu	0.36	0.23	0.50	0.32	0.36	0.47	0.45	0.12	0.17	0.21
Isotopes										
$^{87}Rb/^{86}Sr$	0.284			0.340			0.290		5.222	
$^{87}Sr/^{86}Sr$	0.708566			0.708425			0.707976		0.736026	
$^{87}Sr/^{86}Sr_{335\ Ma}$	0.707213			0.706802			0.706591		0.711127	
$^{147}Sm/^{144}Nd$	0.132			0.128			0.141		0.124	
$^{143}Nd/^{144}Nd$	0.512273			0.512274			0.512314		0.512030	
$^{143}Nd/^{144}Nd_{335Ma}$	0.511984			0.511993			0.512005		0.511758	
$\varepsilon Nd_{335\ Ma}$	-4.4			-4.2			-3.9		-8.8	
$T_{DM\ (Ga)}$	1.4			1.3			1.5		1.7	

Table 8.1: Continued.

which it has a weak positive correlation (Fig. 8.2).

The rocks in this unit are peraluminous (ASI ≈ 0.97-1.30) (Fig. 8.1).

In silicate Earth–normalised diagrams the peraluminous granites have negative anomalies in Ba, Nb, Sr and Ti and positive anomalies in U, K, Pb and Zr and variable P (Fig. 8.7A). Furthermore, these rocks have low contents in REE and all have chondrite-normalised enrichment in LREE relative to HREE, La_N/Lu_N ≈ 3.6-11.5, with negative Eu anomalies, Eu/Eu^* ≈ 0.34-0.64 (Fig. 8.7B).

The rocks have $\varepsilon Nd_{335\ Ma}$ ≈ -8.8 and -6.7 and $^{87}Sr/\ ^{86}Sr_{335\ Ma}$ values of 0.711127 and 0.712135 (Fig. 8.4). In addition, they have $^{147}Sm/^{144}Nd$ ≈ 0.124 and 0.160 and relatively old Nd model ages of 1.7 and 2.3 Ga (Fig. 8.4).

8.2 Valencia del Ventoso Plutonic Complex

8.2.1 Main Pluton Alkaline to Subalkaline Basic-Acid Unit

The main pluton is concentrically zoned with gabbros and diorites at its core, surrounded by quartz diorites to granodiorites and granites at the outer rim (Fig. 4.2). Two groups can be defined in this unit. The first is alkaline to transitional and the second is subalkaline (Fig. 8.8).

The major element concentrations of the alkaline to transitional rocks are SiO_2≈ 47-58 wt %, Na_2O+K_2O ≈ 4.9-7.8 wt % with high FeO_T /MgO ≈ 1.4-4.4 (Fig. 8.8). This group has MgO ≈ 1.4-6.2 wt %, FeO_T ≈ 6.8-11.7 wt %, TiO_2 ≈ 1.0-2.6 wt %, Al_2O_3 ≈ 14.7-20 wt %, CaO ≈ 4.3-9.7 wt %, K_2O ≈ 1.5-3.1 wt % and P_2O_5 ≈ 0.3-0.8 wt % (Fig. 8.9). SiO_2 is negatively correlated with TiO_2, FeO_T, MgO, CaO and, albeit less clearly so, with P_2O_5 (Fig. 8.9).

The rocks of this group are high-K to ultra-high K compositions, alkaline to transitional, metaluminous (ASI ≈ 0.66-1.12), and alkaline to subalkaline in the Borodin index plot (Fig. 8.8).

The major element concentrations of the subalkaline rocks are SiO_2 ≈ 51-73 wt %, Na_2O+K_2O ≈ 2-8.1 wt % with a broad range of FeO_T/MgO ≈ 0.6-4.2 wt % (Fig. 8.8). This group has MgO ≈ 0.3-15.8 wt %, FeO_T ≈ 1.2-10.2 wt %, TiO_2 ≈ 0.1-1.5 wt %, Al_2O_3 ≈ 7.5-18.3 wt %, CaO ≈ 2.2-10.7 wt %, K_2O ≈ 0.7-4.8 wt % and P_2O_5 ≈ 0.1-0.4 wt % (Fig. 8.9). SiO_2 shows a strong correlation with K_2O, and negative correlations with TiO_2, FeO_T, MgO, CaO (Fig. G9). In the diorites and quartz diorites the slope of the MgO vs SiO_2 correlation is much steeper than in the granodiorites and granites. Between 55-60 wt % SiO_2 the rocks show a wide range of Al_2O_3, 12-20 wt % (Fig. 8.9) whereas in the more evolved compositions the Al_2O_3 decreases marking a negative correlation.

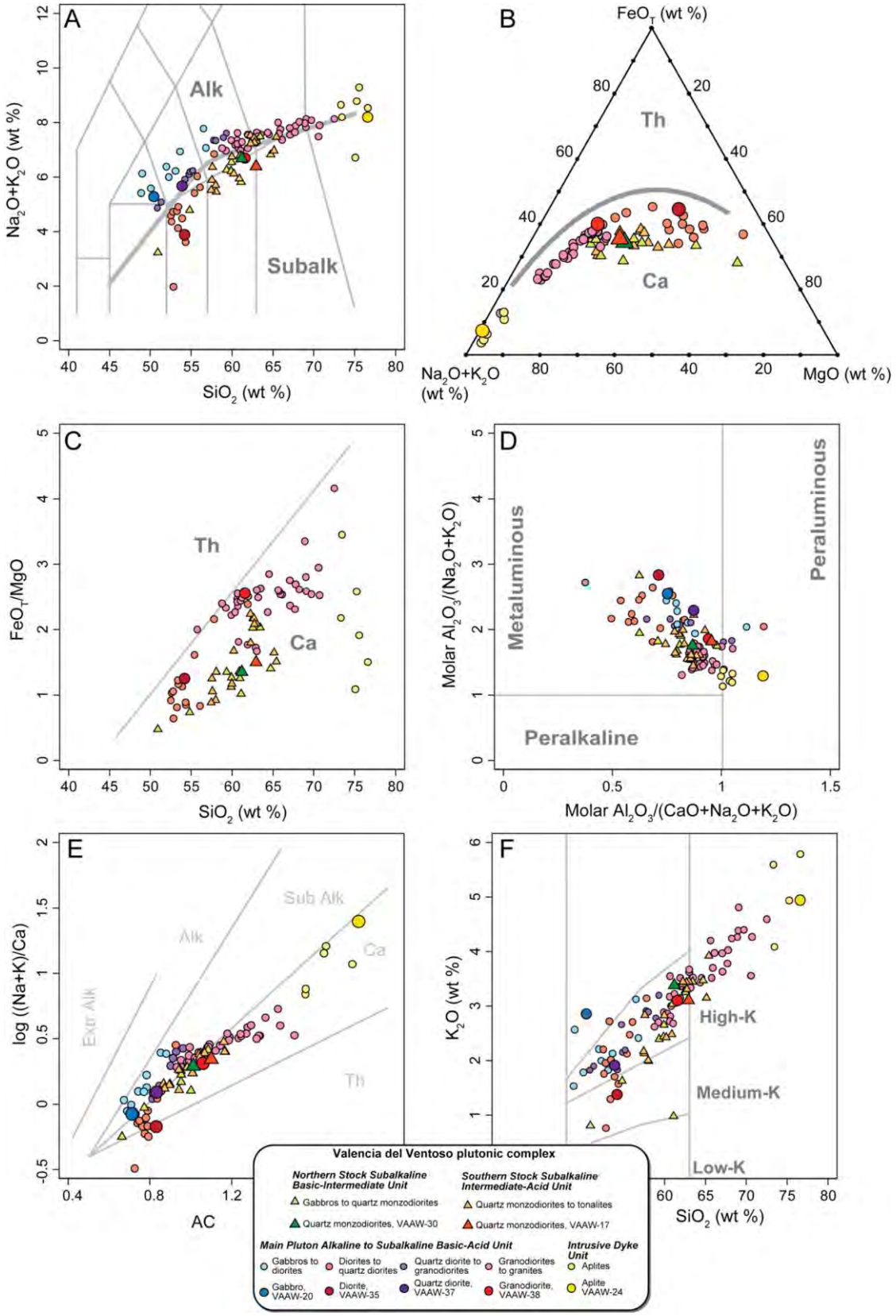

Figure 8.8: Valencia del Ventoso plutonic complex whole-rock compositions. A) Total alkalis vs SiO_2 (TAS) (fields from Le Maitre et al., 1989). B) (Na_2O+K_2O) - FeO_T - MgO (AFM) (fields from Kuno, 1968). C) FeO_T /MgO vs SiO_2 (fields from Frost et al., 2001). D) Molar Al_2O_3/ (Na_2O+K_2O) vs Molar Al_2O_3/ (CaO+ Na_2O+K_2O) (fields from Shand, 1947). E) Borodin index. F) K_2O vs SiO_2 (smaller lighter symbols data from Pons, 1981 and Sarrionandia, 2005). Abbreviations as in Fig. 8.1

The rocks of this second group are high-K, subalkaline, calc-alkaline, metaluminous trending toward peraluminous (ASI ≈ 0.37-1.2), and are subalkaline to tholeiitic in the Borodin index plot (Fig. 8.8).

In silicate Earth–normalised diagrams the alkaline compositions have a weak negative anomaly in Ti and positive anomalies in Ba and K and, to a less extent, Pb and Sr and variable Th, U, Nb and Ta and Zr (Fig. 8.10A). In the same diagrams the transitional compositions have negative anomalies in Nb, Ta, and Ti and positive anomalies in Ba and K and variable Pb, P and Zr (Fig. 8.10C). The subalkaline compositions have negative anomalies in Nb, Ta, Ti and to a lesser extent, P and positive anomalies in K, Pb and Zr, and variable Ba, Th and U (Fig. 8.10E - diorites and quartz diorites; Fig. 8.10G - granodiorites and granites). Furthermore, these rocks all have chondrite-normalised enrichment in LREE relative to HREE, La_N/Lu_N ≈ 3.5-13.1, and negative to flat Eu anomalies, Eu/Eu^* ≈ 0.49-0.92 (Fig. 8.10B, 8.10D, 8.10F and 8.10H).

Both the alkaline and transitional compositions have $\varepsilon Nd_{335\ Ma}$ ≈ -2.5 to -1.5 and $^{87}Sr/\ ^{86}Sr_{335\ Ma}$ values, 0.706383-0.706778, $^{147}Sm/^{144}Nd$ ≈ 0.118-0.143 and the same range of Nd model ages 1.1-1.3 Ga (Fig. 8.11). On the other hand, the subalkaline rocks present a range of $\varepsilon Nd_{335\ Ma}$ ≈ -4.6 to -0.5 and $^{87}Sr/\ ^{86}Sr_{335\ Ma}$ values, 0.705348-0.707251, $^{147}Sm/^{144}Nd$ ≈ 0.114-0.144 and Nd model ages of 1.2-1.5 (Fig. 8.11).

8.2.2 Northern Stock Subalkaline Basic-Intermediate Unit

The Northern stock is composed of a gabbro to quartz monzodiorite association.

Their major element concentrations are SiO_2 ≈ 50-64 wt %, Na_2O+K_2O ≈ 3.2-7.5 wt %, a wide range in FeO_T /MgO ≈ 0.5-2.2 with elevated in K_2O ≈ 0.8-3.4 wt % (Fig. 8.8). They have MgO ≈ 2.4-14.8 wt %, FeO_T ≈ 3.8-7.3 wt %, TiO_2 ≈ 0.4-1.0 wt %, Al_2O_3 ≈ 13.2-16.7 wt %, CaO ≈ 4-9.4 wt % and P_2O_5 ≈ 0.1-0.2 wt % (Fig. 8.9). SiO_2 is positively correlated with K_2O, negative correlations exist with MgO, FeO and CaO (Fig. 8.9).

The rocks are high-K, subalkaline, calc-alkaline, metaluminous (ASI ≈ 0.60-0.98), with a tholeiitic to calc-alkaline Borodin index (Fig. 8.8).

In silicate Earth–normalised diagrams the rocks have positive anomalies in Rb, Th, K and Pb and negative anomalies in Ba, Nb, Ta, Ti and P (Fig. 8.12A). In addition, they show chondrite-normalised enrichment in LREE relative to HREE, La_N/Lu_N ≈ 5.4-14.1, and have negative to positive Eu anomalies, Eu/Eu^* ≈ 0.58-1.29 (Fig. 8.12B).

These rocks have $\varepsilon Nd_{335\ Ma}$ in the range -5.8 to -2.9 and restricted $^{87}Sr/^{86}Sr_{335\ Ma}$, 0.706483-

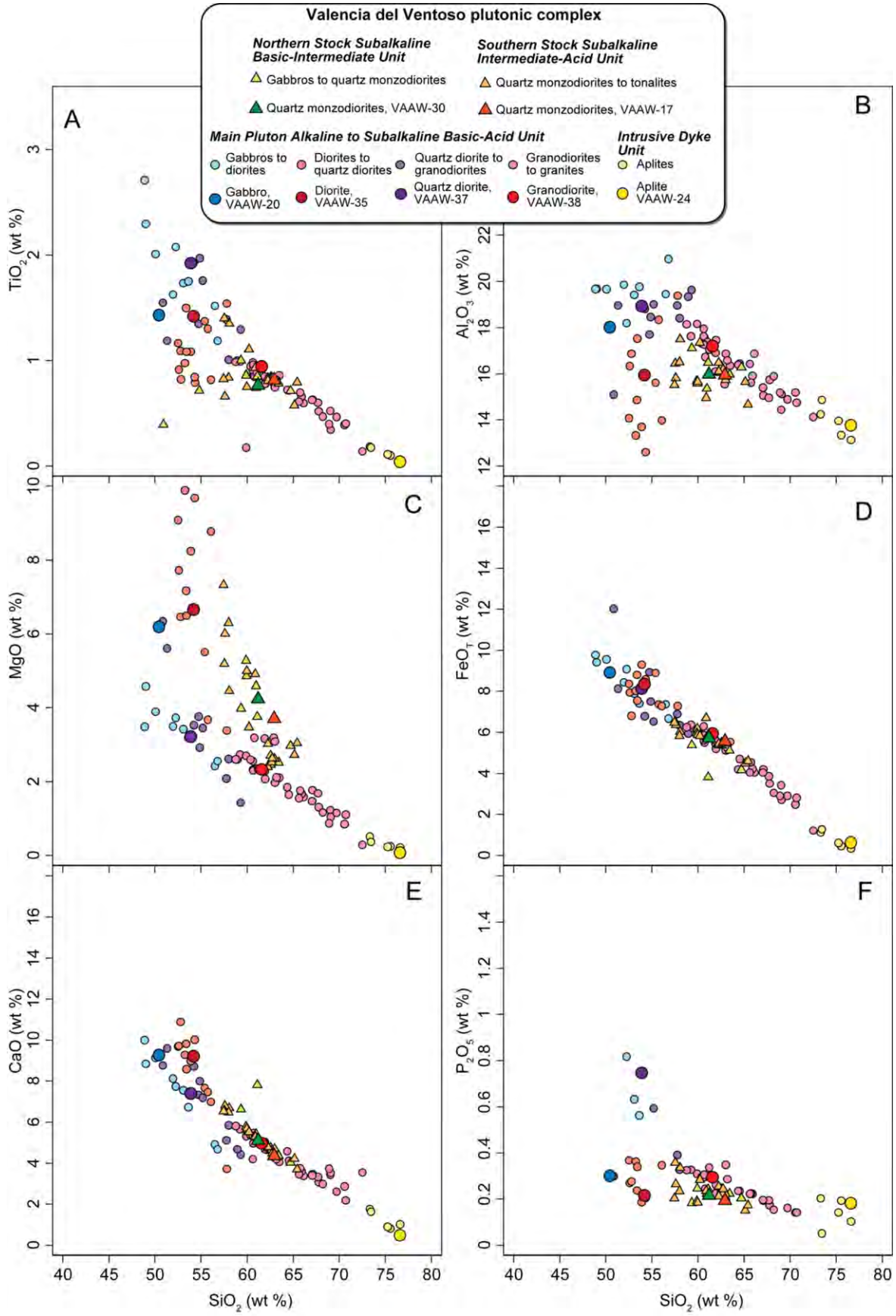

Figure 8.9: Valencia del Ventoso plutonic complex Harker diagrams: A) TiO_2 vs SiO_2 B) Al_2O_3 vs SiO_2. C) MgO vs SiO_2. D) FeO_T vs SiO_2. E) CaO vs SiO_2. F) P_2O_5 vs SiO_2. (smaller lighter symbols data from Pons, 1981 and Sarrionandia, 2005).

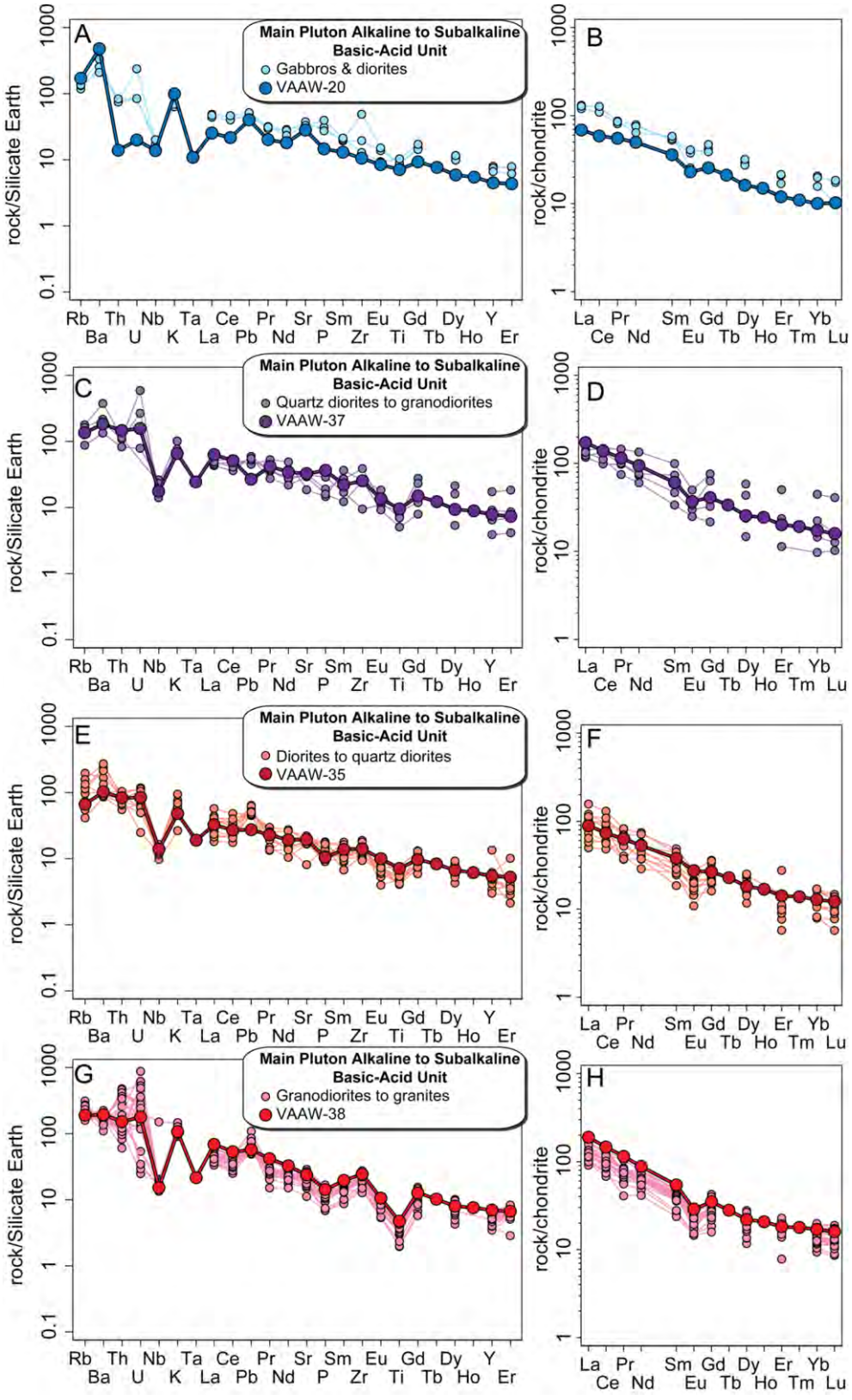

Figure 8.10: Valencia del Ventoso plutonic complex silicate Earth- and chondrite-normalised diagrams (normalization values from McDonough and Sun (1995). A) and B) Main Pluton Alkaline To Subalkaline Basic-Acid Unit gabbros and diorites. C) and D) Main Pluton Alkaline To Subalkaline Basic-Acid Unit quartz diorites to granodiorites. E) and F) Main Pluton Alkaline To Subalkaline Basic-Acid Unit diorites to quartz diorites. G) and H) Main Pluton Alkaline To Subalkaline Basic-Acid Unit granodiorites to granites. (smaller lighter symbols data from Sarrionandia, 2005).

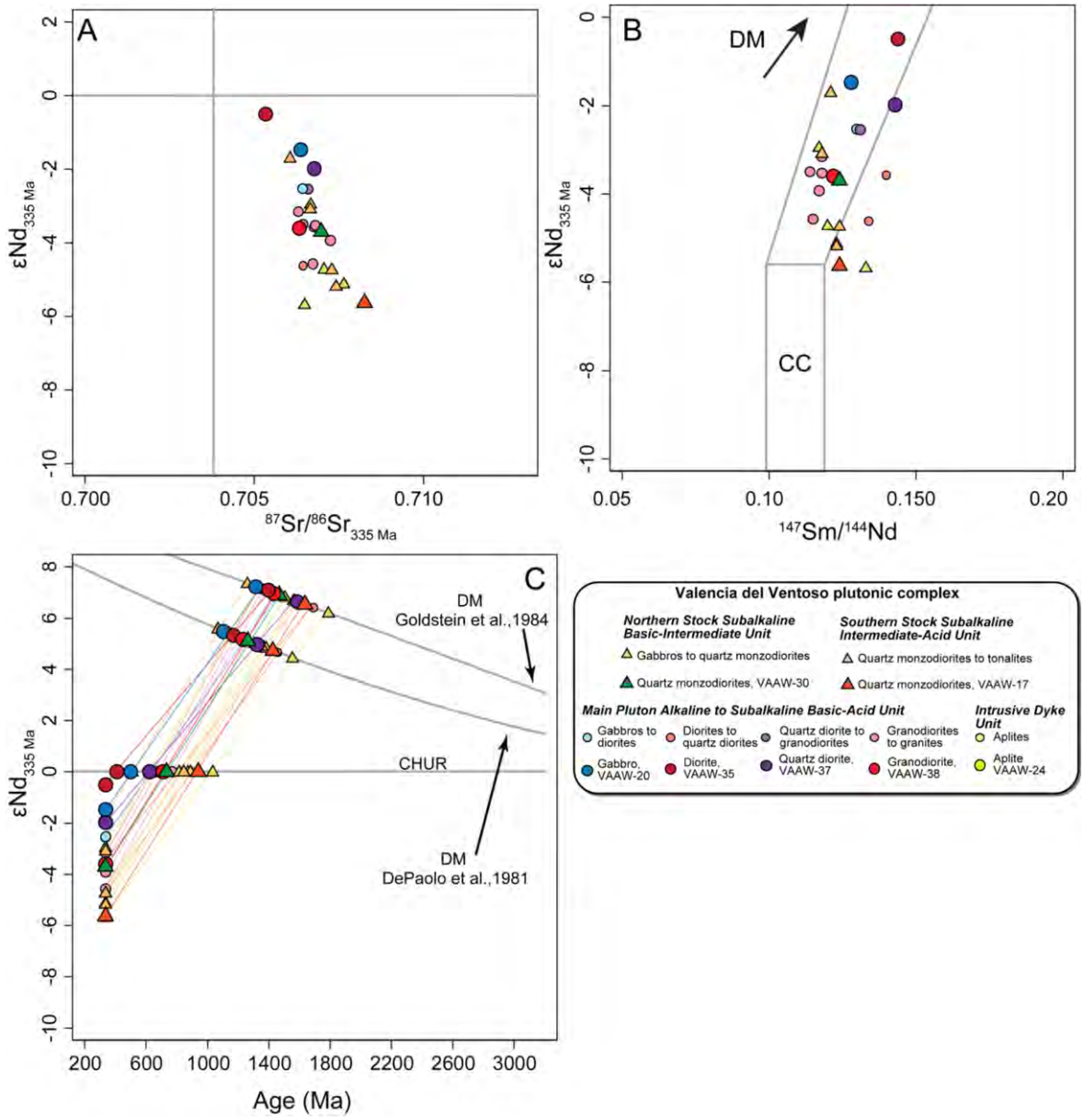

Figure 8.11: Valencia del Ventoso plutonic complex. A) εNd_i vs $^{87}Sr/^{86}Sr$. B) εNd_i vs $^{147}Sm/^{144}Nd$. C) εNd_i vs age. (smaller lighter symbols data from Sarrionandia, 2005). DM, depleted mantle (i.e., MORB-like source); OIB, ocean island basalt source; FM, fertile mantle (derived by 1–7% of partial melting of an OIB source, Swinden et al. 1990); and C) Nd model ages calculated for all rocks using the method of DePaolo, (1981) (TDM) and Goldstein et al., (1984) (TCR). CHUR normalisation taken from DePaolo (1988) and Wasserburg et al. (1981).

0.707643 (Fig. 8.11). Their $^{147}Sm/^{144}Nd$ ranges from 0.117-0.133 and Nd model ages from 1.1-1.6 Ga (Fig. 8.11).

8.2.3 Southern Stock Subalkaline Intermediate-Acid Unit

The Southern stock rocks are quartz diorites, quartz monzodiorites and tonalites.

Their major element concentrations are SiO_2 ≈ 56-64 wt %, Na_2O+K_2O ≈ 5.4-7.5 wt % a

restricted range of FeO_T /MgO ≈ 0.9-2.2 and a K-rich character K_2O ≈ 2.0-3.9 wt % (Fig. 8.8). They have MgO ≈ 2.3-7.2 wt %, FeO_T ≈ 4.4-6.5 wt %, TiO_2 ≈ 0.6-1.4 wt %, Al_2O_3 ≈ 15-17 wt %, CaO ≈ 3.6-6.7 wt %, and P_2O_5 ≈ 0.2-0.4 wt % (Fig. 8.9). As in the Northern Stock, in this unit SiO_2 is positively correlated with K_2O, negative correlations exist with MgO, FeO and CaO (Fig. 8.9).

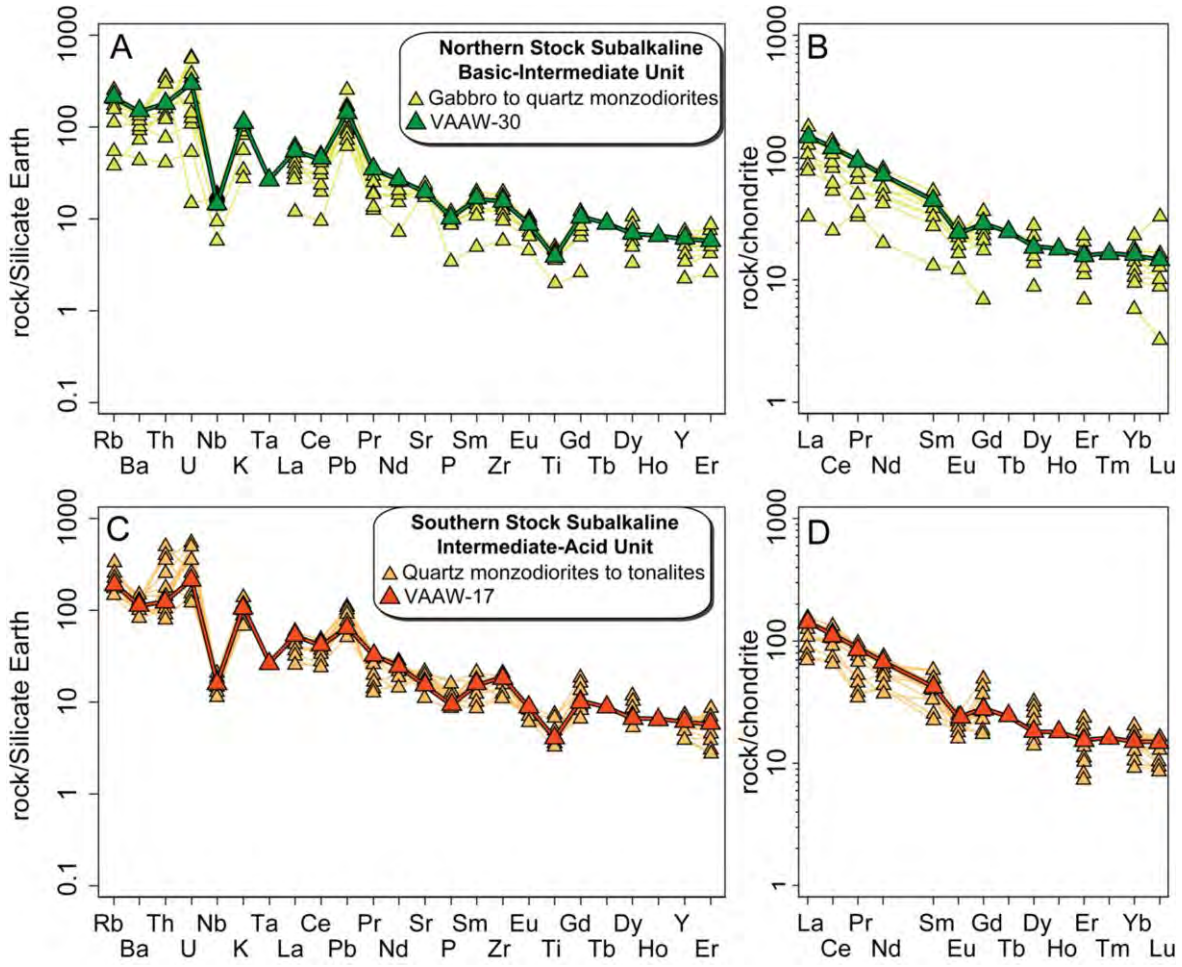

Figure 8.12: Valencia del Ventoso plutonic complex silicate Earth- and chondrite-normalised diagrams (normalization values from McDonough and Sun (1995). A) and B) Northern Stock Subalkaline Basic-Intermediate Unit. C) and D) Southern Stock Subalkaline Intermediate-Acid Unit. (smaller lighter symbols data from Sarrionandia, 2005)

The rocks are high-K, subalkaline, calc-alkaline, metaluminous (ASI ≈ 0.71-0.95), and plot in the calc-alkaline field in the Borodin index diagram (Fig. 8.8).

In silicate Earth–normalised diagrams the rocks have positive anomalies in Rb, Th, K, Pb and Zr and negative anomalies in Ba, Nb, Ta, P and Ti (Fig. 8.12C) with chondrite-normalised show enrichment in LREE relative to HREE, La_N/Lu_N ≈ 7.8-12.6, and negative to almost flat Eu anomalies, Eu/Eu^* ≈ 0.34-0.96 (Fig. 8.12D).

In addition, the Southern Stock shows a variation in $\varepsilon Nd_{335\ Ma}$ of -5.6 to -1.7 and in $^{87}Sr/^{86}Sr_{335\ Ma}$ ≈ 0.706058-0.708252 with $^{147}Sm/^{144}Nd$ ≈ 0.118-0.124 and Nd model ages of 1.1-1.4 Ga comparable to the Northern Stock (Fig. 8.11).

8.2.4 Intrusive, Acid Peraluminous, Dyke Unit

This unit comprises syenite and aplite veins that are spatially restricted to the Valencia del Ventoso plutonic complex.

Their major element concentrations are SiO_2 ≈ 72-76 wt %, Na_2O+K_2O ≈ 7-9 wt % with variable FeO_T/MgO ≈ 1.1-8.9 (Fig. 8.8). They have low contents of MgO ≈ 0.1-0.5 wt %, FeO_T ≈ 0.3-1.2 wt %, TiO_2 ≈ 0-0.2 wt % and CaO ≈ 0.5-1.7 wt %, high Al_2O_3 ≈ 13-14.6 wt %, K_2O ≈ 4.0-6.2 wt % and P_2O_5 ≈ 0.1-0.2 wt % (Fig. 8.9).

These rocks are peraluminous (ASI ≈ 0.99-0.1.19) (Fig. 8.8).

In silicate Earth–normalised diagrams the aplites have negative anomalies in Ba, Nb, La, Ce, Sm and Ti and positive anomalies in Rb, U, K, Pb, P and Zr (Fig. 8.13A). The veins are relatively depleted in REE overall, but show enrichment in LREE relative to HREE, La_N/Lu_N ≈ 2.8-14.1, with negative to positive Eu anomalies in chondrite-normalised diagrams, Eu/Eu^* ≈ 0.34-1.8 (Fig. 8.13B).

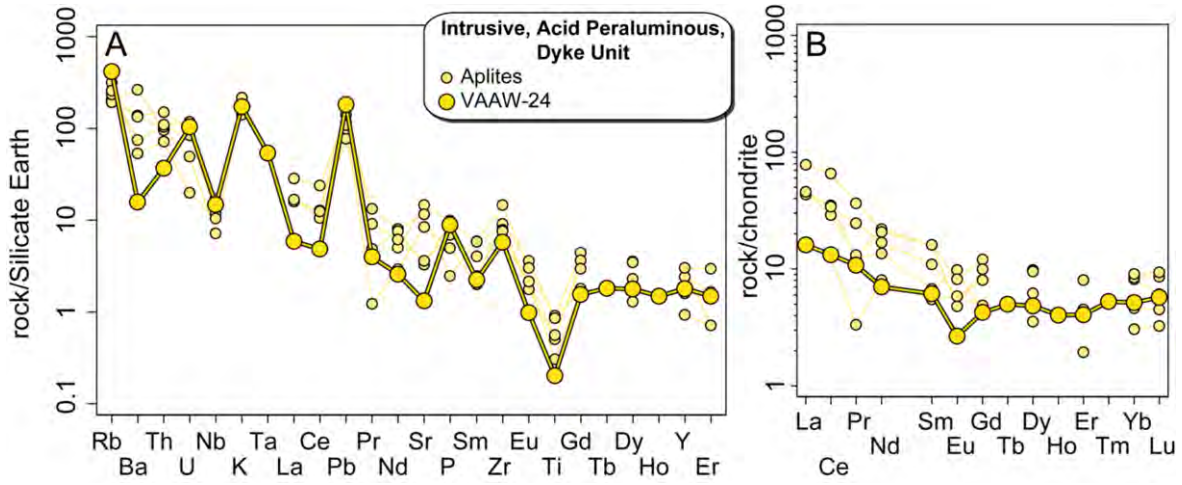

Figure 8.13: Valencia del Ventoso plutonic complex silicate Earth- and chondrite-normalised diagrams (normalization values from McDonough and Sun (1995): A) and B) Intrusive, Acid Peraluminous, Dyke Unit aplites. (smaller lighter symbols data from Sarrionandia, 2005).

8.3 Brovales Pluton

The Brovales pluton is concentrically zoned, it comprises three main rock groups: i) the *Central Subalkaline Intermediate Unit*; ii) the *Intermediate Subalkaline Intermediate Unit*; iii) the *External Subalkaline Acid Unit* and *Intrusive, Acid Peraluminous, Dykes*.

	Valencia del Ventoso plutonic complex							Olivenza-Monesterio basament	
	Northern Stock Subalkaline Basic-Intermediate Unit	Southern Stock Subalkaline Intermediate-Acid Unit	Main Pluton Alkaline To Subalkaline Basic-Acid Unit				Intrusive Dyke Unit		
	Quartz monzodiorite	Quartz monzodiorite	Diorite	Diorite	Quartz diorite	Granodiorite	Aplite	Leucogranite	Metasediment
	VAAW-30	VAAW-17	VAAW-20	VAAW-35	VAAW-37	VAAW-38	VAAW-24	VAAW-41	VAAW-39
Major elements (wt %)									
SiO_2	59.91	61.83	48.63	52.70	52.74	60.69	75.98	78.22	69.03
TiO_2	0.75	0.80	1.38	1.38	1.88	0.93	0.04	0.16	0.68
Al_2O_3	15.63	15.66	17.36	15.50	18.53	16.96	13.65	12.91	14.36
FeO	5.60	5.46	8.59	8.13	7.95	5.86	0.62	0.56	4.42
MnO	0.10	0.09	0.15	0.13	0.10	0.08	0.03	0.01	0.03
MgO	4.14	3.64	5.97	6.48	3.15	2.29	0.07	0.52	2.12
CaO	5.00	4.28	8.93	8.96	7.23	4.89	0.47	0.20	1.36
Na_2O	3.24	3.23	2.33	2.44	3.68	3.53	3.22	6.37	3.35
K_2O	3.31	3.05	2.75	1.34	1.87	3.06	4.90	0.08	2.67
P_2O_5	0.21	0.19	0.29	0.21	0.73	0.29	0.18	0.02	0.20
LOI	0.74	0.70	1.92	1.15	0.54	0.31	0.42	0.56	0.97
Total	98.63	98.93	98.30	98.42	98.40	98.89	99.58	99.61	99.19
Trace elements (ppm)									
Li	24.0	25.0	41.0	14.0	22.0	31.0	10.0	4.0	13.0
Rb	125	119	102	40	81	113	249	2	87
Cs	3.0	4.0	2.0	1.0	2.0	3.0	13.0	0.0	2.0
Be	3.0	3.0	1.0	1.0	2.0	3.0	10.0	4.0	2.0
Sr	391	299	562	384	645	476	26	68	250
Ba	974	738	3163	678	1207	1276	104	9	688
Sc	19.0	18.0	35.0	32.0	25.0	14.0	3.0	4.0	12.0
V	136.0	134.0	200.0	183.0	321.0	134.0	5.0	8.0	91.0
Cr	205.0	166.0	156.0	330.0	18.0	36.0	7.0	2.0	82.0
Co	37.0	40.0	35.0	45.0	40.0	33.0	28.0	38.0	36.0
Ni	85.0	67.0	51.0	103.0	15.0	18.0	2.0	3.0	34.0
Cu	44.0	28.0	38.0	43.0	45.0	19.0	3.0	4.0	8.0
Zn	52.0	43.0	53.0	58.0	40.0	30.0	3.0		15.0
Ga	20.0	20.0	19.0	18.0	23.0	22.0	16.0	25.0	18.0
Y	25.9	26.0	19.2	23.5	33.6	29.8	7.7	27.7	15.6
Nb	9.6	10.6	9.1	9.1	11.5	10.0	9.7	8.6	10.8
Ta	1.0	1.0	0.4	0.7	0.9	0.8	2.0	0.8	0.8
Zr	163	194	110	148	263	256	60	286	237
Hf	5.0	8.2	3.5	4.6	11.1	9.7	2.3	10.2	6.9
Sn	2.0	2.0	0.8	1.6	3.3	3.1	4.8	2.5	1.6
Tl	0.4	0.4	0.7	0.2	0.4	0.4	1.1		0.4
Pb	22	10	6	4	4	9	27	1	2
U	6.10	4.40	0.40	1.70	3.20	3.60	2.10	3.20	1.50
Th	14.4	9.9	1.1	6.6	11.5	12.1	2.9	19.5	8.8
La	35.8	34.1	16.3	21.0	40.9	44.5	3.8	26.9	39.9
Ce	73.8	68.8	36.1	45.1	85.0	89.0	8.1	75.0	79.3
Pr	8.8	8.2	5.1	5.8	10.6	10.6	1.0	7.3	9.0
Nd	33.1	30.8	22.7	24.0	42.8	40.4	3.2	27.4	32.9
Sm	6.64	6.23	5.29	5.59	8.95	7.97	0.91	5.94	5.82
Eu	1.34	1.34	1.29	1.53	2.08	1.63	0.15	0.28	1.27
Gd	5.74	5.62	5.05	5.28	8.12	6.93	0.84	4.97	4.71
Tb	0.89	0.87	0.76	0.82	1.21	1.01	0.18	0.87	0.66
Dy	4.62	4.48	3.97	4.45	6.28	5.39	1.19	5.03	3.12
Ho	0.98	0.98	0.81	0.92	1.32	1.13	0.22	1.06	0.59
Er	2.53	2.49	1.90	2.27	3.22	2.91	0.65	2.87	1.43
Tm	0.41	0.40	0.27	0.34	0.47	0.44	0.13	0.49	0.22
Yb	2.53	2.42	1.61	2.07	2.78	2.74	0.83	3.26	1.34
Lu	0.36	0.37	0.25	0.30	0.39	0.39	0.14	0.48	0.20
Isotopes									
$^{87}Rb/^{86}Sr$	0.896	1.118	0.356	0.292	0.524	0.669		0.112	0.980
$^{87}Sr/^{86}Sr$	0.711253	0.713584	0.708081	0.706740	0.709279	0.709532		0.709309	0.717074
$^{87}Sr/^{86}Sr_{t\ Ma}$	0.706978	0.708252	0.706383	0.705348	0.706778	0.706341		0.708496	0.709954
$^{147}Sm/^{144}Nd$	0.124	0.124	0.128	0.144	0.143	0.122		0.132	0.110
$^{143}Nd/^{144}Nd$	0.512289	0.512190	0.512412	0.512497	0.512419	0.512290		0.512496	0.511766
$^{143}Nd/^{144}Nd_{t\ Ma}$	0.512017	0.511918	0.512131	0.512181	0.512105	0.512022		0.512055	0.511399
$\varepsilon Nd_{335\ Ma}$	-3.7	-5.6	-1.5	-0.5	-2.0	-3.6		1.4	-11.4
$T_{DM\ (Ga)}$	1.3	1.4	1.1	1.2	1.3	1.2		1.0	1.8

Table 8.2: Representative major and trace element and Rb-Sr and Sm-Nd isotope data for the Valencia del Ventoso plutonic complex, a Cambrian leucogranite and a Serie Negra metasediment. Nd model ages calculated for all rocks using the method of DePaolo, (1981) (TDM).

8.3.1 Central Subalkaline Intermediate Unit

The *Central Unit* is formed of quartz diorites to quartz monzodiorites and tonalites to granodiorites with diorite enclaves.

The enclave major element concentrations are SiO_2 ≈ 50-51 wt %, Na_2O+K_2O ≈ 5.1 wt % with FeO_T /MgO ≈ 1.7-2.2 (Fig. 8.14). These rocks have MgO ≈ 5.2-6.3 wt %, TiO_2 ≈ 0.8 wt %, Al_2O_3 ≈ 15 wt %, CaO ≈ 8.4 wt%, K_2O ≈ 1.4 wt %, FeO_T ≈ 10-11 wt % and P_2O_5 ≈ 0.3 wt % (Fig. 8.15).

The enclaves are medium-K, transitional alkaline to subalkaline, metaluminous (ASI ≈ 0.66-0.68), and plot in the subalkaline and calc-alkaline Borodin index diagram (Fig. 8.14).

The plutonic host rock major element concentrations are SiO_2 ≈ 59-67 wt %, Na_2O+K_2O ≈ 6.1-7.1 wt % with FeO_T /MgO ≈ 2.3-3.1 (Fig. 8.14). They have MgO ≈ 1.2-2.4 wt %, FeO_T ≈ 3.5-5.7 wt %, TiO_2 ≈ 0.5-1 wt %, Al_2O_3 ≈ 16.2-17.7 wt %, CaO ≈ 2.9-4.6 wt %, K_2O ≈ 2.7-3.7 wt % and P_2O_5 ≈ 0.2-0.5 wt % (Fig. 8.15).

The main rocks of this unit, that host the enclaves, are subalkaline, calc-alkaline, peraluminous (ASI ≈ 0.98-1.12), they have a calc-alkaline Borodin index (Fig. 8.14).

In the silicate Earth–normalised diagram the diorite enclave has negative anomalies in Nb, Sr, P and Ti and positive anomalies in Rb, U, K, and Sm (Fig. 8.16A). This rock has an almost flat chondrite-normalised REE pattern, La_N/Lu_N ≈ 2.2, and a strong negative Eu anomaly, Eu/Eu^* ≈ 0.45 (Fig. 8.16B). In the silicate Earth–normalised diagram the host quartz diorite and granodiorites have negative anomalies in Nb, Ta, P and Ti and positive anomalies in K, La, Pb and Zr (Fig. 8.16A). These rocks show enrichment in LREE relative to HREE, La_N/Lu_N ≈ 7.6-11.1, and negative Eu anomalies, Eu/Eu^* ≈ 0.65-0.66 (Fig. 8.16B).

The isotopic compositions of all three Brovales pluton unit samples studied here are quite restricted, they have $\varepsilon Nd_{335\ Ma}$ ≈ -4.2 to -3.2 and $^{87}Sr/\ ^{86}Sr_{335\ Ma}$ values 0.707018-0.707543 (Fig. 8.17) with $^{147}Sm/^{144}Nd$ ≈ 0.097-0.132 and Nd model ages from 1.1 to 1.3 Ga (Fig. 8.17). However, published isotopic data for Brovales show more varied compositions with $\varepsilon Nd_{335\ Ma}$ ≈ -5 to -7 and $^{87}Sr/\ ^{86}Sr_{335\ Ma}$ ≈0.7082-0.7096 (Fig. 8.17).

8.3.2 Intermediate Subalkaline Intermediate Unit

This unit is comprises tonalites and granodiorites with coarse-grained, fine-grained, and deformed textures.

The typical major element concentrations are SiO_2 ≈ 61-65 wt %, Na_2O+K_2O ≈ 6.3-7.2

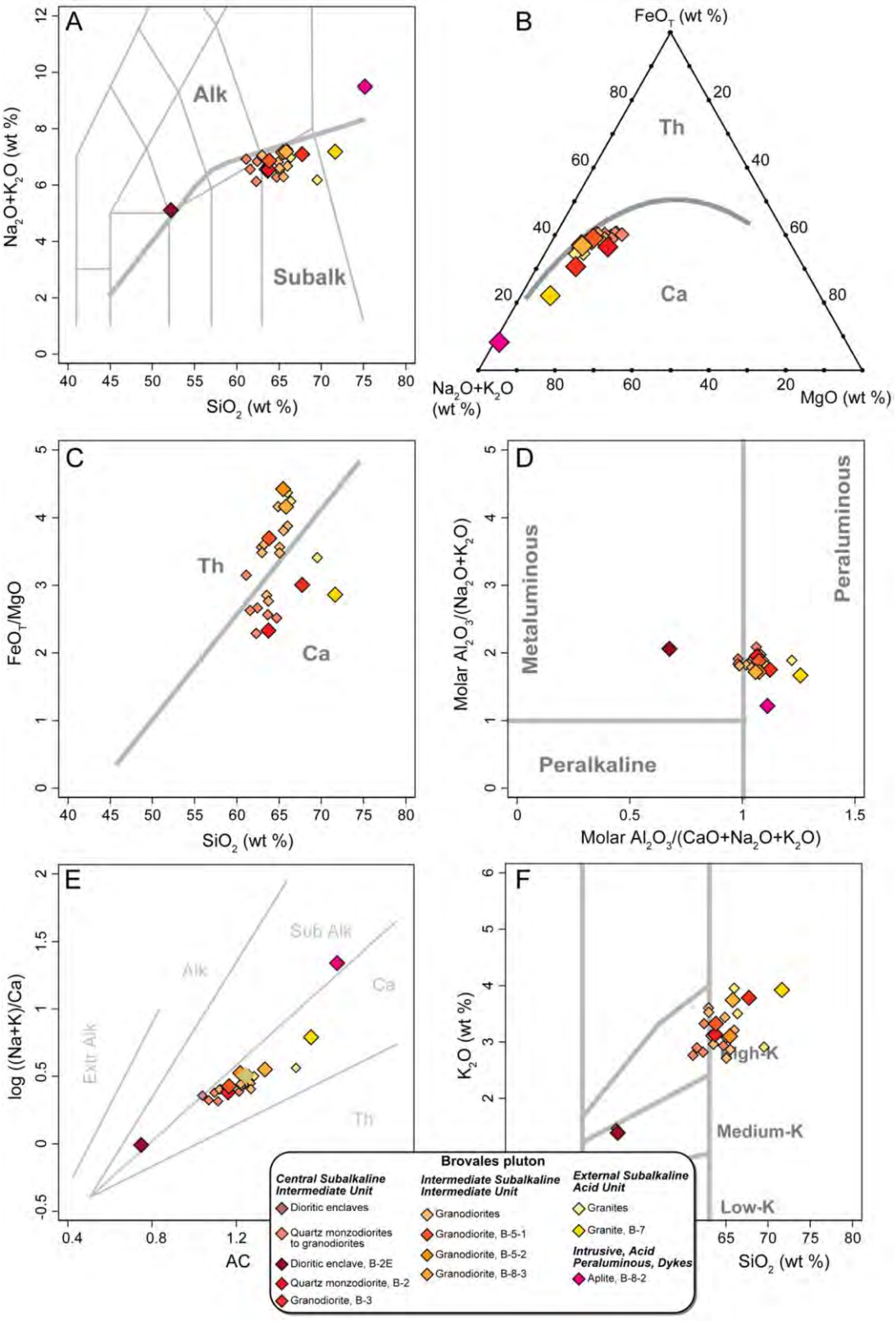

Figure 8.14: Brovales pluton whole-rock compositions: A) Total alkalis vs SiO_2 (TAS) (fields from Le Maitre et al., 1989). B) (Na_2O+K_2O) - FeO_T - MgO (AFM) (fields from Kuno, 1968). C) FeO_T /MgO vs SiO_2 (fields from Frost et al., 2001). D) Molar Al_2O_3/ (Na_2O+K_2O) vs Molar Al_2O_3/ ($CaO+Na_2O+K_2O$) (fields from Shand, 1947). E) Borodin index. F) K_2O vs SiO_2. (smaller lighter symbols data from Pons, 1982). Abbreviations as in Fig. 8.1.

wt % with high FeO_T /MgO ≈ 2.8-4.4 (Fig. 8.14). They have MgO ≈ 1.1-1.8 wt %, FeO_T ≈ 4.6-5.6 wt %, TiO_2 ≈ 0.7-0.9 wt %, Al_2O_3 ≈ 16-17.4 wt %, CaO ≈ 3.3-4.2 wt %, K_2O ≈ 2.6-3.7 wt % and P_2O_5 ≈ 0.2-0.4 wt % (Fig. 8.15).

All these rocks are, subalkaline, calc-alkaline to tholeiitic, peraluminous (ASI ≈ 0.98-1.09), with a subalkaline to calc-alkaline Borodin index (Fig. 8.14).

In silicate Earth–normalised diagrams these samples have negative anomalies in Nb, Ta and Ti and positive anomalies in K, Pb and Zr (Fig. 8.16C). They are enriched in LREE relative to HREE, La_N/Lu_N ≈ 7.2-7.9, and have negative Eu anomalies, Eu/Eu^* ≈ 0.64-0.77 (Fig. 8.16D). Notably, the deformed granodiorite has a lower content in REE than samples (Fig. 8.16D).

8.3.3 External Subalkaline Acid Unit and Intrusive, Acid Peraluminous, Dykes

The *External Unit* comprises monzo- and syenogranites and aplites.

The major element concentrations of the granites are SiO_2≈ 64-71 wt %, Na_2O+K_2O ≈ 6.2-7.2 wt % with variable FeO_T /MgO ≈ 2.9-4.4 (Fig. 8.14). They have low contents of MgO ≈ 0.8-1.1 wt %, FeO_T ≈ 2.2-4.5 wt %, TiO_2 ≈ 0.3-0.7 wt %, and CaO ≈ 1.7-3.2 wt % and high Al_2O_3 ≈ 15.6-16.8 wt %, K_2O ≈ 2.8-3.9 wt % and P_2O_5 ≈ 0.1-0.4 wt% (Fig. 8.15).

The granites are peraluminous (ASI ≈ 1.06-1.30), no Borodin index was calculated because of their high SiO_2 content (Fig. 8.14).

In silicate Earth–normalised diagrams the granite has negative anomalies in Nb, Ta, P and Ti and positive anomalies in K, Pb and Zr (Fig. 8.16E). It is enriched in LREE relative to HREE, La_N/Lu_N ≈ 7.9, with a negative Eu anomaly, Eu/Eu^* ≈ 0.65 (Fig. 8.16F).

The aplite major element concentrations are SiO_2 ≈ 75 wt %, Na_2O+K_2O ≈ 9.5 wt %, with high FeO_T /MgO ≈ 6.5 (Fig. 8.14). This rock has low contents of MgO ≈ 0.1 wt %, FeO_T ≈ 0.8 wt %, TiO_2 ≈ 0.1 wt % and CaO ≈ 0.6 wt %, high Al_2O_3 ≈ 13.5 wt % and K_2O ≈ 7.7 wt % (Fig. 8.15).

It is peraluminous (ASI ≈ 0.98-1.09), again no Borodin index was calculated because of the high SiO_2 content (Fig. 8.14).

In the silicate Earth–normalised diagram the aplite has strong negative anomalies in Nb, Ta, P and Ti and strong positive anomalies in U, K and Pb (Fig. 8.16E). This rock is enriched in LREE and strongly depleted in HREE, La_N/Lu_N ≈ 36.5 with a slight negative Eu anomaly, Eu/Eu^* ≈ 0.84 (Fig. 8.16F).

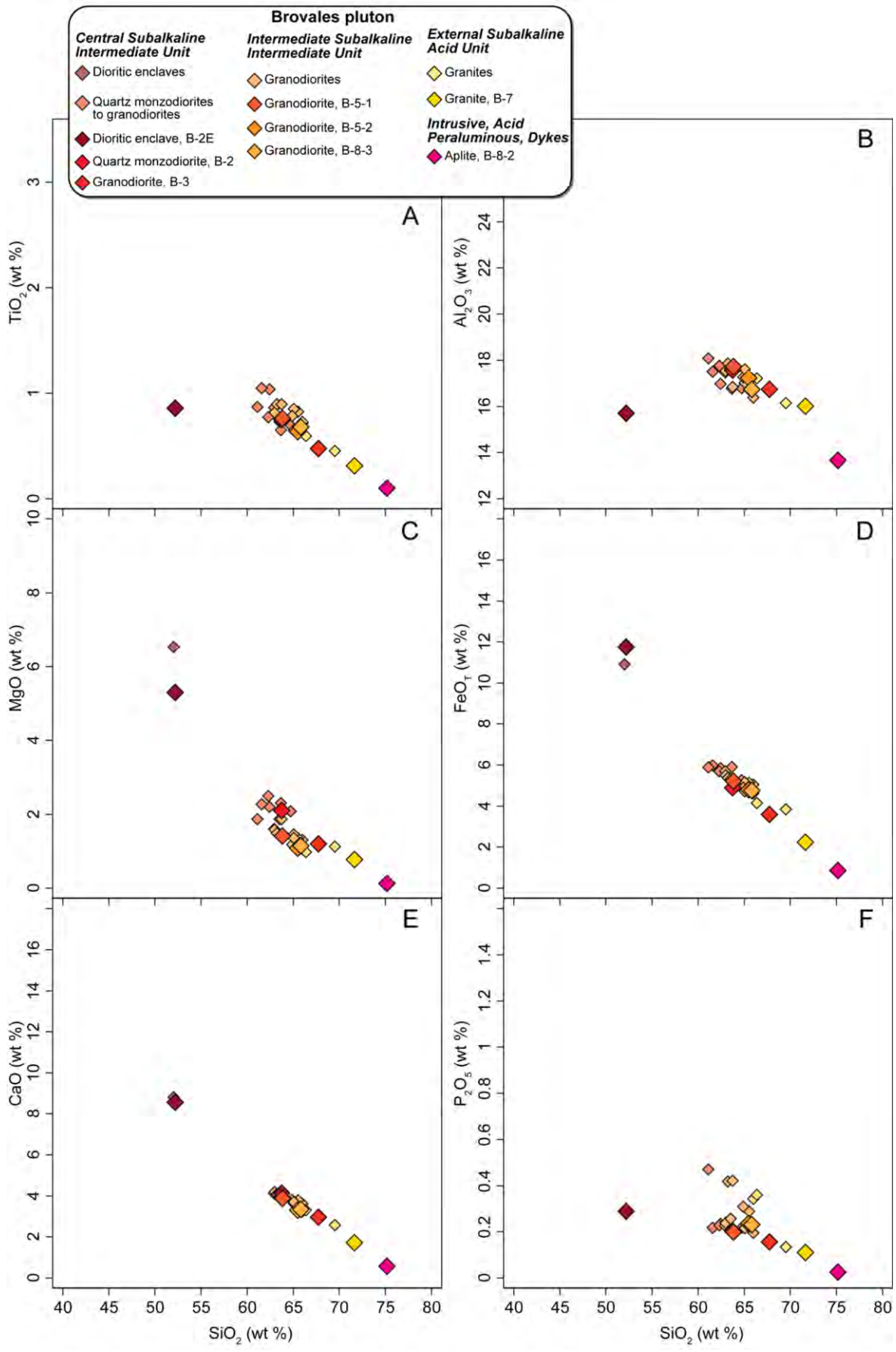

Figure 8.15: Brovales pluton Harker diagrams. A) TiO_2 vs SiO_2. B) Al_2O_3 vs SiO_2. C) MgO vs SiO_2. D) FeO_T vs SiO_2. E) CaO vs SiO_2. F) P_2O_5 vs SiO_2 (smaller lighter symbols data from Pons, 1982).

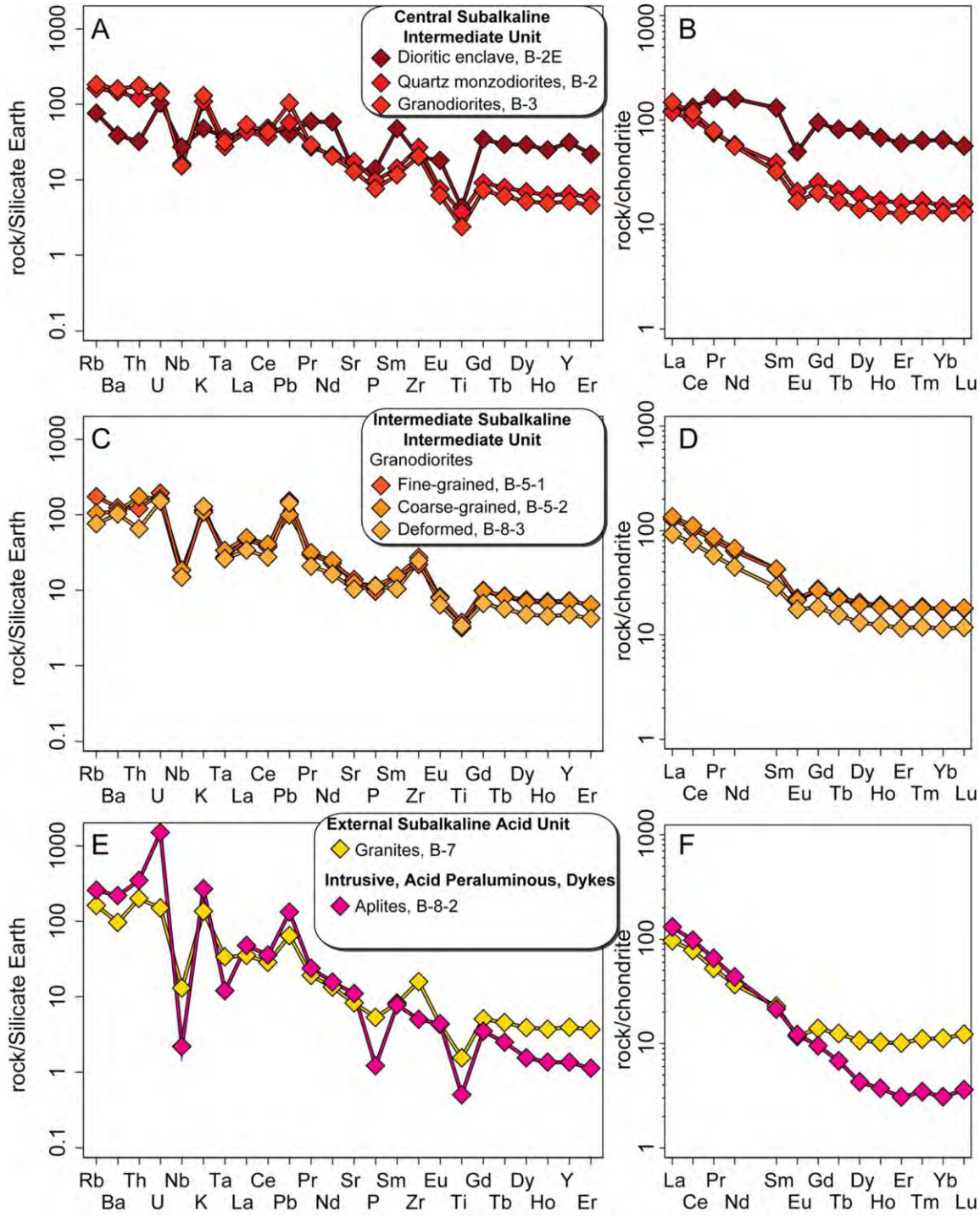

Figure 8.16: Brovales pluton silicate Earth- and chondrite-normalised diagrams (normalisation values from McDonough and Sun (1995). A) and B) Central subalkaline intermediate unit. C) and D) Intermediate subalkaline intermediate unit. E) and F) External subalkaline intermediate unit and Intrusive, acid peraluminous, dykes.

8.4 Cambrian Leucogranite and Serie Negra Metasediment

8.4.1 Cambrian Leucogranite

The leucogranite has a subalkaline composition $SiO_2 \approx 78.2$ wt %, $Na_2O+K_2O \approx 6.5$ wt %.

It is depleted in $K_2O \approx 0.1$ wt % and is peraluminous (ASI=1.18) (Table 8.1). The sample has very low contents of Ba ≈ 9.4 ppm, Sr ≈ 68.7 ppm and Ta ≈ 0.87 ppm but high contents of Zr ≈ 286 ppm and Nb ≈ 8.6 ppm and intermediate contents of Th ≈ 19.5 ppm and U ≈ 3.2 ppm (Table 8.2).

The isotope composition of the leucogranite is $\varepsilon Nd_{510\ Ma}$ of 1.4, $^{87}Sr/^{86}Sr_{510\ Ma}$ of 0.708496, $^{147}Sm/^{144}Nd \approx 0.132$ with a Nd model age of 1.0 Ga (Table 8.2).

8.4.2 Serie Negra Metasediment

The metasediment has a whole-rock composition that plots in the arkose-greywacke fields of Herron (1988) (Table 8.2). It has a high Al_2O_3/SiO_2 ratio ≈ 0.21), intermediate values of $Fe_2O_{3T}+MgO \approx 7.1$ wt % and $K_2O/Na_2O \approx 0.8$ (Table 8.2). Its isotope composition is $\varepsilon Nd_{510\ Ma}$ ≈-11.4, $^{87}Sr/^{86}Sr_{510\ Ma}$ of 0.709954, $^{147}Sm/^{144}Nd \approx 0.110$ with Nd model age of 1.8 Ga (Table 8.2).

8.5 Whole-Rock Compositional Comparison of the Main Units of the Three Plutonic Bodies

The different units from the three plutonic bodies may be correlated into five broad groups (Figure 8.18).

The *Ultramafic-Mafic Group* comprises the Burguillos *Central Ultrabasic-Basic Layered Unit;* and, the Valencia *Northern Stock Subalkaline Basic-Intermediate Unit* gabbros. The most distinctive compositional characteristics of this group are the range of alkaline to subalkaline, principally tholeiitic, compositions and, for a given value of SiO_2, the relatively high concentration of MgO, and low K_2O, TiO_2 and P_2O_5 (Figs 8.2 and 8.9). They have marked positive Pb and negative Nb anomalies (Figs 8.3 and 8.12) and flat to upwards convex chondrite-normalised REE patterns from the LREE to MREE, $La_N/Lu_N \approx 2.8\text{-}13.3$, $La_N/Sm_N \approx 0.9\text{-}3.6$ and $Sm_N/Lu_N \approx 1.5\text{-}5.6$, with no marked Eu anomalies, $Eu/Eu^* \approx 0.77\text{-}1.85$ (Figs 8.3 and 8.12).

The *Alkaline Group* is composed of the Burguillos *Central Alkaline Basic-Intermediate Layered and Acid Unit;* and, some of the rocks from the Valencia *Main Pluton Alkaline to Subalkaline Basic-Acid Unit.* The main compositional characteristics are high K_2O, Al_2O_3, and P_2O_5 ;but relatively low MgO, for a given value of SiO_2 (Figs 8.2 and 8.9). In silicate Earth-normalised diagrams these rocks have no Pb anomaly such as that seen in the previous association and only show a small negative Nb anomaly (Figs 8.5 and 8.10). Chondrite-normalised REE patterns are steeper than the previous group, $La_N/Lu_N \approx 4.7\text{-}16.8$, with variable Eu anomalies, $Eu/Eu^* \approx 0.49\text{-}4.22$, that are positive in the more mafic Burguillos rocks and negative in the more evolved Burguillos and Valencia rocks (Figs 8.5 and 8.10).

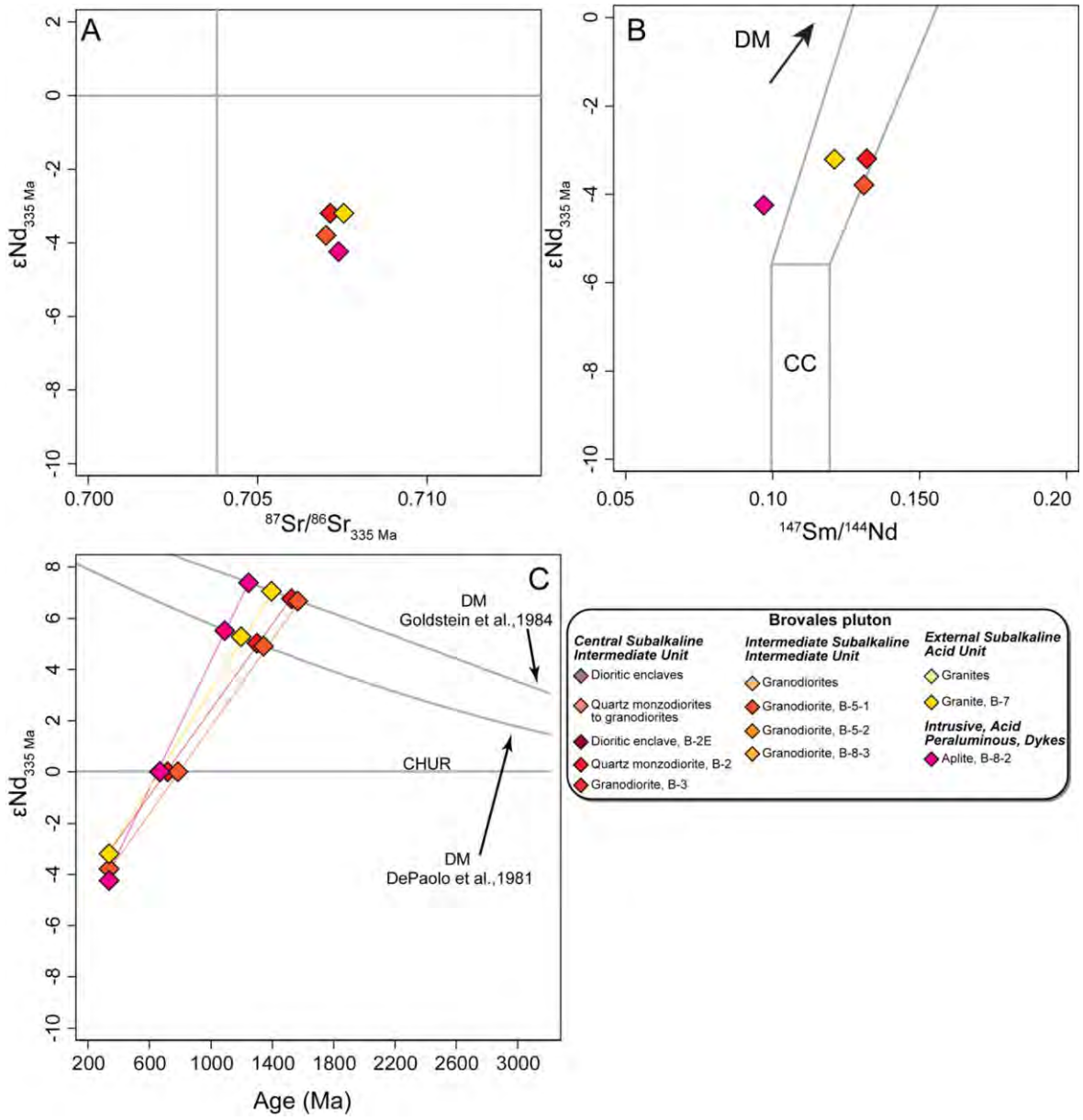

Figure 8.17: Brovales pluton. A) εNd_i vs $^{87}Sr/^{86}Sr$. B) εNd_i vs $^{147}Sm/^{144}Nd$. C) εNd_i vs age. DM, depleted mantle (i.e., MORB-like source); OIB, ocean island basalt source; FM, fertile mantle (derived by 1–7% of partial melting of an OIB source, Swinden et al. 1990); and C) Nd model ages calculated for all rocks using the method of DePaolo, (1981) (TDM) and Goldstein et al., (1984) (TCR). CHUR normalisation taken from DePaolo (1988) and Wasserburg et al. (1981).

The *Subalkaline Mafic-Intermediate Group* includes rocks of the Burguillos *External Subalkaline Intermediate Unit;* the Valencia *Main Pluton Alkaline to Subalkaline Basic-Acid Unit*; and, the Brovales *Central-Intermediate Subalkaline Intermediate Unit* diorite enclave. This group is subalkaline-calc-alkaline-tholeiitic in the classification scheme of Borodin (1987) (Figs 8.1, 8.8 and 8.14). The major element data shows no correlation with SiO_2, although MgO values are relatively high for a given value of SiO_2 (Figs 8.2, 8.9 and 8.15). They have a distinctive negative silicate Earth-

	Brovales pluton							
	Central Subalkaline Intermediate Unit			*Intermediate Subalkaline Intermediate Unit*			*External Subalkaline Acid Unit*	*Intrusive, Acid Peraluminous, Dykes*
	Diorite	Quartz diorite	Granodiorite	Granodiorite	Granodiorite	Granodiorite	Granite	Aplite
	B-2E	B-2	B-3	B-5-1	B-5-2	B-8-3	B-7	B-8-2
Major elements (wt %)								
SiO_2	51.12	62.79	66.72	62.78	64.73	64.97	70.77	74.52
TiO_2	0.84	0.74	0.47	0.75	0.63	0.67	0.31	0.10
Al_2O_3	15.39	17.32	16.49	17.43	17.04	16.53	15.82	13.54
FeO	11.51	4.82	3.55	5.14	4.73	4.71	2.20	0.85
MnO	0.24	0.08	0.06	0.10	0.09	0.09	0.03	0.02
MgO	5.19	2.07	1.18	1.39	1.07	1.13	0.77	0.13
CaO	8.39	4.06	2.91	3.82	3.26	3.30	1.69	0.56
Na_2O	3.65	3.36	3.26	3.49	4.01	3.40	3.22	1.72
K_2O	1.36	3.09	3.73	3.27	3.07	3.70	3.88	7.69
P_2O_5	0.28	0.20	0.15	0.20	0.23	0.23	0.11	0.03
LOI	0.57	0.29	0.25	0.27	0.04	0.04	0.68	0.25
Total	98.54	98.82	98.77	98.63	98.91	98.77	99.48	99.40
Trace elements (ppm)								
Li	13.0	22.4	16.7	21.9	21.8	10.4	8.9	3.3
Rb	46	98	109	104	63	46	97	154
Cs	1.0	2.0	3.0	4.2	4.1	2.7	1.9	1.8
Be	7.1	3.6	3.2	2.8	3.1	2.6	3.4	1.3
Sr	257	349	258	275	247	205	164	219
Ba	259	963	1059	823	731	675	639	1448
Sc	38.1	8.5	4.9	9.1	4.1	4.3	2.7	0.7
V	150.7	58.6	33.8	45.1	30.1	39.9	23.4	10.4
Cr	356.8	68.7	39.1	14.0	14.7	18.5	26.6	23.5
Co	32.1	27.2	22.1	18.1	17.1	21.4	18.7	22.3
Ni	78.3	27.6	11.6	3.0	2.7	3.0	5.8	2.2
Cu	9.1	4.2	4.2	6.6	4.9	8.2	3.5	4.0
Zn	75.9	48.2	45.7	77.9	49.4	84.1	26.5	22.4
Ga	24.3	20.7	19.0	20.3	20.4	18.5	16.9	11.8
Y	134.3	28.0	22.1	31.2	30.5	20.4	17.0	5.8
Nb	17.9	10.7	10.1	9.8	12.1	9.8	8.6	1.5
Ta	1.4	1.0	1.2	1.0	1.2	1.0	1.2	0.4
Zr	213	280	216	231	285	258	167	53
Hf	3.5	2.8	3.6	2.3	2.2	1.1	3.3	0.8
Sn	7.9	2.1	2.7	2.8	2.8	1.9	0.6	0.4
Tl	0.2	0.5	0.5	0.5	0.5	0.3	0.3	0.5
Pb	6	9	16	23	15	21	10	20
U	2.09	2.99	2.91	3.91	3.29	3.09	3.05	30.35
Th	2.6	9.6	14.0	9.6	13.9	5.2	15.8	27.7
La	28.9	28.2	34.7	30.5	32.2	22.0	22.8	30.9
Ce	81.2	62.1	72.0	63.3	68.1	46.1	47.7	59.4
Pr	15.0	7.0	7.3	7.5	8.0	5.3	4.9	6.1
Nd	72.7	26.4	25.7	28.8	30.6	20.5	16.8	19.7
Sm	19.32	5.75	4.75	6.23	6.27	4.24	3.37	3.17
Eu	2.79	1.15	0.95	1.25	1.22	0.99	0.66	0.68
Gd	18.67	5.01	3.98	5.41	5.31	3.64	2.77	1.90
Tb	2.93	0.78	0.60	0.82	0.81	0.56	0.45	0.25
Dy	19.74	4.67	3.46	5.00	4.76	3.24	2.62	1.05
Ho	3.70	0.93	0.73	1.05	1.02	0.68	0.56	0.20
Er	9.62	2.57	2.00	2.80	2.85	1.86	1.62	0.49
Tm	1.56	0.41	0.33	0.45	0.44	0.29	0.27	0.09
Yb	10.38	2.41	2.09	2.82	2.88	1.83	1.81	0.50
Lu	1.38	0.38	0.32	0.44	0.44	0.29	0.30	0.09
Isotopes								
$^{87}Rb/^{86}Sr$		0.813		1.093			1.713	2.034
$^{87}Sr/^{86}Sr$		0.711010		0.712229			0.715710	0.717090
$^{87}Sr/^{86}Sr_{335\ Ma}$		0.707134		0.707018			0.707543	0.707389
$^{147}Sm/^{144}Nd$		0.132		0.131			0.121	0.097
$^{143}Nd/^{144}Nd$		0.512332		0.512299			0.512309	0.512203
$^{143}Nd/^{144}Nd_{335\ Ma}$		0.512043		0.512012			0.512043	0.511990
$\varepsilon Nd_{335\ Ma}$		-3.2		-3.8			-3.2	-4.2
$T_{DM\ (Ga)}$		1.3		1.3			1.2	1.1

Table 8.3: Representative major and trace element and Rb-Sr and Sm-Nd isotope data for the Brovales Pluton. Nd model ages calculated for all rocks using the method of DePaolo, (1981) (TDM).

normalised Nb anomaly and a positive Pb anomaly (Figs 8.6, 8.10 and 8.16). The chondrite-normalised REE patterns are less steep than the alkaline rocks, La_N/Lu_N, 3.4-12.7, and with positive to more pronounced negative Eu anomalies, $Eu/Eu^* \approx 0.36\text{-}1.91$ (Figs 8.6, 8.10 and 8.16).

Some rocks, such as the Brovales enclave, are compositionally transitional between this subalkaline and the above alkaline group. This is seen in the major element Harker diagrams (Figs 8.2, 8.9 and 8.15). They are characterised by a lack of a positive Pb anomaly and only have a slight Nb anomaly in silicate Earth-normalised diagrams (Figs 8.6, 8.10 and 8.16). The chondrite-normalised LREE are enriched relative to HREE, $La_N/Lu_N \approx 2.2\text{-}14.1$, with Eu anomalies that vary from positive, typical of Burguillos alkaline rocks, to negative typical of subalkaline samples, $Eu/Eu^* \approx 0.45\text{-}3.09$ (Figs 8.6, 8.10 and 8.16). The model ages of this group are similar to the alkaline gabbros, which at c. 1 Ga are some of the youngest calculated in the present study (Figs 8.4, 8.11 and 8.17).

The *Subalkaline Intermediate-Felsic Group* comprises rocks of the Burguillos *External Subalkaline Intermediate Unit;* the most of the Valencia *Northern Stock Subalkaline Basic-Intermediate Unit* and *Southern Stock Subalkaline Intermediate-Acid Unit*; and, the Brovales C*entral-Intermediate-External Subalkaline Intermediate* units. The samples in this group plot in the calc-alkaline field (Figs 8.1, 8.8 and 8.14). It is the group with the greatest range of SiO_2, which correlates negatively with all the other major elements except K_2O (Figs 8.2, 8.9 and 8.15). In the silicate Earth-normalised plot they have a positive U anomaly, much greater than in the previous group; but lack the positive Ba anomaly observed in all the other groups except the peraluminous rocks (Figs 8.6, 8.12 and 8.16). The negative Nb anomaly, on the other hand, is more pronounced resulting in a lower value than that for Ta, the same as is observed in the *Ultramafic-Mafic Group* but different from the *Alkaline Group* that have equal silicate Earth-normalised values of these elements (for example compare the relative anomalies of normalised Nb and Ta values in Fig 8.12 and 8.5). The LREE are enriched relative to the HREE, $La_N/Lu_N \approx 5.4\text{-}36.5$ with negative Eu anomalies, $Eu/Eu^* \approx 0.39\text{-}0.84$. The Rb-Sr and Sm-Nd values of this group are more crustal-like than any group except the peraluminous granites (Figs 8.4, 8.11 and 8.17). Notably, the Nd model ages fall between the younger alkaline and older peraluminous ages.

The *Peraluminous Group* is composed of the Burguillos *Acid Peraluminous Unit;* and the Valencia *Intrusive, Acid Peraluminous, Dyke Unit.* These rocks have the highest SiO_2 concentrations (Figs 8.2 and 8.9). In silicate Earth-normalised diagrams both Pb and K show positive anomalies whereas the Nb and Ti anomalies are negative (Figs 8.2 and 8.9). The LREE are enriched relative to MREE , $La_N/Lu_N \approx 2.8\text{-}14.1$ and, $La_N/Sm_N \approx 1.9\text{-}6.7$, but the chondrite-normalised patterns

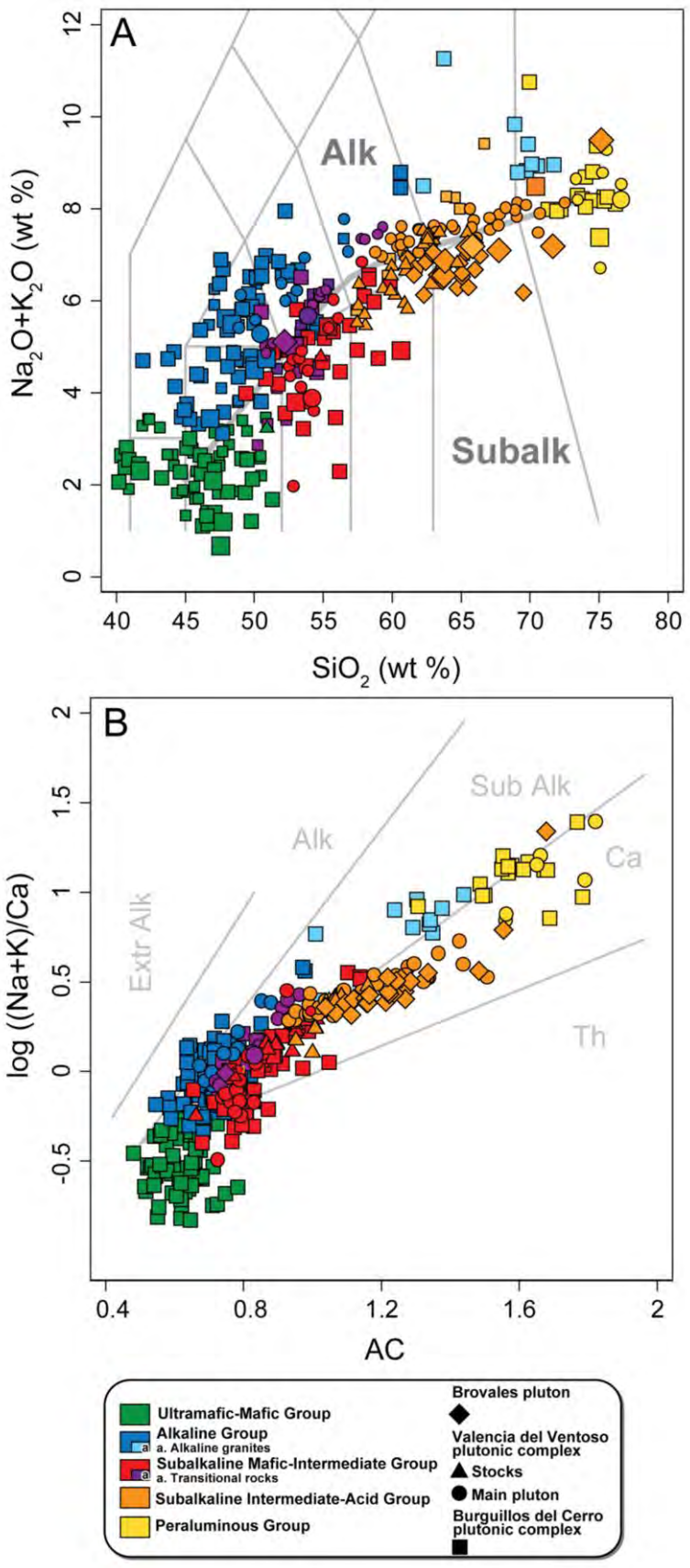

Figure 8.18: A) Total alkalis vs SiO_2 *(TAS) and B)Borodin index plot for all the rocks of the present study, note that independent of the plutonic body the samples may be correlated in five broad compositional groups. Abbreviations as in Fig. 8.1.*

are quite flat from the MREE to the HREE, Sm_N/Lu_N ≈1.1-3.4; Eu anomalies are mainly negative, , Eu/Eu^* ≈ 0.74 (Figs 8.7 and 8.13). The Rb-Sr and Sm-Nd values of these rocks are the most crustal-like of all the units of the three plutonic bodies (Figs 8.4 and 8.11).

Chapter 9: U-Th-Pb Zircon Age and O Isotope Data

9. U-Th-Pb Zircon Ages and O Isotope Data

Zircon was separated from 16 samples of the studied bodies (Table 9.1) using the methods described in Chapter 5. The zircon grains were studied with the SHRIMP for U-Th-Pb dating and, in the case of Burguillos and Brovales, also for oxygen isotopes. The most relevant results are described in the next paragraphs.

9.1 U-Th-Pb Ages

The SHRIMP U-Pb data are summarized in Table 9.1 to 9.5 and Figs 9.1 to 9.10, the full dataset is given in Appendix IV.

9.1.1 Burguillos del Cerro Plutonic Complex

The five samples studied were: a poikilitic amphibole gabbro from the *Central Ultrabasic-Basic Layered Unit*; a diorite and an alkali feldspar granite from the *Central Alkaline Basic-Intermediate Layered and Acid Unit*; a quartz diorite from the *External Subalkaline Intermediate Unit*; and a two-mica granite from the *Acid Peraluminous Unit*. All but the two-mica granite cluster around 336 Ma with a standard deviation of 1.4 (Fig. 9.2A). This value is, therefore, interpreted as the most probable emplacement age of the Complex.

9.1.1.1 Central Ultrabasic-Basic Layered Unit

The studied gabbronorite, sample BUAW-4, contains a few zircon grains. These are colourless stubby, euhedral and equant to elongated bipyramidal prisms (Fig. 9.1A), with sizes from 400 μm x 250 μm to 100 μm x 50 μm (Fig. 9.1A). No inclusions have been observed. Cathodoluminescence imaging reveals that most grains have a fine oscillatory zoning of obvious magmatic origin.

Fifteen grains were analyzed with the SHRIMP. They contained moderate concentrations of U (119-523 ppm) and Th (67-272 ppm) with Th/U = 0.38-0.69 and little common lead (f^{206} < 0.61 %) (Table 9.1). All of them were concordant (discordance -3.2 to 0.8 %) (Fig. 9.2B). The weighted means (errors reported at 2σ) of the uncorrected and 207-corrected $^{206}Pb/^{238}U$ are virtually identical, 336 ± 2 Ma (MSWD = 2.94) and 336 ± 2 Ma (MSWD = 2.63).

9.1.1.2 Central Alkaline Basic-Intermediate Layered and Acid Unit

The diorite, sample BUAW-6, contains abundant zircon. Grains are colourless, free of inclusions, euhedral short bipyramidal prisms with dimensions from 200 μm × 100 μm to 100 μm × 50 μm (Fig. 9.1B). Cathodoluminescence images reveal different internal morphologies: grains with magmatic oscillatory zoning; patchy zonation; and, unzoned grains (Fig. 9.1B).

Figure 9.1 Cathodoluminescence images ages and O isotopes value of representative analysed zircons from the Burguillos del Cerro plutonic complex. A) Central Ultrabasic-Basic Layered Unit poikilitic amphibolitic gabbronorite, (BUAW-4). B) Central Alkaline Basic-Intermediate Layered And Acid Unit diorite, (BUAW-6). C) Central Alkaline Basic-Intermediate Layered And Acid Unit alkali feldspar granite, (BUAW-10). D) External Subalkaline Intermediate Unit quartz diorite, (BUAW-5).

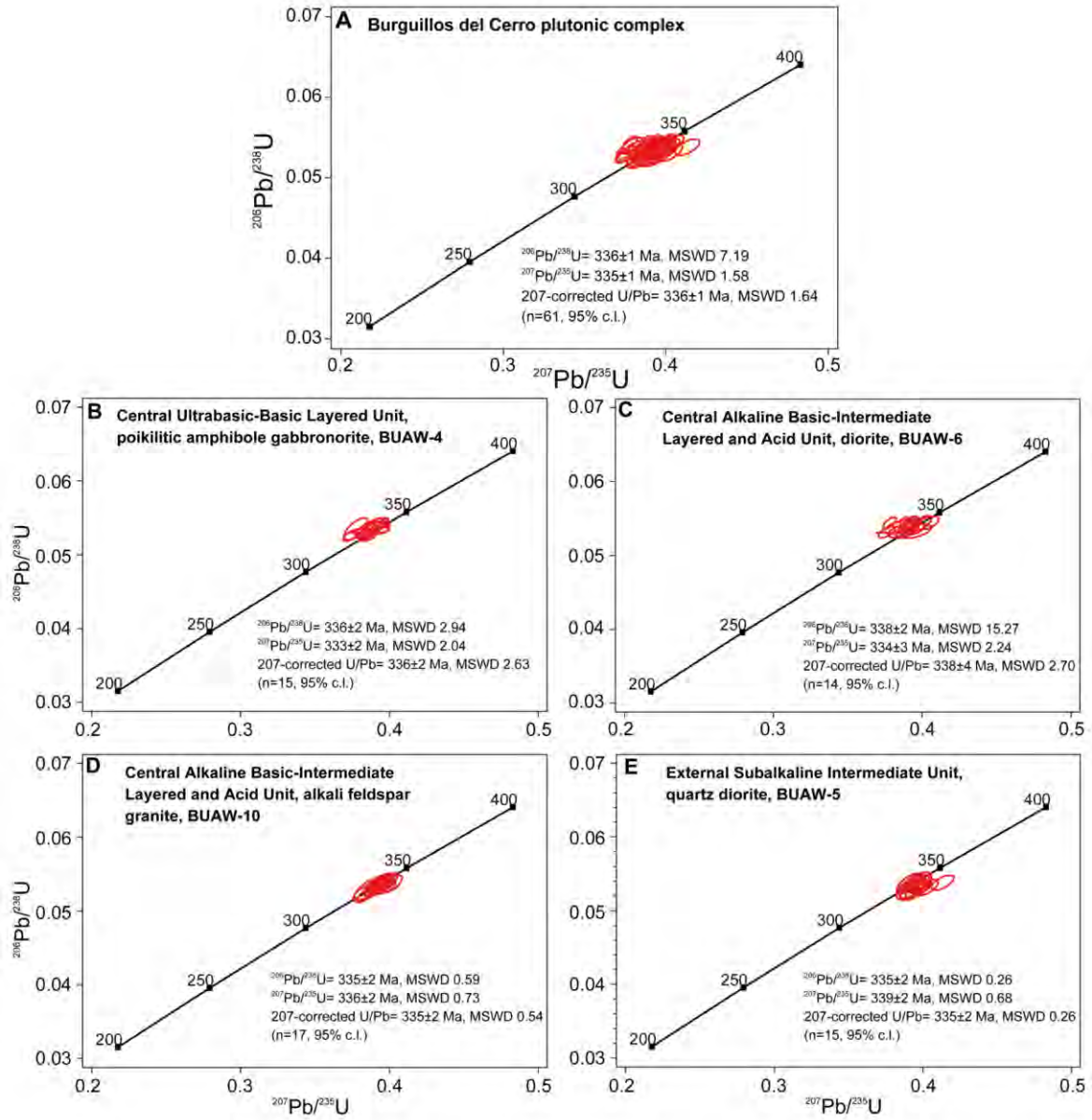

Figure 9.2 A) Wetherill concordia plots for the whole Burguillos del Cerro plutonic complex. Wetherill concordia plots for: B) Central Ultrabasic-Basic Layered Unit poikilitic amphibolitic gabbronorite, (BUAW-4). C) Central Alkaline Basic-Intermediate Layered and Acid Unit diorite, (BUAW-6). D) Central Alkaline Basic-Intermediate Layered and Acid Unit alkali feldspar granite, (BUAW-10). E) External Subalkaline Intermediate Unit quartz diorite, (BUAW-5).

Fourteen grains were analyzed with the SHRIMP. They contained moderate concentrations of U (98-691 ppm) and Th (38-384 ppm) with Th/U = 0.38-0.67 and little common lead (f^{206} < 0.93 %) (Table 9.1). All of them were concordant (discordance -4.8 to 1.0 %) (Fig. 9.2C). The weighted means (errors reported at 2σ) of the uncorrected and 207-corrected $^{206}Pb/^{238}U$ are virtually identical, 338 ± 2 Ma (MSWD = 15.3) and 338 ± 4 Ma (MSWD = 2.7).

The alkali feldspar granite BUAW-10 represents the acid member of this unit. It contains

abundant zircon. Grains are colourless to pinkish, transparent to translucent, free of inclusions, prismatic euhedral to subhedral (Fig. 9.1C) with dimensions around 250 μm x 150 μm (Fig. 9.1C). Cathodoluminescence images reveal oscillatory zoning in most cases (Fig. 9.1C).

Seventeen U-Pb measurements were carried out in 17 different grains. They contained large concentrations of U (333-986 ppm) and moderate values of Th (76-462 ppm) with Th/U = 0.12-0.54 and little common lead (f^{206} < 0.65%) (Table 9.1). All of them were concordant (discordance -0.6 to 1.8 %) (Fig. 9.2D). The weighted means (errors reported at 2σ) of the uncorrected and 207-corrected $^{206}Pb/^{238}U$ are virtually identical, 335 ± 2 Ma (MSWD = 0.59) and 335 ± 2 Ma (MSWD = 0.54).

9.1.1.3 External Subalkaline Intermediate Unit

The quartz diorite BUAW-5 contains abundant large zircons. These are bipyramidal prisms with an average size of 300 μm x 200 μm that, in some cases, may reach up to 400 μm x 300 μm. Most grains are colourless, transparent to translucent, and often have abundant inclusions (Fig. 9.1D). Under the cathodoluminescence microscope most grains show magmatic oscillatory zoning with a core that, in general, is less cathodoluminescent than the rim (Fig. 9.1D).

Fifteen determinations made with the SHRIMP yielded moderate concentrations of U (99-212 ppm) and Th (47-135 ppm) with Th/U = 0.32-0.67 and little common lead (f^{206} < 1.21%) (Table 9.1). All of them were concordant (discordance -0.8 to 3.8%) (Fig. 9.2E). The weighted means (errors reported at 2σ) of the uncorrected and 207-corrected $^{206}Pb/^{238}U$ are virtually identical, 335 ± 2 Ma (MSWD = 0.26) and 335 ± 2 Ma (MSWD = 0.26).

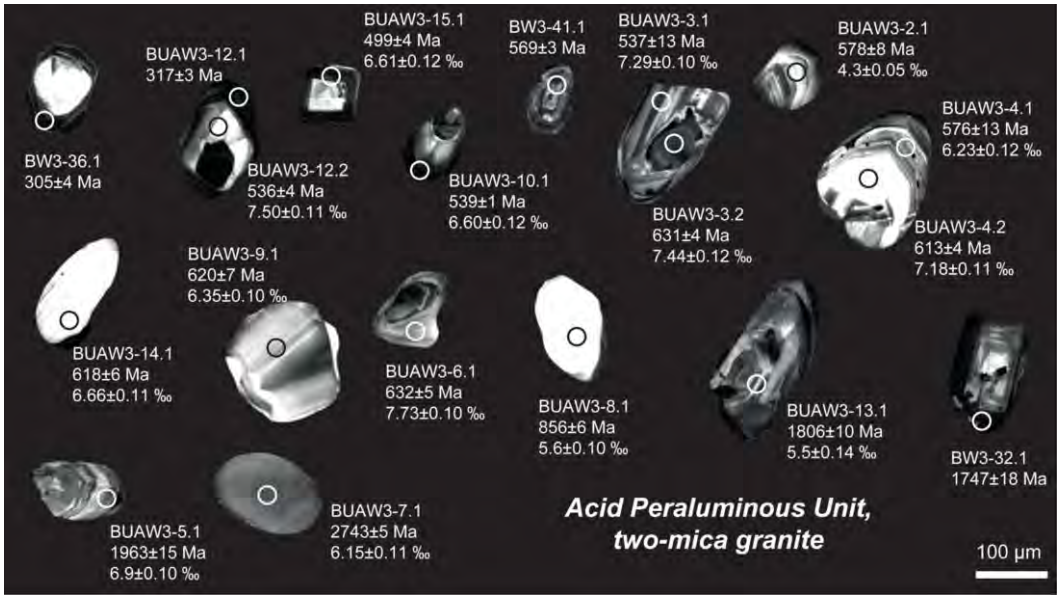

Figure 9.3. A) Cathodoluminescence images ages and O istope values of representative Burguillos del Cerro Acid Peraluminous Unit two-mica granite analysed zircons.

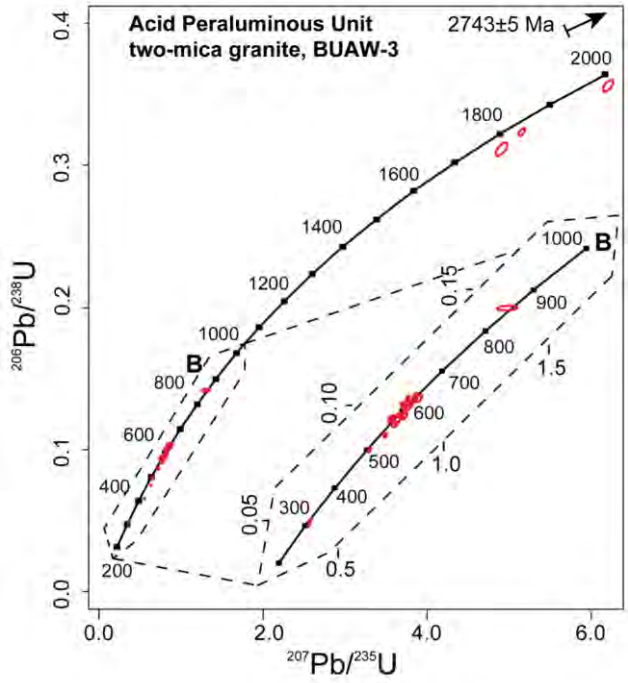

Figure 9.4. A) Wetherill concordia plots for the two-mica granite sample BUAW-3. B) Wetherill Concordia detail of the most abundant age range.

9.1.1.4 Acid Peraluminous Unit

The two-mica granite BUAW-3, in contrast with the rest of the Burguilos samples, contained several morphological populations of zircons with different ages that may be divided into three groups (Table 9.1).

The first group comprises Archean and Paleoproterozoic zircons. One rounded medium size unzoned grain, 100 µm x 100 µm, has an age of 2743±5 Ma (Fig. 9.3 and 9.4). Three Paleoproterozoic grains are medium-sized, 150 µm x 100 µm, prismatic, euhedral with magmatic oscillatory zoning, two grains have Orosirian ages, 1963±15 and 1805±10 Ma and one a Statherian age, 1747±18 Ma (Fig. 9.3 and 9.4). Notably, no Mesoproterozoic zircons were found.

The second group contains Neoproterozoic and lower Cambrian zircons. One rounded high cathodoluminescent zircon is Tonian, 856±6 Ma (Fig. 9.3 and 9.4) but most grains are Ediacaran. These zircons are mainly colourless although some are translucent. Cathodoluminescene imaging reveals two types of zircons: ones with little evidence of magmatic zonation and others with magmatic oscillatory zoning and a core that, in general, is more cathodoluminescent than the rim. The ages range from 634-569 Ma, only two grains have lower

	Conc. (ppm)				Ages (Ma), uncorrected					Age (Ma), ^{207}Pb corrected	
Spot	U	Th	f206%	^{232}Th/^{235}U	^{206}Pb/^{238}U	±err	^{207}Pb/^{235}U	±err	d(%)	^{206}Pb/^{238}U	±err
Sample BUAW-4 (n=15). Central Ultrabasic-Basic Layered Unit, poikilitic amphibole gabbronorite											
BUAW-4-14.1	208	113	0.24	0.56	329.3	3.0	330.6	4.3	0.4	329.1	3.2
BUAW-4-10.1	284	126	0.21	0.45	330.1	3.3	322.5	3.7	-2.4	330.6	3.5
BUAW-4-8.1	276	164	0.06	0.61	330.7	3.2	330.2	3.7	-0.2	330.7	3.4
BUAW-4-11.1	291	195	0.00	0.69	334.6	2.8	335.8	5.7	0.4	334.5	3.3
BUAW-4-13.1	209	140	0.32	0.69	334.1	2.0	328.4	6.2	-1.8	334.5	2.5
BUAW-4-4.1	345	184	0.01	0.55	334.8	4.2	331.4	4.4	-1.0	335.0	4.4
BUAW-4-5.1	213	143	0.20	0.69	335.0	5.8	331.4	6.7	-1.0	335.2	6.2
BUAW-4-7.1	404	266	0.12	0.68	336.3	2.7	339.2	2.6	0.8	336.0	2.7
BUAW-4-6.1	330	133	0.09	0.41	336.0	1.7	334.2	2.2	-0.6	336.1	1.8
BUAW-4-12.1	211	78	0.61	0.38	335.9	6.6	325.2	5.9	-3.2	336.7	6.8
BUAW-4-3.1	296	195	0.15	0.67	338.8	2.8	336.4	5.5	-0.8	338.9	3.2
BUAW-4-2.1	523	272	0.12	0.53	338.7	3.1	331.5	3.6	-2.2	339.2	3.3
BUAW-4-15.1	353	160	-0.14	0.47	341.2	3.2	336.5	3.8	-1.4	341.5	3.4
BUAW-4-9.1	323	146	0.14	0.46	342.5	1.8	339.2	2.0	-1.0	342.7	1.9
BUAW-4-1.1	119	67	-0.02	0.57	343.1	1.9	336.4	2.9	-2.0	343.6	2.1
Sample BUAW-6 (n=14). Central Alkaline Basic-Intermediate Layered and Acid Unit, diorite											
BUAW-6-14.1	369	139	0.10	0.39	333.6	3.0	331.7	2.9	-0.6	333.7	3.1
BUAW-6-8.1	121	65	0.36	0.55	333.3	0.1	322.7	3.5	-3.2	334.1	0.4
BUAW-6-7.1	147	63	0.93	0.44	334.7	5.0	338.3	7.6	1.0	334.4	5.7
BUAW-6-9.1	362	170	0.15	0.48	333.8	3.7	324.2	4.2	-3.0	334.5	3.9
BUAW-6-13.1	225	124	0.12	0.56	334.9	5.0	332.3	7.4	-0.8	335.1	5.6
BUAW-6-1.1	196	84	0.70	0.44	336.0	3.4	338.3	4.4	0.6	335.8	3.7
BUAW-6-3.1	157	74	0.27	0.49	337.9	4.7	330.4	7.1	-2.2	338.4	5.2
BUAW-6-5.1	275	101	0.16	0.38	338.9	4.1	336.8	4.0	-0.6	339.0	4.3
BUAW-6-4.1	98	38	0.40	0.40	339.1	4.5	336.4	4.7	-0.8	339.3	4.8
BUAW-6-6.1	167	110	0.29	0.67	341.3	4.7	343.9	5.8	0.8	341.0	5.0
BUAW-6-12.1	691	384	0.07	0.57	341.4	4.6	341.6	4.8	0.0	341.3	4.8
BUAW-6-2.1	572	248	0.23	0.45	341.7	4.0	335.5	4.0	-1.8	342.1	4.2
BUAW-6-11.1	184	114	0.02	0.63	341.3	3.5	325.6	3.2	-4.8	342.5	3.6
BUAW-6-10.1	441	242	-0.06	0.56	343.3	2.3	332.9	2.4	-3.2	344.1	2.4
Sample BUAW-10 (n=17). Central Alkaline Basic-Intermediate Layered and Acid Unit, alkali feldspar granite											
BUAW-10-12.1	667	270	0.29	0.41	327.1	4.0	329.4	3.7	0.6	326.9	4.2
BUAW-10-4.1	684	269	0.24	0.40	329.3	5.6	329.9	6.1	0.2	329.2	6.0
BUAW-10-2.1	427	125	0.31	0.30	332.1	6.2	330.4	5.9	-0.6	332.2	6.5
BUAW-10-5.1	658	76	0.23	0.12	332.9	5.0	334.4	4.9	0.4	332.7	5.2
BUAW-10-1.1	410	149	0.43	0.37	333.6	4.5	336.5	4.5	0.8	333.3	4.7
BUAW-10-11.1	333	93	0.65	0.29	334.0	4.1	339.8	4.8	1.8	333.5	4.4
BUAW-10-10.1	613	215	0.32	0.36	333.8	4.4	335.6	4.3	0.6	333.6	4.6
BUAW-10-16.1	642	338	0.08	0.54	333.8	5.5	335.0	5.0	0.4	333.7	5.7
BUAW-10-18.2	478	151	0.29	0.32	334.6	5.7	334.4	5.1	0.0	334.6	5.9
BUAW-10-9.2	986	462	0.22	0.48	335.4	6.0	334.2	5.2	-0.4	335.4	6.1
BUAW-10-3.1	407	105	0.32	0.26	335.9	5.5	338.5	5.3	0.8	335.6	5.8
BUAW-10-7.1	477	178	0.34	0.38	336.0	4.8	337.8	4.2	0.6	335.8	4.9
BUAW-10-15.1	623	212	0.51	0.35	336.8	5.3	342.8	5.0	1.8	336.3	5.5
BUAW-10-8.1	375	110	0.44	0.30	338.3	4.7	341.0	4.4	0.8	338.0	4.8
BUAW-10-9.1	437	195	0.32	0.46	338.5	4.2	337.5	3.9	-0.2	338.5	4.4
BUAW-10-6.1	653	225	0.33	0.35	339.5	4.8	338.4	5.1	-0.4	339.5	5.0
BUAW-10-13.1	582	221	0.40	0.39	340.2	4.2	341.5	4.1	0.4	340.0	4.3

Table 9.1. Summary of U-Th-Pb ages obtained for Burguillos del Cerro plutonic complex main units. d(%)=100x(1–206/238 age / 207/235 age); f^{206}%=(common ^{206}Pb/total ^{206}Pb)x100.

	Conc. (ppm)				Ages (Ma), uncorrected					Age (Ma), ^{207}Pb corrected	
Spot	U	Th	f206%	^{232}Th/^{235}U	^{206}Pb/^{238}U	±err	^{207}Pb/^{235}U	±err	d(%)	^{206}Pb/^{238}U	±err
Sample BUAW-5 (n=15). External Subalkaline Intermediate Unit, quartz diorite											
BUAW-5-5.1	112	72	1.02	0.66	332.0	6.7	337.6	7.0	1.6	331.5	7.0
BUAW-5-8.1	166	51	0.38	0.32	332.1	4.4	337.4	4.2	1.6	331.6	4.5
BUAW-5-13.1	182	106	0.46	0.60	333.6	5.4	342.9	6.1	2.8	332.8	5.7
BUAW-5-2.1	122	80	1.21	0.67	333.1	6.3	336.5	6.4	1.0	332.8	6.6
BUAW-5-10.1	130	47	0.66	0.37	333.6	3.7	337.8	6.7	1.2	333.2	4.2
BUAW-5-4.1	105	54	0.37	0.53	333.7	7.9	336.8	8.1	1.0	333.4	8.3
BUAW-5-11.1	101	56	1.21	0.56	334.1	3.9	341.7	4.2	2.2	333.5	4.2
BUAW-5-3.1	109	68	1.15	0.64	333.7	4.2	333.1	4.3	-0.2	333.7	4.4
BUAW-5-12.1	99	58	0.67	0.60	335.2	4.0	340.5	4.9	1.6	334.7	4.3
BUAW-5-14.1	212	109	0.24	0.53	337.7	4.8	351.2	5.4	3.8	336.6	5.1
BUAW-5-9.1	200	118	0.44	0.61	337.0	6.1	334.5	5.7	-0.8	337.1	6.3
BUAW-5-6.1	168	75	0.54	0.46	337.4	5.4	337.3	4.9	0.0	337.4	5.6
BUAW-5-15.1	206	135	0.54	0.67	338.2	4.6	341.3	4.5	1.0	337.9	4.8
BUAW-5-1.1	208	92	0.35	0.45	338.5	6.3	338.9	6.9	0.2	338.4	6.7
BUAW-5-7.1	111	47	0.34	0.43	339.8	4.4	337.4	4.3	-0.8	339.9	4.6
Sample BUAW-3 (n=24). Acid Peraluminous Unit, two-mica granite											
BUAW-3-36.1	577	24	0.16	0.14	304.6	4.3	313.5	4.6	2.8	303.9	4.5
BUAW-3-12.1	703	31	0.09	0.05	316.5	2.9	320.5	3.7	1.2	316.1	3.1
BUAW-3-15.1	459	32	0.11	0.51	498.8	4.1	507.7	4.4	1.8	497.9	4.3
BUAW-3-12.2	281	21	0.08	0.17	536.2	3.9	552.3	4.2	3.0	534.6	4.2
BUAW-3-10.1	674	51	0.19	0.36	539.4	1.3	547.1	1.9	1.4	538.6	1.3
BUAW-3-41.1	433	35	0.19	0.84	568.8	2.7	582.9	3.3	2.4	567.4	2.9
BUAW-3-4.1	43	4	-0.69	0.59	575.9	13.1	584.0	12.0	1.4	575.1	13.9
BUAW-3-2.1	140	11	-0.22	0.64	578.2	7.7	569.5	6.9	-1.6	579.0	8.1
BUAW-3-1.1	260	21	0.15	0.36	580.9	4.8	568.9	7.7	-2.2	582.0	5.5
BUAW-3-11.1	578	48	0.04	1.07	585.2	1.7	588.1	2.8	0.4	584.9	1.9
BUAW-3-35.1	552	46	0.30	0.02	587.3	7.3	605.9	6.4	3.0	585.4	7.6
BUAW-3-37.1	552	47	0.06	0.04	605.2	4.8	605.0	4.5	0.0	605.2	5.2
BUAW-3-40.1	527	45	0.08	0.79	608.6	4.8	615.3	8.4	1.0	607.9	5.6
BUAW-3-4.2	271	23	0.09	0.13	613.1	3.6	604.3	5.1	-1.4	613.9	4.0
BUAW-*3-14.1*	68	6	0.63	0.52	617.7	5.8	611.1	16.3	-1.0	618.3	7.5
BUAW-3-9.1	129	11	-0.13	0.92	620.4	7.4	624.3	6.5	0.6	620.0	7.8
BUAW-3-3.2	241	22	0.57	1.60	631.0	7.4	642.9	7.0	1.8	629.7	7.9
BUAW-3-6.1	226	20	0.12	0.37	632.2	4.8	614.1	4.4	-3.0	634.0	5.1
BUAW-3-3.1	383	34	0.01	0.49	636.9	6.0	634.1	6.7	-0.4	637.1	6.5
BUAW-3-8.1	37	5	0.81	0.57	855.9	5.6	846.9	21.0	-1.0	857.0	8.3
BUAW-3-32.1	550	148	0.03	0.34	1747.3	17.5	1803.7	12.1	3.2	1729.5	21.9
BUAW-3-13.1	215	60	0.07	0.42	1805.9	9.9	1845.0	6.5	2.2	1792.8	12.0
BUAW-3-5.1	277	85	0.04	0.61	1962.9	14.7	2005.5	8.9	2.2	1945.9	18.6
BUAW-3-7.1	271	124	0.00	0.89	2743.3	4.7	2727.4	4.2	-0.6	2753.2	4.7

Table 9.1.Continued.

Cambrian ages, 539±1 and 536±1 Ma (Fig. 9.3 and 9.4). The zircons in the third group are all overgrowths on older grains, they have Variscan ages. The rims are small with low cathodoluminescene, some data apparently reflect a mixed ages, 499±4 Ma, two grains have younger ages 317±3 and 305±4 Ma (Fig. 9.3 and 9.4).

9.1.2 Valencia del Ventoso Plutonic Complex

The six samples studied from this massif were: a diorite, a quartz diorite and a granodiorite from the *Main Pluton Alkaline to Subalkaline Basic-Acid Unit*; a quartz monzodiorite from the *Northern Stock Subalkaline Basic-Intermediate Unit;* a quartz monzodiorite from the *Southern Stock Subalkaline Intermediate-Acid Unit*; and, an aplite from the *Intrusive Dyke Unit*. All U–Pb data are in the range of 334-320 Ma (Fig. 9.6 and Table 9.2).

9.1.2.1 Main Pluton Alkaline to Subalkaline Basic-Acid Unit

Three samples of the main *Main Pluton Alkaline to Subalkaline Basic-Acid Unit* were studied to evaluate the concentric compositional zoning.

The diorite VAAW-35 contained few zircons. They consist of colourless transparent to translucent mostly euhedral short prisms with a size close to 200 μm x 100 μm. They often contain melt inclusions. Cathodoluminescence images reveal that most grains are oscillatory zoned (Fig. 9.5A).

Thirteen U-Pb measurements on the same numbers of zircons yielded variable, high and low, concentrations of U (126-2230 ppm) and Th (44-2444 ppm) with Th/U = 0.1-1.12 and little common lead ($f^{206} < 0.22\%$) (Table 9.2). All of them were concordant (discordance -4.4 to 1 %) (Fig. 9.6A). The weighted means (errors reported at 2σ) of the uncorrected and 207-corrected $^{206}Pb/^{238}U$ are virtually identical, 337 ± 3 Ma (MSWD = 16.6) and 338 ± 3 Ma (MSWD = 15).

The quartz diorite VAAW-37, contained abundant zircon. These are colourless transparent euhedral large bipyramid-terminated prisms with an average size of 300 μm x 200 μm. Some grains are up to 400 μm x 300 μm. The largest zircons are typically fractured and may have large melt inclusions. Under the cathodoluminescence microscope they are dark grey to pale grey, with a marked oscillatory zoning that reveals a core that, in general, is less cathodoluminescent than the rim (Fig. 9.5B).

Twenty-six U-Pb measurements on the same numbers of zircons yielded low to high concentrations of U (85-1174 ppm) and Th (25-682 ppm) with Th/U = 0.23-0.64 and little common lead ($f^{206} < 1.74\%$) (Table 9.2). All of them were concordant (discordance -4.8 to 3.6 %) (Fig. 9.6B). The weighted means (errors reported at 2σ) of the uncorrected and 207-corrected

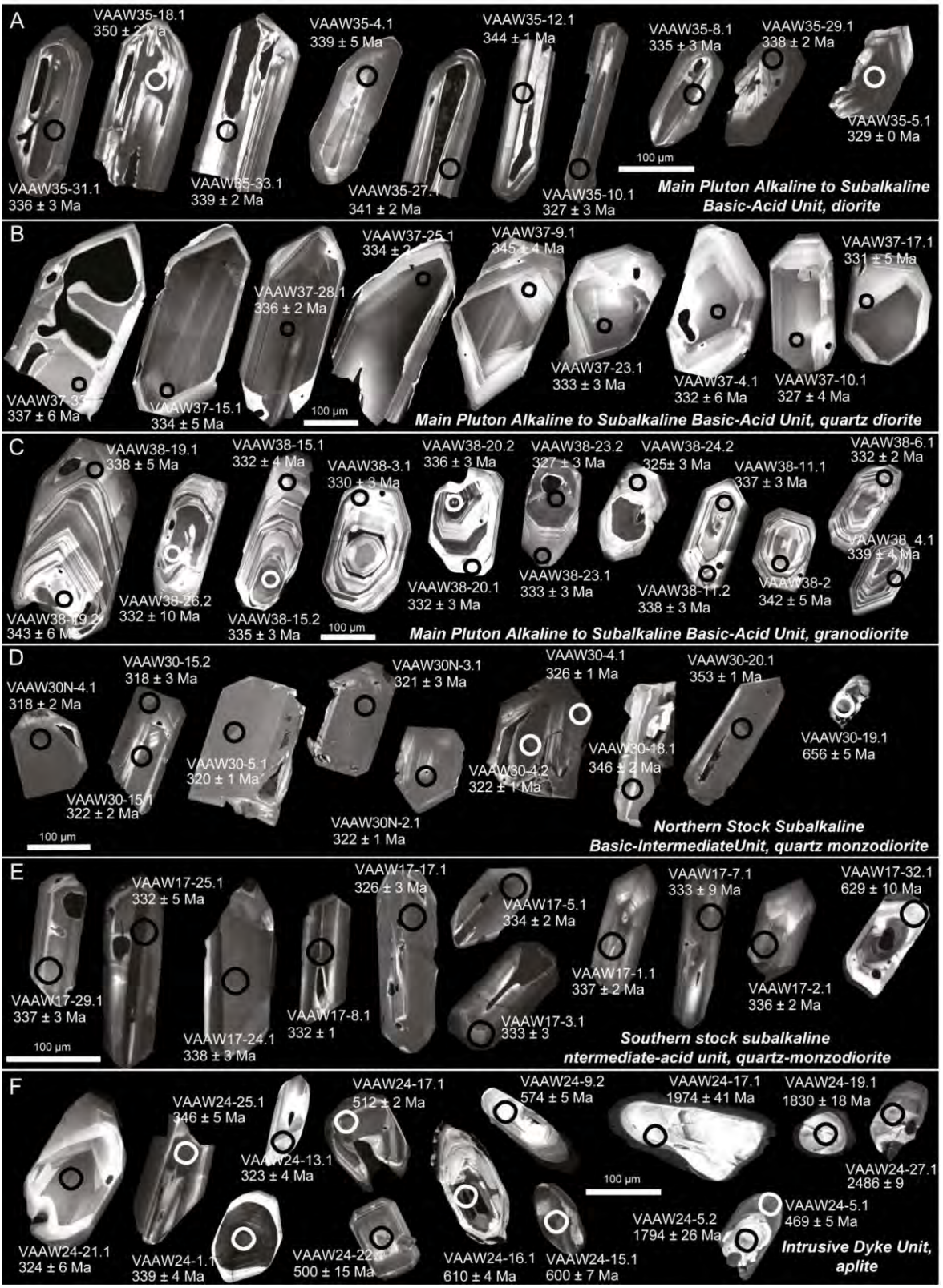

Figure 9.5. Cathodoluminescence images and ages of representative analysed zircons from Valencia del Ventoso plutonic complex. Main Pluton Alkaline To Subalkaline Basic-Acid Unit: A) diorite, B) quartz diorite and C) granodiorite. D) Northern Stock quartz monzodiorite. E) Southern Stock quartz monzodiorite. F) Intrusive Dyke Unit, aplite.

$^{206}Pb/^{238}U$ are virtually identical, 333 ± 2 Ma (MSWD = 0.4) and 333 ± 2 Ma (MSWD = 0.2)

Zircons extracted from the granodiorite VAAW-38 from the outer rim of the pluton are very similar to those from the quartz diorite VAAW-37, and also have similar cathodoluminescene images (Fig. 9.5C).

Twenty-five U-Pb measurements on 17 zircons yielded moderate concentrations of U (86-693 ppm) and Th (26-374 ppm) with Th/U = 0.31-0.56 and little common lead (f^{206} < 1.17%) (Table 9.2). All of them were concordant (discordance -3 to 4.8%) (Fig. 9.6C). The weighted means (errors reported at 2σ) of the uncorrected and 207-corrected $^{206}Pb/^{238}U$ are virtually identical, 336 ± 2 Ma (MSWD = 0.27) and 336 ± 2 Ma (MSWD = 0.20).

9.1.2.2 Northern Stock Subalkaline Basic-Intermediate Unit

Zircons from the quartz monzodiorite VAAW-30 are colourless to pinkish, transparent to translucent, stubby short-medium, 150 μm x 100 μm, euhedral to subhedral prisms which may be rich in inclusions. Cathodoluminescence imaging reveals a monotonous internal structure with little evidence of zonation (Fig. 9.5D).

Fourteen determinations made on 11 different grains with the SHRIMP yielded high concentrations of U (418-6180 ppm) and Th (69-5377 ppm) with Th/U = 0.17-1.08 and little common lead (f^{206} < 0.26%) (Table 9.2). All of them were concordant (discordance -4.2 to 3.4%) (Fig. 9.6D). The weighted means (errors reported at 2σ) of the uncorrected and 207-corrected $^{206}Pb/^{238}U$ are virtually identical, 320 ± 3 Ma (MSWD = 2) and 320 ± 3 Ma (MSWD = 1). Two grains have older $^{206}Pb/^{238}U$ ages of 353±1 and 346±2 Ma (Figs 9.5D and 9.6D). One highly cathodoluminescent pre-magmatic zircon has a $^{206}Pb/^{238}U$ age of 656±5 Ma (Fig. 9.5D).

9.1.2.3 Southern Stock Subalkaline Intermediate-Acid Unit

Zircons of the quartz monzodiorite VAAW-17 are colourless to pinkish, often transparent, euhedral prisms, 100 μm x 50 μm, with pyramidal terminations. The internal morphology is complex: whereas some grains have patchy high and low cathodoluminescent areas other grains are structureless. Some grains contain abundant inclusions that, in some, appear to be melt inclusions (Fig. 9.5E).

Fourteen grains analysed with the SHRIMP yielded high concentrations of U (111-1247 ppm) and Th (21-643 ppm) with Th/U = 0.2-0.74 and little common lead (f^{206} <

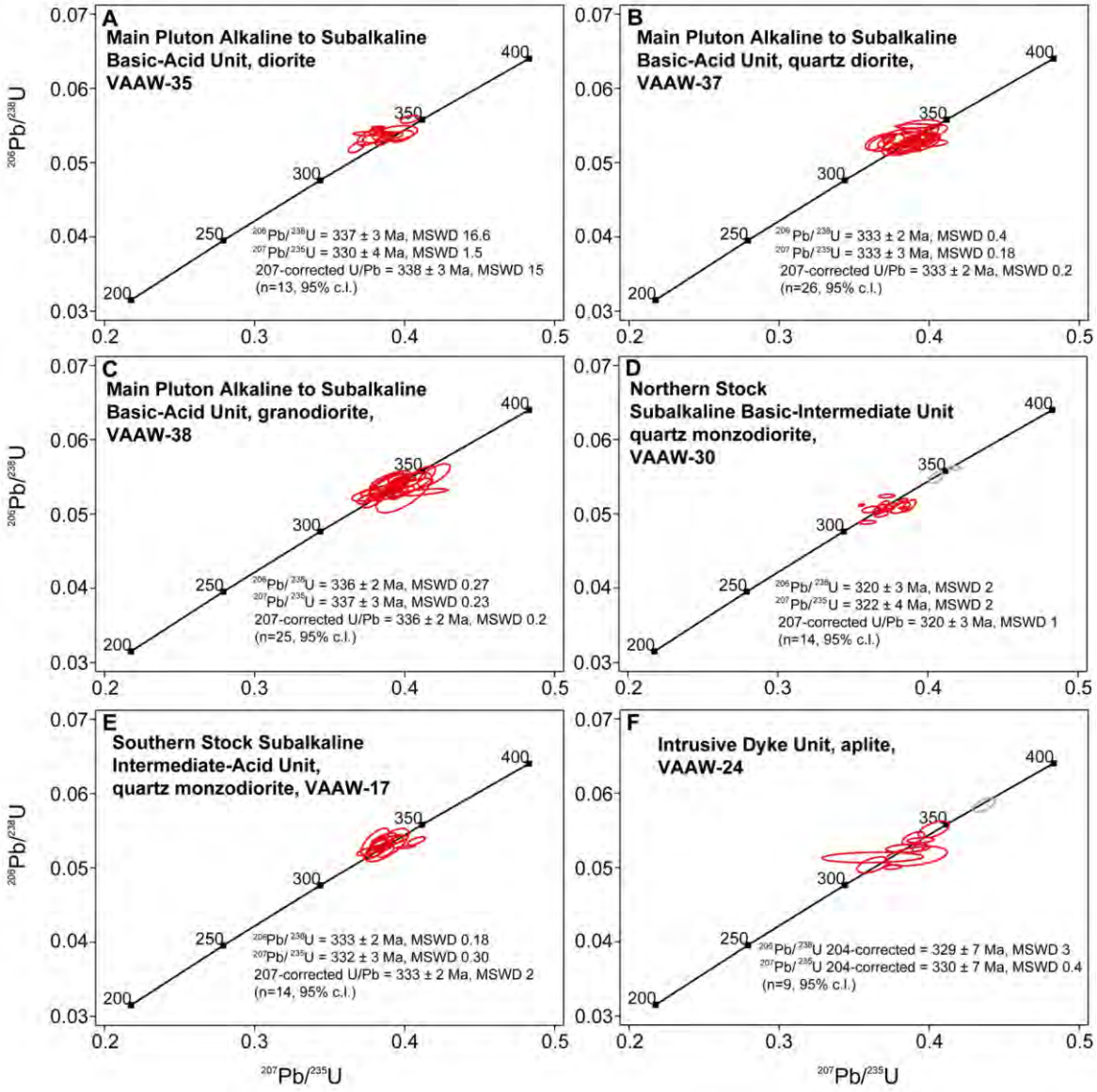

Figure 9.6. Wetherill concordia plots for the Valencia del Ventoso: A) to C) Main Pluton Alkaline to Subalkaline Basic-Acid Unit diorite (VAAW-35), quartz diorite (VAAW-37) and granodiorite (VAAW-38). D) Northern Stock quartz monzodiorite (VAAW-30), grey data not computed for age determination. E) Southern Stock quartz monzodiorite (VAAW-17). F) Intrusive Dyke Unit aplite (VAAW-24), grey data not computed for age determination.

0.73 %) (Table 9.2). All of them were concordant (discordance -2.8 to 3%) (Fig. 9.6E). The weighted means (errors reported at 2σ) of the uncorrected and 207-corrected $^{206}Pb/^{238}U$ are virtually identical, 333 ± 2 Ma (MSWD = 0.18) and 333 ± 2 Ma (MSWD = 2). One grain is morphologically different to the rest (Fig. 9.5E) and appears to be pre-magmatic with a $^{206}Pb/^{238}U$ of 629 ± 10 Ma.

9.1.2.4 Intrusive Dyke Unit

The aplite VAAW-24 has zircons of very different sizes and morphologies which can be

	Conc. (ppm)				Ages (Ma), uncorrected					Age (Ma), ^{207}Pb corrected	
Spot	U	Th	f206%	^{232}Th/^{235}U	^{206}Pb/^{238}U	±err	^{207}Pb/^{235}U	±err	d(%)	^{206}Pb/^{238}U	±err
Sample VAAW-35 (n=13). Main Pluton Alkaline to Subalkaline Basic-Acid Unit, diorite											
VAAW35-10.1	768	520	0.00	0.70	327.3	3.0	318.2	3.4	-2.8	328.0	3.1
VAAW35-5.1	2230	2444	0.04	1.12	329.0	0.3	321.0	1.0	-2.4	329.6	0.3
VAAW35-25.1	1796	1014	0.18	0.58	333.7	3.1	331.5	3.4	-0.6	333.9	3.3
VAAW35-8.1	589	258	0.00	0.45	334.9	3.1	328.6	6.2	-2.0	335.4	3.5
VAAW35-17.1	351	135	0.00	0.39	335.4	4.5	324.9	5.4	-3.2	336.3	5.0
VAAW35-31.1	126	44	-0.51	0.36	336.4	3.4	340.0	4.8	1.0	336.1	3.6
VAAW35-19.1	452	175	0.10	0.40	336.8	2.2	335.3	4.3	-0.4	336.9	2.6
VAAW35-29.1	1445	572	0.22	0.41	337.8	1.6	333.5	2.4	-1.2	338.1	1.7
VAAW35-33.1	135	44	0.00	0.34	338.7	1.5	327.0	8.8	-3.6	339.7	2.3
VAAW35-4.1	216	98	0.00	0.46	338.7	4.9	336.9	9.1	-0.6	338.9	5.7
VAAW35-27.1	438	245	0.17	0.57	340.6	1.8	327.8	3.2	-4.0	341.6	2.0
VAAW35-12.1	489	458	0.00	0.96	343.7	0.7	328.9	2.7	-4.4	344.9	0.9
VAAW35-18.1	1649	162	0.19	0.10	350.3	2.3	344.0	3.8	-1.8	350.8	2.6
Sample VAAW-37 (n=26). Main Pluton Alkaline to Subalkaline Basic-Acid Unit, quartz diorite											
VAAW37-7.1	235	52	0.00	0.23	325.6	1.3	328.5	7.4	0.8	325.4	1.9
VAAW37-7.2	1174	682	0.16	0.60	326.7	3.3	327.5	5.4	0.2	326.7	3.8
VAAW37-10.1	144	70	0.00	0.50	327.1	4.4	329.6	6.7	0.8	327.0	4.9
VAAW37-16.1	393	215	0.00	0.56	328.8	3.2	333.0	4.6	1.2	328.4	3.5
VAAW37-21.1	341	140	0.06	0.42	329.0	4.6	329.6	4.4	0.2	329.0	4.8
VAAW37-12.1	284	127	0.15	0.46	330.1	2.4	336.0	4.2	1.8	329.6	2.7
VAAW37-1.1	164	46	1.74	0.29	330.4	6.0	325.7	6.0	-1.4	330.8	6.3
VAAW37-5.1	204	103	0.56	0.52	330.7	2.2	342.7	6.3	3.6	329.8	2.7
VAAW37-17.1	112	37	0.00	0.34	331.3	5.2	320.7	7.4	-3.4	332.1	5.6
VAAW37-4.1	169	86	0.00	0.52	331.5	5.6	337.4	8.0	1.8	331.0	6.0
VAAW37-18.1	131	43	0.00	0.34	331.7	4.5	316.8	5.5	-4.8	332.9	4.9
VAAW37-26.1	338	190	0.00	0.58	331.9	2.7	331.9	4.1	0.0	331.9	2.9
VAAW37-24.1	166	81	0.00	0.50	332.2	2.9	332.3	3.1	0.0	332.2	3.0
VAAW37-22.1	381	130	0.08	0.35	332.4	4.6	325.1	7.2	-2.2	332.9	5.0
VAAW37-8.1	313	162	0.18	0.53	333.3	2.1	322.0	2.3	-3.6	334.1	2.1
VAAW37-23.2	203	100	0.00	0.51	333.4	3.0	341.6	3.3	2.4	332.8	3.1
VAAW37-11.1	143	70	0.00	0.50	333.6	4.0	335.4	5.0	0.6	333.5	4.4
VAAW37-25.1	327	110	-0.11	0.35	334.1	1.7	342.8	2.7	2.6	333.5	2.0
VAAW37-15.1	169	54	0.00	0.33	334.3	4.7	337.4	4.6	1.0	334.0	4.8
VAAW37-28.1	378	234	0.00	0.64	335.9	1.6	338.3	5.7	0.8	335.8	2.1
VAAW37-19.1	136	41	0.00	0.31	336.5	2.1	341.2	3.5	1.4	336.1	2.3
VAAW37-33.1	164	48	0.00	0.30	336.6	4.6	328.5	8.4	-2.4	337.3	5.2
VAAW37-20.2	345	190	0.00	0.57	338.5	4.6	341.2	4.2	0.8	338.3	4.7
VAAW37-27.1	190	63	-0.24	0.34	341.0	3.5	344.5	4.9	1.0	340.8	3.8
VAAW37-14.1	96	31	0.00	0.34	344.9	1.3	334.3	7.8	-3.2	345.8	2.0
VAAW37-9.1	85	25	0.00	0.30	345.0	3.8	337.2	8.4	-2.4	345.6	4.5
Sample VAAW-38 (n=25). Main Pluton Alkaline to Subalkaline Basic-Acid Unit, granodiorite											
VAAW38-24.2	693	374	0.00	0.55	325.5	3.4	326.3	4.4	0.2	325.5	3.7
VAAW38-23.2	569	272	0.36	0.49	327.4	2.6	324.0	4.8	-1.0	327.6	2.9
VAAW38-3.1	116	40	0.80	0.36	329.7	2.5	332.3	7.5	0.8	329.5	3.0
VAAW38-15.1	152	51	0.44	0.34	331.9	3.9	327.9	10.1	-1.2	332.3	4.7
VAAW38-26.2	241	126	-0.04	0.54	332.2	9.9	341.3	11.2	2.6	331.5	10.5
VAAW38-20.1	166	57	0.00	0.35	332.4	3.5	339.0	3.5	2.0	331.9	3.6
VAAW38-6.1	196	73	0.50	0.38	332.4	1.8	349.1	11.1	4.8	331.0	2.7
VAAW38-23.1	494	154	0.73	0.32	332.6	2.9	340.0	5.5	2.2	332.1	3.3
VAAW38-8.2	204	82	-0.40	0.41	332.7	1.8	325.1	4.0	-2.4	333.3	2.1
VAAW38-8.1	315	107	0.10	0.35	334.3	1.8	335.7	3.3	0.4	334.1	1.9
VAAW38-15.2	353	189	0.00	0.55	335.3	3.1	336.8	3.7	0.4	335.1	3.3
VAAW38-7.1	289	100	0.16	0.36	335.9	1.3	326.1	1.6	-3.0	336.6	1.2
VAAW38-20.2	157	62	0.37	0.41	336.3	3.4	335.2	4.1	-0.4	336.3	3.6
VAAW38-11.1	186	101	0.17	0.56	336.6	3.4	337.4	4.2	0.2	336.6	3.8
VAAW38-9.1	156	59	1.17	0.39	337.7	5.8	334.8	8.4	-0.8	338.0	6.5

Table 9.2. Summary of U-Th-Pb ages obtained for Valencia del Ventoso plutonic complex main units. d(%)=100x(1–206/238 age / 207/235 age); f^{206}%=(common ^{206}Pb/total ^{206}Pb)x100.

	Conc. (ppm)				Ages (Ma), uncorrected					Age (Ma), ^{207}Pb corrected	
Spot	U	Th	f206%	^{232}Th/^{235}U	^{206}Pb/^{238}U	±err	^{207}Pb/^{235}U	±err	d(%)	^{206}Pb/^{238}U	±err
VAAW38-11.2	251	105	0.12	0.43	338.1	3.5	346.1	7.5	2.4	337.5	4.1
VAAW38-19.1	340	118	0.00	0.36	338.4	5.3	332.9	7.2	-1.6	338.9	5.9
VAAW38-4.1	255	103	0.46	0.41	338.7	4.1	337.1	4.6	-0.4	338.9	4.4
VAAW38-5.2	382	206	0.33	0.55	340.2	2.1	337.8	3.6	-0.8	340.4	2.3
VAAW38-17.1	258	99	0.00	0.39	341.7	4.2	342.6	7.6	0.2	341.7	4.9
VAAW38-2.1	181	76	-0.09	0.43	342.1	4.7	334.8	8.3	-2.2	342.6	5.2
VAAW38-13.1	471	187	0.20	0.41	343.0	1.1	341.7	4.4	-0.4	343.1	1.5
VAAW38-19.2	86	26	-0.50	0.31	343.3	6.2	348.5	6.6	1.4	342.8	6.5
VAAW38-5.1	347	118	0.61	0.35	344.3	3.0	337.2	3.0	-2.2	344.8	3.0
VAAW38-14.1	195	71	0.00	0.37	346.7	5.4	355.6	6.5	2.6	346.0	5.8
Sample VAAW-30 (n=17). Northern Stock Subalkaline Basic-Intermediate Unit, quartz monzodiorite											
VAAW30-11.1	1875	1628	0.05	0.89	307.6	1.1	311.8	3.6	1.4	307.3	1.4
VAAW30-6.1	1996	1619	0.06	0.83	314.6	1.9	319.0	2.9	1.4	314.3	2.1
VAAW30-12.1	1400	893	-0.02	0.65	317.7	1.0	321.4	1.9	1.2	317.5	1.3
VAAW30-15.2	1916	2025	0.04	1.08	318.2	2.7	318.2	3.0	0.0	318.2	2.9
VAAW30N-4.1	3678	2292	-0.02	0.64	318.3	2.0	313.7	3.7	-1.4	319.1	2.2
VAAW30-8.1	674	401	0.26	0.61	319.6	3.1	328.2	4.0	2.6	319.0	3.5
VAAW30-5.1	3605	2867	0.00	0.82	319.7	0.7	329.9	2.1	3.0	319.4	0.8
VAAW30-13.1	3021	3132	0.00	1.06	320.2	2.2	322.9	2.8	0.8	320.3	2.5
VAAW30N-3.1	6180	5377	0.03	0.89	321.3	3.2	332.3	2.8	3.4	322.0	3.1
VAAW30N-2.1	2171	2079	0.07	0.98	321.9	0.7	309.0	1.2	-4.2	322.9	0.8
VAAW30-15.1	2318	1410	-0.01	0.62	321.9	2.2	319.8	2.3	-0.6	322.0	2.3
VAAW30-4.2	2446	2016	0.04	0.85	322.2	1.0	325.1	1.7	0.8	322.0	1.1
VAAW30-4.1	2291	1841	0.00	0.82	326.0	0.9	329.6	1.7	1.0	325.8	1.1
VAAW30N-1.1	3349	3289	-0.03	1.01	329.4	1.2	321.5	3.3	-2.4	330.4	1.4
VAAW30-18.1	1428	920	0.00	0.66	345.8	2.3	347.0	2.4	0.4	345.8	2.4
VAAW30-20.1	3513	3443	0.00	1.01	352.5	0.5	354.1	1.8	0.4	352.9	0.6
VAAW30-19.1	418	69	0.00	0.17	656.1	5.0	641.7	6.4	-2.2	657.6	5.7
Sample VAAW-17 (n=15). Southern Stock Subalkaline Intermediate-Acid Unit, quartz monzodiorite											
VAWW17-17.1	706	340	-0.08	0.49	326.2	2.7	326.2	3.8	0.0	326.3	3.1
VAWW17-14.1	458	272	-0.15	0.61	327.8	2.6	332.6	3.3	1.4	327.4	2.8
VAWW17-10.1	388	226	-0.15	0.60	328.3	2.0	325.3	2.2	-1.0	328.5	2.1
VAWW17-19.1	1110	643	0.17	0.59	328.4	2.1	324.2	5.0	-1.2	328.8	2.6
VAWW17-8.1	640	464	0.61	0.74	331.7	0.8	342.1	3.9	3.0	330.9	1.2
VAWW17-25.1	572	367	-0.10	0.66	332.1	5.1	329.7	4.9	-0.8	332.3	5.4
VAWW17-3.1	1247	295	0.10	0.24	332.6	2.9	332.6	3.9	0.0	332.6	3.1
VAWW17-7.1	341	185	0.00	0.56	333.2	8.0	333.1	9.0	0.0	333.3	8.6
VAWW17-5.1	370	214	0.00	0.59	334.0	2.3	329.8	3.8	-1.2	334.4	2.7
VAWW17-22.1	345	214	0.73	0.64	336.1	6.6	327.2	5.7	-2.8	336.8	6.7
VAWW17-29.1	310	170	0.18	0.56	336.6	3.0	334.5	7.4	-0.6	336.8	3.5
VAWW17-2.1	745	198	0.59	0.27	336.7	2.1	347.2	3.6	3.0	335.9	2.3
VAWW17-1.1	401	245	-0.09	0.63	337.1	2.3	337.5	3.0	0.2	337.1	2.5
VAWW17-24.1	322	174	0.32	0.55	337.9	3.2	331.4	5.3	-2.0	338.4	3.5
VAWW17-32.1	111	21	0.00	0.20	628.8	10.1	632.9	13.3	0.6	628.3	11.2

Table 9.2. Continued.

	Conc. (ppm)				Ages (Ma), uncorrected					Age (Ma), ^{207}Pb corrected		Age (Ma), ^{204}Pb corrected	
Spot	U	Th	f206%	^{232}Th/^{235}U	^{206}Pb/^{238}U	±err	^{207}Pb/^{235}U	±err	d(%)	^{206}Pb/^{238}U	±err	^{206}Pb/^{238}U	±err
Sample VAAW-24 (n=22).Intrusive Dyke Unit, aplite													
VAAW24-6.1	884	584	0.73	0.68	317.0	1.5	355.6	3.5	10.8	314.0	1.8	**314.7**	**1.5**
VAAW24-14.1	868	286	0.60	0.34	318.4	4.8	340.4	5.3	6.4	316.6	4.9	**316.5**	**4.7**
VAAW24-13.1	127	51	0.93	0.41	325.6	3.2	355.6	3.7	8.4	323.3	3.5	**322.6**	**3.5**
VAAW24-21.2	194	95	-0.31	0.50	322.7	6.0	321.3	6.9	-0.4	322.9	6.5	**323.7**	**6.1**
VAAW24-4.1	156	95	0.14	0.63	330.7	2.7	337.3	5.3	2.0	330.2	3.1	**330.2**	**2.7**
VAAW24-3.1	709	932	2.88	1.35	340.8	2.5	463.9	3.4	26.6	330.4	2.5	**331.2**	**2.5**
VAAW24-2.1	921	738	-0.02	0.82	336.9	1.7	336.5	2.5	-0.2	336.9	1.8	**336.9**	**1.6**
VAAW24-1.1	1275	604	0.08	0.49	338.7	3.6	337.4	3.7	-0.4	338.9	3.9	**338.5**	**3.7**
VAAW24-25.1	387	211	-0.03	0.56	345.6	4.8	342.5	6.1	-1.0	345.9	5.2	**345.7**	**4.8**
VAAW24-9.1	1608	154	1.01	0.10	369.4	3.7	416.3	4.6	11.2	365.5	4.0	**365.8**	**3.7**
VAAW24-23.1	824	319	0.52	0.40	454.9	3.2	484.5	5.8	6.2	452.3	3.6	**452.7**	**3.2**
VAAW24-5.1	1297	86	1.43	0.07	475.6	4.5	534.9	5.1	11.0	470.1	4.6	**469.1**	**4.5**
VAAW24-22.1	389	212	0.45	0.56	502.3	15.2	509.8	##	1.4	501.6	16.3	**500.2**	**15.3**
VAAW24-17.1	886	47	0.50	0.05	514.4	2.1	540.4	4.6	4.8	512.0	2.6	**512.0**	**2.1**
VAAW24-26.1	470	167	1.51	0.36	525.6	3.1	631.2	7.1	16.8	515.3	3.8	**518.1**	**3.7**
VAAW24-9.2	77	63	0.54	0.83	577.2	5.1	593.5	5.3	2.8	**575.7**	**5.6**	574.3	5.3
VAAW24-15.1	557	619	0.19	1.14	600.4	6.5	628.5	6.4	4.4	**597.6**	**7.0**	599.4	6.6
VAAW24-16.1	428	290	-0.01	0.70	609.5	3.5	617.2	4.9	1.2	**608.8**	**4.1**	609.6	3.6
VAAW24-5.2	178	113	-0.07	0.65	1792.8	26.3	1852.9	##	3.2	**1772.9**	**31.3**	1793.7	26.3
VAAW24-19.1	134	81	0.05	0.62	1831.0	18.5	1849.1	##	1.0	**1824.8**	**23.8**	1830.3	18.4
VAAW24-7.1	130	241	0.00	1.90	1973.6	41.2	1983.7	##	0.6	**1969.5**	**53.3**	1973.6	41.2
VAAW24-27.1	219	79	0.19	0.37	2489.0	8.6	2585.2	5.2	3.8	**2412.8**	**11.9**	2486.0	8.7

Table 9.3 Summary of U-Th-Pb ages obtained for Valencia Intrusive Dyke Unit, aplite. d(%)=100x(1–206/238 age / 207/235 age); f^{206}%=(common ^{206}Pb/total ^{206}Pb)x100.

divided into four groups. The first consists of colourless to brown, often opaque, euhedral short bipyramidal prisms with a size of about 200 μm x 150 μm. Under the cathodoluminescence microscope most grains are grey, with little oscillatory zoning , but a core that, in general, is less cathodoluminescent than the rim (Fig. 9.5F). Nine U-Pb measurements on 9 zircons yielded high concentrations of U (127-1608 ppm) and Th (51-932 ppm) with Th/U = 0.10-1.35. They contain perceptible common lead (f^{206} ≈ -0.31 to 2.88 %) (Table 9.3) and are, therefore, discordant. The discordia, however, is correctable yielding the weighted means (errors reported at 2σ) ^{204}Pb corrected, ^{206}Pb/^{238}U 329 ± 7 Ma (MSWD = 3).

The second group of zircons are stubby short-medium, 100 μm x 100 μm, subhedral short bipyramid-terminated prisms, under the cathodoluminescence microscope the terminations

appear to have a more uniform internal structure (Fig. 9.5F). Five U-Pb measurements on 5 zircons yielded high concentrations of U (389-1297 ppm) and Th (47-217 ppm) with Th/U = 0.05-0.56. They contain perceptible common lead ($f^{206} \approx 0.45$-1.51%) (Table 9.3). The discordia, however, is correctable yielding ^{204}Pb corrected, $^{206}Pb/^{238}U$ ages from *c.* 518 to *c.* 452 Ma (Fig. 9.5F).

The third group of zircons are small, 100 μm x 50 μm, prismatic euhedral grains with rounded terminations. These grains are highly cathodoluminescent (Fig. 9.5F). Three measurements on 3 grains yielded moderate concentrations of U (77-557 ppm) and Th (63-619 ppm) with Th/U = 0.7-1.14 and little common lead ($f^{206} < 1.14\%$) (Table 9.3). All of them were concordant (discordance 1.2 to 4.4%) (Fig. 9.5F). The weighted means (errors reported at 2σ) of the 207-corrected $^{206}Pb/^{238}U$ ages are 576 ± 6 Ma, 599 ± 7 Ma and 610 ± 4 Ma.

The fourth group comprises different grains with varied morphologies, often formed of highly cathodoluminescent cores surrounded by small darker rims (Fig. 9.5F). Four measurements yielded 207-corrected $^{206}Pb/^{238}U$ ages between *c.* 2489 ± 9 to *c.* 1793 ± 26 Ma.

9.1.3 Brovales Pluton

The four samples studied from this pluton are: a quartz monzodiorite from the *Central Subalkaline Intermediate Unit;* a granodiorite from the *Intermediate Subalkaline Intermediate Unit*; a syenogranite from the *External Subalkaline Acid Unit*; and an aplite of the *Intrusive, Acid Peraluminous, Dykes*. Most determinations cluster around 340 Ma but older and younger ages were also found (Fig. 9.8A and 9.8B).

9.1.3.1 Central Subalkaline Intermediate Unit

Zircons from the quartz monzodiorite B-2 are euhedral to subhedral bipyramidal prisms with dimensions about 250 μm x 100 μm (Fig. 9.7A). Most grains are colourless and transparent, although some pinkish to brown translucent crystals are also found. Cathodoluminescence imaging reveals two textural types: some show no or a faint oscillatory zoning and are rich in inclusions; the others show a well-defined oscillatory zoning and have a core that, in general, is more cathodoluminescent than the rim (Fig. 9.7A).

Eight U-Pb measurements on seven zircons yielded moderate to high concentrations of U (143-852 ppm) and Th (50-266 ppm) with Th/U = 0.28-0.43 and little common lead ($f^{206} < 0.84\%$) (Table 9.4). All of them were concordant (discordance -0.4 to 2.4%) (Fig. 9.8C). Five determinations corresponding to unzoned crystals or cores yielded identical weighted means (errors reported at 2σ) of uncorrected and 207-corrected $^{206}Pb/^{238}U$, 339 ± 4 Ma (MSWD = 8.96) and 339 ± 4 Ma (MSWD = 6.78). On the other hand, three rims are younger, averaging at 292 ±

Figure 9.7. Cathodoluminescence images ages and O isotope values of Brovales pluton representative analysed zircons. A) Central Subalkaline Intermediate Unit quartz monzodiorite (B-2). B) Intermediate Subalkaline Intermediate Unit unfoliated fine grain granodiorite (B-5-1). C) External Subalkaline Acid Unit syenogranite (B-7). D) Intrusive, Acid Peraluminous, Dyke deformed aplite (B-8-2).

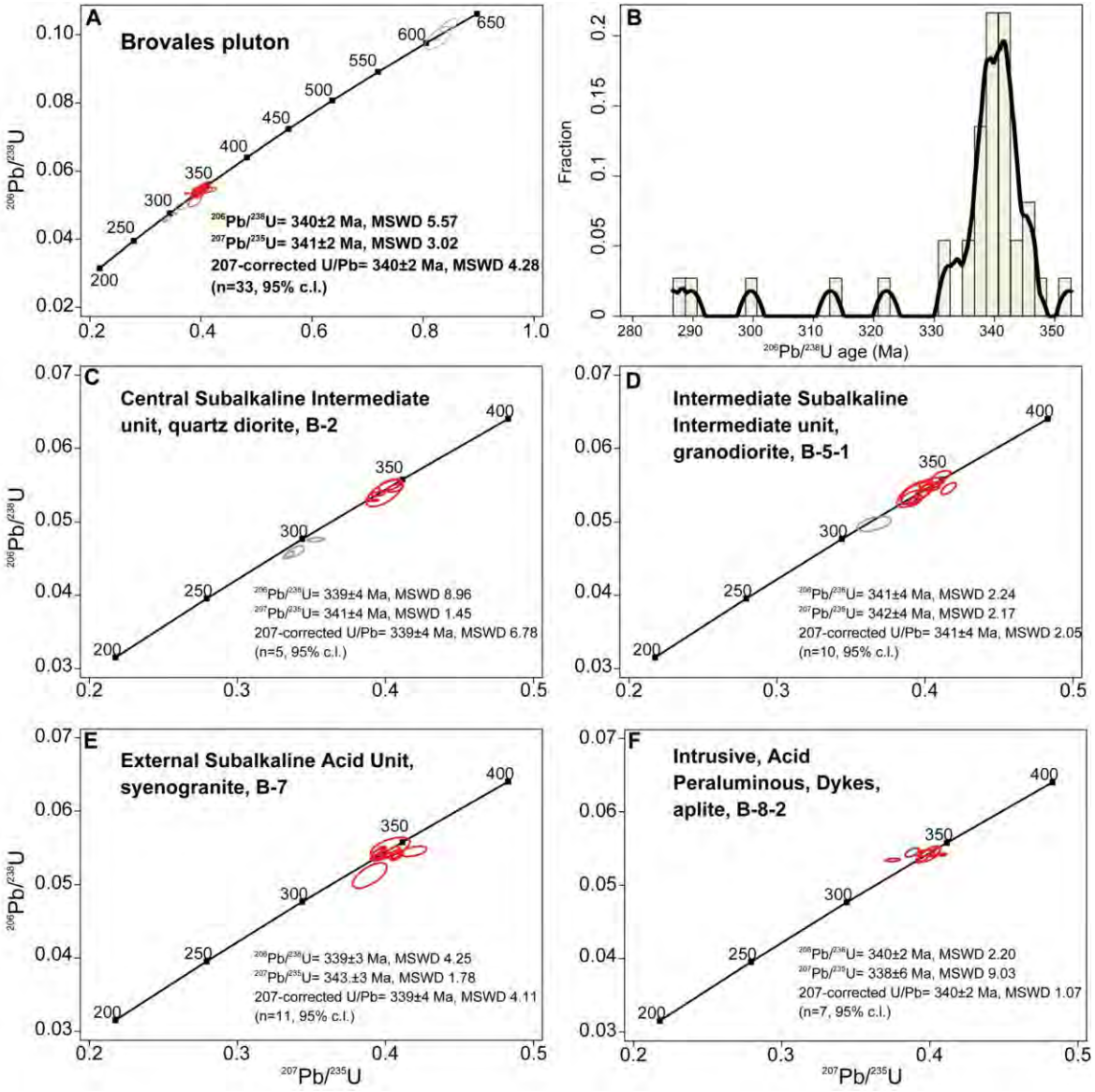

Figure 9.8. A) Wetherill concordia plots for the Brovales pluton, grey data not computed for age determination. B) Frequency and density distribution of U–Pb SHRIMP Variscan ages of the Brovales pluton. Note those younger ages that magmatic crystallisation age (340±2 Ma) represents the second deformation stage that affected principally to Central Unit. Wetherill concordia plots for: C) Central Subalkaline Intermediate Unit quartz diorite (B-2). D) Intermediate Subalkaline Intermediate Unit unfoliated fine grain granodiorite (B-5-1). E) External Subalkaline Acid Unit syenogranite (B-7). F) Intrusive, Acid Peraluminous, Dyke deformed aplite (B-8-2).

4 Ma (Fig. 9.7A and 9.7C).

9.1.3.2 Intermediate Subalkaline Intermediate Unit

The fine-grained granodiorite B-5-1contains abundant but small 125 µm x 75 µm zircons. Most grains are stubby and subhedral to euhedral with pyramidal terminations (Fig. 9.7B). Other grains are more elongated with less well-developed pyramidal terminations (Fig. 9.7B). They are colourless, transparent to translucent, and few of them contain inclusions (Fig. 9.7B).

Cathodoluminescence images reveal oscillatory zoning and the presence of low cathodoluminescent cores in some grains (Fig. 9.7B).

Ten U-Pb measurements on 9 zircons yielded moderate concentrations of U (175-592 ppm) and Th (57-338 ppm) with Th/U = 0.18-0.66 and little common lead (f^{206} < 0.44%) (Table 9.4). All of them were concordant (discordance -1.2 to 3%) (Fig. 9.8D). The weighted means (errors reported at 2σ) of the uncorrected and 207-corrected $^{206}Pb/^{238}U$ are virtually identical, 341 ± 4 Ma (MSWD = 2.24) and 341 ± 4 Ma (MSWD = 2.05). Two other grains are pre-magmatic, with $^{206}Pb/^{238}U$ ages of 630 ± 9 and 606 ± 2 Ma. In addition, one grain, with similar textural features to the magmatic zircons, has a $^{206}Pb/^{238}U$ age of 315 ± 5 Ma (Fig. 9.8D).

9.1.3.3 External Subalkaline Acid Unit

The syenogranite B-7 contained abundant medium to small zircons 200 μm x 150 μm. They are colourless, transparent to translucent euhedral bipyramid-terminated prisms (Fig. 9.7C). Under the cathodoluminescence microscope they show a concentric zonation with high cathodoluminescent cores and darker rims (Fig. 9.7C). Some grains are patchy due to unzoned cathodoluminescent areas (Fig. 9.7C) and often have large melt inclusions (Fig. 9.7C).

Eleven U-Pb measurements on 11 zircons yielded moderate to high concentrations of U (144-956 ppm) and Th (52-381 ppm) with Th/U = 0.21-0.56 and little common lead (f^{206} < 0.63%) (Table 9.4). All of them were concordant (discordance -1.4 to 3.6%) (Fig. 9.8E). The weighted means (errors reported at 2σ) of the uncorrected and 207-corrected $^{206}Pb/^{238}U$ are virtually identical, 339 ± 3 Ma (MSWD = 4.25) and 339 ± 4 Ma (MSWD = 4.11).

9.1.3.4 Intrusive, Acid Peraluminous, Dykes

The aplite B-8-2 contain zircons of different sizes and morphologies. They vary from large, 200 μm x 100 μm, bipyramidal elongated prisms to small 100 μm x 75 μm stubby prisms with short pyramidal terminations (Fig. 9.7D). The zircons are colourless, transparent to translucent. Most grains show oscillatory zoning with a core that, in general, is more cathodoluminescent than the rim (Fig. 9.7D).

Seven U-Pb measurements on 7 zircons yielded low to moderate concentrations of U (93-340 ppm) and Th (39-134 ppm) with Th/U = 0.26-0.94 and little common lead (f^{206} < 0.6%) (Table 9.4). All of them were concordant (discordance -3.8 to 2.2%) (Fig. 9.8F). The weighted means (errors reported at 2σ) of the uncorrected and 207-corrected $^{206}Pb/^{238}U$ are virtually identical, 340 ± 2 Ma (MSWD = 2.20) and 340 ± 2 Ma (MSWD = 1.07). We also found a pre-magmatic grain with a $^{206}Pb/^{238}U$ age of 609 ± 15 (Fig. 9.7D).

	Conc. (ppm)				Ages (Ma), uncorrected					Age (Ma), ^{207}Pb corrected	
Spot	U	Th	f206%	^{232}Th/^{235}U	^{206}Pb/^{238}U	±err	^{207}Pb/^{235}U	±err	d(%)	^{206}Pb/^{238}U	±err
Sample B-2 (n=8).Central subalkaline Intermediate unit, quartz monzodiorite											
B2-1.1*	752	215	0.22	0.29	286.7	2.2	293.2	2.5	2.2	286.2	2.3
B2-5.1*	686	195	0.22	0.29	289.7	3.8	296.4	4.5	2.2	289.1	4.0
B2-6.1*	852	266	0.20	0.32	299.6	1.5	307.0	4.5	2.4	299.0	1.8
B2-13.1	821	236	0.20	0.30	332.6	0.8	335.2	3.1	0.8	332.3	1.0
B2-16.1	819	224	0.13	0.28	337.9	1.7	338.0	3.2	0.0	337.8	1.9
B2-10.1	225	77	0.76	0.35	338.3	8.5	341.0	8.8	0.8	338.0	8.9
B2-16.2	235	99	0.20	0.43	342.7	2.8	346.2	4.0	1.0	342.4	3.1
B2-9.1	143	50	0.84	0.36	345.3	4.1	344.0	5.6	-0.4	345.4	4.5
Sample B-5-1 (n=13). Intermediate Subalkaline Intermediate Unit, granodiorite											
B5-1-13.1*	334	121	0.35	0.37	312.8	5.3	316.3	8.4	1.2	312.5	5.9
B5-1-14.1	448	189	0.11	0.43	332.2	3.4	336.7	3.6	1.4	331.8	3.6
B5-1-5.1	175	59	0.44	0.35	335.0	4.4	334.5	4.8	-0.2	335.0	4.7
B5-1-8.1	295	82	0.28	0.29	337.6	8.2	336.2	8.4	-0.4	337.7	8.6
B5-1-12.1	227	61	0.20	0.27	338.7	7.1	337.5	8.0	-0.4	338.7	7.5
B5-1-1.1	216	65	0.28	0.31	340.1	4.9	341.2	4.5	0.4	340.0	5.1
B5-1-7.1	316	203	0.05	0.66	342.2	3.6	353.0	3.5	3.0	341.3	3.7
B5-1-8.2	512	148	0.16	0.30	342.6	2.3	341.8	2.7	-0.2	342.6	2.4
B5-1-11.1	331	57	0.23	0.18	343.5	2.2	346.5	2.7	0.8	343.2	2.3
B5-1-2.1	431	74	-0.02	0.18	346.7	4.1	344.9	6.0	-0.6	346.8	4.5
B5-1-3.1	282	120	0.35	0.44	352.4	4.0	349.4	4.6	-0.8	352.6	4.3
B5-1-10.1*	592	338	0.07	0.59	605.9	1.5	611.2	2.2	0.8	605.3	1.6
B5-1-6.1*	392	189	0.15	0.49	630.2	8.6	622.7	8.1	-1.2	630.9	9.2
Sample B-7 (n=11). External Subalkaline Acid Unit, Syenogranite											
B7-8.1	498	119	0.19	0.24	322.1	8.1	333.9	8.4	3.6	321.1	8.4
B7-1.1	383	136	0.02	0.36	336.8	2.0	337.9	3.5	0.4	336.7	2.3
B7-4.1	204	113	0.23	0.56	338.5	2.8	347.1	3.0	2.4	337.8	3.0
B7-3.1	186	55	0.48	0.31	338.8	1.9	342.8	3.2	1.2	338.4	2.1
B7-2.1	279	58	0.22	0.21	339.8	2.9	346.4	3.0	2.0	339.2	3.0
B7-9.1	956	381	0.12	0.41	339.3	2.8	339.6	3.0	0.0	339.2	2.9
B7-6.1	144	52	0.31	0.37	342.2	3.8	355.3	6.4	3.6	341.1	4.2
B7-10.1	225	117	0.63	0.53	341.8	3.3	345.0	3.4	1.0	341.5	3.4
B7-7.1	769	229	0.13	0.31	341.3	2.0	337.7	2.3	-1.0	341.5	2.1
B7-11.1	233	118	0.50	0.52	345.3	7.2	343.9	9.6	-0.4	345.4	7.9
B7-5.1	372	113	0.34	0.31	345.2	0.8	340.2	1.9	-1.4	345.5	0.9
Sample B-8-2 (n=8). Intrusive, Acid Peraluminous, Dyke, aplite											
B8-2-4.1	132	39	0.21	0.30	335.6	1.2	323.3	3.6	-3.8	336.5	1.5
B8-2-2.1	190	55	0.50	0.29	338.7	3.8	338.5	3.6	0.0	338.7	3.9
B8-2-3.1	284	71	0.17	0.26	340.1	0.9	348.1	1.6	2.2	339.4	0.9
B8-2-1.1	340	134	0.24	0.40	340.6	5.0	341.7	5.2	0.4	340.5	5.3
B8-2-8.1	269	76	0.37	0.29	341.4	2.5	339.4	4.5	-0.6	341.5	2.8
B8-2-7.1	263	114	0.26	0.44	342.2	2.8	344.0	2.7	0.6	342.0	2.9
B8-2-5.1	182	49	0.08	0.28	341.9	3.0	333.0	3.5	-2.6	342.5	3.2
B8-2-6.1*	93	86	0.60	0.94	608.7	14.9	612.0	13.3	0.6	608.3	15.8

*Table 9.4. Summary of U-Th-Pb ages obtained for Brovales pluton main units. d(%)=100x(1–206/238 age 207/235 age); f^{206}%=(common ^{206}Pb/total ^{206}Pb)x100. * Data no considered for age calculation*

9.1.4 Cambrian Leucogranite and Serie Negra Metasediment

9.1.4.1 Cambrian Leucogranite

Zircons extracted from the leucogranite VAAW-41 have a grain size around 200 μm x 100 μm. They are colourless, often transparent to translucent euhedral to subhedral prisms with short pyramidal terminations. Under the cathodoluminescence microscope they show oscillatory zoning (Fig. 9.9A).

Thirty U-Pb measurements on 25 zircons yielded moderate to large concentrations of U (334-1162 ppm) and Th (109-608 ppm) with Th/U = 0.31-0.78 and little common lead (f^{206} < 0.28%) (Table 9.5). All of them were concordant (discordance -1 to 2.4%) (Fig. 9.10A). The weighted means (errors reported at 2σ) of the uncorrected and 207-corrected $^{206}Pb/^{238}U$ are virtually identical, 509 ± 3 Ma (MSWD = 1.4) and 509 ± 3 Ma (MSWD = 1.2). (Fig. 9.10A).

9.1.4.2 Serie Negra Metasediment

The metasediment VAAW-39 contains zircon with a wide range of sizes and morphologies, as might be expected in a sedimentary sample. For this sample we measured 31 ages, 27 of which are concordant.

The ages obtained may be divided into three groups. The first group is Archean, it comprises two rounded medium size, 100 μm x 50 μm, grain cores, 2721 ± 180 Ma and 2670 ± 210 Ma, one of which has a high cathodoluminescence rim (Fig. 9.9B and 9.10B). The second group is composed of nine Paleoproterozoic zircons including: the aforementioned high cathodoluminescence rim that has a Siderian age, 2470 ± 141 Ma (Fig. 9.9B and 9.10B); two Rhyacian grains with oscillatory magmatic zoning, 2186 ± 50 Ma and 2158 ± 69 Ma (Fig. 9.9B and 9.10B); five Orosirian grains, of variable size and morphology, including small high cathodoluminescence and rounded large zoned zircons, 2018 to 1848 Ma (Fig. 9.9B and 9.10B); and, one Statherian small zoned grain, 1796 ± 34 Ma (Fig. 9.9B and 9.10B). Notably, no Mesoproterozoic zircons were found. The third group is Neoproterozoic. The zircons are 125 μm x 75 μm, prismatic euhedral grains with rounded terminations with high cathodoluminescence (Fig. 9.9B). Two grains are Cryogenian, 699 ± 12 Ma and 676 ± 14 Ma, (Fig. 9.10C) and twelve are Ediacaran (Fig. 9.9B). In the latter, thirteen concordant U-Pb determinations on 12 different grains gave an average $^{206}Pb/^{238}U$ age of 603 ± 7 Ma (MSWD = 3) and an average 207Pb-corrected U-Pb age of 604 ± 7 Ma (MSWD = 2.5) (Fig. 9.10C). The youngest concordant age is 566 ± 10 Ma, it was obtained in the rim of a grain that has a core age of 586 ± 8 Ma (Fig. 9.9B and 9.10B).

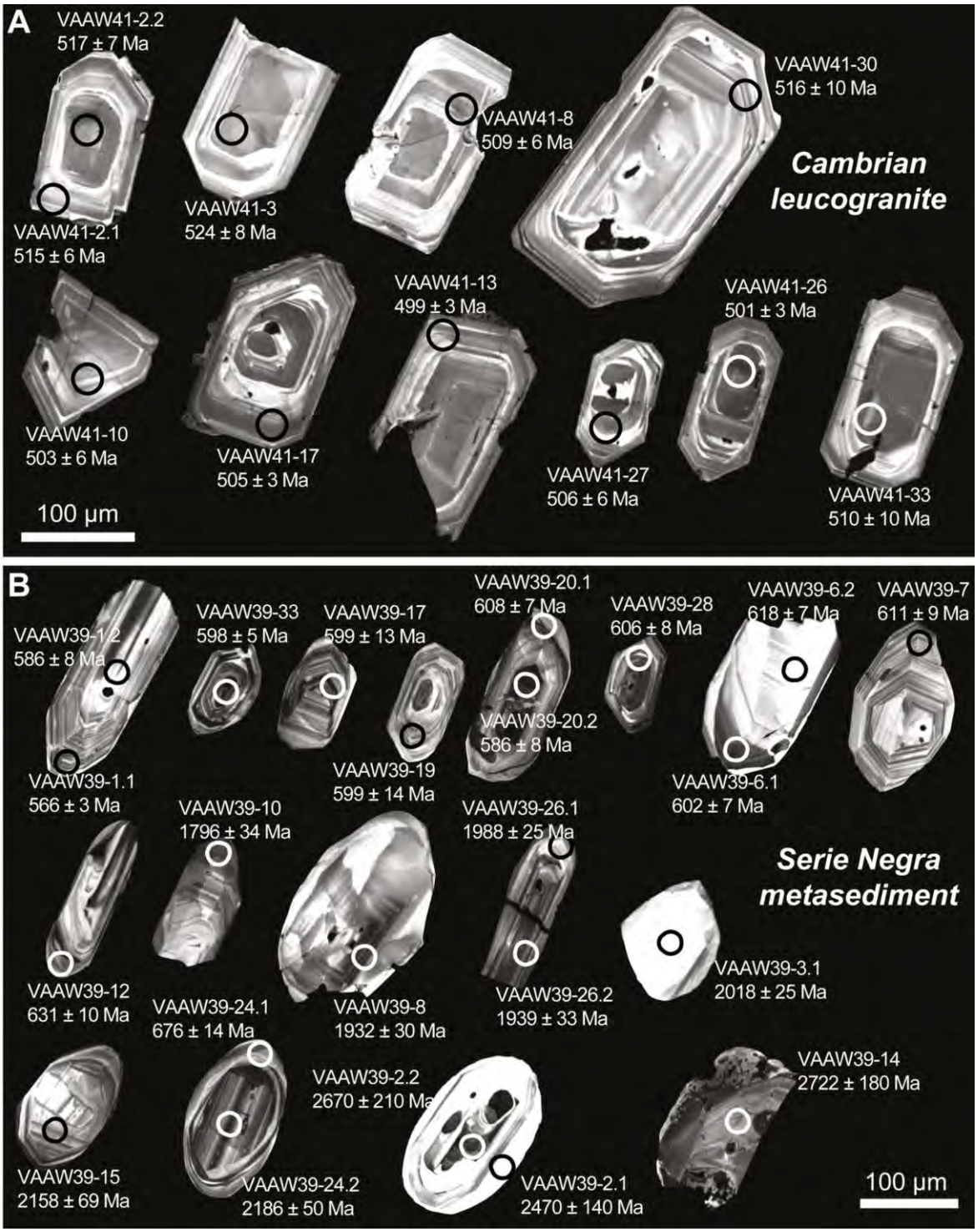

Figure 9.9. Cathodoluminescence images and ages of representative analysed zircons. A) Leucogranite, sample VAAW-41. B) Serie Negra metasediment, sample VAAW-39.

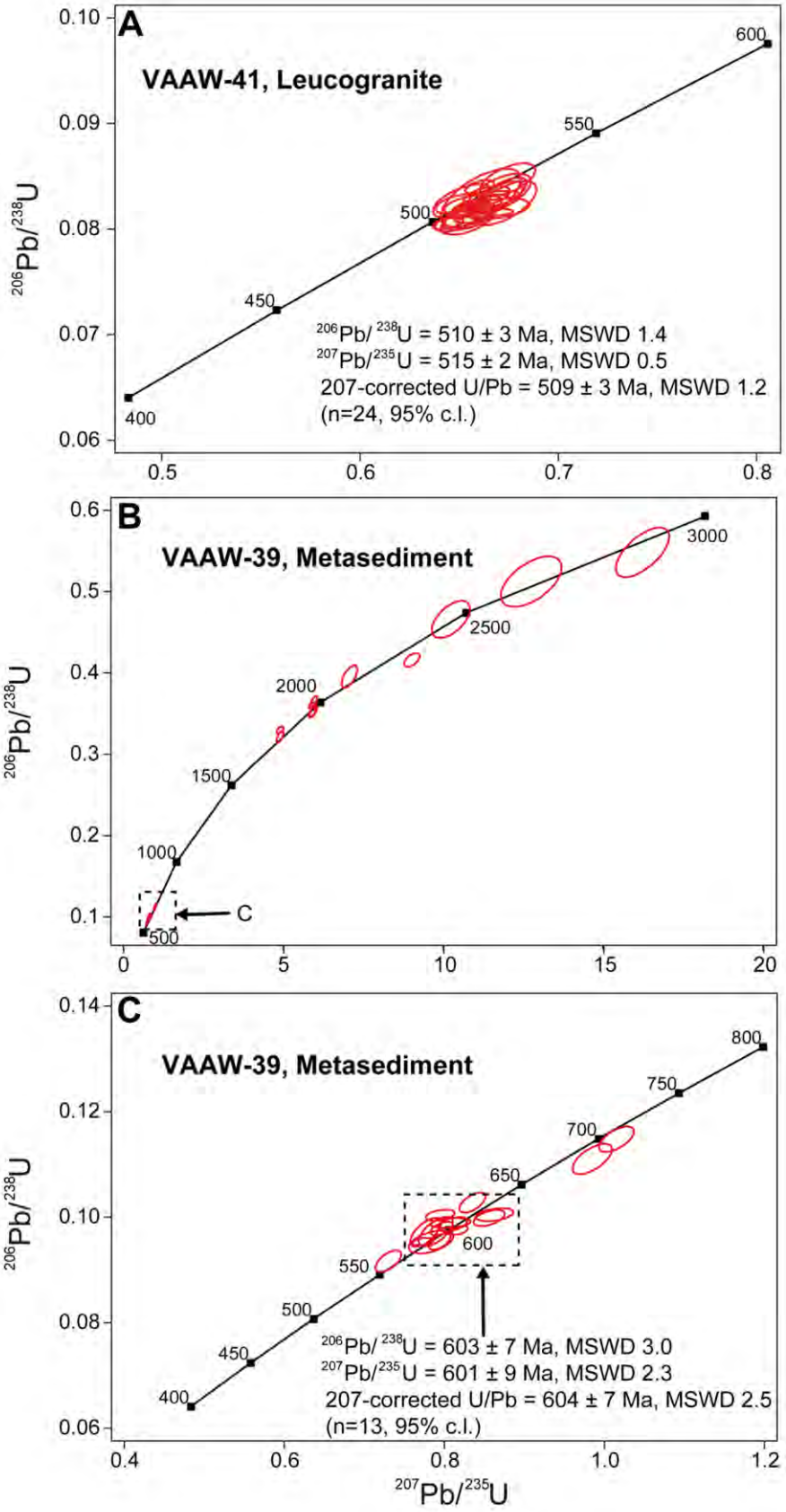

Figure 9.10. Wetherill concordia plots for: A) Leucogranite VAAW-41. B) Serie Negra metasediment VAAW-39. C) Detail of the main Ediacaran cluster ages in which the youngest concordant age is 565±8 Ma.

	Conc. (ppm)				Ages (Ma), uncorrected					Age (Ma), ^{207}Pb corrected	
Spot	U	Th	f206%	^{232}Th/^{235}U	^{206}Pb/^{238}U	±err	^{207}Pb/^{235}U	±err	d(%)	^{206}Pb/^{238}U	±err
Sample VAAW-41 (n=24). Cambrian leucogranite											
VAAW41-13.1	415	144	0.02	0.36	499.3	1.1	504.9	2.3	1.2	498.8	1.3
VAAW41-7.1	735	346	-0.06	0.48	500.3	3.0	507.4	4.0	1.4	499.6	3.3
VAAW41-5.2	334	254	-0.03	0.78	501.4	5.1	511.1	5.9	1.8	500.5	5.6
VAAW41-22.1	1162	608	0.04	0.54	501.7	2.5	512.6	2.6	2.2	500.8	2.6
VAAW41-26.1	918	437	-0.10	0.49	502.2	0.6	512.7	3.2	2.0	501.3	0.9
VAAW41-15.1	453	153	0.05	0.35	503.4	4.7	511.6	5.7	1.6	502.6	5.1
VAAW41-10.1	661	249	0.10	0.39	503.7	3.8	511.0	4.6	1.4	503.1	4.2
VAAW41-17.1	625	240	-0.03	0.39	505.5	0.5	515.7	6.8	2.0	504.5	1.1
VAAW41-27.1	421	164	0.00	0.40	507.6	3.5	520.1	7.4	2.4	506.5	4.3
VAAW41-4.2	761	337	-0.09	0.45	507.5	2.5	511.1	3.0	0.8	507.1	2.6
VAAW41-18.1	669	241	0.02	0.37	507.6	1.7	511.8	2.9	0.8	507.3	2.0
VAAW41-8.1	430	145	0.19	0.35	509.6	3.2	512.6	6.4	0.6	509.4	3.9
VAAW41-33.1	669	274	0.06	0.42	510.6	7.8	522.3	7.3	2.2	509.6	8.2
VAAW41-14.2	609	266	0.10	0.45	510.9	2.3	517.8	3.6	1.4	510.3	2.7
VAAW41-6.1	521	192	0.16	0.38	510.3	2.9	507.9	4.3	-0.4	510.5	3.3
VAAW41-4.1	977	485	0.03	0.51	511.8	5.9	509.5	6.8	-0.4	512.0	6.4
VAAW41-21.1	848	382	0.12	0.46	514.1	5.1	521.0	4.5	1.4	513.4	5.1
VAAW41-11.2	407	161	-0.05	0.41	513.7	10.8	515.0	10.0	0.2	513.5	11.2
VAAW41-2.1	590	225	0.03	0.39	514.7	3.1	516.9	4.6	0.4	514.5	3.4
VAAW41-12.1	480	191	-0.05	0.41	515.1	0.4	520.4	3.7	1.0	514.6	0.8
VAAW41-30.1	366	109	0.00	0.31	516.3	6.9	520.8	7.2	0.8	515.8	7.4
VAAW41-2.2	1032	456	0.28	0.45	517.2	4.5	522.5	4.2	1.0	516.8	4.7
VAAW41-5.1	604	197	0.04	0.33	519.9	1.4	514.6	1.9	-1.0	520.4	1.4
VAAW41-3.1	590	249	0.03	0.43	523.9	5.7	523.3	5.9	-0.2	524.0	6.1
Sample VAAW-39 (n=27).Serie Negra metasediment											
VAAW39-1.1	482	330	0.30	0.70	564.9	7.5	556.4	6.9	-1.6	565.8	8.0
VAAW39-1.2	254	249	0.00	1.00	586.4	9.1	587.3	13.2	0.2	586.4	10.5
VAAW39-20.2	587	160	0.06	0.28	586.8	5.1	593.6	5.0	1.2	586.1	5.4
VAAW39-23.1	421	281	0.10	0.69	586.8	1.8	581.5	4.9	-1.0	587.3	2.2
VAAW39-33.1	563	614	0.00	1.12	597.2	10.1	583.5	8.3	-2.4	598.5	10.4
VAAW39-17.1	218	443	0.00	2.08	598.0	10.6	590.8	9.4	-1.2	598.8	11.2
VAAW39-19.1	123	93	0.56	0.78	599.3	2.1	607.5	3.0	1.4	598.5	2.3
VAAW39-6.1	996	650	-0.04	0.67	601.4	4.2	594.9	5.2	-1.0	602.1	4.8
VAAW39-28.1	348	262	0.00	0.77	606.1	4.8	602.6	7.6	-0.6	606.4	5.5
VAAW39-20.1	415	252	0.23	0.62	607.5	3.1	601.2	11.2	-1.0	608.2	4.4
VAAW39-7.1	104	106	1.18	1.05	613.0	5.7	627.9	7.9	2.4	611.5	6.4
VAAW39-31.1	269	243	0.00	0.93	616.2	3.5	593.9	7.5	-3.8	618.5	4.3
VAAW39-6.2	108	48	0.72	0.46	616.8	4.5	631.5	10.1	2.4	615.3	5.5
VAAW39-12.1	297	106	0.32	0.37	630.1	6.6	616.4	6.2	-2.2	631.4	7.0
VAAW39-24.1	115	41	0.90	0.37	678.2	10.7	696.1	9.6	2.6	676.3	11.4
VAAW39-32.1	327	168	0.08	0.53	699.8	8.6	711.4	7.9	1.6	698.5	9.2
VAAW39-10.1	108	85	0.00	0.81	1797.9	20.5	1803.1	12.8	0.2	1796.3	25.4
VAAW39-11.1	104	64	0.00	0.63	1838.3	12.6	1803.4	12.8	-2.0	1848.3	16.5
VAAW39-8.1	197	323	0.18	1.68	1940.5	16.4	1962.3	9.3	1.2	1932.2	20.0
VAAW39-26.2	148	229	0.07	1.59	1947.0	19.3	1968.1	11.1	1.0	1938.8	24.1
VAAW39-26.1	64	66	0.00	1.06	1981.5	9.5	1964.1	10.7	-0.8	1988.3	14.9
VAAW39-3.1	150	77	0.16	0.53	2008.2	16.5	1971.3	9.1	-1.8	2018.1	16.4
VAAW39-15.1	108	21	0.00	0.20	2148.0	43.6	2120.9	25.9	-1.2	2157.9	57.8
VAAW39-24.2	237	204	0.05	0.88	2242.5	25.0	2341.0	19.1	4.2	2186.3	39.1
VAAW39-2.1	128	68	0.19	0.55	2464.9	75.6	2457.7	49.4	-0.2	2470.1	126.8
VAAW39-2.2	488	228	0.03	0.48	2666.3	102.7	2662.2	66.5	-0.2	2670.4	194.4
VAAW39-14.1	150	62	0.14	0.42	2818.2	90.0	2891.2	44.5	2.6	2721.8	161.0

Table 9.5. Summary of U-Th-Pb ages obtained for a Cambrian leucogranite and Serie Negra metasediment. d(%)=100x(1–206/238 age / 207/235 age); f^{206}%=(common ^{206}Pb/total ^{206}Pb)x100.

9.2 O Isotope Data

The SHRIMP O isotope data are summarized in Figs 9.11 to 9.13, the full dataset is given in Appendix IV.

9.2.1 Burguillos del Cerro Plutonic Complex

9.2.1.1 Central Ultrabasic-Basic Layered Unit

Zircons from the poikilitic amphibole gabbronorite BUAW-4 have a $\delta^{18}O_{(VSMOW)}$ average of 6.28 ± 0.11 ‰ (Fig. 9.11A). The data show a wide dispersion of values from 5.31 ± 0.08 ‰ to 7.38 ± 0.09 ‰ (Fig. 9.11A). The lower $\delta^{18}O_{(VSMOW)}$ are found in the stubby and equant forms whereas the higher values are from the more prismatic zircons (Fig. 9.11A).

9.2.1.2 Central Alkaline Basic-Intermediate Layered and Acid Unit

The diorite BUAW-6 has a uniform $\delta^{18}O_{(VSMOW)}$ with a mean of 6.67 ± 0.10 ‰ (Fig. 9.11B). The alkali feldspar granite BUAW-10, however, is more heterogeneous (Fig. 9.11C). Most grains cluster around the above value, but two grains have a mantle-like compositions *c.* 5.4 ‰ and four grains have crust-like $\delta^{18}O_{(VSMOW)}$ values from *c.* 7.5 ‰ to 8.0 ‰ (Fig. 9.11C). This variation in the O isotopic signature can be correlated with the zircon textural features, the lower values are from cores whereas the higher values are typical of overgrowths or the inner parts of single crystals (Fig. 9.11C).

9.2.1.3 External Subalkaline Intermediate Unit

The $\delta^{18}O_{(VSMOW)}$ of the quartz diorite BUAW-5 ranges from 5.7 ‰ to 6.3 with a mean of 6.03 ± 0.07 ‰ (Fig. 9.11D). Only two grains show more dispersion one has a $\delta^{18}O_{(VSMOW)}$ of 5.36 ± 0.11 ‰ and the second a $\delta^{18}O_{(VSMOW)}$ of 6.96 ± 0.11 ‰ (Fig. 9.11D).

9.2.1.4 Acid Peraluminous Unit

The $\delta^{18}O_{(VSMOW)}$ values of the Archean and Paleoproterozoic zircons from sample BUAW-3 range from 5.5 ‰ to 6.9 ‰ (Fig. 9.12). The main group of Ediacaran zircons have $\delta^{18}O_{(VSMOW)}$ from 4.30 ‰ to 8.28 ‰ with two main populations: the first with an average $\delta^{18}O_{(VSMOW)}$ of 6.57 ± 0.16 ‰ and the second with an average $\delta^{18}O_{(VSMOW)}$ of 7.42 ± 0.16 ‰ (Fig. 9.12). Only three zircons showed an indication of a more mantle-like source with a $\delta^{18}O_{(VSMOW)}$ of 4.30 ± 0.05 ‰, 4.42 ± 0.11 ‰ and 5.04 ± 0.12 ‰ (Fig. 9.12).

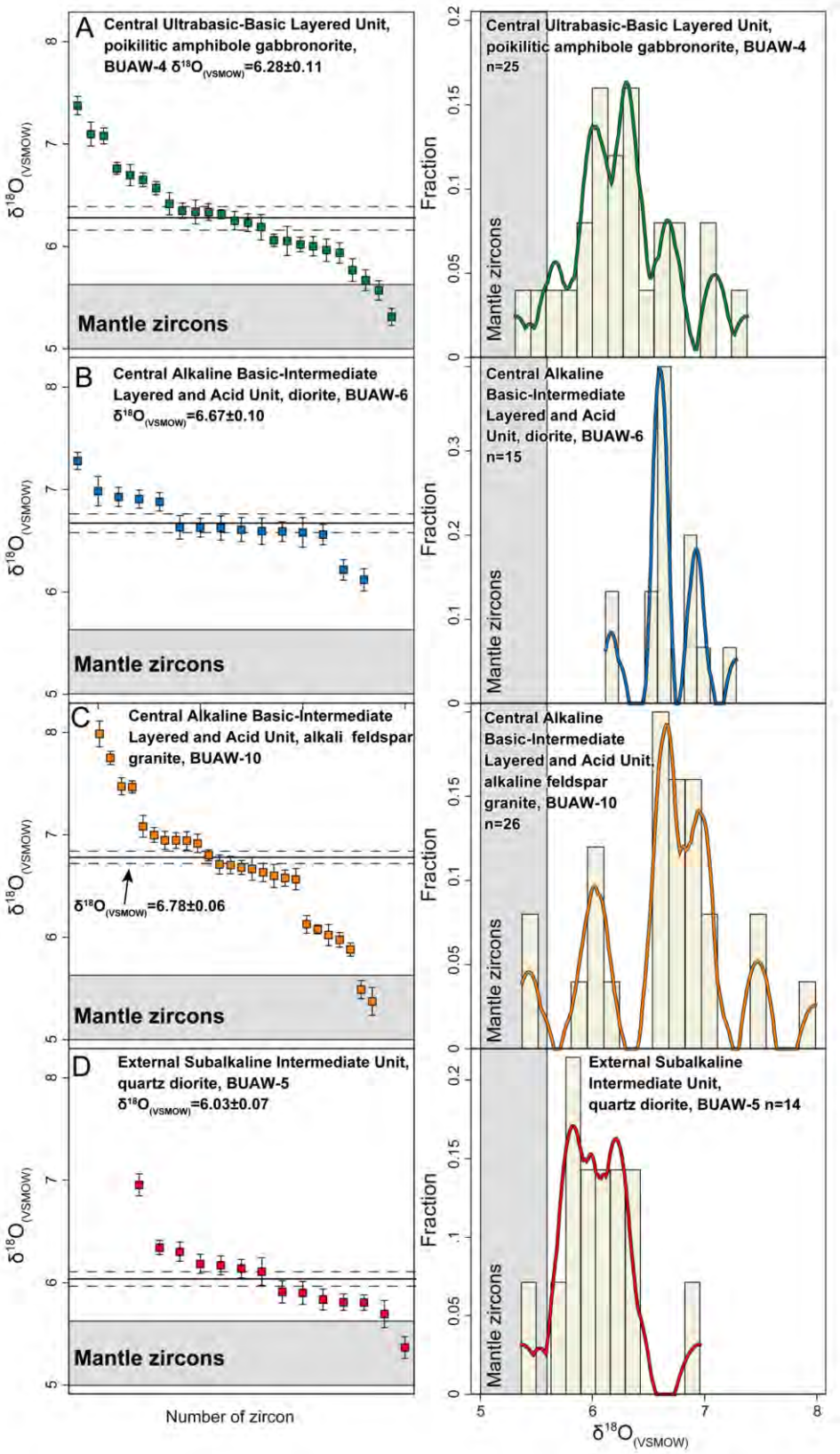

Figure 9.11. Zircon O SHRIMP isotopic composition for the Burguillos del Cerro plutonic complex and frequency and density distribution of: A) Ultrabasic-Basic Layered Unit poikilitic amphibole gabbronorite, (BUAW-4). B) Central Alkaline Basic-Intermediate Layered and Acid Unit diorite, (BUAW-6). C) Central Alkaline Basic-Intermediate Layered and Acid Unit alkali feldspar granite, (BUAW-10). D) External Subalkaline Basic-Intermediate Unit quartz diorite, (BUAW-5).

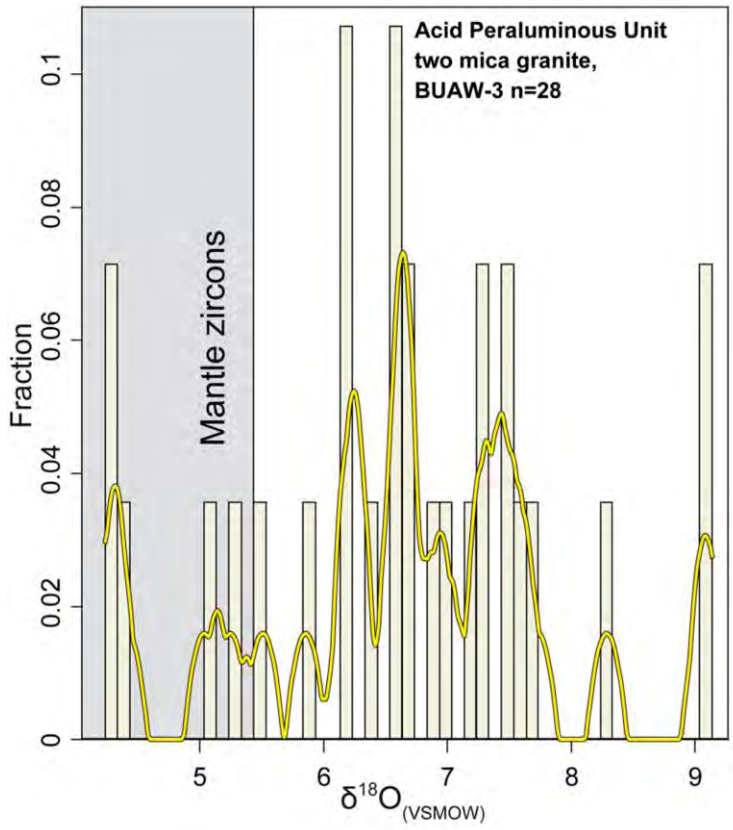

Figure 9.12. SHRIMP zircon O isotope composition of BUAW-3 two-mica granite from the Burguillos del Cerro Acid Peraluminous Unit.

9.2.2 Brovales Pluton

9.2.2.1 Central Subalkaline Intermediate Unit

In zircons from the quartz monzodiorite B-2 $\delta^{18}O_{(VSMOW)}$ ranges from 5.05 ± 0.27 ‰ to 7.61 ± 0.20 ‰ (Figs 9.13A and 9.13B) with a mean value of 6.33 ± 0.48 ‰ (Fig. 9.13A). The lowest values are typically found in the cores of concentric grains whereas the higher values correspond to the rims.

9.2.2.2 Intermediate Subalkaline Intermediate Unit

The granodiorite B-5-1 has $\delta^{18}O_{(VSMOW)}$ between 5.77 ± 0.24 ‰ to 7.95 ± 0.22 ‰ with a mean of 6.79 ± 0.31 ‰ (Fig. 9.13A). One pre-magmatic zircon with 606 ± 2 Ma, on the other hand, has higher $\delta^{18}O_{(VSMOW)}$ of 8.32 ± 0.26 ‰.

9.2.2.3 External Subalkaline Acid Unit

The zircons from syenogranite B-7 have similar oxygen isotope to the granodiorite described above, with $\delta^{18}O_{(VSMOW)}$ ranging from 5.79 ± 0.19 ‰ to 7.60 ± 0.30 ‰ and mean of 6.75 ± 0.30 ‰ (Fig. 9.13A).

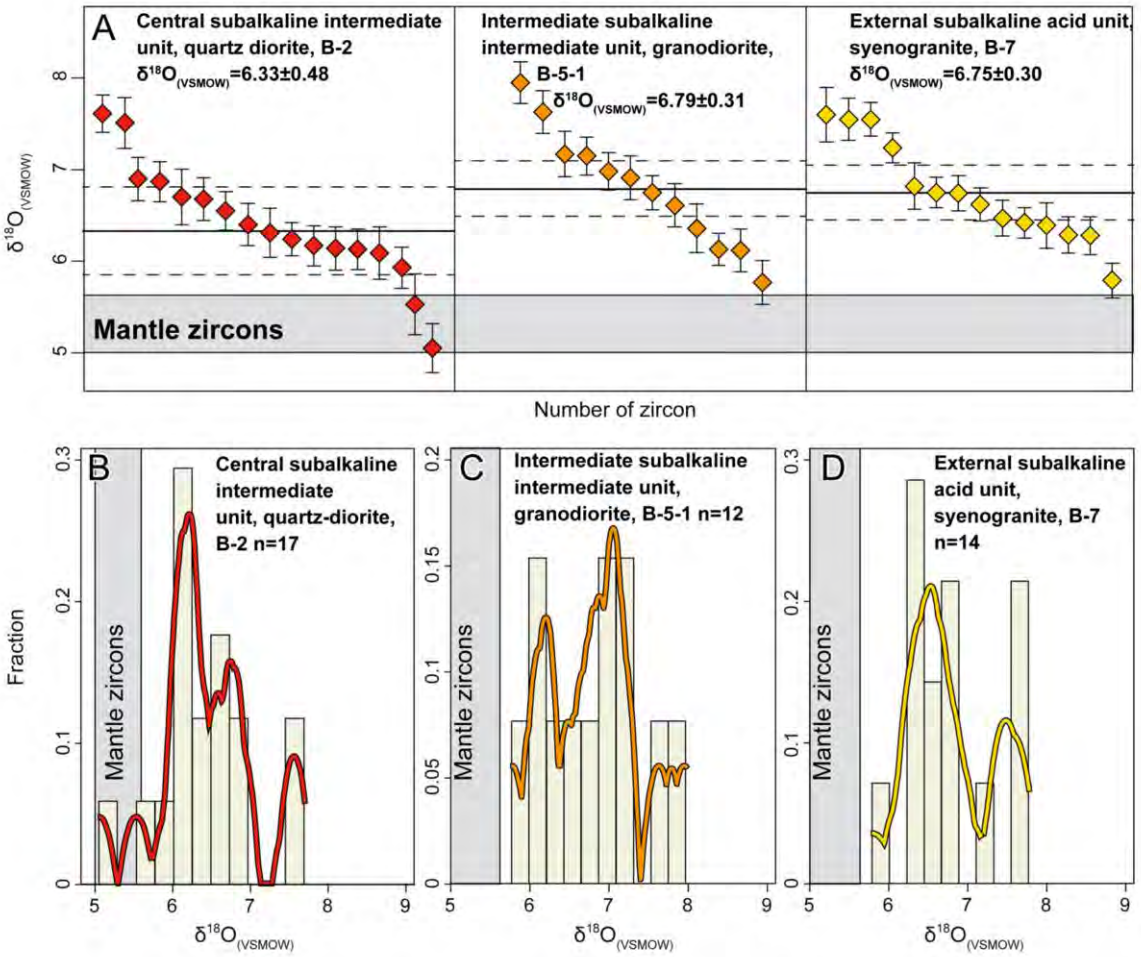

Figure 9.13. A) Zircon O SHRIMP isotopic composition for the three main units of the Brovales pluton, note the wide range of values from mantle-like composition to more crustal influx in all samples. Frequency and density distribution of O isotopic composition of: B) Central Subalkaline Intermediate Unit quartz monzodiorite (B-2). C) Intermediate Subalkaline Intermediate Unit not foliated fine grain granodiorite (B-5-1). D) External Subalkaline Acid Unit syenogranite (B-7).

Chapter 10: P-T Conditions

10. P-T Conditions

The P-T crystallisation conditions of the different units from the three studied complexes have been determined using the following thermobarometric expressions:

i. Zircon-saturation thermometer from Watson and Harrison (1983).
ii. Apatite-saturation thermometer from Harrison and Watson (1984) in metaluminous rocks, using a correction proposed by Bea et al. (1992) for peraluminous compositions.
iii. Two-pyroxene thermobarometers from Putirka (2008) (thermometers 36 and 37 and barometer 39).
iv. Amphibole-plagioclase thermometer from Holland and Blundy (1994).
v. Amphibole-only thermometer from Ridolfi and Renzulli. (2012).
vi. Amphibole-plagioclase thermobarometer from Molina et al. (2015).
vii. Al-in-amphibole barometer from Schmidt (1992).

The results of the thermobarometric calculations are summarised in Figs 10.1 to 10.5 and Table 10.1. Temperatures and pressures determined to be within error for more than one method were considered reliable. The individual results for each method are presented in Appendix V. The emphasis here is on identifying similarities between the units of the different plutonic bodies.

10.1 Zircon and Apatite Saturation Temperatures

The zircon saturation temperatures for the three plutonic bodies are, in general, lower than those of apatite saturation (Fig. 10.1 and Table 10.1). Nevertheless, the two methods gave comparable temperatures for the Burguillos del Cerro *Central Ultrabasic-Basic Layered Unit* and some of the *Central Alkaline Basic-Intermediate Layered and Acid* and *Acid Peraluminous* units and also Brovales pluton units.

Ultramafic and mafic rocks from the Burguillos del Cerro plutonic complex *Central Ultrabasic-Basic Layered Unit* have low zircon saturation temperatures of 354-684 ºC, and for apatite, 488-738 ºC (Fig. 10.1A and Table 10.1). Similarly, the gabbros of the Burguillos *Central Alkaline Basic-Intermediate Layered and Acid Unit* also have low zircon saturation temperatures, 533-787 ºC; although their apatite saturation temperatures are more varied, 621-933 ºC (Fig. 10.1B and Table 10.1). The alkaline gabbros and diorites from the Valencia del Ventoso plutonic complex *Main Pluton Alkaline to Subalkaline Basic-Acid Unit* have comparable zircon 663-822 ºC, and apatite, 780-957 ºC, similar to the Burguillos rocks (Fig. 10.1E and Table 10.1).

The intermediate diorites and quartz diorites from the Burguillos *Central Alkaline Basic-Intermediate Layered and Acid Unit* give two different ranges of zircon and apatite saturation

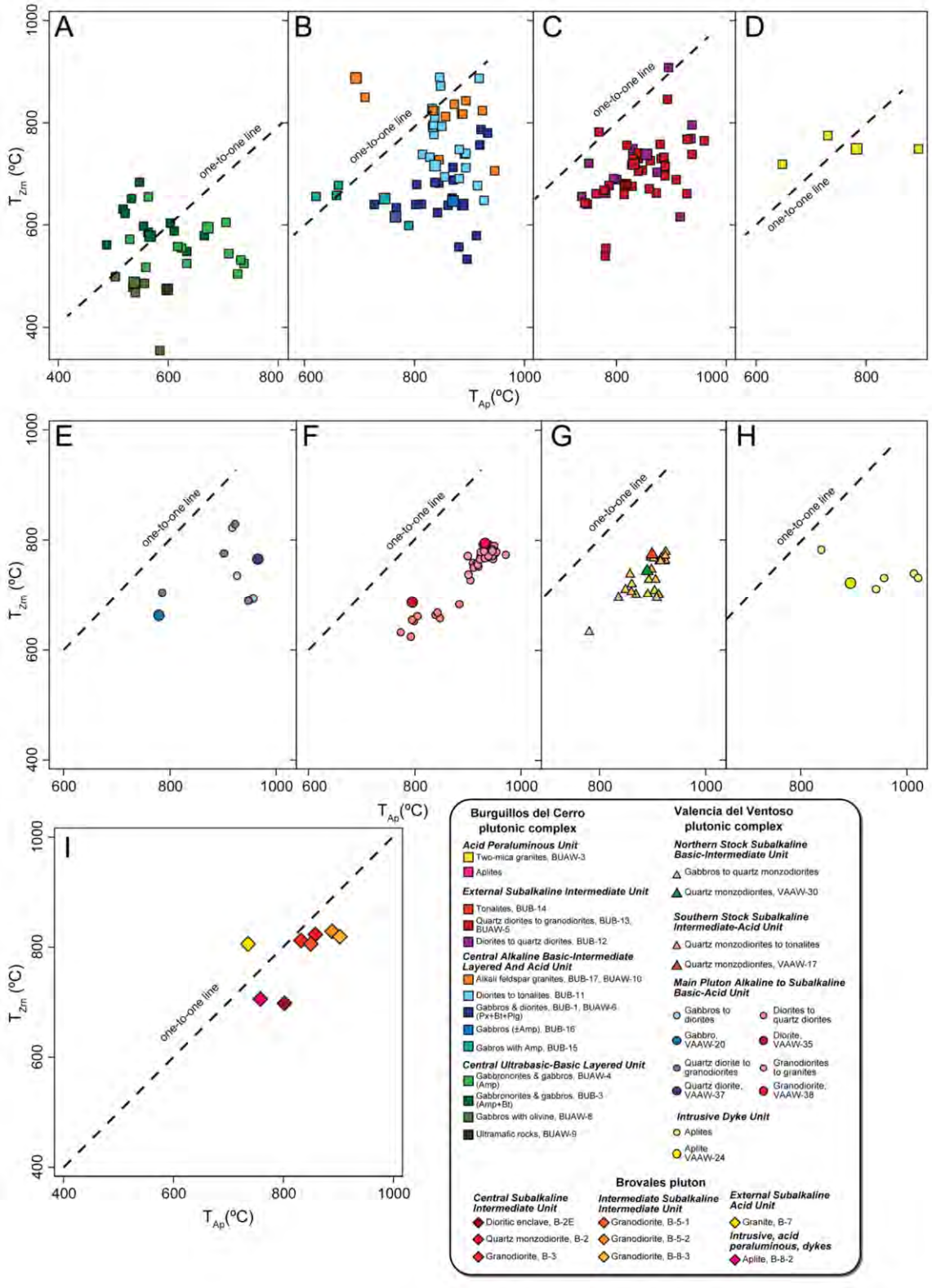

Figure 10.1. Zircon-satuation temperature vs apatite-saturation temperature using the equations of Watson and Harrison (1983), Harrison and Watson (1984) and Bea et al., (1994).

temperatures. The first group has low zircon saturation temperatures, 648-748 ºC, and higher apatite saturation temperatures, 815-927 ºC (Fig. 10.1B). The second group has a more restricted, higher, range of temperatures for zircon, 777-889 ºC, that coincide with the apatite temperatures, 832-886 ºC (Fig. 10.1B). The Burguillos *External Subalkaline Intermediate Unit* intermediate rocks, on the other hand, give very varied zircon and apatite saturation temperatures that have a mean of 707±10 ºC and 840±8 ºC respectively (Fig. 10.1C and Table 10.1).

The diorites from the Valencia *Main Pluton Alkaline to Subalkaline Basic-Acid Unit* have lower zircon saturation temperatures, 535-687 ºC, and apatite saturation temperatures, 774-884 ºC; whereas those of the granodiorites and granites are higher, 726-794 ºC and 900-972 ºC respectively (Fig. 10.1F and Table 10.1). Both the Valencia *Southern Stock Subalkaline Intermediate-Acid Unit* and *Northern Stock Subalkaline Basic-Intermediate Unit* have the same range of temperatures, 713-747ºC for zircon and 859-906ºC for apatite (Fig. 10.1G and Table 10.1).

The intermediate Brovales pluton rocks zircon saturation temperatures are quite restricted in the different units (except the aplites and the dioritic enclave), 806-829 ºC, but the apatite saturation temperatures are more variable, 736-903 ºC (Fig. 10.1I).

The more evolved syenites and alkali feldspar granites from the Burguillos *Central Alkaline Basic-Intermediate Layered and Acid Unit* give similar temperatures, 706-808 ºC, for zircon and, 832-886 ºC, for apatite (Fig. 10.1B).

The Burguillos *Acid Peraluminous Unit* and *Intrusive Dyke Unit* granites and Valencia *Intrusive Acid Peraluminous, dyke* aplites have a limited range of zircon saturation temperatures, 710-780 ºC, by contrast, those for apatite are more varied , 648-1021 ºC (Figs 10.1D and 10.1H).

10.2 Two-pyroxene Thermobarometers

Here we use the orthopyroxene-clinopyroxene thermobarometers of Putirka (2008), which are limited to a compositional range of KD(Fe-Mg)= 1.09±0.14 for equilibrium pairs.

Coexisting orthopyroxene and clinopyroxene is common in the ultramafic and mafic rocks of the Burguillos *Central Ultrabasic-Basic Layered Unit* and in the Valencia *Northern Stock Subalkaline Basic-Intermediate Unit.* Only the Burguillos del Cerro plutonic complex rocks have pairs that may be used in the Putirka (2008) thermobarometer, with KD (Fe-Mg)>0.75, outside the equilibrium range but still acceptable. The lherzolite, BUAW-9, gave temperatures of 940-960 ºC and pressures of *c.* 6 kbar; and, accordingly, the olivine gabbro, BUAW-8, 888-968 ºC and 3-6 kbar (Fig. 10.2).

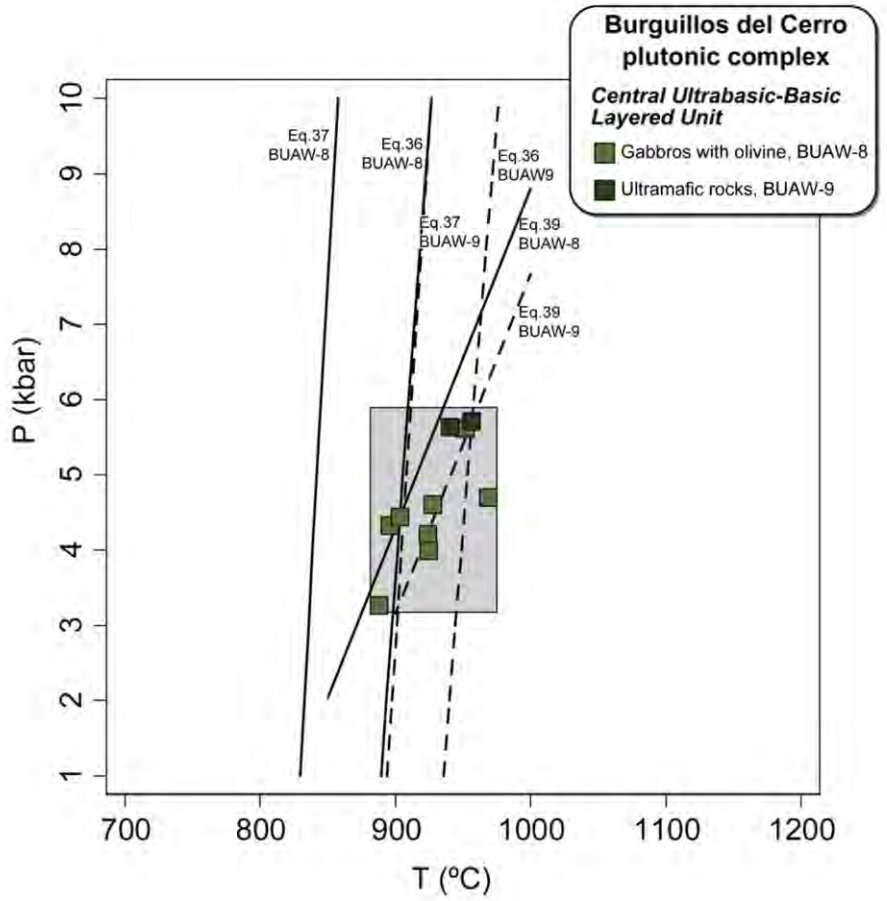

Figure 10.2. Temperature and pressure estimates in ultramafic rocks from the Burguillos Central Ultrabasic-Basic Layered Unit. Calculations performed with two-pyroxene thermobarometric expressions 36 to 39 from Putirka (2008). Grey area best P-T estimates; dotted lines correspond to sample BUAW-9 and solid lines to sample BUAW-8.

10.3 Amphibole-only and Amphibole-Plagioclase Thermobarometers

10.3.1 Thermometers

On the whole the temperatures obtained from the two different amphibole methods compare well with each other. In general the two amphibole thermometers give consistent results in all the Burguillos del Cerro units and also the Valencia *Northern Stock Subalkaline Basic-Intermediate Unit*. By contrast, the amphibole-plagioclase temperatures from the Valencia *Main Pluton Alkaline to Subalkaline Basic-Acid* and *Southern Stock Subalkaline Intermediate-Acid units* are lower than the amphibole-only temperatures.

To determine temperatures we used the edenite-albite-richerterite-anorthite (Ed-Ab-Rich-An) amphibole-plagioclase thermometer of Holland and Blundy (1994). The thermometer of Ridolfi and Renzulli (2012) was also used. The latter permits determination of the temperature of crystallisation of Mg-rich ($Mg/Mg+Fe^{2+}$)>0.5 calcic amphibole, for alkaline and subalkaline

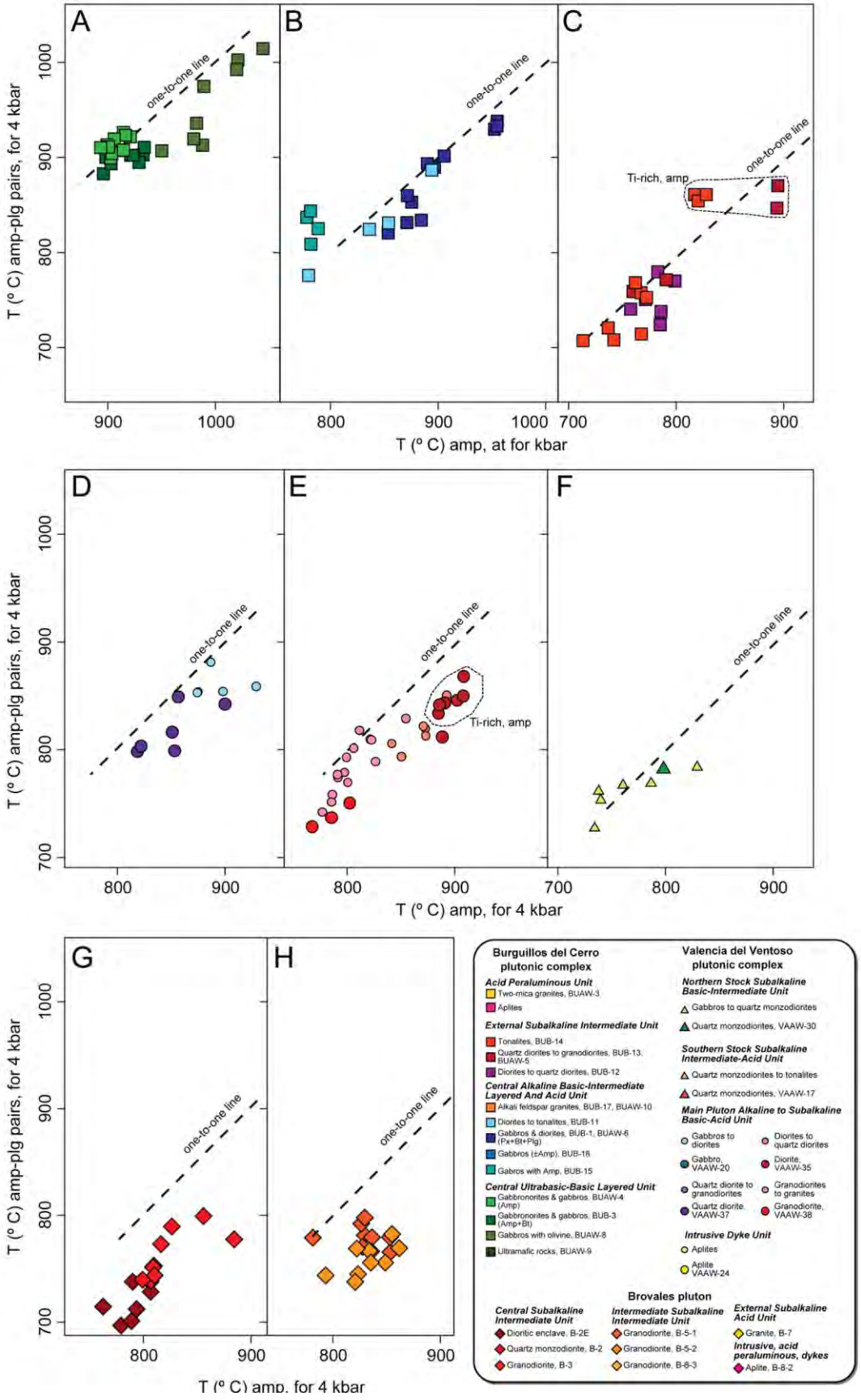

Figure 10.3. Temperature estimates calculated with the amphibole-plagiocase thermometer of Holland and Blundy (1994) and the amphibole-only thermometer of Ridolfi and Renzulli (2012). All data were calculated at 4 kbar.

compositions. Neither thermometer is strongly pressure dependent, estimated temperatures vary from 4-12ºC per kbar, significantly below the 40-50ºC error of the expressions. Good agreement usually exits between the results from the two methods. Here the temperatures were calculated at 4 kbar, within the range given by pyroxenes (see above) and amphibole compositions (see below).

As was indicated in Chapter 6 and Chapter 7, amphibole and plagioclase are present in almost all the units of the three plutonic bodies considered here. However, in many facies they show complex textures that are indicative of disequilibrium. For this reason special attention was paid to the selection of amphibole-plagioclase pairs that were apparently in equilibrium. Selected data are given in Appendix V.

In the Burguillos del Cerro plutonic complex, amphibole-plagioclase pairs were selected for all units except the *Acid Peraluminous Unit* which does not contain amphibole. The olivine gabbros, sample, BUAW-8, of the Burguillos *Central Ultrabasic-Basic Layered Unit,* have an amphibole-plagioclase and amphibole-only temperature range of 907-1044ºC (Fig. 10.A 3A and Table 10. 1). The poikilitic amphibole gabbros, both with and without poikilitic biotite, from the same unit, have a similar high, but more restricted, range of temperatures (Table 10.1): 906-917ºC for both thermometers (Fig. 10.3A). The mafic rocks from the Burguillos *Central Alkaline Basic-Intermediate Layered and Acid Unit* have a variable range of lower temperatures (Fig. 10.3). The temperatures of the amphibole gabbros, 775-853ºC, are lower than those of the gabbros with biotite: 820-955ºC for both thermometers (Fig. 10.3). The most mafic Valencia *Main Pluton Alkaline to Subalkaline Basic-Acid Unit* rocks, the alkaline diorites and quartz diorites, have similarly high temperatures, that were comparable for both thermometers, 798-929ºC (Fig 10.3D).

The intermediate diorites and quartz diorites from Burguillos *Central Alkaline Basic-Intermediate Layered and Acid Unit*, contain amphibole with uniform, relatively high, Ti content. For a plagioclase composition of Ab_{55} and amphiboles with Ti *c.* 0.4 (apfu 23 O), amphibole-plagioclase pairs and the amphibole-only thermometer gave a temperature of 771-894ºC (Fig. 10.3B). The intermediate rocks of the Burguillos *External Subalkaline Intermediate Unit,* on the other hand show that temperatures are dependent on the amphibole Ti content (Fig. 10.3C). Those with higher-Ti, modally less abundant, brown cores have temperatures for $Ab_{50\text{-}60}$ of 817-894ºC, for both methods (Fig. 10.3C). The lower-Ti amphiboles, more abundant dark green rims have temperatures for $Ab_{60\text{-}70}$ of 707-790ºC, for both methods (Fig. 10.3C).

This same Ti content-temperature dependence is observed in the subalkaline diorites from the Valencia *Main Pluton Alkaline to Subalkaline Basic-Acid Unit;* they too have zoned amphiboles with Ti-rich brown cores and lower-Ti dark green rims. The cores amphibole-plagioclase

temperature, for Ab_{60}, is in the range 805-868ºC and amphibole-only 841-908ºC (Fig. 10.3E). The rims amphibole-plagioclase temperature, for Ab_{60-70} is 767-823ºC (Fig. 10.3E). The dark green amphibole has ($Mg/Mg+Fe^{2+}$) *c.* 0.4, which is somewhat outside the range of Mg-rich amphibole compositions valid for the thermometer of Ridolfi and Renzulli (2012). Nevertheless, they give amphibole-only temperatures of 784-841ºC similar to the amphibole-plagioclase pairs and other samples from this unit (Fig. 10.3E). The granodiorites from this same unit, only have unzoned dark green, moderate-Ti, amphiboles that give temperatures lower than the Ti-rich cores but equivalent to the lower-Ti rims: amphibole-plagioclase Ab_{60-70} 728-828ºC and amphibole-only 767-854ºC.

Few of the Valencia *Northern Stock Subalkaline Basic-Intermediate Unit* amphiboles are primary igneous (see Chapters 6 and 7). The scarse equilibrium amphibole-plagioclase pairs gave the same temperature as amphibole-only, 727-856ºC, within the range of the aforementioned green amphibole (Fig. 10.3F).

The Brovales *Central Subalkaline Intermediate Unit* amphibole-plagioclase and amphibole-only temperatures are similar in both the diorite enclave, 697-809ºC, and the host quartz diorite, 739-855ºC, although somewhat more elevated in the latter (Fig. 10.3G and Table 10.1). The Brovales *Intermediate Subalkaline Intermediate Unit* granodiorites have the same amphibole-plagioclase temperatures of 737-798ºC. These rocks have low ($Mg/Mg+Fe^{2+}$) *c.* 0.32-0.4 but like the Valencia *Main Pluton Alkaline to Subalkaline Basic-Acid Unit* subalkaline diorites dark green amphibole rims the amphibole-only temperatures, 782-862ºC are similar to the amphibole-plagioclase pairs and other samples from the pluton (Fig. 10.3H). The granites from the Brovales *External Subalkaline Acid Unit* do not contain amphibole.

10.3.2 Barometers

Pressure calculations were undertaken using the amphibole-plagioclase barometer of Molina et al. (2015) that is based on the pressure dependence of the Al-Si partition between plagioclase and amphibole. Pressures were also calculated using the barometer of Schmidt (1992) that considers amphibole Al content at near-solidus conditions. Agreement between the conditions calculated with the two methods was generally good, particularly when one considers the precision of the methods, ± 1-2 kbar in the case of Molina et al., 2015) and ± 0.5 kbar for Schmidt (1992).

The amphibole-plagioclase barometer of Molina et al. (2015) requires verification that the amphibole-plagioclase pairs are within the defined compositional range used for the calculation

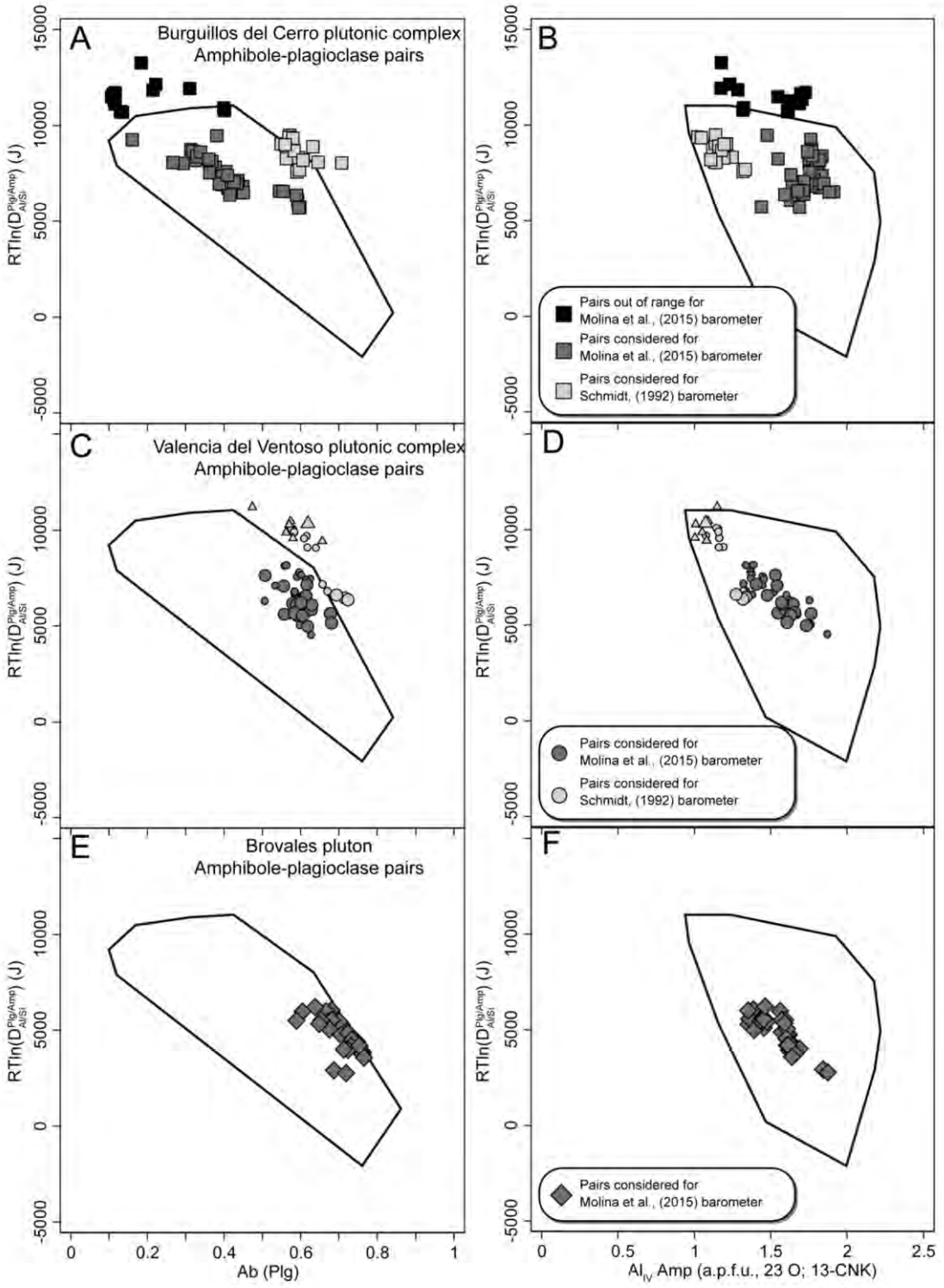

Figure 10.4. Compositional limits for the use of the amphibole-plagioclase barometer of Molina et al., (2015). Note that the amphibole-plagioclase pairs from the intermediate rocks, which are not plotted inside the main fields were not considered. For these rock types pressures were estimated using the Al-in-amphibole barometer of Schmidt (1992). $D_{Al/Si}^{plg/amp}$ *:partition of Si and Al in plagioclase and amphibole, T: Temperature in K and R: gas constant.*

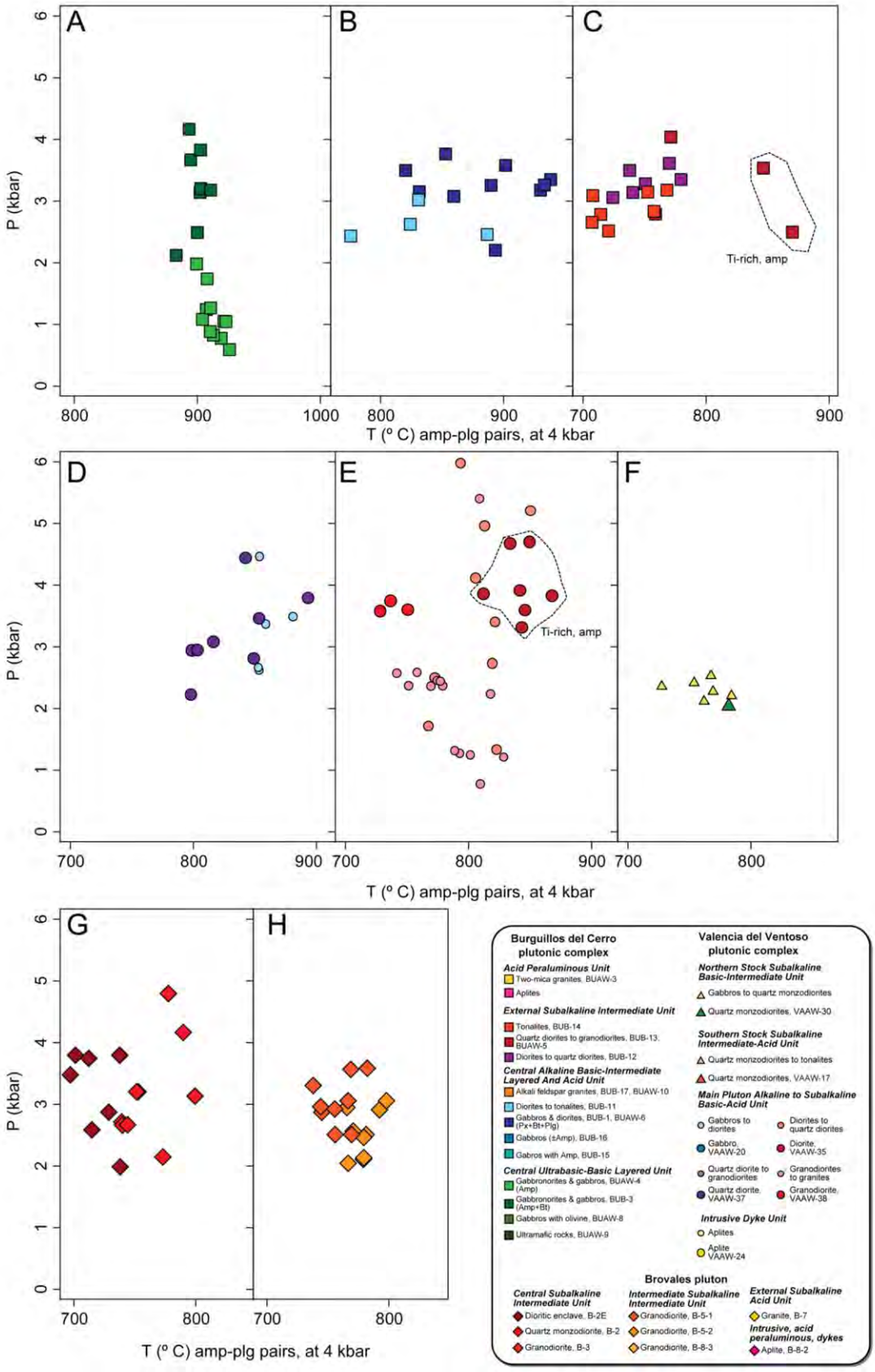

Figure 10.5. Pressure estimates aclculated with the amphibole-plagiolcase barometer of Molina et al., (2015) and, for intermediate rocks, the Al-in-amphibole barometer of Schmidt (1992).

				Zircon saturation T (ºC)					Apatite saturation T (ºC)					Two-pyroxenes T (ºC)					Two-pyroxenes P (kbar)				
Complex	Unit	Rock type	Comment	n	Mean	err	CI		n	Mean	err	CI		n	Mean	err	CI		n	Mean	err	CI	
Burguillos del Cerro plutonic complex	*Central Ultrabasic-Basic Layered Unit*	Ultramafic rocks		7	463.9	18.7	418.1	509.6	7	551.1	12.1	521.6	580.7	3	945.7	5.5	922.2	969.2	3	5.7	0.0	5.6	5.8
		Olivine gabbros												8	922.9	9.7	899.9	945.8	8	4.4	0.2	3.8	5.0
		Poikilitic amphibole and biotite gabros and gabbronorites		12	602.7	11.2	577.9	627.4	12	567.4	15.1	534.3	600.6										
		Poikilitic amphibole gabros and gabbronorites		12	557.3	12.6	529.6	584.9	12	650.9	21.2	604.2	697.6										
	Central Alkaline Basic-Intermediate Layered And Acid Unit	Gabbro with amphibole		6	648.3	10.8	620.6	676.0	6	724.5	38.7	625.0	824.0										
		Gabbro and diorites		21	662.1	14.7	631.5	692.7	21	853.1	12.2	827.6	878.7										
		Quartz diorites to tonalites		22	771.7	14.4	741.7	801.7	22	860.1	7.1	845.3	874.9										
		Alkali feldspar granites		10	812.8	17.4	773.4	852.2	10	846.5	26.4	786.8	906.2										
		Quartz diorites		12	724.8	22.2	676.1	773.6	12	842.3	20.4	797.5	887.2										
	External Subalkaline Intermediate Unit	Quartz monzo diorite to tonalites	Ti-rich amphibole	33	701.3	10.5	680.0	722.6	33	839.3	8.8	821.3	857.3										
			Ti-poor amphibole																				
	Acid Peraluminous Unit	Two mica granite		4	748.0	11.4	711.6	784.4	4	764.5	51.9	599.3	929.7										
Valencia del Ventoso plutonic complex	*Main Pluton Alkaline To Subalkaline Basic-Acid Unit*	Gabbros and diorites		4	728.5	34.5	618.8	838.2	4	895.5	39.4	770.1	1020.9										
		Quartz diorites		5	752.6	25.3	682.4	822.8	5	905.0	31.7	817.1	992.9										
		Diorites	Ti-rich amphibole	11	647.3	12.6	619.3	675.2	11	817.5	9.7	795.8	839.1										
			Ti-poor amphibole																				
	Northern Stock Subalkaline Basic-Intermediate Unit	Granodiorites to granites		30	770.4	2.8	764.6	776.2	30	933.0	3.2	926.5	939.5										
		Quartz monzodiorites		10	738.0	8.8	718.0	758.0	10	897.4	8.3	878.7	916.1										
	Southern Stock Subalkaline Intermediate-Acid Unit	Quartz monzodiorites		14	746.9	7.3	731.2	762.7	14	899.5	5.9	886.8	912.2										
	Intrusive Dyke Unit	Aplites		6	735.8	10.1	709.9	761.7	6	944.3	28.5	871.0	1017.6										
Brovales pluton	*Central Subalkaline Intermediate Unit*	Dioritic enclaves		1	698.0				1	802.0													
		Quartz diorite		2	817.5	5.5			2	845.0	13.0												
	Intermediate Subalkaline Intermediate Unit	Granodiorite	Fine-grained	3	818.0	6.7	789.4	846.6	3	880.7	15.9	812.4	948.9										
			Coarse-grained																				
	External Subalkaline Acid Unit	Granites		1	806.0				1	736.0													
	Intrusive, Acid Peraluminous, Dykes	Aplites		1	706.0				1	758.0													

Table 10.1. Summary of P-T calculations obtained for the main complexes. Precision is given at 1σ and confidence interval (CI) at 95%.

				Amphibole-plagioclase T (ºC)					Amphibole-only T (ºC)					Amphibole-plagioclase P (kbar)					Amphibole P (kbar)				
Complex	Unit	Rock type	Comment	n	Mean	err	CI		n	Mean	err	CI		n	Mean	err	CI		n	Mean	err	CI	
Burguillos del Cerro plutonic complex	*Central Ultrabasic-Basic Layered Unit*	Ultramafic rocks																					
		Olivine gabbros		8	957.4	15.4	920.9	993.8	8	996.8	10.5	972.0	1021.6										
		Poikilitic amphibole and biotite gabros and gabbronorites		8	898.6	3.0	891.6	905.7	8	917.1	5.6	904.0	930.3	8	3.2	0.2	2.7	3.8					
		Poikilitic amphibole gabros and gabbronorites		11	913.1	2.6	907.3	918.8	11	907.7	2.6	901.9	913.5	11	1.1	0.1	0.9	1.4					
		Gabbro with amphibole		4	828.7	7.6	804.4	853.0	4	782.4	2.2	775.3	789.6										
	Central Alkaline Basic-Intermediate Layered And Acid Unit	Gabbro and diorites		11	880.4	13.0	851.4	909.3	11	900.9	11.1	876.1	925.6	10	3.2	0.1	2.9	3.5					
		Quartz diorites to tonalites		5	817.7	21.1	759.2	876.3	5	835.9	19.1	783.0	888.8	4	2.6	0.1	2.2	3.1					
		Alkali feldspar granites																					
	External Subalkaline Intermediate Unit	Quartz diorites		6	750.4	8.5	728.5	772.4	6	780.2	5.8	765.4	795.1						6	3.3	0.1	3.1	3.5
		Quartz monzo diorite to tonalites	Ti-rich amphibole	6	852.4	6.9	834.6	870.2	5	850.7	17.8	801.3	900.2	2.0	3.0	0.5							
			Ti-poor amphibole	9	739.8	8.9	719.2	760.4	9	756.9	7.6	739.4	774.5						9	3.0	0.1	2.7	3.3
	Acid Peraluminous Unit	Two mica granite																					
	Main Pluton Alkaline To Subalkaline Basic-Acid Unit	Gabbros and diorites		5	860.0	5.3	845.2	874.8	5	892.7	10.1	864.6	920.7	5	3.3	0.3	2.4	4.3					
		Quartz diorites		8	831.8	11.9	803.7	860.0	6	850.1	12.0	819.3	880.9	8	3.2	0.2	2.6	3.8					
		Diorites	Ti-rich amphibole	12	832.8	6.1	819.4	846.1	12.0	885.7	4.9	875.0	896.5	16	3.7	0.3	3.1	4.4					
			Ti-poor amphibole	4	792.1	13.3	749.7	834.6	*4*	*812.1*	*11.9*	*774.2*	*849.9*										
Valencia del Ventoso plutonic complex		Granodiorites to granites		5	813.4	4.6	800.5	826.2	5	823.2	8.4	799.8	846.7	7	1.9	0.6	0.4	3.4					
				12	762.4	6.0	749.1	775.7	12	792.6	4.3	783.2	802.0						10	2.8	0.2	2.4	3.2
	Northern Stock Subalkaline Basic-Intermediate Unit	Quartz monzodiorites		7	763.7	7.3	745.9	781.4	8	780.4	16.1	742.3	818.5						8	2.3	0.1	2.2	2.5
	Southern Stock Subalkaline Intermediate-Acid Unit	Quartz monzodiorites																					
	Intrusive Dyke Unit	Aplites																					
	Central Subalkaline Intermediate Unit	Dioritic enclaves		8	722.9	6.9	706.5	739.3	7	792.6	6.5	776.7	808.5	8	3.2	0.2	2.6	3.7					
		Quartz diorite		8	764.3	8.4	744.4	784.1	5	818.1	9.8	790.8	845.4	8	3.2	0.3	2.5	3.9					
Brovales pluton	*Intermediate Subalkaline Intermediate Unit*	Granodiorite	Fine-grained	9	779.2	3.6	770.8	787.6	*9*	*830.4*	*7.0*	*814.3*	*846.5*	9	2.5	0.1	2.2	2.8					
			Coarse-grained	9	758.5	4.9	747.3	769.7	*9*	*832.7*	*7.0*	*816.6*	*848.7*	9	3.0	0.1	2.7	3.3					
	External Subalkaline Acid Unit	Granites																					
	Intrusive, Acid Peraluminous, Dykes	Aplites																					

Table 10.1. Continued.

Complex	Unit	Rock type	Estimation P (kbar)	Estimation T (ºC)
Burguillos del Cerro plutonic complex	Central ultrabasic-basic layered unit	Ultramafic rocks	**6**	**922-969**
		Olivine gabbros	**4-5**	**899-1022**
		Poikilitic amphibole and biotite gabros and gabbronorites	**3-4**	**882-930**
		Poikilitic amphibole gabros and gabbronorites	**1-2**	**902-919**
		Gabbro with amphibole	**-**	**775-853**
	Central Alkaline Basic-Intermediate Layered And Acid Unit	Gabbro and diorites	**3-4**	**851-926**
		Quartz diorites to tonalites	**2-3**	**742-889**
		Alkali feldspar granites		**773-906**
	External Subalkaline Intermediate Unit	Quartz diorites	**3-4**	**728-797**
		Quartz monzo diorite to tonalites	**3-4**	**801-900**
			3	**680-774**
	Acid Peraluminous Unit	Two mica granite	**-**	**-**
Valencia del Ventoso plutonic complex	*Main Pluton Alkaline To Subalkaline Basic-Acid Unit*	Gabbros and diorites	**2-4**	**845-921**
		Quartz diorites	**3-4**	**804-881**
		Diorites	**3-4**	**822-897**
			3-4	**743-839**
		Granodiorites to granites	**0-3**	**800-847**
			2-3	**749-802**
	Northern Stock Subalkaline Basic-Intermediate Unit	Quartz monzodiorites	**2**	**742-819**
	Southern Stock Subalkaline Intermediate-Acid Unit	Quartz monzodiorites	**-**	**-**
	Intrusive Dyke Unit	Aplites	**-**	**-**
Brovales pluton	*Central Subalkaline Intermediate Unit*	Dioritic enclaves	**3-4**	**707-808**
		Quartz diorite	**3-4**	**744-845**
	Intermediate Subalkaline Intermediate Unit	Granodiorite	**2-3**	**771-846**
			3	**747-846**
	External Subalkaline Acid Unit	Granites	**-**	**-**
	Intrusive, Acid Peraluminous, Dykes	Aplites	**-**	**-**

Table 10.1. Continued, summary of P and T results obtained for thre main units of the the three complexes.

(Fig. 10.4). More specifically, these authors indicated that the most important parameters for their barometer are: distribution of Al and Si in plagioclase and amphibole, $D_{Al/Si}^{plg/amp}$; temperature; variation in the plagioclase Ab component; and, variation in Al_{IV} in amphibole (Fig. 10.4). Here we use the temperatures calculated in the previous section.

The Schmidt (1992) barometer was used to calculate the pressure of the amphiboles that did not fulfil the criteria of Molina et al. (2015) (Figs 10.4A to 10.4D). It is based on a linear relation between pressure and amphibole Al content. It may be applied over the temperature range 655-700ºC, to amphiboles in intermediate rocks, tonalites to granodiorites, with the mineral assemblage: amphibole+biotite+plagioclase+orthoclase+quartz+titanite+Fe-Ti oxide+fluid phase+melt. It is suitable, therefore, to estimate the pressures of the Burguillos and Valencia intermediate subalkaline rock amphiboles which fall in the temperature range 745-760ºC.

Gabbros and gabbronorites from the Burguillos *Central Ultrabasic-Basic Layered Unit* give different amphibole-plagioclase pressures. The rocks that contain both poikilitic biotite and amphibole have pressures of 2-4 kbar; whereas those with only poikilitic amphibole have lower pressure, 1-2 kbar (Fig 10.5A). The gabbros and diorites from the Burguillos *Central Alkaline Basic-Intermediate Layered and Acid Unit* have a range of pressures, 2-4-kbar. The same pressure range, 2-4-kbar, was obtained for the alkaline gabbros and quartz diorites from the Valencia *Main Pluton Alkaline to Subalkaline Basic-Acid Unit* (Fig 10.5D).

The Ti-rich amphibole-plagioclase pairs from the intermediate rocks of the Burguillos *External Subalkaline Intermediate Unit* gave a pressure of 2-4 kbar whereas for these pairs including lower-Ti amphiboles pressures calculated using Schmidt (1992) were 3-4 kbar (Fig. 10.5C).

Notably, the subalkaline and alkaline diorites of the Valencia *Main Pluton Alkaline to Subalkaline Basic-Acid Unit* have very variable pressures 1-6 kbar (Fig. 10.5E). Differing from this, the pressures calculated from the amphiboles in the granodiorites of this unit have more typical pressures of 2-4 kbar (Fig. 10.5E). The few amphiboles from the Valencia *Northern Stock Subalkaline Basic-Intermediate Unit* gave pressures of 2 kbar.

The Brovales Pluton units all give comparable pressures: the *Central Unit* diorite enclave 2-4 kbar and quartz diorite 2-5 kbar (Fig. 10.5G); and all fine-grained, coarse-grained and deformed facies of the the *Intermediate Unit* 2-4 kbar (Fig. 10.5H).

10.4 Summary of P-T conditions

Considering all the results obtained from the different thermobarometric methods a crystallisation P-T range can be established for the units of each complex (Table 10.1). Most of

the pressures range from 2-5 kbar and temperatures vary from 900-1000ºC for the ultramafic rocks; 850-930ºC for the mafic rocks; and, 740-850ºC for the intermediate and felsic rocks.

Chapter 11: Discussion

11.1 Paleogeographic Position of the Ossa-Morena Zone During the Cambro-Ordovician and its Subsequent Amalgamation into the Iberian Massif

11.2 Timing and Tectonomagmatic Setting of Variscan Magmatism in the Ossa-Morena Zone

11.3 Magma Sources and Magmatic Processes Involved in the Ossa-Morena Zone Variscan Magmatism.

11. Discussion

11.1 Paleogeographic Position of the Ossa-Morena Zone During the Cambro-Ordovician and its Subsequent Amalgamation into the Iberian Massif

Iberia is a composite of terranes, the paleoposition of these zones prior to their amalgamation and when and how they came to be juxtaposed continues to be the subject of considerable debate. The western sector of the peninsula is dominated by the Iberian Massif, the most extensive expression of the European Variscides that resulted from the collision of Gondwana and Laurentia during the Paleozoic (Burg et al., 1978; Bard et al., 1980; Matte, 1986).

Recently, Bea et al., (2010) proposed a new position for the Central Iberian Zone (CIZ), north of the Saharan Metacraton (Fig. 11.1), further east than previously positioned off Amazonia (Fernández-Suárez et al., 2000; Gutiérrez-Alonso et al., 2003) or the West African Craton (Eguiluz et al., 2000). Similarly, Fernández-Suárez et al., (2014) located the Cantabrian Zone (CZ) next to the Saharan Metacraton and Arabian Nubian Shield and sugggested that it represents a passive margin fragment of the northern fringe of Gondwana (Pastor-Galán, et al., 2013). Shaw et al. (2014) proposed a comparable position for the West Asturian-Leonese Zone (WALZ). Likewise, Díez-Fernández et al., (2010) placed the Galicia Trás-os-Montes (GTOMZ) parautochthonous units close to the Saharan Metacraton (Fig. 11.1). The South Portuguese Zone (SPZ), by contrast, apparently has a paleogeographical affinity with Avalonia (Fig. 11.1).

In agreement with the recently published paleogeographic models, in their reviews of the northern margin of Gondwana, Stampfli et al., (2013) and Torsvik and Cocks (2013) noted that rifting occurred in the transition between the Cadomian and Variscan orogenies. Contemporanous rift-related magmatism has been associated with Rheic Ocean opening (Murphy et al., 2006; Nance et al., 2010; 2012).

We consider it timely, therefore, to contemplate how the Ossa-Morena Zone (OMZ) fits into:

i. New early Paleozoic paleogeographic reconstructions that place other Iberian zones further east than previously thought (Fig. 11.1).
ii. Rheic Ocean opening (Linneman et al., 2004; 2008; Nance et al., 2010; 2012).
iii. Iberia amalgamation (Gutiérrez-Alonso et al., 2004; Martínez-Catalán, 2011; 2012; Simancas et al., 2013).

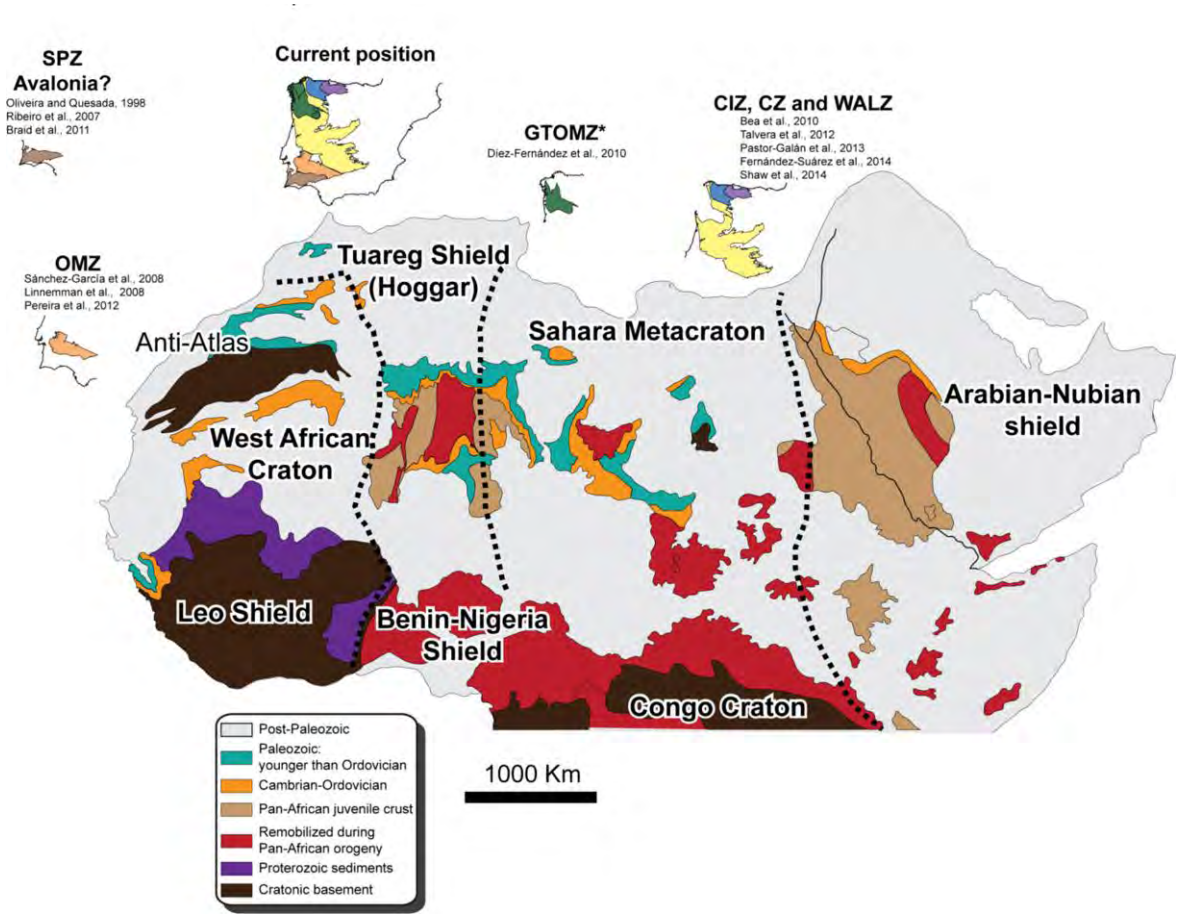

Figure 11.1. The Iberian Massif Zones and their paloegographic position with respect to the north African terranes. The Cratonic regions ages are taken from Avigad et al., (2003). Note that Central Iberian Zone (CIZ), Cantabrian Zone (CZ) and West-Asturian Leonese Zone (WALZ) are close to the Saharan Metacraton and Arabian Nubian Shield (Bea et al., 2010; Talavera et al., 2012; Pastor-Galán et al., 2013; Shaw et al., 2014; Fernández-Suarez et al., 2014). The parauthoctonous units from Galicia-tras-os-Montes Zone is placed between Saharan Metacraton and Tuareg Shield (Díez-Fernandez et al., 2010). The Ossa-Morena Zone (OMZ) was located close to the west Anti-Atlas, West African Craton (Nance and Murphy, 1994; Fernández-Suárez et al., 2002b; Linnemman et al., 2004; 2008; Pereira et al., 2008; 2011; 2012b).

To do this we compiled an extensive database of published geochemical and geochronological data from the OMZ. The dataset includes two new analyses from the current work an OMZ middle Cambrian leucogranite (sample VAAW-41) and a basement metasediment (sample VAAW-39). In addition we collated data from the other Iberian zones and the three main north Gondwana, African, potential paleogeographical terrane candidates: the Anti-Atlas West African Craton; the Tuareg Shield and the Saharan Metacraton. In this way, a new model is developed for the paleogeographic position of the OMZ during the Cambro-Ordovician and for its subsequent amalgamation into the Iberian Massif.

11.1.1 The Tectonomagmatic Evolution of the Ossa-Morena Zone Between the Cadomian (650-550 Ma) and Variscan (390-300 Ma) Orogenies

The OMZ igneous rocks range in age from Precambrian to Permian, thus, they evidence the transition from the Cadomian to Variscan orogenies in the region, including:

i. A Neoproterozoic-Cambrian (590-540 Ma) Cadomian collisional event. (Oschner, 1993; Linnemann et al., 2008).
ii. Early-middle Cambrian (540-500 Ma) early and main rift continental extension-related magmatism. (Expósito, 2000; Sánchez-García et al., 2003; 2010; Simancas et al., 2004).
iii. Cambro-Ordovician (490-470 Ma) incipient ocean basin magmatism (Quesada, 1991; Sanchez-García et al., 2003; Chichorro et al., 2008).
iv. Devonian-Carboniferous Variscan collision and related magmatism (Dallmeyer et al., 1995; Montero et al., 2000; Ordoñez-Casado et al., 2008).

The OMZ Precambrian Cadomian orogenic magmatism, 590-540 Ma, includes subduction-related diorites-granites and basalts now preserved as metabasite amphibolites (Bellon et al., 1979; Schäfer, 1990; Ochsner, 1993). More recently, Sánchez-Lorda et al. (2013) detected a south to north N-MORB to calc-alkaline compositional polarity in the OMZ late Ediacaran magmatism which led them to postulate Gondwana-ward subduction at that time.

The early Cambrian period from 540-520 Ma marked a transition from a collisional to an extensional context (Sanchez-García et al., 2013). The last manifestation of the Cadomian continental magmatic arc, calc-alkaline magmatism, was in the earliest Cambrian (Figs 11.2A, 11.2B and 11.3A) (Oschner, 1993; Linemann et al., 2000; 2008), e.g., the Culebrin tonalite 532±4 Ma (KOBER method, Salman, 2002). By contrast, the early Cambrian magmatism, intercalated in the 'lower detrital formation' sediments is principally composed of peraluminous magmatism (Figs 11.2A and 11.2B). This was produced during initiation of extension, the 'early rift-related event' (e.g., Galindo, 1989; Ochsner, 1993; Galindo and Casquet, 2004; Sánchez-García et al., 2010; 2013). Consistent with this, abundant A_2-type magmatism (Figs 11.3A and 11.3B), such as the Calera de León granite 524±4 Ma (KOBER method, Salman, 2002), marks the initiation of extension in the region (Sanchez-García et al., 2003; 2013).

According to the classification proposed by Eby, (1992) A_2-type compositions form either at convergent margins or represent crustally contaminated A_1-type 'OIB-like' magmas. In support of the latter model OMZ 530-520 Ma S-type magmatism has elemental and isotopic compositions comparable to the basement metasediments, e.g., the Mina Afortunata anatectic dome (532±4 Ma, U-Pb TIMS, Sanchez-García et al., 2008) (Figs 11.2A-B, 11.3A and Fig. 11.5A).

Furthermore, this crustal melt magmatism was coeval with crustally-contaminated N- and E-MORB-like basic magmas preserved for example in the Arroyo Argallón amphibolite (525±13 Ma, U-Pb SHRIMP, Ordoñez-Casado, 1998) (Fig. 11.4A-D) (Gómez-Pugnaire et al., 2003).

In the middle to late Cambrian, from 520-500 Ma, during the 'main rift-related event' (Sanchez-García et al., 2003), plutonic and volcanic mafic magmatism was more abundant. Intercalation of E-MORB-like mafic lavas and tuffs (Fig. 11.4) in the Cambrian 'upper detrital formation' led to the deposition of volcanosedimentary sequences in the central part of the OMZ (517-512 Ma, Sanchez-García et al., 2008; 2010). Following this, widespread OIB, transitional alkaline to tholeiitic, volcanic and plutonic mafic magmatism occurred from 512-505 Ma (Fig. 11.4) (Galindo et al., 1990, Sanchez-García et al., 2010).

Associated with the mafic magmatism was, coeval, extension-related alkaline and anatectic peraluminous intermediate to felsic magmatism (Fig. 11.2C and 11.2D) (Galindo and Casquet, 1985; Galindo et al, 1990; Montero et al., 1999). The Monesterio granodiorite (510±4 Ma, KOBER method, Salman, 2002), for example, comprises peraluminous S-type granitoids (Fig. 11.2C). By contrast, the contemporaneous, within error, alkaline magmatism in the Barrcarota plutonic complex (505±5 Ma Rb-Sr WR, Galindo et al., 1990; 501+5-2 Ma U-Pb TIMS, Oschner, 1993), has a principally A_1-type 'ocean-island' alkaline affinity (Fig. 11.3C and 11.3D). Between these two extremes, other rocks, such as the Castillo granite (502±8 Ma KOBER method, Salman, 2002), are transitional from A_1-type to A_2-type (Fig. 11.3D).

Consistent with the above, our leucogranite, VAAW-41, (509±3 Ma, U-Pb SHRIMP) is A_2-type: either 'convergent margin' or 'crustally contaminated A_1-type' (cf., Eby, 1992). We favour the latter model because, firstly, the magmatism occurred during the 'main rift-related event' not during a collisional episode. Secondly, consistent with a crustal contamination model, field relations reveal extensive interaction between the leucogranite and the host Serie Negra metasediment (VAAW-39, see Chapter 3 Fig 4.13). What is more, other A_2-type magmatism, of the same age in the region, shows evidence of a crustal component (Fig. 11.2D and 11.3C), e.g., the Évora orthogneiss (517± 15 and 505± 5 Ma, U-Pb SHRIMP, Chichorro et al., 2008) and the syenites from the Barcarrota pluton (505±5 Ma Rb-Sr WR, Galindo et al., 1990; 501+5-2 Ma U-Pb TIMS, Oschner, 1993). A variation in εNd reflects the mixed origin of these rocks (Fig. 11.5B).

During the Cambro-Ordovician, 490-470 Ma, rifting progressed resulting in the generation of T- and N-MORB-like mafic rocks (Fig. 11.4), with εNd_t 6-7.5 (Fig. 11.5C). These are notably more primitive than the 520-500 Ma stage E-MORB-like and OIB-like mafic magmatism that

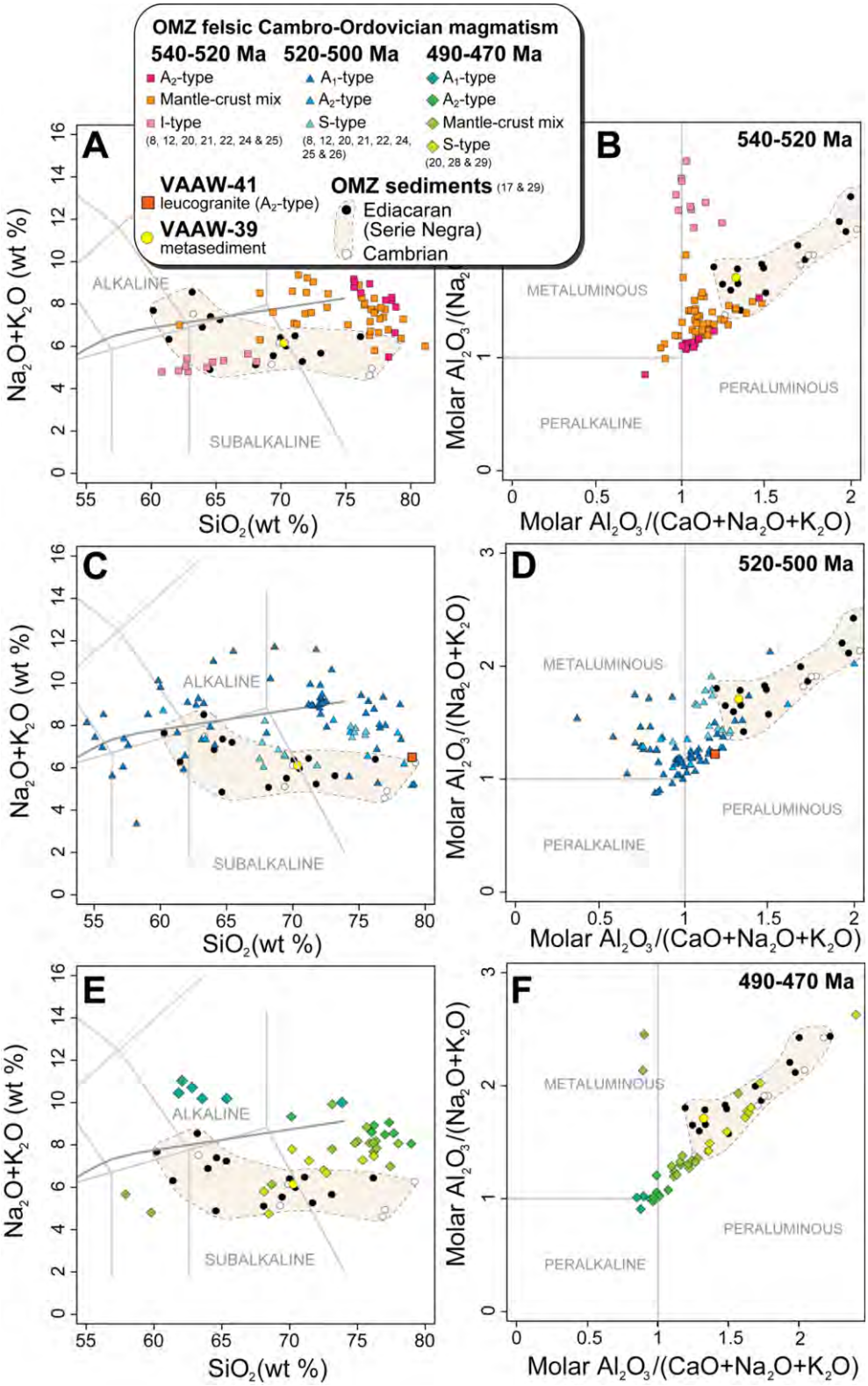

Figure 11.2. Whole-rock major element data of the samples studied in this work and an extensive geochemical database of 540-520 Ma, 520-500 Ma and 490-470 Ma Ossa-Morena Zone (OMZ) magmatism and OMZ sedimentary rocks from Serie Negra and Cambrian units. In the TAS plots (A, C, E), note the discrimination of alkaline and sub-alkaline compositions. The molar (Al_2O_3/(Na_2O+K_2O)) vs. molar (Al_2O_3/(CaO+Na_2O+K_2O)) plots (B, D, F), show the compositional variation of metaluminous, peralkaline and peraluminous samples. Numbers in brackets correspond to the data sources in Appendix I.

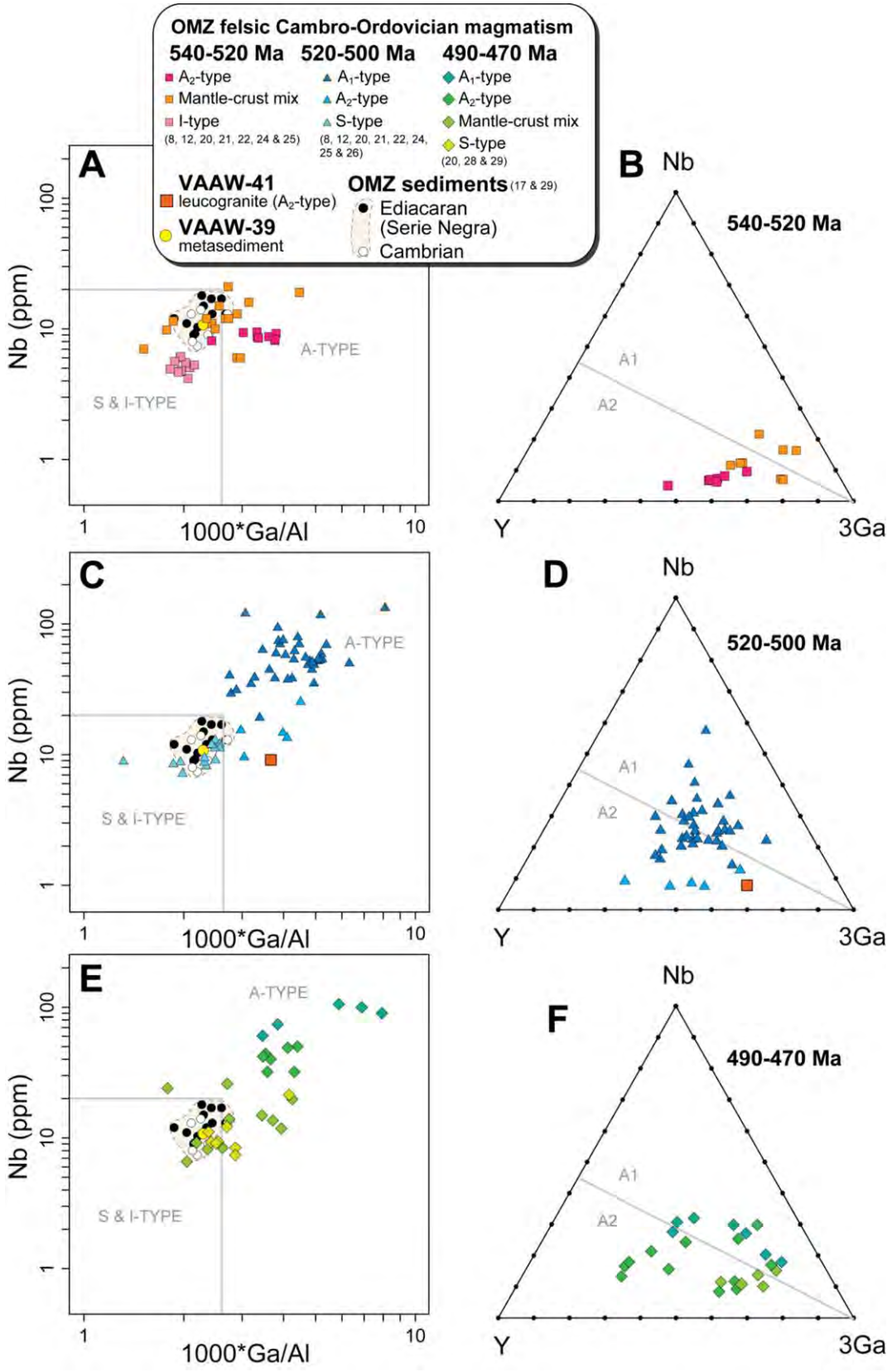

*Figure 11.3. Granitoid discrimination diagrams. The Nb vs 1000*Ga/Al (Whalen et al., 1987) (A, C, E) and the Nb-Y-3Ga A_1- A_2-type granitoids discrimination diagram (Eby, 1992) (B, D, F) show the samples studied here and an extensive geochemical database of 540-520 Ma, 520-500 Ma and 490-470 Ma Ossa-Morena Zone magmatic rocks and sedimentary rocks from Serie Negra and Cambrian units. Numbers in brackets correspond to the data sources in Appendix I.*

have εNd_t 2.5-5 (Fig. 11.5B) (Sanchez-García et al., 2010; Sarrionandia et al., 2012). The N-MORB magmatism apparently resulted from asthenospheric upwelling and proto-ocean basin development (Ordoñez-Casdo, 1998; Chichorro et al., 2008).

Felsic magmatism during the same period was also extension-related peraluminous anatectic and peralkaline anorogenic (Fig. 11.2E and 11.2F) (Sánchez-Carretero et al., 1999; Díez-Fernández et al., 2014). Solá et al. (2008), furthermore, related the coeval peraluminous Urra Formation volcanic rocks to the west in Portugal (488±5 Ma U-Pb SHRIMP) to a north Gondwana extensional event, suggesting that their geochemical affinity was inherited from a crustal source, OMZ Ediacaran calc-alkaline rocks (Fig. 11.3E).

Mixing of mantle- and crust-derived magmas occurred in this period (Figs 11.2E-F and 11.3E). The Carrascal granite (486±7 Ma, U-Pb LA-ICP-MS, Solá, 2007) and the Ribera del Fresno and Las Minillas orthogneisses (473+2-3 Ma, U-Pb TIMS, Schäfer, unpublished data in Oschner, 1993), for example, are interpreted as crustally contaminated alkaline magmas (Fig. 5E) (Oschner, 1993; Solá, 2007). Significantly, both A_1- and A_2-type alkaline rocks crop out in the region (Fig. 5F). The former include the A_1-type peralkaline Almendral granite (470±10 Ma, WR K-Ar, Galindo unpublished data in Casquet and Galindo, 2004) and the latter the A_2-type Aceuchal and Almendradejo orthogneisses (477±5 Ma and 475+10-6 respectively, U-Pb TIMS, Oschern, 1993).

The pattern of the OMZ Cambro-Ordovician magmatism is consistent, both temporally and compositionally, with the diachronous development of a narrow ocean basin related to a rifted volcanic margin, comparable say to the Ethiopian rift Red Sea type model (Pearce, 2008). There, the progression was from E-MORB tholeiitic to OIB-like alkaline and finally T- and N-MORB with a declining crustal input over a period of some 30 million years. Initial felsic magmatism, comparable to the OMZ 'early rift-related event' 540-520 Ma, changed to predominantly intermediate and then bimodal basic-felsic as rifting proceeded, equivalent to the OMZ 'main rift-related event' 520-500 Ma. Finally, the Red Sea context evolved from continental to oceanic crust generation (Wolfenden et al., 2005), as preserved in the OMZ in the 490-470 Ma T- and N-MORB mafic and alkaline and peralkaline felsic magmatism. At some point after *c.* 450 Ma in the OMZ ocean opening was arrested prior to broad ocean basin development. Before *c.* 390 Ma regional rift-related extension changed to collision (Simancas et al., 2001; Braid et al., 2011; Pereira et al., 2012c).

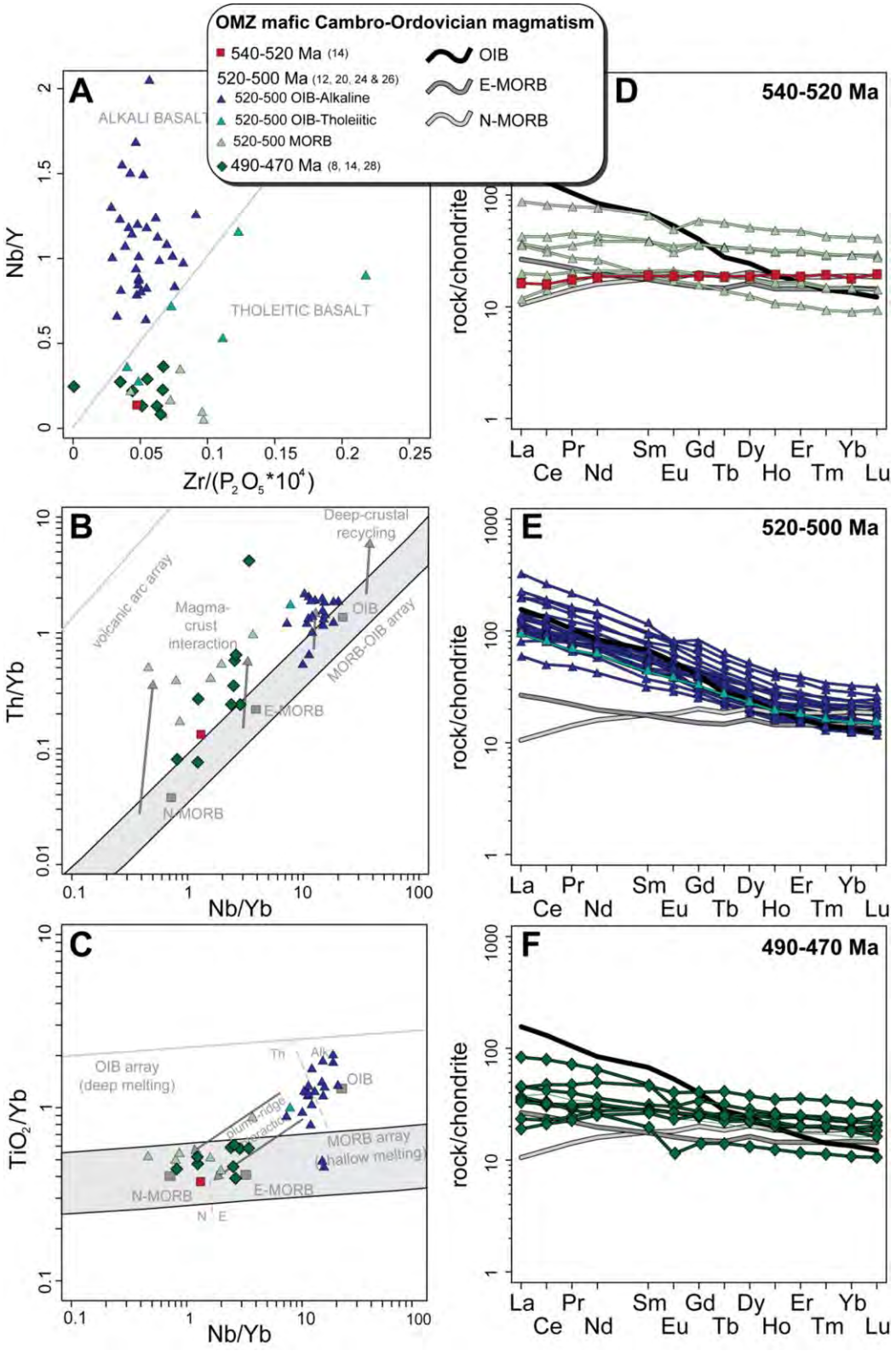

Figure 11.4. Whole-rock minor and trace element diagrams for the Ossa-Morena Zone (OMZ) mafic magmatism 540-520 Ma, 520-500 Ma and 490-470 Ma. Note the alkaline and tholeiitic compositions (A) (after Floyd and Winchester, 1975) and the mantle source affinity (B and C) of each group in Pearce (2008) plots. Chondrite-nomalised REE plots of E) c. 540 to 517 Ma E-MORB like rocks F) 517-512 Ma alkaline/tholeiitic OIB rocks and G) 490-470 Ma T and N-MORB rocks. Normalisation values after McDonough and Sun (1995), the reference mantle source patterns from Sun and McDonough, (1989) are shown in D-F. Numbers in brackets correspond to the data sources in Appendix I.

11.1.2 Geochronological Evidence for the Cambro-Ordovician Paleogeographic Position of the Ossa-Morena Zone

To try to determine the Cambro-Ordovician paleogeographic position of the Ossa-Morena Zone (OMZ) we combine evidence from various geochronologica datasets:

i. Nd model ages from OMZ Cambro-Ordovician igneous rocks; the OMZ Ediacaran to Ordovician sedimentary rocks; and, also, Ediacaran to Cambrian sediments from the OMZ and Central Iberian Zone boundary (Fig. 11.5).
ii. Nd model ages of Pan-African granitoids from the three north African terranes the Anti-Atlas West African Craton; the Tuareg Shield; and the Saharan Metacraton (Fig. 11.5). We consider the Pan-African granitoids as the potential source of Ediacaran to Ordovician OMZ sediments (cf., Bea et al., 2010).
iii. Single and population zircon and whole-rock ages for OMZ sedimentary and magmatic rocks and those of the autochthonous Central Iberian Zone (CIZ) and Cantabrian Zone (CZ) and the Galicia Tras-os-Montes Zone (GTOMZ) parautochthonous units (Fig. 11.6 and 11.10).
iv. Single and population zircon and whole-rock ages of Neoproterozoic and Cambrian sedimentary and magmatic rocks from the three north African terranes (Fig. 11.7, 11.8 and 11.10).

11.1.2.1 Nd Model Ages

11.1.2.1.1 OMZ Cambro-Ordovician Igneous Rocks

The Nd model ages of the OMZ Cambro-Ordovician igneous rocks range from 2.0-0.5 Ga, with main clusters at *c.* 1.7 Ga, *c.* 1.5 Ga, 1.3 Ga, *c.* 1.1 Ga and *c.* 0.5 Ga (Figs 11.5A-D).

Mafic, mantle-derived, early Paleozoic OMZ magmatism may be divided into two main groups. On the one hand the rocks with the youngest Nd model ages, 0.6-0.5 Ga (Fig. 11.5D), close to the *c.* 480 Ma crystallisation age, are those with primitive tholeiitic N-MORB compositions (Fig. 11.5C). This is consistent with the development of a rift/proto-oceanic basin, as suggested above, related to asthenospheric upwelling (Ordoñez-Casado, 1998). By contrast, the E-MORB and OIB magmatism, with an apparently variable crustal input, has older Nd model ages in the range 1.2-0.8 Ga (Fig. 11.5D).

Accordingly, the contemporaneous felsic A_1-type, apparently 'least contaminated', most peralkaline, rocks have a Nd model age of *c.* 0.8 Ga (Figs 11.5C and 11.5D), e.g., the Almendral granite and Aceuchal-Almendradejo orthogneiss, (Oschner, 1993; Casquet and Galindo 2004).

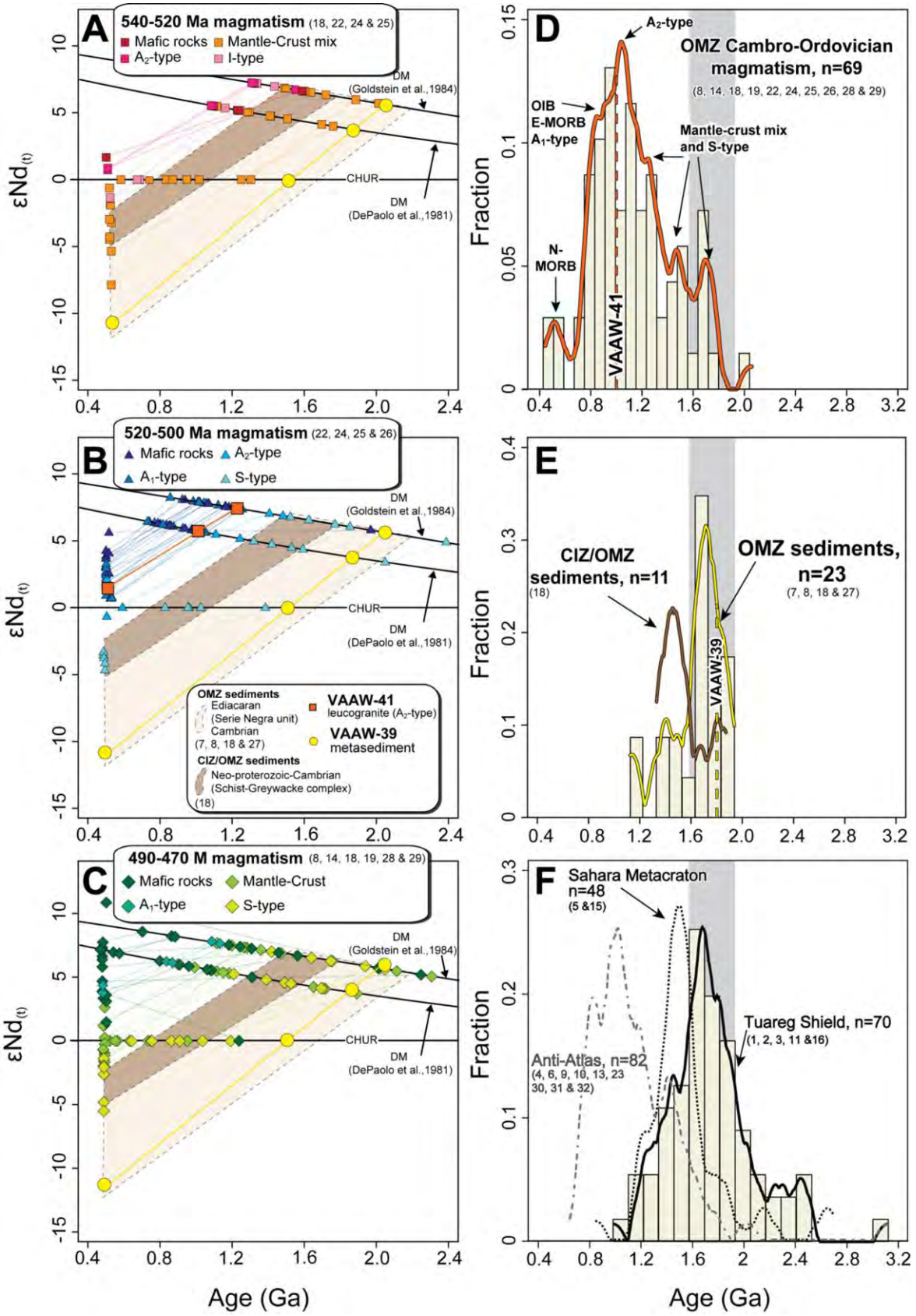
A
540-520 Ma magmatism (18, 22, 24 & 25)
Mafic rocks
Mantle-Crust mix
A2-type
I-type
DM (Goldstein et al.,1984)
CHUR
DM (DePaolo et al.,1981)
εNd(t)
B
520-500 Ma magmatism (22, 24, 25 & 26)
Mafic rocks
A2-type
A1-type
S-type
OMZ sediments
Ediacaran (Serie Negra unit)
Cambrian (7, 8, 18 & 27)
VAAW-41 leucogranite (A2-type)
VAAW-39 metasediment
CIZ/OMZ sediments
Neo-proterozoic-Cambrian (Schist-Greywacke complex) (18)
C
490-470 M magmatism (8, 14, 18, 19, 28 & 29)
Mafic rocks
Mantle-Crust
A1-type
S-type
Age (Ga)
D
A2-type
OMZ Cambro-Ordovician magmatism, n=69
(8, 14, 18, 19, 22, 24, 25, 26, 28 & 29)
OIB
E-MORB
A1-type
Mantle-crust mix and S-type
N-MORB
VAAW-41
Fraction
E
CIZ/OMZ sediments, n=11
(18)
OMZ sediments, n=23
(7, 8, 18 & 27)
VAAW-39
F
Sahara Metacraton n=48
(5 &15)
Tuareg Shield, n=70
(1, 2, 3, 11 &16)
Anti-Atlas, n=82
(4, 6, 9, 10, 13, 23 30, 31 & 32)
Age (Ga)

However, a second group of OMZ A-type rocks, including our leucogranite sample VAAW-41, has an older *c.* 1.0 Ga Nd model age (Fig. 11.5D). This age, it seems, is mixed, because the composition of the rocks is transitional from A_1-type, 'OIB-like', mantle-derived according to Eby (1992), tending to A_2-type. Such compositions, we proposed above, formed by crustal contamination of A_1-type, with an increase in the crustal component, such as in the Castillo granite, giving rise to A_2-type compositions with Nd model ages of up to *c.* 1.2 Ga (e.g., Oschner, 1993; Salman, 2002). This mixing model is supported by field relations that show mingling between the leucogranite and the host Serie Negra metasediment VAAW-39 which has a *c.* 1.8 Nd model age (See Chapter 4, Fig. 4.13).

Contemporaneous crust-derived and strongly crustally contaminated OMZ magmatism such as the Monesterio anatectic dome (Salman, 2004) and Urra volcanosedimentary formation (Solá et al., 2008) has older Nd model ages still, of 2.0-1.3 Ga, with clusters at *c.* 1.7 Ga, *c.* 1.5 Ga and *c.* 1.3 Ga (Fig. 11.5D). Notably, as discussed in detail below, these ages show a similar Nd model age distribution to the OMZ Ediacaran to Ordovician sedimentary rocks (Fig. 11.5D and 11.5E).

Figure 11.5. A-C) Nd isotope compositions of samples studied in the present work and 540-520 Ma, 520-500 Ma and 490-470 Ma Ossa-Morena Zone (OMZ) magmatic rocks. In addition we include Nd isotopic data for OMZ basement metasedimentary rocks from the Serie Negra and Cambrian units as well as OMZ Central Iberian Zone (CIZ) boundary metasediments from the Schist-Greywacke Complex and Cambrian units. For all, the Nd model ages were calculated based on the method of DePaolo, (1981) (T_{DM}) and Goldstein et al., (1984) (T_{CR}). This summary of Nd model (T_{DM}) age distributions includes: D) Histogram of Cambro-Ordovician OMZ magmatic rocks, including our sample VAAW-41, note the variation in age according to mantle or crustal character; E) Histogram of the OMZ metasedimentary rocks, including our sample VAAW-39, note the main peak at c. 1.7 Ga similar to crust-derived or contaminated magmatic rocks in D, the OMZ/CIZ boundary metasediments are shown for comparison; and F) Histogram of the Tuareg Shield Pan-African granitoids, a potential source of OMZ sediments (solid line and thick grey vertical band in D-F) and the other north African regions: the Anti-Atlas, West African Craton (dashed line); and the Saharan Metacraton (dotted line). Notably the Tuareg Shield also has a main peak at c. 1.7 Ga as detected in the OMZ basement in E. Numbers in brackets correspond to the data sources in Appendix I.

11.1.2.1.2 OMZ Sedimentary Rocks

The OMZ Edicaran to Ordovician sedimentary rocks have a Nd model age range of 1.9-1.1 Ga (Fig. 11.5E) (Schäfer et al, 1993; Mullane, 1998 cited in Gutiérrez-Alonso et al., 2003; López-Guijarro et al., 2008). However, this range does not, we suggest, represent the 'real' Nd model age range of the source. As noted above, some of the OMZ Cambro-Ordovician igneous rocks have a Nd model age that corresponds to a mixture between old material derived from the OMZ basement and mantle-derived magmatism, giving a main Nd model age cluster at *c.* 1.1 Ga (Fig. 11.5D). Therefore, the true Nd model age of OMZ sediment end-member should be older than *c.* 1.1 Ga. Accordingly, López-Guijarro et al., (2008) suggested that the 1.6-1.1 Ga Nd model age range from the base to the top of the OMZ Ediacaran-early Cambrian Malcocinado Formation and Cambrian sediments reflected an input of juvenile crust or mantle material. They associated the basal Malcocinado Formation with arc-related magmatism and the upper Cambrian sediments with a rifting context.

In agreement with the above, the Serie Negra Montemolín and Tentudía formations Ediacaran sediments, have a consistently older Nd model age range of 1.9-1.7 Ga, with a mode of *c.* 1.7 Ga (Schäfer et al, 1993; Casquet et al., 2001; Chichorro et al., 2008; López-Guijarro et al., 2008). Passive margin and back-arc basin contexts, both of which are consistent with an input of continental crust, have been suggested (Eguiluz, 1988; Quesada, 1990a) for the formation of these sediments with an old crustal signature (López-Guijarro et al., 2008). Similarly, younger Ordovician-Early Devonian OMZ sediments have a Nd model age range of 1.8-1.6 Ga, related to continental crust input in a passive margin context (López-Guijarro et al., 2006; 2008).

From the above, the best estimate Nd model age for the OMZ sediment source may be the Serie Negra or the Ordovician sediments which have a range of 1.9-1.6 Ga, and a mode at *c.* 1.7 Ga (Fig. 11.5E). Significantly, both the Cambro-Ordovican (Fig. 11.5D) and early Carboniferous Variscan OMZ crust-derived magmatism have a similar Nd model age range 1.9-1.5 Ga with mode of *c.* 1.7 Ga (see next section 11.3) (Bachiller, 1996; Pin et al., 2008; Moita et al., 2009).

11.1.2.1.3 Other Iberian Massif Zones Rocks

Neoproterozoic to Ordovician CIZ and CZ sediments have Nd model ages in the range 2.0-1.3 Ga with a cluster at 1.5 Ga (Gutiérrez-Alonso et al., 2003; Bea et al., 2010; Villaseca et al., 2014), similar to comparable age rocks in the OMZ, 1.9-1.1 Ga. Furthermore, the Cambro-Ordovician crust-derived, CIZ Ollo de Sapo, orthogneisses also have a Nd model age mode of *c.* 1.5 Ga (Bea et al., 2007, 2010; Montero et al., 2007; Talavera et al., 2013) (Fig. 11.5E). Even the southern CIZ Neoproterozic Greywacke Schist Complex and Cambro-Ordovician sediments just

to the north of the boundary with the OMZ have a Nd model age mode of *c.* 1.5 Ga in the range 1.9-1.3 Ga (Fig. 11.5E) (López-Guijarro et al., 2008).

11.1.2.1.4 Potential Sediment Sources: the North Gondwana, African, Basement Granitoids

Bea et al. (2010) summarized the Nd model ages of the Pan-African granitoids from the three main north African Gondwana regions: the Anti-Atlas West African Craton; the Tuareg Shield; and the Saharan Metacraton. These authors considered the Pan-African granitoids as a potential source for the CIZ Ediacaran to Cambrian sedimentary rocks. Similarly, we use the Nd model age data summarized in the present work to identify potential north Gondwana African sources of the OMZ Ediacaran to Ordovician sediments (see Appendix I).

It is worth mentioning that like Bea et al., (2010), we eliminate the Arabian Nubian Shield as a possible OMZ sediment source from the outset because the Nd model age of this region is too young, *c.* 0.74 Ga (Stern, 2002; Moreno et al., 2014). This decision is confirmed by the detrital zircon population ages, see below (Kolodner et al., 2006). In addition, we also rule out the regions of the West African Craton, Tuareg Shield and Saharan Metacraton that have older, *c.* 2.5 Ga, crust signatures greater than the OMZ maximum Nd model ages (Peucat et al., 1996; 2005; 2003; Barth et al., 2002; Bea et al., 2014).

i. The Saharan Metacraton Pan-African granitoids have Nd model ages in the range of 2.3-1.1 Ga, with a minor old cluster at c. 2.7 Ga (Fig. 11.5F). Their Nd model age mode is c. 1.5 Ga (Harms et al., 1990; Bea et al., 2010; 2011) (Fig. 11.5F).
ii. The Anti-Atlas West African Craton Pan-African granitoids, have an asymmetric Nd model age distribution with a continuous range from 1.8-0.8 Ga and small populations at c. 2.2, c. 2.7 and c. 3.0 Ga (Fig. 11.5F). The main population clusters at c. 1.0 Ga (e.g., Blanc et al., 1992; Gasquet et al., 2005; Tahiri et al., 2010) (Fig. 11.5F).
iii. The Tuareg Shield Pan-African granitoids have a continuous Nd model age distribution from 2.5-1.0 Ga, with a minor cluster at c. 3.1 Ga (Fig. 11.5F). Their Nd model age mode is c. 1.7 Ga (e.g., Liegios et al., 1994; Ferré et al., 1996; Abdallah et al., 2007) (Fig. 11.5F).

11.1.2.1.5 Comparison of the North Gondwana, African, Potential Sources with the OMZ and Other Iberian Massif Zones

Above we outlined the new paleogeographic positions for the main Iberian zones, these positions were determined using Nd model ages. The distribution of the Pan-African granitoids from the Sahara Metacraton, match that of the CIZ Cambro-Ordovician crust-derived Ollo de Sapo orthogneisses (Bea et al., 2010; Talavera et al., 2013). The distribution also matches the

northwest Iberia Ediacaran to Ordovician sedimentary rocks (e.g., Fernández-Suárez et al.,2014; Gutiérrez-Alonso et al., 2003; Bea et al., 2010). A link between the CIZ and the Saharan Metacraton was proposed based on the main cluster at *c.* 1.5 Ga in both areas as well as the comparable overall Nd model age distribution of the two regions, 2.3-1.0 Ga (Bea et al., 2010; Talavera et al., 2013).

The CIZ sedimentary Nd model age main cluster is younger, *c.* 1.5 Ga, than the OMZ Ediacaran to Ordovician sedimentary rocks Nd model age distribution, which is centred at *c.* 1.7 Ga (Fig. 11.5E). So, the Saharan Metacraton Pan-African granitoids Nd model ages were also younger than the OMZ Ediacaran to Ordovician sediments (Fig. 11.5E). Furthermore, the paleogeographic link established between this region and the CIZ leads us to exclude this north African terrane as the source of the OMZ sedimentary rocks (Fig. 11.5E and 11.5F).

In comparison with the Anti-Atlas West African Craton, Pan-African granitoids the OMZ Ediacaran to Ordovician sediments have generally older Nd model ages (Fig. 11.5E and 11.5F). The former have more abundant relatively young ages centred at *c.* 1.0 Ga (Fig. 11.5F). Moreover, 1.9-1.6 Ga Nd model ages are scarce to non-existent in the Anti-Atlas West African Craton granitoids (Fig. 11.5F). The OMZ Edicaran and Ordovician sediments generally seem to reflect an input from an older crust, rather than the Anti-Atlas West African Craton more juvenile granitoid crustal signature (Fig. 11.5E and 11.5F).

However, the OMZ Cambrian sediments do include some younger Nd model ages of 1.6-1.1 Ga (López-Guijarro et al., 2008). These ages may be explained by one of two scenarios, or a combination of both:

i. A contribution from a mixed mantle-crustal source consistent with the OMZ Cambrian rifting context and as evidenced by the Nd model ages of crustally contaminated mantle-derived mafic rocks and A-type granites e.g., our leucogranite sample VAAW-41 and its mingled relationship with the Ediacaran basement, sample VAAW-39.
ii. An input of juvenile crust in the late-Ediacaran to early Cambrian sediments, for example the Malcocinado formation, from Cadomian arc-related sediments.
iii. Although the Anti-Atlas West African Craton Pan-African granitoids are apparently not the source of the old-crust signature of the OMZ Ediacaran and Ordovician sediments, we consider that an input from these granitoids may explain the juvenile-crust component character of the OMZ Cambrian sediments.

The Pan-African granitoids from the Tuareg Shield show a wide range of Nd model ages, 2.5-1.0 Ga, centred at *c.* 1.7 Ga (Fig. 11.5F). These granitoids match the main OMZ sediment Nd

model age distribution. In addition, like the OMZ sediments, the Tuareg Shield Pan-African granitoids also have a population of younger Nd model ages. Considered together these characteristics make the Tuareg Shield granitoids the best fit as a source for the OMZ late Ediacaran to early Cambrian sediments (Fig. 11.5E and 11.5F).

Although the OMZ Ediacaran to Ordovician sediments show a great source affinity with the Tuareg Shield, a contribution of more juvenile-crust from the Anti-Atlas West African Craton cannot be ruled out. This, thus, implies that the OMZ was close to the Tuareg Shield but could also have received a sediment contribution from the Anti-Atlas West African Craton placing it to the north-northwest of the former and northeast of the latter (present day coordinates).

Below we discuss the extent to which this conclusion, based on Nd model ages, is supported, by the radiometric ages of the OMZ sedimentary and igneous Neoproterozoic to Ordovician rocks.

11.1.2.2 Radiometric Ages

To clarify further the position of the OMZ during the Cambro-Ordovician, we undertook a study of OMZ detrital and magmatic zircons and compared them with data from the autochthonous (CIZ, CZ) and parautochthonous (GTOMZ) Iberian Massif zones and the north African terranes. To do this we compiled U-Pb single zircon and other radiometric ages for the OMZ, the CIZ, CZ, GTOMZ and the north African Neoproterozoic-Ordovician sediments and Cambro-Ordovician magmatism (see Appendix I). This dataset includes our new age determinations for the VAAW-39 metasediment, maximum sedimentation age 566±10 Ma, and VAAW-41 leucogranite, 509±3 Ma.

11.1.2.2.1 Sedimentary Rocks

11.1.2.2.1.1 The Ossa-Morena Zone

The U-Pb ion microprobe and LA-ICP-MS age determinations on detrital zircons from the OMZ Neoproterozoic to Ordovician sediments reveal an abundance of Neoproterozoic ages (Fig. 11.6). Some 58 % of the data are Ediacaran and Cryogenian, 850-540 Ma. They show a Pan-African peak, so typical of north Gondwana, that includes our newly dated metasediment VAAW-39, at *c.* 600 Ma (Fig. 11.6A). Notably, older Neoproterozoic Tonian ages, 1.0-0.85 Ga, only represent 2 % of data (Fig. 11.6A). However, Paleoproterozic and Archean ages are also abundant, 29 % of the data, with main clusters at *c.* 2.9, *c.* 2.4 and *c.* 1.6 Ga (Fig. 11.6A). Remarkably, the sediments contain very few zircons with Mesoproterozoic ages, <1 %, have ages close to 1.5 Ga (Fig. 11.6A).

11.1.2.2.1.2 The Other Iberian Massif Zones

The OMZ sediment detrital zircons have a broadly comparable age distribution to the other Iberian Massif zones (Fig. 11.6).

In the CIZ Neoproterozoic to Ordovician sediments, Ediacaran and Cryogenian Neoproterozoic ages also abound, 60 % of the data, with a peak at *c.* 615 Ma (e.g., Talavera et al., 2012; Fernández-Suárez et al., 2014; Shaw et al., 2014). Tonian, 7 %, and Mesoproterozoic, 8 %, ages are also common yielding a peak at *c.* 1.0 Ga (Fig. 11.6B). In addition, CIZ sediments contain zircons with Paleoproterozic and Archean ages, 18 % of data, but the main peaks are tighter than in the OMZ, 2.9-2.5 Ga and 2.3-1.9 Ga (Fig. 11.6B).

In the CZ Neoproterozoic to Ordovician sediments, Ediacaran and Cryogenian Neoprotezoic ages are again abundant, 60% of the data, with a peak at *c.* 620 Ma (Fig. 11.6D) (e.g., Fernández-Suárez et al., 2002a; Pastor-Galán et al., 2013; Shaw et al., 2014). As in the CIZ, the CZ contains both Tonian, 1.0-0.85 Ga and Mesoproterozic zircon populations, 17 % of the data, with a well-defined peak at *c.* 1.0 Ga (Fig. 11.6D). Moreover, the Paleoproterozoic and Archean zircons comprise 23 % of the data, with peaks at 2.7-2.4 Ga and *c.* 2.0 Ga, (Fig. 11.6D).

In the GTOMZ the ages of zircons from the parauchthonous units sedimentary rocks were considered. These rocks were deposited from the latest Neoproterozoic to the latest Cambrian (Díez-Fernández et al., 2010). Their zircon populations include Ediacaran and Cryogenian ages, 52 %, with a main cluster at *c.* 650 Ma (Fig. 11.6C). Tonian and Mesoproterozoic zircons are also present, 6 % of the data, but are less abundant than in the CIZ or the CZ (Fig. 11.6C). In addition, Paleoproterozoic zircons, 30 % of the data, are numerous with main populations at 2.3-2.1 Ga and *c.* 1.9 Ga (Fig. 11.6C). Lastly, Archean zircons comprise, 9 % of the data, with a range of 3.5-2.5 Ga and a peak at *c.* 2.7 Ga (Fig. 11.6C) (Díez-Fernández et al., 2010).

When considered in detail, both correlations and differences exist between the detrital zircon age distribution in the OMZ, CIZ, CZ and GTOMZ parauchthonous units sedimentary rocks. Firstly, the Neoproterozoic, Paleoproterozoic and Archean age distributions are comparable (Fig. 11.6). The Paleoproterozoic age distributions, however, show minor variations, 1.9-1.5 Ga ages are more common in the OMZ and in GTOMZ than in the CIZ or CZ (Fig. 11.6). Secondly, a Mesoproterozoic signature, *c.* 1.0 Ga (Fig. 11.6), is well represented in the CIZ and the CZ and is also found in the Ordovician and Devonian sedimentary rocks from the WALZ (Martínez Catalán et al. 2004; 2008). Nevertheless, such Mesoproterozoic ages are scarce in the GTOMZ parautochthonous units and absent in the OMZ (e.g., Linnemann et al.,

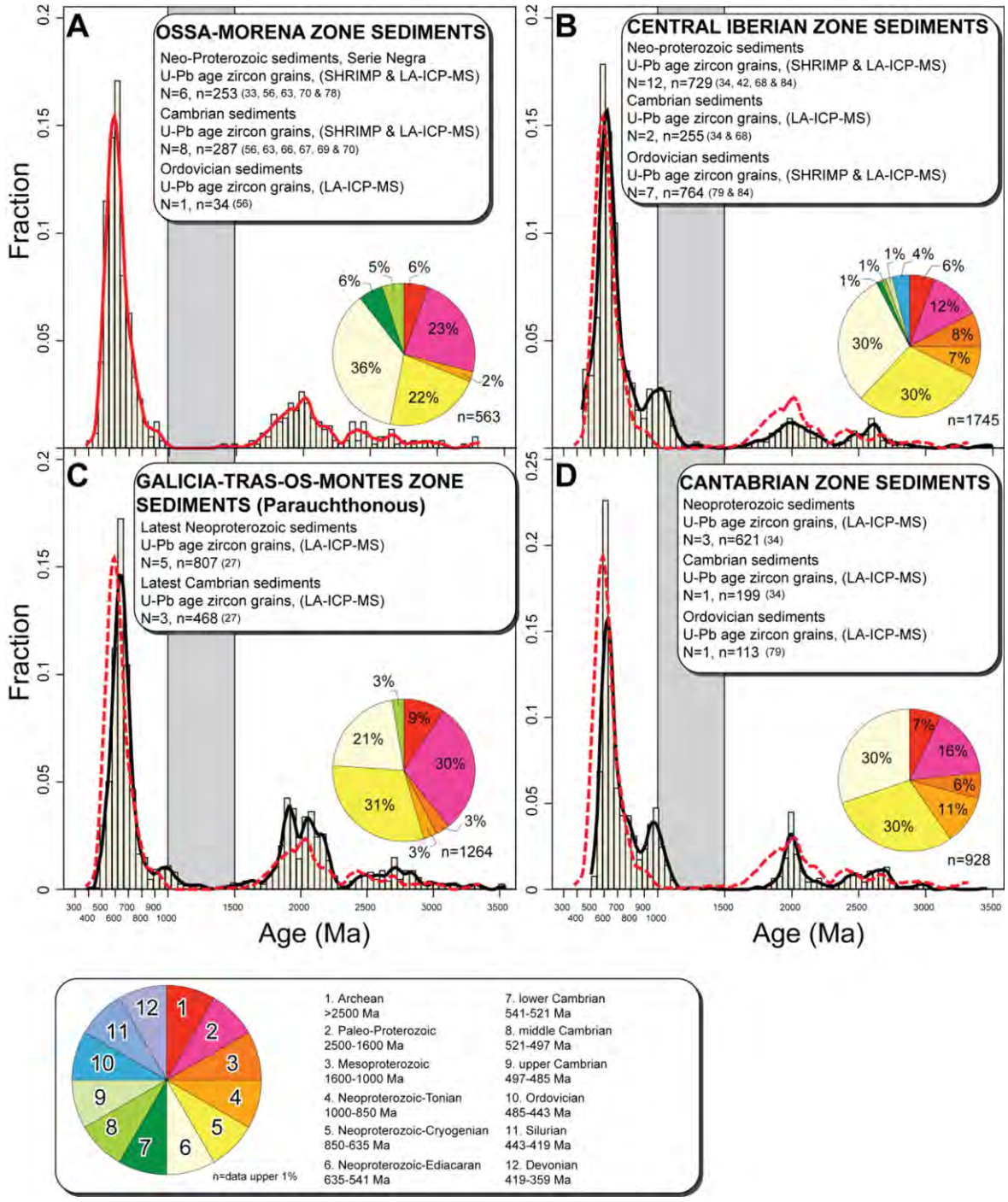

Figure 11.6. Frequency and density distribution of U–Pb SHRIMP and LA-ICP-MS age data for detrital zircons from: A) Ossa-Morena Zone (OMZ) Neoproterozoic and Cambro-Ordovician rocks from the present work and published data. B) Central Iberian Zone (CIZ) Neoproterozoic and Cambro-Ordovician rocks. C) Galicia Tras-os-Montes Zone (GTOMZ) parauchthonous units latest Ediacaran to latest Cambrian sedimentary rocks. E) Cantabrian Zone (CZ) Neoproterozoic and Cambro-Ordovician rocks. To facilitate comparison, all plots include the kernel density distribution of the OMZ ages (thick red/grey line), the Mezoproterozic age range (thick grey vertical band) and pie diagram. Note that Mesoproterozoic zircons are abundant in the CIZ and CZ, less abundant in the GTOMZ and absent in the OMZ. Numbers in brackets correspond to the data sources in Appendix XX.

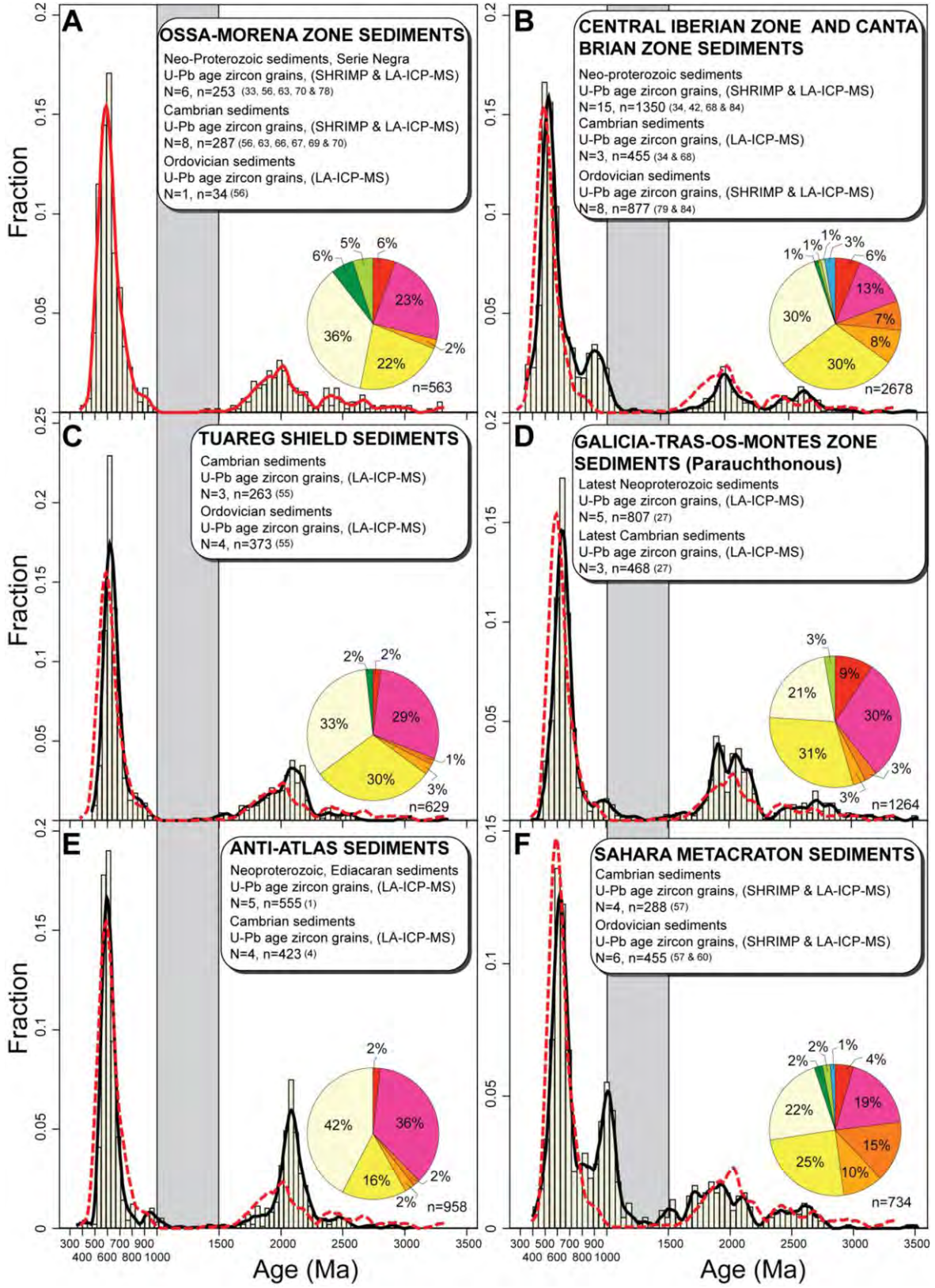
A
OSSA-MORENA ZONE SEDIMENTS
Neo-Proterozoic sediments, Serie Negra
U-Pb age zircon grains, (SHRIMP & LA-ICP-MS)
N=6, n=253 (33, 56, 63, 70 & 78)
Cambrian sediments
U-Pb age zircon grains, (SHRIMP & LA-ICP-MS)
N=8, n=287 (56, 63, 66, 67, 69 & 70)
Ordovician sediments
U-Pb age zircon grains, (LA-ICP-MS)
N=1, n=34 (56)
5%
6%
6%
23%
36%
2%
22%
n=563
B
CENTRAL IBERIAN ZONE AND CANTA BRIAN ZONE SEDIMENTS
Neo-proterozoic sediments
U-Pb age zircon grains, (SHRIMP & LA-ICP-MS)
N=15, n=1350 (34, 42, 68 & 84)
Cambrian sediments
U-Pb age zircon grains, (LA-ICP-MS)
N=3, n=455 (34 & 68)
Ordovician sediments
U-Pb age zircon grains, (SHRIMP & LA-ICP-MS)
N=8, n=877 (79 & 84)
1%
1%
1%
3%
6%
13%
30%
7%
8%
30%
n=2678
C
TUAREG SHIELD SEDIMENTS
Cambrian sediments
U-Pb age zircon grains, (LA-ICP-MS)
N=3, n=263 (55)
Ordovician sediments
U-Pb age zircon grains, (LA-ICP-MS)
N=4, n=373 (55)
2%
2%
29%
33%
1%
30%
3%
n=629
D
GALICIA-TRAS-OS-MONTES ZONE SEDIMENTS (Parauchthonous)
Latest Neoproterozoic sediments
U-Pb age zircon grains, (LA-ICP-MS)
N=5, n=807 (27)
Latest Cambrian sediments
U-Pb age zircon grains, (LA-ICP-MS)
N=3, n=468 (27)
3%
9%
21%
30%
31%
3%
3%
n=1264
E
ANTI-ATLAS SEDIMENTS
Neoproterozoic, Ediacaran sediments
U-Pb age zircon grains, (LA-ICP-MS)
N=5, n=555 (1)
Cambrian sediments
U-Pb age zircon grains, (LA-ICP-MS)
N=4, n=423 (4)
2%
42%
36%
16%
2%
2%
n=958
F
SAHARA METACRATON SEDIMENTS
Cambrian sediments
U-Pb age zircon grains, (SHRIMP & LA-ICP-MS)
N=4, n=288 (57)
Ordovician sediments
U-Pb age zircon grains, (SHRIMP & LA-ICP-MS)
N=6, n=455 (57 & 60)
2%
2%
1%
4%
22%
19%
15%
25%
10%
n=734
Fraction
Age (Ma)
300 500 700 900
400 600 800 1000
1500
2000
2500
3000
3500

2008; Díez-Fernández et al., 2010; Pereira et al. 2011). Thirdly, some differences can be established in the Tonian zircons distributions, they are more abundant in the CIZ and the CZ than in the GTOMZ and the OMZ (Fig. 11.6).

Significantly, age distributions observed in the Iberian zones, in conjunction with the absence of a main Mesoproterozoic population, 1.5-1.3 Ga, have been defined as the characteristic sedimentary zircon age distribution for north Gondwana (e.g., Nance and Murphy, 1994; Linnemann et al., 2004; Nance et al., 2008) rather than Amazonia or Baltica (e.g., Teixeira et al., 1989; Bingen et al., 2003; Bogdanova et al., 2008). However, there are some differences in the Iberian zones zircon age distributions compared with those typical of north Gondwana, these are discussed in the next section.

11.1.2.2.1.3 The North Gondwana, African, Terranes

The Cambrian Saharan Metacraton, and Arabian Nubian Shield sediments, like the Neoproterozoic to Ordovician Central Iberian Zone and Cantabrian Zone sediments (Kolodner et al., 2006), have abundant Neoproterozoic zircons (Meinhold et al., 2011; Morton et al., compiled in Meinhold et al., 2013). Ediacaran and Cryogenian, comprise 47% of the data, with a main peak at *c.* 615 Ma (Fig. 11.7F). They also have abundant Archean ages, some 23% of the data, with small peaks at 2.8-2.5 Ga and 2.2-1.7 Ga (Fig. 11.7F). The Saharan Metacraton sediments also have a significant population of Mesoproterozoic and early Neoproterozoic, Tonian, ages, with a main peak at *c.* 1.0 Ga (Fig. 11.7F).

The sediment detrital zircons age pattern of the Anti-Atlas West African Craton, reveals even more abundant Neoprotezoic Ediacaran and Cryogenian ages, 71% of the data, with the typical pan-African north Gondwana peak at *c.* 600 Ma (Fig. 11.7E) (Abati et al., 2010; Avigad et

Figure 11.7. Frequency and density distribution of U–Pb SHRIMP and LA-ICP-MS age data for detrital zircons from: A) Ossa-Morena Zone (OMZ) Neoproterozoic and Cambro-Ordovician rocks from the present work and published data. B) Central Iberian Zone (CIZ) and Cantabrian Zone (CZ) Neoproterozoic and Cambro-Ordovician rocks. C) Tuareg Shield Cambro-Ordovician rocks. D) Galicia Tras-os-Montes Zone (GTOMZ) parauchthonous units late Ediacaran to late Cambrian sedimentary rocks. E) Anti-Atlas, West African Craton, Neoproterozoic to Cambrian sedimentary rocks. F) Saharan Metacraton Cambro-Ordovician sedimentary rocks. To facilitate comparison, all plots include the kernel density distribution of the OMZ ages (thick red/grey line). Mezoproterozic age range (thick grey vertical band) and pie diagram as in Figure 11.6. Note the coincidence of the OMZ and Tuareg Shield patterns, in both Mezoproterozic ages are absent. Numbers in brackets correspond to the data sources in Appendix I

al., 2012). Paleoproterozic ages are abundant, 36 % of the data, with a main peak centred at *c.* 2.2 Ga and a minor peak *c.* 2.5 Ga (Fig. 11.7E) (Abati et al., 2010). The Anti-Atlas West African Craton Archean zircon population is scarce, only 2 % (Fig. 11.7E). The Ediacaran sedimentary rocks in this region are few older Neoproterozoic Tonian ages and Mesoproterozoic ages are absent (Abati et al., 2010). However, in the Anti-Atlas West African Craton Cambrian sedimentary rocks Tonian ages are more abundant, centred *c.* 950 Ma, and some Mesoproterozoic ages *c.* 1.0 Ga, have also been described (Fig. 11.8C) (Avigad et al., 2012).

The Cambro-Orodovican Tuareg Shield sediments present a bimodal detrital zircon age distribution with Neoproterozoic Cryogenian and Ediacaran ages comprising 63 % of the data with a peak at *c.* 615 Ma (Fig. 11.7C) and abundant Paleoproterozic and Archean ages, 31 % of the data, with a main peak at 2.2-1.5 Ga (Fig. 11.7C). The Cambro-Orodovican Tuareg Shield sediments also have a Mesoproterozic gap, only 1 % of data have an age of *c.* 1.5 Ga, and there is no detectable *c.* 1.0 Ga peak (Fig. 11.7C).

11.1.2.2.1.4 Comparison of the OMZ and Other Iberian Massif Zones with Detrital Zircon Radiometric Ages of the North Gondwana, African, Potential Sources

Comparison of detrital zircon populations in Neoproterozoic to Ordovician sedimentary rocks from the CIZ, CZ, GTOMZ parautochthonous units and WALZ (not shown) Ordovician to Devonian sedimentary rocks, with the north African terranes (Fig. 11.7) revealed a northeast Gondwana (current coordinates) source for the zircon populations. The CIZ, CZ and WALZ have been linked to the Saharan Metacraton (Bea et al., 2010; Talavera et al., 2013) and the Arabian Nubian Shield (Fernández-Suárez et al., 2014; Shaw et al., 2014).

Díez-Fernández et al., (2010) defined an intermediate position between the Saharan Metacraton and West African Craton for the GTOMZ parautochthonous units. These authors established the GTOMZ paleogeographic position based on the abundance of Cryogenian, Tonian and Mesoproterozoic ages, 1.2-0.75 Ga, which are less abundant in the West African Craton but well-represented in the Saharan Metacraton (Fig. 11.7E and 11.7F).

The presence of Mesoproterozoic zircons, *c.* 1.0 Ga, and the abundance of Cryogenian and Tonian ages in the CIZ, CZ and GTOMZ parautochthonous units are the main differences with respect to the OMZ (Fig. 11.7D and 11.7E). Thus the Saharan Metacraton is ruled out as the possible paleogeographic source for the OMZ (Fig. 11.7E).

The two other potential zircon population sources for the OMZ in a north Gondwana context are the Anti-Atlas West African Craton and the Tuareg Shield (Fig. 11.7A to 11.7C). The

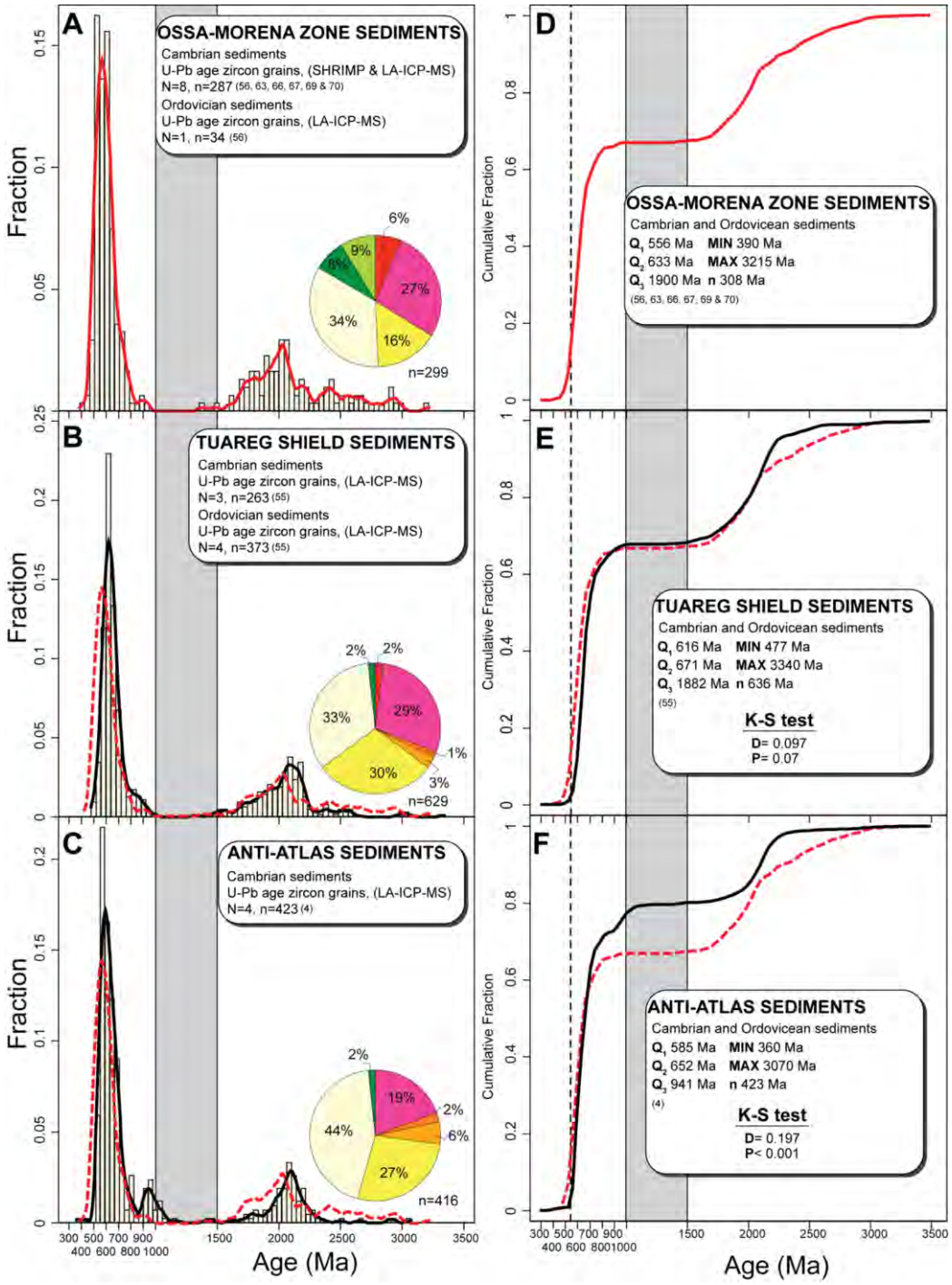

Figure 11.8. Frequency and density distribution of U–Pb SHRIMP and LA-ICP-MS age data for detrital zircons from: A) Ossa-Morena Zone (OMZ) Cambro-Ordovician rocks. B) Tuareg Shield Cambro-Ordovician rocks. C) Anti-Atlas, West African Craton, Cambrian sedimentary rocks. Cumulative fraction diagrams from the same rocks of: D) OMZ, E) Tuareg Shield and F) Anti-Atlas, West African Craton. To facilitate comparison, all plots include the kernel density distribution of the OMZ ages in Figs B to C and cumulative fraction in Figs E and F (thick red/grey line), the Mesoproterozic age range (thick grey vertical band) and pie diagram as in Figure 11.6. We add statistical parametres for zircon population and the Kolmogorov-Smirnov test (K-S) result of comparised the OMZ with the Tuareg Shield and Anti-Atlas sediments in Figs D, E and F. Note the coincidence of the OMZ and Tuareg Shield patterns. Numbers in brackets correspond to the data sources in Appendix I.

detrital zircon age distributions of the Anti-Atlas West African Craton and Tuareg Shield sediments are both similar to the OMZ sediment zircon population, for example the abundance of Neoproterozoic, Paleoproterozoic and Archean ages in the OMZ and those regions (Fig. 11.7). Also, the absence of Mesoproterozoic ages, *c.* 1.0 Ga, in the three areas is particularly significant (Fig. 11.7A to 11.7C). However, there are some differences between the Anti-Atlas West African Craton and the OMZ: late Cryogenian and Tonian ages are more abundant in the latter, in particular for comparable Ediacaran age sedimentary rocks (cf., Linnemann et al., 2008; Abati et al., 2010); The Paleoproterozic zircon distribution in the Anti-Atlas West African Craton is notably centred at *c.* 2.2 Ga with few representative ages at 1.9-1.5 Ga whereas this age range is common in the OMZ and there is a comparable zircon population in the Tuareg Shield (Fig. 11.7A and 11.7C). Equally, Linnemann et al., (2011) noted that the 1.9-1.5 Ga zircon population is absent in the West African Craton but is typical in rocks from the western Hoggar of the Tuareg Shield (cf., Drost et al., 2011) (Fig. 11.7A and 11.7C).

To look in more detail at the similarities and differences in the detrital zircon ages we focussed in on the populations from the Cambro-Ordovician sedimentary rocks from the OMZ, Tuareg Shield and Anti-Atlas West African Craton (Fig. 11.8). The zircon age distribution in the OMZ Cambro-Ordovician sediments is quite similar to the whole detrital zircon population that also includes the Ediacaran rocks (Fig. 11.7A and 11.8A). This is not the case for the Anti-Atlas West African Craton Ediacaran and Cambro-Ordovician sedimentary rocks zircon populations (cf., Abati et al., 2010; Avigad et al., 2012). The OMZ detrital zircon age distribution matches better with the Tuareg Shield than the Anti-Atlas West African Craton (Fig. 11.8A, 11.8B and 11.8C). The differences are particularly appreciable in the Anti-Atlas West African Craton late Tonian to early Mesoproterozic ages, 1.2-0.95 Ga, which are scarce to absent in both the OMZ and the Tuareg Shield (Fig. 11.8B and 11.8C). Furthermore, the Paleoproterozic zircons are more abundant in the OMZ and the Tuareg Shield, *c.* 28 % of the data, than in the Anti-Atlas West African Craton, 19 % of the data. This difference in Paleoproterozic variation is evidenced by fewer ages in the range 1.9-1.5 Ga in the Anti-Atlas West African Craton (e.g., Avigad et al., 2012) than in the Tuareg Shield (Linnemann et al., 2011) or the OMZ (Fig. 11.8A, 11.8B and 11.8C). Another important difference is in the Archean zircons which make up 6 % of the OMZ data and is present although scarce in the Tuareg Shield, 2 %, but virtually absent, <<1 %, in the Anti-Atlas, West African Craton Cambro-Ordovician sediments (Fig. 11.8A, 11.8B and 11.8C).

Differences between the zircon populations in the three zones are quite clear in cumulative fraction plots (Fig. 11.8D to 11.8F). The OMZ Cambro-Ordovician sediments match the Tuareg Shield pattern almost perfectly, only showing differences in the Cambrian and Archean ages (Fig.

11.8E). Comparable age sediments from the Anti-Atlas West African Craton show very marked differences, the plots highlight the aforementioned late Tonian to early Mesoproterozoic zircon Anti-Atlas West African Craton population and also the abundance of 1.9-1.5 Ga zircon in the OMZ (Fig. 11.8F).

We used the two-sample Kolmogorov-Smirnov test (K-S) to make a quantitative comparison of the zircon populations (cf., Berry et al., 2001; Fernández-Suárez et al., 2014). This test evaluates the maximum probability difference (D) between two cumulative distribution functions. Two populations can be considered to be from the same source if the probability value (P) corresponds to a confidence level of 95% ($P \geq 0.05$) (Guynn and Gehrels, 2010). Shaw et al., (2014) performed a K-S test on the Ordovician CIZ, CZ and WALZ Amorican quartzite. The results showed a potential source area for these terranes as the Saharan Metacraton and Arabian Nubian Shield. In the present work we carried out this test to assess the similarities and differences between the OMZ, Anti-Atlas West African Craton and Tuareg Shield. We took into account the analytical error of each measurement (Guynn and Gehrels, 2010). Another factor that had to be considered was the relative abundance of Cambrian zircons in the OMZ compared with similar age rocks from either the Tuareg Shield or Anti-Atlas West African Craton, as observed in the histogram and density zircon distributions. This could skew the comparison of the populations, so the K-S test was only performed on Precambrian detrital zircons from the Cambro-Ordovician sediments (> 541 Ma) (Fig. 11.8D to 11.8F).

The K-S test revealed a great affinity between the OMZ and Tuareg Shield Cambro-Ordovician sediments (D 0.097, P 0.07), and so supports the connection between these two regions observed in the age histograms and density distributions (Fig. 11.8E). The Anti-Atlas West African Craton Cambrian sediments, by contrast, have a different cumulative distribution and the K-S test rejects the possibility that this population had the same source as the OMZ (D 0.197, $P<0.001$) (Fig. 11.8F).

So, of the three possible north Gondwana African terranes, the Tuareg Shield and the Anti-Atlas West African Craton have affinities with the OMZ zircon population whereas the Saharan Metacraton does not. The Tuareg Shield zircon distribution matches the OMZ more closely than the Anti-Atlas West African Craton. Therefore, we consider the Tuareg Shield as the main sediment source for the OMZ although we do not rule out a concomitant contribution from the Anti-Atlas West African Craton.

Consequently, the above scenario is consistent with the aforementioned Nd model age distribution in the Tuareg Shield, peak at *c.* 1.7 Ga, and the OMZ peak at *c.* 1.7 Ga, with a

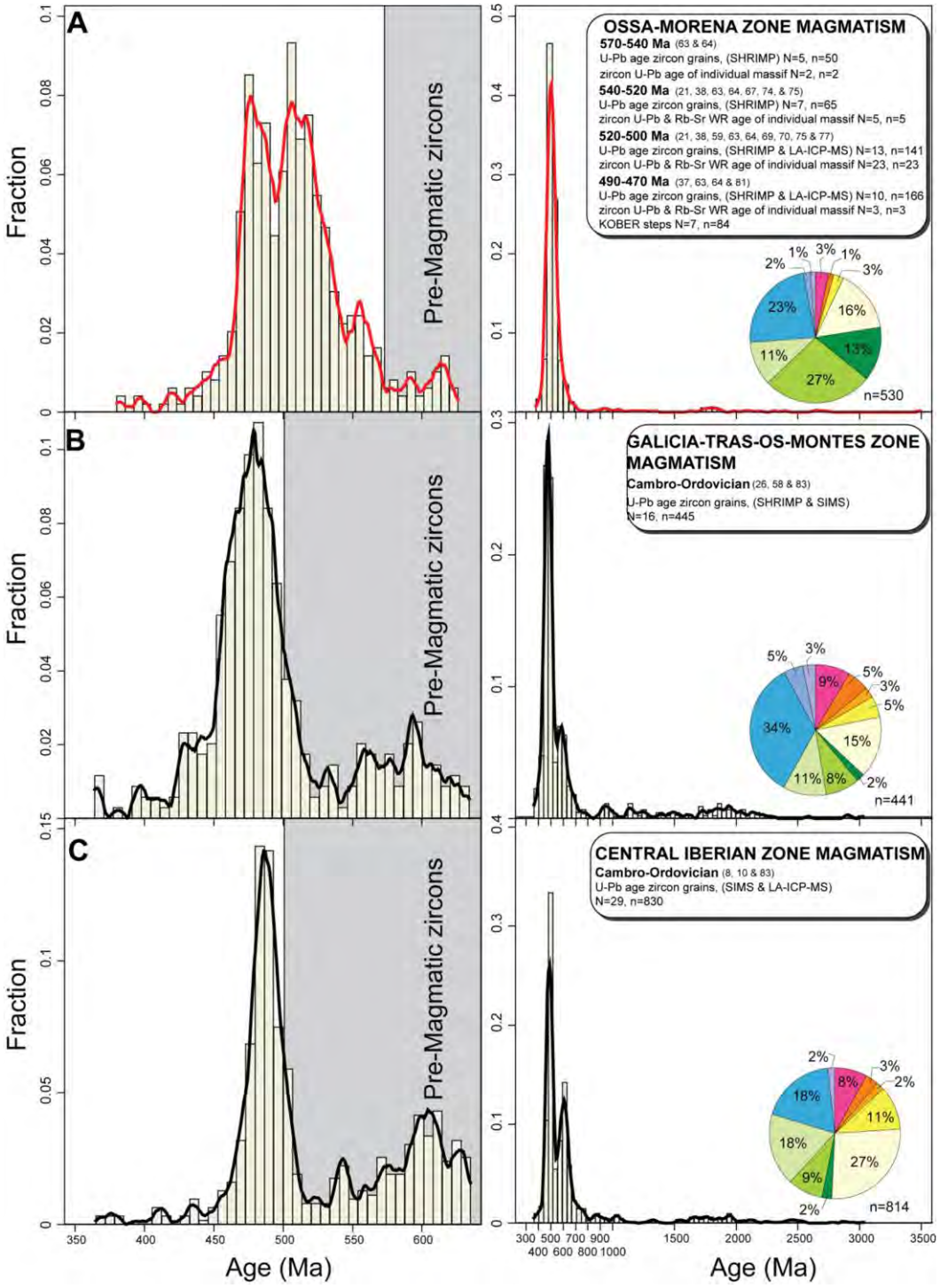

Figure 11.9. Frequency and density distribution of U–Pb ion microprobe, LA-ICP-MS and massif crystallisation ages of magmatic rocks from: A) Ossa-Morena Zone (OMZ) Cambro-Ordovician rocks, note the three main magmatic peaks at c. 540 Ma, c. 512 Ma and c. 480 Ma. Ages older than c. 570 Ma correspond to pre-magmatic zircons. B) Galicia Tras-os-Montes Zone (GTOMZ) parauchthonous units with Cambro-Ordovician magmatic event with an age range of 490-470 Ma centred at c. 480 Ma. Note the abundant pre-magmatic zircons at c. 615 Ma C) Central Iberian Zone (CIZ) Cambro-Ordovician magmatic rocks, note the main c. 480 Ma peak and the extraordinary abundance of pre-magmatic, here ages older than c. 490 Ma are pre-magmatic, centred at c. 615 Ma. Pie diagram age sections as in Figure 11.6. Numbers in brackets correspond to the data sources in Appendix I.

corollary contribution from the Anti-Atlas West African Craton, peak at *c.* 1.0 Ga.

11.1.2.2.2 Igneous Rocks Pre-magmatic and Magmatic Zircons

To complement the Nd model age and detrital zircon data, we also consider the magmatic and pre-magmatic zircon age data from the OMZ, CIZ, GTOMZ parautochthonous units and the three north African terranes.

11.1.2.2.2.1 The Ossa-Morena Zone

As described in section 11.1.1, OMZ Cadomian to Variscan magmatism occurred in three main stages: Neoproterozoic-Cambrian Cadomian (650-540 Ma), Cambro-Ordovician (540-450 Ma) and Devonian-Carboniferous Variscan (390-305 Ma). Rift-related magmatic events were recorded by the OMZ zircons with peaks at *c.* 550 Ma, *c.* 520 Ma and *c.* 480 Ma (Fig. 11.9A). The OMZ pre-magmatic ages include Neoproterozoic, mostly Ediacaran *c.* 615 Ma dates, as well as less common Paleoproterozoic and Archean ages, conspicuously once more Mesoproterozoic ages are absent (Fig. 11.9A).

11.1.2.2.2.2 The Other Iberian Massif Zones

In the CIZ, Ordovician magmatism is only preserved in peraluminous metavolcanic rocks and metagranites of the Ollo de Sapo Formation (Parga-Pondal et al., 1964; Díez-Montes et al., 2010; Montero et al., 2009a). The magmatism occurred from 496-474 Ma with the peak of activity, marked by new zircon formation, at *c.* 480 Ma (Fig. 11.9C) (Solá et al., 2005, Bea et al., 2007; Montero et al., 2007; Talavera et al., 2013). Pre-magmatic ages are extraordinarily abundant in these rocks. They include Neoproterozoic ages, again Ediacaran *c.* 615 Ma, that comprise 27 % of the data as well as Paleoproterozoic and Archean ages. Notably, the CIZ meta-igneous rocks also have Mesoproterozoic ages with a peak at *c.* 1.1 Ga (Fig. 13C).

In the GTOMZ parautochthonous units Cambro-Ordovician magmatism comprises varied calc-alkaline, peraluminous, alkaline and peralkaline metagranites and metavolcanic rocks (e.g., Arenas, 1984; Montero et al., 1998). The magmatism occurred from 500-470 Ma (Fig. 11.9B). There was a change in the composition of the magmatism over time:

i. Calc-alkaline 500-490 Ma (Rodríguez et al., 2007; Abati et al., 20102b).
ii. Peraluminous felsic 498-462 Ma (Talavera et al., 2013) coeval with alkaline to peralkaline felsic 475-470 (Montero et al., 2009b; Díez-Fernández et al., 2012). As in the CIZ the magmatic peak was at *c.* 480 Ma (Fig. 11.9B) (Montero et al., 2009b; Abati et al., 2010b; Díez-Fernández et al., 2012; Talavera et al., 2013).

Also, as in the CIZ, peraluminous metagranites and metavolcanic rocks have abundant pre-

magmatic zircons (Fig. 11.9C) (Talavera et al., 2013). These include: Neoproterozoic Ediacaran and Cryogenian ages, centred at *c.* 615 Ma, 15 % of data; and, Mesoproterozoic, Tonian, ages in the range 1.2-1.0 Ga. The GTOMZ rocks also have numerous Paleoproterozoic, 2.3-1.6 Ga, ages (Fig. 11.9C).

The pattern of CIZ and GTOMZ parauchthonous units magmatic ages is quite different from the OMZ. The first two only show a magmatic peak at *c.* 480 Ma whereas the OMZ, in addition to *c.* 480 Ma, also has older peaks *c.* 520 Ma and *c.* 550 Ma (Fig. 11.9). The difference in the age of the magmatic events led Montero et al., (2009a) to propose a different, albeit unspecified, paleogeographic position for the OMZ relative to the CIZ. This suggestion is also supported by the pre-magmatic age data, the CIZ and GTOMZ both have Mesoproterozoic ages that are absent in the OMZ.

11.1.2.2.2.3 The North Gondwana, African, Terranes

The Saharan Metacraton granitoids have Neoproterozoic pre-magmatic zircon age of *c.* 615 Ma also found in the OMZ, CIZ and GTOMZ parauchthonous units. Furthermore, they also contain abundant Archean, Paleoproterozoic, and most significantly Mesoproterozoic ages, *c.* 1.0 Ga, like the CIZ and GTOMZ igneous and meta-igneous rocks (Fig. 11.10D).

The Neoproterozoic magmatic events recorded in the Anti-Atlas West African Craton have an asymmetric distribution, with main Ediacaran peaks at *c.* 600 Ma and *c.* 560 Ma (Fig. 11.10C). The Anti-Atlas West African Craton, also records abundant Paleoproterozoic magmatism at *c.* 2.0 Ga that is not found in the OMZ (cf., Barbey et al., 2004; Peucat et al., 2005) (Fig. 11.10C).

With respect to the Tuareg Shield the first thing to mention is that, unfortunately, there are few published single zircon ages, the compiled geochronological data includes Rb-Sr WR and U-Pb population zircon ages (Fig. 11.10B). Bertrand et al. (1986) dated Ediacaran, *c.* 615 Ma, granitoids in the north of the region. Ediacaran magmatism was also described in Central Hoggar (Liégeois et al., 2003; Abdallah et al., 2007) and in the Eastern Nigeria province 650-570 Ma (e.g., Ferré et al., 1996; Ekwueme and Kröner, 1998). Other regional Neoproterozoic magmatism includes granitoids in the Nigerian Air region, 750-650 Ma (Liégeois et al., 1994) (Fig. 11.10B). Somewhat older Neoproterozoic Tonian 870-800 Ma, granitoids crop out in western-central Hoggar as do Paleoproterozoic Eburnean, *c.* 2.5 and *c.* 2.0 Ga granitoids (Fig. 11.10B) (e.g., Caby, 2003). In addition, Paleoproterozoic zircons, 1.9-1.8 Ga, were described in the western Hoggar HT metamorphic terranes (Peucat et al., 1996; 2003; Bruguier et al., 2008). Archean zircons are present as pre-magmatic ages in Pan-African granites from the Hoggar (Abdallah et al., 2007) and some outcrops of the West Nigeria terrane (*c.* 3.5 Ga Kröner et al., 2001).

The youngest igneous event in the Tuareg Shield was a major Cambrian alkaline magmatic event forming the alkaline-peralkaline Iforas province, *c.* 556 Ma, the Tisselliline pluton, *c.* 555 Ma and the Taourirt magmatic province at *c.* 525 Ma (Fig. 11.10B) (e.g., Azzouni-Sekkal et al., 2003; Caby, 2003). The Taourirt, and other magmatic provinces, are interpreted as a post-collisional alkaline magmatic event related to the mega-shear zones movements in a transtensional setting that provoked asthenosphere upwelling and melting (Azzouni-Sekkal et al., 2003). As might be expected interaction of mantle-derived magmatism and old-crustal basement, have been described in the Taourit province resulting in a mixed Nd model age range of 1.7-1.1 Ga.

11.1.2.2.2.4 Comparison of the OMZ and Other Iberian Massif Zones Pre-magmatic and Magmatic Zircon Radiometric Ages with the North Gondwana, African, Terranes

Bea et al., (2010) compared magmatic and pre-magmatic zircon age data from the CIZ orthogneisses and north African granitoids in their study of the early Paleozoic palaeographic position of the CIZ. Based on this and the aforementioned Nd model ages they concluded that, at that time, the CIZ was located further east than had previously been thought, next to the Saharan Metacraton. A similar scenario was proposed for the GTOMZ parauchthonous units peraluminous magmatism (Talavera et al., 2013).

The West African Craton is not the best fit with the timing of the OMZ events defined by the pre-magmatic and magmatic ages. Although 550-500 Ma ages are found in both the OMZ and the Anti-Atlas West African Craton, the distribution of the Cambrian west African ages does not match that of the OMZ. In the Anti-Atlas West African Craton the older ages are more abundant than in the OMZ or, for that matter, the CIZ or GTOMZ parautochthonous units (Fig. 11.10A and 11.10C). Furthermore, the Ordovician *c.* 480 Ma magmatic event identified in the OMZ, CIZ and GTOMZ parautochthonous units is hardly represented in the Anti-Atlas West African Craton magmatic rocks (Fig. 11.10C). In fact, the Anti-Atlas West African Craton and OMZ rift-related magmatism was, seemingly, diachronous (see below). It began in the latest Ediacaran in the former (Thomas et al., 2002; 2004; Walsh et al., 2012) but later, in the Cambrian 'early and main rift-related events' in the OMZ (Sánchez-García et al., 2008; 2010).

Revealingly perhaps, the youngest Tuareg Shield Taourit magmatic province alkaline event was contemporaneous with the OMZ 'early rift-related event' at 540-520 Ma (Sánchez-García et al., 2008; 2010). Consistent with this, is the coeval OMZ abundant alkaline magmatism with a clear crustal contribution and, we have suggested, mixed Nd model age range of 1.7-1.0 Ga (Fig. 11.5A). Alkaline magmatism comparable to that in the OMZ was also described in the Anti-Atlas

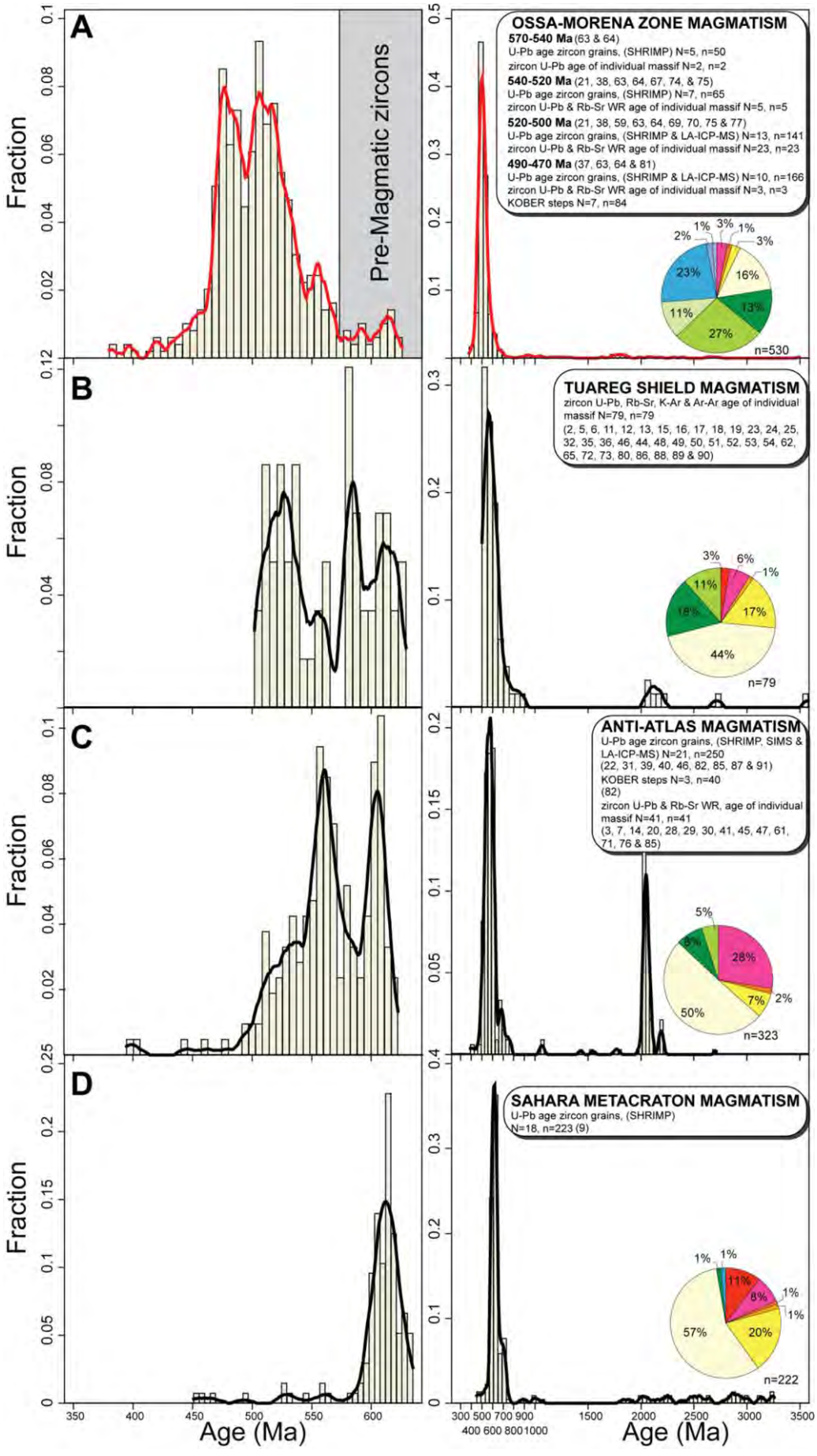
A
Pre-Magmatic zircons
OSSA-MORENA ZONE MAGMATISM
570-540 Ma (63 & 64)
U-Pb age zircon grains, (SHRIMP) N=5, n=50
zircon U-Pb age of individual massif N=2, n=2
540-520 Ma (21, 38, 63, 64, 67, 74, & 75)
U-Pb age zircon grains, (SHRIMP) N=7, n=65
zircon U-Pb & Rb-Sr WR age of individual massif N=5, n=5
520-500 Ma (21, 38, 59, 63, 64, 69, 70, 75 & 77)
U-Pb age zircon grains, (SHRIMP & LA-ICP-MS) N=13, n=141
zircon U-Pb & Rb-Sr WR age of individual massif N=23, n=23
490-470 Ma (37, 63, 64 & 81)
U-Pb age zircon grains, (SHRIMP & LA-ICP-MS) N=10, n=166
zircon U-Pb & Rb-Sr WR age of individual massif N=3, n=3
KOBER steps N=7, n=84
2%
1%
3%
1%
3%
23%
16%
13%
11%
27%
n=530
B
TUAREG SHIELD MAGMATISM
zircon U-Pb, Rb-Sr, K-Ar & Ar-Ar age of individual massif N=79, n=79
(2, 5, 6, 11, 12, 13, 15, 16, 17, 18, 19, 23, 24, 25, 32, 35, 36, 46, 44, 48, 49, 50, 51, 52, 53, 54, 62, 65, 72, 73, 80, 86, 88, 89 & 90)
3%
6%
1%
11%
18%
17%
44%
n=79
C
ANTI-ATLAS MAGMATISM
U-Pb age zircon grains, (SHRIMP, SIMS & LA-ICP-MS) N=21, n=250
(22, 31, 39, 40, 46, 82, 85, 87 & 91)
KOBER steps N=3, n=40
(82)
zircon U-Pb & Rb-Sr WR, age of individual massif N=41, n=41
(3, 7, 14, 20, 28, 29, 30, 41, 45, 47, 61, 71, 76 & 85)
5%
28%
7%
2%
50%
n=323
D
SAHARA METACRATON MAGMATISM
U-Pb age zircon grains, (SHRIMP)
N=18, n=223 (9)
1%
1%
11%
8%
1%
1%
57%
20%
n=222
Fraction
Age (Ma)
350
400
450
500
550
600
300 500 700 900
400 600 800 1000
1500
2000
2500
3000
3500

West African Craton, but it is older and therefore also apparently diachronous with the OMZ and Tuareg Shield alkaline event (cf., Álvaro et al., 2014 and references therein). The coeval alkaline provinces in the OMZ and the Tuareg Shield record a tectonomagmatic event that is recognizable in both regions implying that the terranes were proximal during the Cambro-Ordovician.

In short, all geochronological evidence, be it Nd model ages, dates of detrital zircons in sedimentary rocks or pre-magmatic and magmatic ages, is consistent with the OMZ having a clear input from, and being adjacent to, the Tuareg Shield during the early Paleozoic. The relationship between this 'more easterly than previously thought' paleogeographic position of the OMZ, during the Cambro-Ordovician and the connection with the recently suggested more easterly paleogeographic positions of the other Iberian Massif zones is discussed in the next section. In our new model we contemplated Cambro-Ordovician stratigraphic similarities and differences between the OMZ and the other Iberian Massif zones and the north African terranes. This, with the geochronological evidence permits us to propose a tectonomagmatic scenario for the amalgamation of Iberia culminating in the Variscan orogeny.

11.1.3 A New Paleogeographic Position for the OMZ During the Cambro-Ordovician

As mentioned previously, Stampfli et al., (2013) and Torsvik and Cocks (2013) identified an early Paleozoic rifting event in the northern part of Gondwana in the transition between the Cadomian and Variscan orogenies. Associated magmatism has been suggested to be a consequence of west to east (present day coordinates) Rheic ocean opening and associated separation of micro-terranes from the northern margin of Gondwana (Fig. 15A) (Murphy et al., 2006; Nance et al., 2010; 2012).

Figure 11.10. Frequency and density distribution of U–Pb ion microprobe, LA-ICP-MS and whole-rock crystallisation ages of magmatic rocks from: A) Ossa-Morena Zone (OMZ) Cambro-Ordovician rocks, note the three main magmatic peaks at c. 540 Ma, c. 512 Ma and c. 480 Ma. Ages older than c. 570 Ma correspond to pre-magmatic zircons. B) Tuareg Shield granitoids crystallisation ages with a main peak at c. 525 Ma, here all ages are magmatic. C) Anti-Atlas, West African Craton granitoids with a main cluster at c. 570 Ma and c. 600 Ma, note the asymmetric distribution and that the c. 480 Ma magmatic event is scarcely represented. D) Saharan Metacraton granitoids, migmatites and orthogneisses ages, note the peak at c. 615 Ma. Pie diagram age periods as in Figure 11.6. Numbers in brackets correspond to the reference data sources in Appendix I.

The question is then, if the new paleogeographic positions recently suggested for the Iberian Massif zones, detailed above, and the interpretation of their Cambro-Ordovician magmatism are consistent with this scenario. Before we begin to address this point, it is worth mentioning that Braid et al., (2011) concluded that, at this time, the SPZ was part of Avalonia on the other side of the Rheic Ocean close to Laurentia, so it is not considered further here.

11.1.3.1 The Previously Accepted Paleogeographic Position of the Ossa-Morena Zone

A Cambro-Ordovician west African paleogeographic position, adjacent to the Anti-Atlas West African Craton, has been suggested for the OMZ (Murphy and Nance, 1989; Nance and Murphy, 1996). This scenario was proposed based on paleontological evidence that indicated that the OMZ and other Cadomian-related areas had fauna typical of the periphery of Gondwana (Robardet et al., 1994; Robardet and Gutiérrez-Marco, 2004). Paleomagnetic data was also interpreted to suggest a north Africa position at that time (e.g., Torsvik et al., 1992; Stampfli et al., 2002). Other evidence that positioned the OMZ close to the West African Craton was the detrital zircon population in the sedimentary rocks (Nance and Murphy, 1994; Linnemman et al., 2008; Pereira et al.; 2011; 2012b). As noted above this connection was based on the abundance of OMZ Neoproterozoic, Paleoproterozoic and Archean ages (Fig. 11.7). The main argument that connected the OMZ with the West African Craton was the absence, in both terranes, of Mesoproterozoic ages, c. 1.0 Ga (Fig. 11.7).

1 1.1.3.2 Towards a New Paleogeographic Position for the Ossa-Morena Zone

Álvaro et al., (2014) reviewed the relationship between the western sector of the Anti-Atlas West African Craton and the OMZ. They noted that there was a difference in the age and timing of several important lithologies. Firstly, in the western Anti-Atlas West African Craton Cryogenian and Ediacaran sedimentary sequences are well-developed, whereas in the OMZ only Ediacaran, Serie Negra, sediments crop out. Secondly, the two regions have different zircon ages in arc-related syn-orogenic basins, specifically the Ediacaran sedimentary rocks in both areas have different maximum sedimentation ages: 630-610 Ma in the Anti-Atlas West African Craton and 590-545 Ma in the OMZ. In addition, these authors noted the presence of, albeit minor, Mesoproterozoic zircons, *c.* 1.0 Ga, in Cambrian sediments in the Anti-Atlas West African Craton which are absent in the same sediments in the OMZ (Fig. 11.8C). Thirdly, there was a variation in the timing of key tectonomagmatic events, such as calc-alkaline arc-related magmatism, in the Anti-Atlas West African Craton, 615-579 Ma, and the OMZ, 582-535 Ma (Fig. 11.10A and 11.10C) (Álvaro et al., 2014). As noted above, the post-collisonal magmatism in the Anti-Atlas West African Craton occurred at 577-552 Ma, whereas in the OMZ comparable magmatism, i.e.,

the 'early rift-related event', happened later at 530-527 Ma (Fig. 11.10A and 11.10C) (Sánchez-García et al., 2008; 2010). Rift propagation in both areas marks a southwest to northeast trend, present day coordinates.

So, the Cambro-Ordovician progression of events in the Anti-Atlas West African Craton and the OMZ was apparently from the southwest to the northeast. In agreement with this, the arguments presented here link the OMZ and the Tuareg Shield. This leads us to propose that if the OMZ was close to the Anti-Atlas West African Craton then it was in a more northeasterly rather than westerly position.

11.1.3.2.1 Geochronological Evidence

As described above the OMZ sedimentary detrital zircon population is similar to both those in the Anti-Atlas West African Craton and the Tuareg Shield, with a real paucity of *c.* 1.0 Ga zircons in the three areas (Fig. 11.8B and 11.8C). We presented evidence that favours a sediment input into the OMZ from the Tuareg Shield. Specifically, the Nd model age of the OMZ Ediacaran, syn-orogenic deposits, and Ordovician, passive margin deposits, *c.* 1.7 Ga, reflect an old Pan-African crustal input. To our knowledge the Tuareg Shield is the only terrane along the northern Gondwana margin that has comparable model ages, *c.* 1.7 Ga (Fig. 11.5). The OMZ detrital zircons also have late Cryogenian-Tonian and Archean populations that are more scarce in the Anti-Atlas West African Craton than in the Tuareg Shield. Furthermore, Paleoproterozoic ages of 1.9-1.5 Ga are typical in the OMZ Cambrian sedimentary rocks, this age distribution matches the Tuareg Shield rather than the Anti-Atlas West African Craton, as shown in the Kolmogorov-Smirnov test (Fig. 11.8).

The tectonomagmatic events are diachronic between the OMZ, later, and the Anti-Atlas West African Craton, earlier. By contrast, the mantle-derived, rift-related alkaline magmatism in the Tuareg Shield, *c.* 525 Ma, was coeval with the OMZ *c.* 520 Ma 'early rift-related event' identified by Sánchez-García et al., (2003) (Fig. 11.10). Additionally, the alkaline rocks in both the OMZ and the Tuareg Shield have an old crustal contribution mixed with a juvenile *c.* 1.0 Ga mantle or crustal component which resulted in a Nd model age range for this magmatism of 1.7-1.0 Ga (Azzouni-Sekkal et al., 2003; Sánchez-García et al., 2013) (Fig. 11.5).

11.1.3.2.2 Stratigraphical Evidence

In the Tuareg Shield, the Tassili Ouan Ahaggar basin, southeast Hoggar, records the transition from a closed to open marine environment during the Cambro-Ordovician (Beuf et al., 1971). Linnemann et al., (2011) studied the zircon population in this sedimentary record, data considered in the present work, and established a model of basin evolution. Basal early Cambrian

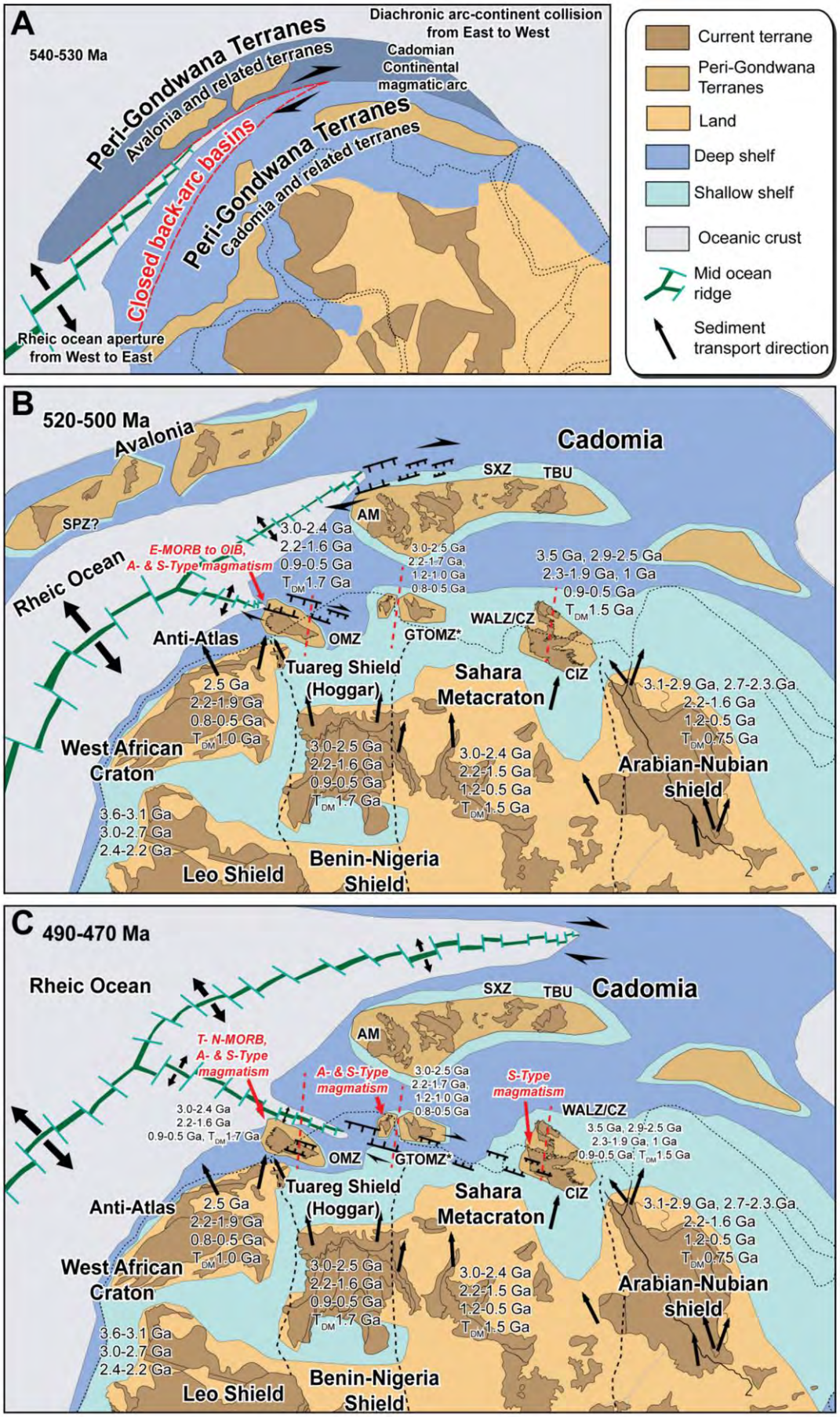
A
540-530 Ma
Diachronic arc-continent collision from East to West
Peri-Gondwana Terranes
Avalonia and related terranes
Cadomian Continental magmatic arc
Closed back-arc basins
Peri-Gondwana Terranes
Cadomia and related terranes
Rheic ocean aperture from West to East
Current terrane
Peri-Gondwana Terranes
Land
Deep shelf
Shallow shelf
Oceanic crust
Mid ocean ridge
Sediment transport direction
B
520-500 Ma
Avalonia
Cadomia
SXZ
TBU
AM
SPZ?
Rheic Ocean
E-MORB to OIB, A- & S-Type magmatism
3.0-2.4 Ga
2.2-1.6 Ga
0.9-0.5 Ga
T_DM 1.7 Ga
3.0-2.5 Ga
2.2-1.7 Ga,
1.2-1.0 Ga
0.8-0.5 Ga
3.5 Ga, 2.9-2.5 Ga
2.3-1.9 Ga, 1 Ga
0.9-0.5 Ga
T_DM 1.5 Ga
WALZ/CZ
Anti-Atlas
OMZ
GTOMZ*
Tuareg Shield (Hoggar)
Sahara Metacraton
CIZ
2.5 Ga
2.2-1.9 Ga
0.8-0.5 Ga
T_DM 1.0 Ga
3.1-2.9 Ga, 2.7-2.3 Ga
2.2-1.6 Ga
1.2-0.5 Ga
T_DM 0.75 Ga
West African Craton
3.0-2.5 Ga
2.2-1.6 Ga
0.9-0.5 Ga
T_DM 1.7 Ga
3.0-2.4 Ga
2.2-1.5 Ga
1.2-0.5 Ga
T_DM 1.5 Ga
Arabian-Nubian shield
3.6-3.1 Ga
3.0-2.7 Ga
2.4-2.2 Ga
Leo Shield
Benin-Nigeria Shield
C
490-470 Ma
Rheic Ocean
SXZ
TBU
Cadomia
AM
T- N-MORB, A- & S-Type magmatism
A- & S-Type magmatism
S-Type magmatism
3.0-2.4 Ga
2.2-1.6 Ga
0.9-0.5 Ga, T_DM 1.7 Ga
3.0-2.5 Ga
2.2-1.7 Ga,
1.2-1.0 Ga
0.8-0.5 Ga
WALZ/CZ
3.5 Ga, 2.9-2.5 Ga
2.3-1.9 Ga, 1 Ga
0.9-0.5 Ga, T_DM 1.5 Ga
OMZ
GTOMZ*
Tuareg Shield (Hoggar)
Sahara Metacraton
CIZ
Anti-Atlas
2.5 Ga
2.2-1.9 Ga
0.8-0.5 Ga
T_DM 1.0 Ga
3.1-2.9 Ga, 2.7-2.3 Ga
2.2-1.6 Ga
1.2-0.5 Ga
T_DM 0.75 Ga
West African Craton
3.0-2.5 Ga
2.2-1.6 Ga
0.9-0.5 Ga
T_DM 1.7 Ga
3.0-2.4 Ga
2.2-1.5 Ga
1.2-0.5 Ga
T_DM 1.5 Ga
Arabian-Nubian shield
3.6-3.1 Ga
3.0-2.7 Ga
2.4-2.2 Ga
Leo Shield
Benin-Nigeria Shield

deltaic deposits unconformably overlie Precambrian basement. These oldest sediments grade upwards into shallow marine Cambrian deposits that are, in turn, overlain by Ordovician marine sandstones and glacial sediments. The sedimentary sequence culminates in monotonous deeper water Silurian shales and Devonian marine sandstones (Beuf et al., 1971; Ghienne et al., 2007a,b).

Linnemann et al. (2011) suggested that the Tassili Ouan Ahaggar basin developed related to Rheic Ocean opening during the Cambro-Ordovician. The sedimentation record reflects an important change from continental deposits, that only contain detrital zircons from cratonic areas, to marine deposition with a clear input of Pan-African rocks, exposed as rift shoulders related to the Rheic Ocean opening (Linnemann et al., 2011).

Similarities can be established between the sedimentary sequences in the Tassili Ouan Ahaggar basin and the OMZ. In both cases Cambrian deposits unconformably overlie Precambrian basement. The early Cambrian series in the OMZ and the Tuareg Shield are fluvial to shallow marine deposits that have been related to a Rheic Ocean rifting context (cf., Sánchez-García et al., 2010; Linnemann et al., 2011). Analagous rifting in the Anti-Atlas West African Craton began slightly earlier, in the earliest Cambrian (Álvaro, 2014) consistent with diachronous

Figure 11.11 Paleogeographic reconstructions of northem Gondwana: A) Transition from continental magmatic arc to west to east Rheic Ocean opening that resulted in micro-terranes separation from northern Gondwana during the Precambrian-Cambrian transition (based on Linnemann et al., 2008 and Torsvik and Cocks, 2013). B) Middle to late Cambrian rift progression provoked the separation of Peri-Gondwana terranes Avalonia, South Portuguese Zone-like (SPZ?) then Cadomia (AM: Armonican Massif; SXZ: Saxo-Thuringian Zone; TBU: Tepla-Barrandian Unit) (after Linnemann et al., 2008). This 520-500 Ma period, contemporaneous with the 'main rift-related event' in the Ossa-Morena Zone (OMZ), is associated with initiation of a 'Gondwana-ward' branch of the Rheic Ocean to the west (paleogeographic position) of the OMZ close to Tuareg Shield. This new paleoposition is adjacent to that recent defined for the Galicia Tras-os-Montes Zone parauchthonous units (GTOMZ), West-Asturian Leonese Zone (WALZ), Cantabrian Zone (CZ) and Central Iberian Zone (CIZ) close to the Saharan Metacraton. C) Ordovician, 490-470 Ma, rifting evolution with passive margin formation, that resulted in generation of oceanic crust in the west in the OMZ, whereas in the GTOMZ and CIZ magmatism was incipient rift propagation related. For clarity, we include the main detrital zircon ages of the OMZ, CIZ and the three north African terrane rocks as well as a summary of magmatism during Rheic Ocean branch opening from west to east. In addition, shallow and deep ocean and land morphology are shown, according to Torsvik and Cocks, (2013) and the bathimetric gradient established for the OMZ and CIZ after Robardet and Guitiérrez-Marco (2004). Dashed lines correspond to Figure 11.10 cross-sections. Cratonic regions age ranges are taken from the compilation in the present work and from compilations by Pereira et al., (2008) and Drost et al., (2011). Sediment transport directions from Avigad et al., (2003) and Shaw et al., (2014).*

west to east ocean opening. Early Ordovician deposits, in the OMZ and Tuareg Shield, are detrital to open marine sediments although these are somewhat deeper in the former (Beuf et al., 1971; Giese et al., 1994). Similarly, late Ordovician to Silurian deposits in both the Tuareg Shield Tassili Ouan Ahaggar basin and the OMZ are characterized by monotonous black marine shelf shales (Beuf et al., 1971; Gutiérrez-Marco et al., 1998), which subsequently progressed to more shallow-marine Devonian terrigenous series (Beuf et al., 1971, Oliveira et al., 1991).

11.1.4 Cambro-Ordovician Rifting and Separation of Micro-terranes from the Northern Margin of Gondwana Related to West to East opening of the Rheic Ocean

11.1.4.1 Stratigraphical and Paleontological Evidence

An indication of somewhat deeper sedimentation in the OMZ is consistent with a more northerly marginal paleoposition with respect to the Tuareg Shield and also with a Cambro-Ordovician northeasterly sediment transport direction (Beuf et al., 1971). Nevertheless, the overall correlation between the OMZ and the Tuareg Shield Tassili Ouan Ahaggar basin links the two regions. It marks a Cambro-Ordovician change of continental deposition to marine sedimentation interpreted to be related to rifting and Rheic Ocean opening off north Gondwana (Murphy et al., 2006; Nance et al., 2010).

Analogous, albeit diachronous, rifting is also recorded elsewhere along the north Gondwana margin. The stratigraphic sequences of the Anti-Atlas West African Craton and part of the European Variscan Massif preserve evidence of an early Cambrian rifting stage that evolved to a passive margin context during the Ordovician (Drost et al., 2011; Álvaro et al., 2014). In addition, Cambro-Ordovician rifting, admittedly not as extensively developed as in the OMZ, has also been described in other Iberian Massif zones, for example in the CIZ and CZ (cf., Robardet and Gutierraz-Marco; 2004; Pastor-Galán et al., 2013). Early Cambrian CIZ shallow marine deposits (Liñán et al., 2002) are coeval with the OMZ Cambrian marine carbonate unit and upper detrital formation (Liñán and Quesada, 1990). However, these rocks have been interpreted differently in the two regions. In the CIZ calm shallow-marine deposition occurred prior to Cambro-Ordovician rifting (Simancas et al., 2004) whereas in the OMZ coeval sedimentation resulted from turbiditic and shelf siliciclastic deposition during a collapse-related extensional process (Fig. 11.1A and 11.12A) (Liñán and Quesada, 1990; Sanchez-García et al., 2003).

Drawing on paleontological evidence Robardet and Gutiérrez-Marco (1990a; 1990b; 2004) concluded that there was no doubt that both the OMZ and CIZ have north Gondwana type

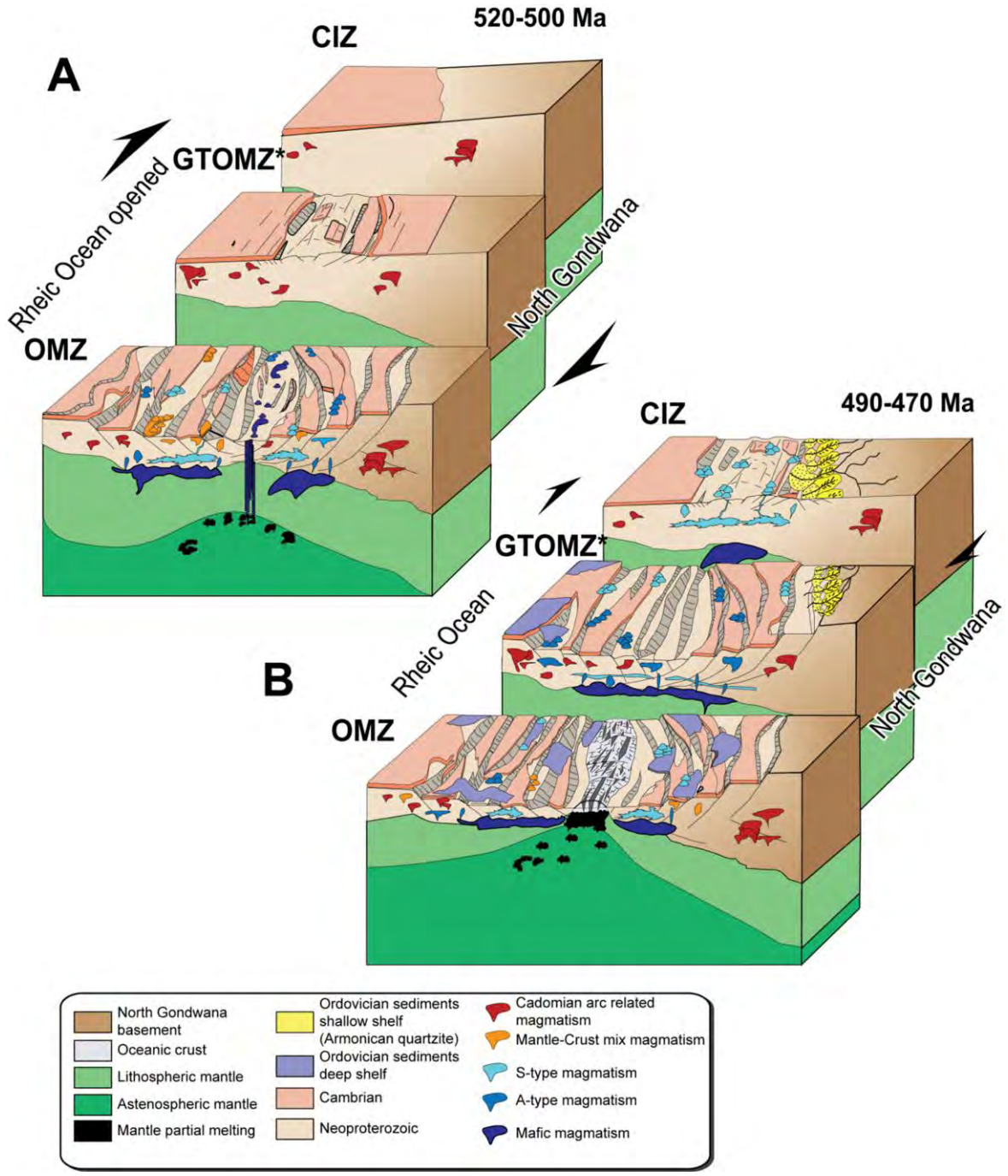

Figure 11.12 Model for the formation of the 'Gondwana-ward' Rheic Ocean branch that propagated from west to east during: A) The c. 520-500 Ma, 'main rift-related event' period during which there was: generation of A-type, S-type, mantle-crust mixed and E-MORB to OIB mafic magmatism in the Ossa-Morena Zone (OMZ); and, collapse-related extension that affected Cambrian sedimentary successions. Notably this magmatic event is absent in the Galicia Tras-os-Montes Zone parauchthonous units (GTOMZ) and the Central Iberian Zone (CIZ) that were close to the Saharan Metacraton. B) Ordovician, c. 490-470 Ma, oceanic crust generation in the OMZ resulted from rift progression, with generation of A- and S-type magmatism further east in the GTOMZ*, whereas in the CIZ more limited rifting generated S-type magmatism during the same period. Note that during the Ordovician a deeper marine context is suggested for the OMZ and shallow deposition conditions were defined for the CIZ with Armorican quartzite sedimentation (Robardet and Guitiérrez-Marco, 2004).*

sediments and faunas. However, whereas the Cambrian sedimentation was similar in the two regions, the Lower Ordovician-Lower Devonian successions differ appreciably. The stratigraphical and paleontological indications suggest that the OMZ was situated in a deep ocean that shallowed eastward to the GTOMZ and became shallower still in the WALZ, CZ and CIZ (Figs 11.11B and 11.12B).

Evidence for the eastward shallowing also includes the Lower Ordovician, 477-465 Ma, Armorican Quartzite (i.e., Gutiérrez-Marco et al., 2002; Gutiérrez-Alonso et al., 2007). This facies is interpreted as an off-shore Gondwana passive margin unit deposited on a wide, stable and shallow marine platform. Whereas the quartzite is well-exposed in the CIZ and CZ (Barrios Formation) it is not present in the OMZ (Fig. 11.12B) (Robardet and Gutiérrez-Marco, 1990a; 1990b; 2004). In the OMZ the Ordovician succession comprises deeper water shaley and silty deposits and is thus characteristic of a more distal deeper environment (Fig. 16B). Accordingly, a bathimetric gradient has been established from deeper, OMZ, to shallow, CIZ (Fig. 11.1B and 11.12B) (Hammann and Henry, 1978; Gutiérrez-Marco et al., 1998). This earlier initiation and more extensive progression of rifting is, once more, consistent with the west to east opening of the Rheic Ocean (cf., Nance et al., 2012).

Linking back to geochronological constraints, Shaw et al., (2014) studied U-Pb detrital zircon age data from the Armorican Quartzite to constrain the provenance variability of the CZ, WALZ and CIZ along the Early Ordovician north Gondwana margin. They concluded that their data were consistent with the proposed easterly off-shore Saharan Metacraton and Arabian Nubian Shield location of the zones proposed by Bea et al., (2010), Pastor-Galán et al., (2013), Talavera et al., (2013), Fernández-Suárez et al., (2014) and Shaw et al., (2014).

11.1.4.2 Magmatic Evidence

It is worth underlining that the timing and composition of early Palaeozoic magmatism in the Iberian Massif zones detailed above is equally consistent with the west to east opening of the Rheic Ocean and also with the new paleogeographic positions. As can be deduced from the range of magmatic ages presented, Cambro-Ordovician magmatism began earlier and was more protracted in the more westerly OMZ than the more easterly, Cambro-Ordovician coordinates, CIZ (Fig. 11.12A). It was also more prolonged than in the GTOMZ parautochthonous units, which have also recently been situated more easterly off the Saharan Metacraton (Figs 11.1B and 11.12A) (Díez-Fernández et al., 2010; Talavera et al., 2013).

The OMZ Cambro-Ordovician, plutonic rocks *c.* 520-470 Ma have an anorogenic character related to progression of extension that started in the early Cambrian (Fig. 11.12) (Ochsner,

1993; Sánchez-García et al., 2010). This extensional event is characterized by bimodal magmatism comprising mafic and felsic rocks, best exposed in the west of the OMZ, and by the generation of alkaline magmas, (Fig. 11.12A and 11.12B). The CIZ magmatism during the same period is restricted to *c.* 480 Ma calc-alkaline to peraluminous metagranite and metavolcanic orthogneisses that contain abundant pre-magmatic zircons. Bea et al. (2007) interpreted the numerous inherited zircons to reflect a fast crustal melt magma generation and emplacement related to intrusion of mantle-derived mafic magmas at the base of the crust in an extensional environment (Fig. 11.12B) (cf., Díez-Montes et al., 2010; Talavera et al., 2013). This led Bea et al., (2007) to conclude that their model was consistent with the hypothesis of fragmentation and dispersal of terranes from the northern margin of Gondwana. Accordingly, Rubio-Ordoñez et al. (2012), recently identified an Early Ordovician tonalitic-granodioritic belt in the CIZ.

Similar to the CIZ, the GTOMZ parautochthonous units contains *c.* 480 Ma S-type and A_1-type granites, no coeval mafic rocks crop out indicating that rifting did not progress as much as in the OMZ (Fig. 11.12B) (Montero et al., 2009b; Díez-Fernández et al., 2012). So the weaker Ordovician magmatic expression in the GTOMZ and CIZ father east, Cambro-Ordovician coordinates, than the OMZ, is consistent with production related to an eastward propagating rift. We suggest, that the rift was a 'Gondwana-ward' branch of the Rheic Ocean rather than the main ocean itself (Figs 11.1 and 11.12).

The sedimentological and magmatic evidence lead us to suggest that the OMZ was located to the west of the other Iberian Massif zones during the Cambro-Ordovician. Nevertheless, stratigraphical evidence, detailed above, and the apparent sedimentary contributions from both the Tuareg Shield and the Anti-Atlas West African Craton place it further east than its previously accepted paleogeographic position off the western Anti-Atlas West African Craton (Murphy and Nance, 1991; Nance and Murphy, 1994) (Fig. 11.1B). Our new scenario suggests a more easterly Anti-Atlas, West African Craton to northwest Tuareg Shield, Cambro-Ordovician paleogeographic position of the OMZ. This fits with the contemporaneous paleogeographic reconstruction of the north Gondwana terranes that establishes a more eastern paleogeographic position for the Cadomian terrane (Stampfli et al., 2002; Simancas et al., 2009; Torsvik and Cox, 2013).

11.1.5 The Amalgamation of Iberia

We suggest that the OMZ preserves a Gondwana-ward southerly branch of the Rheic Ocean that opened diachronously from west to east rather than the main ocean (cf., Linnemann et al., 2008). The regional Cambro-Ordovician magmatic evolution, stratigraphic constraints and

paleogeographic position all fit with a rifted volcanic margin, Ethiopian rift Red Sea type model. Extension-related A-type and S-type felsic magmatism and E-MORB and OIB mafic magmatism intruded from 530-500 Ma. Then, as the rifting progressed, a narrow ocean basin opened forming T and N-MORB ocean crust in the westerly OMZ (Figs 11.1 and 11.12). Further east, in the GTOMZ terrane, coeval extension is reflected by Ordovician mantle-derived A_1-type granites and subsequent crustal melt S-type granitoids. Further eastward still in the CIZ, where rifting did not progress so extensively, no mantle-derived magmatic expression is evident other than provocation of a crustal partial melting event that produced the S-type Ollo de Sapo orthogneisses with abundant pre-magmatic zircons (Figs 11.1 and 11.12).

The new early Paleozoic paleogeographic position of the OMZ presented here is further east (present day coordinates) than previously thought (e.g., Sánchez-García et al., 2008; Pereria et al., 2012c). Notably, it does not require 180° rotation of the OMZ as in some other models (e.g., Eguiluz et al., 2000). With respect to the amalgamation of the Iberian Massif terranes at some point after *c.* 450 Ma and before *c.* 390 Ma regional rift-related extension changed to collision. This resulted in sinistral transpressional juxtaposition of the OMZ and the CIZ, along the Badajoz-Cordoba shear zone during the Variscan Orogeny (Matte, 2002; Robardet and Gutiérrez-Marco, 2004; Simancas et al., 2006; Pereira et al., 2010a).

The Variscan orogeny in the Iberian Massif resulted in shortening which generated thrusts and folds (Simancas et al., 2013). The consequences of this process were crustal thickening in the CIZ, subsequent voluminous magmatism (Bea, 2012), and the generation of the Variscan orocline (Guitérrez-Alonso et al., 2004; Martínez-Catalán, 2011; Simancas et al., 2013). In the OMZ the regional Variscan structures preserve evidence of an initial collisional event between 390-345 Ma (Simancas et al., 2003; Pereira et al., 2012c). This was followed, from 345-330 Ma, by an intra-orogenic extension-related event (Apraiz and Eguíluz, 2002; Pereira et al., 2009; Rosas et al., 2008) with associated bimodal magmatism from 350-320 Ma (e.g., Casquet and Galindo, 2004). A subsequent collisional event, 330-305 Ma, closed the Variscan orogenic cycle in the region (Simancas et al., 2003; 2006; Azor et al., 2008).

11.2 Timing and Tectonomagmatic Setting of Variscan Magmatism in the Ossa-Morena Zone

Widespread magmatism occurred as a result of the juxtaposition of the Ossa-Morena Zone (OMZ), the Central Iberian Zone (CIZ) and the South Portuguese Zone (SPZ) during the latest Devonian-earliest Carboniferous Variscan Orogeny (Matte, 2001 and references therein). The magmatism has an overall calc-alkaline character and has been linked with subduction (e.g., Pons, 1982; Giese et al. 1994; Quesada et al., 1994; Castro et al., 1996; Sarrionandia, 2005). It is not clear, however, whether all calc-alkaline rocks should be directly linked with active or ancient subduction zones (e.g., Arculus, 2003; Pearce, 2008; Maurice et al., 2009; Scarrow et al., 2009).

Various studies have identified a short-lived intra-orogenic extensional event in the region during the main Variscan collision, 350-330 Ma (Apraiz and Eguíluz, 2002; Simancas et al., 2003; Pereira et al., 2007; 2009; Rosas et al., 2008). At the same time there was:

i. Sedimentary basin development (Quesada et al., 1990a; Giese et al., 1994; Simancas et al. 2003)
ii. Mid-crustal intraplating of the 'IBERSEIS Reflective Body' of ultramafic-mafic sills (Simancas et al., 2003; Carbonell et al., 2004; Palomeras et al., 2011; Brown et al., 2012)
iii. Extensive mineralization related to an extensional context (Tornos et al., 2006; Romero et al., 2006);
iv. High-temperature low-pressure metamorphism (Bard, 1969; Ordoñez-Casado, 1998; Pereira et al., 2003; 2007; 2009; Díaz-Azpiroz et al., 2004; 2006)
v. The main OMZ Variscan magmatism (Dallmeyer et al. 1995; Montero et al., 2000; Ordóñez-Casado, 2008).

The compositional diversity of the OMZ Variscan plutons, ultramafic-rocks, gabbros and diorites through quartz diorites to granodiorites and granites, detailed in the previous chapters suggests complex interplay of magmas derived from mantle and crustal sources. The aim is to determine the tectonomagmatic context of the plutonic complexes studied here and what this may reveal about the derivation and interaction of mantle- and crust-derived magmas during orogenesis.

11.2.1 Timing of OMZ Variscan Magmatism

New precise SHRIMP U-Pb ages for the Burguillos del Cerro plutonic complex, the Valencia del Ventoso plutonic complex and the Brovales pluton permit consideration of:

i. The geochronological and tectonomagmatic constraints on the emplacement of the

Olivenza-Monesterio, Ossa-Morena Variscan plutons

ii. The possible link between the plutons and the IBERSEIS Reflective Body

iii. More generally, the petrogenetic implications of mantle- and crust-derived magma interaction during orogenesis.

11.2.1.1 Geochronological Constraints: Emplacement of the Burguillos, Valencia and Brovales Complexes

The geochronological results obtained in this study define a Carboniferous Variscan age range, 340-320 Ma Visean-Bashkirian, for the three complexes (Table 11.1). This constrains their emplacement to between the two Variscan collisional events and connects them with the intra-orogenic episode of extension/transtension.

The new average ^{207}Pb-corrected age of 336±1 Ma for the Burguillos plutonic complex falls within the range of A-Ar ages, 342-329 Ma, determined for gabbros and diorites from the complex by García-Casquero (1991). The gabbro ages, paradoxically, were considered erroneous, the consequence of resetting of older ages as a result of Variscan diorite intrusion. Given the alkaline nature of the magmatism García-Casquero (1991) associated production of the ultramafic and mafic rocks of the complex with a known Cambro-Ordovician OMZ rifting event (see previous). Our results, conversely, show that all the units of the Burguillos del Cerro plutonic complex were contemporaneous. The exception is the two-mica granite of the A*cid Peraluminous Unit* for which the only Variscan ages obtained were in thin low cathodoluminescent overgrowth rims in just two zircons, 305±4 Ma and 317±3 Ma; the other ages determinied in this rock being pre-magmatic and pre-Variscan (see Chapter 9). In any case, field relations and ages obtained for comparable rock types in other complexes relate the two-mica granites compositionally and temporally to the *Peraluminous Group* (see section 11.3.1.3). Moreover, the abundant pre-magmatic zircons found in these rocks indicates rapid emplacement and crystallisation favouring preservation of pre-existing, inherited, accessory minerals. The presence of abundant pre-magmatic zircons suggests a clear crustal influence in the *Acid Peraluminous Group*. This, associated with their peraluminous character, points towards a crustal melting event coeval with the Burguillos del Cerro plutonic complex.

The average ^{207}Pb-corrected age of 334±2 Ma for the Valencia del Ventoso plutonic complex is 15 million years younger than the previously published age of 349±28 Ma, WR Rb-Sr (Sarrionandia and Carracedo, 2007). Only the Valencia, *Northern Stock Subalkaline Basic-Intermediate Unit* has a somewhat younger age than the other rocks, 320±3 Ma. This indicates that mafic, presumably mantle-derived, magmatism related to the Valencia del Ventoso plutonic complex

Complex	Unit	Rock type	Sample	^{207}Pb-corrected age (Ma)
Burguillos del Cerro plutonic complex	*Central Ultrabasic-Basic Layered Unit*	Poikilitic amphibole gabros and gabbronorites	BUAW-4	**336±2**
	Central Alkaline Basic-Intermediate Layered and Acid Unit	Gabbro and diorites	BUAW-6	**338±4**
		Alkali feldspar granites	BUAW-10	**335±2**
	External Subalkaline Intermediate Unit	Quartz diorites to tonalites	BUAW-5	**335±2**
Valencia del Ventoso plutonic complex	*Main Pluton Alkaline to Subalkaline Basic-Acid Unit*	Diorites	VAAW-35	**338±3**
		Quartz diorites	VAAW-37	**333±2**
		Granodiorites to granites	VAAW-38	**336±2**
	Northern Stock Subalkaline Basic-Intermediate Unit	Quartz monzodiorites	VAAW-17	**333±2**
	Southern Stock Subalkaline Intermediate-Acid Unit	Quartz monzodiorites	VAAW-30	**320±2**
	Intrusive Dyke Unit	Aplites	VAAW-24	**329±2**
Brovales pluton	*Central Subalkaline Intermediate Unit*	Quartz diorites	B-2	**339±4**
	Intermediate Subalkaline Intermediate Unit	Granodiorites	B-5-1	**341±4**
	External Subalkaline Acid Unit	Granites	B-7	**339±4**
	Intrusive, Acid Peraluminous, Dykes	Aplites	B-8-2	**340±2**

Table 11.1. Summary of U-Pb ages from this study for rocks from the Burguillos del Cerro, Valencia del Ventoso and Brovales complexes.

emplacement continued, at least, until that time. Even the dated aplite from the *Intrusive Dyke Unit* has the same age, 329±7 Ma, within error, as the main pluton (Table 11.1). This sample, like the Burguillos two-mica granite, contains numerous pre-magmatic zircons implying, as in that case, a crustal component in these rocks.

The average ^{207}Pb -corrected age of 340±2 Ma for the Brovales pluton is within error of that obtained by Montero et al., (2000) (342±4 Ma, Pb-Pb Kober method). In the present work we dated the four main units of the pluton all of which were found to have the same age (Table

11.1). The emplacement of all the Brovales pluton facies occurred, therefore, during the Variscan orogeny (cf., Pons, 1982; Casquet and Galindo, 2004) in contrast to previous suggestions of their relation to pre-Variscan magmatism (Eguíluz et al., 2004; Palacios et al., 2010).

The Brovales pluton also limits the age of the intra-orogenic extension-related event and the second collisional event, 330-305 Ma (Simancas et al., 2003; 2006; Azor et al., 2008). As indicated above the Brovales *Intermediate Subalkaline Intermediate Unit* includes a deformed facies. The deformation pattern is particularly evident in the granodiorites associated with the Monesterio thrust (Chapter 4, Fig. 4.12). The plan-view teardrop shape of the intrusion is extended along the fault which strikes parallel to the granodiorite foliation (Eguiluz et al., 2004; Expósito, 2000). The granodiorites comprise both deformed and undeformed facies which indicates syn-magmatic deformation that is also detected in the aplitic dyke rocks (Chapter 4, Fig. 4.11). We suggest that the foliated to unfoliated facies are related to syn-magmatic regional stress affecting a heterogeneous crystallizing mush: the more solid portions could have given rise to the deformed facies; whereas, more liquid-rich magmas, where the fluid phase absorbed the deformation, may have subsequently crystallised to the undeformed facies. Moita et al., (2009) described a similar process for foliated, weakly foliated and unfoliated granodioritic rocks from the Évora massif. Some zircons from the Brovales *Central and Intermediate Subalkaline Intermediate units* have U-Pb dates younger, *c.* 300 Ma, than the main cluster interpreted as the crystallisation age (see Chapter 8). The age of the deformed aplite 340±2 Ma, of the *Intrusive, Acid Peraluminous, dykes*, cuts the deformed granodiorite (Chapter 4, Fig. 4.11) marking the transition from the first compressional event to an extensional context. The younger ages of the *Central Subalkaline Intermediate Units*, *c.* 300 Ma, apparently records the second collisional event.

11.2.1.2 Geochronological Contraints: Other OMZ Variscan Plutonic Rocks

So Burguillos, Valencia and Brovales complexes rocks which are compositionally varied, alkaline, subalkaline, metaluminous and peraluminous, and were generated at the same time in the same tectonomagmatic context. As such, the association is very different from typical S-type, crustal magmatism, described elsewhere in the Variscan. The compositional variety noted above recurs nevertheless in the Variscan magmatism throughout the OMZ (Fig. 11.13, cf., Casquet and Galindo, 2004). Contemporaneous bodies that present comparable features to the studied complexes are: the Santa Olalla and Agua Blanca plutonic complex that comprises ultramafic to felsic rock (Fig. 11.13, 344±3 Ma U-Pb SHRIMP Ordoñez-Casado et al., 2008; cf., Romero et al.,

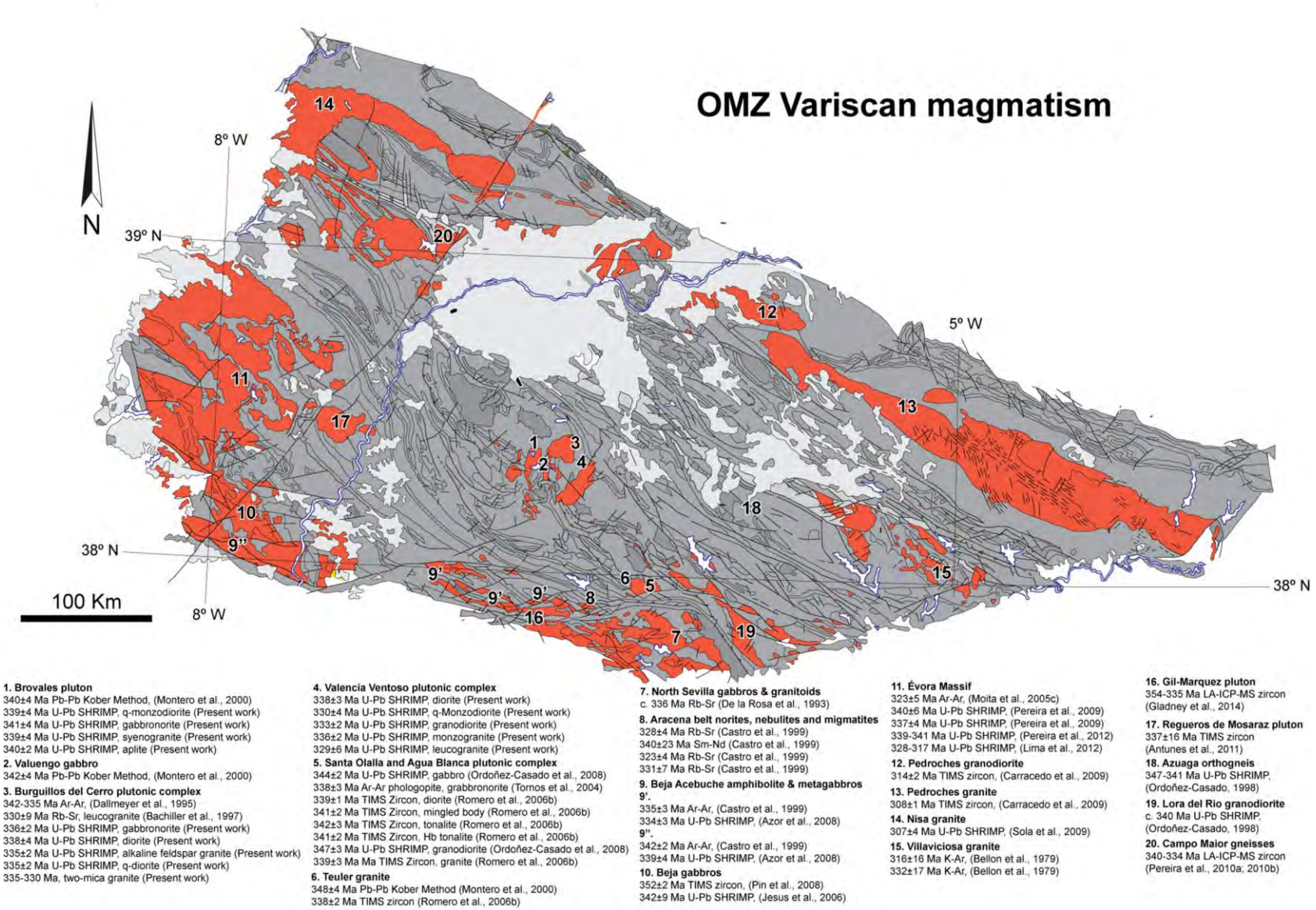

Figure 11.13. The Ossa-Morena Zone showing the Variscan magmatism and published ages for the early Carboniferous magmatism.

2006a; 2006b) with associated Ni-Cu-PGE ore mineralization (Ortega et al., 2004; Tornos et al., 2005; 2006; Piña et al., 2010); the Évora Massif composed of felsic and minor mafic rocks (340-324 Ma U-Pb SHRIMP, Lima et al., 2012; 341±2 and 331±9 Ma U-Pb SHRIMP, Pereira et al., 2015); and the Beja Igneous complex composed of ultramafic to mafic rocks (342±9 Ma U-Pb SHRIMP, Jesus et al., 2007 and *c.* 350 Ma U-Pb TIMS, Pin et al., 2008).

Geochronological data including single zircon and whole-rock ages from a range of complexes indicate that OMZ Variscan magmatism extended from 350 Ma to 320 Ma (Fig. 11.14A).

11.2.1.3 Tectonomagmatic Constraints: Emplacement of the Burguillos, Valencia and Brovales Complexes

The meta-igneous series Beja-Acebuches amphibolite unit, at the contact of the OMZ and the SPZ, is of particular significance for the interpretation of the region. This unit has a T-MORB signature (Munhá et al., 1986; Fonseca and Ribeiro, 1993; Castro et al., 1996) and has previously been interpreted as an ophiolitic complex marking the Rheic Ocean suture (e.g., Quesada et al., 1994; Matte, 2001). Azor et al., (2008), however, have dated the mafic protolith of the Beja-Acebuches amphibolite unit at 340-332 Ma, U-Pb SHRIMP (Fig. 11.13 and 11.14), remarkably close to the accepted exhumation age, *c.* 330 Ma amphibole Ar-Ar (Fig. 11.14) (Dallmeyer et al., 1993; Castro et al., 1999). This age is significantly younger than the initial collision related to the closure of the Rheic Ocean during the latest Devonian–earliest Carboniferous, 370-355 Ma (Fig., 11.14) (Azor et al., 2008; Nance et al., 2010; 2012; Braid et al., 2011; Pereira et al., 2012b).

Thus, the protolith age does not fit with the Beja-Acebuches amphibolite unit being a remnant of the Rheic Ocean. Other evidence also suggests that it is not ocean crust that was consumed, by subduction, before the earliest Carboniferous. The OMZ Visean-Serpukhovian, 345-320 Ma, magmatism (e.g., Dallmeyer et al., 1995; Montero et al., 2000; Ordoñez-Casado et al., 2008; Pereira et al., 2009), is coeval with Visean, 345-320 Ma, magmatism in the SPZ (e.g., De la Rosa et al., 1993; Barrei et al., 2002; Dunning et al., 2002; Gladney et al., 2014). It is difficult to explain contemporaneous magmatism both north, OMZ, and south, SPZ, of a zone boundary related to an arc context.

The Early Carboniferous OMZ magmatic event was coeval with a high-T low-P event which has Visean-Serpukhovian age: in the Évora Massif (340±6 and 337±4, U-Pb SHRIMP, Pereira et al., 2009); in the Aracena metamorphic belt (351±58, 331±27 and 323±4, Rb-Sr Castro et al., 1999); and in the Lora del Rio Massif (*c.* 340 Ma, U-Pb SHRIMP, Ordoñez-Casado,

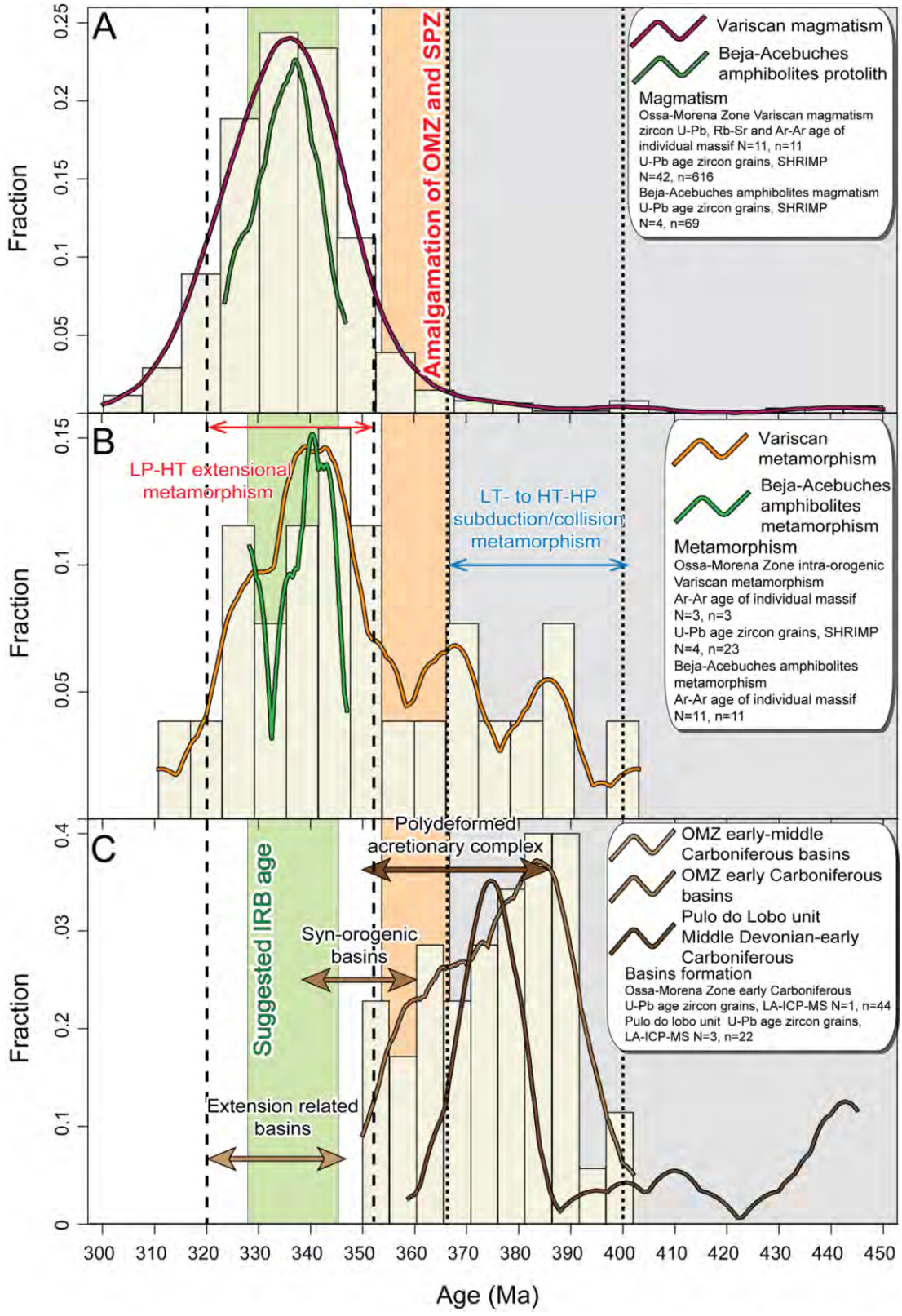

Figure 11.14. Frequency and density distribution of U–Pb ion microprobe, LA-ICP-MS and whole-rock ages of: A) Variscan magmatic rocks from the Ossa-Morena Zone, note the main magmatic peak c. 335 Ma. Ages older than c. 350 Ma are from pre-magmatic zircons. B) Metamorphic events in the Ossa-Morena Zone and C) Detrital zircon distribution in Devonian-Early Carboniferous basins, arrows indicate the age range for basin formation. In addition we indicate the suggested age for IRB formation as well as the age range of the Ossa-Morena Zone and South Portugese Zone amalgamation. Data sources are given in Appendix I.

1998).(Fig. 11.14) (Apraiz and Eguíluz, 2002; Pereira et al., 2003; 2007; Díaz-Azpiroz et al., 2004; 2006). A low-T to high-T high-P metamorphic event occurred from 390-370 Ma (Fig. 11.14) (Araújo et al. 2005; Moita et al., 2005c); metamorphism associated with decompression and shearing began later at *c.* 340 Ma (Pereira et al., 2010a; 2010b).

In agreement with the above, an Early Devonian subduction-related polydeformed accretionary prism, the Pulo do Lobo formation (Fig., 11.14) (Oliveira, 1990; Silva et al., 1990; Braid et al., 2010) is unconformably overlain by Late Devonian sediments e.g., the Ferreira-Ficalho and Chança groups that crop out throughout the SPZ (Oliveira, 1990). The maximum sedimentation age of this complex is *c.* 360 Ma (Fig. 11.14) (Braid et al., 2011) which constrains the upper age limit of the subduction process in that region to that period (Schermerhörn, 1971; Simancas et al., 2009). In addition, other units adjacent to the Beja-Acebuches amphibolite unit also reflect latest Devonian–earliest Carboniferous juxtaposition of the OMZ-SPZ. For example the Moura Cubito unit, interpreted as an allochtonous accretionary complex related to Early Devonian subduction, comprises blocks of oceanic crust and OMZ-SPZ continental crust. Fonseca et al., (1999) suggested that they were obducted during a Late Devonian collision. Furthermore, by the Early Carboniferous the OMZ and SPZ sediments had similar palynological characteristics suggesting that the two terranes were already joined (Pereira et al., 2006).

The final main line of evidence for the Rheic Ocean closure in the latest Devonian–earliest Carboniferous comes from detrital zircons. Early Carboniferous, Tournaisian-Visean, turbidites deposited in syn-orogenic basins in the OMZ, Cabrela formation, and the SPZ, Mértola formation, located at both sides of the suggested Rheic Ocean suture, have Late Devonian detrital zircons populations 390-360 Ma (Fig. 11.14). Pereira et al., (2012b) suggested that these zircons result from intra-oceanic arc erosion, related to Rheic Ocean closure.

All evidence, therefore, points towards active subduction having ceased prior the latest Devonian–earliest Carboniferous (cf., Woodcock et al., 2007; Azor et al., 2008; Braid et al., 2011; Pereira et al., 2012b).

11.2.1.4 The Link between the IBERSEIS Reflective Body and Intra-Orogenic Extension-Related Magmatism

The Olivenza-Monesterio antiform Carboniferous plutonic, 340-320 Ma, complexes are, therefore, too young to have formed in a subduction zone environment. Here we propose a model for their generation related to the IBERSEIS Reflective Body (IRB, Simancas et al., 2003) (Fig. 11.15).

The IRB was detected, along some 50 km of the IBERSEIS deep seismic profile (Chapter

2, Fig. 2.10), it comprises strongly reflective layers which have been interpreted as Early Carboniferous ultramafic–mafic igneous bodies hosted in the middle crust of the northern SPZ, OMZ and southern CIZ (Carbonell et al., 2004; Simancas et al., 2006; Palomeras et al., 2011). A collisional event between 390-345 Ma preceded the IRB emplacement (Fig. 11.15A) (Simancas et al., 2001; Expósito et al., 2002). The IRB then formed from 345-335 Ma in an intra-orogenic extensional/transtensional setting, associated with Carboniferous sedimentary basin formation but unrelated to the pre-Carboniferous suprasubduction zone context (Fig. 11.14 and 11.15B) (Simancas et al., 2003; 2006; Azor et al., 2008).

The main IRB-related intra-orogenic extensional/transtensional event was contemporaneous with the generation of extensive mafic mantle-derived and, in turn, felsic crustal melt magmatism throughout the OMZ. As the overall regime progressed to transpressional, the Beja-Acebuches amphibolite unit was rapidly exhumed and so could be, we suggest, a surface expression of the IRB-associated magmatism (Fig. 11.15C). Following the extension/transtension, pluton emplacement style was conditioned by the transition to the second collisional event. The Burguillos del Cerro pluton was emplaced into the hinge of a recumbent fold, the axial trace of which traverses the body (Expósito, 2000) (Figs 11.15C and 11.15E). The intrusion of the plan view teardrop shaped Brovales pluton, on the other hand, was controlled by the Monesterio thrust. This is reflected in its elongation along the fault line and the marked deformation foliation that has the same strike as the thrust (Eguiluz et al., 2004; Expósito, 2000) (Figs 11.15E). The elongated oval Valencia del Ventoso plutonic complex cuts the main Variscan first collisional event structures and older granitoids plutons (Figs 11.15E).

The complexes studied in the present work are geographical proximal and temporally and compositionally similarity to, the IRB–related, Santa Olalla Agua Blanca plutonic complex (Tornos et al., 2006), Beja Igneous complex (Pin et al., 2008) and the Évora Massif (Moita et al., 2009; 2015; Lima et al., 2013). This leads us to suggest that all the plutonic bodies were generated in the same tectonomagmatic context; intra-orogenic extension; this may well be the case for much of the OMZ regional early Carboniferous magmatism. We suggest that the second collisional event started later than previously thought by Simancas et al. (2006) and Azor et al. (2008) *c.* 325 Ma because of the continuation of the mafic magmatism until 320±3 Ma, Valencia, *Northern Stock Subalkaline Basic-Intermediate Unit* (Fig. 11.15D).

A scenario is envisaged in which, during an overall convergent context, the Early Carboniferous extensional event (Simancas et al., 2003; 2006; Palomeras et al., 2011; Brown et al., 2012) was related to a thermal anomaly that affected northern Gondwana, Laurentia and Iberia (Murphy et al., 1999; Simancas et al., 2003; 2009). Although simply invoking an intra-orogenic

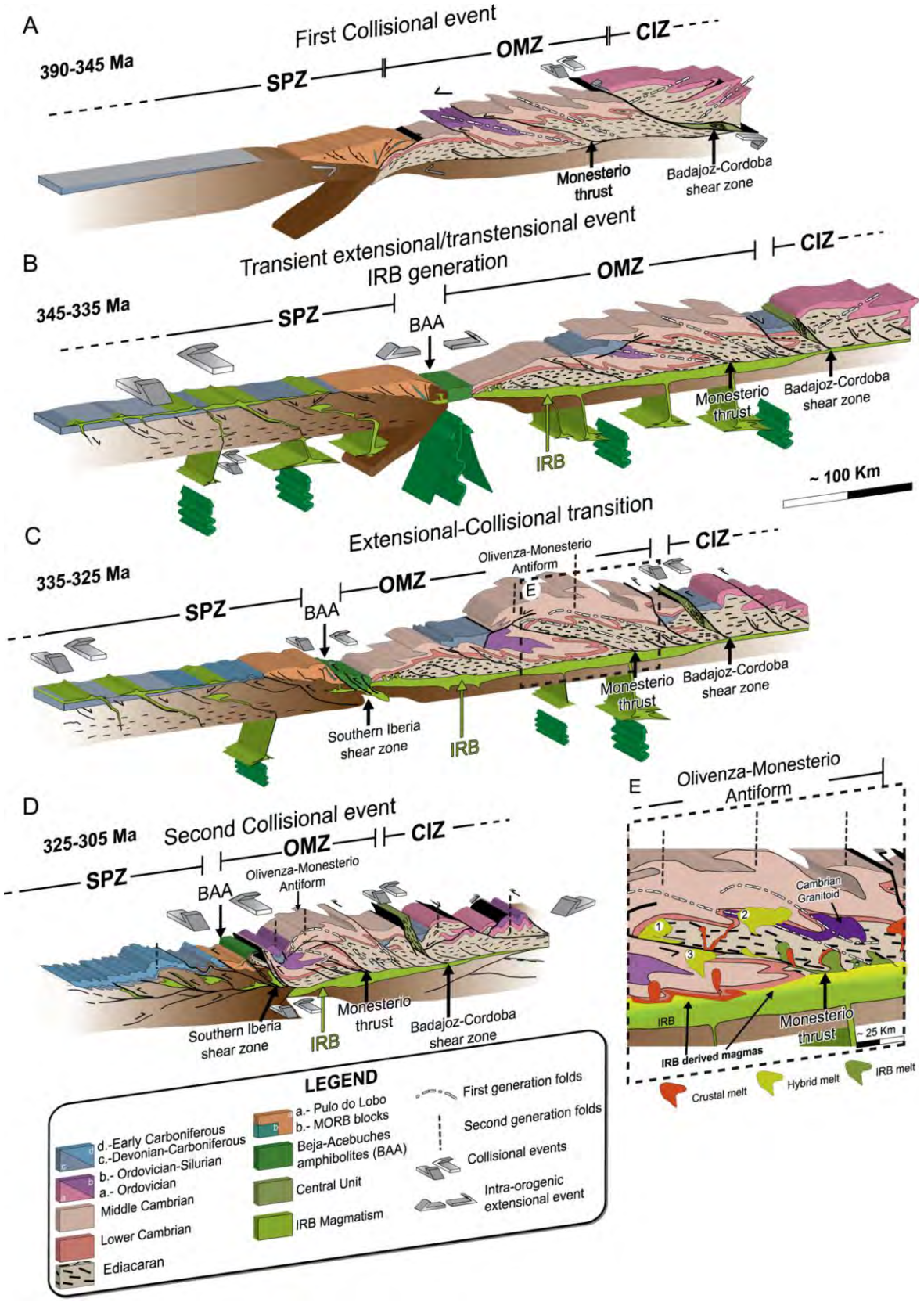
A
First Collisional event
390-345 Ma
SPZ
OMZ
CIZ
Monesterio thrust
Badajoz-Cordoba shear zone
B
Transient extensional/transtensional event
IRB generation
345-335 Ma
SPZ
BAA
OMZ
CIZ
IRB
Monesterio thrust
Badajoz-Cordoba shear zone
~ 100 Km
C
Extensional-Collisional transition
335-325 Ma
SPZ
BAA
OMZ
Olivenza-Monesterio Antiform
E
CIZ
Southern Iberia shear zone
IRB
Monesterio thrust
Badajoz-Cordoba shear zone
D
Second Collisional event
325-305 Ma
SPZ
BAA
OMZ
Olivenza-Monesterio Antiform
CIZ
Southern Iberia shear zone
IRB
Monesterio thrust
Badajoz-Cordoba shear zone
E
Olivenza-Monesterio Antiform
Cambrian Granitoid
1
2
3
IRB
Monesterio thrust
~ 25 Km
IRB derived magmas
Crustal melt
Hybrid melt
IRB melt
LEGEND
d.-Early Carboniferous
c.-Devonian-Carboniferous
b.- Ordovician-Silurian
a.- Ordovician
Middle Cambrian
Lower Cambrian
Ediacaran
a.- Pulo do Lobo
b.- MORB blocks
Beja-Acebuches amphibolites (BAA)
Central Unit
IRB Magmatism
First generation folds
Second generation folds
Collisional events
Intra-orogenic extensional event

thermal anomaly might explain the IRB in the OMZ it is perhaps relying too much on coincidence to suggest it as a general model for under- and intraplate magmatism. Alternative processes could include delamination or slab breakoff (e.g., Averbruch and Piromallo 2012), or small-scale convection (e.g., Kaislaniemi et al. 2014). More simply, low-degree adiabatic mantle melting may also be associated with lithospheric extension in the absence of a thermal anomaly (cf., McKenzie and Bickle, 1988; Latin and White, 1990; 1993). Another alternative is oroclinal bending comparable to that proposed for the Iberian Massif during the Late Carboniferous (e.g., Gutierrez-Alonso et al., 2011; Weil et al., 2012).

11.2.2 Petrogenetic Implications of the Emplacement of the Burguillos, Valencia and Brovales Complexes

Independent of the exact tectonomagmatic context of formation of the IRB it is clear that it formed in the middle crust during an extensional event that was temporally and spatially coincident with the generation of the OMZ Variscan Early Carboniferous mafic magmatism (Figs 11.15E). Coeval crustal partial melting is also recorded in the OMZ Variscan plutons (Pons, 1982; García-Casquero, 1991; Casquet et al., 2001; Ordoñez-Casado et al., 2008; Pereira et al., 2009; present work). Notably, the principal geochemical characteristic of the aforementioned magmatism is their whole-rock calc-alkaline composition which, as indicated above, has to date been associated with a subduction processes (e.g., Pons, 1982; Ribeiro et al., 1995; Sarrionandia, 2005; Moita et al., 2015).

Here, we propose the OMZ Variscan 'calc-alkaline' mafic–felsic plutons were emplaced unrelated to subduction. A 'calc-alkaline' composition may be obtained by mixing between alkaline mafic mantle-derived and peraluminous felsic crustal-derived magma (e.g., Rock, 1991; Prelevic et al., 2004) or melting of either an enriched lithospheric mantle or lower crust (e.g., Liegéois et al., 1998). The mixing model is supported by Bonin (2004), in his classic, extensively

Figure 11.15. Model of the evolution of the Ossa-Morena Zone and the adjacent South Portuguese Zone and Central Iberian Zone, from the Middle Devonian to the Late Carboniferous, modified from Azor et al., (2008) and Simancas et al., (2009). A) First collisional event. B) Early Carboniferous transient extensional/transtensional event when the IBERSEIS Reflective Body was emplaced. C) Transition from extensional/transtensional to the second collisional event when the Burguillos, Valencia and Brovales complexes were emplaced. D) Second collisional event. E) Schematic model explaining the Olivenza-Monesterio antiform magmatism as the product of magma mixing. Note that some plutons were emplaced within pre-existing structures, such as 1. Burguillos del Cerro plutonic complex; 2. The Valencia del Ventoso plutonic complex cuts pre-existing structures and older granitoids; and, 3. The Brovales pluton.

cited, work. He considered the interaction of mafic and felsic magmas from, respectively, mantle and crustal sources in a post-collisional setting.

Mafic-felsic mixing has also been invoked in the formation of other Variscan plutonic complexes in the OMZ, such as Regueros de Monsaraz (Antunes et al., 2010) or the Évora Massif (Moita et al., 2009; Pereira et al., 2015). More broadly, in the Iberian Massif several plutonic complexes show evidence of 'calc-alkaline' hybrid magmatism, for example in both the SPZ (Castro et al., 1991; De la Rosa et al., 1993) and the CIZ (Donaire et al., 1999; Carracedo et al., 2009; Scarrow et al., 2009; Molina et al., 2009; 2012). Similarly, further east in the Variscan, in the Bohemian Massif, Janousek et al., (2004) concluded that mafic-felsic mixing was also an important process in the generation of calc-alkaline rocks.

So, extension resulted in emplacement of the Burguillos del Cerro, Valencia del Ventoso and Brovales plutonic complexes mafic-intermediate bodies related to intraplating of the IRB, which in turn provoked localized crustal melting. The mafic and felsic magmatism is contemporaneous in age although the former is volumetrically more abundant than the latter. In addition, differentiation was apparently an important process in the generation of the OMZ Variscan 'calc-alkaline' rocks.

11.3 Magma Sources and Magmatic Processes Involved in the Ossa-Morena Zone Variscan Magmatism

11.3.1 Magma Sources

To develop a petrogenetic model for hybrid igneous bodies such as the ones considered in this study it is necessary to identify the different magma sources potentially involved in their generation. From our data, combined with that of the literature, three main magmatic sources, two of which are mantle-derived and the other crustal, seem to have participated in the generation of the OMZ Variscan igneous rocks. The heterogenous ultramafic to felsic Burguillos del Cerro and, to a lesser extent, Valencia del Ventoso plutonic complexes reveal most about the individual sources. The Brovales pluton, on the other hand, is apparently a more homogeneous mix of magmas derived from the three sources.

In the three complexes considered, we have recognised two main groups of basic compositions derived from mantle partial melting: the first is subalkaline and tholeiitic; the second is alkaline

11.3.1.1 Tholeiitic Mantle Source

Both Pons (1982) and Sarrionandia (2005) invoked a contribution from a tholeiitic source in the generation of the OMZ Variscan plutons, albeit subduction-modified in the latter case.

Tholeiitic rocks are well represented in the *Central Ultrabasic-Basic Layered Unit* of Burguillos; the only identified occurrence in Valencia is the gabbros of the *Northern Stock in the Subalkaline Basic-Intermediate Unit*; they are absent in Brovales. These subalkaline basic rocks are grouped together as the Ultramafic-Mafic Group (Fig. 11.16).

The *Ultramafic-Mafic Group* samples are CIPW olivine- and hypersthene-normative. Some however are nepheline-normative. The rocks are MgO-rich and are mostly subalkaline although, depending on the classification scheme, some tend towards alkaline (Fig. 11.16A). In the classification of Borodin (1987) they are all tholeiitic (Fig. 11.16). In the 'geochemical fingerprinting' diagrams of Pearce (2008), the Ultramafic-Mafic Group and other OMZ Variscan tholeiites are transitional between N-MORB and E-MORB (Fig. 11.16C and 11.16D). However, they are often displaced from the mante array, perhaps as the result of involvement of a lithospheric component(s) (Fig. 11.16C).

These rocks have low contents of immobile incompatible elements similar to MORB oceanic tholeiites, although Rb, K, Pb and Sr may be locally enriched (Fig. 11.17A). Chondrite-

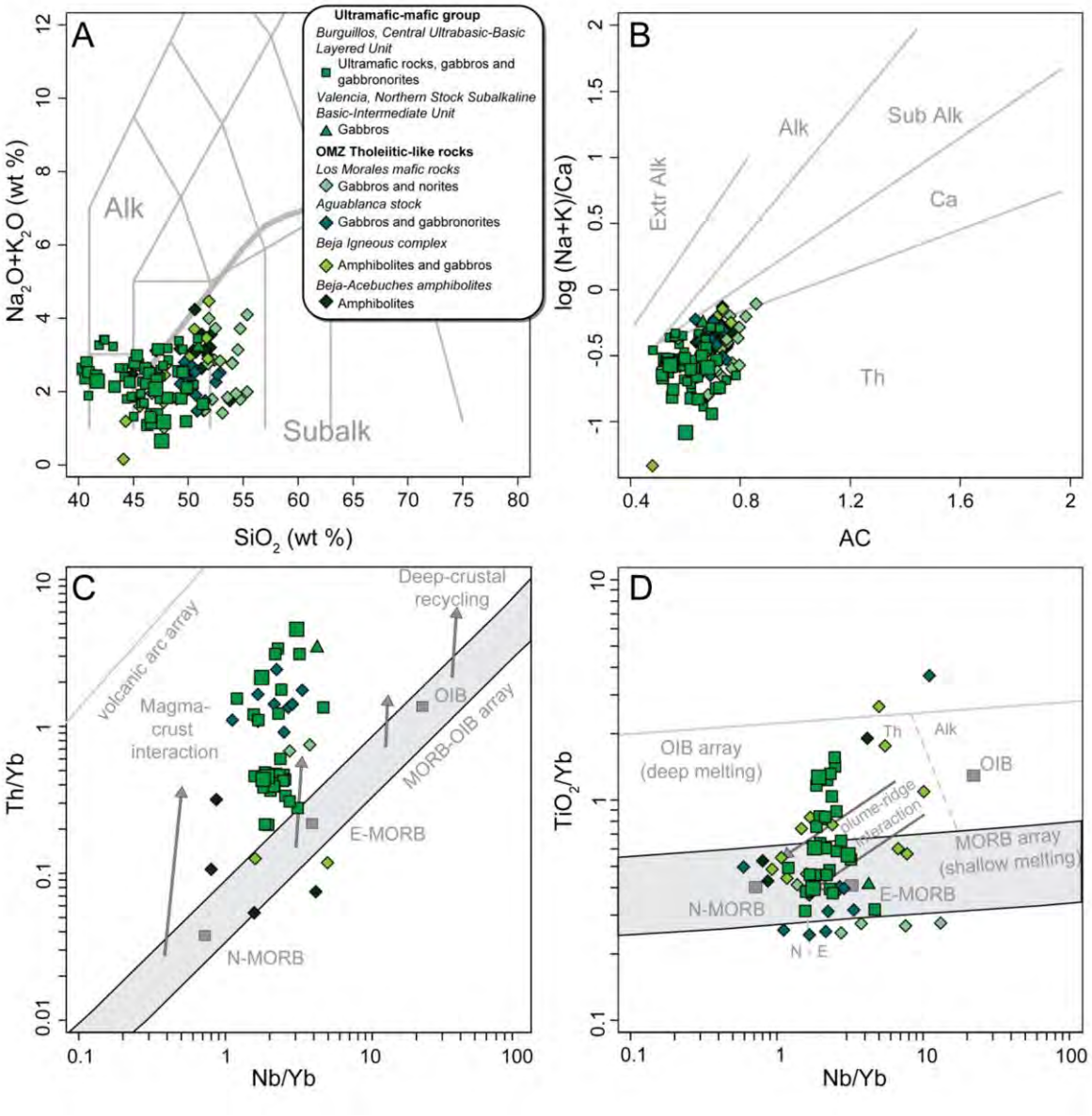

Figure 11.16. Whole-rock compositions of the Ultramafic-Mafic Group and the OMZ Variscan tholeiite-like rocks (Pons, 1982; Castro et al., 1996; El-Hmidi, 2000; Casquet et al., 2001; Piña, 2006; Tornos et al., 2006; Azor et al., 2008; Pin et al., 2008) in: A) the TAS plot (fields from Le Maitre et al., 1989) B) Borodin. (1988) classification diagram, note the sub-alkaline and tholeiite-like features, C) and D) mantle source affinity plots (Pearce, 2008).

normalised REE patterns vary from quite flat, 25 to 60 times chondrite, to enriched in LREE relative to HREE, La_N/Lu_N 0.5-3.6, without appreciable Eu anomalies, Eu/Eu* 0.8-1.2 ($Eu^*=Eu_N/\sqrt{(Sm_N*Gd_N)}$) (Fig. 11.17B).

The *Ultramafic-Mafic Group* also have enriched isotopic values, $^{87}Sr/^{86}Sr_{335\ Ma}$ 0.70524-0.707940, $\varepsilon Nd_{335\ Ma}$ -5.7 to -2.18 and $^{147}Sm/^{144}Nd$ 0.133-0.202 (Fig. 11.18B) with old model ages, 1.3-2.7 Ga, resulting, we suggest, from a lithospheric component(s). In agreement with this the

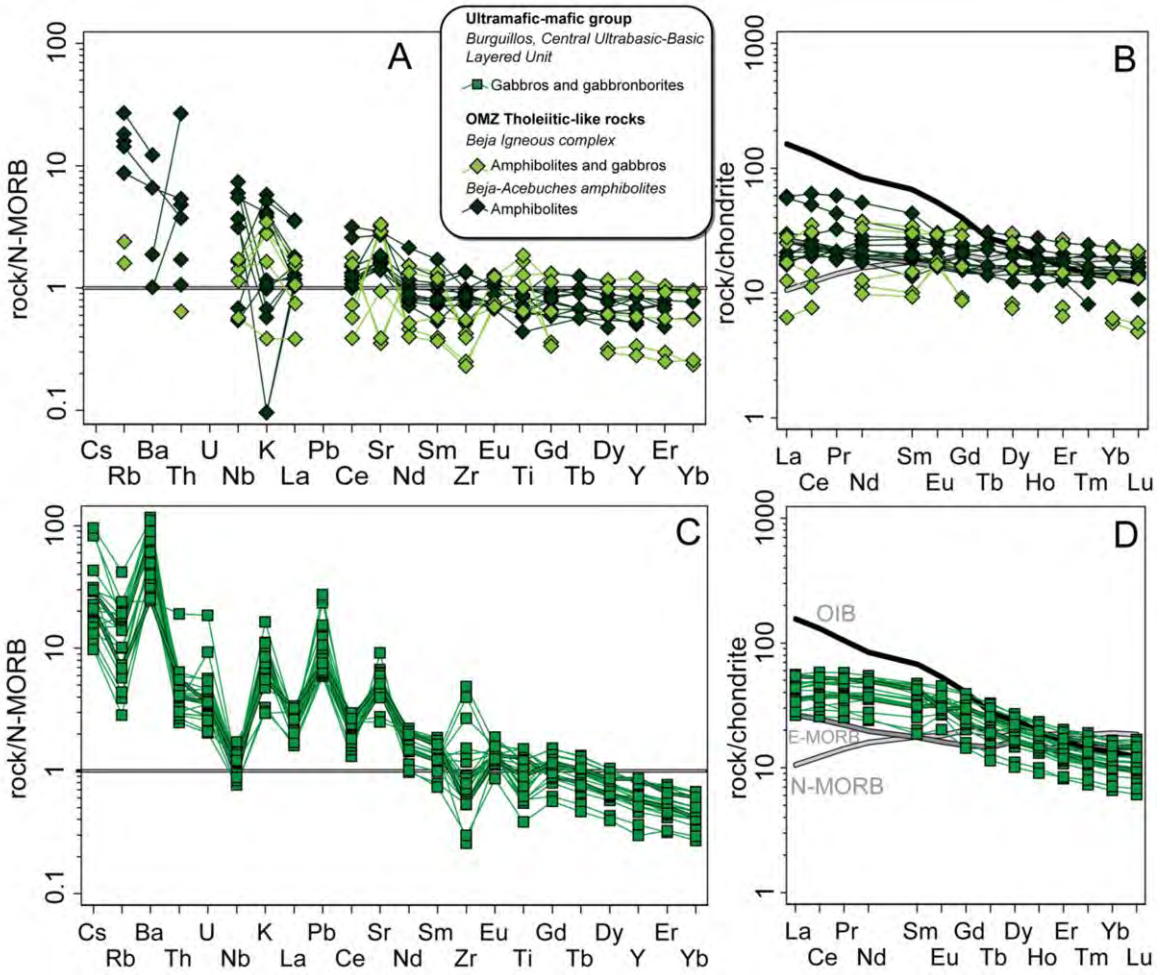

Figure 11.17. N-MORB-normalised and (normalisation values from Hofmann, 1988) and chondrite-normalised diagrams (normalization values from McDonough and Sun, 1995) for: A) and C) the OMZ Variscan tholeiitic-like rocks (Castro et al., 1996; Azor et al., 2008; Pin et al., 2008) and B) and D) the Ultramafic-Mafic Group.

zircon O isotopes measured in a poikilitic amphibole gabbronorite, vary from $\delta^{18}O_{(VSMOW)}$ 5.3 to 7.4, which we interpret to reflect involvement of both mantle and crustal components.

The compositional range of the *Ultramafic-Mafic Group* is similar to other OMZ Variscan tholeiitic magmatic rocks interpreted to have derived from a depleted source, e.g., the Beja Igneous complex mafic rocks (Jesus et al., 2007; Pin et al., 2008) and the Aracena-Acebuches metabasite amphibolites, considered to be metamorphosed N-MORB to T-MORB (Bard, 1969; Munhá et al., 1986; Castro et al., 1996) (Fig. 11.16). Nevertheless, our *Ultramafic-Mafic Group* has some differences compared to the OMZ Variscan tholeiitic magmatism, for example greater enrichment in incompatible elements such as Ba and Pb, although the HFS are comparable (Fig. 11.17C). Differences are also apparent in the chondrite-normalised patterns, LREE are more

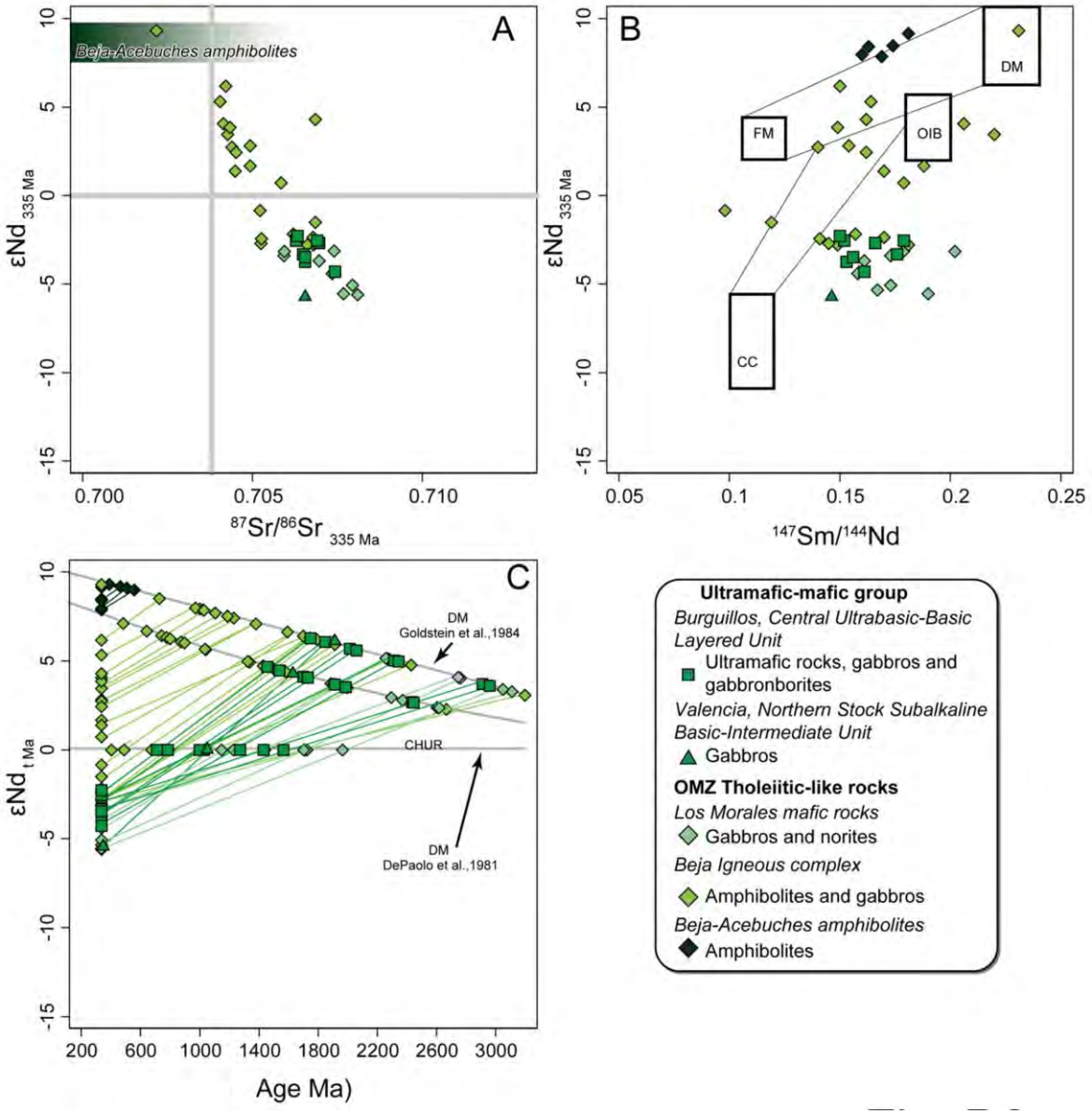

Figure 11.18. Isotope values for the Ultramafic-Mafic Group and the OMZ Variscan tholeiitic-like rocks (Pons, 1982; Castro et al., 1996; El-Hmidi, 2000; Casquet et al., 2001; Piña, 2006; Tornos et al., 2006; Azor et al., 2008; Pin et al., 2008): A) $\varepsilon Nd_{335\ Ma}$ vs $^{87}Sr/^{86}Sr_{335\ Ma}$; B) $\varepsilon Nd_{335\ Ma}$ vs $^{147}Sm/^{144}Nd$, DM, depleted mantle (i.e., MORB-like source); OIB, ocean island basalt source; FM, fertile mantle (derived by 1–7% of partial melting of an OIB source, Swinden et al. 1990); and C) Nd model ages calculated for all rocks using the method of DePaolo, (1981) (T_{DM}) and Goldstein et al., (1984) (T_{CR}). CHUR normalisation taken from DePaolo (1988) and Wasserburg et al. (1981).

enriched relative to HREE, La_N/Lu_N 2.8-5.6, and Eu anomalies are more evident, Eu, Eu/Eu* 0.8-1.4 (Fig. 11.17D).

The isotopic composition of the OMZ Variscan tholeiitic magmatism, varies from primitive to more enriched (Fig. 11.18). Significantly, the Aracena-Acebuches metabasite amphibolites have high, primitive, values of $\varepsilon Nd_{335\ Ma}$ 7.5 to 10, which are in the range of the Beja

Igneous complex mafic rocks (Castro et al., 1996; Casquet et al., 2001; Pin et al., 2008). The model ages of these rocks are similar the age of the protolith, indicating partial melting of a depleted source, *c.* 335 Ma (Fig. 11.18C). Other Beja tholeiitic rocks show evidence of progressive enrichment with $^{87}Sr/^{86}Sr_{335\ Ma}$ 0.700404-0.706847 and $\varepsilon Nd_{335\ Ma}$ 6.18 to -5 (Fig. 11.18A) and model ages that vary from 0.5-2.6 Ga (11.18C). Pin et al. (2008) interpreted this variation as the result of crustal contamination of the tholeiitic magmas.

Experimental petrology, trace element modelling and isotope data all indicate that tholeiitic magmas are produced by low-pressure, relatively high-degree melting of normal, depleted to slightly enriched, asthenospheric mantle (e.g., Jaques and Green, 1980). When such melting occurred in the OMZ is contrained by the Beja-Acebuches T-MORB composition amphibolites, *c.* 335 Ma (Munhá et al., 1986; Castro et al., 1996), dated at 330-340 Ma, U-Pb SHRIMP (Azor et al., 2008).

11.3.1.2 Alkaline Mantle Source

Sarrionandia (2005) attributed the production of a volumetrically minor alkaline component in the Valencia del Ventoso complex to melting of a metasomatised spinel-bearing hydrated mantle lithosphere. The lack of HREE depletion having led him to exclude garnet as a residual source phase. In agreement with this Casquet and Galindo (2004) considered that the main source of the Variscan post-collisional, high-K, magnesian calc-alkaline magmatism was the metasomatised, so by inference lithospheric, subcontinental mantle. Nonetheless, defining the alkaline source using regional comparison, as done above for the tholeiite composition, and reconciling it with that component is more difficult.

Alkaline rocks are an important part of the *Central Alkaline Basic-Intermediate Layered and Acid Unit* of Burguillos and the *Main Pluton Alkaline to Subalkaline Basic-Acid Unit* of Valencia (Fig. 11.19A). Together they form the *Alkaline Group*.

The petrography and mineral chemistry of the *Alkaline Group* attest to their alkaline nature: diopsidic clinopyroxene, high-Ti pargasite and magnesiohastingsite, abundant biotite, and apatite and, in the more evolved rocks, meso-perthites. The rocks are Ne-normative with basic alkaline, high-K to ultra-high K compositions (Fig. 11.19A). In the Pearce (2008) diagrams, this group is transitional between N-MORB and E-MORB like the tholeiitic *Ultramafic-Mafic Group* but is displaced towards more alkaline compositions (Fig. 11.19C and 11.19D). The rocks are LREE-enriched relative to HREE, La_N/Lu_N 4.8-16.8, and lack a more pronounced depletion in Nb relative to Ta in normalised diagrams (Fig. 11.20; see Fig., GC5). *The Alkaline Group* may be divided in two subgroups on the basis of Eu anomaly, Eu/Eu*, the first subgroup has a marked

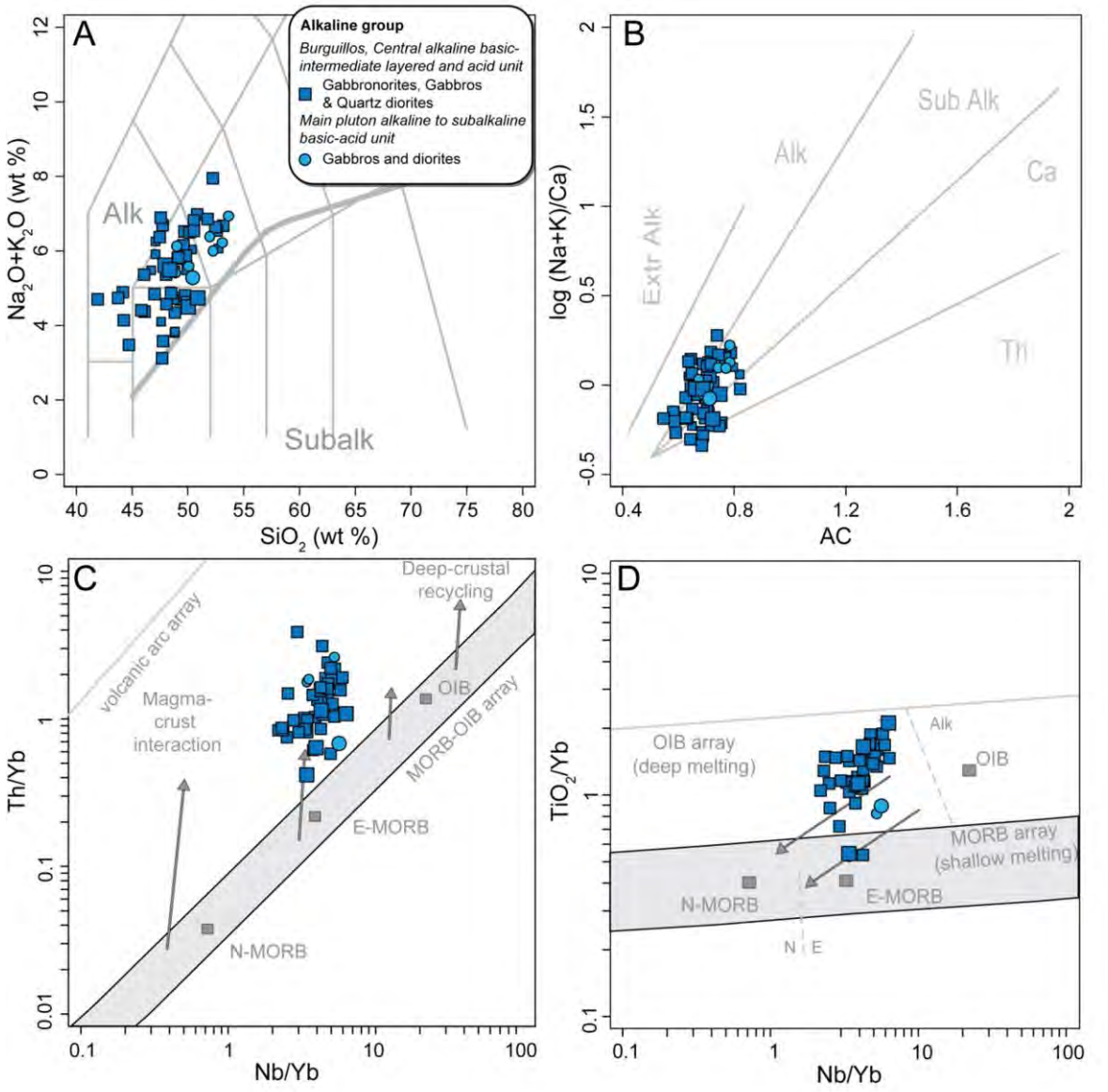

Figure 11.19. Whole-rock composition of the Alkaline Group including data from the present work and from Sarrionandia (2005) and Pon, (1982), in: A) the TAS plot (fields from Le Maitre et al., 1989); B) Borodin. (1988) classification diagram; C) and D) mantle source affinity plots (Pearce, 2008).

a positive anomaly, Eu/Eu* 1.2-4.2, the second has a variable negative anomaly, Eu/Eu* 0.5-0.9 (Fig. 11.20). These differences are the result of plagioclase accumulation which will be considered in section 11.3.2.2.1.

The *Alkaline Group* has elevated $^{87}Sr/^{86}Sr_{335Ma}$ between 0.705895 to 0.707223, εNd_{335Ma} -3.8 to -1.2 and Nd model ages of 1.0 to 1.4 Ga remarkably older than their zircon crystallisation ages (Fig. 11.21). These values, inconsistent with mantle-derived rocks, may reflect an anomolous source composition or a mixed mantle-crustal signature. Deciphering these two posibilities is a difficult question that may not have a simple answer: to what extent does the isotopic enrichment

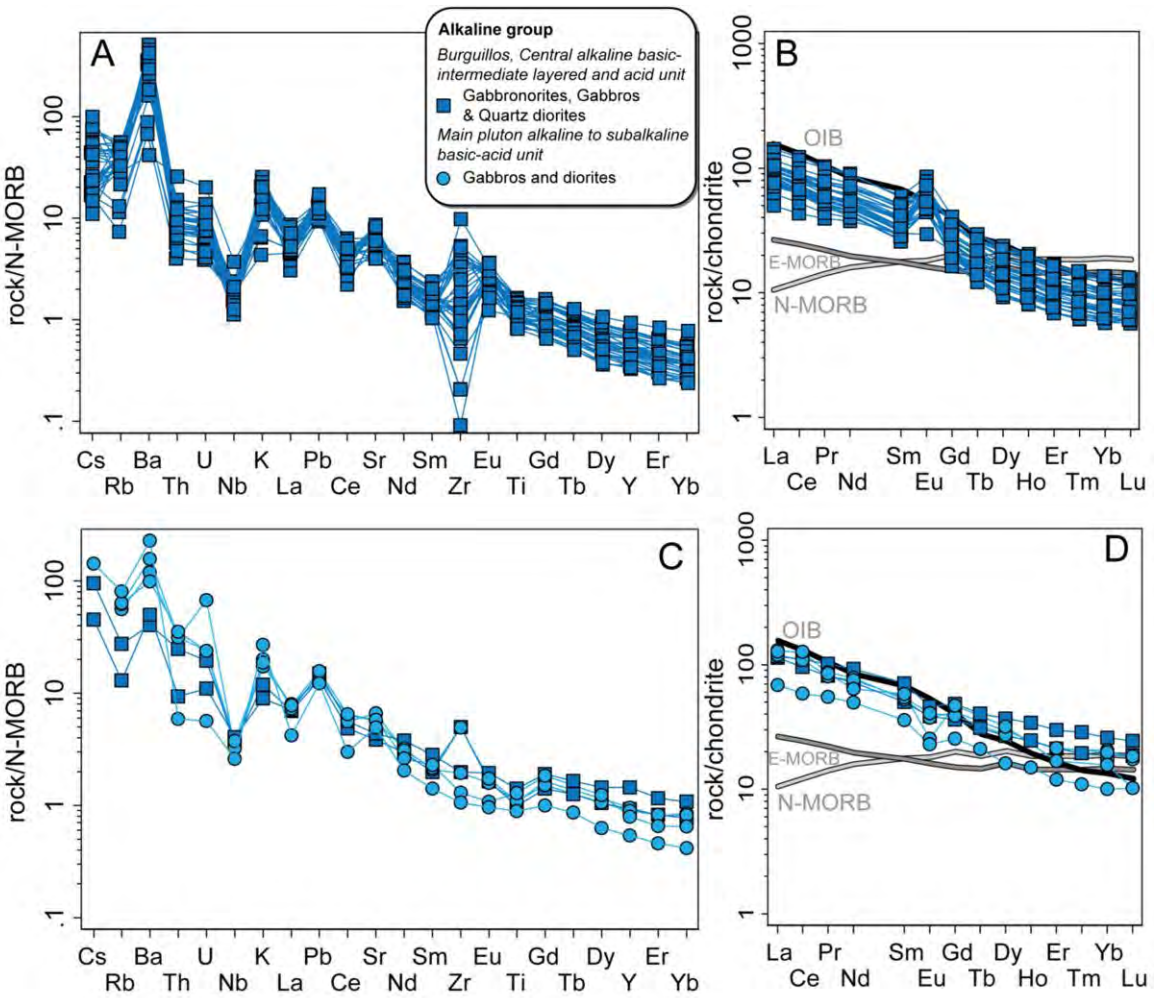

Figure 11.20. N-MORB-normalised (normalisation values from Hofmann, 1988) and chondrite-normalised diagrams (normalisation values from McDonough and Sun, 1995) for the Alkaline Group including data from the present work and from Sarrionandia (2005).

result from temporal evolution of an enriched mantle component, crustal contamination of a mantle-derived melt, or a combination of both? This is addressed in section 11.3.2.2.3 below. As in the tholeiites, the zircon O isotopes measured in a diorite and alkali felspar granite vary from mantle to crustal values $\delta^{18}O_{(VSMOW)}$ 5.4 to 8.0.

Pilet et al., (2008) presented a model limiting alkaline magma production to the lithosphere. They deduced that enrichment resulted from melting of metasomatic volatile- and alkali-rich amphibole veins, frozen low-degree melts, that would be unstable in the asthenosphere (see below, section 11.3.3). This is in agreement with the suggestion of involvement of recycled, metasomatised lithospheric mantle in alkaline magma production (e.g., Lloyd and Bailey, 1975; Sun and Hanson, 1975). These models eliminate the necessity for subduction-related recycled enriched components such as ocean crust and sediment in the alkaline source (e.g., Hofmann, 1997).

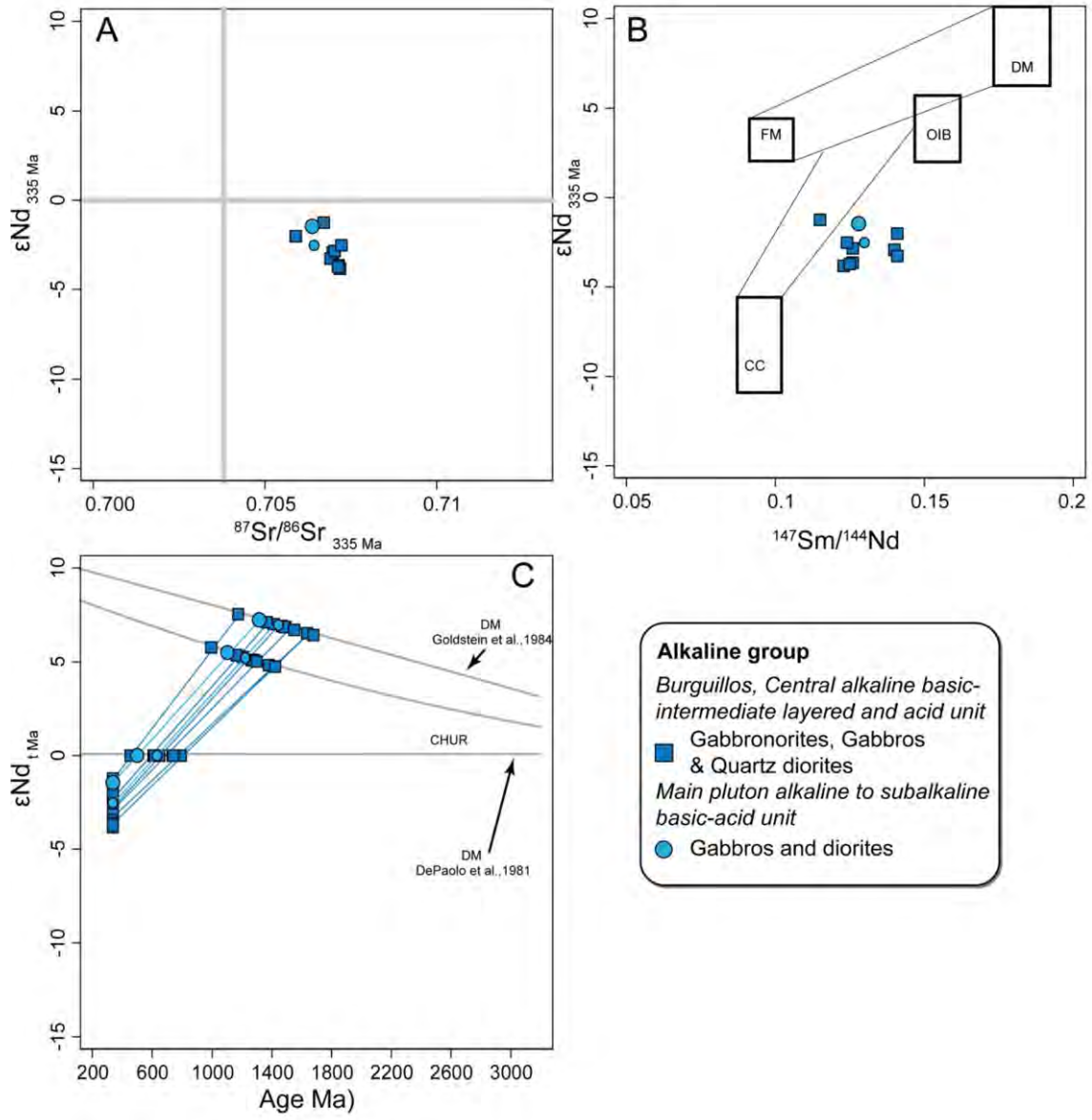

Figure 11.21. Isotope values of the Alkaline Group include data from present work and from Sarrioanadia (2005); A) $\varepsilon Nd_{335\,Ma}$ vs. $^{87}Sr/^{86}Sr_{335\,Ma}$, B) $\varepsilon Nd_{335\,Ma}$ vs.$^{147}Sm/^{144}Nd$, DM, depleted mantle (i.e. MORB-like source); OIB, ocean island basalt source; FM, fertile mantle (derived by 1–7% of partial melting of an OIB source Swinden et al. 1990). and C) Nd model ages calculated for all rocks using the method of DePaolo, (1981) (T_{DM}) and Goldstein et al., (1984) (T_{CR}). CHUR normalisation according to DePaolo (1988) and Wasserburg et al. (1981).

Notably, the OMZ mafic-intermediate rocks contain hydrous, F- and Cl-rich ferromagnesian minerals, biotite and amphibole (see Chapter 7). These characteristics are consistent with their production by melting of a hydrated metasomatised mantle lithosphere source.

The timing of Variscan alkaline magma production in the OMZ is constrained, to a great extent, by our new *c.* 335 Ma age for a diorite and an alkaline feldspar granite from the Burguillos, Central Alkaline Basic-Intermediate Layered and Acid Unit.

11.3.1.3 Crustal Source

Crustal melting, related both temporally and spatially to the aforementioned high-T low-P metamorphic event was a third source of magma.

The crustal component is clearly identifiable in the Burguillos two-mica granites and aplites, and, to a lesser extent, in the Valencia aplites. Together these rocks form the *Peraluminous Group* (Fig 11.22). Other OMZ examples of crustal-derived rocks include the two-mica granites and aplites from Évora Massif and the Beja Igneous complex (Fig. 11.22, Pin et al., 2008; Pereira

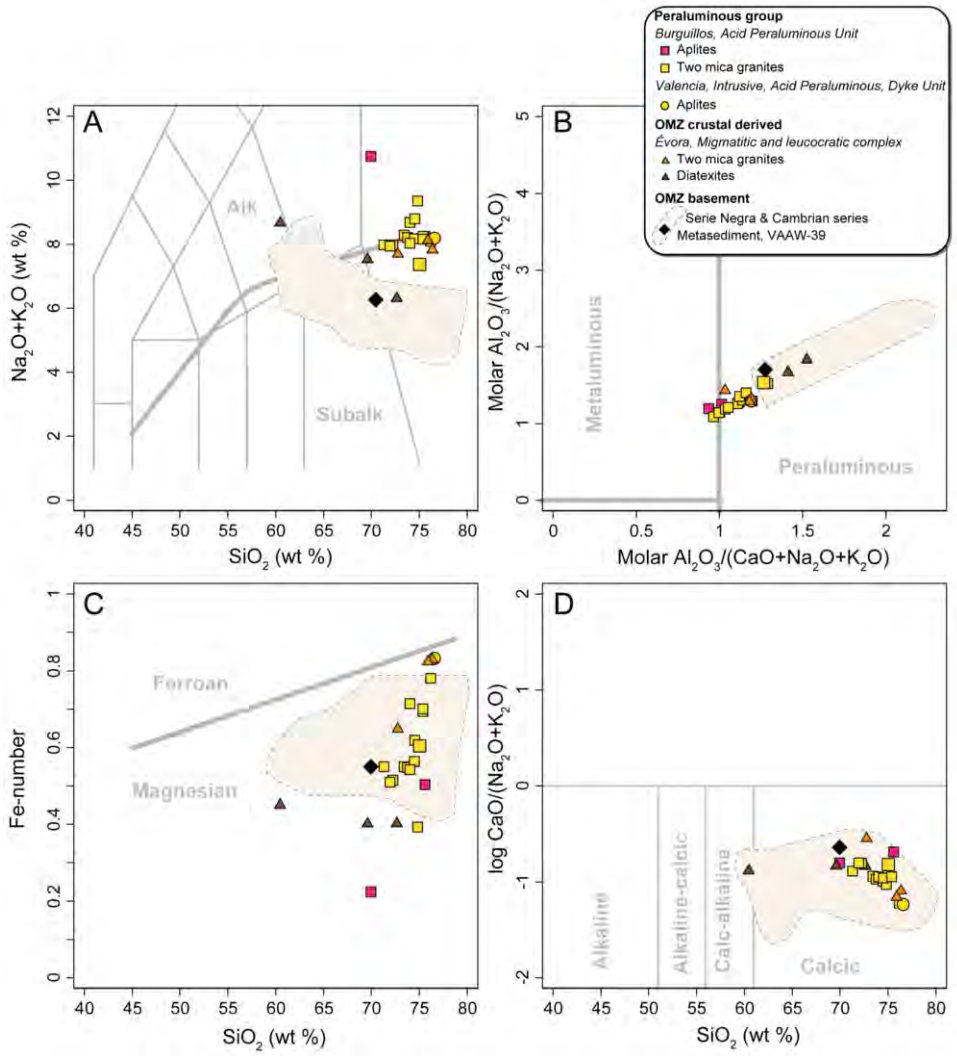

Figure 11.22. Whole-rock composition of the Peraluminous Group and comparable OMZ Variscan crustal-derived rocks (Pereira et al., 2008; Moita et al., 2009) and representative data of the OMZ basement (Schäfer, 1990; López-Gijarro et al., 2006; Pereira et al., 2006) in: A) the TAS plot (fields from Le Maitre et al., 1989); B) Molar (Al_2O_3/ (Na_2O+K_2O)) vs. molar (Al_2O_3/ (CaO+Na_2O+K_2O)); C) Fe-number vs. SiO_2 plot (Frost et al., 2001); and, D) Peacock (1931) diagram.

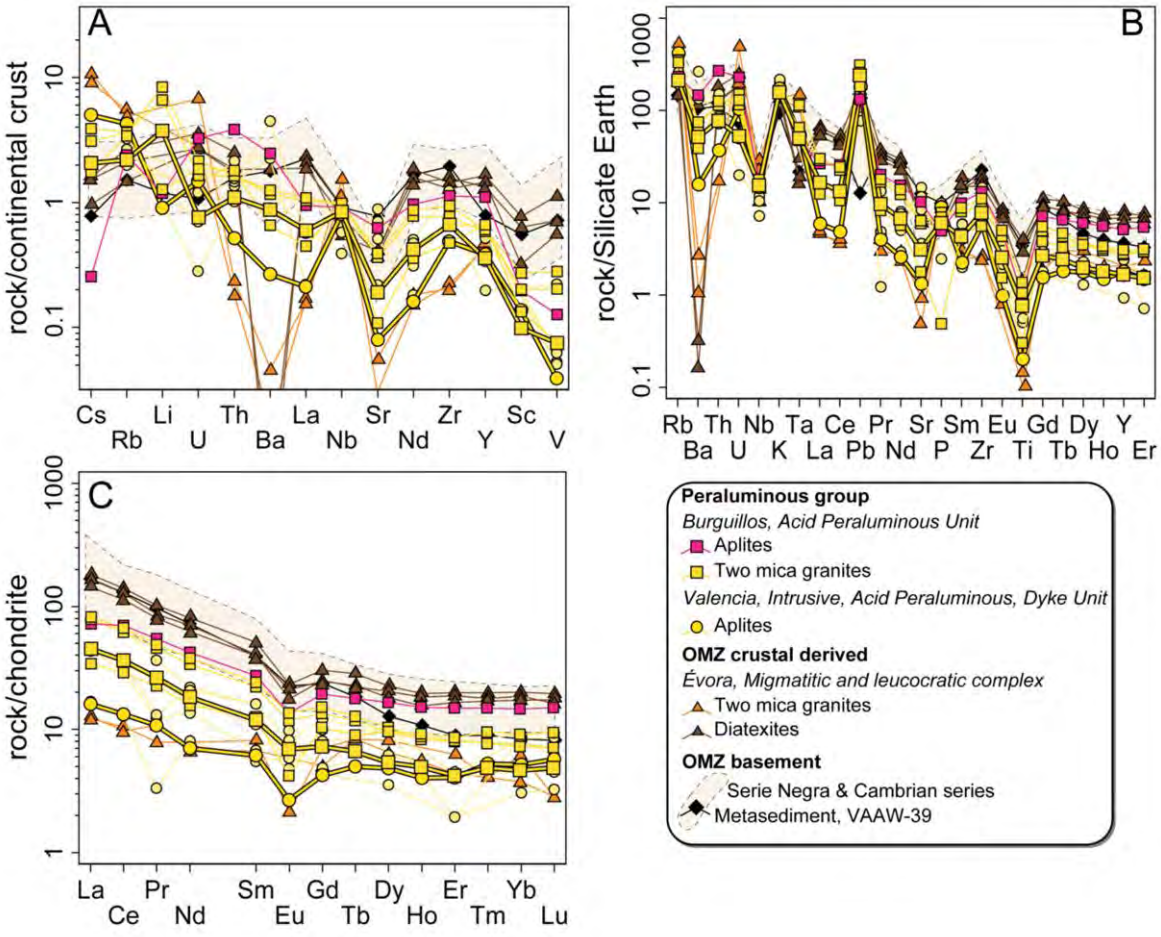

Figure 11.23. The Peraluminous Group: A) Continental crust-nomalised trace elements plots (normalisation values of Rudnick and Fountain, 1995); B) Silicate Earth-normalised trace element plots; and, C) chondrite-nomalised REE plots (normalisation values of McDonough and Sun, 1995) The grey field represents the composition of the OMZ basement (Schäfer, 1990; López-Gijarro, 2006; Pereira et al., 2006) and other OMZ crustal-derived rocks (data source: Moita et al., 2009).

et al., 2009; Moita et al., 2009).

All the *Peraluminous Group* rocks contain primary-looking muscovite and rare cordierite, thus being corrundum-normative. The rocks have peraluminous compositions (Fig. 11.22A and 11.22B). In the classification scheme of Frost et al. (2001) they are magnesian and according to Peacock (1931) calcic (Fig. 11.22C and 11.22D). Their major element compositions are typical of crustal-derived S-type magmas (e.g., Barbarin, 1999; Frost et al., 2001; Montero et al., 2009) (Fig. 11.22).

Rocks included in the *Peraluminous Group* show marked enrichments in alkali elements, especially Li; and negative Sr anomalies (Fig. 11.23A). In silicate Earth-normalised diagrams the two-mica granites have negative anomalies in Ba, Nb, Sr, P and Ti and positive anomalies in U, K and Pb, the latter being typical of a crustal-derived signature (Fig. 11.23B). The chondrite-

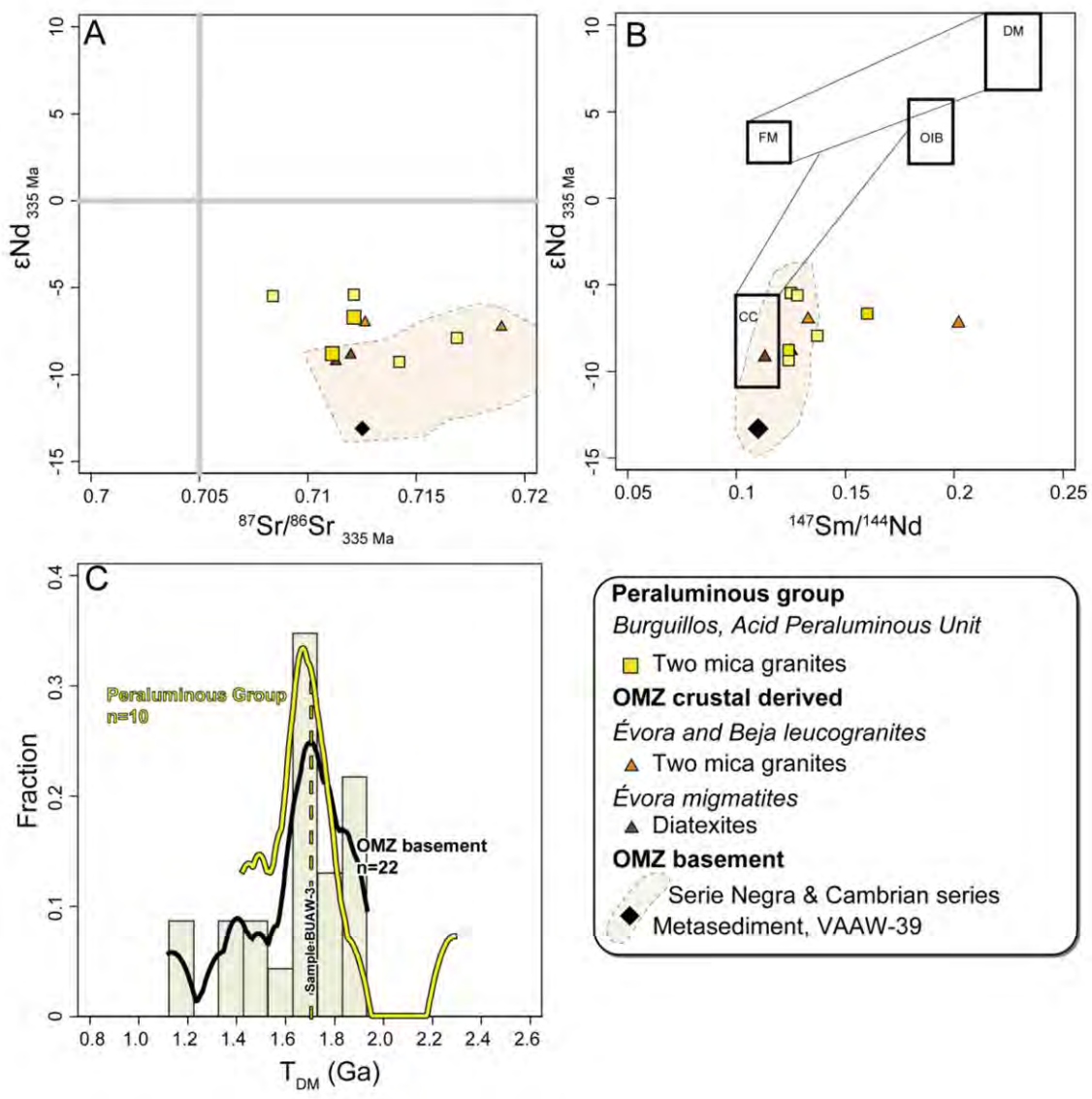

Figure 11.24. Isotope values for the Peraluminous Group including data from the present work and from Bachiller, (1996), other OMZ crustal-derived rocks (Pin et al., 2008; Moita et al., 2009) and the OMZ basement (Casquet et al. 2001; Casquet and Galindo, 2004): A) $\varepsilon Nd_{335\ Ma}$ vs $^{87}Sr/^{86}Sr_{335\ Ma}$; B) $\varepsilon Nd_{335\ Ma}$ vs.$^{147}Sm/^{144}Nd$, DM - depleted mantle (i.e. MORB-like source); OIB - ocean island basalt source; FM - fertile mantle (derived by 1–7% of partial melting of an OIB source Swinden et al. 1990); and, C) Nd model age density distribution of Peraluminous Group and other coeval crustal-derived rocks (Bachiller, 1996; Pin et al., 2008; Moita et al., 2009) compared with the histogram and density distribution of the OMZ basement Nd model ages (Schäfer, 1990; Casquet et al., 2001; Chichorro et al., 2008; López-Guijarro et al., 2008). Note that the two distributions are centred at 1.7-1.8 Ga.The Nd model ages were calculated based on the method of DePaolo, (1981) (T_{DM}). CHUR normalisation was according to DePaolo (1988) and Wasserburg et al. (1981).

normalised REE patterns of the OMZ metasedimentary basement-like diatexitic compositions are parallel with those of the evolved, crustal-derived two-mica granites and aplites, the latter albeit with lower values (Fig. 11.23C).

The *Peraluminous Group* rocks have elevated $^{87}Sr/^{86}Sr_{335\ Ma}$ 0.708375-0.716912 and low $\varepsilon Nd_{335\ Ma}$ -10 to -5, an isotopic composition that overlaps with OMZ basement and other crustal-derived rocks (Fig. 11.24A and 11.24B). In addition, they have Nd model ages of 2.3-1.4 Ga centred at *c.* 1.7 Ga (Fig. 11.24C), which correlate with OMZ crustal-derived rocks and, significantly, the distribution of clusters in OMZ basement ages (Fig. 11.24C). We suggest, therefore, that the *Peraluminous Group* rocks had an OMZ basement, Serie Negra, source.

The U-Pb SHRIMP age of the Valencia aplite, 329±7 Ma, marks the timing of crustal melting. In the two-mica granite from the Burguillos, on the other hand, the only Variscan ages obtained were from thin U-rich low-cathodoluminescent overgrowth rims in just two zircons: 305±4 Ma and 317±3 Ma, whihc are probably too low because of Pb-loss. Field relations, however, reflect clear syn-plutonic intrusive interaction between the *Acid Peraluminous Unit* and other Burguillos units dated at *c.* 335 Ma (see Chapter 9). Furthermore, other OMZ crustal-derived granites, e.g., Arriolos, have an age of 337±4 (U-Pb SHRIMP, Pereira et al., 2009) (Fig. 11.25A). This suggests that the *Peraluminous Group* rocks are coeval with the main OMZ Variscan mafic magmatism, accordingly, these rocks fit a Rb-Sr WR *c.* 330 Ma slope (Fig. 11.25B).

The *Peraluminous Group* rocks also contain abundant pre-magmatic zircons: Archean to Paleoproterozoic; Neoproterozoic Tonian and, mainly, Ediacaran, *c.* 600 Ma; and, some lower Cambrian ages. Mesoproterozoic ages are notably absent. This distribution clearly correlates with OMZ basement zircon age distribution (Fig. 11.25A) and other OMZ crustal-derived granites (e.g., Pereira et al., 2008; 2009). The main Ediacaran grains could be from Cadomian-arc magmatism, 620-570 Ma, which is considered to be the Serie Negra metasedimentary basement source (Fig. 11.25A).

The older pre-magmatic zircon oxygen isotope values from the Burguillos *Acid Peraluminous Unit* two-mica granites all reveal both mantle and crustal components, 5.5-6.9 $\delta^{18}O_{(VSMOW)}$ (Fig. 11.25C). The more abundant Cadomian Ediacaran zircons have a broader range of $\delta^{18}O_{(VSMOW)}$ compositions of 4.30 ± 0.05 to 8.28 ± 0.11 (Fig. 11.25C). These data fit with the $\delta^{18}O_{(VSMOW)}$ 4-10 range measured in OMZ Serie Negra detrital and inherited zircons (Chichorro et al., 2014) and most likely reflects source crustal recycling and crust–mantle interactions (cf., Valley et al., 2005). The abundant pre-magmatic zircons preserved in the Peraluminous Group rocks and in comparable OMZ granites (Pereira et al., 2009) are consistent with a low melt-fraction

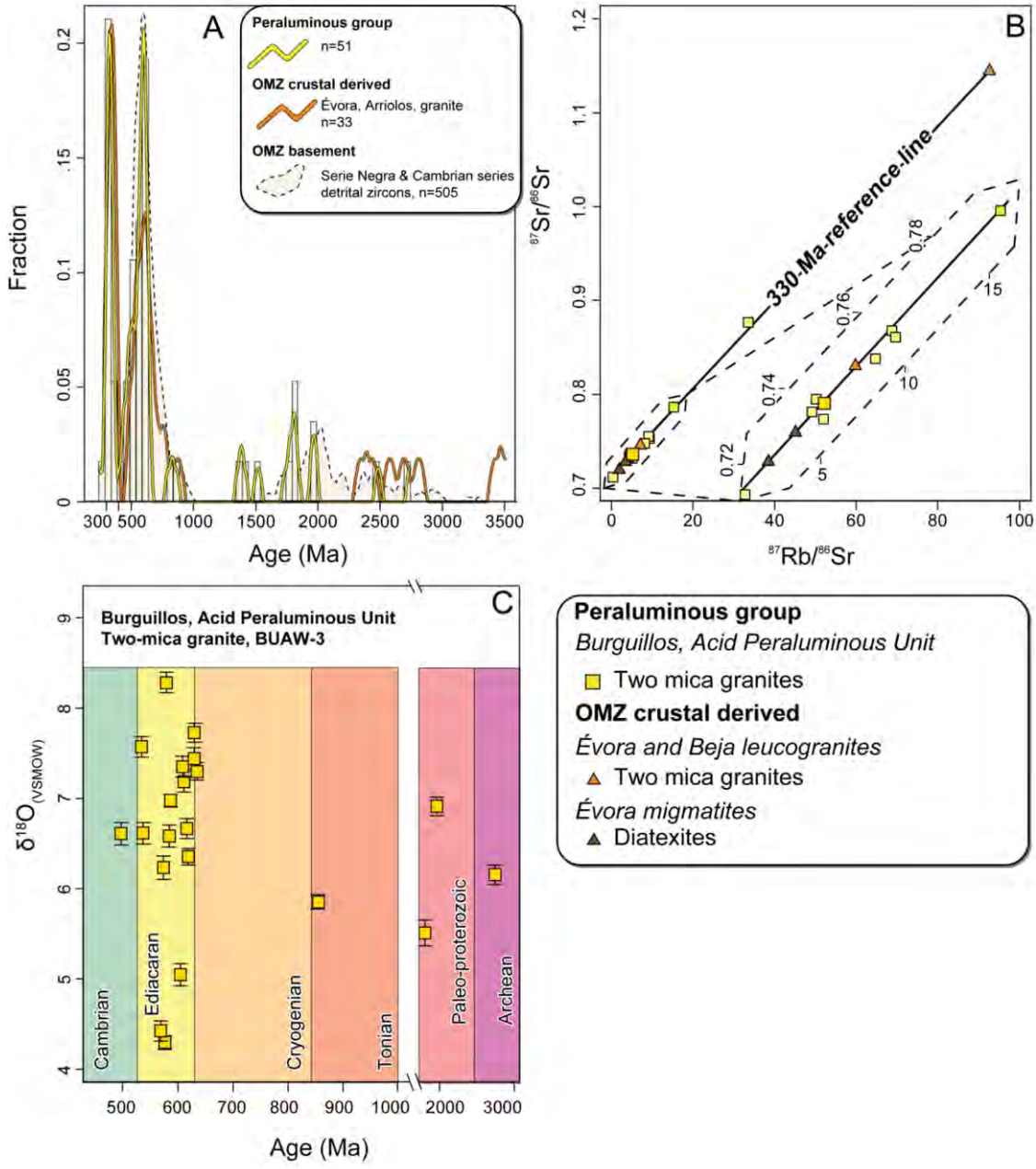

Figure 11.25. A) Frequency and density distribution of Peraluminous Group U–Pb SHRIMP ages other coeval crustal-derived granites (Arriolos granite, Pereira et al., 2008; 2009) and, a field, the OMZ basement detrital zircons (Schäfer et al., 1993; Ordoñez-Casado, 1998; Fernández-Suárez et al., 2002; Linnemann et al., 2008; Pereira et al., 2010a; 2010b; 2011; 2012b). Note that the two-mica granite and aplite pre-magmatic zircon age distribution matches the OMZ basement pattern; B) $^{87}Rb/^{86}Sr$ vs $^{87}Sr/^{86}Sr$ diagram with a reference line at c. 330 Ma (errochron obtained by Bachiller et al., 1997). Note that the Peraluminous Group (shadow symbols from Bachiller, 1996) and other coeval crustal-derived rocks (Pin et al., 2008; Moita et al., 2009) fit with this reference age. C) SHRIMP zircon O isotope compositions of the Peraluminous Group two-mica granite.

migmatisation process (cf., Bea, 1991; Montero et al., 2004; Bea et al., 2007). Coalescence of such low degree melts above the critical melt percentage (cf., Arzi, 1978; Wickham, 1987) into small reservoirs would have led to pre-magmatic zircon preservation rather than new grain crystallisation (Montero et al., 2004; Bea et al., 2007).

11.3.2 Magmatic Processes

Considering the petrological, mineral chemistry and whole-rock compositional data in the context of the mantle and crustal sources identified, at least three interaction processes are evident:

i. Mixing and mingling
ii. Accumulation
iii. Fractional crystallisation

11.3.2.1 Evidence for Mixing and Mingling

11.3.2.1.1 Mafic Mixing

Regarding the mantle-derived magmas, mixing occurred between the tholeiitic and alkaline compositions. The best examples of this process are found in the Burguillos *Central Ultrabasic-Basic Layered Unit* and *Central Alkaline Basic-Intermediate Layered and Acid Unit*, components of the *Ultramafic-Mafic and Alkaline Groups* respectively.

The results of our thermobarometric calculations (see Chapter 10) for these two groups indicate, within error, that they all crystallised at mid-crustal levels, *c.* 4 kbar, at around 800-900ºC. The observed mineralogical and compositional variations cannot, therefore, be attributed to P-T variations, but instead reflect real differences in the composition of the liquid from which they crystallised.

11.3.2.1.1.1 Petrographic and Mineral Chemistry Evidence for Mixing

Petrographically the mafic rocks from the *Ultramafic-Mafic and Alkaline Groups* are quite different (see Chapter 6). The most obvious distinction is the predominance of amphibole in the former and of biotite in the latter. The relative proportions of the two phases varies from rocks in which the only ferromagnesian phase is poikilitic amphibole to those in which it is biotite. Nonetheless, a gradation is evident, the *Ultramafic-Mafic Group* contains some gabbronorites with both poikilitic amphibole and biotite and the *Alkaline Group* includes some amphibole gabbros.

Clinopyroxene was an early crystallisation phase. In the *Ultramafic-Mafic Group* rocks the clinopyroxene is transitional between alkaline and subalkaline (Fig. 7.4). In the *Alkaline Group* gabbros with biotite, it has a clear alkaline affinity. Notably, the amphibole gabbros from the

Alkaline Group have two generations of clinopyroxene: one with a subalkaline affinity, the other being markedly alkaline (Fig. 7.4).

As in the case of the clinopyroxenes, the *Ultramafic-Mafic Group* amphiboles are transitional between alkaline and subalkaline whereas the *Alkaline Group* amphiboles are mainly alkaline. Molina et al., (2009) established a relationship between K_2O and Na_2O/K_2O amphibole/liquid partitioning. Their equation permits the use of mineral compositions to determine, for a given value of SiO_2, the concentration in Na_2O and K_2O of the liquid in equilibrium with the crystallising amphibole (Fig. 11.26 and 11.27). Data in Appendix VI.

Applied to our case we found that all the Ti-rich amphibole cores of the *Ultramafic-Mafic Group* rocks are in equilibrium with liquid compositions with high, alkaline, Na_2O+K_2O liquid contents (Fig. 11.26A and 11.26B). The Ti-poor amphiboles, by contrast, have variable alkaline to subalkaline Na_2O+K_2O, liquid compositions, (Fig. 11.26A y 11.26B).These results fit well with those deduced from the mineral chemistry characteristics.

In the *Alkaline Group*, the true biotite- and clinopyroxene-bearing gabbros, in which amphibole is a minor, or often absent, phase have high, alkaline, Na_2O+K_2O liquid contents, (Fig. 11.26C). The amphibole in the *Alkaline Group* 'transitional' amphibole gabbros on the other hand has moderate Ti, and corresponding lower, transitional alkaline-subalkaline Na_2O+K_2O liquid values (Fig. 11.26C).

It is noteworthy that calculation of the $Na_2O + K_2O$ of the liquid in equilibrium with the amphibole is the same as the measured whole-rock values in the *Alkaline Group* (Fig. 11.26). The *Ultramafic-Mafic Group* whole-rock measured Na_2O+K_2O are slightly different from the calculated values (Fig. 11.26).

The data evidence that the *Ultramafic-Mafic Group* amphiboles crystalllised in two contrasting compositional environments: i. alkaline Ti-rich, cores ii. subalkaline Ti-poor, rims and individual crystals. Remarkably, the *Alkaline Group* transitional amphibole gabbros show these same variations.

Biotite formed in the early stages of crystallisation, its textural relationship with amphibole indicates that it formed first in the mafic rocks of both the *Ultramafic-Mafic Group* and *Alkaline Group*. It is a diagnostic mineral in the gabbros of the *Alkaline Group*, characterised by high Ti content (0.7-0.8 a.p.f.u., 22 O) and relatively low Si+Al (7.8-8 a.p.f.u., 22O). In the gabbros and gabbronorites of the *Ultramafic-Mafic Group*, though, it is a minor phase with lower Ti (0.6-0.7 a.p.f.u., 22 O) and higher Si+Al (7.9-8.1 a.p.f.u., 22 O). The phlogopites in the ultramafic rocks of the *Ultramafic-Mafic Group* have lower Ti still (0-0.2 a.p.f.u., 22 O) and even higher Si+Al

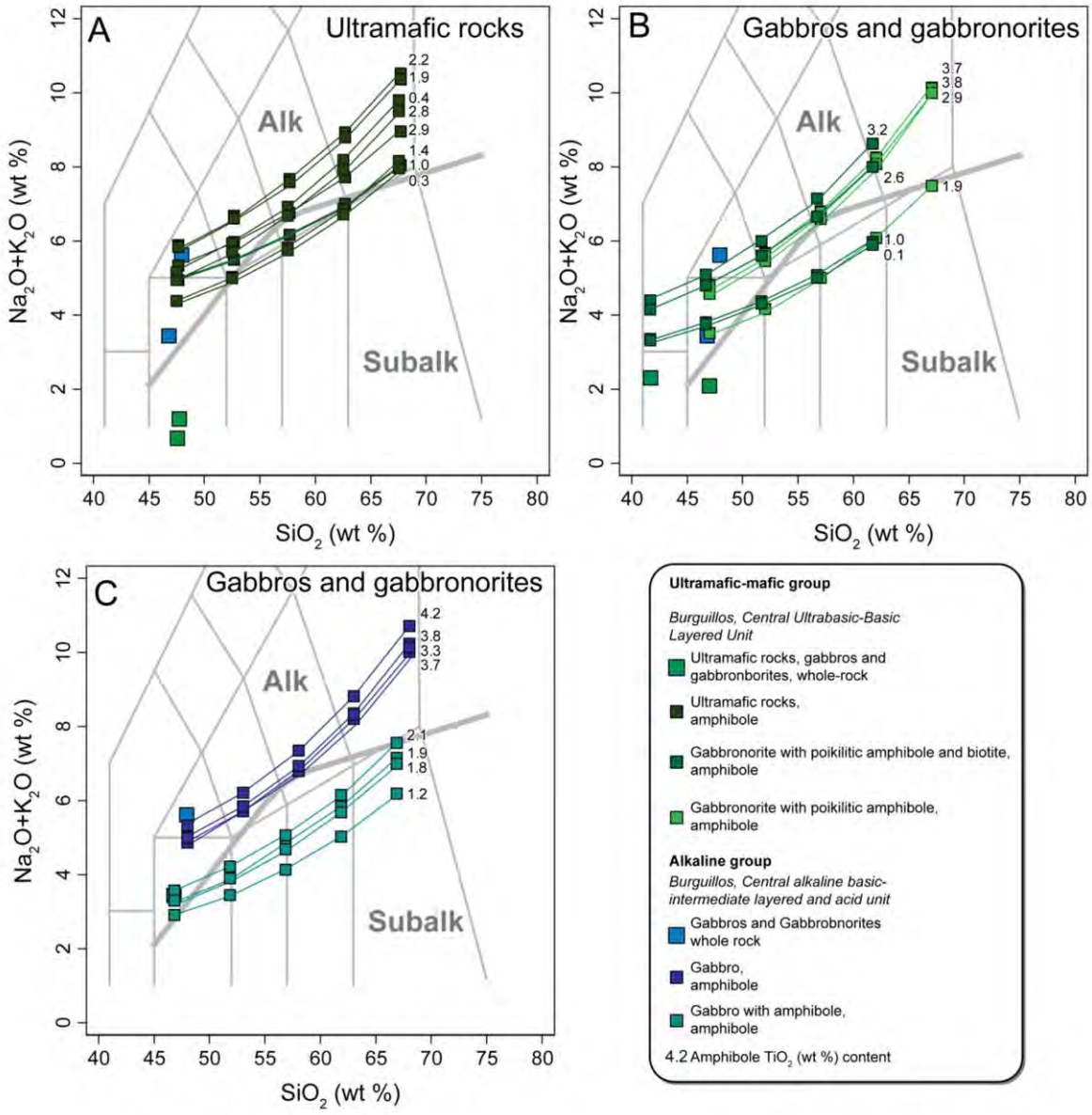

Figure 11.26. Melt compositions as a function of melt silica content calculated from representative amphibole compositions, over a SiO_2 range from the whole-rock composition to 20 % more. Kd values used in the calculations from Molina et al., (2009). Results were plotted in the TAS diagram (fields from Le Maitre et al., 1989): A) and B) Ultramafic-Mafic Group; and, C) Alkaline Group mafic rocks. Numbers indicate the amphibole TiO_2 (wt %) content.

(8.1-8.3 a.p.f.u., 22O). Higher Ti and, particularly, a more marked deficiency in Si+Al cation saturation in the tetrahedral layer of the biotites indicate a change from subalkaline to alkaline compositions (cf, Mitchell and Bergman, 1991).

Plagioclases in the gabbros *s. s.* of the *Alkaline Group* are clean and untransformed or altered and have a homogeneous composition, An_{50-60}. In contrast to this, the amphibole gabbros of that same group and the gabbros and gabbronorites of the *Ultramafic-Mafic Group* have patchy

disequilibrium textures and two stages of growth: second phase bytownite An_{70-90} rimming earlier formed cores of labradorite An_{50-70}, as was seen in the plagioclase of the gabbros of the *Alkaline Group*.

This compositional variation reveals that the less calcic plagioclase, labradorite, crystallised from more alkaline magmas, those that gave rise to the *Alkaline Group*. These more sodic compositions were in disequilibrium in the *Ultramafic-Mafic Group* magma, from which bytownite formed. The An_{50-60} composition is typical for liquidus plagioclase in alkali basalts, whereas plagioclases crystallised from tholeiitic magmas tend to be more Ca-rich bytownite (Smith and Brown, 1988).

11.3.2.1.1.2 Whole-Rock Composition Evidence for Mixing

The *Ultramafic-Mafic Group* are richer in MgO and CaO but poorer in Al_2O_3, K_2O and P_2O_5 than the *Alkaline Group* gabbros (See Chapter 8) as was reflected in the mineral associations. The Burguillos amphibole gabbros *s. s.* mark a transition from the *Ultramafic-Mafic* to *Alkaline Group*. Despite these differences all these rocks are generally quite similar isotopically which suggests a common source. Although the *Ultramafic-Mafic Group* have higher $^{147}Sm/^{144}Nd$ and so older Nd model ages. Modelling of magma mixing is considered in detail below in section 11.3.2.2.3.

11.3.2.1.2 Mafic-Felsic Mixing

11.3.2.1.2.1 Field Evidence

Field relations reveal extensive interaction, mingling, of mafic, intermediate and felsic magmas (see Chapter 4, Fig. 4.5, 4.6 and 4.10). Hybridisation is particularly evident in the Burguillos *External Subalkaline Intermediate Unit* and between the *Central Alkaline Basic-Intermediate Layered and Acid Unit* and the *Acid Peraluminous Unit*. In Valencia the mingling is observed in the *Main Pluton Alkaline-Subalkaline Basic-Acid Unit*. In Brovales interaction exists between dioritic enclaves and the *Central Subalkaline Intermediate Unit* and also between the granodiorite facies of the *Intermediate Subalkaline Intermediate Unit*. In all complexes the mixing gives rise to the rocks of the *Subalkaline Mafic-Intermediate Group* and *Subalkaline Intermediate-Acid Group*.

11.3.2.1.2.2 Petrographic and Mineral Chemistry Evidence

The amphibole compositions and the content of Na_2O+K_2O in the liquids calculated to be in equilibrium with them register compositional changes during crystallisation. All the *Alkaline Group* intermediate rocks Ti-rich amphiboles crystallised from an alkaline magma, as was the case for the amphiboles from this group's mafic rocks (Fig. 11.26C and 11.27A). By contrast, the amphiboles with lower Ti were in equilibrium with a transitional alkaline to subalkaline magma

(Fig. 11.27A). As would be expected the alkaline granite amphiboles have concentrations of Na_2O+K_2O that indicate equilibrium with an alkaline magma (Fig. 11.27A). Data in Appendix VI.

The *Subalkaline Mafic-Intermediate* and *Intermediate-Felsic* groups transitional rocks contain both high-Ti and lower-Ti amphiboles that records a change from alkaline to subalkaline magma compositions (Fig. 11.27B). The main *Subalkaline Mafic-Intermediate Group* amphiboles, on the other hand, have variable Ti contents but are all in equilibrium with a subalkaline magma (Fig. 11.27C). The *Subalkaline Intermediate-Felsic Group* more Ti-rich amphibole crystallised in equilibrium with an alkaline magma and the lower-Ti amphibole a subalkaline one (Fig. 11.27D).

The biotites in the *Subalkaline Mafic-Intermediate* and *Intermediate-Felsic* groups are compositionally varied, as is typical in mixed magmas, reflecting changes in the magma from which they crystallised (e.g., Prelevic et al., 2004). Many units contain biotite that records a transition from subsaturated to oversaturated compositions. For example the Burguillos *External Subalkaline Intermediate Unit* and the Valencia *Main Pluton Alkaline to Subalkaline Basic-Acid Unit* rocks have biotites with Ti-rich cores and Ti-poor rims. All the biotites from the Valencia *Southern Stock Subalkaline Intermediate-Acid Unit* and the three Brovales units, however, only reflect Ti-poor oversaturated hybrid magma. The Valencia *Northern Stock Subalkaline Mafic-Intermediate Unit* biotites, on the other hand, are the only ones that are solely Ti-poor but with a sub-saturated tetrahedral layer.

Plagioclase from the *Subalkaline Mafic-Intermediate Group* have disequilibrium textures as, for example in the rocks from the Burguillos *External Subalkaline Intermediate Unit* and the most mafic rocks of the Valencia *Main Pluton Alkaline-Subalkaline Basic-Acid Unit*. As in the mafic rocks cores are generally more calcic albeit labradoritic here, rims and individual crystals are less calcic andesine.

11.3.2.1.2.3 Major and Trace Element and Isotopic Evidence

The variety of alkaline–tholeiitic–calc-alkaline–peraluminous compositions observed in the three studied complexes (see Chapter 8, Fig. 8.18) is characteristic of mixed magmatism (cf.,

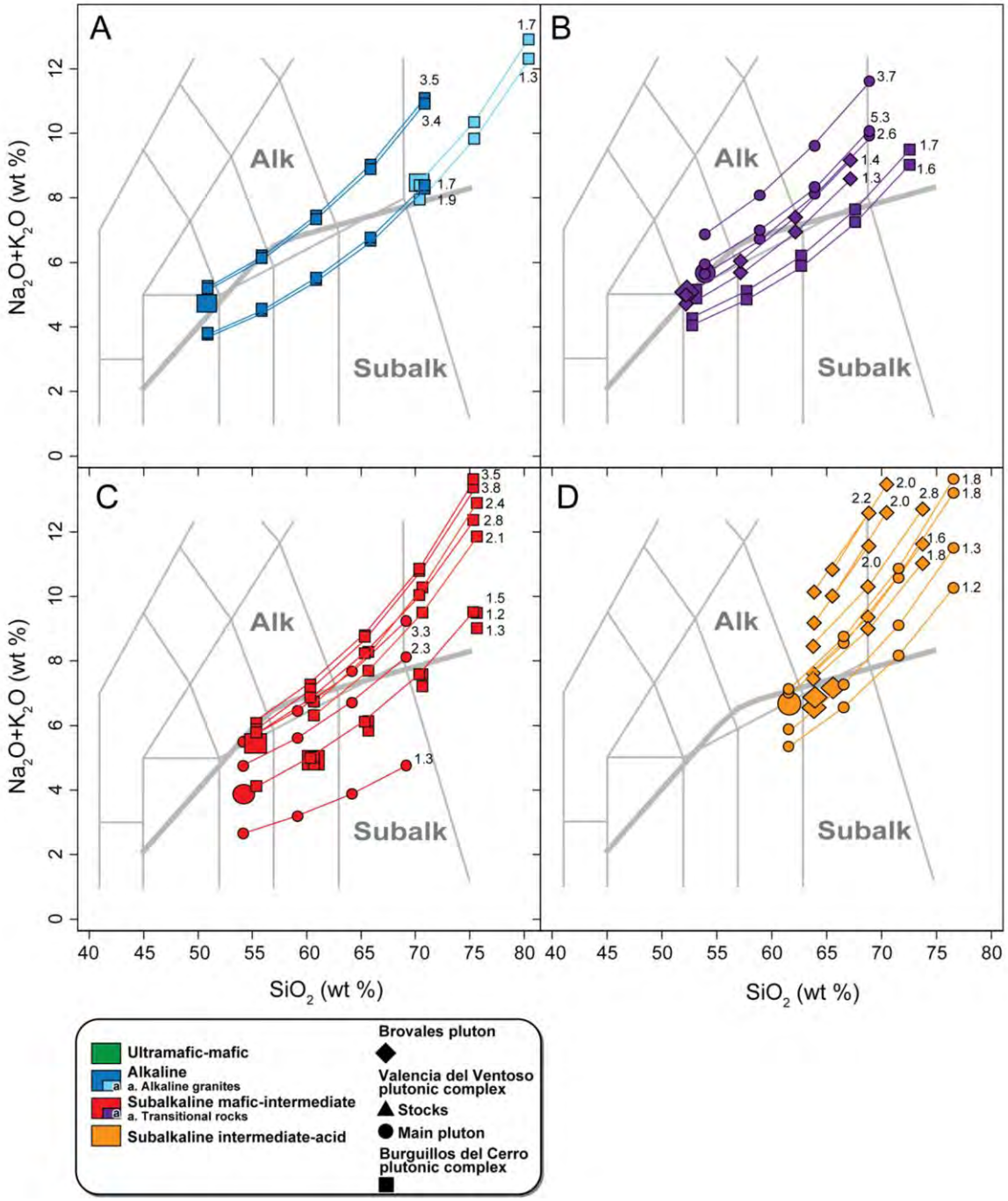

Figure 11.27. Melt compositions as a function of melt silica content calculated from representative amphibole compositions, over a SiO_2 range from the whole-rock composition to 20 % more. Kd values used in the calculations from Molina et al., (2009). Results were plotted in the TAS diagram (fields from Le Maitre et al., 1989): A) Alkaline Group intermediate and felsic rocks, B) to C) Subalkaline Mafic-Intermediate and Intermediate-Felsic groups. Numbers indicate the amphibole TiO_2 (wt %) content.

Kay and Kay, 1985; Carlier et al., 1997; Bonin et al., 1998; Roberts et al., 2000; Prelevic et al., 2004; Scarrow et al., 2009). Accordingly, the major and trace elements variations are gradational between the compositional groups. The Rb-Sr and Sm-Nd isotopes vary from primitive Bulk Earth compositions to more crustal compositions that trend towards host-rock Serie Negra and Cambrian metasediments (see Chapter 8). Significantly, comparable isotopic ranges are observed in other OMZ contemporaneous compositionally similar plutons in which mingling is also observed in the field, such as the Santa Olalla plutonic complex and Regueros de Monsaraz (Ordoñez-Casado et al., 2008; Antunes et al., 2008). The mixing hypothesis is supported by our new geochronological data that show the compositionally diverse plutonic rocks were coeval (Fig. 11.14).

More specifically, in the TAS and Harker diagrams and trace element and Rb-Sr and Sm-Nd isotope diagrams the two subalkaline groups, *Subalkaline Mafic-Intermediate* and *Intermediate-Felsic* groups have compositions that lie, respectively, between the *Ultramafic-Mafic* and *Alkaline* groups and the *Peraluminous Acid Group* (see Chapter 8, Fig. 8.18). The mode of the zircon O isotope values in the *Subalkaline Mafic-Intermediate Group* is 6.0 $\delta^{18}O_{(VSMOW)}$, is intermediate between the mantle, 5.5 $\delta^{18}O_{(VSMOW)}$, and crustal, 7.0 $\delta^{18}O_{(VSMOW)}$, values measured in the sample.

The possible mixing models between the mafic and felsic components are presented in section 11.3.2.2.3, prior to that the effects of mineral accumulation and fractionation are considered.

11.3.2.2 Modelling of Differentiation Processes

In addition to hybridisation the three complexes were also subject to magmatic fractionation leading to the formation of cumulate and fractionated rocks. In this chapter we model the processes affecting each of the compositional groups with an aim to identify rocks that represent parental liquid magmas.

11.3.2.2.1 Accumulation

The rocks of the *Ultramafic-Mafic Group* and the *Alkaline Group*, mainly represented in the Burguillos del Cerro plutonic complex, show layering and compositional banding at outcrop scale (see Chapter 4) and unequivocal cumulitic textures at microscopic scale (see Chapter 6). The *Ultramafic-Mafic Group* cumulus minerals are clinopyroxene and olivine accompanied by minor plagioclase. The main cumulus mineral in the *Alkaline Group*, by contrast, is plagioclase. Cumulus textures have also been described in the *Subalkaline Mafic Intermediate Group*, in the Valencia del Ventoso plutonic complex (Pons, 1982; Sarrioanandia, 2005).

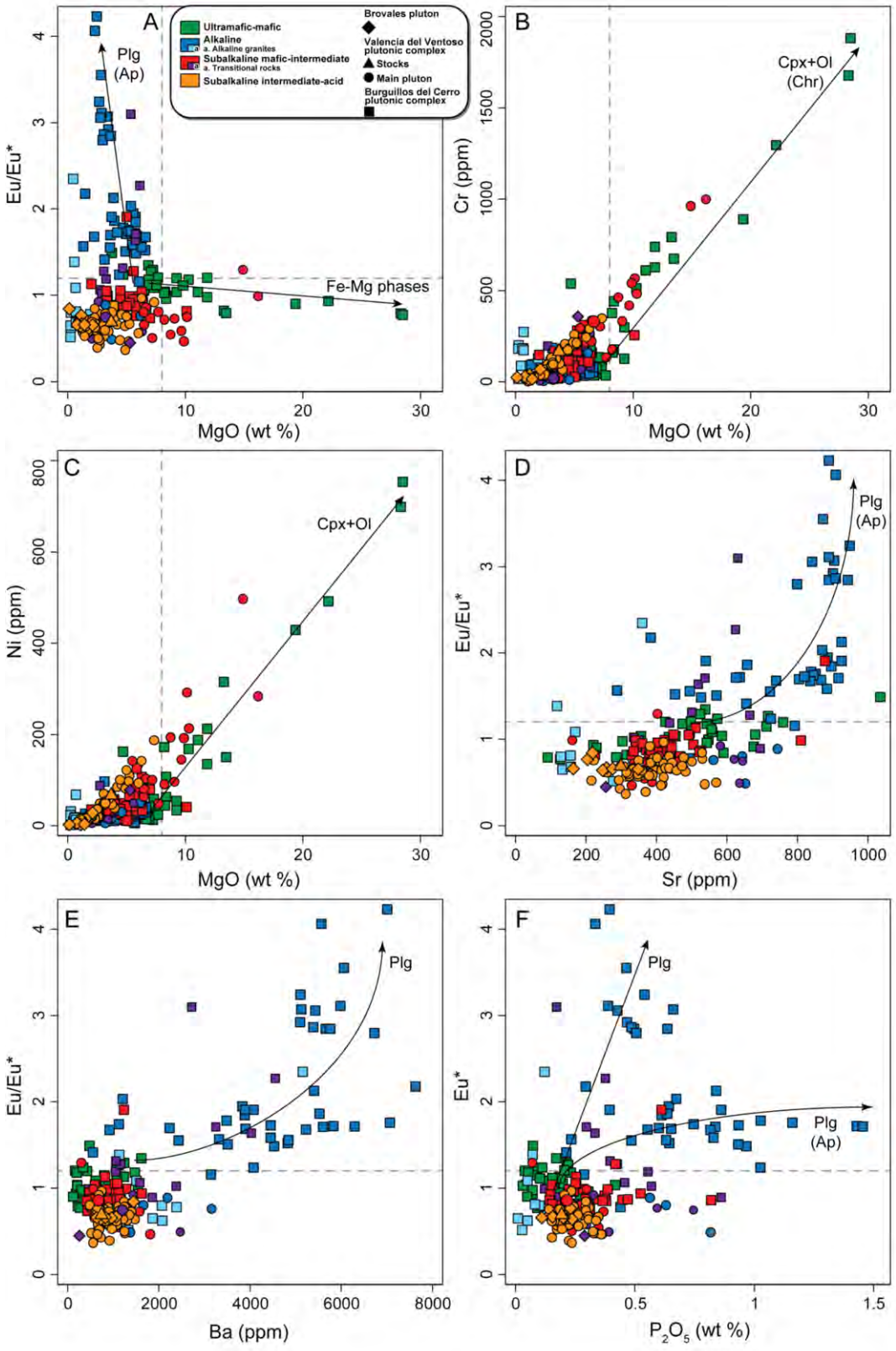

Figure 11.28. Parameters that indicate accumulation of plagioclase and ferromagnesian minerals for the main rock groups defined in the present work: A) Eu/Eu ($Eu^*=Eu_N/\sqrt{(Sm_N*Gd_N)}$) vs MgO (wt %); B) Cr (ppm) vs MgO (wt %); C) Ni (ppm) vs MgO (wt %); D) Eu/Eu* vs Sr (ppm); E) Eu/Eu* vs P_2O_5 (wt %). Ol: Olivine; Opx: Orthopyroxene; Cpx: Clinopyroxene; Amp: Amphibole; Bt: Biotite; Plg: Plagioclase; Ap: Apatite.*

Whole-rock compositions reflect two different trends depending on the cumulus phase involved (Fig. 11.28 and 11.29). The first reflects the importance of ferromagnesian minerals and is detected by elevated MgO, Cr and Ni. The second is dominated by plagioclase which is evident in variable Eu anomalies (Fig. 11.28).

Accumulation of ferromagnesian minerals was an important process in the *Ultramafic-Mafic Group* and some samples of the *Subalkaline Mafic-Intermediate Group* (Fig. 11.28A). High MgO in these groups correlates positively with elevated Cr and Ni, consistent with the main minerals being olivine and clinopyroxene with acccesory minerals such as chromite also playing a role (Fig. 11.28B and 11.28C).

The variation in Al_2O_3 and CaO of the mafic and intermediate rocks of the *Alkaline Group,* on the other hand, is determined by plagioclase accumulation, as recorded by variable positive Eu anomalies (Fig. 11.28A) and the correlation between this parameter and trace elements that are compatible in plagioclase, such as Sr and Ba (Fig. 11.28D and 11.28E). Apatite accumulation is apparent in the rocks with positive Eu anomalies and also high P_2O_5, emphasised in part, by their inclusion in the segregating plagioclase (Fig. 11.28F). Relatively it constant MgO precludes significant involvement of ferromagnesian minerals in the cumulus assemblage (Fig. 11.28A).

To identify the parental magma compositions we projected *Ultramafic-Mafic* and *Alkaline group* whole-rock compositions with all available mineral chemistry data for the respective groups together with a compositional field of typical basaltic magma. The compositional variations in the *Ultramafic-Mafic Group,* show two accumulation trends: the first towards olivine and pyroxenes; the second towards plagioclase and amphibole (Fig. 11.29A to 11.29D). The *Alkaline Group* rocks define a single trend towards plagioclase (Fig. 11.29E and 11.29F). Given the relationship between an increase in MgO and ferromagnesian mineral accumulation and Eu/Eu*> 1 and plagioclase accumulation we applied a filter to the dataset to remove the composition effect of an excess of these minerals: MgO< 8 wt% and 0.8<Eu/Eu*<1.2. The few samples that pass this filter and also fall in the typical basalt magma compositional field are considered parental liquid magma compositions (Fig. 11.29).

Field, petrographic and compositional data all indicate that the *Ultramafic-Mafic Group* rocks are predominantly cumulitic. Nevertheless, we only consider gravitational segregation to have been an important process in the ultramafic facies that comprise both cumulus and intercumulus phases. In the mafic gabbros and gabbronorites of this unit only cumulus, not intercumulus, phases are identified (see Chapter 6). As discussed above, the evolution of the gabbros and gabbronorites is determined by the coeval crystallisation of amphibole and plagioclase. This

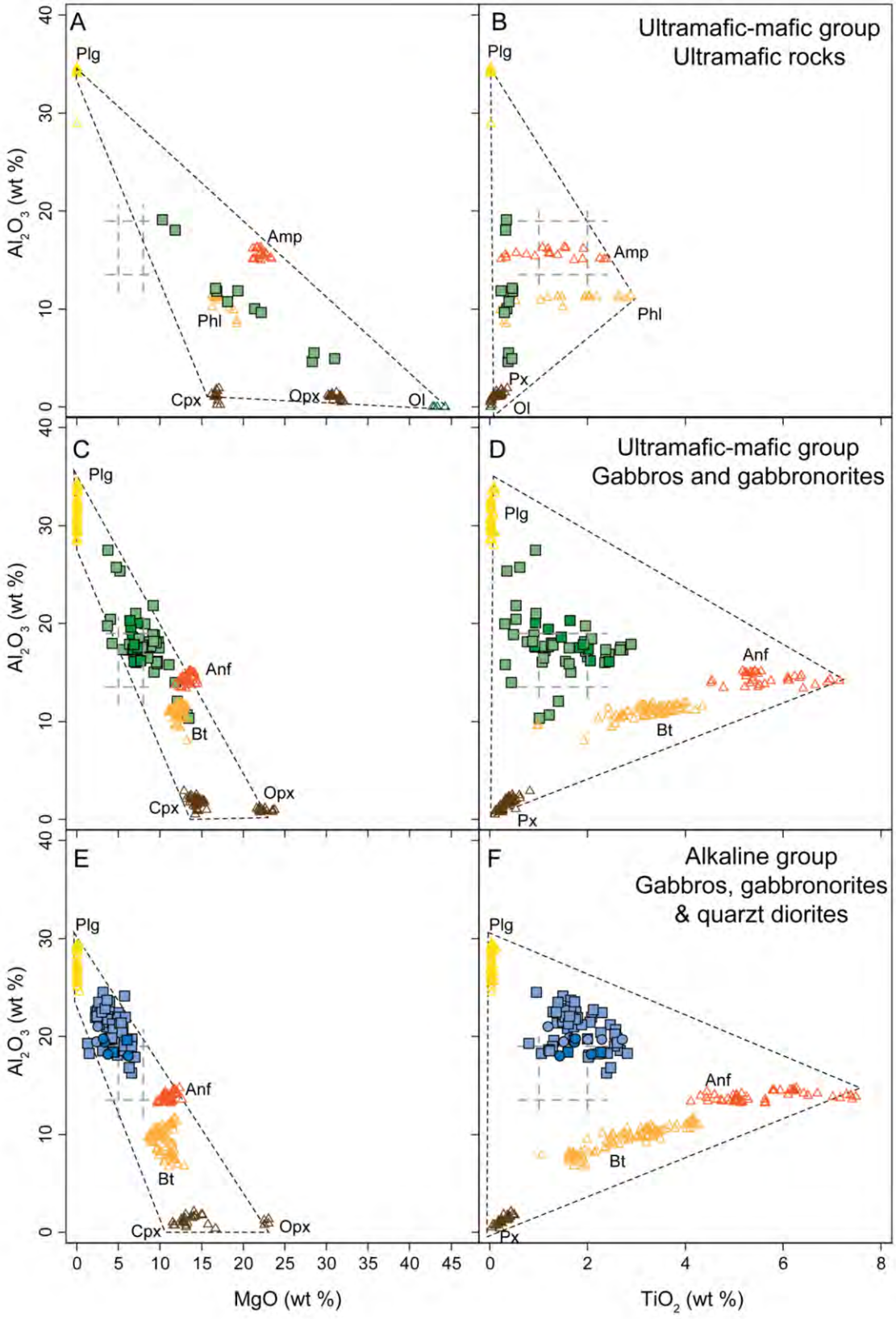

Fig. 11.29. Major element compositions of the Ultramafic-Mafic and Alkaline groups and representative minerals from each group, to evaluate the cumulitic processes as function of Al_2O_3, MgO and TiO_2 (wt %) content. Broken grey lines indicate a typical basaltic composition, taken from Pearce (1996). Ol: Olivine; Opx: Orthopyroxene; Cpx: Clinopyroxene; Amp: Amphibole; Bt: Biotite; Plg: Plagioclase; Ap: Apatite.

textural evidence is consistent with formation of these rocks by in situ crystallisation (cf., Langmuir, 1989). This process is also indicated by the trace element compositional variations. These gabbros and gabbronorites have concentrations in incompatible element, including the REE, much higher than the ultramafic rocks. This fits with the model of Langmuir (1989): the ultramafic rocks represent the 'cumulate pile' of abundant segregated olivine and clinopyroxene, whereas the gabbros and gabronorites are the 'solidification zone' where amphibole and plagioclase formed in situ (cf., Hermann et al., 2001).

11.3.2.2.2 Fractionation

The studied complexes were also affected by fractional crystallisation. Two main lines of fractionation are identified: from basic to acid in the *Alkaline Group*; and, from intermediate to acid in the *Subalkaline Intermediate-Acid Group* (Fig. 11.30). The general aspects of the models are defined in Appendix VI, these include: the starting compositions parental melts and end-point compositions, the minerals involved in the fractionation, their compositions and relative proportions, and the degrees of crystallisation.

For the alkaline fractionation trend a hypothetical parental melt was fixed as the mean composition of the non-cumulate basic alkaline rocks (see previous section 11.3.1, Fig. 11.30). The mean composition of the alkaline feldspar granites was considered to be the end-point of the fractionation (Fig. 11.30; Table 11.2). As was shown in Chapter 6 and Chapter 7, *the Alkaline Group* mineral association and mineral compositions vary from the basic to the intermediate and acid rocks (Fig. 11.30). For this reason the modelling was considered in two steps.

The first stage of alkaline crystallisation was modelled from the parental composition to the most evolved intermediate composition of the group (Table 11.2). The minerals fractionated were those observed in the rocks: orthopyroxene, clinopyroxene, biotite and plagioclase with accessory apatite, ilmenite and magnetite (Fig. 11.31). The major element fractional crystallisation model that gave the best fit was 60% crystallisation, with minerals proportions of 59% labradorite plagioclase, 15% biotite, 11% orthopyroxene, 11% clinopyroxene, 2% apatite, 1% magnetite and 2% ilmenite (Fig. 11.31 and Table 11.2). The residual values between the calculated results and the measured samples were less than 2 for all elements (Table 11.2). The fractionated assemblage is compositionally comparable to the *Alkaline Group* mafic cumulitic rocks (Table 11.2).

The second stage of alkaline crystallisation was modelled from the end-point of the first crystallisation stage to the mean composition of the alkaline granites (Table 11.2). The minerals fractionated were those that are characteristic of the intermediate alkaline rocks: amphibole,

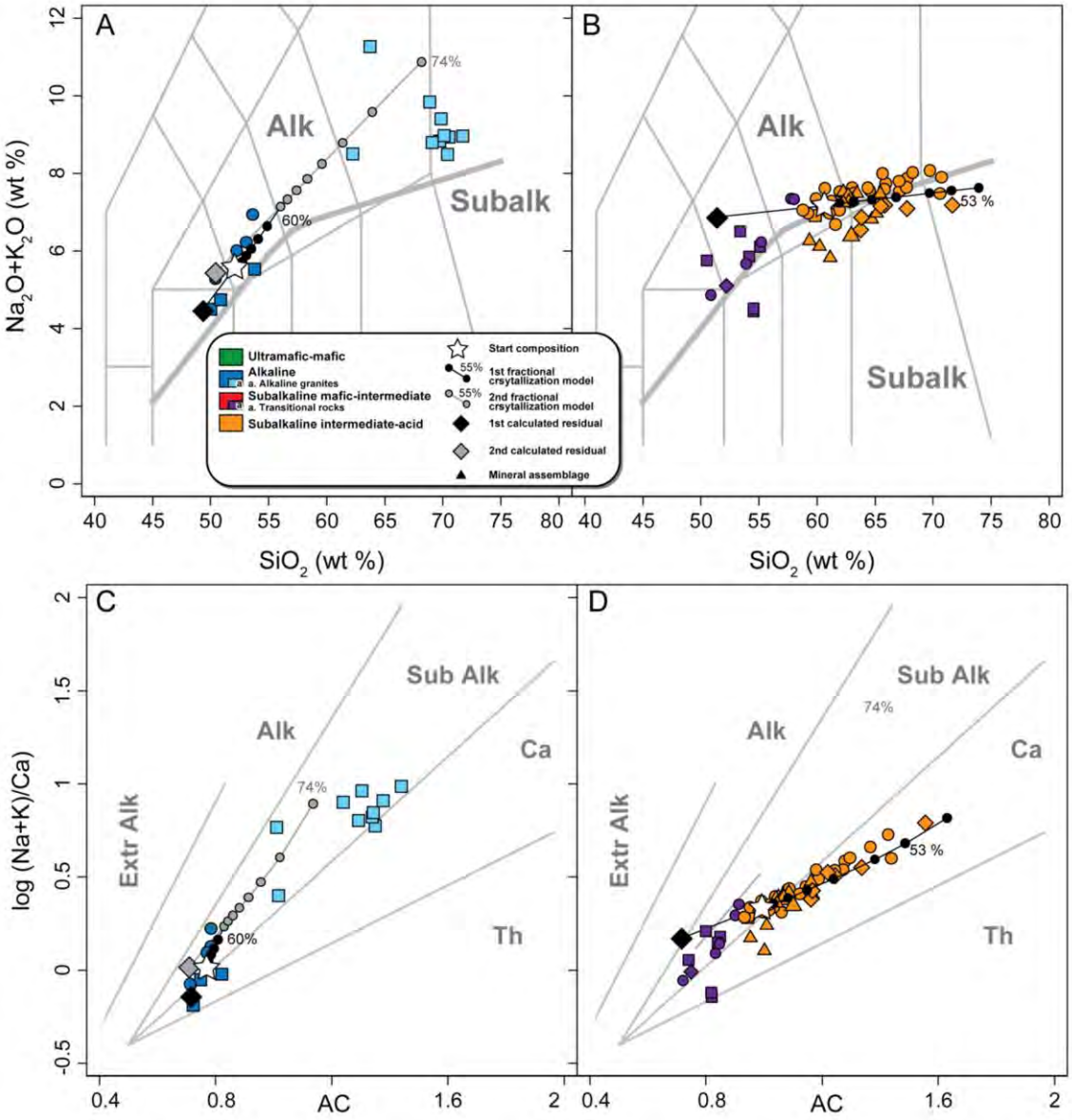

Figure 11.30. Major element compositions of the Alkaline and Subalkaline Intermediate-Felsic groups showing the fractional crystallisation model: A) and B) TAS plot (fields from Le Maitre et al., 1989); and, C) and D) Borodin. (1988) classification diagram.

biotite, and plagioclase with accessory ilmenite. The major element fractional crystallisation model that gave the best fit was 72% crystallisation of the remaining 40% of original magma, 28.8% of the total making 88.8% crystallisation in all, with minerals proportions of 50% andesine plagioclase, 37% hastingsite amphibole, 12% biotite and 1% ilmenite (Fig. 11.31 and Table 11.2). The residual values between the calculated results and the measured samples were less than 2 for all elements (Table 11.2). The fractionated assemblage is compositionally comparable to the *Alkaline Group* intermediate cumulitic rocks.

	Alkaline group, first fractional crystallisation stage				
	11% Opx, 11% Cpx, 15% Bt, 59% Plg, 2% Ap, 1% Mt, 2 %Ilm				
	Fractionated assemblage	Parental composition	Calculated, 60 % frac.	Observed	Residuals
Major elements (wt %)					
SiO2	49.4	52.13	56.06	56.53	0.47
TiO2	2.02	1.8	1.5	1.52	0.02
Al2O3	19.87	18.82	17.41	19.44	2.03
FeO	8.35	8.04	7.64	7.35	-0.29
MnO	0.24	0.12		0.05	0.05
MgO	5.05	4.48	3.7	2.42	-1.28
CaO	10.02	8.56	6.55	4.92	-1.64
Na2O	3.05	3.66	4.51	4.65	0.14
K2O	1.4	1.91	2.63	3.12	0.5
P2O5	0.6	0.48			
	Alkaline group, second fractional crystallisation stage				
	37 % Amp, 12% Bt, 50% Plg, 1 %Ilm				
	Fractionated assemblage	Parental composition	Calculated, 74 % frac.	Observed	Residuals
Major elements (wt %)					
SiO2	50.44	56.06	70.71	70.04	-0.66
TiO2	1.94	1.5	0.31	0.36	0.06
Al2O3	18.5	17.41	14.43	15.47	1.04
FeO	9.89	7.64	1.63	2.71	1.08
MnO	0.18			0.05	0.05
MgO	5.06	3.7	0.08	0.45	0.37
CaO	8.56	6.55	1.19	1.82	0.63
Na2O	3.89	4.51	6.13	4.48	-1.65
K2O	1.53	2.63	5.52	4.55	-0.98
P2O5				0.06	0.06
	Sub-alkaline mafic-intermediate group, fractional crystallisation model				
	22 % Amp, 17 % Bt, 59 % Plg, 1% Ap, 1% Mt				
	Fracctionated assemblage	Parental composition	Calculated, 53 % frac.	Observed	Residuals
Major elements (wt %)					
SiO2	51.12	60.68	71.2	70.89	-0.32
TiO2	1.39	0.86	0.29	0.35	0.06
Al2O3	19.84	17.39	14.81	14.73	-0.08
FeO	9.05	5.84	2.38	2.35	-0.03
MnO	0.11	0.08		0.03	0.03
MgO	4	2.54	0.97	0.85	-0.12
CaO	7.48	5.15	2.66	2.8	0.14
Na2O	4.69	4.19	3.66	3.69	0.03
K2O	2.03	2.99	4.03	4.17	0.14
P2O5	0.29	0.29		0.15	0.15

Table 11.2. Summary of the fractional crystallisation model for the Alkaline Group, in two stages, and for the Subalkaline Intermediate-Felsic Group, single stage.

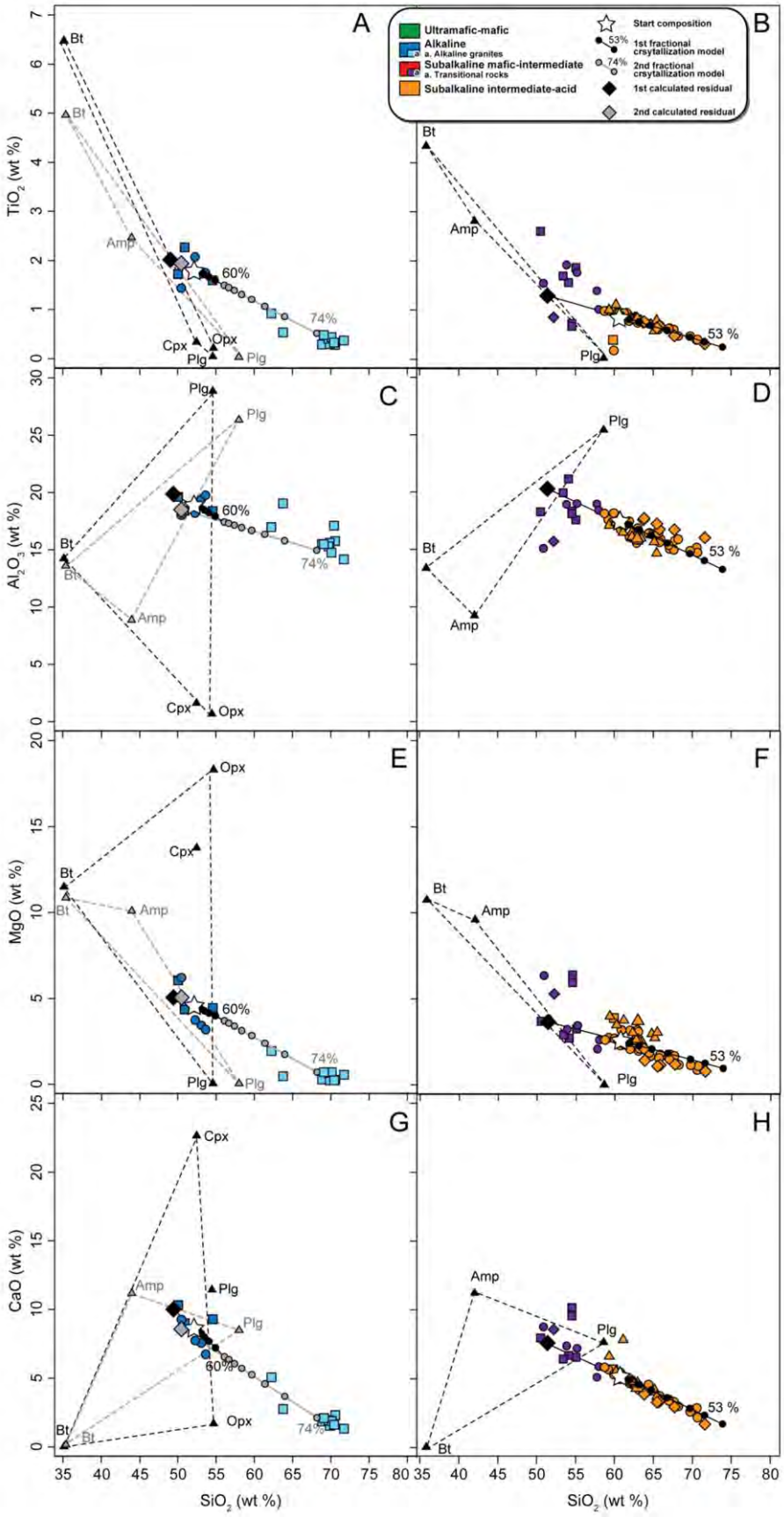

Figure 11.31. Harker diagrams of the Alkaline and Subalkaline Intermediate-Felsic groups showing the fractional crystallisation model: A) and B) TiO_2 vs SiO_2; C) and D) Al_2O_3 vs SiO_2; E) and F) MgO vs SiO_2; and, G) and H) CaO vs SiO_2 (wt %). Opx: Orthopyroxene; Cpx: Clinopyroxene; Amp: Amphibole; Bt: Biotite; Plg: Plagioclase.

The subalkaline fractionation trend was modelled as a one step process. The parental composition was fixed as the average of the least-evolved rocks of the *Subalkaline Intermediate-Felsic Group* (Fig. 11.30 and Table 11.2). The end-point was the average of the most-evolved rocks of the group (Fig. 11.30 and Table 11.2). The minerals fractionated were those observed in the samples: amphibole, biotite and plagioclase with accessory apatite and magnetite (Fig. 11.31). The major element fractional crystallisation model that gave the best fit was 53% crystallisation, with minerals proportions of 59% andesine plagioclase, 22 % hastingsite-edenite amphibole, 17% biotite, 1% apatite and 1% magnetite (Fig. 11.31, Table 11.2). The residual values between the calculated results and the measured samples were less than 1 for all elements (Table 11.2). The fractionated assemblage is compositionally comparable to the *Subalkaline Mafic-Intermediate Group* transitional rocks (Fig. 11.30 and 11.31).

The alkaline fractional crystallisation model supports the evolution of the *Alkaline Group* from basic through intermediate to acid compositions (Fig. 11.30). The subalkaline model, on the other hand, is not so clear. It crosses from transitional-mildly alkaline to subalkaline compositions (Fig. F15). We suggest that this effect is related to the hybrid nature of the group (Fig. 11.30).

11.3.2.2.3 Magma mixing

As has been shown throughout this work field, petrological, and compositional data all point towards magma mixing being a significant process in the generation of the rocks under consideration. Different possible hybridisation trends are identified involving three different sources: two basic mantle-derived the first alkaline from the lithosphere and the second tholeiitic from the asthenosphere, the third an acid crustal peraluminous partial melt of basement metasediments. The objective of this section is an evaluation of the mixing processes. Of all the groups the *Sub-alkaline Mafic-Intermediate* is the one that reveals most about the hybridisation processes.

Given that the mafic rocks studied here, and other comparable OMZ rocks, show evidence of crustal contamination (cf., Casquet et al., 2001; Tornos et al., 2006; Pin et al., 2008), the selection of mixing end-members requires particular care. Appendix VI.

11.3.2.2.3.1 Model End-members

In the case of the mafic tholeiitic end-member at first sight the the best candidates might appear to be the OMZ rocks with a tholeiitic affinity (see section 11.3.) (cf., Castro et al., 1996; Pin et al., 2008). Nevertheless these rocks have been affected by metamorphism, for example the Beja Acebuches amphibolites, and crustal contamination, for example the Beja Igneous complex gabbros. These processes may have modified their compositions, but despite this they clearly

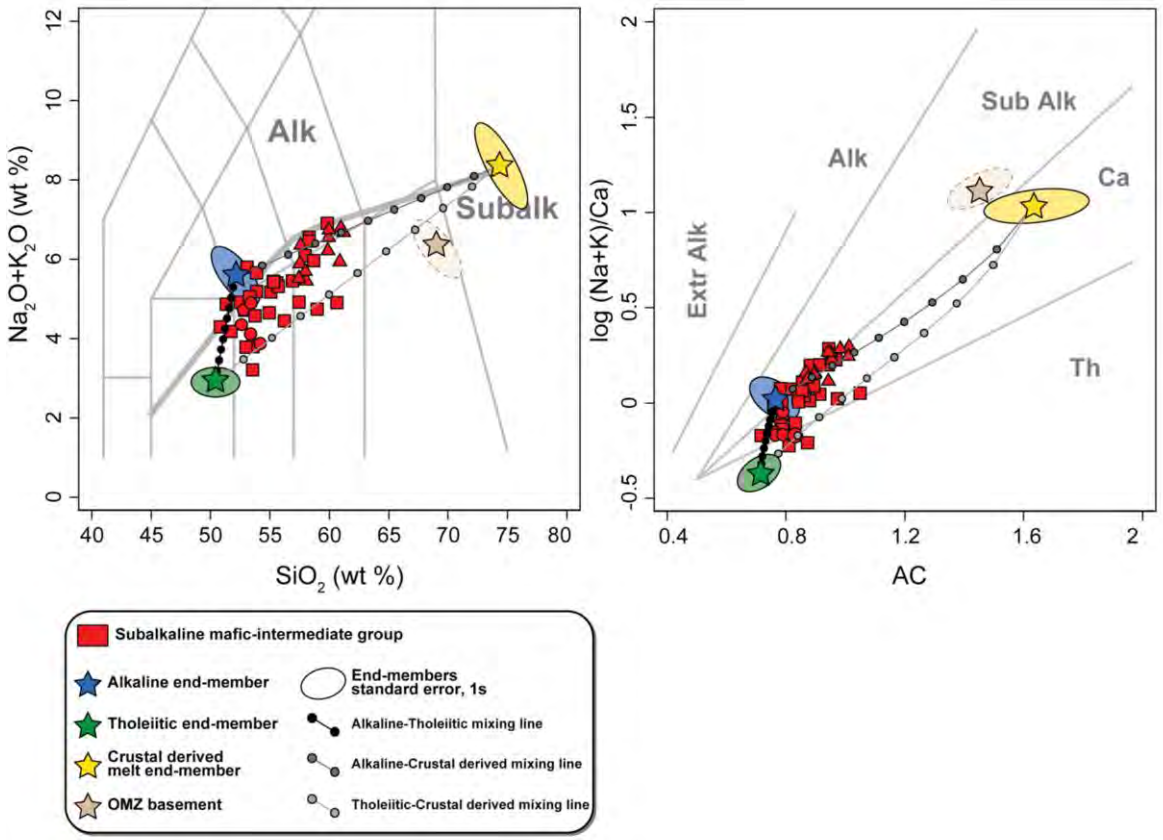

Figure 11.32. Major element compositions of the Subalkaline Mafic-Intermediate Group showing the three component magma mixing model: left, TAS plot (fields from Le Maitre et al., 1989); and, right, Borodin. (1988) classification diagram. The end-members considered were: tholeiitic N-MORB from White and Hofmann, (1982) and Sun and Mcdonough, (1989); and, alkaline and crustal-derived melt end-members from the present work. In addition we include a representative composition of OMZ basement (Schäfer, 1990; López-Gijarro et al., 2006; Pereira et al., 2006; present work). Shaded areas are the standard error interval at 1σ. We also include the simple pure mixing lines between end-members.

preserve some tholeiitic traits such as normative hypersthene. Given that the most abundant tholeiites are N-MORB (e.g., White and Hofmann, 1982; Hofman, 1988; Sun and Mcdonough, 1989), we selected this composition as the tholeiitic end-member for the mixing model (White and Hofmann, 1982; Sun and Mcdonough, 1989).

The definition of the mafic alkaline end-member is more problematic given the varied compositions that may be derived by partial melting of a mantle lithosphere source (Pilet et al., 2011) and the fact that the OMZ alkaline rocks are, to a greater or lesser extent, affected by crustal contamination. Given these complications we decided to use an average of the parental composition of the first stage of the alkaline crystallisation series (see 11.3.2.2.2). This composition may be considered an 'alkaline minimum' for the magma mixing model.

The crustal component in the mixing is well-defined as the *Peraluminous Group* granites, partial melts of the OMZ metasedimentary basement, e.g., the Serie Negra (see section 11.3.1). An average basement composition was also considered to evaluate crustal assimilation.

11.3.2.2.3.2 Modelling the End-member Mixing

The *Subalkaline Mafic-Intermediate Group* rocks are considered to be the products of magma mixing - they have a broad compositional range but with no clear trends such as those related to fractionation in the *Alkaline and Subalkaline Intermediate-Felsic* groups (Fig. 11.32 to 11.34). All the same, the possibility that some of the compositional variation is attributable to this process must be taken into account. Fractional crystallisation would essentially drive the whole-rock compositions in a direction that may overlap with crustal contamination. The complexity of the system prevents the fractionation effect from being assessed, for this reason estimates of the amount contamination may be considered maximums.

Assimilation of ≥ 50% of crustal material would require to cause the compositional variation observed in the hybrid rocks (Fig. 11.32 to 11.34). Contamination is much more efficient, however, if melts are involved (Sparks and Marshall, 1986; Poli et al., 1996; Bea, 2012). In addition the crustal-melt peraluminous granites have more evolved compositions than the OMZ basement, being partial melt leucocratic segregates of it. So a lower proportion of the component would be required to produce the same compositional effect.

The majority of the *Subalkaline Mafic-Intermediate Group* lies within the triangle formed by the three hypothetical mixing lines between the end-members (Fig. 11.32 to 11.34). So the compositional space defined by the end-member joins constrains the subalkaline hybrid rocks (Fig. 11.32A) including a transition from more alkaline-like to more tholeiite-like (Fig. 11.32B). The major element Harker diagrams show that the compositional variation of the hybrid rocks may be explained by a mix of the three end-members (Fig. 11.33). For a given SiO_2 content the major element concentrations vary between the end-member compositions (Fig. 11.33). The proportion of crustal component never exceeds 40%. The relative proportions of the mafic end-members is much more variable, although the alkaline component usually dominates (Fig. 11.33).

The trace element concentrations are very varied in the hybrid rocks, this is consistent with the heterogeneous mixing process and the limitations discussed above regarding identification of the end-member compositions. Despite this, the variation in many trace elements may be explained in terms of the selected end-members (Fig. 11.34).

The whole-rock major and trace element isotope compositions fit with the mixing

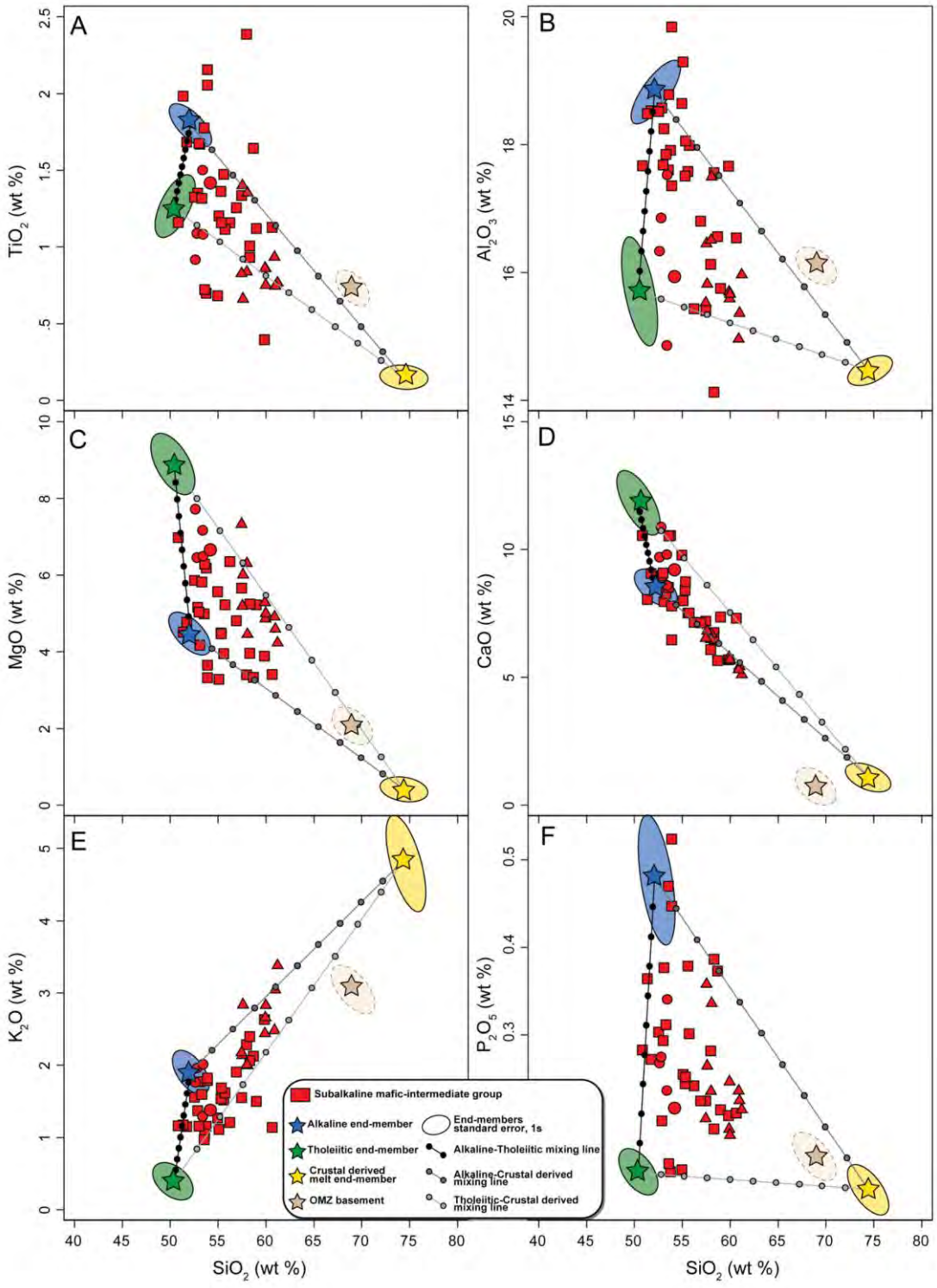

Figure 11.33. Harker diagrams of the Subalkaline Mafic-Intermediate Group showing the three component magma mixing model A) TiO_2 vs SiO_2; B) Al_2O_3 vs SiO_2; C) MgO vs SiO_2; D) CaO vs SiO_2 ; E) K_2O vs SiO_2; and, F) P_2O_5 vs SiO_2 (wt %). The end-members considered were: tholeiitic N-MORB from White and Hofmann, (1982) and Sun and McDonough, (1989); and, alkaline and crustal-derived melt end-members from the present work. In addition we include a representative composition of OMZ basement (Schäfer, 1990; López-Gijarro et al., 2006; Pereira et al., 2006; present work). Shaded areas are the standard error interval at 1σ. We also include the simple pure mixing lines between end-members.

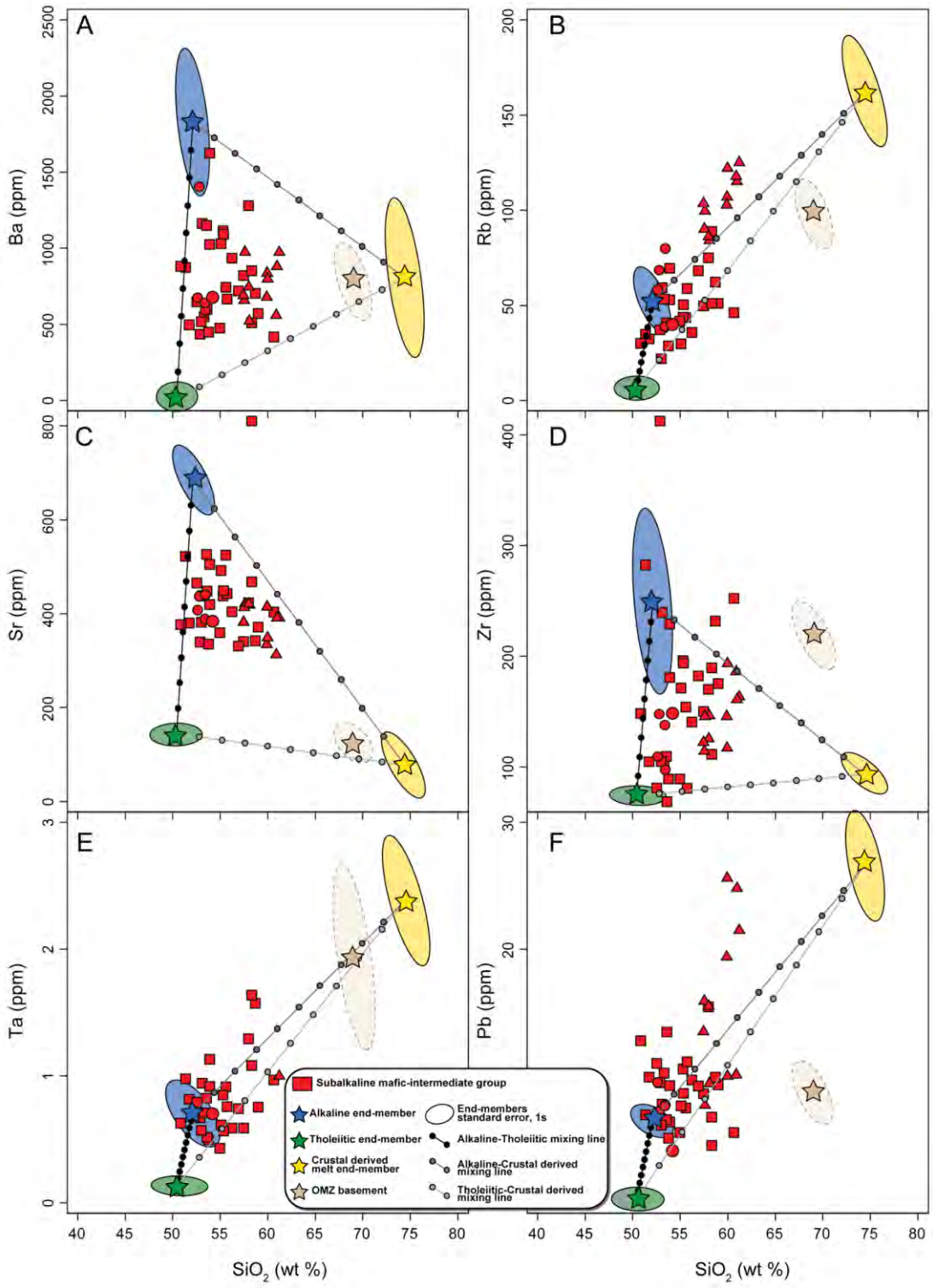

Figure 11.34. Harker diagrams of trace elements for the Subalkaline Mafic-Intermediate Group showing the three component magma mixing model: A) Ba vs SiO_2; B) Rb vs SiO_2; C) Sr vs SiO_2; D) Zr vs SiO2; E) Ta vs SiO_2; and, F) Pb vs SiO_2 (wt %). The end-members considered were: tholeiitic N-MORB from White and Hofmann, (1982) and Sun and McDonough, (1989); and, alkaline and crustal-derived melt end-members from the present work. In addition we include a representative composition of OMZ basement (Schäfer, 1990; López-Gijarro et al., 2006; Pereira et al., 2006; present work). Shaded areas are the standard error interval at 1σ. We also include the simple pure mixing lines between end-members.

hypothesis showing progressive enrichment. Both the *Subalkaline Mafic-Intermediate* and *Subalkaline Intermediate-Felsic* groups hybrid compositions have $\varepsilon Nd_{335\ Ma}$ and $^{87}Sr/^{86}Sr_{335\ Ma}$ that are mid way between the mafic alkaline and felsic peraluminous compositions (Fig. 11.35). Other OMZ hybrid rocks fall on the same trend, e.g., the Santa-Olalla and Aguablanca complexes (Casquet et al., 2001; Tornos et al., 2006) (Fig. 11.35).

The tholeiite-peraluminous mixing line shows that the OMZ tholeiites are affected by the crustal contamination, for example the Beja Igneous complex (Pin et al., 2008). In addition, tholeiite-peraluminous mixing can explain some of the isotopic compositional variations of the *Ultramafic-Mafic Group* (Fig. 11.35C and 11.35D). Mafic alkaline-like and tholeiite-like magmas also mixed (see section 11.3.2.1.1 Mafic mixing). The isotopic composition of the *Ultramafic-Mafic Group* is similar to the *Alkaline Group* although the former has higher values of $^{147}Sm/^{144}Nd$ (Fig. 11.35C and 11.35D). The observed ratios are consistent with crustal-melt contamination of a mafic alkaline-subalkaline mix. (Fig. 11.35D), which fits with the field and compositional data regarding the nature of the *Ultramafic-Mafic Group*.

The broad agreement between the proportion of crustal contamination indicated by the elemental and isotopic modelling is relevant in addressing the aforementioned question of whether the observed isotopic enrichment resulted from the temporal evolution of an enriched mantle component, crustal contamination of a mantle-derived melt, or a combination of both. The agreement between the two indicators, elemental and isotopic, suggests that long-term evolution of an enriched component was not the main cause of the isotopic enrichment (cf. Scarrow et al., 2009b). If it had been an important effect the isotopic data should reflect a greater amount of contamination than the elemental data. Thus it would appear that the lithospheric source enrichment occurred shortly before the melt-generation event (cf., Pilet et al., 2008; 2011) (Fig. 11.36).

11.3.3 Tectonomagmatic Context

11.3.3.1 Intra-Orogenic Calc-Alkaline Magmatism

We conclude that the OMZ Variscan magmatism 'calc-alkaline' mafic–felsic plutons were emplaced unrelated to subduction. In agreement with our modelling it is well-established that a calc-alkaline composition may be obtained by mixing between alkaline mafic mantle-derived and peraluminous felsic crustal-derived magma (e.g., Rock, 1991; Prelevic et al., 2004; Scarrow et al., 2009) or melting of either an enriched lithospheric mantle or lower crust (e.g., Liegéois et al., 1998). The mixing model is supported by Bonin (2004), in his classic, extensively cited, work. He considered the interaction of mafic and felsic magmas from, respectively, mantle and crustal

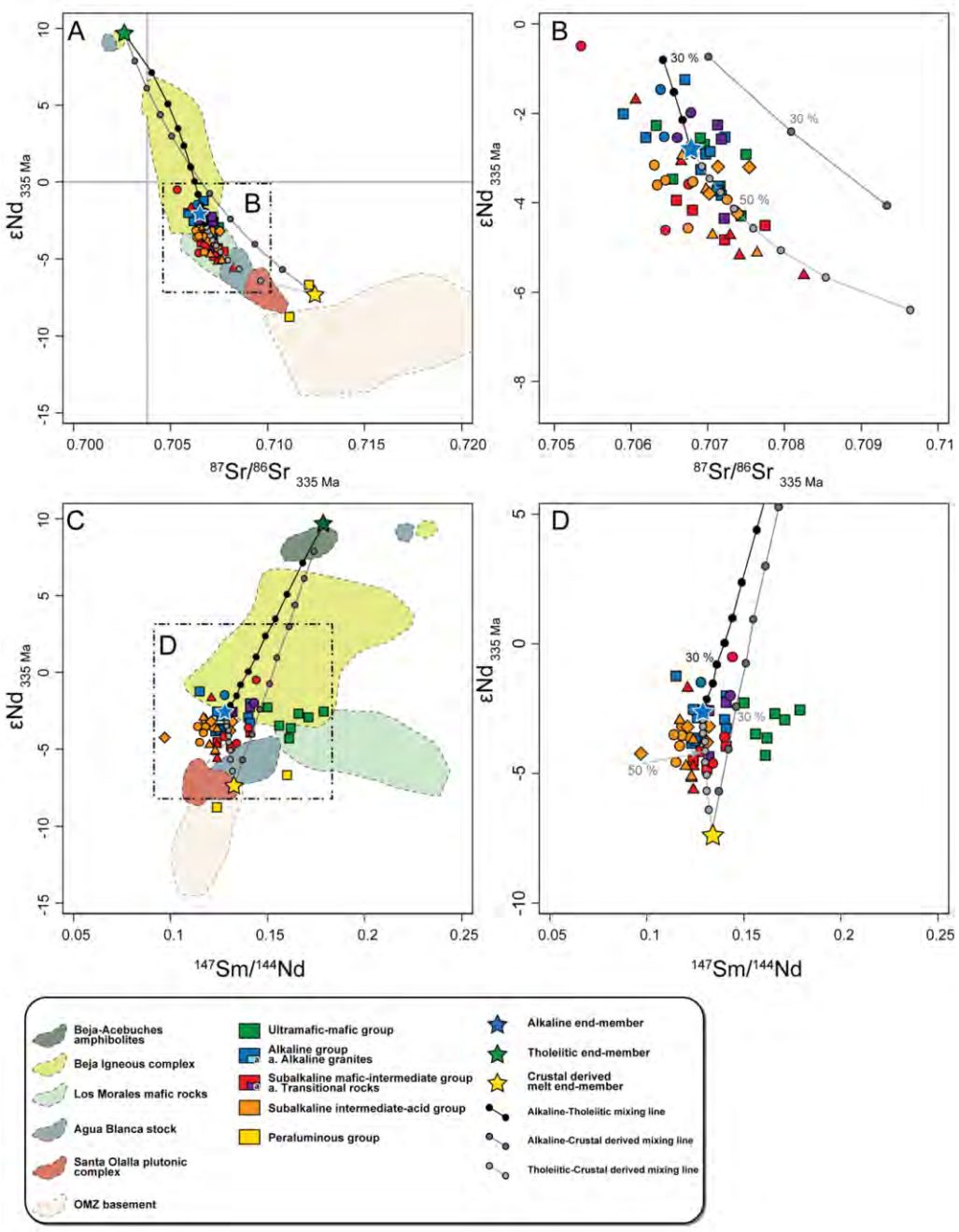

Figure 11.35. Isotope values of the groups defined in present work: A) $\varepsilon Nd_{335\,Ma}$ vs. $^{87}Sr/^{86}Sr_{335\,Ma}$, note the enriched compositions that head towards host-rock OMZ metasediments (cf., Casquet et al. 2001). Similar trends are observed in coeval OMZ plutons: the Beja Igneous complex, Los Morales mafic rocks, Agua-Blanca Stock and Santa Olalla Plutonic complex (El-Hmidi, 2000; Casquet et al., 2001; Salman, 2002; Tornos et al., 2006; Pin et al., 2008). B) Detail of the isotopic composition of the magma mixing model; C) $\varepsilon Nd_{335\,Ma}$ vs.$^{147}Sm/^{144}Nd$ for the aforementioned rocks and other OMZ Variscan intrusive rocks: Beja-Acebuche amphibolites; Beja Igneous complex, Los Morales mafic rocks, Agua-Blanca Stock and Santa Olalla Plutonic complex (Castro et al., 1996; El-Hmidi, 2000; Casquet et al., 2001; Salman, 2002; Tornos et al., 2006; Pin et al., 2008) and the OMZ basement (Schäfer, 1990; Casquet et al., 2001; Chichorro et al., 2008; López-Guijarro et al., 2008). D) Detail of the $\varepsilon Nd_{335\,Ma}$ vs $^{147}Sm/^{144}Nd$ isotopic values of the groups defined in the present work and isotopic magma mixing lines.

sources in a post-collisional setting.

Not that it is the main aim of this study, but having decoupled the formation of the OMZ Variscan magmatism from subduction a tectonomagmatic context consistent with our new petrogenetic model should be sought. In the OMZ various authors have suggested that Variscan metamophism and magmatism was the result of intra-orogenic extension (Simancas et al., 2003; Pereira et al., 2009).

Extensional/transtensional processes associated with intra-continental orogenesis are generally associated with the later stages of continental accretion, in all cases they are post-orogenic (Shaw, 1991; Cunningham, 2005; Dyksterhuis and Müller, 2008; Meira et al., 2015). The main consequence of the extension/transtension is thinning of the lithosphere by extensive shear zones (Aitken et al., 2009; Pereira et al., 2009). Ensuing upwelling of the asthenosphere causes mantle melting and emplacement of mafic magmatism in the thinned lithosphere (Fig. 11.36) (Raimondo et al., 2014; Meira et al., 2015).

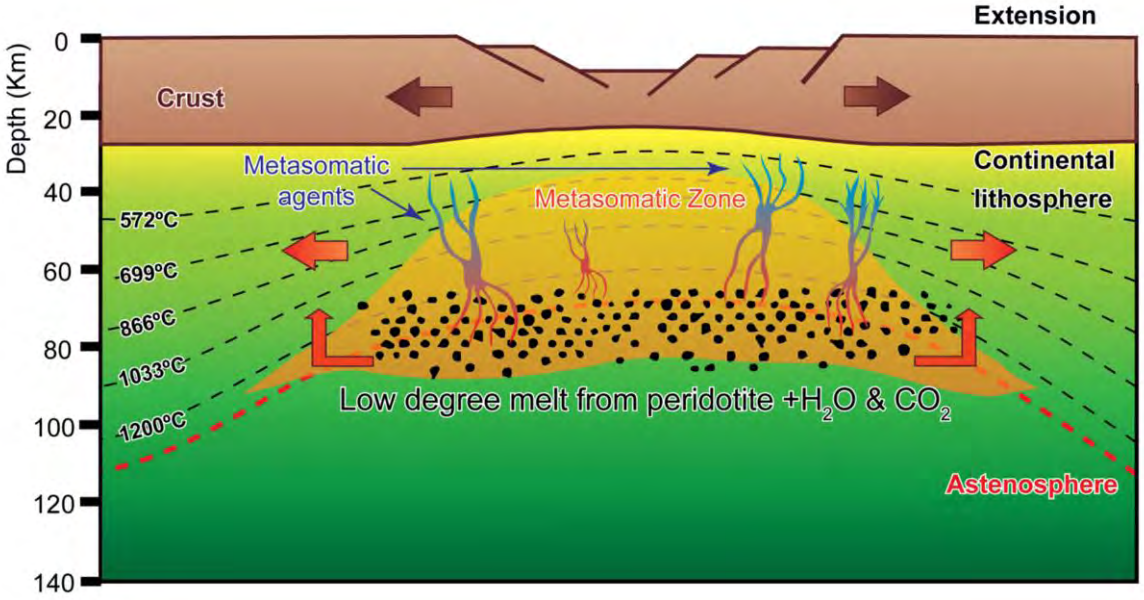

Figure 11.36. Schematic model for metasomatism of the continental lithospheric manntle associated with extension, modified from Pilet et al., (2011). Note that the asthenosphere upwelling generates metasomatic agents resulting in a metasomatic zone in the adjacent lithosphere.

11.3.3.2 Extension of the Lithosphere: Melt Volume and Composition

A key question is 'what would be the effect of ascent of the mantle astheosphere?'. We suggest that the models of McKenzie and Bickle (1988) regarding the volume and composition of melts of the asthenospheric mantle generated by extension of the lithosphere may provide a

good explanation for the OMZ Variscan magmatism. They used a predicted initial geotherm and knowledge about the variation and composition of the melt fraction as a function of pressure and temperature to obtained parameterised convective models. The composition of the magma produced is mainly a function of the melt fraction which itself depends on adiabatic melting during upwelling. McKenzie and Bickle (1988) concluded that extension of the continental lithosphere generates little melt unless the stretching, β, factor (the ratio of the final to the initial surface area) >2 and the mantle potential temperature (T_p) is T_p> 1380°C (Fig. 11.37). Above these values, alkali basalts are generated with melts becoming more tholeiitic as the amount of melting increases. It is particularly significant for our case that these authors noted that large quantities of melt may be generated by uniform stretching pure shear lithospheric extension, in particular at continental margins, where there is a tendency to underestimate the β factor (McKenzie and Bickle, 1988; Latin and White, 1990).

The stretching factor, mantle potential temperature and lithosphere thickness affect the melting process: more stretching, more heat or a thinner lithosphere all result in more magma production. For an elevated mantle potential temperature, 1480 ºC, such as would be the case for a plume, large volumes of magma would be generated even for a low stretching factor (Fig. 11.37). A mantle with a normal potential temperature, 1280ºC, would produce less melt for a comparable stretching factor (Fig. 11.37). In the absence of evidence for plume involvement, e.g., extremely large volumes of tholeiitic magma such as flood basalts, the two variables that may come into play in the OMZ Variscan case are the stretching factor and the lithosphere thickness.

11.3.3.3 The Ossa-Morena Zone Variscan Case

Rather than forward modelling determining results from causes as undertaken by McKenzie and Bickle (1988), in the case of the OMZ Variscan magmatism we have an inverse problem that starts from the results to obtain the cause. At *c.* 340 Ma a limited volume of alkaline and tholeiitic magma was emplaced in the OMZ middle crust. Temporally associated with this the transition from the first collisional event to the intra-orogenic extensional event was more of a thermal relaxation than an extensional collapse. Nevertheless, the extension is widely recognised, for example in adjacent terranes in northern Gondwana and Avalonia-Laurentia as recorded in the development of Carboniferous sedimentary basins (Simancas et al., 2009; Marillier and Verhoef, 1989; Bouabdelli and Piqué, 1996) and the generation of mafic-felsic magmatism and mafic underplating (e.g., Dessureau et al., 2000; Houari and Hoepffner, 2003) (Fig. 11.38).

Considering ballpark figures, a beta factor of 2 to 2.5 may be considered reasonable for the change in the OMZ lithosphere at that time (F. Simancas, pers. comm.) (Fig. 11.37). Accordingly,

the contemporaneous subsidence recorded in the Pedroches or Santos de Maimona sedimentary basins of some 1-2 km depth (Quesada et al., 1990c; Expósito, 2000; Armendariz et al.,

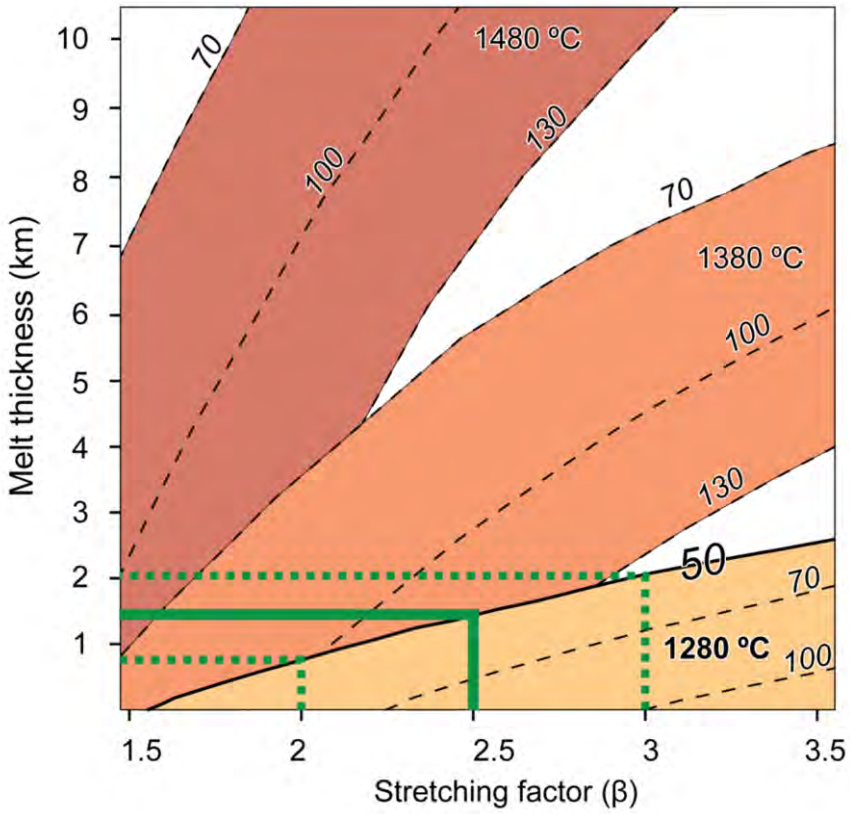

Figure 11.37. Melt thicknesses generated as a function of stretching factor (β), potential mantle temperature (bold captions) and lithosphere thickness (italic captions) modified from McKenzie and Bickle (1989.) Note that 1-2 km melt thickness results from a stretching factor of 2-2.5 for a normal mantle potential temperature, 1280 ºC, and lithosphere thickness of c. 50 km.

2008; Pous et al., 2011) is also consistent with a stretching factor of 2-2.5 (cf., White and McKenzie, 1989). The absence of evidence for plume involvement, so considering a normal mantle potential temperature of 1280ºC, leads to a requirement of somewhat thinned lithosphere, 50 km, to produce a limited amount, 1-2 km, of melt (cf., McKenzie and Bickle, 1988, Fig. 11.37).

It should be borne in mind, moreover, that McKenzie and Bickle (1988) consider a dry system whereas the OMZ hydrous ferromagnesian phases in the mafic rocks indicate that the magmatism had a somewhat elevated water content which would facilitate melting. Furthermore, the stretching factor was most likely irregular across the region, more of a boudin-like than regular variation in lithospheric thickness. More stretched thin, neck, zones are reflected in the

magmatism recorded in the Beja-Acebuches metagabbros and amphibolites (cf., Castro, 1996) and the Los Pedroches sedimentary basin (Armendariz et al., 2008), as well as, we suggest, albeit

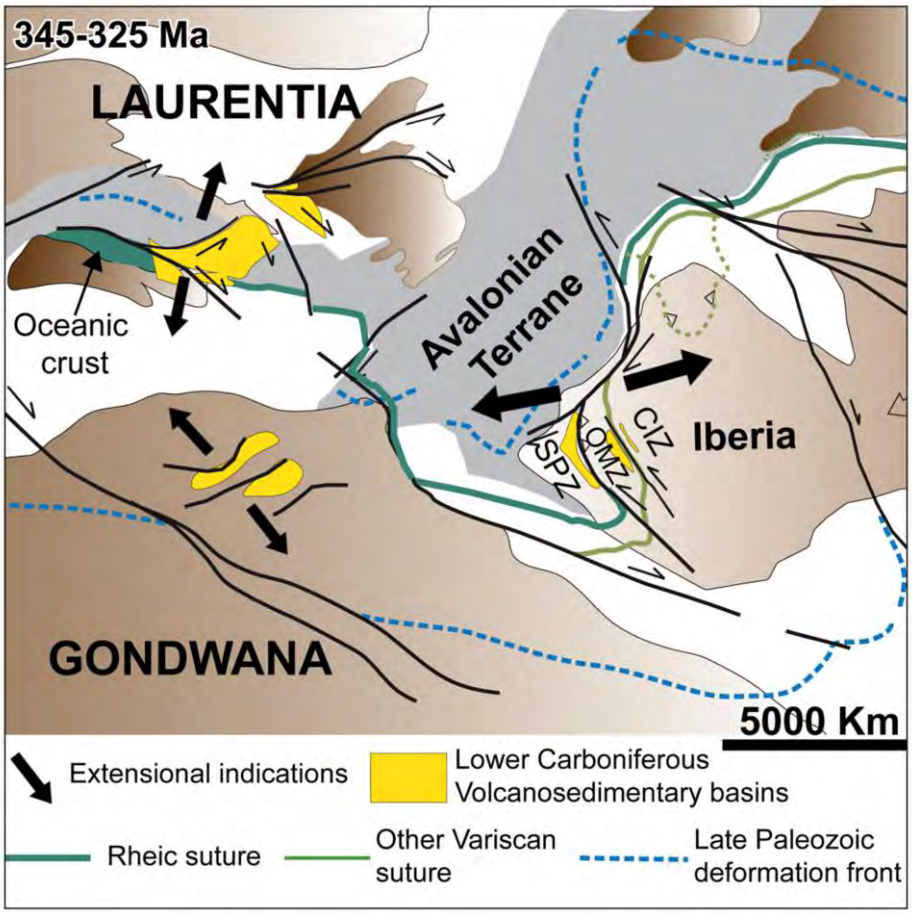

Figure 11.38. Middle Carboniferous reconstruction of the Variscan orogeny, modified from Azor et al., (2008) and Simancas et al., (2009), showing: A) the Visean-Bashkirian transition when the IBERSEIS Reflective Body was emplaced in the Iberian massif middle crust; and, B) other coeval extensional episodes associated with basin development and magmatism in Gondwana and Laurentia.

to a lesser extent, in the hinge of the Olivenza-Monesterio antiform, e.g., Burguillos del Cerro plutonic complex. So the amount of magma produced may have varied locally.

As noted by Latin and White (1990) adiabatic decompression during lithospheric stretching will lead to melting of the asthenosphere if the geotherm intersects the solidus. But, they also observed that the process may produce melt from enriched lithospheric mantle containing small amounts of volatile-bearing phases e.g., pargasite, phlogopite and carbonate (Green 1973; Harte, 1983; Wyllie, 1987; McKenzie, 1989; Latin et a., 1999). Pilet et al., (2011) concluded that melting of the mantle lithosphere, provoked by extension and asthenospheric upwelling would preferentially extract enriched melts of metasomatic volatile- and alkali-rich amphibole veins (Fig.

11.36). In accordance with this, as noted above, Casquet and Galindo (2004) considered that the main source of the Variscan post-collisional high-K magnesian calc-alkaline magmatism was the metasomatised, so by inference lithospheric, subcontinental mantle. So, we suggest that in the OMZ ascent of asthenospheric tholeiitic magma would have, at least locally, raised the temperature of the lithospheric mantle that was already susceptible to melting as a result of extension-related adiabatic uplift. The combined effect could have given rise to fusion of heterogeneous metasomatised lithospheric mantle producing alkaline melts that rose, together with the asthenosphere-derived tholeiites and coalesced forming intrusive bodies located in the middle crust. The connection between this leads us to be able to underline that the magmatism associated with this event was both subalkaline and alkaline.

11.3.3.4 The Role of the IBERSEIS Reflective Body - Mafic Magma Intraplating

The IBERSEIS Reflective Body (IRB) is a high amplitude reflectivity layer located in the OMZ middle crust (Fig. 11.39), its relationship with major structural features and its petrophysical properties led to it being interpreted as early Carboniferous, 345-335 Ma, mantle-derived ultramafic and mafic sills (Simancas et al., 2003; Carbonell et al., 2004; Palomeras et al., 2009; 2011; Brown et al., 2012). Its emplacement is, therefore, coeval with intra-orogenic extension and regional magmatism (Simancas et al., 2003; Pereira et al., 2009, Fig. 11.14). Various authors have connected the IRB with generation of Variscan OMZ ultramafic-mafic to intermediate plutons (Tornos et al., 2005; 2006; Ordoñez-Casado et al., 2008). Although the one km of melt suggested above by the McKenzie and Bickle (1989) model for the OMZ Variscan case may seem low related to the IRB *c.* 5 km thickness of the reflector (Simancas et al., 2003). The reflectors are actually interpreted as a package of highly reflective bodies, mafic rocks, intercalated with lower and middle crustal metasediments (Flecha et al., 2009). This is consistent with numerous thin sills, so an actual magma thickness of considerably less than 5 km.

Here we suggest that mafic magma emplacement may have been the driving force of the main OMZ Variscan magmatism, with mafic magmas causing the crustal melting rather than resulting from it. If this is the case then the IRB may comprise both subalkaline and alkaline compositions.

Gerya and Burg (2007) considered the relatively common, albeit apparently paradoxical, matter of how relatively dense ultramafic or mafic magma can rise and emplace in the middle crust. Using multiphysics modelling they proposed a solution related to the emplacement of melts that are positive buoyancy compared to the lithospheric mantle. Variation in the crustal rheology, as consequence of variable temperature, results in differing intrusion dynamics and

geometry giving rise to a range of bodies from pipes and dykes to deeper plutons and shallower sills. Initial normal faulting result in subsidence but continued magma emplacement would lead to surface uplift. This is consistent with the idea of mafic magma emplacement compensating crustal thinning (e.g., Thybo and Artemieva, 2013).

To consider to the effect to which underplating and intraplating of mafic magma would have on crustal partial melting Bea (2012) undertook numerical modelling of a large mafic sill (5×60 km) with an initial T of 1300 °C (see Fig. 12 in Bea, 2012). He concluded, in agreement with Huppert and Sparks (1989), that conductive heat transfer from crystallizing mafic magma to the surrounding crust was the most effective mechanism to provoke melting (Fig. 11.39). This process generated small-scale crustal magma chambers *c.* 0.9 M.y. post-intrusion. Underplating only resulted in a crustal melt chamber above the mafic sill whereas intraplating generated crustal melt both above and below the sill (Fig. 11.39). Given that crustal-derived magmas are less dense than mafic magma only in the latter case would they rise through the mafic sill favouring magma mixing (Fig. 11.39). This fits very well with the field relations observed in the three studied complexes which permit identification of the different components of the numerical model.

11.3.3.5 The OMZ Variscan Hybrid Plutons

Mid-crustal emplacement of mafic magma is the tectonomagmatic context of the rocks studied in this thesis.

In Burguillos, a pulse of alkaline magma preserved by the *Alkaline Group* formed the main pluton. This initial magma was an open system affected by various differentiation processes. The alkaline magma mixed with a more minor subalkaline tholeiitic component, which was itself subject to accumulation processes forming the *Ultramafic and Mafic Group* (Fig. 11.39). The hybrid alkaline-subakaline transitional mafic magma subsequently mixed with peraluminous crustal melt, presumably at the base of the pluton (cf. Bea 2012) to produce the *Subalkaline Mafic-Intermediate Group*, (Fig. 11.39). This less dense subalkaline mix intruded the main alkaline body resulting in the Burguillos *External Subalkaline Intermediate Unit*, The crustal melt above the upper pluton boundary did not mix, however, because of the relative density contrast. The unmixed crustal magmas were preserved as the *Peraluminous Group*.

Another important factor may be that for interaction to occur, components of a mix need to have similar rheological properties. Sparks and Marshall (1986) observed that ultramafic and felsic components have viscosities that are too different to interact mixing only happening when more similar intermediate compositions are approached. Ultramafic and felsic components may simply have been too dissimilar to interact: felsic magma at 850 ºC with 1% H_2O would have a

viscosity of c. 10^7 Pa s whereas similarly hydrated mafic magma at 1300 ºC would have a viscosity of c. 10^2 Pa s (Giordano et al., 2008).

By analogy, hybrid rocks must, then, reflect end-members that have similar rheological properties, in particular viscosity (Sparks and Marshall, 1986; Jellinek et al., 1999). Mafic to felsic magmas viscosities vary with H_2O content. A mafic magma at *c.* 1000 ºC, with 1-3 wt % H_2O would have a viscosity of 10^4-10^7 Pa s and have a 60% melt fraction (Weidendorfer et al., 2014). A felsic magma at the same temperature and H_2O de 1-2 wt (%) would have similar viscosities, 10^5-10^6 Pa s, but a much greater melt fraction of 80% (Weidendorfer et al., 2014). In this rheological window the mafic and felsic magmas could mix to form hybrid rocks such as those of the Burguillos *External Subalkaline Intermediate Unit*. Weidendorfer, et al., (2014) defined a range of properties for intermediate hybrid rocks that fall in the magma mixing rheological window: viscosity 10^3-10^5 Pa s, 1-3 wt % H_2O and a temperature of 1100-1000 ºC. By inference then the hybrid rocks must have had end-members with such rheological properties. The high crystal fraction, some 40 % in the mafic component is consistent with the cores of the mineral phases in the hybrid rocks recording a different, previous, pre-mix stage of crystallisation.

In Valencia the initial alkaline component was volumetrically less important although some remnants of it are preserved, such as in the Ti-rich mineral chemistry of early formed mineral phases typical in the *Subalkaline Mafic-Intermediate Group*. On the whole, though, the hybrid *Subalkaline Intermediate-Acid Group* mafic-alkaline felsic-peraluminous mingled plutonic complex is more homogeneous than Burguillos del Cerro, although Valencia does include two stocks. The *Southern Stock*, comprises relatively homogeneous mafic-alkaline into felsic-peraluminous hybrid rocks. The *Northern Stock*, on the other hand, evidences a mafic tholeiitic component. This intruded some 10 million years later than the other bodies, it has an elongated lenticular shape with an emplacement-related foliation and a faulted southern contact with the Valencia del Ventoso main pluton. We suggest that it formed by late-stage release of melt through tension-gash opening in an already solidified crust; a comparable process to the transtensional Riedel fault association of tardi-orogenic lamprophyre dykes (Scarrow et al., 2011 and references therein). All the above rocks are cut by veins of the *Peraluminous Group*.

Brovales, like the Valencia Southern Stock, is a relatively homogeneous *Subalkaline Intermediate -Acid Group* mafic-alkaline felsic-peraluminous mix that fractionated from intermediate to acid compositions.

So, the compositional variations of the three plutonic complexes fit well with the sill, IRB, model.

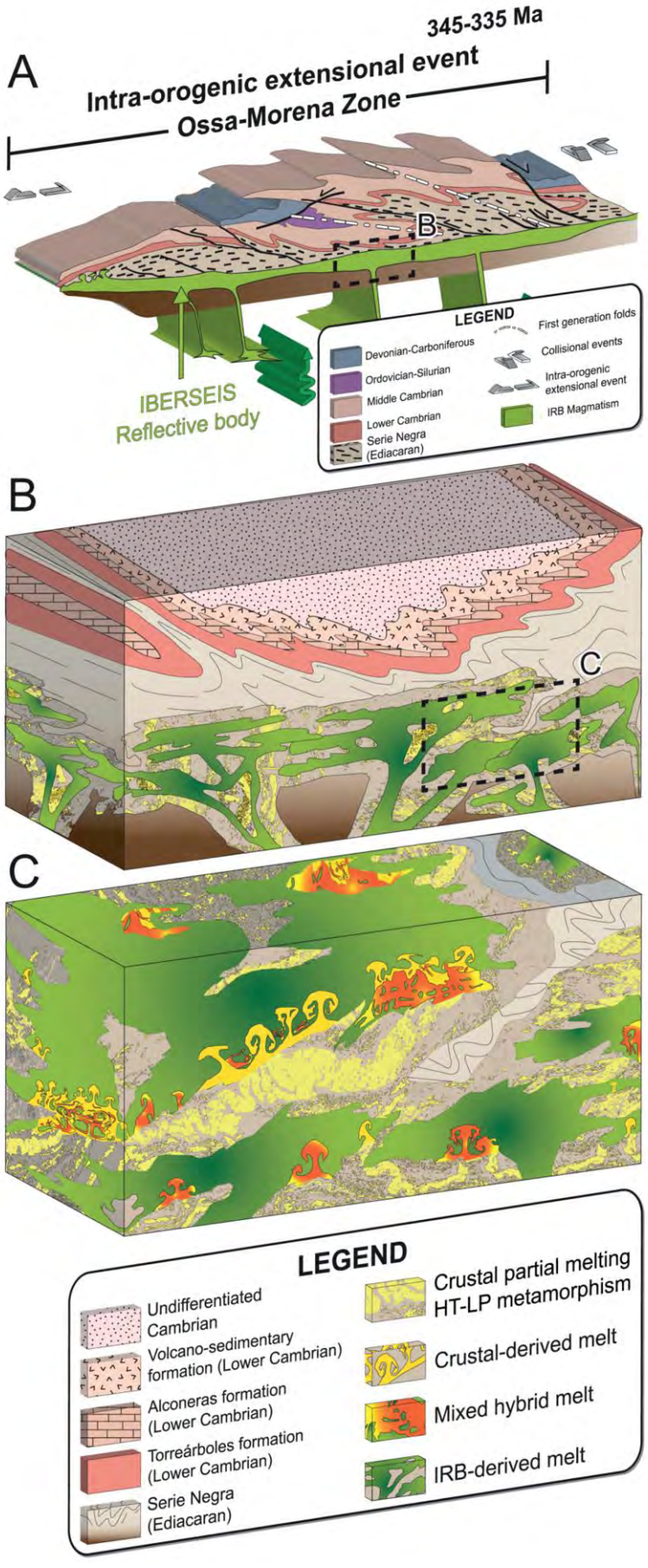
A
345-335 Ma
Intra-orogenic extensional event
Ossa-Morena Zone
B
IBERSEIS
Reflective body
LEGEND
Devonian-Carboniferous
Ordovician-Silurian
Middle Cambrian
Lower Cambrian
Serie Negra
(Ediacaran)
First generation folds
Collisional events
Intra-orogenic
extensional event
IRB Magmatism
B
C
C
LEGEND
Undifferentiated
Cambrian
Volcano-sedimentary
formation (Lower Cambrian)
Alconeras formation
(Lower Cambrian)
Torreárboles formation
(Lower Cambrian)
Serie Negra
(Ediacaran)
Crustal partial melting
HT-LP metamorphism
Crustal-derived melt
Mixed hybrid melt
IRB-derived melt

Further evidence that supports this interpretation is the regional high-T low-P metamorphic event (Pereira et al., 2009; Castro et al., 1999; and Ordoñez-Casado, 1998). Our thermobarometric results, pressures of *c.* 3-4 kbar, 9-12 km, and temperatures varying from 900-1000ºC for the ultramafic rocks to 850-930ºC for the mafic rocks; and, 740-850ºC for the intermediate and felsic rocks. All underpinned by the rocks' ultramafic to mafic composition.

The Burguillos del Cerro plutonic may apparently preserve the upper contact of an alkaline mafic body with the country rock: the *Ultramafic-Mafic* and *Alkaline* groups representing the pluton itself; the *Peraluminous Group* the 'pure' basement crustal-derived melt, and the *Subalkaline groups* that, significantly, intrude the *Ultramafic-Mafic* and *Alkaline* groups, the ascending basal pluton-country rock contact mixed magma which was also preserved, as in Valencia and Brovales (Fig. 11.39).

11.3.4 Concluding Remarks

Our model agrees with the conclusions of Franke (2014) in his far-reaching review of the Variscan orogen topography. He noted that timing and distribution of the Variscan magmatism and high-T metamorphism was not consistent with a model of extensional collapse. The lithospheric extension and heating were interpreted as a result of the Tethyan rifting. That process weakened the lower and middle crust so that stacking was unfeasible, resulting in a 'failed' orogen. The high-T conditions were also invoked to explain the abundant granitoids and the input of mafic components from: Variscan and Cadomian crust and Cadomian metasomatised lithospheric mantle 'mimicking subduction-related magmatism'

So the role of mafic magmatism in orogenesis is changeable. During the Variscan in the CIZ, the mafic magmatism played a minor role resulting from adiabatic melting of lithospheric mantle that was uplifted related to late-orogenic extentional collapse that followed extensive mid-crustal melt felsic magmatism (Scarrow et al, 2009). In the same orogen in the OMZ, however, mafic magmatism drove the crustal melting rather than resulting from it:, extension-related adiabatic asthenospheric and lithospheric mantle melts rose, emplaced at mid-crustal levels and melted the surrounding country rock producing volumetrically minor felsic magmatism. These mixed to produce hybrid rocks.

Figure 11.39. Schematic representations of A) The Early Carboniferous transient extensional/transtensional event during which the IBERSEIS Reflective Body (IRB) was emplaced, modified from Azor et al., (2008) and Simancas et al., (2009); B) Emplacement of the IRB in the middle crust as numerous sills that provoked the high-T low-P metamorphic event and crustal partial melting; C) Detail of the interaction of mantle- and crustal-derived melts, magma mixing results in a hybrid magma at the borders of the mafic intrusion.

Conclusions

Conclusiones

Conclusions

1. The age of the Ossa-Morena Zone Variscan magmatism was determined by SHRIMP U-Pb zircon dating of three plutonic bodies. The Burguillos del Cerro plutonic complex ages all cluster around 336 ± 1 Ma. The Valencia del Ventoso Main Pluton and the Southern Stock have an age of 334 ± 2 Ma whereas the Northern Stock is somewhat younger, 320 ± 3 Ma. The Brovales pluton units were dated at 340 ± 2 Ma. The results obtained define a Carboniferous, Visean-Bashkirian, 340-320 Ma age for three compositionally diverse plutonic complexes, this is interpreted as their emplacement age. Pre-magmatic zircons were principally found in the peraluminous Burguillos two-mica granites and Valencia aplites. They include an older population of Archean and Paleoproterozoic ages and a younger Neoproterozoic and lower Cambrian age population. Inherited Neoproterozoic, Ediacaran, zircons were also found in the Valencia stocks and the Brovales Intermediate Unit. Notably, no Mesoproterozoic zircons were found. The pre-magmatic ages have the same distribution as the OMZ Serie Negra metasedimentary basement which is considered to be their source.

2. The petrographic, mineral chemistry, whole-rock major and trace element geochemistry and Sr and Nd isotopic characteristics of the Burguillos del Cerro, Valencia del Ventoso and Brovales plutonic complexes permit correlation of their units into five broad groups: the Ultramafic-Mafic Group; the Alkaline Group; two Subalkaline groups one being Mafic-Intermediate and the other Intermediate-Felsic; and a Peraluminous Group. Three different sources are identified in the group compositions: two basic mantle-derived, the first alkaline from the lithosphere and the second tholeiitic from the asthenosphere, and a third crustal-derived acid peraluminous partial melt of Ossa-Morena Zone basement metasediments. These compositionally heterogeneous magmas mixed and crystallised leading to the formation of hybrid, cumulate and fractionated rocks giving rise to 'diorites and diorites': some produced by mingling of basic alkaline-subalkaline and acid peraluminous components; and, others fractionated from basic alkaline parental compositions. The Burguillos del Cerro pluton is a predominantly alkaline mafic body that was emplaced in the middle crust: the Ultramafic-Mafic and Alkaline groups represent the pluton itself; the Peraluminous Group the 'pure' basement crustal-derived melt, and the Subalkaline groups that, significantly, intrude the Ultramafic-Mafic and Alkaline groups, the ascending basal pluton-country rock contact mixed magma that are also preserved in the Valencia and Brovales plutonic bodies.

3. The Carboniferous, Visean-Bashkirian, 340-320 Ma age determined for the Burguillos del Cerro, Valencia del Ventoso and Brovales complexes decouples their formation from a subduction-related tectonomagmatic context. They were emplaced instead between two Variscan collisional events related to an intra-orogenic episode of extension/transtension coeval with: sedimentary basin development; high-temperature low-pressure metamorphism; and mid-crustal intraplating of the 'IBERSEIS Reflective Body' interpreted as ultramafic-mafic sills.

4. The Burguillos, Valencia and Brovales complexes varied compositions were generated at the same time and in the same tectonomagmatic context- intra-orogenic extension/transtension. Asthenospheric upwelling of a normal potential temperature mantle as a result of the extension produced a limited amount of melt, 1-2 km. Ascent of the asthenospheric, tholeiitic, magma raised the temperature of the lithospheric mantle. This combined with the effect of extension-related adiabatic uplift provoked fusion of a heterogeneous metasomatised lithospheric mantle producing alkaline melts. These rose together with the asthenosphere-derived tholeiites. Coalescence of the tholeiitic and alkaline mafic magmas formed intraplated intrusions, the IBERSEIS reflective body, in the middle crust. The mafic mantle-derived melts caused localised partial crustal melting producing volumetrically minor felsic magmas that mixed and fractionated generating the compositionally varied Burguillos, del Cerro, Valencia del Ventoso and Brovales complexes.

5. The pre-Variscan paleogeographic position of the Ossa-Morena Zone was further east than has previously been suggested. In the Cambro-Ordovician it was one of a series of north Gondwana terranes that subsequently amalgamated to form Iberia during the Variscan Orogeny. Geochronological data, be it Nd model ages, ages of detrital zircons in sedimentary rocks or pre-magmatic and magmatic ages, are consistent with the Ossa-Morena Zone having a clear input from the Tuareg Shield north Gondwana, African, terrane. This places it in a more easterly paleogeographic position than off the western Anti-Atlas West African Craton as was previously thought. Between the Cadomian and Variscan orogenies terranes rifted off northern Gondwana as the Rheic Ocean opened. The Ordovician magmatic expression of this extension is weaker in the more easterly (Paleozoic position) Central Iberian Zone and Galicia Tras-os-Montes Zone than in the more westerly (Paleozoic position, proposed in this work) Ossa-Morena Zone. Furthermore, stratigraphical and paleontological indications suggest that the Ossa-Morena Zone

was situated in a deep ocean that shallowed eastward to the Galicia Tras-os-Montes Zone and became shallower still in the Central Iberian Zone. So all evidence is consistent with the Cambro-Ordovician rocks of the Ossa-Morena Zone preserving an eastward propagating rift, a 'Gondwana-ward' Rheic Ocean branch, that was subsequently preserved in the Badajoz- Cordoba sinistral transpressive shear zone during the Variscan juxtaposition of the Ossa-Morena Zone and the Central Iberian Zone.

Conclusiones

1. Las dataciones de U-Pb en circón realizadas con SHRIMP revelan que las rocas de los complejos estudiados en esta tesis se formaron en un mismo periodo de tiempo 340-320 Ma (Viseense-Bashkiriense). El complejo plutónico de Burguillos del Cerro tiene una edad de formación de 336 ± 1 Ma. Para el plutón principal y el Stock Sur del complejo de Valencia del Ventoso se obtuvo una edad de 334 ± 2 Ma. Por otro lado, para el Stock Norte, del mismo complejo, la edad obtenida fue 320 ± 3 Ma. Por último, el plutón de Brovales tiene una edad de 340 ± 2 Ma. En las distintas unidades, que dan forma a los complejos estudiados, se describen circones pre-magmáticos, muy abundantes en los granitos y aplitas peraluminosos de Burguillos y Valencia. Estos circones se agrupan, atendiendo a su edad, en distintas poblaciones; Arcaicos, Paleoproterozoicos, Neoproterozoicos resaltando los circones Ediacarenses y Cámbricos basales. Cabe destacar que no fueron encontrados circones con edades Mesoproterozoicas. Esta población de circones heredados presenta la misma distribución que los circones detríticos caracterizados en las rocas del basamento de la Zona de Ossa-Morena, especialmente para la Serie Negra. Por lo tanto, la fuente de los circones pre-magmáticos se le atribuye a este basamento.

2. Del estudio petrográfico, del quimismo de las fases minerales y de la composición de elementos mayores, trazas e isotópico, Sr y Nd, de roca total se llevó a cabo la caracterización del complejo plutónico de Burguillos del Cerro, el complejo plutónico de Valencia del Ventoso y del plutón de Brovales. Este proceso permitió agrupar las distintas unidades definidas en cada uno de ellos en cinco grandes grupos composicionales: el *Grupo Ultramáfico-Máfico*; el *Grupo Alcalino*; dos grupos *Subalcalino*s uno de características máficas e intermedias y otro de características intermedias a félsicas; y el *Grupo Peraluminoso*. De esta clasificación se identificaron tres potenciales fuentes: dos de características máficas, la primera alcalina relacionada con un manto litosférico metasomatizado y la segunda toleiitica asociada al proceso de fusión parcial de un manto astenosférico. La tercera fuente de magmas se relaciona con la fusión parcial de los metasedimentos de la Zona de Ossa-Morena, como por ejemplo la Serie Nerga. En estos magmas, composicionalmente heterogéneos, tuvieron lugar procesos de acumulación y fraccionación además de procesos de interacción entre ellos dando como resultados composiciones híbridas por mezcla de magmas. El complejo plutónico de Burguillos del Cerro esta formado esencialmente por rocas máficas alcalinas que se emplazaron en niveles de la corteza media. Los

grupos Ultramáfico-Máfico y Alcalino dan la forma, casi en su totalidad, a este complejo. El Grupo Peraluminoso representa el magma, 'puro', derivado de la corteza. Por otro lado los grupos Sub-alcalinos, que además intuyen a los grupos Ultramáfico-Máfico y Alcalino, representarían las rocas híbridas, rocas que se preservan en mayor medida en el complejo de Valencia del Ventoso y en plutón de Brovales.

3. La edad Carbonífera, Viseense-Bashkiriense, obtenida en los complejos de Burguillos, Valencia y Brovales desvincula un contexto tectonomagmático relacionado con subducción como el marco donde se formaron estas rocas. Estos complejos plutónicos se emplazaron entre dos eventos colisionales durante la orogenia Varisca, asociados a un proceso de extensión/transtensión intra-orogénica en el que además se produjo un evento metamórfico de alta temperatura y baja presión así como el desarrollo de cuencas sedimentarias. En este evento se relaciona al reflector sísmico IBERSEIS como el producto de la intrusión de rocas ultramáficas y máficas en la corteza media.

4. Los complejos plutónicos de Burguillos, Valencia y Brovales, composicionalmente muy heterogeneos, se formaron en el mismo periodo de tiempo y en el mismo contexto tectonomagmático de extensión/transtensión intra-orogénica. El ascenso de la astenosfera, sin anomalía térmica asociada, en relación al proceso extensional puede generar pequeños volúmenes de fundidos de 1-2 km de potencia. El ascenso de estos magmas astenosféricos, de afinidad toleiitica, junto con el proceso de levantamiento, adiabático, del manto provocaron la fusión de un manto litosférico metasomatizado dando lugar a fundidos máficos alcalinos. La coalescencia de estos magmas como sills de pequeño espesor explicaría la formación del reflector IBERSEIS en la corteza media. Además el emplazamiento de estas rocas provocaría, por transferencia de calor, la fusión parcial del basamento circundante dando lugar a la formación de pequeñas cantidades de magmas félsicos. La coexistencia de estos magmas facilitaría los procesos de mezcla de magmas preservados en las rocas de características híbridas de los complejos de Burguillos, Valencia y Brovales.

5. En esta tesis ha sido considerado el contexto paleogeográfico de la Zona de Ossa-Morena durante el transito Cámbrico-Ordovício antes de la orogenia Varisca. Los datos geocronológicos, como son las distribuciones de las edades modelo de Nd, circones detríticos en rocas sedimentarias y circones magmáticos y pre-magmáticos en rocas ígneas indican que la Zona

de Ossa-Morena estaría localizada en las proximidades del Escudo del Tuareg durante el transito Cámbrico-Ordovíco, posición más oriental, coordenadas actuales, que la establecida previamente en las cercanías del Escudo Oeste Africano en la región del Anti-Atlas. En este periodo de tiempo se enmarca, además, la apertura del Océano Rhéico a lo largo del margen norte de Gondwana. En consecuencia la expresión magmática de este evento se registra de manera más leve en los terrenos, de acuerdo con su posición paleogeográfica en el Paleozoico, situados en la parte más oriental, como es el caso de la Zona Centro-Ibérica o los terrenos parautóctonos de la Zona de Galicia Tras-os-Montes. Mientras que el evento magmático Cámbrico-Ordovícico es más evidente en las zonas localizadas en una posición paleogeográfica más occidental, como la que se propone en este trabajo para la Zona de Ossa-Morena. Los datos paleontológicos y estratigráficos ponen de manifiesto unas condiciones de sedimentación más profunda para la Zona de Ossa-Morena que para las zonas paleogeográficamente más orientales, como la Zona Centro-Ibérica, en las que se establecen unas condiciones de sedimentación someras. Todas estas evidencias apoyan un modelo para el tránsito Cámbrico-Ordovícico de la Zona de Ossa-Morena se corresponderían con una propagación de una 'rama' o 'brazo' del Océano Rhéico que se preservaría actualmente en la zona de cizalla transpresiva izquierda de Badajoz-Cordoba, como consecuencia de la amalgamación de la Zona Centro-Ibérica y la Zona de Ossa-Morena durante la orogenia Varisca.

References

References

Abad, I., Nieto, F., Velilla, N., Simancas, J.F., 2004. La Zona Sudportuguesa: Metamorfismo. In: Vera, J.A. (ed.). Geología de España, SGE-IGME, Madrid, Spain, 209-211.

Ábalos, B., Gil Ibarguchi, J.I., Eguíluz, L., 1991. Cadomian subduction/collision and Variscan transpression in the Badajoz-Córdoba shear belt, southwest Spain. Tectonophysics 199, 51-72.

Ábalos, B., 1992. Variscan shear-zone deformation of late Pre-Cambrian basement in SW Iberia: implications for circum-Atlantic pre-Mesozoic tectonics. Journal of Structural Geology 14, 807-823.

Ábalos, B., Díaz-Cusi, J., 1995. Correlation between seismic anisotropy and major geological structures in SW Iberia: A case study on continental lithosphere deformation: Tectonics 14, 1021-1040.

Abati, J., Aghzer, A.M., Gerdes, A., Ennih, N., 2010a. Detrital zircon ages of Neoproterozoic sequences of the Moroccan Anti-Atlas belt. Precambrian Research 181, 115-128.

Abati, J., Gerdes, A., Fernández-Suárez, J., Arenas, R.,Whitehouse, M.J., Díez Fernández, R., 2010b. Magmatism and early-Variscan continental subduction in the northern Gondwana margin recorded in zircons from the basal units of Galicia, NW Spain. Geological Society of America Bulletin 122, 219–235.

Abdallah, N., Liégeois, J.P., De Waele, B., Fezaa, N., Ouabadi, A., 2007. The Temaguessine Fe-cordierite orbicular granite (Central Hoggar, Algeria): U-Pb SHRIMP age, petrology, origin and geodynamical consequences for the late Pan-African magmatism of the Tuareg shield. Journal of African Earth Sciences 49, 153-178.

Acef, K., Liégeois, J.P., Ouabadi, A., Latouche, L., 2003. The Anfeg post-collisional Pan-African high-K calc-alkaline batholith (Central Hoggar, Algeria), result of the LATEA microcontinent metacratonization. Journal of African Earth Sciences 37, 295-311.

Aït Malek, H., Gasquet, D., Bertrand, J.M., Leterrier, J., 1998. Géochronoligie U-Pb sur zirocn de granitöides éburnéens et panafricains dans les boutonnières protérozoïques d'lgherm, du Kerdous et du Bas Drâa (Anti-Atlas occidental, Maroc). Comptes Rendus de l'Académie des Sciences Paris 327, 819-826.

Aitken, A.R.A., Betts, P.G., Ailleres, L., 2009. Lithosphere The architecture, kinematics, and lithospheric processes of a compressional intraplate orogen occurring under Gondwana assembly: The Petermann orogeny, central Australia. Lithosphere 1, 1343-357.

Alía, M., 1963. Rasgos estructurales de la Baja Extremadura. Boletín de la Real Sociedad Española de Historia Natural 61, 51-72.

Almarza, J., 1996. Petrología y geoquímica de los yacimientos de uranio del Sureste de Badajoz. Ph.D. thesis, University of Sevilla.

Álvaro, J.J., Bellido, F., Gasquet, D., Pereira, M.F., Quesada, C., Sánchez-García, T., 2014. Diachronism in the late Neoproterozoic–Cambrian arc-rift transition of North Gondwana: A comparison of Morocco and the Iberian Ossa-Morena Zone. Journal of African Earth Sciences 98, 113-132.

Antunes, I.M.H.R., Neiva, A.M.R., Silva, M.M.V.G., Corfu, F., 2008. Geochemistry of S-type granitic rocks from the reversely zoned Castelo Branco pluton (central Portugal). Lithos 103, 445–465.

Antunes, A.I.M., Santos, J.F., Azevedo, M.R., Corfu, F, 2011. New U-Pb zircon age contraints for the emplacement of the Reguengos de Monsaraz Massif (Ossa Morena Zone). Seventh Hutton Symposium on Granites and Related Rocks, Avila Spain, 9 p.

Apalategui, O., Barranco, E., Contreras, F., Delgado, M., Roldán, F.J., Quesada, C., 1983. Mapa de la hoja Nº 916 Aroche. Instituto Geológico y Minero, scale 1:50,000. Spain.

Apalategui, D., Barranco, E., Contreras, F., Delgado, M., Roldan, F.J. 1984. Mapa de la hoja Nº 917 Aracena. Instituto Geológico y Minero, scale 1:50,000. Spain.

Apalategui, O., Borrero, J.D., Higueras, P., 1985a. División en grupo de rocas en Ossa-Morena oriental. Temas Geologicos y Mineros 8, 73-80.

Apalategui, O., Borrero, J.D, Eguíluz, L., Roldán, F.J., Garrote, A., Higueras, P., Liñán, E., Palacios, T., 1985b. Mapa de la Hoja Nº 918 Azuaga. Instituto Geológico y Minero, scale 1:50,000. Spain.

Apalategui, O., Jorquera, A., Villalobos, M., Egíluz, L., 1988. Mapa de la Hoja Nº 801 Olivenza. Instituto Geológico y Minero, scale 1:50,000. Spain.

Apraiz, A., Eguiluz, L., 1996. El nucleo metamórfico de Valuengo (Zona de Ossa-Morena, Macizo Ibérico): petrografía, termobarometría y evolución geodinámica. Revista de la Sociedad Geológica de España 9, 29-49.

Apraiz, A., 1998. Geología de los macizos de Lora del Río y Valuengo (Zona de Ossa Morena): Evolución tectonometamórfica y significado geodinámico. Ph.D. thesis, University of País

Vasco.

Apraiz, A., Eguiluz, L., 2002. Hercynian tectono-thermal evolution associated with crustal extension and exhumation of the Lora del Río metamorphic core complex (Ossa-Morena zone, Iberian Massif, SW Spain). International Journal of Earth Sciences 91, 76-92.

Araújo, A., Fonseca, P., Munhá, J., Moita, P., Pedro, J., Ribeiro, A., 2005. The Moura Phyllonitic Complex: An accretionary complex related with obduction in the southern Iberia Variscan suture. Geodinamica Acta 18, 375–388.

Arculus, R.J., 2003. Use and abuse of terms calcalkaline and calcalkalic. Journal of Petrology 44, 929–935.

Ardizone, J., Mezcua, J., Socias, I., 1989. Mapa aeromagnético de España Peninsular, Instituto Geográfico Nacional, Madrid, Spain.

Arenas, R., 1984. Características y significado del volcanismo ordovícico-silúrico de la serie autóctona envolvente del Macizo de Cabo Ortegal (Galicia, NW de España). Revista de Materiales y Procesos Geológicos 2, 135–144.

Arenas, R., 1985. Evolución petrológica y geoquímica de la Unidad Alóctona inferior del complejo de metamórfico básico ultrabásico de Cabo Ortegal (Unidad de Moeche) y del Silúrico parautóctono, Cadena Hercínica Ibérica (NW de España). Ph.D., thesis University Complutense de Madrid, 543 p.

Arenas, R., Martínez-Catalán, J.R., Guitérrez-Marco, J.C., Díaz-García, F., 2004. Zona de Galicia-tras-os-Montes: Introducción. In: Vera, J.A. (ed.). Geología de España, SGE-IGME, Madrid, Spain, 133–135.

Arenas, R., Martínez Catalán, J.R., Sánchez Martínez, S., Fernández-Suárez, J., Andonaegui, P., Pearce, J.A., Corfu, F., 2007. The Vila de Cruces ophiolite: a remnant of the early Rheic Ocean in the Variscan suture of Galicia (northwest Iberian Massif). Journal of Geology 115, 129–148.

Arenas, R., Sánchez Martínez, S., Gerdes, A., Albert, R., Díez Fernández, R., Andonaegui, P., 2013. Re-interpreting the Devonian ophiolites involved in the Variscan suture: U–Pb and Lu–Hf zircon data of the Moeche Ophiolite (Cabo Ortegal Complex, NW Iberia). International Journal of Earth Sciences 103, 1385–1402.

Arenas, R., Díez Fernández, R., Sánchez Martínez, S., Gerdes, A., Fernández-Suárez, J., Albert, R., 2014. Two-stage collision: exploring the birth of Pangea in the Variscan terranes. Gondwana Research 25, 756–763.

Armendariz, M., López-Guijarro, R., Quesada, C., Pin, C., Bellido, F., 2008. Genesis and evolution of a syn-orogenic basin in transpression: Insights from petrography, geochemistry and Sm–Nd systematics in the Variscan Pedroches basin (Mississippian, SW Iberia). Tectonophysics 461, 395-413.

Arriola, A., Eguíluz, L., Fernández-Carrasco, J., Garrote, A., 1984. Individualización de diferentes dominios y unidades en el anticlinorio Olivenza-Monesterio. Cuadernos del Laboratorio Geologico de Laxe 8, 147-168.

Arzi, A.A., 1978. Critical phenomena in the rheology of partially molten rocks. Tectonophysics 74, 173-184.

Avigad, D., Kolodner, K., McWilliams, M., Persing, H.M., Weissbrod, T., 2003. Origin of northern Gondwana Cambrian sandstone as revealed by SHRIMP dating of detrital zircons. Geology, 31, 227–230

Avigad, D., Gerdes, A., Morag, N., Bechstädt, T., 2012. Coupled U–Pb–Hf of detrital zircons of Cambrian sandstones from Morocco and Sardinia: Implications for provenance and Precambrian crustal evolution of North Africa. Gondwana Research 21, 690-703.

Azor, A., 1994. Evolución tectonometamórfica del límite entre las Zonas Centroibérica y de Ossa-Morena (Cordillera Varisca, SO de España). Ph. D., thesis Univerity of Granada, 295 p.

Azor, A., González-Lodeiro, F., Martínez-Poyatos, D., Simancas, J.F., 1994a. Regional significance of kilometric-scale NE-vergent recumbent folds associated with E- to SE-directed shear on the southern border of the Central Iberian Zone (Hornachos-Olivas region, Variscan Belt, Iberian Peninsula). International Journal of Earth Science (Geol Rundschau) 83, 377-387.

Azor, A., González-Lodeiro, F., Simancas, J.F., 1994b. Tectonic evolution of the boundary between the Central Iberian and Ossa-Morena Zones (Variscan Belt, southwest Spain). Tectonics 13, 45-61.

Azor, A., Expósito, I., González-Lodeiro, F., Simancas, J.F., Martínez-Poyatos, D., 2004. La Zona de Ossa-Morena: Estructura y Metamorfismo. In: Vera, J.A. (ed.). Geología de España, SGE-IGME, Madrid, Spain, 173-179.

Azor, A., Rubatto, D., Simancas, J.F., González Lodeiro, F., Martínez-Poyatos, D.J., Martín-Parra, L.M., Maas, J., 2008. Rheic Ocean ophiolitic remnants in southern Iberia questioned by SHRIMP U-Pb zircon ages on the Beja-Acebuches amphibolites. Tectonics 27, TC5006.

Azzouni-Sekkal, A., Liegeois, J.P., Bechiri- Benmerzoug, F., Belaidi-Zinet, S. and Bonin, B., 2003. The "Taourirt" magmatic province, a marker of the closing stage of the Pan-African orogeny in the Tuareg Shield: review of available data and Sr-Nd isotope evidence. Journal of African Earth Sciences 37, 331–350.

Bachiller, N., 1996. Las alteraciones hidrotermales de los leucogranitos del complejo intrusivo de Burguillos del Cerro (Badajoz): edad, geoquímica y modelo de procedencia y evolución de los fluidos. Unpublished Bachelor thesis, University Complutense of Madrid.

Bachiller, N., Galindo, C., Darbyshire, D.P.F., Casquet, C., 1997. Geocronología Rb–Sr de los leucogranitos del complejo plutónico de Burguillos del Cerro (Badajoz). Geogaceta 21, 29–30.

Baeza-Rojano, L.J., Rúiz-García, C., Ruiz-Montes, M., 1978. Presencia de formaciones vulcanosedimentarias y mineralizaciones de hierro asociadas en el eje magmatico La Coronada-Villaviciosa de Córdoba. Boletín Geológico y Minero 89, 431-437.

Bandrés, A., Eguiluz, L., Pin, C., Paquette, J.L., Ordóñez-Casado, B., Le Fèvre, B., Ortega, L.A., Gil-Ibarguchi, J.I., 2004. The northern Ossa-Morena Cadomian batholith (Iberian Massif): magmatic arc origin and early evolution. International Journal of Earth Science (Geol Rundschau) 93, 860-885.

Barbarin, B., 1999. A review of the relationships between granitoid types, their origins and their geodynamic environments. Lithos 46, 605–626.

Barbey, P., Bertrand, J.M., Angoua, S., Dautel, D., 1989. Petrology and U/Pb geochronology of the Telohat migmatites, Aleksod, Central Hoggar, Algeria. Contributions to Mineralogy and Petrology 101, 207-219.

Barbey, P., Nachit, H., Pons, J., 2001. Magma-host interactions during differentiation and emplacement of a shallowlevel, zoned granitic pluton (Tarcouate pluton, Morocco): implications for magma emplacement. Lithos 58, 125–143.

Barbey, P., Oberli, F., Burg, J.P., Nachit, H., Pons, J., Meier, M., 2004. The Palaeoproterozoic in western Anti-Atlas (Morocco): a clarification. Journal of African Earth Sciences 39, 239-245.

Bard, J.P., 1969. Le métamorphisme regional progressif de Sierra de Aracena en Andalousie occidentale (Espagne). Ph.D. thesis, Universit of Montpellier, 379 pp.

Bard, J.P., 1971. Sur l'alternance des zones métamorphiques dans le segment hercynien sud-ibérique; comparasion de la variabilité des caracteres géotectoniques de ces zones avec les

orogenès "orthotectoniques". Boletín Geológico y Minero 82, 324-345.

Bard, J.P., Capdevila, R., Matte, P, Ribeiro, A., 1973. Geotectonic Model for the Iberian Variscan Orogen. Nature 241, 50-52.

Bard, J.P., 1977. Signification tectonique des métatholeites d'affinité abyssale de la ceinture de base pression d'Aracena (Huelva, Espagne). Bulletin de la societe geologique de France 19, 385–393.

Bard, J.P., Moine, B., 1979. Acebuches amphibolites in the Aracena hercynian metamorphic belt (southwest Spain): Geochemical variations and basaltic affinities. Lithos 12, 271-282.

Bard, J.P., Burg, J.P., Matte, P, Ribeiro, A., 1980. La chaîne hercynienne d'Europe occidentale en termes de tectonique des plaques. In: Cogné, J., Slansky, M., (eds), Colloque C6, Géologie de l'Europe-26°, Paris, 7-17.

Bard, J.P., 1992. Les complexes intrusifs acide-basique calco-alcalins de la chaîne varisque sud-ibérique et leurs liaisons avec les grands cisaillements transpressifs de Badajoz-Cordue et de la zone sud-ibérique: proposition de modèles géodynamiques impliquant des processus de subduction continentale. Comptes Rendus de l'Academie de Science de Paris 314, 711-716.

Barriga, F.J.A.S., Carvalho, D., Ribeiro, A., 1997. Introduction to the Pyrite Belt. In: Barriga, F.J.A.S., Carvalho, D., (eds). Geology and VMS Deposits of the Iberian Pyrite Belt, Guidebook series 27, 1-20.

Barth, M.G., Rudnick, R.L., Carlson, R.W., Horn, I., McDonough, W.F., 2002. Re-Os and U-Pb geochronological constraints on the eclogite-tonalite connection in the Archean Man Shield, West Africa. Precambrian Research 118, 267-283.

Bea, F., Sánchez-González, J.G., Serrano-Pinto, M., 1987. Una compilación geoquímica (elementos mayors) para los granitoids del Macizo Hespérico. In: Bea, F., Carnicero, A., Gonzalo, J.C., López-Plaza., M., Rodriguez-Alonso, M.D., (eds), Geología de los granitoids y rocas asociadas del Macizo Hepérico. Rueda, Madrid, 87-193.

Bea, F.,1991. Geochrmical modelling of low melt-fraction anatexis in a peraluminous system: the Peña Negra Complex (central Spain). Geochimica et Cosmochimica Acta 55, 1859-1874.

Bea, F., Pereira, M.D., Corretgé, L.G., Fershtater, G.B., 1994. Differentiation of strongly peraluminous, perphoshorous granites. The Pedrobernardo pluton, central Spain. Geochemica et Cosmochimica Acta 58, 2609-2628.

Bea, F., 2004. La naturaleza del magmatismo de la Zona Centroibérica: consideraciones generales y ensayo de correlación. In: Vera, J.A. (ed.). Geología de España, SGE-IGME, Madrid,

Spain, 128-133.

Bea, F., Montero, P., González-Lodeiro, F., Talavera, C., Molina, J. F., Scarrow, J. H., Whitehouse, M. J., Zinger, T. F., 2006a. Zircon thermometry and U-Pb ion-microprobe dating of the gabbros and associated migmatites of the Variscan Toledo Anatectic Complex, Central Iberia. Journal of the Geological Society, London 163, 847-855.

Bea, F., Montero, P., Talavera, C., Zinger, T., 2006b. A revised Ordovician age for the oldest magmatism of Central Iberia. U-Pb ion microprobe and LA-ICP-MS dating of the Miranda do Douro orthogneiss. Geologica Acta 4, 395–401.

Bea, F., Montero, P., Talavera, C., Abu Anbar, M., Scarrow, J.H., Molina, J.F., Moreno, J.A., 2010. The palaeogeographic position of Central Iberia in Gondwana during the Ordovician: evidence from zircon chronology and Nd isotopes. Terra Nova 22, 341-346.

Bea, F., Montero, P., Abu-Anbar, M., Molina, J.F., Scarrow, J.H., 2011. The Bir Safsaf Precambrian inlier of South West Egypt revisited. A model for ~1.5 Ga TDM late Pan-African granite generation by crustal reworking. Lithos 125, 897-914.

Bea, F., 2012. The sources of energy for crustal melting and the geochemistry of heat-producing elements. Lithos 153, 278-291.

Bea, F., Montero, P., Haissen, F., Rjimati, E., Molina, J.F., Scarrow, J.H, 2014. Kalsilite-bearing plutonic rocks: The deep-seated Archean Awsard massif of the Reguibat Rise, South Morocco, West African Craton. Review Earth-Science Reviews 138, 1-24.

Bellido, F., González-Lodeiro, F., Klein, F., Martínez-Catalán, J., Pablo-Maciá, J.G., 1987. Las rocas graníticas hercínicas del Norte de Galicia y Occidente de Asturias. Memorias del Instituto Geologico Minero de España 101, 1-157.

Bellon, H., Blanchere, H., Crousilles, M., Deloche, C., Dixsaut, C., Hertritch, B., Prost-Dame, V., Rossi, P.H., Simon, D., Tamain, G., 1979. Radiochronologie, évolution téctono-magmatique et implications métallogéniques dans les cadomo-variscides du Sud-Est Hespérique. Bulletin de la Société Géologique de France 21, 113-120.

Bendaoud, A., Ouzegane, K., Godard, G., Liegeois, J.-P., Kienast, J.-R., Bruguier, O., Drareni, A., 2008. Geochronology and metamorphic P-T-X evolution of the Eburnean granulite-facies metapelites of Tidjenouine (Central Hoggar, Algeria): witness of the LATEA metacratonic evolution. Geological Society, London, Special Publications 297, 111-146.

Berry, R.F., Jenner, G.A., Meffre, S., Tubrett, M.N., 2001, A North American provenance for

Neoproterozoic to Cambrian sandstones in Tasmania? Earth and Planetary Science Letters 192, 207-222.

Bertrand, J.M., Meriem, D., Lapique, F., Michard, A., Dautel, D., Gravelle, M., 1986a. Nouvelles donn ees sur l'age de la tectonique pan-africaine dans le rameau oriental de la cha^ıne Pharusienne (région de Timgaouine, Hoggar, Algérie). Comptes Rendus de l'Académie des Sciences Paris 302, 437–440.

Bertrand, J.M., Michard, A., Boulier, A.M., Dautel, D., 1986b. Structure and U/Pb geochronology of central Hoggar (Algeria): a reappraisal of its Pan-African evolution. Tectonics 5, 955-972.

Beuf, S., Biju-Duval, B., de Charpal, O., Rognon, P., Gariel, O., Bennacef, A., 1971. Les Grés du Paléozoique inférieur au Sahara. Publications de línstitut Francais du Pétrole 18, 1-464.

Bingen, B., Nordgulen, Ø., Sigmond, E.M.O., Tucker, R., Mansfeld, J., Hogdahl, K., 2003. Relations between 1.19–1.13 Ga continental magmatism, sedimentation and metamorphism, Sveconorwegian province, S Norway. Precambrian Research 124, 215-241.

Black, L.P., Kamo, S.L., Allen, C.M., Aleinikoff, J.A., Davis, D.W., Korsch, J.R., Foudolis, C., 2003. TEMORA 1: a new zircon standard for Phanerozoic U–Pb geochonology. Chemical Geology 200, 155–170.

Black, L.P., Kamo, S.L., Allen, C.M., Davis, D.W., Aleinikoff, J.N., Valley, J.W., Mundil, R., Campbell, I.H., Korsch, R.J., Williams, I.S., Foudoulis. C., 2004. Improved 206 Pb/238 U microprobe geochronology by the monitoring of a trace-element-related matrix effect; SHRIMP, ID–TIMS, ELA–ICP–MS and oxygen isotope documentation for a series of zircon standards. Chemical Geology 205, 115-140.

Blanc, A., Bernard-Griffiths, J., Caby, R., Caruba, C., Caruba, R., Dars, R., Fourcade, S., Peucat, J.J., 1992. U-Pb dating and isotopic signature of the alkaline ring complexes of Bou Naga (Mauritania): its bearing on late Proterozoic plate tectonics around the West African Craton. Journal of African Earth Sciences 14, 301–311.

Bogdanova, S.V., Bingen, B., Gorbatschev, R., Kheraskova, T.N., Kozlov, V.I., Puchkov, V.N., Volozh, Y.A., 2008. The East European Craton (Baltica) before and during the assembly of Rodinia. Precambrian Research 160, 23-45.

Bonin, B., Azzouni-Sekkal, A., Bussy, F., Ferrag, S., 1998. Alkali-calcic and alkaline post- orogenic (PO) granite magmatism: petrologic constraints and geodynamic settings. Lithos 45, 45–70.

Bonin, B., 2004. Do coeval mafic and felsic magmas in post-collisional to within-plate regimes

necessarily imply two contrasting, mantle and crustal, sources? A review. Lithos 78, 1–24.

Booth-Rea, G., Simancas, J.F., Azor, A., Azañón, J.M., González Lodeiro, F., Fonseca, P.E., 2006. HP–LT Variscan metamorphism in the Cubito–Moura schists (Ossa-Morena Zone, southern Iberia). Comptes Rendus Geoscience 338, 1260-1267.

Borodin, L.S., 1987. Petrochemical Trends and classification of the Gabbro-Granitoid Series. International Geology Review 11, 1189-1198

Bouabdelli, M., Piqué, A., 1996. Du bassin sur décrochement au basin d'avant-pays: dynamique du bassin d'Azrou-Khénifra (Maroc hercynien central). Journal of African Earth Sciences 22, 213–224.

Braid, J.A., Murphy J.B., Quesada C., 2010. Structural analysis of an accretionary prism in a continental collisional setting, the Late Paleozoic Pulo do Lobo Zone, Southern Iberia. Gondwana Research 17, 422-439.

Braid, J.A., Murphy J.B., Quesada C., 2011. Tectonic escape of a crustal fragment during the closure of the Rheic Ocean: U-Pb detrital zircon data from the Late Palaeozoic Pulo do Lobo and South Portuguese zones, southern Iberia. Journal of the Geological Society, London 168, 383-392.

Brey, G.P., Köhler, T., 1990. Geothermobarometry in Four-phase Lherzolites II. New Thermobarometers, and Practical Assessment of Existing Thermobarometers. Journal of Petrology 31, 1353-1378.

Brown, M., 2007. Crustal melting and melt extraction, ascent and emplacement in orogens: mechanisms and consequences. Journal of the Geological Society, London 164, 709–730.

Brown, M., 2010. Melting of the continental crust during orogenesis: The thermal, rheological and compositional consequences of melt transport from lower to upper continental crust. Canadian Journal of Earth Sciences 47, 655-694.

Brown, D., Zhang, X., Palomeras, I., Simancas, J.F., Carbonell, R., Juhlin, C., Salisbury, M., 2012. Petrophysical analysis of a mid-crustal reflector in the IBERSEIS profile, SW Spain. Tectonophysics 550–553, 35–46.

Bruguier, O., Bosch, D., Caby, R., Galland, B., Hammor, D., 2008. Sampling an active continental paleo-margin: a LA-ICP-MS U–Pb zircon study from the Adrar des Iforas (Mali). Geochimica et Cosmochimica Acta 72, A118.

Brun, J.P, Pons, J., 1981. Strain patterns of pluton emplacement in a crust undergoing non-coaxial deformation, Sierra Morena, Southern Spain. Journal of Structural Geology 3, 219-229.

Burg J.P., Matte, P., 1978. A cross section trough the French Massif central and the scope of its Variscan geodynamic evolution. Zeitschrift der Deutschen Geologischen Gesellschaft 109, 429-460.

Burg J.P., Iglesias, M., Laurent, P., Matte, P., Ribeiro, A., 1981. Variscan intracontinental deformation: the Coimbra-Badajoz shear zone (SW Iberia Peninsula). Tectonophysics 78, 161-177.

Caby, R., Andreopoulos-Renaud, U., Gravelle, M., 1982. Cadre géologique et géochronologie U/Pb sur zircon des batholites précoces dans le segment pan-africain du Hoggar central (Algérie). Bulletin Société Géologique France 24, 677–684.

Caby, R., Andreopoulos-Renaud, U., Lancelot, J.R., 1985. Les phases tardives de l'orogéné se pan-africaine dans l'Adrar des Iforas oriental (Mali): lithostratigraphie des formations molassiques et géochronologie U/Pb sur zircon de deux massifs intrusifs. Precambrian Research 28, 187–199.

Caby, R., Andreopoulos-Renaud, U., 1989. Age U–Pb a 620 Ma d'un pluton synorog_enique de l'Adrar des Iforas (Mali). Cons_equences pour l'age de la phase majeure de l'orog_ene pan-africaine. Comptes Rendus de l'Acadèmie des Sciences Paris 308, 307–314.

Caby, R., Andreopoulos-Renaud, U., Pin, C., 1989. Late Proterozoic arc-continent and continent-continent collision in the Pan-African trans-Saharan belt of Mali. Canadian Journal of Earth Sciences 26, 1136–1146.

Caby, R., 2003. Terrane assembly and geodynamic evolution of central-western Hoggar: a synthesis. Journal of African Earth Sciences 37, 133-159.

Caen-Vachette, M., Umeji, A.C., 1983. Whole-rock Rb–Sr dating of two monzogranites in southern Nigeria and their implications on the age of the Pan-African orogenic cycle. Journal of African Earth Sciences 1, 339-342.

Capdevila, R., Matte, P., Paredes, J., 1971. La nature du Précambrien et ses relations avec le Paleozoïque dans la Sierra Morena centrale (Sud de l'Espagne). Comptes Rendus de l'Academie des Sciences de Paris 273, 1359–1362.

Carbonell, R., Simancas, J.F., Juhlin, C., Pous, J., Pérez-Estaún, A., González-Lodeiro, F., Muñoz, G., Heise, W., Ayarza, P., 2004. Geophysical evidence of a mantle derived intrusion in SW Iberia. Geophysical Research Letters 31, L11601.

Carey, S.W., 1955. The orocline concept in geotectonics: Proceedings of the Royal Society of Tasmania 89, 255–288.

Carlier, G., Lorand, J.P., Audebaud, E., Kienast, J.R., 1997. Petrology of an unusual orthopyroxene-bearing minette suite from southeastern Peru, Eastern Andean Cordillera: Al-rich lamproites contaminated by peraluminous granites. Journal of Volcanology and Geothermal Research 75, 59–87.

Carrilho-Lopes, J.M., Munha, J.M., Oliveira, V.M.J., 1990. In: VIII Semana de Geoquímica, Abstracts, University of Lisboa.

Carrilho-Lopes, J.M., Munha, J.M., Wu, C.T., Oliveira, V.M.J., 1998. O complexo plutónico de Monforte-Santa Eulalia (Alentejo-NE, Portugal Central): caracterizaçao geoquímica e consideraçoes petrogenéticas. Comuicaçoes Instituto Geologico e Mineiro 83, 127-142.

Carvalhosa, B.A., 1965. Contribuçao para o conhecimiento geologico da regiao entre Portel y Ficalho (Alentejo). Memoria Serviçio Geologico Portugal 11, 1-130.

Carvalhosa, A., Carvalho, A., Alves, C., Pina, H., 1969. Carta Geológica de Portugal 40-A Évora. Instituto Geológico e Mineiro, scale 1:50.000. Portugal.

Carvalhosa, A., Zbyszewski, G., 1994. Carta Geológica de Portugal 35-D Montemor-o-Novo. Instituto Geológico e Mineiro, scale 1:50.000. Portugal.

Casquet, C., Galindo, C., Tornos, F., Velasco, F., Canales, A., 2001. The Aguablanca Cu–Ni ore depos- it (Extremadura, Spain), a case of synorogenic orthomagmatic mineralization: age and iso- tope composition of magmas (Sr, Nd) and ore (S). Ore Geology Reviews 18, 237–250.

Casquet, C., Galindo, C., 2004. Magmatismo varisco y postvarisco en la Zona de Ossa-Morena. In: Vera, J.A., (ed.), Geología de España. Sociedad Geológica de España-Instituto Geológico Minero España, Madrid, 194-199.

Castro, A., Fernández, C., De la Rosa, J., Moreno-Ventas, I., Rogers, G., 1996a. Significance of MORB-derived amphibolites from the Aracena Metamorphic Belt, Southwest Spain. Journal of Petrology 37, 235–260.

Castro, A., Fernández, C., De La Rosa, J. D., Moreno-Ventas, I., El-Hmidi, H., El-Biad, M., Bergamin, J.F., Sánchez, N., 1996b. Triple-junction migration during Paleozoic Plate convergence: the Aracena metamorphic belt, Hercynian massif, Spain. Geologische Rundschau 85, 108-185.

Castro, A., Fernández, C., El-Hmidi, H., El-Biad, M., Díaz, M., De la Rosa, J., Stuart, F., 1999. Age constrains to the relationships between magmatism, metamorphism and tectonism in the Aracena metamorphic belt, southern Spain. International Journal Earth Sciences 88,

26–37.

Chacón, J., Fernández-Carrasco, J., Mitrofanov, F., Timofeev, B.V., 1984. Primeras dataciones microfitopaleontológicas en el sector de Valverde de Burguillos-Jerez de los Caballeros (Anticlinorio de Olivenza-Monesterio). Cuaderno Laboratorio Xeoloxico de Laxe 8, 211-220.

Chalot-Prat, F., Gasquet, D., Roger, J., Hassenforder, B., Chevremont, P., Baudin, T., Razin, P., Benlakhdim, A., Benssaou, M., Mortaji, A., 2001. Mémoire explicatif, Carte géologique Maroc (1/50000), Feuille Sidi Bou addi. Notes et Mémoires Servicie Géologique Maroc, No. 415 bis. MICEM/BRGM.

Cheilletz, A., Bertrand, J.M., Charoy, B., Moulahoum, O., Bouabsa, L., Farrar, E., Zimmerman, J.L., Dautel, D., Archibald, D.A., Boullier, A.M., 1992. Geochimie et gèochronologie Rb–Sr, K–Ar et 39Ar–40Ar des complexes granitiques Pan-Africains de la région de Tamanrasset (Algérie): relations avec les minéralisations Sn–W associées et l'evolution tectonique du Hoggar central. Bulletin Société Géologique France 163, 733–750.

Chichorro, M., Pereira, M.F., Apraiz, A., Silva, J.B., 2004. High temperature–Low pressure tectonites from the Boa Fé Fault Zone (Évora Massif, Ossa Morena Zone, Portugal): evidences for transtensional tectonics. Geogaceta 34, 43–46.

Chichorro, M., 2006. A Evolução Tectónica da Zona de Cisalhamento de Montemor-o-Novo (Sudoeste da Zona de Ossa Morena – Área de Santiago do Escoural – Cabrela). Ph.D. thesis, University of Évora.

Chichorro, M., Pereira, M.F., Díaz-Azpíroz, M., Williams, I.S., Fernández, C., Pin, Ch., Silva, J.B., 2008. Cambrian ensialic rift-related magmatism in the Ossa-Morena zone (Évora–Aracena metamorphic belt, SW Iberian Massif): Sm–Nd isotopes and SHRIMP zircon U–Th–Pb geochronology. Tectonophysics 461, 91–113.

Chichorro, M., Solá, A.R., Pereira, M.F., Sánchez García, T., Ferreira, A., Silva, J.B., Armstrong, R. 2014. Intra-crustal recycling and crustal-mantle interactions in North Gondwana revealed by oxygen isotopic composition of Neoproterozoic to Ordovician zircons from SW Iberia rocks. Gondwana 15 Abstracts, 33.

Claoue-Long, J., Compston, W., Roberts, J., Fanning, C.M., 1995. Two carboniferous ages: a comparison of SHRIMP zircon dating with conventional zircon ages & 40Ar/39Ar analysis, In Berggren, W.A., Kent, D.V., Aubry, M.P., Hardenbol, J. (eds). Geochronology, Time Scales & Stratigraphic Correlation. SEPM Special Publication 54, 1-22.

Clemens, J.D., 1998. Observations on the origins and ascent mechanisms of granitic magmas. Journal of the Geological Society, London 155, 843–851.

Clemens, J.D., 2006. Melting of the continental crust: fluid regimes, melting reactions, and source-rock fertility. In: Brown, M., Rushmer, T., (eds), Evolution and Differentiation of the Continental Crust. Cambridge University Press, Cambridge, 297-331.

Compston, W., Williams, I.S., Kirschvink, J.L., Zichao, Z., Guogan, M., 1992. Zircon U-Pb ages for the Early Cambrian time-scale. Journal of the Geological Society, London 149, 171-184.

Condie, K.C., 2014. Growth of continental crust: a balance between preservation and recycling Mineralogical Magazine 78, 623-637.

Corretgé, L.G., Bea, F., Súarez, O., 1985. Las caracteristicas geoquímicas del Batolito de Cabeza de Araya (Cáceres, España): Implicaciones petrogenéticas. Trabajos de Geología 15, 219-238.

Corretgé, L.G., Suárez, O., Galán, G., 1990. West Asturian Leonese Zone: Igneous rocks. In: Dallmeyer, R.D., Martínez-García, E., (eds), Pre-mesozoic geology of Iberia. Springer, Berlin, 115-128.

Crespo-Blanc, A., 1987. El macizo de Aracena (Macizo Ibérico meridional): Propuesta de división sobre la base de nuevos datos estructurales y petrográficos. Boletín Geológico y Minero 98, 507-515.

Crespo-Blanc, A., Orozco, M., 1988. The Southern Iberian Shear Zone: A major boundary in the Hercynian folded belt. Tectonophysics 148, 221-227.

Crespo-Blanc, A., 1989. Evolución geotectónica del contacto entre la Zona de Ossa-Morena y la Zona Surportuguesa en las sierras de Aracena y Aroche (Macizo Ibérico meridional): un contacto mayor en la Cadena Hercínica europea. Ph.D. thesis, University of Granada, 324 p.

Crespo-Blanc, A., Orozco, M., 1991. The boundary between the Ossa-Morena and South Portuguese Zones (Southern Iberia): a major suture in the European Hercynian Chain. Geologische Rundschau 80, 691-702.

Crespo-Blanc, A., 1992. Structure and kinematics of a sinistral transpressive suture between the Ossa-Morena and the South Portuguese Zones, South Iberian Massif. Journal Geological Society of London 149, 401-411.

Cunningham, D., Tectonic setting and structural evolution of the Late Cenozoic Gobi Altai orogen, Geological Society, London, Special Publications 2010, 338, 361-387.

Dada, S.S., Lancelot, J.R., Briqueu, L., 1989a. Age and origin of the annular charnockitic complex at Toro, Northern Nigeria: U–Pb and Rb–Sr evidence. Journal of African Earth Sciences 9, 227-234.

Dada, S.S., Respaut, J.P., 1989b. La monzonite à fayalite de Bauchi (bauchite), nouveau témoin d'un magmatisme syntectonique panafricain au nord du Nigéria. Comptes Rendus de l'Académie des Sciences Paris 309, 887–892.

Dada, S.S., Tubosun, I.A., Lancelot, J.R., Lar, A.U., 1993. Late Archean U–Pb age for the reactivated basement of Northeastern Nigeria. Journal of African Earth Sciences 16, 405-412.

Dallmeyer, R., Fonseca, P.E., Quesada, C., Ribeiro, A., 1993. 40Ar/39Ar mineral age constraints for the tectonothermal evolution of a Variscan suture in southwest Iberia. Tectonophysics 222, 177-194.

Dallmeyer, R.D., García-Casquero, J.L., Quesada, C., 1995. 40Ar/39Ar mineral age constraints on the emplacement of the Burguillos del Cerro Igneous complex (Ossa-Morena zone, SW Iberia). Boletín Geológico y Minero 106, 203–214.

D'Aubisson de Voisins, J.F., 1891. Traité de géognosie. Levrault, Strasbourg, 2, 665 p.

De la Rosa, J.D., 1992. Petrología de las rocas básicas y granitoides del batolito de la Sierra Norte de Sevilla, Zona Sur Portuguesa, Macizo Ibérico. Ph.D. thesis, University of Sevilla, 312 p.

De la Rosa, J.D., Rogers, G., Castro, A., 1993. Relaciones 87Sr/86Sr de rocas básicas y granitoids del batolito de la Sierra Norte de Sevilla. Revista de la Sociedad Geológica de España 6, 141-149.

De la Rosa, J.D., Jenner, G., Castro, A., 2002. A study of inherited zircons in granitoid rocks from the South Portuguese and Ossa-Morena Zones, Iberian Massif: support for the exotic origin of the South Portuguese Zone. Tectonophysics 352, 245-256.

Deer, W.A., Howie, R.A., Zussman, J., 1997. Rock-forming minerals. 2B. Double chain silicates. The Geological Society, London, 784 p.

Delgado-Quesada, M., Pascual, E., Fenoll-Hach-Ali, P., 1981. A geological and metallogenic study of some ocurrences of magnetite and sulphides in Sierra Morena (NNW of Córdoba, Spain). Estudios Geológicos 34, 461-474.

DePaolo, D.J., 1981. Neodymium isotopes in the Colorado Front Range and implications for crust formation and mantle evolution in the Proterozoic. Nature 291, 193–197.

DePaolo, D.J., 1988. Neodymium Isotope Geochemistry. An Introduction. Minerals and Rocks (Series 20). Springer-Verlag, New York, 187 p.

Dessureau, G., Piper, D.J.W., Pe-Piper, G., 2000. Geochemical evolution of Earliest Carboniferous continental tholeiitic basalts along a crustal-scale shear zone, southwestern Maritimes basin, eastern Canada. Lithos 50, 27–50.

Díaz-Azpiroz, M., Fernández, C., 2000. Análisis de la variación del tamaño de grano en las metabasitas de la serie de Acebuches (Macizo Ibérico meridional). Geotemas 1, 229-231.

Díaz-Azpiroz, M., 2001. Evolución tectono-metamórfica del dominio de alto grado de la banda metamórfica de Aracena. Ph.D. thesis, University of Huelva.

Díaz-Azpiroz, M., Castro, A., Fernández, C., 2001. Caracterización petrológica y geoquímica de los granitos metaluminosos tardíos del dominio continental de la banda metamórfica de Aracena (Macizo Ibérico meridional). Geogaceta 30, 41-44.

Díaz-Azpiroz, M., Fernández, C., 2003. Characterization of tectono-metamorphic events using crystal size distribution (CSD) diagrams. A case study from the Acebuches metabasites (SW Spain). Journal of Structural Geology 25, 935-947.

Díaz-Azpiroz, M., Castro, A., Fernández, C., López, S., Fernández-Caliani, J.C., Moreno-Ventas, I., 2004. The contact between the Ossa Morena and the South Portuguese zones. Characteristics and significance of the Aracena metamorphic belt, in its central sector between Aroche and Aracena (Huelva). Journal of Iberian Geology 30, 23-51.

Díaz-Azpiroz, M., Fernández, C., Castro, A., El-Biad, M., 2006. Tectonometamorphic evolution of the Aracena metamorphic belt (SW Spain) resulting from ridge-trench interaction during Variscan plate convergence. Tectonics 25, TC1001.

Díez-Balda, M.A., 1986. El Complejo Esquisto-Grauwáckico, las series Paleozoicas, y la estructura Hercínica al sur de Salamanca. Ph.D thesis University of Salamanca.

Díez-Balda, M.A., Martínez-Catalán, J.R., Ayarza, P., 1995. Syn-collisional extensional collapse parallel to the orogenic trend in a domain of steep tectonics: the Salamanca Detachment Zone (Central Iberian Zone, Spain). Journal of Structural Geology 17, 163–182.

Díez-Balda, M.A., Vegas, R., González Lodeiro, F., 1990. Central-Iberian Zone. Autochthonous Sequences. Structure. In: Dallmeyer, R.D., Martínez García, E. (eds) Pre-Mesozoic Geology of Iberia. Springer-Verlag, 172–188.

Díez-Fernández, R., Martínez-Catalán. J.R., Gerdes, A., Abati, J., Arenas, R., Fernández-Suárez, J., 2010. U–Pb ages of detrital zircons from the Basal allochthonous units of NW Iberia:

Provenance and paleoposition on the northern margin of Gondwana during the Neoproterozoic and Paleozoic. Gondwana Research 18, 385-399.

Díez-Fernandez, R., Castiñeiras, P., Gómez-Barreiro, J., 2012. Age constraints on Lower Paleozoic convection system: Magmatic events in the NW Iberian Gondwana margin. Gondwana Research 21, 1066-1079.

Díez-Fernández, R., Pereira, M.F., Foster, D.A., 2014. Peralkaline and alkaline magmatism of the Ossa-Morena zone (SW Iberia): Age, source, and implications for the Paleozoic evolution of Gondwanan lithosphere. Lithosphere, L379.1.

Díez-Montes, A., Navidad, M., González-Lodeiro, F., Martínez-Catalán, J.R., 2004. El Ollo de Sapo. In: Vera, J.A. (ed.). Geología de España. Sociedad Geológica de España-Instituto Geológico y Minero, Madrid, 69-72.

Díez-Montes, A., Martínez-Catalán, J.R., Bellido-Mulas, F., 2010. Role of the Ollo de Sapo massive felsic volcanism of NW Iberia in the Early Ordovician dynamics of northern Gondwana. Gondwana Research 17, 363-376.

D'Lemos, R.S., Inglis, J.D., Samson, S.D., 2006. A newly discovered orogenic event in Morocco: Neoproterozic ages for supposed Eburnean basement of the Bou Azzer inlier, Anti-Atlas Mountains. Precambrian Research 147, 65-78.

Dornsiepen, U.F., 1979. Rb/Sr whole rock ages within the European Hercynian: a review. Krystalinikum 14, 33-49.

Drost, K., Gerdes, A., Jeffries, T., Linnemann, U., Storey, C., 2011. Provenance of Neoproterozoic and early Paleozoic siliciclastic rocks of the Teplá- Barrandian unit (Bohemian Massif): Evidence from U–Pb detrital zircon ages. Gondwana Research 19, 213-231.

Ducrot, J., Lancelot, J.R., 1977. Probleme de la limite Precambrien-Cambrien; etude radiochronologique par la methode U /Pb sur zircons du volcan du Jbel Boho Anti-Atlas marocain). Canadian Journal Earth Science 14, 2771 -2777.

Dupuy, C., Dostal, J., Bard, J.P., 1979. Trace element geochemistry of paleozoic amphibolites from SW Spain. Tschermaks Mineralogische und Petrographische Mitteilungen 26, 87-93.

Dyksterhuis, S., Müller, R.D., 2008, Cause and evolution of intraplate orogeny in Australia, Geology 36, 495-498.

Eby, G.N., 1992. Chemical subdivision of A-type granitoids: petrogenetic and tectonic implications. Geology 20, 641-644.

Eddif, A., Gasquet, D., Hoepffner, C., Levresse, G., 2007. Age of the Wirgane granodiorite intrusions (Western High-Atlas, Morocco): New U–Pb constraints. Journal of African Earth Sciences 47, 227-231.

Eden, C.P., Andrews, J., 1990. Middle to Upper Devonian melanges in SW Spain and their relationship to the Meneage Formation in south Cornwall. Proceedings of the Ussher Society 7, 217-222.

Eden, C., 1991. Tectonostratigraphic analysis of the northern extent of the oceanic exotic terrane, northwestern Huelva province, Spain. Ph.D. thesis, University of Southampton.

Eguiluz, L., 1988. Petrogénesis de rocas ígneas y metamórficas en el antiforme de Burguillos Monesterio. Macizo Ibérico Meridional. Ph.D. thesis, University of Pais Vasco, 649 p.

Eguiluz, L., Apraiz, A., Ábalos, B., Martínez-Torres, L.M., 1995. Evolution de la zone d'Ossa Morena (Espagne) au course du Protérozoique supérieur: Corrélations avec l'orogène cadomien nord armoricain. Geólogie de France 3, 35-47.

Eguiluz, L., Gil-Ibarguchi, J.I., Ábalos, B., Apraiz, A., 2000. Superposed Hercynian and Cadomian orogenic cycles in the Ossa-Morena zone and related areas of the Iberian Massif. Geological Society of America Bulletin 112, 1398-1413.

Eguiluz, L., Carracedo, M., Sarrionandia, F., Apalategui, O., 2004. Nuevos datos tectono-estructurales del Macizo de Brovales (Antiforma de Olivenza-Monesterio): relación con el cabalgamiento de Monesterio. Geogaceta 35, 83-56.

Ekwueme, B.N., Kröner, A., 1998. Single zircon evaporation ages from the Oban Massif, southeastern Nigeria. Journal of African Earth Sciences 26, 195-205.

El-Biad, M., 2000. Generación de granitoides en ambientes geológicamente contrastados del Macizo Ibérico. Limitaciones experimentales entre 2 y 15 kbar. Ph.D. thesis, University of Huelva.

El-Hmidi, H., 2000. Petrología y geoquímica de los sistemas andesíticos ricos en Mg: estudio petrológico y experimental de las noritas de la Banda Metamórfica de Aracena, SO de España. Ph.D. thesis, University of Huelva, 239 p.

England, P.C., Thompson, A., 1986. Some thermal and tectonic models for crustal melting in continental collision zones. Geological Society of London, Special Publication 19, 83-94.

Errami, E., Bonin, B., Laduron, D., Lasri, L., 2009. Petrology and geodynamic significance of the post-collisionalPan-African magmatism in the Eastern Saghro area (Anti-Atlas, Morocco). Journal of African Earth Sciences 55, 105-124.

Escuder-Viruete, J., Arenas, R., Martínez-Catalán, J.R., 1994. Tectonothermal evolution associated with Variscan crustal extension in the Tormes gneissic dome (NW Salamanca, Iberian Massif, Spain). Tectonophysics 238, 117-138.

Escuder-Viruete, J., Indares, A., Arenas, R., 2000. P-T paths derived from garnet growth zoning in an extensional setting: an example from the Tormes Gneissic Dome (Iberian Massif, Spain). Journal of Petrology 41, 1488-1518.

Expósito, I., 2000. Evolución Estructural de la mitad septentrional de la Zona de Ossa-Morena y su relación con el límite Zona Ossa-Morena/Zona Centroibérica. Ph.D. thesis, University of Granada, 291 p.

Expósito, I., Simancas, J.F., González-Lodeiro, F., Azor, A., Martínez-Poyatos, D.J., 2002. Estructura de la mitad septentrional de la zona de Ossa- Morena: Deformación en el bloque inferior de un cabalgamiento cortical de evolución compleja. Revista de la Sociedad Geológica de España 15, 3-14.

Expósito, I., Simancas, J.F., González-Lodeiro, F., Bea, F., Montero, P., Salman, K., 2003. Metamorphic and deformational imprint of Cambrian-Lower Ordovician rifting in the Ossa-Morena Zone (Iberian Massif, Spain). Journal of Structural Geology 25, 2077-2087.

Eyal, M., Litvinovsky, B., Jahnb, B.M., Zanvilevicha, A., Katzira, Y., 2010. Origin and evolution of post-collisional magmatism: coeval Neoproterozoic calc-alkaline and alkaline suites of the Sinai Peninsula. Chemical Geology 269, 153-179.

Farias, P., Gallastegui, G., González-Lodeiro, F., Marquínez, J., Martín Parra, L.M., Martínez Catalán, J.R., Pablo Maciá, J.G., Rodríguez Fernández, L.R., 1987. Aportaciones al conocimiento de la litoestratigrafía y estructura de Galicia Central. Mem Faculdade Ciências Univ Porto 1,411-431

Ferkous, K., Monié, P., 2002. Neoproterozoic shearing and auriferous hydrothermalism along the lithospheric N-S East In Ouzzal shear zone (western Hoggar, Algeria, North Africa). Journal of African Earth Sciences 35, 399-415.

Fernández-Carrasco, J., Coullaut, J.L., Aguilar, J.M., 1981. Mapa de la hoja no. 875 (Jerez de los Caballeros) del Mapa Geológico de Españaa a escala 1: 50.000. IGME.

Fernández, M., Marzán, I., Correia, A., Ramalho, E., 1998. Heat flow, heat production, and lithospheric thermal regime in the Iberian Peninsula. Tectonophysics 291, 29-53.

Fernández-Suárez, J., Gutierrez-Alonso, G., Jenner, G.A., Jacson, S.E., 1998. Geochronology and geochemistry of the Pola de Allande granitoids (northern Spain): their bearing on the

Cadomian-Avalonian evolution of northwest Iberia. Canadian Journal of Earth Sciences 35, 1-15.

Fernández-Suárez, J., Gutiérrez-Alonso, G., Jenner, G.A., Tubrett, M.N., 2000. New ideas on the Proterozoic–Early Palaeozoic evolution of NW Iberia: insights from U–Pb detrital zircon ages. Precambrian Research 102, 185-206.

Fernández-Suárez, J., Gutiérrez-Alonso, G., Cox, R., Jenner, G.A., 2002a. Assembly of the Armorica microplate: a strike-slip terrane delivery? Evidence from U–Pb ages of detrital zircons. Journal of Geology 110, 619-626.

Fernández-Suárez, J., Gutiérrez-Alonso, G., Jeffries, T.E., 2002b. The importance of along-margin terrane transport in northern Gondwana: insights from detrital zircon parentage in Neoproterozoic rocks from Iberia and Brittany. Earth and Planetary Science Letters 204, 75-88.

Fernández-Suárez, J., Gutiérrez-Alonso, G., Pastor-Galán, D., Hofmann, M., Murphy, J.B., Linnemann, U., 2014. The Ediacaran–Early Cambrian detrital zircon record of NW Iberia: possible sources and paleogeographic constraints. International Journal of Earth Sciences 103, 1335-1357.

Ferré, E., Déléris, J., Bouchez, J.L., Lar, A.U., Peucat, J.J., 1996. The Pan-African reactivation of Eburnean and Archaean provinces in Nigeria: structural and isotopic data. Journal of the Geological Society, London 153, 719-728.

Ferré, E., Gleizes, G., Caby, R., 2002. Obliquely convergent tectonics and granite emplacement in the Trans-Saharan belt of Eastern Nigeria: a synthesis. Precambrian Research 114, 199-219.

Floyd, P.A., Winchester, J.A., 1975. Magma-type and tectonic setting discrimination using immobile elements. Earth Planetary Science Letters 27, 211-218.

Fonseca, P., Ribeiro, A., 1993. Tectonics of the Beja-Acebuches ophiolite: A major suture in the Iberian Variscan Foldbelt. Geologische Rundschau 82, 40-447.

Foucault, A., Paquet, J., 1971. Sur l'importance d'une tectogènese dans la region central des Cordillères Bétiques (S. de la Arana, prov. Grenade, Espagne). Comptes Rendus de la Académie des Sciences de Paris 272, 2756-2758.

Franke, W., 2014, Topography of the Variscan orogen in Europe: failed–not collapsed. International Journal of Earth Sciences 103, 1471-1499.

Fricke, W., 1941. Die Geologie des Grenzebietes zwischen nordöstlicher Sierra Morena und Extremadura. Ph.D. thesis, University of Berlin, 91 p.

Frost, B.R., Barnes, C.G., Collins, W.J., Arculus, R.J., Ellis, D.J., Frost, C.D., 2001. A geochemical classification for granitic rocks. Journal of Petrology 42, 2033-2048.

Fyfe, W.S., 1973. The Granulite Facies, Partial Melting and the Archaean Crust. Philosophical Transactions of the Royal Society of London, Series A 273, 457-461.

Gabaldón, V., Garrote, A., Quesada, C., 1983. Las cuencas de Valdeinfierno y Benajarafe (Tournaisiense-Viseense). Caracterización sedimentológica e implicaciones regionals. Dominio de Sierra Albarrana (Zona de Ossa-Morena). Comunicaciones Servicio Geológico de Portugal 69, 209-218.

Gabaldón, V., Férnadez-Gianotti, J., Rubio-Campos, J.C., Baeza-Rojano, L., 1993. .Mapa de la Hoja Nº 900 La Cardenchosa. Instituto Geológico y Minero, scale 1:50,000. Spain.

Gabaldón et al., 2001. Geologic map of Iberia. Instituto Geologico y Minero, scale 1:1,000,000. Spain.

Galadí-Enríquez, E., Galindo-Zaldívar, Simancas, F., Expósito, I., 2000. Geometría del granito de La Bazana a partir de datos gravimétricos (Zona de Ossa-Morena, Macizo Ibérico). Geogaceta 28, 51-54.

Galadí-Enríquez, E., Galindo-Zaldívar, Simancas, F., Expósito, I., 2003. Diapiric emplacement in the upper crust of a granitic body: the La Bazana granite (SW Spain). Tectonophysics 361, 83-96.

Galindo, C., Casquet, C., 1985. Caracterización geoquímica del complejo plutónico Táliga-Barcarrota (Badajoz). Cuadernos Laboratorio Xeolóxico de Laxe 9, 46-62.

Galindo, C., Portugal-Ferreira, M.R., 1988. Petrology and chronology of the San Amaro peralkaline ortogneisses (Badajoz, Ossa-Morena Zone). Memórias e Noticias , University of Coimbra 108, 45-67.

Galindo, C. 1989. Petrología y geocronología del Complejo Plutónico Táliga-Barcarrota (Badajoz). Ph.D. thesis, University Complutense Madrid, 261 p.

Galindo, C., Portugal-Ferreira, M.R., Casquet, C., Regencio-Macedo, C.A., 1990. Dataciones Rb-Sr en el Complejo plutónico Táliga-Barcarrota (CPTB). Geogaceta 8, 7-10.

Galindo, C., Muñoz, M., Casquet, C., 1991. El enjambre filoniano básico intrusivo en el Complejo plutónico Táliga-Barcarrota (Ossa-Morena, Badajoz). Geogaceta 10, 87-90.

Galindo, C., Casquet, C., 2004. El magmatismo prevarisco de la Zona de Ossa-Morena. In: Vera, J.A., (ed.), Geología de España. Sociedad Geológica de España-Instituto Geológico Minero

España, Madrid, 190-194.

Gallastegui, G., Aramburu, C., Barba, P, Fernández, L.P., Cuesta, A., 1992. El vulcanismo del Paleozoico inferior de la Zona Cantábrica (NO de España). In: Rabano, I., Gutiérrez-Marco, J.C., Saavedra, J., (eds), El Paleozoico inferior de Ibero-Armorica. Universidad de Extremadura, Badajoz, 435-452.

Gallastegui, G., Suárez, O., Cuesta, A., 2004. Zona Cantábrica: Magmatismo. In: Vera, J.A. (ed.). Geología de España, SGE-IGME, Madrid, Spain, 47-49.

García-Casquero, J.L., 1991. El complejo plutónico de Burguillos del Cerro (Badajoz). Ph.D. thesis, University of Salamanca 376 p.

García-Lobón, J.L., 2004. Petrofísica e interpretación integrada de datos aeromagnéticos, radiométricos y gravimétricos. Aplicaciones a los complejos ígneos del área de Monesterio. Ph.D. thesis, University Politecnica of Madrid, 544 p.

García-Lobón J.L., Rey-Moral, C., Ayala, C., 2006. Comprehensive petrophysics of rocks from the Monesterio Antiform (Ossa-Morena Zone, SW Spain). Journal of Applied Geophysics 59, 190-204.

García-Portero, J., 1980. El Precámbrico y las rocas ígneas de los alrededores de Fuente Obejuna (provincial de Cordoba). Ph.D thesis, University of Pais Vasco.

Garrote, A., Sámchez-Carretero, R., 1979. Granitos post-cinemáticos de tendencia alcalina en Ossa-Morena: el stock de La Cardenchosa (provincial de Córdoba). Acta Geológica Hispania 14, 90-96.

Gasquet, D., Roger, J., Chalot-Prat, F., Hassenforder, B., Baudin, T., Chevremont, P., Cocherie, A., Benlakhdim, A., Zouhair, M., Cheilletz, A., Archibald, D., 2001. Le magmatisme polycyclique des boutonnie`res de la Tagragra d Akka et du Kerdous-Tafeltast (Anti-Atlas occidental, Maroc). In: 2e`me Coll. Intern.Magmatisme, Métamorphisme et Minéralisations Associées, Marrakech, Mai 2001. Abstract 30.

Gasquet, D., Chevremont, P., Baudin, T., Chalot-Prat, F., Guerrot, C., Cocherie, A., Roger, J., Hassenforder, B., Cheilletz, A., 2004. Polycyclic magmatism in the Tagragra d_Akka and Kerdous–Tafeltast inliers (Western Anti-Atlas, Morocco). Journal of African Earth Sciences 39, 267-275.

Gasquet, D., Levresse, G., Cheilletz, A., Azizi-Samir, M.R., Mouttaqi, A., 2005. Contribution to a geodynamic reconstruction of the Anti-Atlas (Morocco) during Pan-African times with the emphasis on inversion tectonics and metallogenic activity at the Precambrian-Cambrian

transition. Precambrian Research 140, 157-182.

Gerya, T.V., Burg, J.-P., 2007. Intrusion of ultramafic magmatic bodies into the continental crust: Numerical simulation. Physics of the Earth and Planetary Interiors 160, 124-142.

Ghienne, J.F., Le Heron, D.P., Moreau, J., Denis, M., Denoux, M., 2007a. The Late Ordovician glacial sedimentary system of the North Gondwana platform. In: Hambrey, M.J., Christoffersen, P., Glasser, N.F., Hubbard, B. (eds), Glacial Sedimentary Processes and Products, IAS Special Publication Number 19 of the International Association of Sedimentologists. Blackwell Publishing, 296-319.

Ghienne, J.F., Boumendjel, K., Paris, F., Videt, B., 2007b. The Cambrian–Ordovician succession in the Ougarta Range (western Algeris, North Africa) and interferrence of the late Ordovician glaciation on the development of the Lower Palaeozoic transgression on northern Gondwana. Bulletin of Geosciences 82, 183-214.

Giese, U., Bühn, B., 1993. Early Paleozoic rifting and bimodal volcanisim in Ossa-Morena Zone of South-West Spain. Geologische Rundschau 83, 143-160.

Giese, U., Von Hoegen, R., Hoymann, K.H., Kramm, U., Walter, R., 1994. The Paleozoic evolution of the Ossa Morena Zone and its boundary to the South Portuguese Zone in SW Spain: Geological constrains and geodynamic interpretation of a suture in the Iberian Variscan orogen. Neues Jahrbuch für Geologie und Paläontologie, Abhandlungen 192, 383-412.

Giese, U., Von Hoegen, R.V., Hollman, G., Walter, R., 1994. Geology of the southwestern Iberia Meseta I. The Paleozoic of the Ossa-Morena Zone north and south of the Olivenza-Monesterio Anticline (Huelva province, SW Spain). Neues Jahrbuch für Geologie und Paläontologie, Abhandlungen 192, 293-331.

Gilbert, M.C., Helz, R.T., Popp, R.K., Spear, F.S., 1982. Experimental studies of amphibole stability: Mineralogical Society of America. Review Mineralogy and Geochemistry 9B, 231-268.

Giordano, D., Russel, J.K., Dingwell, D.B., 2008 Viscosity of magmatic liquids: A model. Earth and Planetary Science Letters 271, 123-134.

Gladney, E.R., Braid, J.A., Murphy, J.B., Quesada, V., McFarlane, R.M., 2014. U–Pb geochronology and petrology of the late Paleozoic Gil Marquez pluton: magmatism in the Variscan suture zone, southern Iberia, during continental collision and the amalgamation of Pangea. International Journal of Earth Science 103, 1433-1451.

Goldstein, S.L., Onions, R.K., Hamilton, P.J,. 1984. A Sm-Nd Isotopic Study of Atmospheric Dusts and Particulates from Major River Systems. Earth and Planetary Science Letters 70, 221-236.

Gómez-Pugnaire, M.T., Azor, A., Fernández-Soler, J.M., López Sánchez-Vizcaíno, V., 2003. The amphibolites from the Ossa-Morena/Central Iberian Variscan suture (Southwestern Iberian Massif): geochemistry and tectonic interpretation. Lithos 68, 23-42.

Gonçalves, F., 1971. Subsidios para o conhecimiento geológico do Nordeste de Alentejano. Memoria Serviçio Geologico Portugal 18, 1-62.

González, A., 1996. Análisis de señales sísmicas. Estudio de la estructura de la litosfera en el margen suroccidental ibérico. Ph.D. thesis, University Complutense of Madrid, 307 p.

González-Menéndez, L., 2002. Petrología del batolito de Nisa-Alburquerque. Revista de la Sociedad Geológica de España 15, 233-246.

González-Menéndez, L., Bea, F., 2004. El batolito de Nisa-Alburquerque. In: Vera, J.A., (ed.), Geología de España. Sociedad Geológica de España-Instituto Geológico Minero España, Madrid, 120-122.

González-Menéndez, L., Azor, A., Pereira, M.D., Acosta, A., 2006. Petrogénesis del plutón de Santa Eulalia (Alto Alentejo, Portugal). Revista de la Sociedad Geológica de España 19, 69-86.

González-Menéndez, L., Solá, A.R., 2011. Late Variscan Santa Eulalia Complex and the Nisa-Alburquerque Batholith. In: Scarrow, J.H., (ed.), Pre-meeting field trip Southern Iberia Traverse, field guide. VII Hutton Symposium on Granites and Related Rocks, Avila, 49-61.

Govindaraju, K., Potts, P.J., Webb, P.C., Watson, J.S., 1994. 1994 Report on Whin Sill Dolerite WS-E from England and Pitscurrie Micrograbbro PM-S from Scotland: assessment by one hundred and four international laboratories. Geostandards Newsletters 18, 211-300.

Green, D.H. 1973. Experirnental melting studies on model upper mantle compositions at high pressure under both water saturated and water-undersaturated conditions. Earth and Planetary Science Letters 19, 37-53.

Gutiérrez-Alonso, G., Fernánndez-Suárez, J., Jeffries, T.E., Jenner, G.A., Tubrett, M.N., Cox, R., Jackson, S.E., 2003. Terrane accretion and dispersal in the northern Gondwana margin. An early Paleozoic analogue of a longlived active margin. Tectonophysics 365, 221-232.

Gutiérrez-Alonso, G., Fernández-Suárez, J., Weil, A.B., 2004. Orocline triggered lithospheric delamination. Geological Society of America Special Paper 383, 121-130.

Gutiérrez-Marco, J.C., Rábano, I., Robardet, M., 1984. Estudio bioestratigráfico del Ordovícico en el synclinal del Valle (provincial de Sevilla, SO de Espoaña). Memórias e Noticias , University of Coimbra 97, 12-37.

Gutiérrez-Marco, J.C., Robardet, M., Piçarra, J.M., 1998. Silurian Stratigraphy and Paleogeography of the Iberian Peninsula (Spain and Portugal). Temas Geológico-Mineros 23, 13-44.

Gutiérrez-Marco, J.C., San José, M.A., Pieren, A.P., 1990. Central-Iberian Zone, Autochthonous sequences: post-Cambrian Palaeozoic Stratigraphy. In: Dallmeyer, R.D., Martinez-García, E., (eds), Pre-Mesozoic Geology of Iberia. Springer-Verlag, Berlin Heidelbelberg, 160-171.

Gutiérrez-Marco, J.C., Robardet, M., Rábano, I., Sarmiento, G.N., San José-Lancha, M.A., Herranz, P., Pieren-Pidal, A.P., 2002. Ordovician. In: Gibbons, W., Moreno, T., (eds), The Geology of Spain. Geological Society, London, 31-49.

Guynn, J., and Gehrels, G.E., 2010, Comparison of detrital zircon age distributions using the K-S test: Tucson, Arizona LaserChron Center. https:// sites .google .com /a/laserchron .org /laserchron /home / (December 2014).

Hadj-Kaddour, Z., Liégeois, J.P., Demaiffe, D., Caby, R., 1998. The alkaline–peralkaline granitic post-collisional Tin Zebane dyke swarm Pan-African Tuareg shield, Algeria: prevalent mantle signature and late agpaitic differentiation. Lithos 45, 223-243.

Hammann, W., Henry, J.L., 1978. Quelques espèces de Calymenella, Eohomalonotus et Kerfornella (Trilobita, Ptychopariida) de l'Ordovicien du Massif Armoricain et de la Péninsule Ibérique. Senckenbergiana lethaea 59, 401-429.

Harms, U., Schandelmeier, H., Darbyshire, D.P.F., 1990. Pan-African reworked early / middle Proterozoic crust in NE Africa W of the Nile: Sr and Nd isotope evidence. Journal of Geological Society of London 147, 859-872.

Harte, B. 1983. Mantle peridotites and processes—the kimberlite sample. In: Hawkesworth, C.J. and Norry, M.J., (eds) Continental Basalts and Mantle Xenoliths. Nantwich: Shiva, 46-91 pp.

Haydoutov, I., 1989. Precambrian ophiolites, Cambrian island arc, and Variscan suture in the South Carpathian–Balkan region. Geology 17, 905-908.

Henry, B., Liegeois, J.P., Nouar, O., Derder, M.E.M., Bayou, B., Bruguier, O., Ouabadi, A., Belhai, D., Amenna, M., Hemmi, A., Ayache, M., 2009. Repeated granitoid intrusions during the Neoproterozoic along the western boundary of the Saharan metacraton, Eastern Hoggar, Tuareg shield, Algeria: an AMS and U-Pb zircon age study. Tectonophysics 474, 417-434.

Hermann, J., Müntener, O., Günther, D., 2001. Differentiation of mafic magma in a continental crust-to-mantle transition zone. Journal of Petrology 42, 189-206.

Herron, M. M. 1988. Geochemical classification of terrigenous sands and shales from core or log data. Journal of Sedimentary Petrology 58, 820-829.

Hofmann, A.W., 1988. Chemical differentiation of the Earth: the relationship between mantle, continental crust, and oceanic crust: Earth and Planetary Science Letters 90, 297-314.

Hofmann, A.W., 1997. Mantle geochemistry: the message from oceanic volcanism. Nature 385, 219-229.

Houari, M.R., Hoepffner, C.H., 2003. Late Carboniferous dextral wrench-dominated transpression along the North African craton margin (eastern High-Atlas, Morocco). Journal of African Earth Sciences 37, 11-24.

Huppert, H.E., Sparks, S.J., 1989. The generation of granitic magmas by intrusion of basalt into continental crust. Journal of Petrology 29, 599-624.

Ickert, R.B., Hiess, J., Williams, I.S., Holden, P., Ireland, T.R., Lanc, P., Schram, N., Foster, J.J., Clement, S.W., 2008. Determining high precision, in situ, oxygen isotope ratios with SHRIMP II: analyses of MPI-DING silicate-glass reference materials and zircon from contrasting granites. Chemical Geology 257, 114-128.

Inglis, J.D., MacLean, J.S., Samson, S.D., D_Lemos, R.S., Admou, H., Hefferan, K., 2004. A precise U-Pb zircon age for the Bleida granodiorite, Anti-Atlas, Morocco: implications for the timing of deformation and terrane assembly in the eastern Anti-Atlas. Journal of African Earth Sciences 39, 277-283.

Inglis, J.D., D'Lemos, R.S., Samson, S.D., Admou, H., 2005. Geochronological Constraints on Late Precambrian Intrusion, Metamorphism, and Tectonism in the Anti-Atlas Mountains. The Journal of Geology 113, 439-450.

Jaques, A.L., Green, D.H., 1979. Determination of liquid compositions in experimental, high pressure melting of peridotite. American Mineralogist 64, 1312-1321.

Jellinek, A.M., Kerr, R.C., Griffiths, R.W., 1999. Mixing and compositional stratification produced by natural convection 1. Experiments and their application to Earth's core and mantle. Journal of Geophysical Research 104: doi: 10.1029.

Jesus, A.P., Munha, J., Mateus, A., Tassinari, C., Nutman, A.P., 2007. The Beja layered gabbroic sequence (Ossa-Morena Zone, southern Portugal): Geochronology and geodynamic implications, Geodinamica Acta 20, 139-157.

Julivert, M., Fonboté, J.M., Ribeiro, A., Nabais-Conde, L.E., 1972. Mapa tectócnico de la Península Ibérica y Baleares. Spain Instituto Geológico y Minero, scale 1:1.000,000.

Kay, S.M., Kay, R.W., 1985, Aleutian tholeiitic and calc alkaline magma series: The mafic phenocrysts. Contributions to Mineralogy and Petrology 90, 276-290.

Kemp, A.I.S., Wormald, R., Whitehouse, M.J., Price, R.C., 2005. Hf isotopes in zircon reveal contrasting sources and crystallization histories for alkaline to peralkaline granites of Temora, southeastern Australia. Geology 33, 979-800.

Kolodner, K., Avigad, D., McWilliams, M., Wooden, J.L., Weissbrod, T., Feinstein, S., 2006. Provenance of north Gondwana Cambrian–Ordovician sandstone: U-Pb SHRIMP dating of detrital zircons from Israel and Jordan. Geological Magazine 143, 367-391.

Kossmat, F., 1927. Gliederung des varistischen gebirgsbaues. Abh Sächs Geol Landesamtes 1, p 39.

Kröner, A., Ekwueme, B.N., Pidgeon, R.T., 2001. The Oldest Rocks in West Africa: SHRIMP Zircon Age for Early Archean Migmatitic Orthogneiss at Kaduna, Northern Nigeria. The Journal of Geology 109, 399-406.

Kroner, U., Romer, R.L., 2013. Two plates-Many subduction zones: The Variscan orogeny reconsidered. Gondwana Research 24, 298-329.

Kuno, H., 1968. Differentiation of basalt magmas. In: Hess, H.H. and Poldervaart, A. A. (eds) Basalts: The Poldervaart Treatise on Rocks of Basaltic Composition, 2. New York: Interscience, 623-688.

Küster, D., 1995. Rb–Sr isotope systematics of muscovite from Pan-African pegmatites of Western and Northeastern Africa. Mineralogy and Petrology 55, 71-83.

Lancelot, J.R., Boullier, A.M., Maluski, H., Ducrot, J., 1983. Deformation and related radiochronology in a Late Pan-Africam Mylonitic shear Zone, Adrar des Iforas (Mali). Contributions to Mineralogy and Petrology 82, 312-326.

Langmuir, C.H., 1989. Geochemical consequences of in situ crystallization. Nature 340, 199-205.

Latin, D., White, N., 1990. Generating melt during lithospheric exlension: pure shear vs. simple shear. Geology 18, 327-331.

Latin, D.M., Dixon, J.E., Fitton, J.G., 1990. Rift-related Magmatism in the North Sea Basin. In Blundell, D.J. and .Gibbs, A.D. (eds); Tectonic evolution of the North Sea rifts. Oxford University Press Oxford: Clarendon Press, 101-104 p.

Le Maitre, R.W., 1989. A Classification of Igneous Rocks and Glossary of Terms. Recommendations of the IUGS Commission on the Systematics of Igneous Rocks. Oxford: Blackwell, 256 p.

Leake, B.E., Woolley, A.F., Arps, C.E.S., Birch, W.D., Gilbert, M.C., Grice, J.D., Hawthore, F.C., Kato, A., Kisch, H.J., Krivovichev, V.G., Linthour, K., Laird, J., Mandarion, J., 1997. Nomenclature of amphiboles. Report of the Subcommittee on Amphiboles of the International Mineralogical Association Commission on the New Mineral Names. Canadian Mineralogist 9, 623-651.

Leterrier, J., Maury, R.C., Thonon, P., Girard, D., Marchal, M., 1982. Clinopyroxene composition as a method of identification of the magmatic affinities of Paleo-volcanic series. Earth Planetary Science Letters 59, 139-154.

Liégeois, J.P., Bertrand, J.M., Black, R., 1987. The subducfion- and collision-related Pan-African composite batholith of the Adrar des Iforas (Mali): a review. Geological Journal 22,185-211.

Liégeois, J.P., Black, R., Navez, J., Latouche, L., 1994. Early and late pan- African orogenies in the Air assembly of terranes (Tuareg Shield, Niger). Precambrian Research 67, 59-88.

Liégeois, J.P., Navez, J., Hertogen, J., Black, R., 1998. Contrasting origin of post-collisional high-K calc-alkaline and shoshonitic versus alkaline and peralkaline granitoids. The use of sliding normalization. Lithos 45, 1-28.

Liégeois, J.P., Latouche, L., Boughara, M., Navez, J., Guiraud, M., 2003. The LATEA metacraton (Central Hoggar, Tuareg shield, Algeria): behaviour of an old passive margin during the Pan-African orogeny. Journal of African Earth Sciences 37, 161-190.

Lima, S.M., Corfu, F., Neiva, A.M.R., J. M. F. Ramos, J.M.F., 2012. Dissecting Complex Magmatic Processes: an in-depth U–Pb Study of the Pavia Pluton, Ossa–Morena Zone, Portugal. Journal of Petrology 53, 1887-1911.

Lima, S.M., Neiva, A.M.R., Ramos, J.M.F., 2013. Adakitic-like magmatism in western Ossa–Morena Zone (Portugal): Geochemical and isotopic constraints of the Pavia pluton. Lithos 160-161, 98-116.

Linnemann, U., Gehmlich, M., Tichomirowa, M., Buschmann, B., Nasdala, L., Jonas, P., Lützner, H., Bombach, K., 2000. From Cadomian subduction to Early Palaeozoic rifting: the evolution of Saxo-Thuringia at the margin of Gondwana in the light of single zircon geochronology and basin development (Central European Variscides, Germany). In: Franke, W., Haak, V., Oncken, O., Tanner, D. (eds), Orogenic Processes — Quantification

and Modelling in the Variscan Belt of Central Europe: The Geological Society of London, London, Special Publication 179, 131-153.

Linnemann, U., McNaughton, N.J., Romer, R.L., Gehmlich, M., Drost, K., Tonk, C., 2004. West African provenance for Saxo-Thuringia (Bohemian Massif): did Armorica ever leave pre-Pangean Gondwana? U/Pb-SHRIMP zircon evidence and the Nd-isotopic record. International Journal of Earth Sciences 93, 683-705.

Linnemann, U., Pereira, M.F., Jeffries, T., Drost, K., Gerdes, A., 2008. Cadomian Orogeny and the opening of the Rheic Ocean: new insights in the diachrony of geotectonic processes constrained by LA-ICP-MS U-Pb zircon dating (Ossa-Morena and Saxo- Thuringian Zones, Iberian and Bohemian Massifs. Tectonophysics 461, 21-43.

Linnemann, U., Ouzegane, K., Drareni, A., Hofmann, M., Becker, S., Gärtner, A., Sagawe, A., 2011. Sands of West Gondwana: An archive of secular magmatism and plateinteractions–A case study from the Cambro-Ordovician section of the Tassili Ouan Ahaggar (Algerian Sahara) using U–Pb–LA-ICP-MS detrital zircon ages. Lithos 123, 188-203.

Liñán, E., 1978. Bioestratigrafía de la Sierra de Córdoba. Ph.D thesis, University of Granada, 212 p.

Liñán, E., Perejón, A., 1981. Precambriam-Cambrian boundary and correlactions from southwestern and central parts of Spain. Geological Magazine 121, 221-228.

Liñán, E., 1984. Los iconofósiles de la Formación Torreárboles (Precambrico?-Cambrico inferior) en los alrededores de Fuente Cantos, Badajoz. Cuaderno Laboratorio Xeoloxico de Laxe 8, 283-314.

Liñán, E., Quesada, C., 1990. Stratigraphy: Rift phase. In: Dallmeyer, R.D., Martínez-García, E., (eds), Pre-mesozoic geology of Iberia. Springer, Berlin, 259-271.

Liñan, E., Gámez-Vintaned, J.A., 1993. Lower Cambrian palaeogeography of the Iberian Península and its relations with some neighbouring European areas. Bulletin Société Géologique France 164, 831-842.

Liñán, E., Gozalo, R., Palacios, T., Gámez Vintaned, J.A., Ugidos, J.M., Mayoral, E., 2002. Cambrian. In: Gibbons, W., Moreno, T. (eds), The Geology of Spain. Geological Society of London, London, 17-29.

Lloyd, F.E., Bailey, D.K., 1975. Light element metasomatism of the continental mantle: The evidence and the consequences. Physics and Chemistry of the Earth 9, 389-416.

López Sánchez-Vizcaíno, V., Gómez-Pugnaire, M.T., Azor, A., Fernández-Soler, J.M., 2003. Phase

diagram sections applied to amphibolites: a case study from the Ossa-Morena/Central Iberian Variscan suture (Southwestern Iberian Massif). Lithos 68, 1-21.

López-Guijarro, R., 2006. Ambiente geodinámico y procedencia de las rocas sedimentarias precámbricas de las zonas de Ossa Morena y Centroibérica a través del análisis geoquímico. Boletín Geológico y Minero 117, 499-505.

López-Guijarro, R., Armendáriz, M., Quesada, C., Fernández-Suárez, J., Murphy, J.B., Pin, Ch., Bellido, F., 2008. Ediacaran-Palaeozoic tectonic evolution of the Ossa Morena and Central Iberian zones (SW Iberia) as revealed by Sm–Nd isotope systematics. Tectonophysics 461, 202-214.

Lotze, F., 1945. Zur Gliederung der Variszíden der Iberischen Meseta. Geotekt Forsch 6,78-92.

Lotze, F., 1956b. Über Sardischen bewegungen in Spanien und ihre Bezeiehungen zur assyntischen faltung. Geotektonische Symposium zu Ehren von Hans Stille, Stuttgart, 129-139.

Lunar, R., García-palomero, F., Ortega, L., Sierra, J., Moreno, T., Prichard, H., 1997. Ni-Cu-(PGM) mineralization associated with mafic and ultramafic rocks: the recently discovered Aguablanca ore deposit, SW Spain. In Papuen, H., (ed.), Mineral Deposits: Research and Exploration. Where Do They Meet? Balkema, Rotterdam.

Marcos, A., 1973. Las series del Paleozoico inferior y la estructura herciniana del occidente de Asturias (NW de España). Trabajos de Geología 6, 3-113.

Marcos, A., Martínez, F.J., Julivert, M., Pulgar, J.A., 1980. Mapa y memoria de explicativa de la Hoja nº 50 (Cangas del Narcea) del Mapa Geológico de España a escala 1:50.000 (2ª serie). IGME, Madrid.

Marcos, A., Martínez-Catalán, J.R., Guitérrez-Marco, J.C., Pérez-Estaún, A., 2004. Zona Asturoccidental-Leonesa: Estratigrafía y paleogeografía. In: Vera, J.A. (ed.). Geología de España, SGE-IGME, Madrid, Spain, 49-54.

Marillier, F., Verhoef, J., 1989. Crustal thickness under the Gulf of St. Lawrence, Northern Appalachians, from gravity and deep seismic data: Canadian Journal of Earth Sciences 26, 1517-1532.

Martín-Algarra, A., 1983. Evolucíon, geológica alpine del contacto entre las Zonas Internas y las Zonas Externas de la Cordillera Bética. Ph.D. thesis, University of Granada, 1171 p.

Martín-Agarra, A., Messina, A., Perrone, V., Russo, S., Maate, A., Martín-Martín, M., 2000. A los real, in the internal domains of the Betic-Rif Orogen (Spain and Morocco): Evidence from

conglomerates and consequences for Alpine geodynamic evolution. Journal of Geology 108, 447-467.

Martínez-Catalán, J.R., 1985. Estratigrafía y estructura del Domo de Lugo (Sector Oeste de la Zona Asturoccidental-leonesa). Corpus Geologicum Gallaeciae (2ª Serie) 2, 1-291.

Martínez-Catalán, J.R., Arenas, R., Díaz García, F., Abati, J., 1999. Allochthonous units in the Variscan belt of NW Iberia: Terranes and accretionary history. In: Sinha, A.K. (ed.), Basement Tectonics. Kluwer Academic Publishers, Amsterdam, 65-84.

Martínez-Catalán, J.R., Fernández-Suárez, J., Jenner, G.A., Belousova, E., Díez Montes, A., 2004. Provenance constraints from detrital zircon U–Pb ages in the NW Iberian Massif: implications for Paleozoic plateconfiguration and Variscan evolution. Journal of the Geological Society 161, 461-473.

Martínez-Catalán J.R., Arenas R., Díaz García F., Gómez-Barreiro J., González Cuadra P., Abati J., Castiñeiras P., Fernández-Suárez J,. Sánchez Martínez S., Andonaegui P., Gónzalez Clavijo E., Díez Montes A., Rubio Pascual F.J., Valle Aguado, B., 2007. Space and time in the tectonic evolution of the northwestern Iberian Massif. Implications for the Variscan belt. In: Hatcher R.D. Jr, Carlson M.P., McBride J.H. Martínez Catalán J.R. (eds) 4-D framework of continental crust. Geol Soc Am Memoir, 200, 403-423.

Martínez-Catalán, J.R., Fernández-Suárez, J., Meireles, C., González-Clavijo, E., Belousova, E., Saeed, A., 2008. U–Pb detrital circón ages in synorogenic deposits of the NW Iberian Masif (Variscan Belt): interplay of Devonian–Carbonifeorus sedimentation and thrust tectonics. Journal of the Geological Society 165, 687-698.

Martínez-Catalán, J.R., Arenas, R., Abati, J., Sánchez Martínez, S., Díaz García, F., Fernández-Suárez, J., González Cuadra, P., Castiñeiras, P., Gómez Barreiro, J., Díez Montes, A., González Clavijo, E., Rubio Pascual, F.J., Andonaegui, P, Jeffries, T.E., Alcock, J.E., Díez Fernández, R., López Carmona, A., 2009. A rootless suture and the loss of the roots of a mountain chain: the Variscan belt of NW Iberia. Comptes Rendues Geoscience 341, 114-126.

Martínez-Catalán, J.R., 2011. Are the oroclines of the Variscan belt related to late Variscan strike-slip tectonics? Terra Nova 23, 241-247.

Martínez-Catalán, J.R., 2012. The Central Iberian arc, an orocline centered in the Iberian Massif and some implications for the Variscan belt. International Journal of Earth Sciences 110,

1299-1314.

Martínez-García, E., 1973. Deformación y Metamorfismo en la zona de Sanabria (Provincias de Zamora, León y Orense, Noroeste de España). Stvdia Geológica Salamanticensia V, 7-106 (ed.) Geología de España. Sociedad Geológica de España and Instituto Geológico y Minero de España, 21-25.

Martínez-Poyatos, D., 1997. Estructura del borde meridional de la Zona Centroibérica y su relación con el contacto entre las Zonas Centroibérica y de Ossa-Morena. Ph.D. thesis, University of Granada, 222 p.

Maruyama, S., Liou, J.G. Suzuki, K., 1982. The Peristerite Gap in Low-Grade Metamorphic Rocks. Contributions to Mineralogy and Petrology 81, 268-276.

Marzán, I., Fernández, M., Cabal, J., 1996. Estudio geotérmico en la mitad occidental de España. Geogaceta 20, 745-748.

Mata, J., Munhá, J., 1986. Geodynamic significance of high grade metamorphic rocks from Delogados-Campo Maior (Tomar-Badajoz-Cordoba shear zone). Maleo 2, 28.

Matte, P., 1986. Tectonics and PlateTectonics Model for the Variscan Belt of Europe. Tectonophysics 126, 329-374.

Matte, P., Ribeiro, A., 1975. Forme et orientation de l'ellipsoide de déformationj dans la virgation hercynienne de Galicice. Relations avec le plissement et hypothèses sur la génèse de lárc ibéro-armonican. Comptes Rendus de l'Académie des Sciences Paris 280, 2825-2828.

Matte, P., 2001. The Variscan collage and orogeny (480–290 Ma) and the tectonic defini- tion of the Armorica microplate: a review. Terra Nova 13, 122-128.

Matte, P., 2002. Variscides between the Appalachians and the Urals: Similarities and differences between Paleozoic subduction and collision belts. In: Martínez-Catalán, J.R., Hatcher, R.D., Arenas, R., Díaz-García, F.,(eds), Variscan-Appalachian dynamics: The building of the late Paleozoic basement. Geological Society of America Special Publication 364, 239-251.

Mayringer, F., Treloar, P.J., Gerdes, A., Finger, F., Shengelia, D., 2011. New age data from the Dzirula massif, Georgia: implications for the evolution of the Caucasian Variscides. American Journal of Science 311, 404-441.

McDonough, W.F., Sun, S.S., 1995. The composition of the Earth. Chemical Geology 120, 223-253.

McKenzie, D., Bickle, M.J., 1988. The volume and composition of melt generated by extension

of the lithosphere, Journal of Petrology 29, 625-697.

McKenzie, D., 1989. Some remarks on the movement of small melt fractions in the mantle. Earth and Planetary Science Letters 95, 53-72.

Meinhold, G., Morton, A.C., Fanning, C.M., Frei, D., Howard, J.P., Phillips, R.J., Strogen, D., Whitham, A.G., 2011. Evidence from detrital zircons for recycling of Mesoproterozoic and Neoproterozoic crust recorded in Paleozoic and Mesozoic sandstones of southern Libya. Earth and Planetary Science Letters 312, 164-175.

Meinhold, G., Morton, A.C., Avigad, D., 2013. New insights into peri-Gondwana paleogeography and the Gondwana super-fan system from detrital zircon U–Pb ages. Gondwana Research 23, 661-665.

Meira, V.T., García-Casco, A., Juliani, C., Almeida, R.P., Schorscher, J.H.D., 2015. The role of intracontinental deformation in supercontinent assembly: insights from the Ribeira Belt, Southeastern Brazil (Neoproterozoic West Gondwana). Terra Nova 27, 206-217.

Melou, M., Oulebbsir, L. Paris, F., 1999. Brachiopodes et chitinozoaires ordoviciens dans le NE du Sahara algerien: implications stratigraphicques et paleogeographiques. Geobios, 32, 692-717.

Michard, A., Soulaimani, A., Hoepffner, C., Ouanaimi, H., Baidder, L., Rjimati, E.C., Saddiqi, O., 2010. The South-Western Branch of the Variscan Belt: evidence from Morocco. Tectonophysics 492, 1-24.

Mitchell, R.H., Bergman, S.C., 1991. Petrology of Lamproites. Springer, New York, 447 p.

Moita, P., Pereira, M.F., Santos, J., 2005a. Tonalites from the Hospitais massif (Ossa–Morena Zone, SW Iberian Massif, Portugal). I: geological setting and petrography. Geogaceta 37, 51-54.

Moita, P., Santos, J., Pereira, M.F., 2005b. Tonalites from the Hospitais massif (Ossa-Morena Zone, SW Iberian Massif, Portugal). II: geochemistry and petrogenesis. Geogaceta 37, 55-58.

Moita, P., Munhá, J., Fonseca, P.E., Pedro, J., Tassinari, C.C.G., Araújo, A., Palácios, T., 2005c. Phase equilibria and geochronology of Ossa-Morena eclogites, paper presented at XIV Semana de Geoquímica/ VIII Congresso de Geoquímica dos Países de Língua Portuguesa, Univ. De Aveiro, Aveiro, Portugal.

Moita P., Santos, J.F., Pereira M.F., 2009. Layered granitoids: Interaction between continental crust recycling processes and mantle-derived magmatism. Examples from the Évora Massif

(Ossa–Morena Zone, southwest Iberia, Portugal). Lithos 111, 125-141.

Moita, P., Dantos, J.F., Pereira, M.F., Costa, MM., Corfu, F., 2015. The quartz-dioritic Hospitais intrusion (SW Iberian Massif) and its mafic microgranular enclaves-Evidence for mineral clustering. Lithos 224-225, 78-100

Molina, J.F., Scarrow, J.H., Montero, P., Bea, F., 2009. High-Ti amphibole as a petrogenetic indicator of magma chemistry: evidence for mildly alkalic-hybrid melts during evolution of Variscan basic–ultrabasic magmatism of Central Iberia. Contributions to Mineralogy and Petrology 158, 69-98.

Montero, P., Bea, F., 1998. Accurate determination of 87Rb/86Sr and 147Sm/144Nd ratios by inductively-coupled-plasma mass spectrometry in isotope geoscience: an alternative to isotope dilution analysis. Analytica Chimica Acta 358, 227-233.

Montero, P., Floor, P., Corretgé, L.G., 1998. The accumulation of rare-earth elements and high-field-strength elements in peralkaline granitic rocks: the Galiñeiro orthogneisic complex, North western Spain. Canadian Mineralogy 36, 683-700.

Montero, P., Salman, K., Zinger, T., Bea, F., 1999. Rb-Sr and single-zircon grain 207Pb/206Pb chronology of the Monesterio Granodiorite and related Migmatites. Evidence of a late Cambrian melting in the Ossa-Morena Zone, Iberian Massif. Estudios Geológicos 55, 3-8.

Montero, P., Salman, K., Zinger, T., Bea, F., 1999. Rb-Sr and single-zircon grain 207Pb/206Pb chronology of the Monesterio Granodiorite and related Migmatites. Evidence of a late Cambrian melting in the Ossa-Morena Zone, Iberian Massif. Estudios Geológicos 55, 3-8.

Montero, P., Salman, K., Bea, F., Azor, A., Exposito, I., González-Lodeiro, F., Martine Poyatos, D.J., Simancas, J.F., 2000. New data on the geochronology of the Ossa Morena Zone, Iberian Massif. Basement Tectonics 15, 136-138.

Montero, P., Bea, F., Zinger, T.F., Scarrow, J.H., Molina, J.F., Whitehouse, M.J., 2004. 55 million years of continuous anatexis in central Iberia: single zircon dating of the Peña Negra Complex. Journal of the Geological Society, London 161, 255-264.

Montero, P., Bea, F., González-Lodeiro, F., Talavera, C., Whitehouse, M., 2007. Zircon crystallization age and protholith history of the metavolcanic rocks and metagranites of the Ollo de Sapo Domain in central Spain. Implications for the Neoproterozoic to Early-Paleozoic evolution of Iberia. Geological Magazine 144, 963-976.

Montero, P., Talavera, C., Bea, F, González-Lodeiro, F., Whitehouse, M., 2009a. Zircon Geochronology of the Ollo de Sapo Formation and the age of the Cambro-Ordovician

rifting in Iberia. Journal of Geology 117, 174-191.

Montero, P., Bea, F., Corretge, L.G., Floor, P., Whitehouse, M.J., 2009b. U–Pb ion microprobe dating and Sr and Nd isotope geology of the Galiñeiro Igneous Complex. A model for the peraluminous/peralkaline duality of the Cambro-Ordovician magmatism of Iberia. Lithos 107, 227-238.

Moreno, J.A., Molina, J.F., Montero, P., Abu Anbar, M., Scarrow, J., Cambeses, A., Bea, F., 2014. Unraveling sources of A-type magmas in juvenile continental crust: Constraints from compositionally diverse Ediacaran post-collisional granitoids in the Katerina Ring Complex, southern Sinai, Egypt. Lithos 192-195, 56-85.

Morimoto, N., Fabries, J., Ferguson, A.K., Ginzburg, I.V., Ross, M., Seifeit, F.A., Zussman, J., 1988. Nomenclature of pyroxenes. American Mineralogist 73, 1123-1133.

Morton, A.C., Whitham, A., Howard, J., Fanning, M., Abutarruma, Y., El Dieb, M., Elkatarry, F.M., Hamhoom, A.M., Lüning, S., Phillips, R., Thusu, B., 2013. Using heavy minerals to test the stratigraphic framework of the Al Kufrah Basin. In: Salem, M.J. (ed.), Geology of Southern Libya.

Mueller, S., Prodehl, C., Mendes, A.S., Sousa-Moreira, V., 1973. Crustal structure in the Southwestern part of the Iberian Peninsula. Tectonophysics 20, 307-318.

Mullane, E., 1998. The geochemistry of the South Portuguese Zone, Spain and Portugal. Ph.D. thesis, University Southampton, 260 p.

Munhá, J., 1983. Low-Grade Regional Metamorphism in the Iberian Pyrite Belt. Comini. Serv. Geol. Portugal 69, 3-35.

Munhá, J., Oliveira, J.T., Ribeiro, A., Oliveira, V., Quesada, C., Kerrich, R., 1986. Beja- Acebuches ophiolite characterization and geodynamic significance. Maleo 2, 31.

Murphy, J.B., Nance, R.D., 1989. A model for the evolution of the Avalonian–Cadomian belt. Geology 17, 735-738.

Murphy, J.B., Gutiérrez-Alonso, G., Nance, R.D., Fernández-Suárez, J., Keppie, J.D., Quesada, C., Strachan, R.A., Dostal, J., 2006. Origin of the Rheic Ocean: rifting along a Neoproterozoic suture? Geology 34, 325-328.

Nance, R.D., Murphy, J.B., 1994. Contrasting basement isotopic signatures and the palinspastic restoration of peripheral orogens: example from the Neoproterozoic Avalonian–Cadomian belt. Geology 22, 617-620.

Nance, R.D., Murphy, J.B., 1996. Basement isotopic signatures and Neoproterozoic paleogeography of Avalonian-Cadomian and related terranes in the circum-North Atlantic. In: Nance, R.D., Thompson, M.D., (eds), Avalonia and Related Peri-Godnwanan Terranes of the Circum-North Atlantic: Boulder, Colorado. Geological Society of America Special Paper 51, 333-346.

Nance, R.F., Murphy, J.B., Strachan, R.A., Keppie, J.D., Gutiérrez-Alonso, G., Fernández-Suárez, J., Quesada, C., Linnemann, U., D'Lemos, R., Pisarevsky, S.A., 2008. Neoproterozoic-early Paleozoic tectonostratigraphy and palaeogeography of the peri-Gondwanan terranes: Amazonian v. West African connections. In: Ennih, N., Liégeois, J.P., (eds), The Boundaries of the West African Craton. Geological Society of London Special Publication 297, 345-383.

Nance R.D., Gutiérrez-Alonso, G., Keppie J.D., Linnemann, U., Murphy J.B., Quesada, C, Strachan, R.A., Woodcock, N.H., 2010. Evolution of the Rheic Ocean. Gondwana Research 17, 194-222.

Nance D.R., Gutiérrez-Alonso, G., Keppie D.J., Linnemann, U., Murphy B.J., Quesada, C, Strachan, A.R., Woodcock, N.H., 2012. A brief history of the Rheic Ocean. Geoscience Frontiers 3, 125-135.

Navas-Parejo, P., 2012. Paleozoic stratigraphy and Paleogeography of the Maláguide Complex (Betic Cordillera) and other Western Mediterranean related domains (Calabria-Peloritani Terrane). Ph.D. thesis, University of Granada, 429 p.

Okay, N., Zack, T., Okay, A.I., Barth, M., 2010. Sinistral transport along the Trans- European Suture Zone: detrital zircon–rutile geochronology and sandstone petrography from the Carboniferous flysch of the Pontides. Geological Magazine 148, 380-403.

Okeke, P.I., Fitton, J.G., 1982. Petrology of the Kirawa volcanics and geochronology of some Gwoza rocks. Nigerian Journal of Mining and Geology 19, 231-242.

Oliveira, J.T., Cunha, T., Streel, M., Vanguertaine, M., 1986. Dating the Horta da Torre Formation, a new lithostratigraphic unit of the Ferreira-Ficalho Group, South-Portuguese Zone: geological consequences. Comunicações Serviços Geológicos de Portugal 72, 129-135.

Oliveira, J.T., 1990. The South Portuguese Zone. Stratigraphy and Synsedimentary tecnonism. In: Dallmeyer, R.D., Martínez-García, E., (eds), Pre-Mesozoic geology of Iberia. Springer, Berlin, 334-347.

Oliveira, J.T., Oliveira, R., Piçarra, J.M., 1991. Traços gerais da evoluçao tectono-estratigráfica da

Zona de Ossa-Morena, em Portugal. Cuaderno Laboratorio Xeoloxico de Laxe 16, 221-250.

Oliveira, J.T., Almeida, J.P., Carvalho, D., Carvalhosa, A., Ferreira, J.N., Gonçalves, F., Oliveira, V., Ribeiro, A., Ribeira, ML., Silva, A.F., Noronha, F., Toun, T., 1992. Carta Geológica de Portugal. Sociedad Geológica de Portugal.

Oliveira, J.T., Pereira, E., Piçarra. J.M., Young, T., Romano, M., 1992. O Paleozoico Inferior de Portugal: síntese da estratigrafia e da evoluçao paleogeográfica. In: Guitiérrez-Marco, J.C., Saavedra, I., Rábano, I., (eds), Paleozoico inferior de Ibero-América. Universidad de Extremadura, Badajoz, 359-375.

Ordoñez-Casado, B., 1998. Geocghronological studies of the Pre-Mesozoic basement of the Iberian Massif: the Ossa Morena zone and the Allochthonous' Complexes within the Central Iberian zone. Ph.D. thesis, Swiss Federal Institute of Technology, Zurich, 235 p.

Ordoñez-Casado, B., Martín-Izard, A., García-Nieto, J., 2008. SHRIMP-zircon U–Pb dating of the Ni–Cu–PGE mineralized Aguablanca gabbro and Santa Olalla granodiorite: Confirmation of an Early Carboniferous metallogenic epoch in the Variscan Massif of the Iberian Peninsula. Ore Geology Reviews 34, 343-353.

Ortega, L., Lunar, R., García-Palomero, F., Moreno, T., Prichard, H., 2001. Removilización de minerales del grupo del platino en el yacimiento de Ni-Cu-EGP de Aguablanca (Badajoz). Boletín de la Sociedad Geológica de Mineralogía 24, 175-176.

Ortega, L., Lunar, R., García-Palomero, F., Moreno, T., Martin-Estevez, J.R., Prichard, H.M., Fisher, P.C., 2004. The Aguablanca Ni–Cu–PGE deposit, Southwestern Iberia: magmatic ore-forming processes and retrograde evolution. Canadian Mineralogist 42, 325-350.

Ortega-Gironés, E., González Lodeiro, F., 1986. La discordancia intra-Alcudiense en el dominio meridional de la Zona Centroibérica. Breviora Geológica Astúrica 27, 27-32.

Oschner, A., 1993. U-Pb geochronology of the Upper Proterozoic lower Paleozoic geodynamic evolution in the Ossa-Morena Zone (SW Iberia): Constrains on the Timming of the Cadomian Orogeny. Ph.D. thesis, University of Zürich, 293 p.

Palomeras, I., Carbonell, R., Flecha, I., Simancas, J.F., Ayarza, P., Matas, J., Martínez Poyatos, D., Azor, A., González Lodeiro, F., Pérez Estaún, A., 2009. Nature of the lithosphere across the Variscan orogen of SW Iberia: dense wide-angle seismic reflection data. Journal of Geophysical Research 114, B02302.

Palomeras, I., Carbonell., R., Atarza, P., Fernández, M., Simancas, J.F., Martínez-Poyatos, D.J., González-Lodeiro, F., Pérez-Estaún, A., 2011. Geophysical model of the lithosphere across

the Variscan Belt of SW-Iberia: Multidisciplinary assessment. Tectonophysics 508, 42-51.

Paquette, J.L., Caby, R., Djouadi, M.T., Bouchez, J.L., 1998. U–Pb dating of the end of the Pan-African orogeny in the Tuareg shield: the post-collisional syn-shear Tioueine pluton (Western Hoggar, Algeria). Lithos 45, 245-253.

Parga-Pondal, I., Matte, P., Capdevila, R., 1964. Introduction à la géologie de 'l'Ollo de Sapo', Formation porphyrode antesilurienne du nord ouest de l'Espagne. Notas y Comunicaciones del Instituto Geolo¤gico y Minero de España 76, 119-153.

Pascual, E., Pérez-Lorente, F., 1975. El magmatismo ácido superficial al sur de Villanueva del Rey-Villaviciosa de Córdoba (Sierra Morena, Cordoba). Cuadernos geológicos de la Universidad de Granada 6, 15-30.

Pastor-Galán, D., Gutiérrez-Alonso, G., Murphy, J.B., Fernández-Suárez, J., Hofmann, M., Linnemann, U., 2013. Provenance analysis of the Paleozoic sequences of the northern Gondwana margin in NW Iberia: Passive margin to Variscan collision and orocline development. Gondwana Research 23, 1089-1103.

Patiño-Douce, A.E., Castro, A., El-Biad, M., 1997. Thermal evolution and tectonic implications of spinel-cordierite granulites from the Aracena Metamorphic Belt, Southwest Spain. GAC/MAC Annual Meeting 22.

Peacock, M.A., 1931. Classification of igneous rock series. Journal of Geology 39, 54-67.

Pearce, J.A., 1996. A user's guide to basalt discrimination diagrams. Trace element geochemistry of volcanic rocks: applications for massive sulphide exploration. Wyman D.A. (ed) Geological Association of Canada, Short Course Notes.

Pearce, J.A., 2008. Geochemical fingerprinting of oceanic basalts with applications to ophiolite classification and the search for Archean oceanic crust. Lithos 100, 14-48.

Pereira, M.F., Silva, J.B., 2001. The Northeast Alentejo Neoproterozoic-Lower Cambrian Succession (Portugal): Implications for regional correlations in the Ossa-Morena Zone (Iberian Massif). Geogaceta 30: 106-109.

Pereira, M.F., Silva, J.B., Chichorro, M., 2003. Internal Structure of the Évora High-grade Terrains and the Montemor-o-Novo Shear Zone (Ossa–Morena Zone, Portugal). Geogaceta 33, 79-82.

Pereira, M.F., Quesada, C., 2006. Ediacaran to Visean crustal growth processes in the Ossa-Morena zone (SW Iberia). IGCP 497 Evora Meeting 2006: Conference Abstracts and Field Trip Guide. Publicaciones del Instituto Geológico y Minero de España, Madrid, 1-115.

Pereira, M.F., Chichorro, M., Linnemann, U., Eguiluz, L., Silva, J.B., 2006. Inherited arc signature in Ediacaran and Early Cambrian basins of the Ossa-Morena Zone (Iberian Massif, Portugal): paleogeographic link with European and North African Cadomian correlatives. Precambrian Research 144, 297-315.

Pereira, M.F., Silva, J.B., Chichorro, M., Moita, P., Santos, J.F., Apraiz, A. Ribeiro, C., 2007a. Crustal growth and deformational processes in the Northern Gondwana margin: Constraints from the Évora Massif (Ossa-Morena Zone, SW Iberia, Portugal). In: Linnemann, U., Nance, R.D., Kraft, P., Zulauf, G. (eds), The Evolution of the Rheic Ocean: From Avalonian–Cadomian Active Margin to Alleghenian–Variscan Collision. Special Paper Geological Society of America 423, 333-358.

Pereira, M.F., Apraiz, A., Silva, J.B., Chichorro, M., 2007b. Tectonothermal analysis of high-temperature mylonitization in the Coimbra–Córdoba shear zone (SW Iberian Massif, Ouguela tectonic unit, Portugal): Evidence of intra-continental transcurrent transport during the amalgamation of Pangea. Tectonophysics 461, 378-394.

Pereira, M.F., Chichorro, M., Williams, I.S., Silva, J.B., 2008. Zircon U-Pb geochronology of paragneisses and biotite granite from the SW Iberian Massif (Portugal): evidence for a palaeogeographical linl between the Ossa-Morena Ediacaran basin and the West African craton. Geological Society, London, Special Publications 297, 385-408.

Pereira, M.F., Chichorro M., Williams, I., Silva J.B., Fernandez C., Díaz-Azpíroz M., Apraiz A., Castro, A. 2009. Variscan intra-orogenic extensional tectonics in the Ossa-Morena Zone (Évora-Aracena-Lora del Río metamorphic belt, SW Iberian Massif): SHRIMP zircon U-Th-Pb geochronology. Geological Society, London, Special Publications 327, 215-237.

Pereira, M.F., Apraiz, A., Chichorro, M., Silva, J.B., Armstrong, R.A., 2010a. Exhumation of high-pressure rocks in northern Gondwana during the Early Carboniferours (Coimbra–Cordoba shear zone, SW Iberian Massif): Tectonothermal analysis and U–Th–Pb SHRIMP in-situ zircon geochronology. Gondwana Research 17, 440-460.

Pereira, M.F., Silva, J.B., Drost, K., Chichorro, M., Apraiz, A., 2010b. Relative timing of transcurrent displacements in northern Gondwana: U–Pb laser ablation ICP-MS zircon and monazite geochronology of gneisses and sheared granites from the western Iberian Massif (Portugal). Gondwana Research 17, 461-481.

Pereira, M.F., Chichorro, M., Solá, A.R., Silva, J.B., Sánchez-García, T., Bellido, F., 2011. Tracing the Cadomian magmatism with detrital/inherited zircon ages by in-situ U–Pb SHRIMP geochronology (Ossa-Morena Zone, SW Iberian Massif). Lithos 123, 204-217.

Pereira, M.F., Chichorro, M., Silva, J.B., Ordóñez-Casado, B., Lee, J.K.W., Williams, I.S., 2012a. Early Carboniferous wrenching, exhumation of high-grade metamorphic rocks and basin instability in SW Iberia: Constraints derived from structural geology and U–Pb and 40Ar–39Ar geochronology. Tectonophysics 558-559, 28-44.

Pereira, M.F., Solá, A.R., Chichorro, M., Lopes, L., Gerdes, A., Silva, J.B., 2012b. North-Gondwana assembly, break-up and paleogeography: U–Pb isotope evidence from detrital and igneous zircons of Ediacaran and Cambrian rocks of SW Iberia. Gondwana Research 22, 866-881.

Pereira, M.F., Chichorro, M., Johnston, S.T., Gutiérrez-Alonso, G., Silva, J.B., Linnemann, U., Hofmann, M., Drost, K., 2012c. The missing Rheic Ocean magmatic arcs: Provenance analysis of Late Paleozoic sedimentary clastic rocks of SW Iberia. Gondwana Research 22, 882-891.

Pereira, M.F., Chichorro, M., Moita, P., Santos, J.F., Solá, A.M.R., Williams, I.S., Silva, J.B., Armstrong, R.A., 2015. The multistage crystallization of zircon in calc alkaline granitoids: U–Pb age constraints on the timing of Variscan tectonic activity in SW Iberia, International Journal of Earth Science, doi 10.1007.

Pérez-Estaún, A., Bastida, F., Alonso, J.L., Marquínez, J., Aller, J., Álvarez-Marrón, J., Marcos, A., Pulgar, J.A., 1988. A thin-skined tectonics model for an arcuate fold and thrust belt: The Cantabrian Zone (Variscan Ibero-Armonican Arc). Tectonics 7, 517-537.

Pérez-Estaún, A., 2004. Zona Cantábrica: Estratigrafía. In: Vera, J.A. (ed.). Geología de España, SGE-IGME, Madrid, Spain, 26-42.

Pérez-Estaún, A., Bea, F., 2004. Macizo Ibérico, in: Vera, J.A. (ed.), Geología de España, Madrid, SGE-IGME, Madrid, Spain, 19-230.

Pérez-Estaún, A., Bea, F., Bastida, F., Marcos, A., Martínez Catalán, J.R., Martínez Poyatos, D., Arenas, R., Díaz García, F., Azor, A., Simancas, J.F., González- Lodeiro, F., 2004. La cordillera Varisca Europea: El Macizo Ibérico. In: Vera, J.A. (ed.), IGME, Madrid, 19-228.

Peucat, J.J., Capdevila, R., Drareni, A., Choukroune, P., Fanning, C.M., Bernard-Griffiths, J., Fourcade, S., 1996. Major and trace element geochemistry and isotope (Sr, Nd, Pb, O) systematics of an Archaean basement involved in a 2.0 Ga very high-temperature (1000°C) metamorphic event: In Ouzzal Massif, Hoggar, Algeria. Journal of Metamorphic Geology 14, 667-692.

Peucat, J.J., Drareni, A., Latouche, L., Deloule, E., Vidal, P., 2003. U-Pb zircon (TIMS and SIMS)

and Sm-Nd whole-rock geochronology of the Gour Oumelalen granulitic basement, Hoggar massif, Tuareg shield, Algeria. Journal of African Earth Sciences 37, 229-239.

Peucat, J.J., Capdevila, R., Drareni, A., Mahdjoub, Y., Kahoui, M., 2005. The Eglab massif in the West African Craton (Algeria), an original segment of the Eburnean orogenic belt: petrology, geochemistry and geochronology. Precambrian Research 136, 309-352.

Pilet, S., Baker, M.B., Stolper, E.M., 2008. Metasomatized Lithosphere and the Origin of Alkaline Lavas. Science, 320, 916-919.

Pilet, S., Baker, M.B., Müntener, O., Stolper, E.M., 2011. Monte Carlo Simulations of Metasomatic Enrichment in the Lithosphere and Implications for the Source of Alkaline Basalts. Journal of Petrology 52, 1415-1442.

Pin, C., Paquette, J.L., Fonseca, P., 1999. 350 Ma (U–Pb zircon) igneous emplacement age and Sm-Nd isotopic study of the Beja gabbroic complex (S Portugal), XV Reunión Geología del Oeste Peninsular, Badajoz, Spain. Journal of Conference Abstracts 4, 1019.

Pin, Ch., Liñán, E., Pascual, E., Donaire, T., Valenzuela, A., 2002. Late Neoproterozoic crustal growth in the European Variscides: Nd isotope and geochemical evidence from the Sierra de Córdoba andesites (Ossa-Morena Zone, Southern Spain). Tectonophysics 352, 133-151.

Pin, C., Fonseca, P.E., Paquette, J.L., Castro, P., Matte, P., 2008. The ca. 350 Ma Beja Igneous Complex: A record of transcurrent slab break-off in the Southern Iberia Variscan Belt?. Tectonophysics 461, 356-377.

Pinto, M.S., 1984. Granitóides Caledónicos e Hercínicos na Zona de Ossa-Morena (Portugal). Memórias e Noticias Publicaçoes do Museo e Laboratório mineralógico e geológico da Universidad de Coimbra 97, 81-94.

Piña, R., 2006. El yacimiento de Ni-Cu-EGP de Aguablanca (Badajoz): Caracterización y modelización metalogénica. Ph.D. thesis, Universty Complutense of Madrid.

Pitcher, W.S., 1993. The Nature and Origin of Granite. Chapman and Hall, London, 321 p.

Poli, G., Tommasini, S., Halliday, A.N., 1996. Trace element and isotopic exchange during acid-basic magma interaction processes. Transactions of the Royal Society of Edinburgh: Earth Sciences, 87, 225-232.

Pons, J., 1982. Un Modele d'evolution de Complexes plutoniques: Gabbros et Granitöides de la Sierra Morena Occidentale. Ph.D. thesis, University of Paul Salvatier Touluse, 451 p.

Pous, J., Poyatos, D.M., Heise, W., Monteiro Santos, F., Galindo-Zaldívar, J., Ibarra, P., Pedrera, A., Ruiz-Constán, A., Anahnah, F., Gonçalves, R., Mateus, A., 2013. Constraints on the crustal structure of the internal Variscan Belt in SW Europe: A magnetotelluric transect along the eastern part of Central Iberian Zone, Iberian Massif. Journal of Geophysical Research 116, doi:10.1029.

Prelevic, D., Foley, S.F., Cvetkovic, V., Romer, R.L., 2004. Origin of minette by mixing of lamproite and dacite magmas in Veliki Majdan, Serbia. Journal of Petrology 45, 759-792.

Prodehl, C., Sousa-Moreira, V., Mueller, S.T., Mendes, A.S., 1975. Deepseismic sounding experiments in central and southern Portugal. Proc. of the 14th General Assembly of the European Seismological Comission, Berlin, 261-266.

Quesada, C., Apalategui, O., Eguiluz, L., Liñán, E., Palacios, T., 1990a. Ossa-Morena Zone: precambrian. In: Dallmeyer, R.D., Martínez-García, E., (eds), Pre-mesozoic geology of Iberia. Springer, Berlin, 250-258.

Quesada, C., 1990. Precambrian successions in SW Iberia: their relationship to Cadomian orogenic events. In: D'Lemos, R.S., Strachan, R.A., Topley, C.G., (eds), The Cadomian orogeny. Geological Society of Special Publication, London 51, 553-562.

Quesada, C., Robardet, M., Gabladón, V., 1990b. Stratigraphy: Synorogenic Phase (Upper Devonian-Carboniferous-Lower Permian). In: Dallmeyer, R.D., Martínez-García, E., (eds), Pre-mesozoic geology of Iberia. Springer, Berlin, 273-279.

Quesada, C., 1991. Geological constraints on the Paleozoic tectonic evolution of tectonostratigraphic Terranes in the Iberian Massif. Tectonophysics 185, 225-245.

Quesada, C., Fonseca, P., Munhá, J., Oliveira, J.T., Ribeiro, A., 1994. The Beja-Acebuches Ophiolite (southern Iberia Variscan fold belt): Geological characterization and geodynamic significance. Boletín Geológico y Minero 105, 3-49.

Quesada, C., Sánchez-García, T., Bellido, F., López-Guijarro, R., Armendáriz, M., Braid, J., 2006. Introduction: the Ossa-Morena zone-from Neoproterozoic arc through Early Palaeozoic rifting to late Palaeozoic orogeny. In: Pereira, M.F., Quesada, C. (eds), Ediacaran to Visean Crustal Growth Processes in the Ossa-Morena Zone (SW Iberia). IGCP 497 Evora Meeting 2006: Conference Abstracts and Field Trip Guide. Publicaciones del Instituto Geológico y Minero de España, Madrid, 51-73.

Raimondo, T., Hand, M., Collins, W.J., 2014. Compressional intracontinental orogens: ancient and modern perspectives. Earth-Science Reviews 130, 128-153.

Rapp, R.P., Watson, E.B., 1995. Dehydration melting of metabasalt at 8–32 kbar: Implications for continental growth and crust–mantle recycling. Journal of Petrology 36, 891-931.

Ribeiro, A., Pereira E., Díaz, R., 1990. Structure in the NW of the Iberian Peninsula. In: Dallmeyer, R.D., Martinez-García, E., (eds), Pre-Mesozoic Geology of Iberia. Springer-Verlag, Berlin Heidelbelberg, 221-236.

Ribeiro, A., Dias, R., Silva, J.B., 1995. Genesis of the Ibero-Armorican Arc. Geodinamica Acta 8, 173-184.

Ribeiro, A., Munhá J., Dias, R., Mateus, A., Pereira, E., Ribeiro, L., Fonseca, P., Araujo, A., Oliveira, T., Romao, J., Chaminé, H., Coke, C., Pedro, J., 2007. Geodynamic evolution of the SW Europe Variscides. Tectonics, 26, TC6009.

Ridolfi, F., Renzulli, A., 2012. Calcic amphiboles in calc-alkaline and alkaline magmas: thermobarometric and chemometric empirical equations valid up to 1,130° C and 2.2 GPa. Contributions to Mineralogy and Petrology 163, 877-895.

Robardet, M., 1981. Late Ordovician tillites in the Iberian Peninsula. In: Hambrey, M.J., Harlant, W.B., (eds), Earth Pre-Pleistocene Glacial record. Cambridge University, Cambridge, 585-589.

Robardet, M., Gutiérrez-Marco, J.C., 1990a. Stratigraphy: Passive Margin Phase (Ordovician-Silurian-Devonian). In: Dallmeyer, R.D., Martínez-García, E., (eds), Pre-mesozoic geology of Iberia. Springer, Berlin, 267-272.

Robardet, M., Gutiérrez-Marco, J.C., 1990b. Sedimentary and faunal domains in the Iberian Peninsula during Lower Paleozoic times. In: Dallmeyer, R.D., Martínez-García, E., (eds), Pre-mesozoic geology of Iberia. Springer, Berlin, 383-395.

Robardet, M., Verniers, J., Feist, R., Paris, F., 1994, Le Paléozoique antévarisque de France, contexte paléogéographique et géodynamique. Géologie de la France 3, 3-31.

Robardet, M., 2003. The Armorica 'microplate': fact or fiction? Critical review of the concept and contradictory palaeobiogeographical data. Palaeogeography, Palaeoclimatology, Palaeoecology 195, 125-148.

Robardet, M., Gutiérrez-Marco, J.C., 2004. The Ordovician, Silurian and Devonian sedimentary rocks of the Ossa-Morena Zone (SW Iberian Peninsula, Spain). Journal of Iberian Geology 30, 73-92.

Roberts, M.P., Pin, C, Clemens, J.C., Paquette, J.L., 2000. Petrogenesis of Mafic to Felsic Plutonic Rock Associations: the Calc-alkaline Querigut Complex, French Pyrenees Journal of

Petrology 41, 809-844.

Roberts, N.M.W., Van Kranendonk, M.J., Parman, S, Clift, P.D. 2015. Continent formation through time. Geological Society, London, Special Publications, 389, 362 p.

Rock, N.M.S., 1991. Lamprophyres. Blackie, Glasgow, 285 p.

Rodríguez, J., Paquette, J.L., Gil Ibarguchi, J.I., 2007. U–Pb dating of Lower Ordovician alkaline magmatism in the Gondwana margin (Malpica-Tui complex, Iberian Massif): latest continental events before oceanic spreading. In: Arenas, R., Martínez Catalán, J.R., Abati, J., Sánchez Martínez, S. (eds), IGCP 497—The Rheic Ocean: its origin, evolution and correlatives. The rootless Variscan suture of NW Iberia (Galicia, Spain). Field trip guide & Conference abstracts. Instituto Geologico y Minero de Espana, A Coruña, Spain, 163-164.

Romero, I., Lunar, R., Capote, R., Quesada, C., Dunning, G.R., Piña. R., Ortega, L., 2006b. U–Pb age constraints on Variscan magmatism and Ni–Cu–PGE metallogeny in the Ossa–Morena Zone (SW Iberia). Journal of the Geological Society, London 163, 837-846.

Rosas, F.M., Marques, F.O., Ballèvre, M., Tassinari, C., 2008 Geodynamic evolution of the SW Variscides: Orogenic collapse shown by new tectonometamorphic and isotopic data from western Ossa-Morena Zone, SW Iberia. Tectonics 27, TC002333.

Rubio-Ordóñez, A., Valverde-Vaquero, P., Corretgé, L.G., Cuesta-Fernández, A., Gallastegui, G., Fernández-González, M., Gerdes, A., 2012. An Early Ordovician tonalitic–granodioritic belt along the Schistose-Greywacke Domain of the Central Iberian Zone (Iberian Massif, Variscan Belt). Geological Magazine 149, 927-939.

Rubio-Pascual, J., Matas, J., Martín-Parra, L.M., 2013. High-pressure metamorphism in the Early Variscan subduction complex of the SW Iberian Massif. Tectonophysics 592, 187-199.

Rudnick, R.L., Fountain, D.M., 1995. Nature and composition of the continental crust: a lower crustal perspective. Reviews of Geophysics 33, 267-267.

Sáez, R., Almodovar, G.R., Barriga, F.J.A.S., 1997. Mineral exploation in the Iberian Pyrite Belt. SGA news 3, 7-10.

Salman, K., 2002. Estudio petrológico, geoquímico y Geocronológico de los granitoides del área Monesterio-Cala, Zona de Ossa-Morena (Macizo Ibérico). Ph.D. thesis, University of Granada, 232 p.

Samson, S.D., Inglis, J.D., D'Lemos, R.S., Admou, H., Blichert-Toft, J., Hefferan, K., 2004. Geochronological, geochemical, and Nd–Hf isotopic constraints on the origin of Neoproterozoic plagiogranites in the Tasriwine ophiolite, Anti-Atlas orogen, Morocco.

Precambrian Research 135, 133-147.

Sánchez Martínez, S., Arenas, R., Gerdes, A., Castiñeiras, P., Potrel, A., Fernández-Suárez, J., 2011. Isotope geochemistry and revised geochronology of the Purrido Ophiolite (Cabo Ortegal Complex, NW Iberian Massif): Devonian magmatism with mixed sources and involved Mesoproterozoic basement. Journal of the Geological Society 168, 733-750.

Sánchez Martínez, S., Gerdes, A., Arenas, R., Abati, J., 2012. The Bazar Ophiolite of NW Iberia: a relic of the Iapetus–Tornquist Ocean in the Variscan suture. Terra Nova 24, 283-294.

Sánchez-Carretero, R., Carracedo, M., Eguiluz, L., Garrote, A., Apalategui, O., 1989. El magmatismo calcoalcalino del Precámbrico terminal en la Zona de Ossa-Morena (Macizo Ibérico). Revista de la Sociedad Geológica de España 2, 7-21.

Sánchez-Carretero, R., Eguiluz, L., Pascual, E., Carracedo, M., 1990. Ossa-Morena Zone: igneous rocks. In: Dallmeyer, R.D., Martínez-García, E., (eds), Pre-mesozoic geology of Iberia. Springer, Berlin, 292-313

Sánchez-Carretero, R., Carracedo, M., Eguiluz, L., Olazabal, A.A., 1999. Magmatismo alcalino tardicadomiense en la zona de Ossa Morena (Macizo Ibérico): Cartografía, petrografía y geoquímica preliminary del Macizo del Almendral. Geogaceta 26, 87-90.

Sánchez-España, J., Velasco, F., Boyce, A.J., Fallick, A.E., 2003. Source and evolution of ore-forming hydrothermal fluids in the northern Iberian Pyrite Belt massive sulphide deposits (SW Spain): evidence from fluid inclusions and stable isotopes. Minerali Deposita 38, 519-537.

Sánchez-García, T., Bellido, F., Quesada, C., 2003. Geodynamic setting and geochemical signatures of Cambrian-Ordovician rift-related igneous rocks (Ossa-Morena Zone, SW Iberia). Tectonophysics 365, 233-255.

Sánchez-García, T., Quesada, C., Bellido, F., Dunning, G., González de Tanago, J., 2008. Two-step magma flooding of the upper crust during rifting: the Early Paleozoic of the Ossa-Morena zone (SW Iberia). Tectonophysics 461, 72-90.

Sánchez-García, T., Bellido, F., Pereira, M.F., Chichorro, M., Quesada, C., Pin. Ch., Silva. J.B., 2010. Rift-related volcanism predating the birth of the Rheic Ocean. Gondwana Research 17, 392-407.

Sánchez-García, T., Pereira, M.F., Bellido, F., Chichorro, M., Silva, J.B., Valverde-Vaquero, P., Pin, Ch., Solá, A.R., 2013. Early Cambrian granitoids of North Gondwana margin in the transition from a convergent setting to intra-continental rifting (Ossa-Morena Zone, SW

Iberia). International Journal of Earth Sciences, 103, 1203-1218.

Sánchez-Jiménez, N., 2004. estructura gravimétrica y magnética de la corteza del suroeste peninsular (Zona Surportuguesa y Zona de Ossa-Morena). Ph.D. thesis, University Complutense of Madrid, 244 p.

Sánchez-Lorda, M.E., Sarrionandia, F., Ábalos, B., Carracedo, M., Eguiluz, L., Gil-Ibarbuchi, J.I., 2013. Geochemistry and paleotectonic setting of Ediacaran metabasites from the Ossa-Morena Zone (SW Iberia). International Journal of Earth Sciences, 103, 1263-1286.

Santos, J.F., Mata, J., Gonçalves, F., Munhá, J.M., 1987. Contribuiçao para o conhecimento geológicopetrológico da regiao de Santa Suzana: o Complexo Vulcano-sedimentar de Toca da Moura. Comunicacoes Servicios Geológicos Portugal 73, 29-40.

Sarrionandia, F., 2005. Estudio petrológico del complejo plutónico de Valencia del Ventoso (Badajoz). Ph.D. thesis, University of Pais Vasco, 477 p.

Sarrionandia, F., Carracedo, M., 2007. Geocronología Rb-Sr y Sm-Nd del complejo plutónico de Valencia del Ventoso (Badajoz). Geogaceta 41, 207-210.

Sarrionandia, F., Carracedo, M., Eguíluz, L., Ábalos, B., 2011. Caracterización de los granitoides variscos de tipo I (ACG) de la Zona de Ossa-Morena (Macizo Hespérico): Unidad Ácida del Plutón de Valencia del Ventoso (Badajoz). Geogaceta 50, 43-46.

Sarrionandia, F., Carracedo-Sánchez, M., Eguíluz, E., Ábalos, B., Rodríguez, J., Pin, C., Gil Ibarguchi, J.I., 2012. Cambrian rift-related magmatism in the Ossa-Morena Zone (Iberian Massif): Geochemical and geophysical evidence of Gondwana break-up. Tectonophysics 570-571, 135-150.

Scarrow, J.H. Bea, F., Montero, P., Molina, J.F., 2009a. Shoshonites, vaugnerites and potassic lamprophyres: similarities and differences between 'ultra'-high-K rocks. Earth and Environmental Science Transactions of the Royal Society of Edinburgh 99, 159-175.

Scarrow, J.H., Molina, J.F., Bea, F., Montero, P., 2009b. Within-plate calc-alkaline rocks: Insights from alkaline mafic magma–peraluminous crustal melt hybrid appinites of the Central Iberian Variscan continental collision. Lithos 110, 50-64.

Scarrow, J.H., Molina, J.F., Bea, F., Montero, P., Vaughan, A.P.M., 2011. Lamprophyre dikes as tectonic markers of late orogenic transtension timing and kinematics: A case study from the Central Iberian Zone. Tectonics, 30, doi:10.1029.

Schäfer, H.J., 1990. Geochronological investigations in the Ossa-Morena Zone, SW Spain. Ph. D. thesis, Swiss Federal Institute of Technology, Zurich, 153 p.

Schäfer, H.J., Gebauner, D., Nägler, T.F., Eguiluz, L., 1993. Conventional and ion-microprobe U-Pb dating of detrital zircons of the Tentudia Group (Serie Negra, SW Spain): implications for zircon systematics, stratigraphy, tectonics and the Precambrian/Cambrian boundary. Contributions to Mineralogy and Petrology 113, 289-299.

Schermerhörn, L.J.G., 1971. An outline stratigraphy of the Iberian Pyrite Belt. Boletín Geológico Minero 82, 239-268.

Schmelzbach, C., Simancas, J.F., Juhlin, C., Carbonell, R., 2008. Seismic reflection imaging over the South Portuguese Zone foldand- thrust belt, SW Iberia. Journal of Geophysical Research 113, B08301.

Shand, S.J., 1947. Eruptive Rocks. Their Genesis, Composition, Classification, and Their Relation to Ore-Deposits with a Chapter on Meteorite. New York, John Wiley & Sons, 360 p.

Shaw, A., 1991. The Petrogenesis of Hercynian Granites, French Massif Central, Ph.D. thesis, University of London, 570p.

Shaw, J., Gutiérrez-Alonso, G., Johnston, S.T., Pastor-Galán, D., 2014. Provenance variability along the Early Ordovician north Gondwana margin: Paleogeographic and tectonic implications of U-Pb detrital zircon ages from the Armorican Quartzite of the Iberian Variscan belt. Geological Society of America Bulletin, doi: 10.1130/.

Silva, J.B., Oliveira, J.T., Ribeiro, A., 1990. The South Portugese Zone. Structural outline. In: Dallmeyer, R.D., Martínez-García, E., (eds), Pre-mesozoic geology of Iberia. Springer, Berlin, 334-362.

Simancas, F., 1983. Geología de la extremidad oriental de la Zona Sudportuguesa. Ph.D. thesis, University of Granada, 439 p.

Simancas, F., Galindo-Zaldivar, J. and Azor, A., 2000. Three-dimensional shape and emplacement of the Cardenchosa deformed pluton (Variscan Orogen, southwestern Iberian Massif). Journal of Structural Geology 22, 489-503.

Simancas, J.F., Martínez-Poyatos, D.J., Expósito, I., Azor, I., González-Lodeiro, F., 2001. The structure of a major suture zone in the SW Iberian Massif: The Ossa-Morena/Central Iberian contact. Tectonophysics. 332, 295- 308.

Simancas, J.F., Carbonell, R., González-Lodeiro, F., Pérez-Estaún, A., Juhlin, C., Ayarza, P., Kashubin, A., Azor, A., Martínez-Poyatos, D.J., Almodóvar, G.R., Pascual, E., Sáez, R., Expósito, I., 2003. Crustal structure of the transpressional Variscan orogen of SW Iberia: SW Iberia deep seismic reflection profile (IBERSEIS). Tectonics 22, 1062.

Simancas, J.F., Expósito, I., Azor, A., Martínez-Poyatos, D., González-Lodeiro, F., 2004. From the Cadomian orogenesis to the Early Palaeozoic Variscan rifting in Southwest Iberia. Journal of Iberian Geology 30, 53-71.

Simancas, J.F., 2004. La Zona Sudportuguesa: Estructura. In: Vera, J.A. (ed.). Geología de España, SGE-IGME, Madrid, Spain, 211-215.

Simancas, J.F., Tahiri, A., Azor, A., González-Lodeiro, F., Martínez Poyatos, D.J., El Hadi, H., 2005. The tectonic frame of the Variscan –Alleghanian orogeny in southern Europe and northern Africa. Tectonophysics 398, 181-198.

Simancas, J.F., Carbonell, R., González-Lodeiro, F., Pérez-Estaún, A., Juhlin, C., Ayarza, P., Kashubin, A., Azor, A., Martínez-Poyatos, D.J., Saez, R., Almodovar, G.R., Pascual, E., 2006. Transpressional collision tectonics and mantle plume dynamics: The Variscides of southwestern Iberia. In: Gee, D.G., Stephenson, R.A., (eds), European Lithosphere Dynamics. Memoirs Geological Society of London 32, 345-354.

Simancas, J.F., Azor, A., Martínez-Poyatos, D.J., Thahiri, A., El-Hadi, H., González-Lodeiro, F., Pérez-Estaún, A., Carbonell, R., 2009. Tectonic relationships of Southwest Iberia with the allochthons of Northwest Iberia and the Moroccan Variscides. Comptes Rendus Geoscience 341, 103-113.

Simancas, J.F., Ayarza, P., Azor, A., Carbonell, R., Martínez-Poyatos, D., Pérez-Estaún, A., González-Lodeiro, F., 2013. A Seismic geotraverse across the Iberian Variscides: Orogenic shortening, collisional magmatism, and oroclline development. Tectonics 32, 417-432.

Smith, J.V., and Brown, W.L., 1988. Feldspar minerals: 1.Crystal structures, physical, chemical, and microtextural properties. Springer-Verlag, Berlin, 828 p.

Snelling, N.J., 1964. Age Determination Unit. Institute Geological Scince, Annual Report, 30-40.

Socías, I., Mezcua, J., Lynam, J., Del Potro, R., 1991. Interpretation of an aeromagnetic survey in the Spanish mainland. Earth and Planetary Science Letters 105, 55-64.

Solá, A.R., Montero, P., Neiva, A.M.R., Zinger, T., Bea, F., 2005. Pb/Pb age of the Carrascal Massif, central Portugal. Geochimica et Cosmochimica Acta 69, A856-A856.

Solá, A.R., 2007. Relaçoes petrogeoquímicas dos maciços graníticos do NE Alentejano. Ph.D. thesis, University of Coimbra, 405 p.

Solá, A.R., Pereira, M.F., Williams, I.S., Ribeiro, M.L., Neiva, A.M.R., Montero, P., Bea, F., Zinger, T., 2008. New insights from U-Pb zircon dating of Early Ordovician magmatism on northern Gondwana margin: The Urra Formation (SW Iberian Massif, Portugal).

Tectonophysics 461, 114-129.

Solá, A.R., Williams, I.S. Neiva, A.M.R., Ribeiro, M.L., 2009. U-Th-Pb SHRIMP ages and oxygen isotope composition of zircon from two contrasting late Variscan granitoids, Nisa-Albuquerque batholiths, SW Iberian Massif: petrologic and regional implications. Lithos 111, 156-167.

Sparks, R.S.J., Marshall, L.A., 1986. Thermal and mechanical constraints on mixing between mafic and silicic magmas. Journal of Volcanology and Geothermal Research 29, 99-124.

Stampfli, G.M., Borel, G.D., 2002. A plate tectonic model for the Paleozoic and Mesozoic constrained by dynamic plateboundaries and restored synthetic oceanic isochrones. Earth and Planetary Science Letters 196, 17-33.

Stampfli, G.M., von Raumer, J., Borel, G.D., 2002. Paleozoic evolution of per-Variscan terranes: From Gondwana to the Variscan collision. Im Martínez-Catalan, J.R., Hatcher, R.D., Arenas, R., Díaz-García, F., (eds). Variscan-Appalachian dynamics: The building of the late Paleozoic basement: Boulder, Colorado. Geological Society of America Special Paper 364, 263-280.

Stampfli, G.M., Hochard, C., Vérard, C., Wilhem, C., von Raumer, J., 2013. The formation of Pangea. Tectonophysics 593, 1-19.

Stern, R.J., 2002. Crustal evolution in the East African Orogen: a neodymium isotopic perspective. Journal of African Earth Sciences 34, 109-117.

Sun, S.S., Hanson, G.N., 1975. Origin of Ross Island basanitoid and limitations upon the heterogenity of mantle sources for alkali basalts and nephelinites. Contributions to Mineralogy and Petrology 52, 77-106.

Sun, S., McDonough, W. F., 1989. Chemical and isotopic systematics of oceanic basalts: Implications for mantle composition and processes. In: Saunder, A.D., Norry, M. J., (eds), Magmatism in the Ocean Basins. Geological Society Special Publication 42, 313-345.

Swinden, H.S., Jenner, G.A., Fryer, B.J., Hertogen, J., Roddick, J.C., 1990. Petrogenesis and paleotectonic history of the Wild Bight Group, an Ordovician rifted island arc in central Newfoundland. Contributions to Mineralogy and Petrology 105, 219-241.

Tahiri, A., Montero, P., El Hadi, H., Martinez Poyatos, D., Azor, A., Bea, F., Simancas, F., González-Lodeiro, F. 2010. Geochronological data on the Rabat–Tiflet granitoids: their bearing on the tectonics of the Moroccan Variscides. Journal of African Earth Sciences 57, 1-13.

Tait, J.A., Bachtadse, V., Soffel, H., 1996. Eastern Variscan fold belt: paleomagnetic evidence for oroclinal bending. Geology 24, 871–874.

Talavera, C., Montero, P., Martínez-Poyatos, D., Williams, I.S., 2012. Ediacaran to Lower Ordovician age for rocks ascribed to the Schist–Graywacke Complex (Iberian Massif, Spain): Evidence from detrital zircon SHRIMP U–Pb geochronology. Gondwana Research 22, 928-942.

Talavera, C., Montero, P., Bea, F., González Lodeiro, F., Whitehouse, M., 2013. U–Pb Zircon geochronology of the Cambro-Ordovician metagranites and metavolcanic rocks of central and NW Iberia. International Journal of Earth Sciences 102, 1-23.

Teixeira, W., Tassinari, C.C.G., Cordani, U.G., Kawashita, K., 1989. A review of the geochronology of the Amazonian craton: Tectonic implications. Precambrian Research 42, 213-227.

Thomas, R.J., Chevallier, L.P., Gresse, P.G., Harmer, R.E., Eglington, B.M., Armstrong, R.A., de Beer, C.H., Martini, J.E.J., de Kock, G.S., Macey, P.H., Ingram, B.A., 2002. Precambrian evolution of the Sirwa Window, Anti- Atlas Orogen, Morocco. Precambrian Research 118, 1-57.

Thomas, R.J., Fekkak, A., Ennih, N., Errami, E., Loughlin, S.C,. Gresse, P.G., Chevallier, L.P., Lie´geois, J.-P., 2004. A new lithostratigraphic framework for the Anti-Atlas Orogen, Morocco. Journal of African Earth Sciences 39, 217-226.

Thybo, H., Artemieva, I.M., 2013. Magmatic underplating-not only in extensional settings. AGU Fall Meeting Abstracts 1, 08.

Tischendorf, G., Förster, H.-J., Gottesmann, B., Rieder, M., 2007. True and brittle micas: composition and solid-solution series. Mineralogical Magazine 71, 285-320.

Tornos, F., Casquet, C., Relvas, M.R.S.J., 2005. Transpressional tectonics, lower crust decoupling and intrusion of deep mafic sills: a model for the unusual metallogenesis of SW Iberia. Ore Geology Reviews 27, 133-163.

Tornos, F., Galindo, C., Casquet, C., Rodríguez Pevida, L., Martínez, C., Martínez, E., Velasco, F., Iriondo, A., 2006. The Aguablanca Ni–(Cu) sulfide deposit, SW Spain: geologic and geochemical controls and the relationship with a midcrustal layered mafic complex. Mineralium Deposita 41, 737-769.

Torsvik, T.H., Smethurst, M.A., Van der Voo, R., Trench, A., Abrahamsen, N., Halvorsen, E., 1992, Baltica. A synopsis of Vendian-Permian paleomagnetic data and their paleotectonic

implications: Earth-Science Reviews 33, 133-152.

Torsvik, T.H., Cocks, L.R.M., 2013. Gondwana from top to base in space and time. Gondwana Research 24, 999-1030.

Tougarinov, A.I., Knorre, K.G., Shanin, L.L., Prokofieva, L.N., 1968. The geochronology of some Precambrian rocks of southern West Africa. Canadian Journal of Earth Sciences 5, 639-642.

Tounmmite, A., Liegeois, J.P., Gasquet, D., Bruguier, O., Beraaouz, E.H., 2013. Ikenne Field, geochemistry and Sr-Nd isotopes of the Pan-African granitoids from the Tifnoute Valley (Sirwa, Anti-Atlas, Morocco): a post-collisional event in a metacratonic setting. Mineralogy and Petrology 107, 739-763.

Tubosun, I.A., Lancelot, J.R., Rahaman, M.A., Ocan, O., 1984. U–Pb Panafrican ages of two charnockite-granite association from southwestern Nigeria. Contribution to Mineralogy and Petrology 88, 188-195.

Valley, J.W., 2003. Oxygen isotopes in zircon. In: Hanchar, J.M., Hoskin, P.W.O. (eds), Zircon, Reviews in Mineralogy and Geochemistry, 53. Mineralogical Society of America/Geochemical Society, Washington, DC, 343-385.

Valley, J.W., Lackey, J.S., Cavosie, A.J., Clechenko, C.C., Spicuzza, M.J., Basei, M.A.S., Bindeman, I.N., Ferreira, V.P., Sial, A.N., King, E.M., Peck, W.H., Sinha, A.K., Wei, C.S., 2005. 4.4 billion years of crustal maturation: oxygen isotope ratios of magmatic zircon. Contributions to Mineralogy and Petrology 150, 561-580.

van Breemen, O., Pidgeon, R.T., Bowden, P., 1977. Age and isotopic studies of some panafrican granites from Northcentral Nigeria. Precambrian Research 4, 307-319.

Villaseca, C., Merino, E., Oyarzun, R., Orejana, D., Pérez-Soba, C., Chicharro, E., 2014. Contrasting chemical and isotopic signatures from Neoproterozoic metasedimentary rocks in the Central Iberian Zone (Spain) of pre-Variscan Europe: Implications for terrane analysis and EarlyOrdovician magmatic belts. Precambrian Research 245, 131-145.

von Raumer, J.F., Neubauer, F. (eds), 1993. Pre-Mesozoic Geology in the Alps. Springer, Berlin Heidelberg. 677 p.

Wagner, R.H., 1978. The Valdeinfierno sequence (Prov. Cordoba): its tectonic, sedimentary and floral significance. Annales de la Société Géologique du Nord (Lille) 98, 59-66.

Wagner, R.H., Coquel, R., Broutin, J., 1983. Mississipian floras of the Sierra Morena, SW Spain: a progress report. In: Lemos de Sousa, M.J., (ed.), Contributions to the Carboniferous

geology and palaeontology of the Iberian Peninsula. University of Porto, 101-126.

Walsh, G.J., Aleinikoff, J.N., Benziane, F., Yazidi, A., Armstrong, T.R., 2002. U–Pb zircon geochronology of the Paleoproterozoic Tagragra de Tata inlier and its Neoproterozoic cover, western Anti-Atlas, Morocco. Precambrian Research 117, 1-20.

Walsh, G.J., Benziane, F., Aleinikoff, J.N., Harrison, R.W., Yazidi, A., Burton, W.C., Quick, J.E., Saadane, A., 2012. Neoproterozoic tectonic evolution of the Jebel Saghro and Bou Azzer–El Graara inliers, eastern and central Anti-Atlas, Morocco. Precambrian Research 216-219, 23-62.

Wasserburg, G.J., Jacousen, S.B., DePaolo, D.J., McCulloch, M.T., Wen, T. 1981. Precise determination of ratios, Sm and Nd isotopic abundances in standard solutions. Geochimica et Cosmochimica Acta 45, 2311-2323.

Weidendorfer, D., Mattsson, H.B., Ulmer, .P, 2014. Dynamics of Magma Mixing in Partially Crystallized Magma Chambers: Textural and Petrological Constraints from the Basal Complex of the Austurhorn Intrusion (SE Iceland). Journal of Petrology 55, 1865-1903.

Whalen, J.B., Currie, K.L., Chappell, B.W., 1987. A-type granites: geochemical characteristics, discrimination and petrogenesis. Contributions to Mineralogy and Petrology 95, 407-419.

White, W.M., Hofmann, A.W., 1982. Sr and Nd isotope geochemistry of oceanic basalts and mantle evolution. Nature 296, 821-825.

White, R.S., McKenzie, D.P., 1989. Magmatism at rift zones: the generation of volcanic continental margins and flood basalts. Journal of Geophysical Research 94, 7685-7729.

Wickham, S.M., 1987. Crustal anatexis and granite petrogenesis during low-pressure regional metamorphism: the Trois Seigneurs Massif, Pyrenees, France. Journal of Petrology 28, 127-169.

Wiedenbeck, M., Hanchar, J.M., Peck, W.H., Sylvester, P. Valley, J., Whitehouse, M.J., Kronz, A. Morishita, Y., Nasdala, L., Fiebig, J., Franchi, I., Girard, J.-P., Greenwood, R.C., Hinton, R., Kita, N., Mason, P.R.D., Norman, M., Ogasawara, M., Piccoli, P.M., Rhede, D., Satoh, H., Schulz-Dobrick, B., Skår, O., Spicuzza, M.J., Terada, K., Tindle, A., Togashi, S., Vennemann, T., Xie, Q., Zheng, Y.-F., 2004. Further Characterisation of the 91500 Zircon Crystal. Geostandards and Geoanalytical Research 28, 9-39.

Williams, I.S., Claesson, S., 1987. Isotopic evidence for the Precambrian provenance and Caledonian metamorphism of high grade paragneisses from the Seve Nappes, Scandinavian Caledonides. II: Ion microprobe zircon U-Th-Pb. Contribution to Mineralogy

and Petrology 97, 205-217.

Wolfenden, E., , Ebinger, C., Yitgu, G., Renne, P.R., Kelley, S.P., 2005. Evolution of a volcanic rifted margin: Southern Red Sea, Ethiopia. Geological Society of America Bulletin 117, 846-864.

Wyllie, P.J., 1987. Metasomatism and fluid generation in mantle xenoliths: experimental. in P.H. Nixon, (ed.), Mantle Xenoliths, Wiley, New York. 609-621 p.

Zhang, X., Maoa, Q., Zhzng, H., Zhaia, M., Yang, Y., Hub, Z., 2011. Mafic and felsic magma interaction during the construction of high-K calc-alkaline plutons within a metacratonic passive margin: the Early Permian Guyang batholith from the northern North China Craton. Lithos 125, 569-591.

Tesis Doctoral

2015

ugr Universidad de Granada
Departamento de Mineralogía y Petrología
Programa Doctorado Ciencias de la Tierra